europhysics
conference
abstracts

24th European Physical Society Conference on

Controlled Fusion and Plasma Physics

Berchtesgaden, 9th-13th June 1997

Editors: M. Schittenhelm, R. Bartiromo and F. Wagner

Contributed Papers, Part I

Published by: The European Physical Society

Series Editor: Prof. R. Pick, Paris

Managing Editor: G. Thomas, Geneva

Volume 21A
Part I

24th European Physical Society Conference on

Controlled Fusion and Plasma Physics

Kongresshaus Berchtesgaden, Germany

9 - 13 June 1997

Editors: M. Schittenhelm, R. Bartiromo and F. Wagner

europhysics
conference
abstracts

24th European Physical Society Conference on

Controlled Fusion and Plasma Physics

Berchtesgaden, 9th-13th June 1997

Editors: M. Schittenhelm, R. Bartiromo and F. Wagner

Contributed Papers, Part I

Published by: The European Physical Society

Series Editor: Prof. R. Pick, Paris

Managing Editor: G. Thomas, Geneva

Volume 21A
Part I

EUROPHYSICS CONFERENCE ABSTRACTS is published
by the European Physical Society, ©1997

The Proceedings may be purchased from Max-Planck-Institut für Plasmaphysik, Boltzmannstrasse 2, 85748 Garching, Germany.

Preface

The 24th European Physical Society Conference on Controlled Fusion and Plasma Physics, under the auspices of the Plasma Physics Division of the European Physical Society, was hosted by the Max-Planck-Institut für Plasmaphysik Garching, Germany. Following the guidelines of the Board of the EPS Plasma Physics Division, the 1997 Conference included topics from the areas of: Tokamaks; Stellarators; Alternative Magnetic Confinement Schemes; Magnetic Confinement Theory and Modelling; Plasma Edge Physics; Plasma Heating; Current Drive and Profile Control; Diagnostics; Basic Collisionless Plasma Physics; Highly Compressed and Non Stationary Plasmas.

The scientific programme and paper selection were the responsibility of the International Programme Committee appointed by the Board of the EPS Plasma Physics Division. The Programme Committee selected 523 contributed papers (out of 651 submitted abstracts) for presentation as posters in four sessions at the meeting. Guideline for the composition of the poster session was to display the various contributions of larger teams in one session and to place teams of similar goals and interests into different sessions.

As in the past, the Proceedings are printed after the meeting, giving authors the opportunity to present their latest results in four-page papers. According to EPS Plasma Physics Division regulations, the Conference Proceedings contain the four-page papers of all those contributions for which at least one author was a registered participant at the Conference. All submitted papers satisfy this condition. 51 papers were not presented at the Conference and not submitted to the Scientific Secretary though they had originally been accepted by the Programme Committee. This caused some problems in the organisation of the poster sessions. As only in a few cases the cancellation had technical reasons, it is strongly recommended for future conferences that along with the submission of an abstract a guarantee has to be provided that an accepted paper will be presented

The four volumes of the proceedings will be mailed to all registered participants of the Conference. The papers of the 8 Review Lectures and 20 Topical Lectures will be published in a Special Issue of the journal 'Plasma Physics and Controlled Fusion', which will also be mailed to all registered participants.

M. Schittenhelm, R. Bartiromo and F. Wagner

July 1997

Programme Committee

R. Bartiromo	IGI del CNR, Italy - Chairman
E. Ascasibar	CIEMAT, Madrid, Spain
D. Gresillon	LPMI/EP, Palaiseau, France
R.D. Hazeltine	Texas University, USA
F. Hofmann	CRPP/EPFL, Lausanne, Switzerland
A. Litvak	IAP, Nizhny Novgorod, Russia
L. Stenflo	Umea University, Sweden
F. Sluijter	Eindhoven University, Netherlands
D.F.H. Start	JET Joint Undertaking, Abingdon, U. Kingdom
U. Samm	Forschungszentrum Jülich, Germany
F. Serra	Universidad Technica, Lisboa, Portugal
T. Todd	UKAEA Fusion, Abingdon, United Kingdom
F. Wagner	IPP, Garching, Germany
R. Weynants	ERM, Brussels, Belgium

Local Organising Committee

F. Wagner	Chairman
G. Zankl	Vice Chairman
M. Schittenhelm	Scientific Secretary
A. Eggeling (Ms).....	Conference Secretary
T. Geist	
H. Jahreiss	Finance Officer
Ch. Stahlberg (Ms)	
K.-H. Steuer	

Acknowledgements

The Conference Organisers gratefully acknowledge financial support from the following:

Accel Instruments GmbH
Bayerische Vereinsbank AG
Cray Research GmbH
BESTEC GmbH
European Commission
Kurdirektion Berchtesgaden
Oxford Instruments
Spinner GmbH
Max-Planck-Institut für Plasmaphysik

Contents of
Europhysics Conference Abstracts
Volume 21A (Part I - Part IV)

Index of Contributed Papers

Contributed Papers

Contents of Part I (Poster Session 1)

Contents of Part II (Poster Session 2)

Contents of Part III (Poster Session 3)

Contents of Part IV (Poster Session 4)

H-mode confinement on ASDEX Upgrade

Discharge optimisation and the control of MHD modes

M.F.F.Nave[1], G.T.A. Huysmans, B.Balet, B. de Esch, R. Gianella, C.Gowers, T.Jones, R.Konig, P.Lomas, V.V.Parail, F.Rimini, B.Schunke, P.Thomas

JET Joint Undertaking, Abingdon, Oxon. OX14 3EA, UK.
[1]Associação EURATOM/IST, Lisbon, Portugal

Introduction

JET hot-ion H-modes are limited by modes in the core, associated with the sawtooth instability, as well as by modes near the edge such as outer modes and ELMs [1]. Since the hot-ion H-modes are characterised by a confinement which increases with time, the best performance is obtained when both core and edge MHD phenomena occur late in the heating phase. Thus, to achieve high performance, it is very important to increase the MHD stability of such plasmas. Although, it has not been possible to eliminate entirely the MHD modes, successful measures are taken to delay their onset. Particularly successful results, reported here, are those of experiments aimed at delaying the outer modes, by the controlled reduction of the plasma current (current ramp-down).

Experimental and theoretical results for two optimisation techniques routinely used at JET, will be reported: a) current ramp-down, and b) continuous gas fuelling. We look into the possibility of using both techniques to delay MHD modes observed near the edge. Transport and edge MHD stability analysis for both types of optimisation techniques have been performed, using the ideal MHD code MISHKA-1 /2/, and transport codes TRANSP /3/ (interpretation), JETTO /4/ and PRETOR /5/ (predictive studies).

Edge modes observed to limit JET high performance plasmas

Outer modes and ELMs, account for over 70% of the limitations observed in JET hot-ion H-modes /1/. Outer modes are MHD oscillations observed near the edge of the plasma, with typical mode numbers m=4-7, n=1. The mode structure observed in SXR data is consistent with that of external kinks /6/. Giant ELMs are observed late in the heating phase, from a few ms to a few hundred ms after the onset of the outer mode. Their nature is not yet clear.

In hot-ion H-mode discharges, large pressure gradients and currents densities develop at the edge. Ballooning and kink stability analysis of several discharges shows that, in general, both outer modes and ELMs occur near the external kink marginal stability. The first giant ELM, however, is observed as the discharge approaches the ballooning limit.

Current Ramp Down

The external kink stability depends on the value of the current-density in the outer 5 cm of the plasma. Theoretical analysis therefore suggests that a decrease in edge current-density, which could be achieved by decreasing the plasma current during the heating phase, improves the external kink stability and may delay the outer modes. This was indeed confirmed by experimental results. A comparison of discharges with and without current ramp-down (typically 0.3-0.5 MA/s) clearly shows that in most cases, n=1 MHD modes near the edge can be delayed, resulting in a substantial improvement in performance (fig.1).

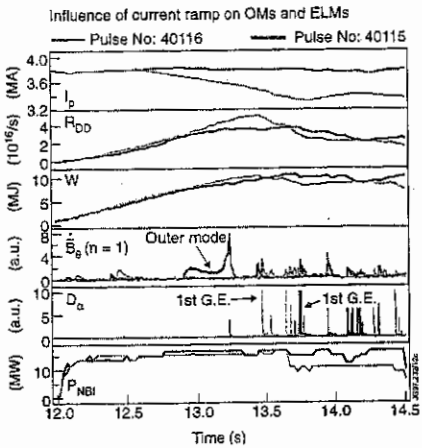

Fig. 1 - With Ip ramped down the outer mode is delayed by 500 ms, allowing an improvement in the neutron rate of 45%. The first giant ELM occurs 300 ms earlier.

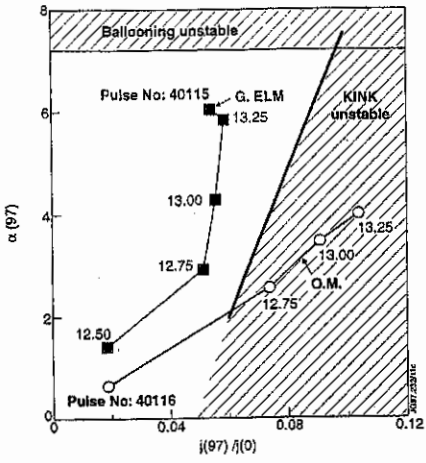

Fig. 2 - Trajectories in the (α, j) diagram, for discharges with and without an I_p ramp. With I_p down the plasma is more stable to external kinks and more ballooning unstable.(The current densit is taken at 97% of the flux surface.)

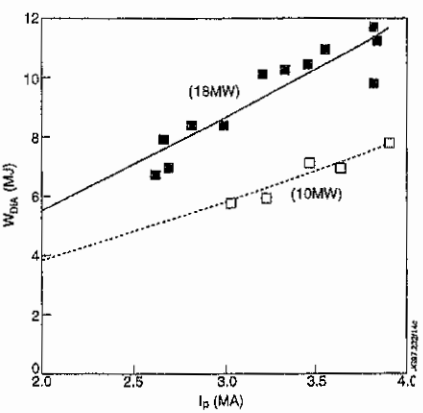

Fig. 3 - Plasma stored energy versus I_p at the time of the 1st Giant ELM.

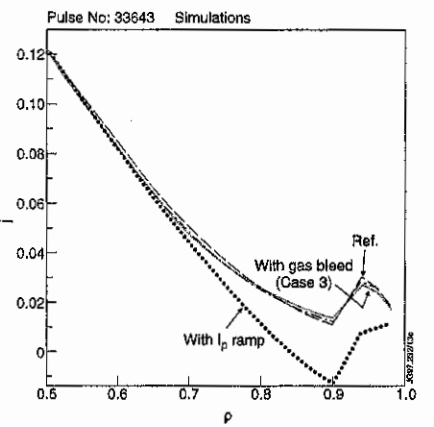

Fig. 4- Typical changes in j_{EDGE} calculated for #33643 (Ref.)in simulations: a) with gas bleed (see fig.6) and b) with a current ramp down (dI/dt=0.4 MA/s).

The evolution of the discharges in the (α, j_{EDGE}) stability diagram shows that with I_p ramped down, the plasma is more stable to external kinks. (fig.2). This is due to the reduced edge current (as illustrated in fig.4). There is a change of sign in the electric field, which decreases the Ohmic current in the outer region.

However, while the duration of the period free of outer modes increases, the ELM-free period is normally observed to decrease (fig. 1). Transport simulations show that with I_p ramped down, grad(p) at the edge does not change significantly. However, a typical B_p decrease of ~10%, increases $\alpha = \text{grad}(p)/B_p^2$ making the discharge more ballooning unstable (fig. 2).

Experiments carried out at different values of plasma current show that the plasma stored energy attained at the time of the first giant ELM and the ELM-free period are proportional to the plasma current, i.e. $W \alpha I_p^{\alpha}$, where $\alpha \geq 1$, for a given plasma configuration and input power (fig. 3). Thus from the point of view of controlling the giant ELMs, it is better to operate at high plasma current.

Gas bleed

Another technique currently used at JET to improve performance, is that of injection of cold gas at the edge of the plasma. This is done in two stages: a gas puff before the formation of the X-point, and a lower continuous gas injection during the early heating phase, known as gas bleeding. The initial gas puff is particularly useful in low power NBI heated discharges ($P_{NBI} \leq 10$ MW) since it reduces the shine through, improving the deposition of NBI power in the core of the plasma. After the initial puff, a continuous injection of gas is observed to reduce Z_{eff} (see fig. 5). In the following we assess the potential of gas bleed as a technique to delay both outer modes and ELMs.

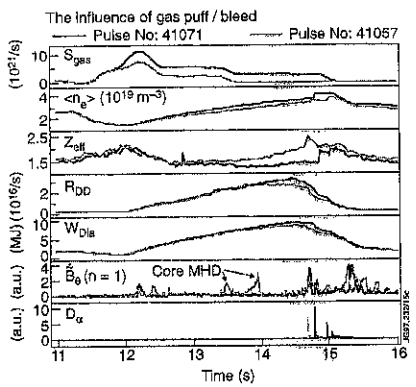

Figure 5 - A comparison of similar discharges (P_{NBI}=10MW) with different levels of gas puff/bleed)

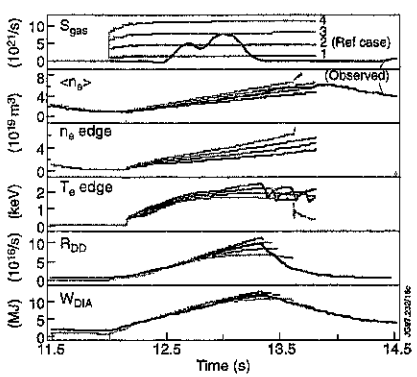

Figure 6. Simulations with different gas levels for highest R_{DD} discharge with the MK I divertor (#33643 with PNBI=20MW). The R_{DD} plots were stopped at the 1st critical value reached, either α_{crit} or j_{crit}

Gas bleeding has been found to reduce Z_{eff} both in ELM-free /7/ and in ELMy H-modes /8/. In accord with transport simulations, with the lower Z_{eff} an improvement in the neutron rate is observed. In hot-ion H-modes at present gas levels, no significant change is observed in the

occurrence of outer modes and ELMs. However, in some discharges gas bleed is observed to delay core MHD modes (fig.5). (This needs further investigation.)

By increasing the edge density, and consequently cooling the plasma, one could in principle decrease both the bootstrap and the Ohmic currents at the edge, making both the external kinks and ballooning modes more stable. Transport simulations were carried out, assuming a neo-classical model for the H-mode transport barrier, where the H-mode barrier has the width of the poloidal Larmour radius /9/.

For the levels of gas used at present, simulations indicate no significant change in grad(p). In addition, the predicted and observed cooling of the edge plasma is too small to cause any significant change in j_{EDGE}. Further cooling of the edge, by further increasing the gas source, would have a beneficial effect in both the external kink stability and the ballooning stability, however core confinement would deteriorate since increasing the edge density would increase the heat losses. Fig. 6 shows the results of simulations for different levels of a constant gas source. In each case the time of occurrence of an α_{crit} and a j_{crit} at the edge was registered. Very little difference was found between cases 1-3 (see fig. 4). In case 4, MHD events are delayed by ~ 200ms, however no improvement in R_{DD} is obtained.

Conclusion

In accord with theoretical predictions, observations show that ramping down I_p delays the outer mode. Improvements in the neutron yield of 45 % have been obtained.

The improvement in performance which can be achieved by delaying the outer mode is eventually halted by an earlier onset of a giant ELM. It is clear from observations at different values of the plasma current, that from the point of view of controlling the giant ELMs, it is better to operate at high plasma currents.

MHD observations at different values of I_p, confirm the interpretation of outer modes as external kinks, while indicating that the giant ELMs occur as the ballooning limit is approached.

The effect of gas bleeding on the edge MHD stability has been studied. For the levels of gas routinely used, no significant improvement in either kink or ballooning stability is expected. Further increase in the edge density, would cool the plasma edge, delaying both ballooning and external kink modes, however performance would not improve due to the increased heat losses. Observations show that gas bleed is an effective way to reduce Z_{eff}.

References:

/1/ Nave et al., JET Report JET-P(96)14 (1996), accept for publication in Nuclear Fusion

/2/ A.B.Mikhailovskii et al., JET Report JET-P(96)25 (1996), accept for public. in Reports of Plasma Physics

/3/ R.J. Goldston et al., J.Comput. Phys. 43 (1981) 61

/4/ G. Cenacchi and A. Taroni, Raporto ENEA RT/T1B 88(5) 1988

/5/ D. Boucher and P.H. Rebut, Proc. IAEA Techn. Comm. meeting on Avc. in Simulation and Moddeling of Thermonuclear Plasmas, Montreal, Canada, 1992, IAEA Vienna (1993) 142

/6/ T Hender et al., this conference

/7/ F. Rimini et al., this conference

/8/ Saibene et al., this conference

/9/ A. Cherubini et al., Plasma Phys. Control Fusion 38 (1996) ,1421

INVESTIGATION OF IMPURITY EQUILIBRIUM AT JET

M. Romanelli [1] **, B. Alper, A. W. Edwards, R. Giannella,**
R. D. Gill, L. C. Ingesson, M. Ottaviani
JET Joint Undertaking, Abingdon, Oxfordshire, OX14 3EA, UK
[1] Imperial College, London, SW7 2BZ, UK

INTRODUCTION

High performance JET discharges are characterised by large auxiliary heating in the form of neutral beam injection which drives the plasma column to rotate toroidally at frequencies in excess of 18 kHz. In this condition the thermal velocity of heavy impurities such as nickel (Z=28), iron (Z=26) etc. is comparable to their rotational velocity so that the centrifugal force and the friction between heavy ions and rotating plasma become important in evaluating the equilibrium distribution of the impurities and their flux. Impurity transport in the Pfirsch-Schlüter regime has been studied including the above effects. The model is valid for trace impurities ($Z_I^2 n_I << n_i$), that are found to be in high collisionality regime far from the plasma centre ($0.6 < \rho < 1$) even in very hot plasmas ($T_I \approx 10$ keV).

IMPURITY BACKGROUND-IONS EQUILIBRIUM

The classical cross field diffusion of impurity ions in a hydrogen plasma is due mainly to the collision between protons and impurity. Since heavy impurities typically fall in the Pfirsch-Schlüter collisional regime (at least at the plasma edge where the temperature is lower) it is interesting to solve the equilibrium equations in this regime including the centrifugal force term. Let m_I, Z_I be the impurity mass and charge while we indicate with m_i, Z_i the background ions mass and electric charge. Trace impurities are sufficiently diluted that they do not influence the background plasma but they are affected by the self consistent electric and magnetic field. Following Braginskii [1], the force balance equations for ions electrons and impurities in the limit $m_I >> m_i$ are

$$
\begin{aligned}
0 &= -\nabla p_e - n_e e(\vec{E} + \vec{V}_e \times \vec{B}) + \vec{F}_{ei} + \vec{F}_{eI} , \\
\vec{F}_c^{\,i} &= -\nabla p_i + Z_i n_i e(\vec{E} + \vec{V}_i \times \vec{B}) + \vec{F}_{iI} + \vec{F}_{ie} , \\
\vec{F}_c^{\,I} &= -\nabla p_I + Z_I n_I e(\vec{E} + \vec{V}_I \times \vec{B}) + \vec{F}_{Ii} + \vec{F}_{Ie} ,
\end{aligned}
\qquad (1)
$$

where the friction term involved in the Pfirsch-Schlüter transport is $\vec{F}_{ij} = -m_i n_i \upsilon_{ij} C_1 \vec{u}_{\parallel} - C_2 n_i \nabla_{\parallel} T_i$ and $\vec{u} = \vec{v}_i - \vec{v}_j$. The term $\vec{F}_c = -mn\Omega^2 R^2 \vec{e}_R$ is the centrifugal force, R is the distance between the rotating point and the rotation axis, $\vec{e}_R$ is the unit vector in the direction of the line perpendicular to the rotation axis at the rotating point. The friction terms in the perpendicular component of the velocities are of the order $\delta = \frac{\rho}{L}$ defined as the ratio between the ion Larmor radius and the scale length of the system. The radial component of the zero order perpendicular velocity for both ions and impurities is zero. The poloidal component is

$$V^0_{\perp\theta} = \frac{\partial p_I}{\partial r}\frac{1}{n_I e Z_I B_T} - \frac{m_I \Omega^2 (R_0 + r\cos\theta)\cos\theta}{eZ_I B_T} - \frac{E_r}{B_T} \quad . \tag{2}$$

The radial electric field is already set by the ions-electrons equilibrium and is supposed not to be changed by the trace impurity particles. The condition $V^0_{\perp\theta I} = V^0_{\perp\theta i}$, together with the assumption that impurity and background ions are rotating at the same toroidal speed yields the (first order in δ) equilibrium equation which can be analytically solved for the impurity density assuming the temperature varies slowly with the radius. The solution, which takes into account also the poloidal distribution of the background ions, is a function of r and θ (eq. 3)

$$n_I = n_I(0)\left(\frac{n_i(r)}{n_i(0)}\right)^{\frac{Z_I}{Z_i}} \exp\left[\frac{\Omega^2}{2T} m_I \left(1 - \frac{m_i}{m_I}\frac{Z_I T_e}{T + Z_i T_e}\right)\left(R^2 - R_0^{\,2}\right) - \frac{\Omega^2}{2}\frac{Z_I}{Z_i}\frac{m_i}{T + Z_i T_e}\left(r^2 - 2rR_0\right)\right]$$

where $R = R_0 + r\cos\theta$.

For a peaked background-ion density profile (for example a Gaussian shaped radial profile of width Λ) eq. 3 predicts that the centrifugal force displaces the density peak of heavy impurities when $\Lambda \approx \sqrt{Z_I T_i / \Omega^2 (m_I - Zm_i)}$ while strongly on-axis peaked background ion-density profile ($\Lambda << \sqrt{Z_I T_i / \Omega^2 (m_I - Zm_i)}$) leads to strongly on-axis peaked impurity-density profile. When the background-ion density profile is slightly hollow then the impurity density is expected to be strongly peaked off axis and the centrifugal term to produce a poloidal asymmetry.

OBSERVED IMPURITY EQUILIBRIA

In a hot plasma ($T_i \approx 10$ keV) in which nickel particles are present the charge state (Helium like) Ni^{26+} constitutes 90 % of the species and radiates in the soft X-ray (SXR) frequency range together with Ni^{27+} which is only 1% of the species, so the Ni SXR radiation is dominated by Ni^{26+} and is proportional to its density. The radiation emitted by Ni during impurity injection experiments [4] has been reconstructed over the poloidal section by SXR tomography. The quasi steady state, in which the emissivity change on a very slow time scale compared with the fast time scale of the impurity entering, is reached after 60ms from the injection and in high performance JET discharges lasts for 0.1 s. Two different kinds of impurity-density equilibria predicted by eq. 3 are observed

-off axis peaked impurity density

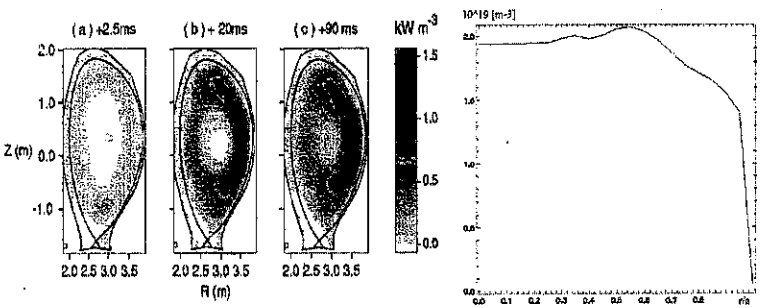

Figure 1: *Radiation from injected Ni in a hot ion H mode plasma (#34476, Ti=11 keV,* $\Omega = 1.2 \times 10^5 \, rad / s$ *). The radiation is initially symmetric. A poloidal asymmetry [2,3] develops after 10ms from the injection and the emissivity remains stationary for 0.1s. On the right is the background ion density profile.*

-on axis peaked impurity density

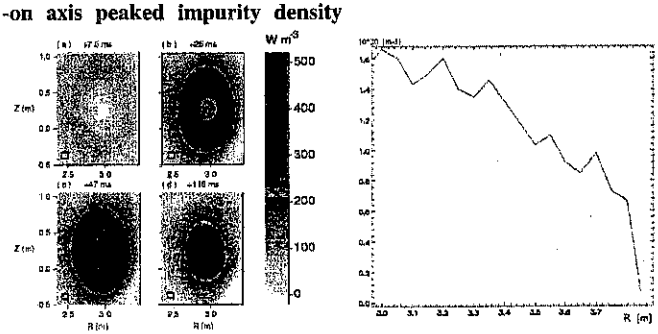

Figure 2: *Radiation from injected nickel in optimised shear plasma (#40051). The impurity particles strongly peak in the centre as expected from the peaked background-ion density profile. On the right the Electron density at the time of injection is reported.*

DEVELOPMENT OF THE POLOIDAL ASYMMETRY AND ASSOCIATED FLUX

The time scale on which the poloidal asymmetry develops is related to the time the impurity need to be accelerated toroidally (τ_{eq}). For Ni^{26+} in the shot #34476 the equilibration time is of the order of 10ms; for the shot #40051 no asymmetry is expected since the rotational speed is very low. During the 10 ms the friction on the magnetic surface leads to a zero order (in $\varepsilon = r/R$) radial flux $\Gamma_N = -\frac{C_1 m_i n_i}{ZeB_\theta \tau_{iN}} u_\parallel$ where $u_\parallel(t) = \Omega \mathrm{Re}^{-t/\tau_{eq}}$. The average of Γ_N over the magnetic surface gives $\langle \Gamma_N \rangle = -\frac{C_1 m_i n_i}{ZeB_{\theta 0} \tau_{iN}} \Omega R_0 e^{-t/\tau_{eq}}$. The initial radial velocity associated with the above flux is for nickel (#34476) $v_r \approx -30\, m/s$; therefore the impurity particles will travel a distance $\lambda = \tau_{eq} |v_r| \approx 30\ cm$ before reaching the equilibrium with the background-ions. This may explain the strong pinch velocity and the fast transport seen in the first ms after the impurity injection.

CONCLUSIONS

It has been shown that neoclassical transport theory can describe heavy impurity transport in JET plasmas. In particular the following features could be explained :

- Off-axis peaking of heavy impurities (due to a hollow background density profile)
- Strong impurity-density asymmetry on magnetic surfaces (due to the centrifugal force)
- Strong impurity flux in the first ms of impurity injection experiments in NBI heated plasmas (due to a slow transfer of toroidal momentum between background ions and heavy impurities)

REFERENCES

[1] P H Rutherford, 'Impurity transport in the P-S regime', The Physics of Fluids, Vol. 17, No 9, September 1974

[2] B Alper, A W Edwards, R D Gill, L C Ingesson, M Romanelli, J Wesson, K-D Zastrow, 'Strong asymmetries in impurity distributions of JET plasmas' , Proceedings of the 23rd EPS conference, Kiev, Ukraine, 24-28 June 1996, Vol. 1 pag. 163

[3] J Wesson, 'Poloidal distribution of impurities in a rotating Tokamak plasma', to be published in Nuclear Fusion

[4] R. Giannella *et al.*,'Poloidal asymmetry of impurity in co- and counter injection experiments at JET', Proc. 19th EPS, Innsbruck, Austria, Vol. 1 pag. 279

A Comparison of Soft X-Ray Activity in High Performance JET Discharges

B. Alper, A.W. Edwards, A. Fasoli, R.D. Gill, L.C. Ingesson, M. Romanelli

JET Joint Undertaking, Abingdon, Oxon, OX14 3EA, UK.

Introduction: The study of MHD phenomena has been carried out at JET in unprecedented detail using the new 282 channel soft X-ray diode system [1] in conjunction with the CATS fast data acquisition system [2]. In particular the MHD phenomena occurring during the two principal routes to high fusion yield, namely the hot ion H-mode (HI) and the optimised shear (OS) discharges during Mark II divertor operation have investigated.

Performance Limiting MHD Phenomena: In Hot Ion H-Modes there are 3 distinct phenomena clearly associated with performance limitation; namely: 1) Giant ELMs, 2) Outer Modes and 3) Sawteeth. Giant ELMs, occurring 1-2 seconds into the Hot Ion H-mode phase always lead to a loss of confinement with 5-10% of the stored energy lost in <200μs. This is followed by a more gradual but permanent fall in energy confinement. The ELMs are associated with bursts of SXR emission from the divertor at or near the tiles and by emission from inside the plasma in the outboard upper region[3]. This is shown in **Figure 1** where data from identically-viewing channels at octants 4 & 8 are compared. These data, which are from the new higher bandwidth (200kHz) system show that the bursts in SXR emission have structure down to timescales of ~10μs. Little or no correlation is apparent between the two octants indicating the SXR bursts are probably due to highly localised phenomena.

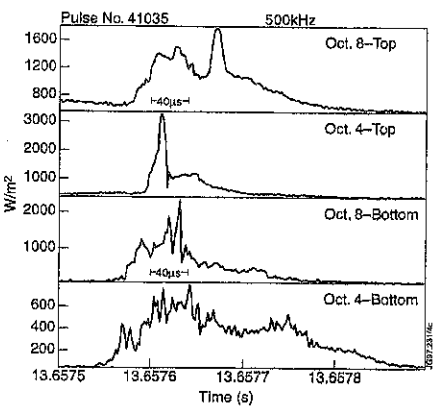

***Fig.1.** SXR emission during an ELM showing little correlation between the two octants*

The **outer mode** has been identified as an ideal external kink [4] and is located close to the plasma boundary. In Mark II divertor operation it appears with various growth patterns as illustrated in **Figure 2.** It can occur as a series of short duration (~5ms) bursts (see 2(a) &(b)), as a rapidly growing precursor to a giant ELM , (see 2(c)&(d)) or as a quasi-continuous mode lasting ~100ms (see 2(e)&(f)).

The mode is always associated with a rise in H-alpha radiation (2(a),(c) &(e)) and frequently with a rise in edge T_e (see 2(b)). Ramping down the plasma current usually improves plasma performance by suppressing the quasi - continuous mode but does not remove the outer mode completely

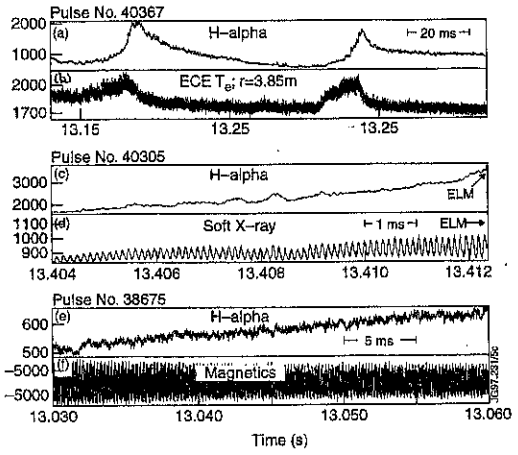

Fig.2. Three examples of outer modes in HI discharges; (a),(b) as short pulses, (c),(d) as an ELM precursor and (e),(f) as a quasi-continuous mode.

Sawteeth are largely suppressed during the Hot-Ion phase. Those that do occur at times of high performance have a global character with SXR excursions extending to the plasma edge[5]. Prior to Mark II operation this would lead to a global 'X-event' (combined sawtooth and ELM) producing a dramatic loss in confinement [6] but here no associated ELM appears and a correspondingly less dramatic loss in confinement results.

In **Optimised Shear Discharges,** although many MHD phenomena are observed (and some are discussed below) only one has a clear and unambiguous correlation with a loss in plasma confinement. This mode, seen in the L-mode confinement phase, has an n=1 structure and is global in character with all SXR channels (with reasonable SXR emission) responding to the mode. It has been identified as a global pressure driven kink mode[7]. SXR data in **Figure 3** show the appearance of such a mode which in this case occurs soon after formation of the internal transport barrier. It lasts only about 6ms and shows a characteristic rapid fall in frequency from ~35 kHz initially (corresponding to the core rotation frequency) to ~12kHz at the end. A rapid but temporary fall in neutron yield occurs similar to a sawtooth. Emission profiles from a vertical camera, **Figure 4,** show that the core has an m=1 structure. A phase inversion occurs only on the high field (inner) side indicating an m=2 structure locked to the m=1 with constructive interference on the low field (outer) side. When this mode occurs well after the formation of the transport barrier, it usually locks to the wall in less than 1 ms and leads to a rapid and dramatic disruption[7].

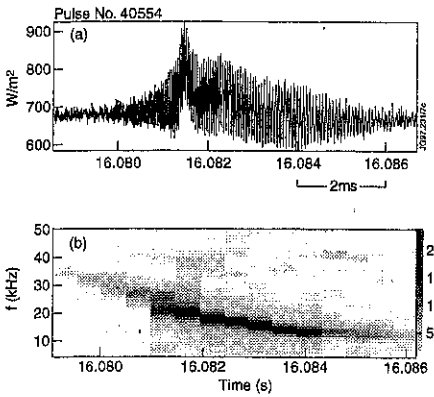

*Fig.3 **(a)** Line integrated SXR emission and **(b)** the corresponding frequency spectrum of a global n=1 kink mode in an OS discharge.*

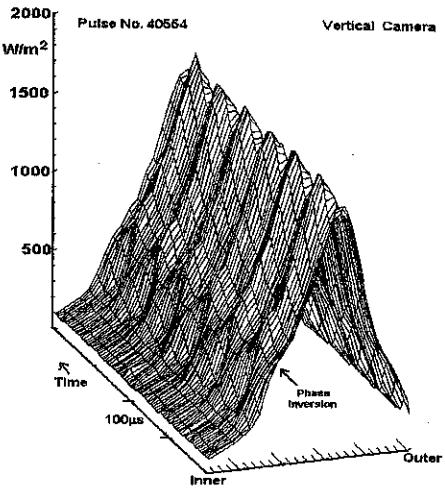

Fig.4. SXR emission profile for the global n=1 kink, showing a phase inversion on the inboard (high field) side only

A New Low-Frequency Mode (Picket Fence

An unusual mode has been observed for the first time in Optimised Shear discharges. It regularly appears at low frequency (200 - 700 Hz) during the L-mode phase, usually after the formation of the internal transport barrier. Its characteristic feature of a regular series of spikes in the H-alpha and magnetics time traces - reminiscent of a 'Picket Fence' - are shown in **Figure 5.** The mode disappears abruptly at the L-H transition. Its localisation is close to the separatrix. Note the abrupt fall in T_e with each cycle at R= 3.82m.

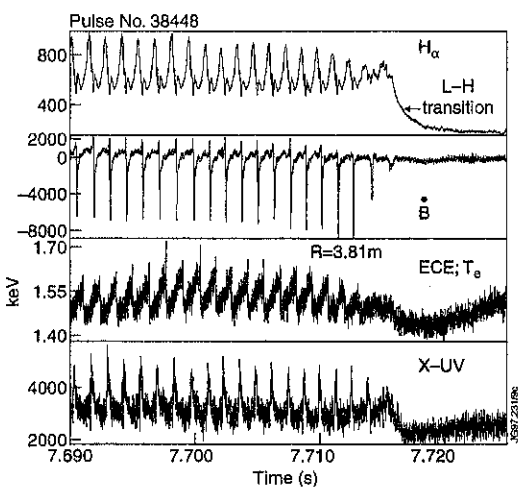

Fig.5. An example of the 'picket fence' mode seen in various edge plasma diagnostics. It terminates with the onset of the H-mode.

The mode as seen from a toroidal array of magnetic coils has a pulsed n=1 structure and is **counter-rotating,** i.e. opposite to the clockwise NBI-driven rotation of the plasma core. SXR tomographic reconstruction generally shows a bulk counter-clockwise motion of the plasma core at the same low frequency with an amplitude of 4-6 mm. ECE measurements show a sinusoidal modulation of T_e predominately where the gradients are largest - close to the internal transport barrier[8]. The mode may play a role in maintaining the OS discharges in L-mode and has also been observed in high current 'steady state' discharges as they periodically drop into L-mode.

High Frequency Modes

Some evidence for a weak excitation of TAE modes near the plasma core at a frequency of ~150 kHz has been observed with the new higher bandwidth SXR diagnostic in the highest performance OS discharge, 40554, corresponding to a displacement amplitude of ~3mm. MHD modes with frequencies from 60 kHz up to our normal bandwidth limit of 100kHz are regularly observed in the magnetics signals during the high performance phases of both types of discharges. These are less commonly seen in the SXR data but, when present, are usually associated with n ~2-3 modes in the plasma core. Occasionally, in OS discharges, modes are present in the plasma core which are driven by the beating of two RF antennae. These is no evidence that any of these modes affect plasma confinement.

Summary

Using the multi-channel, soft X-ray and CATS diagnostic systems, MHD events which play a significant role in limiting the fusion yield of high performance plasmas in JET have been studied in some detail. The complexity of both ELMs and the newly observed picket fence mode have become apparent. An understanding of the nature of outer modes and bulk pressure driven kink modes has led to the implementation of operational techniques to minimise their effects on plasma performance.

References

[1] B. Alper *et al* Rev. Sci. Instrum. **68**, 778 (1997)
[2] K. Blackler and A.W. Edwards, IEEE Trans. Nucl. Sci. **41**,111 (1994)
[3] R.D. Gill *et al* , Cont. Fus. Plas. Phys. (Kiev,1996), Vol.1,167.
[4] T. Hender *et al* , this conference
[5] M. Nave et al, Nucl. Fus. **35**, 409 (1995)
[6] J. Wesson, Phys. Rev. Lett. **77**, 5214 (1996)
[7] G. Huysmans *et al*, this conference
[8] F. Soldner *et al* , this conference

An Interpretive/Predictive Study of the JET Mark II Divertors for ELMy H-modes in JET

R Simonini, G Corrigan, M Fichtmueller, R Monk, G Radford, J Spence, A Taroni
JET Joint Undertaking, Abingdon, Oxon, OX14 3EA, United Kingdom

INTRODUCTION

At JET, the current Mark IIA divertor will be followed by the more closed Mark II GB, which was designed specifically to test the ITER Gas Box concept. This paper details modelling studies and results concerning the relative merits of the various configurations.

The computational model has been assessed by a campaign of calculations to simulate the phase between ELMs in H modes using the EDGE2D/U code[1]. The transport model has been tested by simulating experimental data on radiation and target profiles, especially j_{sat} and T_e, for horizontal and vertical Mark IIA configurations.

MODEL AND TESTS

For our tests, we have chosen Mark IIA shots #37937 and #37940, with horizontal and vertical targets, respectively.

The upstream midplane density at the outer separatrix n_{es} as well as the electron and ion input power P_e and P_i are specified as input parameters. Boundary conditions toward walls are decay lengths of λ_T=2.0 cm and λ_n=2.5 cm for temperature and density, respectively. For impurities, we have assumed ∇n_z=0 at the boundary-core interface, for all charge stages.

The simulations performed refer to ELMy H modes, but the ELMs themselves have not been modelled, the more modest aim being to simulate the plasma behaviour between ELMs. This is possible because, if ELMs are not very frequent ($\leq$ 10 Hz), the plasma behaviour including the boundary region will be essentially determined by the ELM-free period. Actually, calculations show that even though the pulses are not in a steady state between ELMs and carbon accumulates outside the divertor, quasi-stationary levels of radiation, pressure and ion saturation current are reached in a few tens of milliseconds because the non-retained fraction of carbon does not radiate appreciably. As a consequence, we have used the results of previous studies [2,3] of Hot-ion ELM-free H-mode pure plasmas, which have suggested the particle diffusion coefficient $D_\perp \approx 0.1 m^2/s$ with an inward particle pinch term $V \approx 4.5$ m/s, and $\chi_e \approx 0.2$ m^2/s, $\chi_i \approx 0.4$ m^2/s

The chemical sputtering yield is from Ref [4], assuming a uniform wall temperature of 300° C, with a reducing factor so as to have a total effective yield $\approx$1%. A significantly higher yield would induce high recycling conditions, inconsistent with experimental data. On the other hand, chemical sputtering yields are poorly known, ranging from 0.6% to 5% according to various models described in the literature.

In all simulations, the total radiated power in the boundary region is only partially (≈40%) accounted for by the computed carbon distribution. The missing radiation could be due in part to some metal impurity (the presence of nickel in the discharges is confirmed by spectroscopic signals, but its contribution in the boundary region is unknown). The missing radiation is imposed in the code by means of an analytic formula.

For shot #37937, the power radiated near the X point between ELMs is less than 1MW, even though the total NBI power is about 11 MW. However, the stored energy is varying rapidly, with $dW_{dia}/dt \approx 5$ MW. Good agreement with experimental data is obtained by imposing the boundary condition that the separatrix density is $n_s=10^{19}$ m^{-3}, and the electron and ion input powers into the computational layer, a few cm inside the separatrix, are P_e=1 MW and P_i=2 MW. These numbers take into account not only dW/dt but also other losses such as charge exchange and beam shine through losses. With this choice, the total radiated power is P_{rad}=0.7MW. Fig. 1 shows the experimental and computed profiles of the ion saturation current density j_{sat} and the electron temperature T_e as a function of distance from the separatrix along the outer divertor target.Similar agreement is obtained for the inner target.

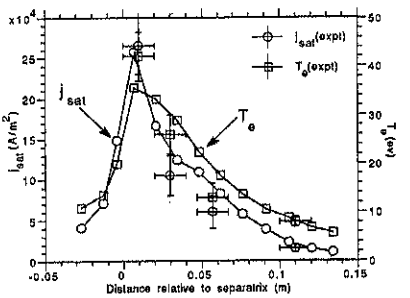

Fig.1 Experimental and computed j_{sat} and T_e along the outer divertor target for pulse #37937

Other diagnostics are available from spectroscopy. Fig.2 shows experimental time evolution profiles of three D_α signals compared with the computed levels at the simulated time, and the photon fluxes from visible and VUV spectroscopy due to C^{2+} and C^{3+}.

Similar levels of agreement are obtained for discharge # 37940 (vertical target plate configuration). The parameters of the simulation were the same, the only difference being the boundary condition of the density

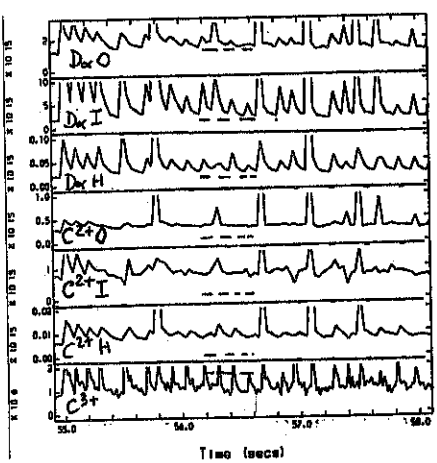

Fig.2 Experimental (solid) and computed (dashed) photon fluxes for pulse #37937

at the separatrix n_s=0.7×10^{19} m^{-3} (in accordance with the fact that from the PPF signal NEX/WAL, the average boundary density $<n_b>\approx$2.0×10^{19} m^{-3} and 1.5×10^{19} m^{-3} for discharges #37937 and 37940, respectively).

A number of tests show that most results are not very sensitive to different hypotheses on the recycling of the ions leaving the SOL in the perpendicular direction.

PREDICTIVE MODELLING: Comparison between Mark IIAP and Mark IIGB

Predictions for Mark II GB and comparisons with Mark IIAP (plugged by-pass leaks) have also been carried out by assuming the same input data (and very similar plasma volumes) and changing only the equilibrium and divertor configurations. Possible effects depending on variations of the separatrix density or main plasma confinement properties, which would require a full edge-core coupled model like the JETTO-SANCO-EDGE2D-NIMBUS chain [3], have not been taken into account. The calculations have all assumed n_s=10^{19}m^{-3}, P_e=1MW, P_i=2MW. It turns out that the production of carbon is virtually the same for all configurations (≈8×10^{20} s^{-1}), even though at the outer strike point, T_e decreases from 35 eV (horizontal Mark IIAP-H) to 14 eV (vertical Mark II GB-V) while n_e increases from 1.3×10^{19} m^{-3} to 2.3×10^{19} m^{-3}). Also virtually the same is the fraction of carbon outside the divertor (in excess of 95%). However, the horizontal Mark IIs are more leaky, resulting in a total carbon content about twice that of the vertical Mark II GB V, which is marginally better than Mark IIAP-V.

Fig. 3 shows the profile of Z_{eff} along the separatrix, from the outer to the inner target. There are only small differences between Mark IIAPs and GBs (Z_{eff}-1 is lower in GB-V than AP-V by ≈15%). T_e at the midplane depends mostly on whether the configuration is AP or GB, whereas T_e at the targets depends essentially on whether it is H or V. Similar considerations apply to n_e.

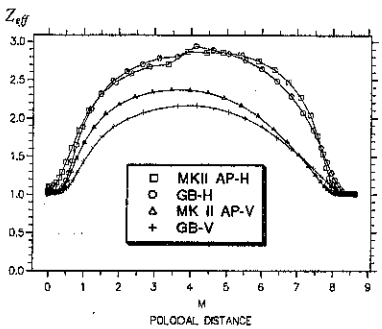

Fig.3 Poloidal profiles of Zeff at separatrix for vertical and horizontal Mark II AP and Mark II GB

In view of the possibility of modifying the geometry of the GB divertor, for example by removing the septum and/or changing the material of the private region plate, we have assessed the importance of possible options by removing the septum and artificially switching off the sputtering in various portions of the chamber.

In the case of Mark II GB-V, Fig. 4 shows the profile of Z_{eff} along the separatrix, for various conditions. The effective sputtering yields vary up to 20%. While the temperature and density profiles in the SOL are virtually indistinguishable, Z_{eff} -1 varies up to 40%. These two effects

are compatible because even though most of the carbon produced is entrenched in the divertor, the leaked fraction builds up outside in regions of high temperature where it does not radiate, and the carbon left in the divertor is not sufficient to alter the profiles appreciably.

Note that, in contrast to these low-recycling discharges at rather high temperature, previous calculations [5] for high-recycling or detached regimes have shown that the details of the geometry, in particular the presence and the material of the septum, can be much more important.

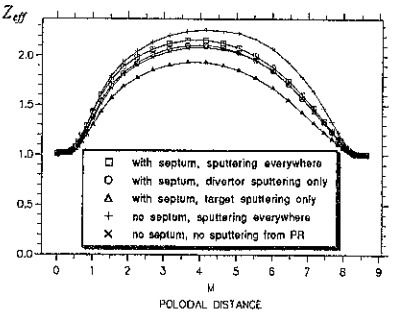

Fig.4 Poloidal profiles of Z_{eff} at separatrix for different options in vertical Mark II GB.

CONCLUSIONS

The chain of codes EGDE2D/NIMBUS is able to reproduce important experimental features observed in the attached, moderate recycling phase between ELMs in ELMy H-mode discharges in JET. However, there are difficulties in getting radiation and carbon stage distribution and content at the same time, due to uncertainties in the model, especially sputtering, and the lack of a proper coupling to the core plasma.

In the regimes considered, the predictive runs indicate that in terms of Z_{eff} at separatrix the Mark II GB divertor should perform in a similar way as the Mark II AP, with GB-V slightly better AP-V, and details of wall and material in the divertor are not as important as in high-recycling or detached regimes.

ACKNOWLEDGMENTS

H.Guo, K.D.Lawson and G.C.Vlases have contributed with experimental information and useful discussions.

REFERENCES

[1] R.Simonini et al, Contrib. Plasma Phys. 34(1994)368

[2] G.K.McCormick et al., 12th PSI Conference, St.Raphael, France 1996

[3] A.Taroni et. al, 16th IAEA Fusion Energy Conf., Montreal, Canada 1996, IAEA-CN-64/D3-3

[4] B.V.Mech, A.A.Haasz, J.W.Davis, 12th PSI Conference, St.Raphael, France 1996

[5] R.Simonini et al, 22nd EPS Conference, Kiev,Ukraine, 20C-II(1996)823

Power Step-Down Experiments in the JET MkII Divertor Configuration

F B Marcus, B Balet, J P Christiansen, H P L De Esch, N Deliyanakis, R Giannella, C Gowers, G T A Huysmans, O N Jarvis, T T C Jones, R Koenig, P Lomas, V V Parail, F Rimini, P Smeulders, A Taroni, P Thomas, N H Zornig

JET Joint Undertaking, Abingdon, Oxon, OX14 3EA, U.K.

Introduction

This paper focuses on experiments that extend the duration of high performance deuterium plasma discharges in the hot-ion ELM-free H-mode regime in JET. The goals of these experiments are to: quantify plasma confinement in quasi-steady regimes; study instability behaviour in quasi-steady regimes; optimise the plasma performance and duration; determine the conditions for maximising fusion Q in quasi-steady regimes. Extension of the transient regime towards quasi-steady conditions is achieved by using a power step-down method. The Mark II divertor configuration most recently installed in JET has a more closed geometry and better recycling control than the previous Mark I. For more detailed information, an extensive study and comparison of power step-down discharges in Mark I and Mark II configurations is being published [1].

Energy Balance and Confinement Scaling

Global scaling laws for confinement times in the ELM-free H-mode regime are investigated for their validity in quasi-steady-state and hot-ion regimes. The ELM-free H-mode scaling law [2] for predicting the confinement time for total plasma energy (giving similar times as thermal ITER-H93-P scaling) is:

$$\tau_{EF,TOT} \equiv 0.045\, I_p^{0.87}\, B^{0.45}\, P^{-0.55}\, M^{0.43}\, R^{1.84}\, n^{0.03}\, \varepsilon^{-0.02}\, \kappa^{0.53}$$

Power step-down at different levels of plasma stored energy provides insight into the behaviour of the plasma loss power and its scaling. In the Mark II configuration, discharges with long periods free of any instabilities, at 2.8 MA and 2.8 T, for Pulses 38100, 38102, 38104, each had different power step-down timing, as shown in Fig. 1. All the discharges have similar energy confinement times of about 0.6-0.8 s, the same range as predicted from ELM-free H-mode total energy scaling. After the power step-down occurs, the experimentally measured confinement time tends to increase from a level 10-20% below the scaling prediction to a level 10-20% above it.

Instabilities

Step-down discharges provide a useful vehicle for the study of instability events, since parameters change very slowly, particularly edge pressure gradients. Fig. 1 shows that in Pulse 38100, the stored energy declines slowly, excluding a global pressure limit as a cause of instability. During the power step-down phase from 13.3 s to 13.9 s in Pulse 38100, the gradient of the edge electron pressure P_e remains unchanged, and the gradient of the ion pressure P_i, measured by CXRS, decreases slightly. The only discernible precursor activity appears on a magnetic pickup coil sensitive to the ~10^4 Hz frequency characteristic of the "outer mode", kink instability and begins about 100 ms before the Giant ELM at 13.9 s. Sawtooth crashes do not directly contribute to performance degradation.

The MISHKA I stability code was used to analyse the stability of a JETTO simulation of Pulse 38100 with respect to ballooning modes and the n=1 external kink mode. Fig. 2 shows the 97% flux value of the current density and the normalised edge pressure gradient at the maximum gradient in the transport barrier, with the growth rate of the n=1 kink mode. The edge current density becomes nearly constant after step-down, and the edge pressure gradient falls, staying near or below the ballooning limit. The plasma is close to the external kink limit, and the growth rate increases continuously even after power step-down, because of the reduction in the edge pressure gradient. [The pressure gradient is a stabilising term.] This increasing kink instability may therefore be the reason why an outer mode is observed even though the stored energy is decreasing.

Within a given series of discharges, the ELMs tend to occur at a given density, but different stored energies, for example: Pulses 38100, 38102, 38104, 38106, 38109, some of which are shown in Fig. 1. The limiting density increases approximately linearly with plasma current. This result indicates that an additional mechanism may result in Giant ELMs besides ballooning and kinks. One possibility is the resistive MHD model of ELM's (see eq. 4.10 in [5]), since the separatrix density usually increases as the main plasma density.

Neutral Beam Optimisation

Experiments were performed to optimise the choice of beam energy, since at JET there are two beam boxes, one at 140 keV, the other at 80 keV. Fig. 3 illustrates the effects of beam energy with two identical discharges apart from the choice of beam energy after power step-down, Pulse 38102 (see also Fig. 1) and Pulse 38103. The 140 keV beams in Pulse 38102 maintain the stored energy and neutron production rate at a noticeably higher level.

To explore extreme variations of heating waveforms, a series of 3.4 T and 3.8 MA discharges were compared, with a current ramp down to stabilise the outer mode, shown in Fig. 4. The heating waveforms include full beam power heating of 19 MW for 1.5 s in Pulse

40346, a power step-down to 10 MW after 0.9 s in Pulse 40367, and a constant power of 10 MW in Pulse 40365. The interesting feature of these discharges is that their behaviour tends to be confinement limited, without significant effects from the outer mode instability. ELMs and sawtooth crashes cause only temporary energy loss. Pulse 40365 enters the H-mode and is ELM free during the entire 2.5 s heating period, and the stored energy nearly becomes constant at a 9 MW level of heating and power loss. Pulse 40346 achieves a higher stored energy and neutron rate, but transiently. Its stored energy has nearly reached an equilibrium in stored energy with a power loss equal to the heating power of 19 MW before a series of ELMs. The power step-down Pulse 40367 reaches quasi-steady state, then undergoes a series of ELMs during 13.6 to 13.8 s, but recovers afterwards. The slowest density, stored energy, and neutron rate evolution is in 40365.

Conclusions on Maximising Performance during Extended Operation

As shown in Fig. 4, the ratio of the observed neutron rate to the square of the plasma stored energy is nearly constant, decreasing very slowly with time. A consequence is that since the neutron rate and the loss power both scale as W^2, the steady state value of their ratio is approximately constant. The ratio of the d-t extrapolated power (using TRANSP for a 50-50 mixture) to the heating power, in the high power discharge 40346 and the quasi-steady discharge 40365 is typically 0.4. The ratio for the power step-down discharge is 0.6, somewhat less than in the Mark I divertor, where discharge 34236 reached 0.75. These numbers all increase slightly to give a larger effective fusion Q when other effects are included.

The optimisation of the performance of power step-down discharges in terms of neutron yield, discharge duration and fusion Q involve the following: the power step-down should eliminate low and keep high energy beams; conditions of minimum recycling should be provided; the fusion power and ion fusion reactivity at a given plasma stored energy should be maximised by high initial power; the initial and final power levels should be sufficient to enter and to maintain the ELM-free H-mode; the plasma confinement should be maximised by high plasma current, toroidal field and additional confinement enhancement above ELM-free scaling laws.

[1] MARCUS, F.B. et al., "A Power Step-Down Approach to Extended High Performance of ELM-free H-modes in JET," accepted for publication, Nucl. Fusion.
[2] THOMSEN, K., CAMPBELL, D.J., CORDEY, J.G., Nucl. Fusion 34 (1994) 131.
[3] JET TEAM (presented by P. R. Thomas), in Plasma Phys. and Cont. Fusion Res. 1996 (Proc. 16th Int. Conf. Montreal, 1996), IAEA, Vienna (1996), Paper IAEA-CN-64/A3-2.
[4] NAVE, M.F.F. et al., "An Overview of MHD Activity at the Termination of JET Hot-ion H-Modes, JET Preprint JET-P(96)14, May 1996, submitted for publication in Nucl. Fusion.
[5] CHANKIN, A.V., JET Preprint JET-P(97)02, subm to Plasma Phys. and Cont. Fusion.

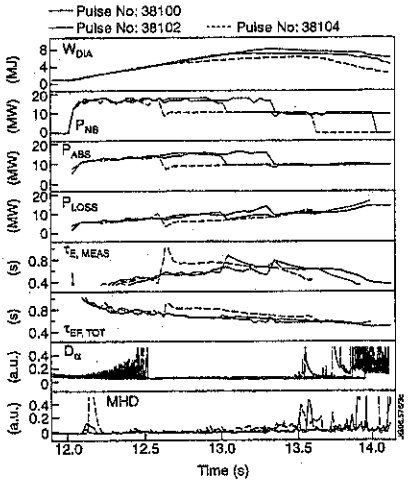

Fig. 1. Stored energy frrom the diamagnetic loop, injected neutral beam power, absorbed heating power, plasma loss power, energy confinement time and confinement time from ELM–free H–mode total energy scaling law, D_α recycling light, and edge MHD activity for power step–down Pulses 38100, 38102, 38104 with different step–down times in the Mark II divertor configuration.

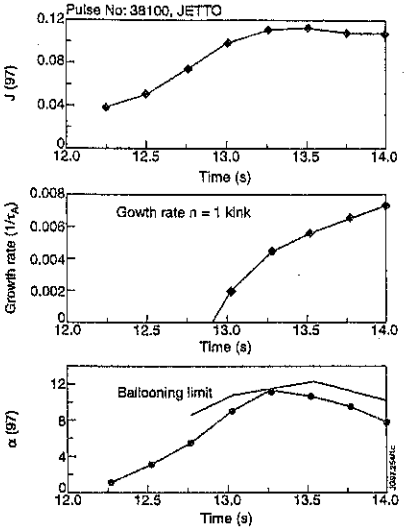

Fig. 2. Current density at the 97% flux surface, growth rate of the n=1 kink mode, and normalised pressure gradient at the 97% flux surface, for Pulse 38100.

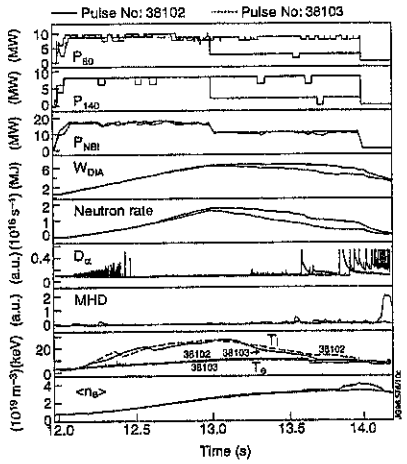

Fig. 3. Total injected beam power, 80 keV AND 140 keV contributions, stored energy from the diamagnetic loop, global neutron rate from fission chambers, D_α recycling light and edge MHD activity at 10^4 Hz measured by a comb–filtered magnetic probe for power step–down Pulses 38102 and 38103 in the Mark II divertor.

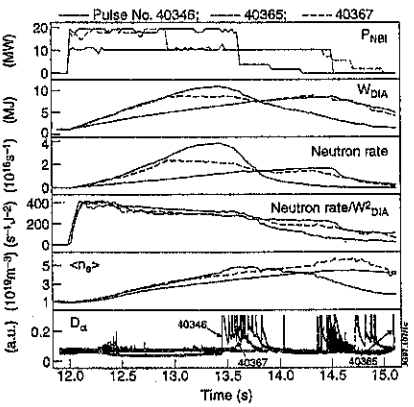

Fig. 4. Beam heating power, stored plasma energy, neutron production rate and its ratio to the square of the stored plasma energy, volume averaged density, and edge recycling light for Pulses 40346, 40365, 40367.

MHD Stability Analysis of Optimised Shear Discharges in JET

G.T.A. Huysmans, B. Alper, Y. Baranov, G.A. Cottrell, D. Kadau, D. O'Brien and W. Zwingmann
JET Joint Undertaking, Abingdon, OX14 3EA, UK.

Introduction

In JET, high neutron rates (< 5.6 10^{16} n/s) have been achieved in the so-called optimised shear scenario (see Fig. 1) [1]. Early heating of the plasma during the current ramp leads to the formation of a transport barrier and consequently very peaked pressure profiles (see Fig.5). Due to the continued ramp of the current the plasma stays in L mode even with the large heating power. Disruptions are common in the optimised shear discharges. They can be avoided by adjusting the heating power wave form and also by going from L to H mode. The internal transport barrier however decays during the H-mode phase and the best performance is usually obtained in the L mode phase.

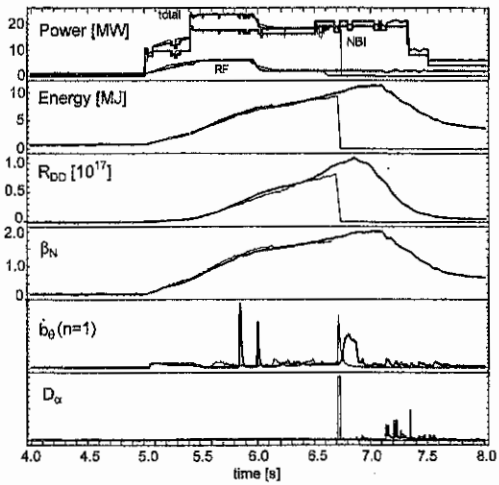

Fig. 1 Time traces of the heating power, the reaction rate, the stored energy, normalised beta, the n=1 MHD signal and the D_α signal for two nearly identical discharges: 40847 (fat lines) and 40848 (thin lines) which ends in a disruption.

Tomographic reconstruction of the disruption precursor

In some cases the disruption in the optimised shear discharges is preceded by a clear n=1 precursor [2]. Fig. 2 shows the disruption precursor in discharge #39430 as seen in a central SXR channel. The mode initially rotates with the plasma rotation frequency at 30 kHz. Then the mode slows down and locks to the wall leading to the disruption.

The data from the JET 198 channel SXR system has been used for a tomographic reconstruction of the SXR emission profile. The newly developed tomography code is based on a straight field line flux surface co-ordinate system and uses B-splines and Fourier harmonics to represent the emission profile. Singular value decomposition is used to fit the coefficient to the measurements.

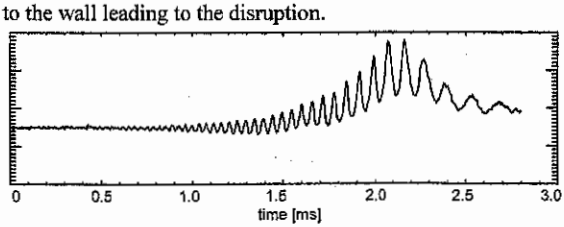

Fig. 2 The precursor of the disruption in discharge #39430 as seen in a central SXR channel.

Fig.4a shows the result of the tomographic inversion of the disruption precursor using m = 0, 1 and 2 as the poloidal harmonics. It shows the difference in SXR emissivity in the poloidal plane between two time slices half a period of the precursor oscillation apart.

Comparison SXR reconstruction with calculated mode structures

MHD Stability analysis shows an global n=1 ideal mode to be unstable at the time of the disruption precursor. The mode extends over the whole plasma radius with a m=2 dominant harmonic (see Fig. 3). To compare the calculated mode structure with the structure obtained from the tomographic inversion, the calculated displacement has to be multiplied with the gradient of the equilibrium SXR emission profile. This equilibrium profile is obtained by tomographic inversion of the time averaged SXR signals. Due to the extreme peakedness of the equilibrium profile, only the perturbation in the plasma centre remains visible.

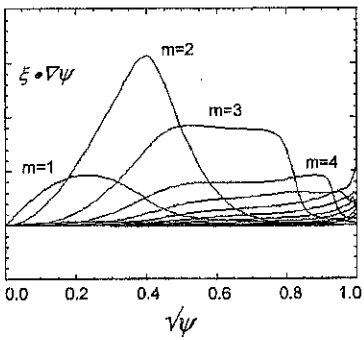

Fig.3 The poloidal harmonics of the perpendicular displacement of the n=1 mode found unstable in discharge 39430 at the time of the disruption precursor.

In Fig. 4a and 4b the SXR emissivity contours are compared from the calculated mode structure and from the tomographic inversion. Good agreement is found. However due to the peaking of the SXR emission profile only information of the m=1 and m=2 harmonics can be obtained.

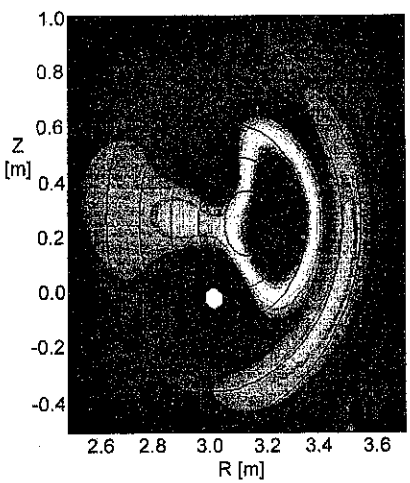

Fig.4a The difference between two time slices of the SXR tomographic reconstruction of the disruption precursor in #39430. The closed curves are the equilibrium flux surfaces.

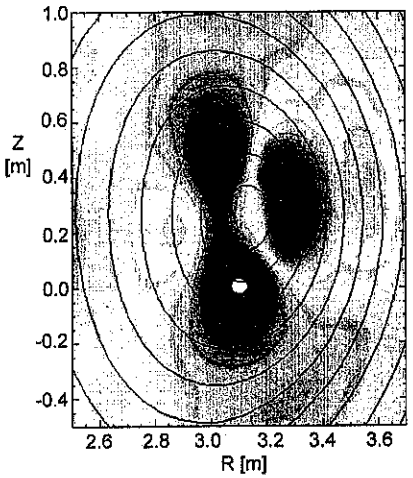

Fig.4b The simulated perturbation of the SXR emission based on the n=1 mode in fig.3.

MHD Stability limits

One of the highest performance optimised shear discharges #40847 (see Fig.1) has been analysed with respect to the ideal MHD stability limits. The pressure profiles (see Fig.5) and the q-profiles are taken from a TRANSP analysis of this discharge [3]. Shortly after the start of the main heating the pressure profile becomes extremely peaked due to the formation of a transport barrier. Later this barrier moves radially outward resulting in less peaked pressure profile. The q-profiles are monotonic with low shear in the plasma centre, q on axis is relatively constant at about 1.5.

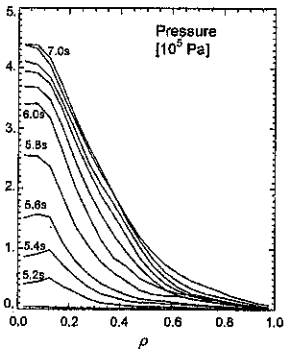

Fig.5 The evolution of the pressure profile in one of the highest performance discharges, #40847.

The MISHKA-1 ideal MHD stability code [4] was used to calculate the stability limit for the n=1 mode as discussed in the previous section. The stability limits are shown in Fig. 6a. It shows a very low limit on β_N of about 1.0 starting at t = 5.5s. This is due to the extreme peaking of the pressure profile. With the reduction of the peaking factor the marginal value for β_N increases to 2.0 at t = 7.0 seconds. The reduced slope of the β_N trace is due to the reduced heating power after t = 6.0s. This reduction was found to be necessary to avoid a disruption at this time, consistent with the calculated MHD stability limits. Fig.6b shows the evolution of the discharge as a function of the normalised beta and the pressure profile peaking factor, illustrating the strong influence of the peaking factor on the stability limits.

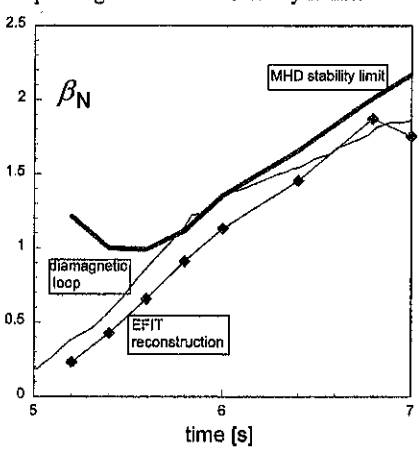

Fig.6a The MHD stability limit due to a global n=1 pressure driven kink mode as a function of time for discharge 40847. ($\beta_N=\beta$ / (I[MA]/a[m]B[T]). Included is the time evolution of β_N.

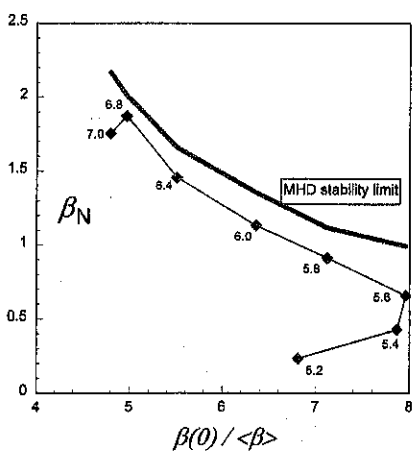

Fig.6b The evolution of the peaking factor of the pressure profile(from TRANSP data) and the normalised beta (β_N). Included is the MHD stability limit.

It was found experimentally that a transition from L to H mode can avoid the disruption. To compare the stability of the pressure profile during the L and H-mode phase, the marginally stable pressure profile was calculated for a peaked pressure profile with and without an edge pedestal (see Fig. 7).

The pressure profile with the edge pedestal allows much higher stable normalised beta values. The maximum β_N for the H-mode type pressure profile is 2.1, for the L-mode profile 1.15, i.e. the addition of an edge pedestal by going from L to H-mode moves the plasma away from the ideal MHD stability limit.

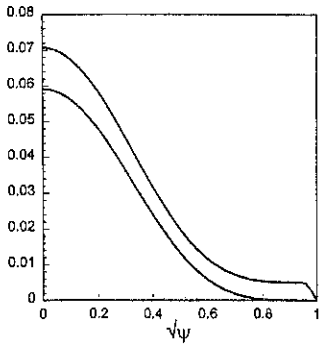

Fig. 7 Two marginally stable pressure profiles, with (β_N=2.1) and without (β_N=1.15) an edge pedestal.

Conclusions

The JET optimised shear discharges frequently terminate in a disruption. Tomographic inversion of the disruption precursor shows an n=1 mode in the plasma centre with dominant poloidal harmonics of m=2 and m=1. The mode structure obtained from the tomography agrees well with predictions based on the calculated mode structure of an n=1 global pressure driven kink mode.

Ideal MHD stability analysis of the optimised shear discharges show that the plasma is close to the stability limit for most of the heating pulse. The maximum normalised beta was found to be a strong function of the peaking of the pressure profile, in agreement with results from DIII-D [5] and TFTR [6]. Initially the beta limit is very low, due to the extreme peaking of the pressure profile. As the internal transport barrier moves outward in radius, the normalised beta of the MHD stability limit rises. The plasma beta is following the MHD stability limit. This is partly due to the adjustment of the heating waveform, which is essential to avoid an early disruption and partly due to relaxations of the pressure profile due to modes with a similar mode structure as the disruption precursor.

References

[1] A.C.C. Sips et al., *Operation at high performance in shear optimised plasmas in JET*, this conference.
[2] B. Alper et al., *A comparison of soft X-ray activity in high performance JET discharge'*, this conference.
[3] G.A. Cottrell et al., *Modelling of JET optimised shear discharges*, this conference.
[4] A.B. Mikhailovskii, G.T.A. Huysmans, W.O.K. Kerner and S.E. Sharapov, *Optimisation of Computational MHD Normal-mode Analysis in Tokamaks*, JET P(96) 25.
[5] DIII-D Team, *DIII-D Tokamak concept improvement research*, 16th IAEA Fusion Energy Conf., Montreal 1996, F1-CN-64/O1-6.
[6] J. Manickam et al., *MHD Stability Studies in Reversed Shear Plasmas*, 16th IAEA Fusion Energy Conf., Montreal 1996, IAEA-CN-64/A5-2.
T.C. Hender et al., *Stability of TFTR Reverse Shear Discharges*, 23rd EPS Conf. Contr. Fusion and Plasma Physics, Kiev 1996, Vol. 20C, p31.

MODELLING OF ALFVEN EIGENMODES IN HIGH PERFORMANCE DISCHARGES ON JET

W. Kerner, D. Borba[1], J.Candy[2], A. Fasoli[3], R. Heeter[4] and S. Sharapov

JET Joint Undertaking, Abingdon, Oxon, OX14 3EA, UK

[1]Associação EURATOM / IST, Av Rovisco Pais 1096, Lisbon, Portugal

[2]Institute for Fusion Studies, The University of Texas at Austin, Texas 7812

[3]CRPP-EPFL, Ass. Euratom-Swiss Confederation, CH-1007, Lausanne, Switzerland

[4]Princeton Plasma Physics Laboratory, P.O.Box 451, Princeton, NJ 08543 USA

INTRODUCTION

The confinement of alpha particles in JET DTE1 experiments as well as of energetic ions generated by high-power additional heating in JET discharges can be degraded by Global Alfvén Eigenmodes (AE). It is of great interest to analyse such AE instabilities in conjunction with the observed performance limits of JET, where the energetic ions are generated by Neutral Beam Injection (NBI) and Radio Frequency heating (RF) or by fusion-born alpha particles in JET DTE1 D-T discharges. Theoretical modelling and diagnostic results are combined to study the excitation of AE in high performance JET discharges. The study is based on a typical Hot-ion H-mode with $B_T = 3.4T$, $I_p = 3.4MA$, $\langle n_e \rangle = 3 \times 10^{19} m^{-3}$, and optimized shear discharges with q(0) ~ $q_{\min} \approx 1.5$, $\langle n_e \rangle = 2 \times 10^{19} m^{-3}$ both with auxiliary heating power of $P_{NBI} < 20MW$ and $P_{RF} < 10MW$. The ion temperature is $T_i(0) = 10 - 25keV$ and the electron temperature is of the order of $T_e(0) = 10keV$. These discharges are extrapolated to operation with deuterium-tritium (DT) using transport predictions (TRANSP).

THEORETICAL MODEL

A hybrid fluid-particle model has been developed, where the background plasma together with the plasma waves is described by the fluid part. The energetic ions need to be treated by the kinetic model. The model comprises two stages, the linear stability analysis and the nonlinear evolution of the system. In the linear phase the energy exchange between the coherent plasma normal- mode and the energetic ions is evaluated by δW_{hot}. The perturbative approach utilising the MHD normal-mode is justified for a small drive as given by the alpha particle distribution in JET and ITER. It requires a high heating power density from NBI and RF to drive non-eigenmodes unstable .

The CASTOR-K code evaluates both drive and dampings for general tokamak configurations, general orbits and realistic fast particle distributions. The nonlinear evolution of the wave and particle distribution is descibed by a self consistent weak turbulence model and is evaluated by the FAC code. The nonlinear simulations give the scaling of the saturated amplitude

$$\frac{\delta B}{B_0} = C\left(\frac{\gamma}{\omega}\right)^2 \quad , \tag{1}$$

where the proportionality factor is close to one $C \approx 1$. Thus, the saturated amplitude can be extracted from the linear analysis. Further, it is found that the orbit stochasticity threshold

$$\frac{\delta B}{B_{0\ stoch}} > \frac{\delta B}{B_{\max}} \sim 10^{-4} \quad , \tag{2}$$

is difficult to reach in JET plasmas.

DIAGNOSTICS

Systematic measurements of magnetohydrodynamic (MHD) activity have been done using the synchronous detection system of the AE Active and Passive Diagnostics. Recently, an improved diagnostic based on a set of eight magnetic coils with 1 MHz sampling rate for a 1 second time intervall has become operational thus allowing to monitor frequencies up to 500 kHz in time.

RESULTS

I) **NBI** : Theory reveals that 140 keV beams can drive TAE unstable in Hot ion H-mode only for high-n (n >14). The modelling for a slowing-down distribution shows that the drive is increased for 140 keV ions with increasing n with n ~ 14 being marginal unstable. As shown in Fig. 1 the stability limit is reached in some JET discharges. Although magnetic fluctuations with n=1 to 10 were observed with frequencies around 400 kHz there is no conclusive evidence that these are AE.

II) **RF** : From the modelling it is found that the energetic ion tail (E>500 keV) can drive TAE modes unstable (see Fig. 2). Interpretation of JET ICRH discharges yields that an estimate of the energy stored in the fast ions is given by $W_f = P_{RF} \cdot t_{sd} / 8$, where t_{sd} is the ion-electron slowing down time in the plasma centre [1]. This leads to a tail temperature for the fast ions of $T_f \approx 700 KeV$ for the case of 4 MW RF power. Experimentally it is found that low-n (n=2 to 5) TAEs in optimized shear and medium-n (n=5 to 11) TAEs in Hot-ion H-mode are unstable for RF power larger than 4 MW. EAEs are observed for RF power larger than 6MW as shown in Figs. 3 and 4. A large data base of these results was established at JET.

III) **α-particles** : The modelling for a slowing-down distribution indicates that the drive is reduced for 3.5 MeV α 's with increasing toroidal mode number n. From theory it follows that alphas can drive AE unstable in Hot-ion H-mode discharges for n=5 to 10 (KTAE) as well as in optimized shear configurations for n=2 to 4 (TAE). Thus direct AE excitation by α 's is predicted in DTE1 discharges with a fusion power in excess of 10 MW. These AE should be detectable by the high resolution diagnostic.

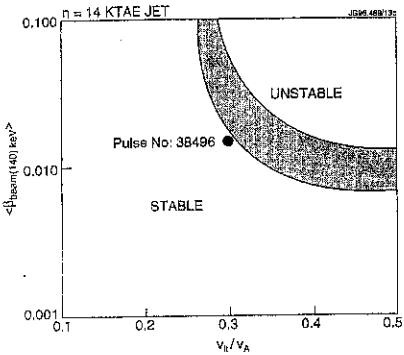

Fig. 1 Stability diagram for NBI drive.

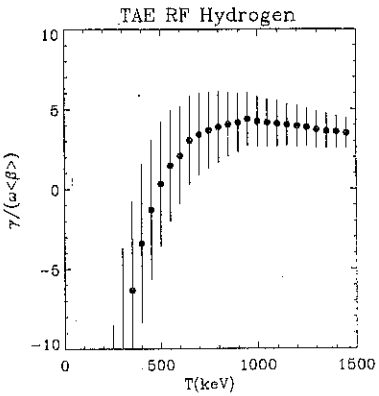

Fig. 2 Modelling of the growth rate of a n=5 TAE mode in the presence of RF generated ions due to on-axis heating.

CONCLUSIONS

It is predicted that the fusion born α 's can drive AE unstable both in JET Hot-ion H-mode and optimised shear D-T discharges, when the fusion power exceeds 10MW. Since the AE amplitudes are predicted to saturate at small amplitudes, no significant α - particle loss or redistribution should occur.

The drive provided by RF generated fast ions is sufficient to drive AE and EAE unstable both in Hot-ion H-mode and optimised shear discharges. The experimental identification of frequencies and mode numbers agrees well with the modelling. It is, however difficult to measure the saturated AE amplitudes in the plasma centre, which is needed for further benchmark tests on the theory . Extremely difficult is the measurement of the energetic particle redistribution, in particular when losses are not pronounced.

[1] L-G Eriksson, private communication

AE activity on optimised shear

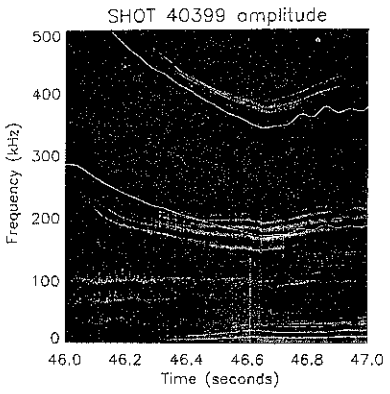

Fig.3 Spectrogram of the magnetic fluctuations measured by a pick-up MHD coil. The Alfvén frequency on axis is indicated.

Continuum gap structure

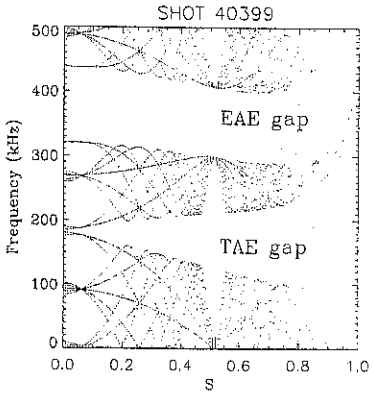

Fig.4 Alfvén continuum gap structure for shot 40399 at t=46.5 s.

Alpha particles in DTE1

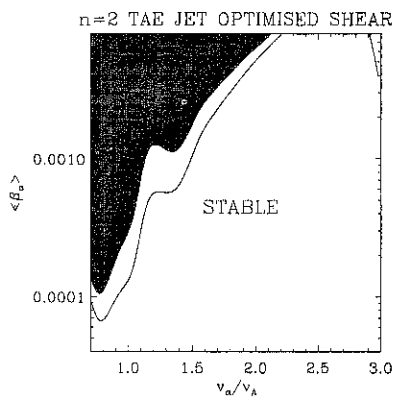

Fig.5 Stabilty diagram for optimized shear equivalent D-T discharges

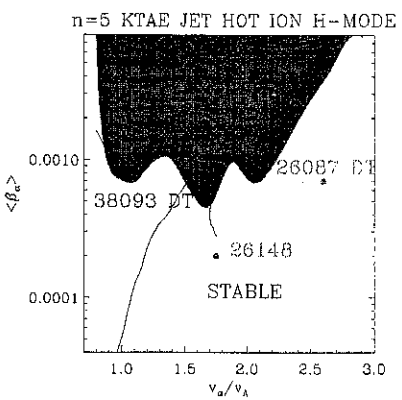

Fig. 6 Stability diagram for Hot-ion H-mode equivalent D-T discharges

Identification of outer modes in JET

T C Hender*, B Alper and G T A Huysmans
Jet Joint Undertaking, Abingdon, Oxon, OX14 3EA, UK
*UKAEA Fusion, Culham, Abingdon, Oxon, OX14 3DB, UK

Introduction

The Hot Ion H-mode is one of the operating regimes used to attain high performance (ie high neutron yield) in JET. In this regime a low density target plasma is heated with substantial neutral beam power ($\geq$15MW); the low target density allows good beam penetration to the plasma core and gives rise to long ion-electron equipartition times, so that the ions become substantially hotter than the electrons (typically T_i~20-30keV, T_e~10-15keV). Since the ions are the fusing species $T_i > T_e$ tends to optimise neutron yield (in D-D and D-T plasmas) for a given stored energy. The Hot Ion regime is transient and almost always terminated by MHD [1]. This MHD may be in the plasma core (sawtooth or fishbone) or at the plasma edge (giant ELM or 'outer mode'). Discussion of the origin of the so called outer mode is the subject of this paper. Experimentally the outer mode is observed to generally have a toroidal mode number n=1 (though n=5 has been observed) and have poloidal mode numbers in the range m=4-5. It has a frequency of ~10kHz and is observed to occur in the outer ~20% of the plasma (hence its name). Although confined to the plasma periphery the outer mode causes a global degradation of energy confinement (see Fig 1) and poses a significant limitation to high performance operation in JET Hot Ion H-modes; therefore a physics understanding of it is important.

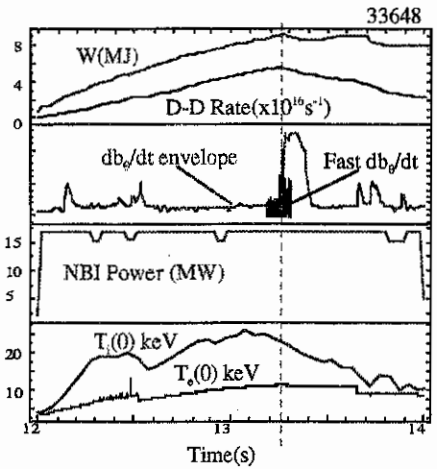

Fig 1 Hot Ion mode discharge (with T_i~$2T_e$) in which performance is limited by an outer mode at ~13.25s (visible on db_θ/dt traces). In this discharge there is a continual density rise which accounts for continued increase in stored energy while the ion temperature begins to decline.

MHD Stability

In the Hot Ion H-mode large edge temperature and density gradients occur. The combination of the high edge temperatures channelling ohmic current near the edge and the bootstrap effect,

gives rise to large edge current gradients; an effect which is confirmed by detailed transport simulations. The edge pressure gradients can approach the ideal ballooning limit, while the edge current gradients can drive low-n edge kink modes (sometimes known as peeling modes). The stability of these edge kink modes has been calculated with the free boundary resistive and ideal toroidal MHD codes, CASTOR and MISHKA. Stability calculations based on equilibria from transport simulations of specific discharges show (within error bars) that the low-n (n=1 and 2) ideal kink modes are unstable when outer modes are observed (Fig 2).

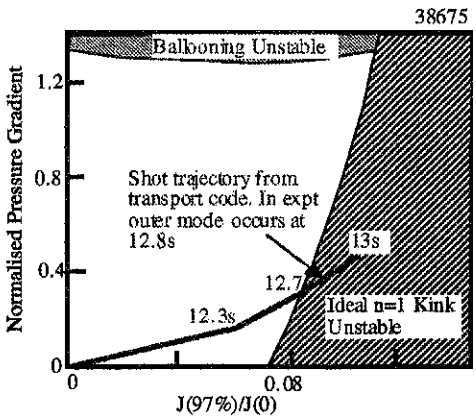

Fig 2 Stability of pulse 38675 in which an outer mode occurs at 12.8s. At this time the pulse is unstable to the external kink mode but far from ballooning instability.

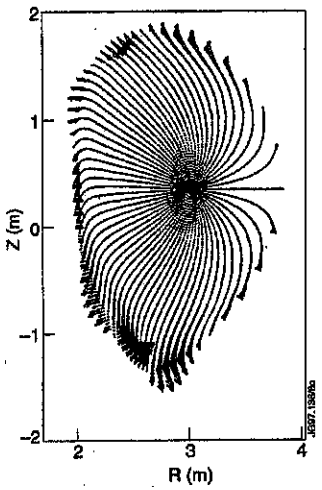

Fig 3 Velocity vectors for n=1 kink mode

The coincidence between the n=1 external kink stability boundary and the outer mode being observed combined with the edge localisation of the external kink mode (Fig 3), which is an observed feature of the outer mode, strongly suggests that the outer mode is a current driven external kink. A further convincing identification of the outer mode as an edge kink mode comes from a comparison of theory predictions with SXR data.

SXR Comparison

JET has an extensive SXR system with 9 arrays of diodes giving 197 chordal views at a given toroidal angle. The filtering on these diodes is such that they are sensitive down to temperatures of ~2keV (very near the edge in Hot Ion discharges). The outer mode is particularly visible on SXR chords which are tangential to the edge region of the plasma. To compare the SXR data with theory an average emission profile is computed from experimental data (not a flux surface quantity), displaced using the ideal kink mode displacement vectors, and the SXR line integral views computed. For dominantly toroidal rotation an equivalence between time and toroidal

angle exists, allowing time histories of the SXR channels to be computed and compared with experiment (see figure); excellent agreement is found both in relative phase (Fig 4).

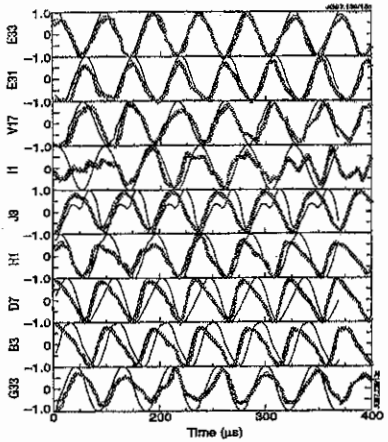

Fig 4 Comparison for pulse 37431 of observed outer mode oscillations (thick lines) with theory (thin lines) for a range of outer SXR channels (see Fig 5).

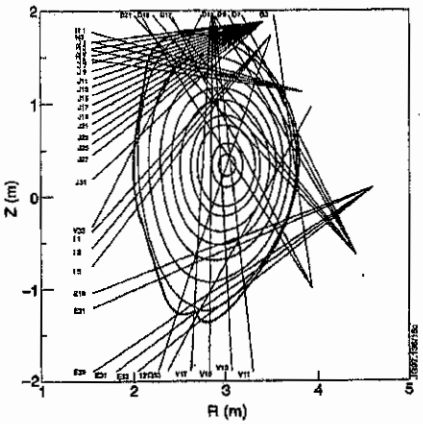

Fig 5 SXR channels on which an outer mode oscillation with amplitude > 50Wm^{-2} is observed. The plasma surfaces shown include the kink distortion at an amplitude which matches the SXR oscillations.

There is good agreement between theory and experiment, for a given camera, on the relative amplitudes of the outer mode SXR oscillations. By fixing the absolute amplitude of the linear kink mode eigenfunctions by matching to a given channel (E33 in the X-point region is used here) the boundary distortions due to the outer mode can be seen (Fig 5). These distortions are largest at the X-point (~10cm) and the upper stagnation point and are significantly smaller on the mid-plane (~1cm).

In these external kink mode computations the separatrix geometry is approximated by truncating at some flux value; 99% of the separatrix value for the computations presented above. The edge-q value due to this truncation affects the dominant poloidal mode number forming the kink mode eigenfunction. For the comparison in Fig 4 q_ψ=4.8 which causes the dominant harmonic to be m=5. Other edge truncations have been examined causing the m=4 or 6 harmonics to be dominant but the agreement with experiment is somewhat worse.

Tearing Mode SXR comparison

Comparisons with experiment have also been made for resistive (island forming) edge kink modes. These remain unstable as the edge current is reduced below the threshold to drive ideal modes being driven by current gradients within the plasma. A different technique is required to compute the theory SXR chord integrals, since the ideal MHD assumption that the plasma (and

hence the SXR emissivity) moves with the perturbed flux surfaces is no longer valid. Instead it is assumed that the SXR emission is constant on a perturbed field line and that the emission on that field line is specified as a function of its average radius. The emissivity profile used is determined by a flux surface averaged tomographic reconstruction. Use of this procedure shows a much poorer comparison of relative phase with experiment for the resistive island forming mode (see Fig 6) than for the ideal mode (Fig 7).

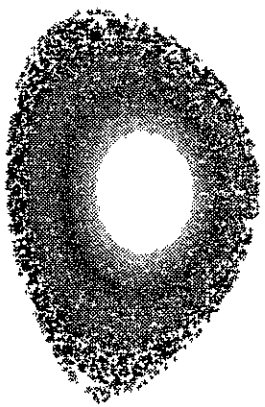

Fig 6 Poincare puncture plot showing magnetic islands near edge formed by tearing mode, particularly in X-point region

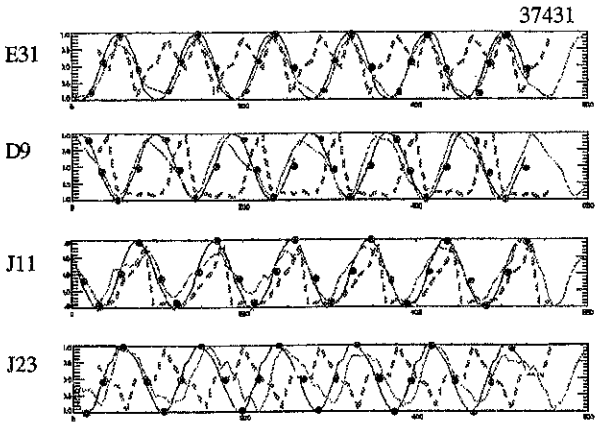

Fig 7 Comparison of experiment and ideal (line with dots) and tearing mode theory (broken line) predictions of outer mode SXR oscillations

Summary and Discussion

The outer mode poses a serious performance limit for the Hot Ion H-mode. The comparison presented with stability boundaries, location and detailed SXR reconstruction strongly suggests outer mode is caused by the ideal external kink (or peeling) mode. This identification of the outer mode as driven by edge current gradient suggests methods for its avoidance by ramping the plasma current down; this is discussed in more detail in Ref [2]. This technique is now routinely used to suppress outer modes in Hot Ion discharges.

Acknowledgement

The UKAEA author was jointly funded by the UK Department of Trade and Industry and EURATOM

Reference

[1] M F F Nave et al, JET Pre-print, JET-P(6)14
[2] M F F Nave et al, this conf.

JET discharges with low geodesic curvature

F. Alladio[1], **F. Crisanti**[1], A. Mancuso[1], P. Micozzi[1], O. Tudisco[1]; P. Lomas[2], B. Schunke[2], V. Riccardo[2]

[1]Associazione Euratom-ENEA sulla Fusione, C.P. 65 Frascati (Roma), Italy,
[2]JET Joint Undertaking, Abigdon, Oxon, OX14 3DB, UK

1. Introduction

DIII-D has shown that highly triangular and elongated discharges are characterised by increased confinement properties [1]. A possible explanation of these improvements is the reduction of the magnetic field lines geodesic curvature [2].

Low geodesic curvature implies reduced particle drifts and therefore lowers the neo-classical transport and quenches a number of MHD instabilities. The radial electric field can be affected as well by the reduction of the geodesic curvature. In fact the contribution of the rotation to the electric field can be written [3] as $\left|\vec{E}_r\right|_{\vec{v}\times\vec{B}} \propto G(\psi)RB_p$, where R is the distance from the symmetry axis of the cylindrical co-ordinate (R,ϕ,Z), B_p is the poloidal magnetic field, ψ is the poloidal flux and $G(\psi)$ is a surface function, which depends upon the magnetic configuration. For large anomalous parallel viscosity ($\nu_{eff} >> \nu_{\parallel}^{NC}$) $G(\psi)$ can be written (for $t>>1/\nu_{eff}$) as $S_G/\rho_m\alpha\nu_{eff}$, where S_G is the momentum source (proportional to the NBI power), ρ_m is the mass density and the parameter $\alpha \propto (1+2\hat{q}^2)/q^2$ is the effective increase of the plasma moment of inertia [4], due to the compression of the flux tubes. Therefore the radial electric field, neglecting the pressure gradient and fixing all other quantities, behaves like $\left|\vec{E}_r\right|_{\vec{v}\times\vec{B}} \propto \alpha^{-1}$. A scan of plasma equilibrium configurations has been done varying the plasma aspect ratio (A) the elongation (κ) and the triangularity (δ) [5]. The calculations results has swown that the parameters α is always strongly correlated with the geodesic curvature. In particular α is decreasing with κ at any aspect ratio and at any triangularity. The dependence from the triangularity changes with the apect ratio: for the aspect ratio of JET ($A \approx 3.5$) α has a minimun for $\delta \approx 0.4$, whereas for the aspect ratio of DIII-D ($A \approx 2.5$) α decreases monotonly. These behaviours are confirmed from the DIII-D [2] and from the JET experimental data.

2. JET experimental data

In order to compare the effective plasma moment of inertia with the experimental parameters of the plasma equilibrium a number of JET discharges have been examinated. The data base has been formed selecting discharges with fixed safety factor at the edge ($3.3 < q_{95} < 3.5$) and fixed toroidal field ($2.5 < B_T < 2.6$ T), but with different elongation and triangularity. In Fig.1 shows the volume averaged α versus κ (1a) and δ (1b).The volume average is performed through the range $0.60 < \rho < 0.95$ of the equivalent minor radius, as this is the region where the effect of the radial electric field is relevant.

To study the energy confinement of highly shaped JET discharges the previous data base has been used, together with a second data base selected using discharges at higher safety factor at the edge ($4.4 < q_{95} < 4.6$) and with toroidal field in the range $2.6 < B_T < 3.5$ T. All the disharges where heated by neutral beam injection with $P_{NBI} \geq 8$MW.

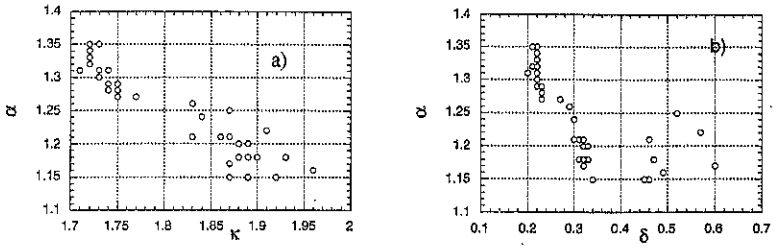

Fig 1 - Correlation of α parameter with elongation (k) and triangularity(δ). Only discharges with 3.3<q95<3.5 and P_{TOT}>8 MW have been plotted.

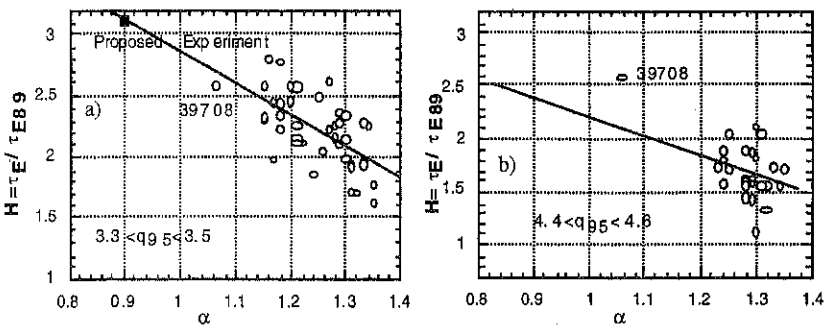

Fig 2a-b) Correlation of α parameter with the improved confinement $H=\tau_E/\tau_{E89}$; two different q values are selected.

In Fig 2a) and 2b) the factor of confinement improvement $H=\tau_E/\tau_{ITER89}$ is reported versus the volume averaged α for the two set of discharges. Even though the spread of the points is large, it can be observed that the parameter H increases as α decreases. This increase of the confinement improvement with the decrease of α is mainly due to the increase of κ, but some improvement comes also from the incerease of the triangularity, at least for $\delta \leq 0.3$.

From this experimental evidence a dedicated discharge with the minimum achievable α ($\alpha \approx 1.05$) has been designed and produced, without modifying the standard connection of the JET poloidal field circuit; moreover this request has pushed to use a relatively low plasma current I_p=2.0MA. The toroidal field was B_T=2.6T giving a q_{95}=4.55.

In Fig. 3 the equilibrium configuration reconstructed by the code EFIT is shown along with a few relevant waveforms (shot #39708). The power injected was quite small (P_{NBI} = 7MW), due to some problems in the injection system. In spite of the limited power quite good plasma performances have been achieved (H ≈ 2.7); moreover (see Fig 2a and 2b) the obtained confinement is the one predicted by a linear fitting of the data base at higher plasma current. Comparing the result with the linear fitting for the discharges at similar q_{95} the confinement is still better.

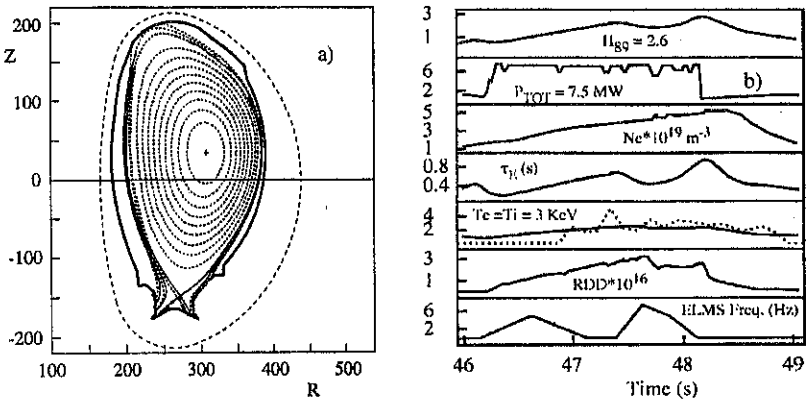

Fig 3 - a) EFIT equilibirium reconstroction. --- b) Temporal evolution of: 1] Improved confinement H89. 2] Total power; 3] Electron density. 4] Confinement time. 5] Electron and ion temperature. 6] Neturun flux. 7] Elms frequency

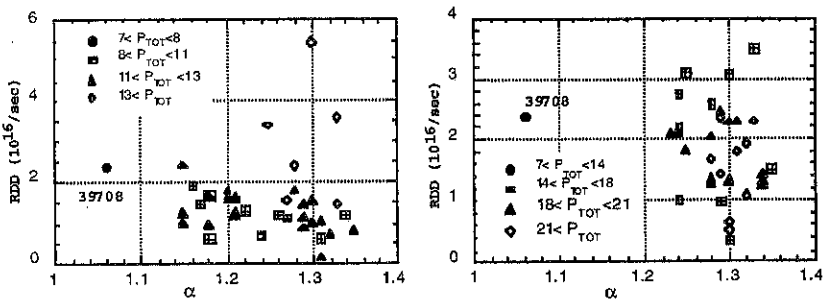

Fig 4 - Neutron yield for the two data set of discharges at q=3.5 (a) and q=4.5 (b), compared with the experiment at low a. The data are clustered for ranges of additional power.

The neutron emission is quite large ($R_{DD} \approx 2.4\ 10^{16}$/sec), especially as it is obtained with a limited injected power (see Fig.4).

3. Future experiments and conclusions

A study of possible plasma equilibria (Fig.5) shows that on JET the parameter α can be pushed down to $\alpha \approx 0.9$ at $I_p \approx 2.8$ MA; the foreseen elongation for this equilibrium is $\kappa \approx 2.1$ with an average triangularity $\delta \approx 0.4$. This plasma shape can be obtained unbalancing, up and down, the total current flowing in the poloidal windings PF2 and PF3 and selecting a different number of turn for each coil. A preliminar analysis of the vertical stability, using the code MAXFEA, gives a grow rate $\gamma \approx 600$, that should be controlled by the JET vertical control sytem. Fig 2a shows the expected confinement improvement, as extrapolated by the linear fitting of the data: an H factor of the order of 3 should be obtained. It has to be noted that in

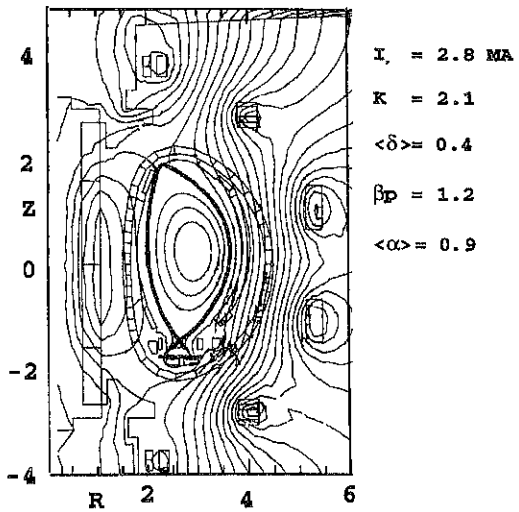

Fig 5 - Projected Experiement, trying to minimise the magnetic inertia α

this proposed experiment the magnetic inertia factor α would be comparable with the one of DIII-D in VH mode [2].

If the proposed experiment will be realised in the next future, it will be possible to determine whether the magnetic inertia is definitely relevant for the energy confinement, or if the reduction of the geodesic curvature in the improved confinement regimes is driven by the change of some other parameter.

References

[1] E.A. Lazarus et al., Proc. of IAEA, Seville 1994, p.609

[2] F. Alladio, F. Crisanti, S. Mancuso, P. Micozzi, K.H. Burrel, L.L. Lao, M.S. Chu, T.H. Osborne, R. Giannella, P. Lomas, D. O'Brien, XXXVII APS meeting of Plasma Physics, November 6-10, 1995, Louisville, Kentucky, paper 6Q.29.

[3] F. Alladio and P. Micozzi, ENEA Report, RT/ERG/FUS/95/21

[4] S.P. Hirshman, Nucl. Fusion **18** (1978), 917

[5] F. Alladio, F. Crisanti, S. Mancuso, P. Micozzi. IV PDTA Symposium (Symp. on plasma dynamic theory and applic.) November 1995.

Modelling Neutral Particle Analyzer Measurements of High Energy Fusion Alpha–Particle Distributions in JET

KG McClements[1], RO Dendy[1] and A Gondhalekar[2]

[1] UKAEA Fusion, Culham, Abingdon, Oxfordshire, OX14 3DB, UK
(UKAEA/Euratom Fusion Association)

[2] JET Joint Undertaking, Abingdon, Oxfordshire, OX14 3EA, UK

1. Introduction

A neutral particle analyzer (NPA) on JET has been used to measure the energy distribution of ions heated by waves in the ion cyclotron range of frequencies (ICRF) [1,2]. The NPA measures a vertical line integral through the plasma centre of the heated ion energy distribution weighted by the local neutralization probability. In this paper we address the question of interpreting NPA measurements in terms of a time–evolving alpha–particle velocity distribution. The NPA has already been used to measure MeV ICRF–heated helium–3 ions in JET, with injected helium–4 atoms providing charge exchange [3]. The same instrumentation has been used to measure alpha–particles in TFTR [4]: in this case an ablating lithium pellet was used to produce a sufficient density of hydrogen–like and helium–like ions for a detectable flux of helium–4 atoms to be formed. Helium–4 beam injection may be used in the JET deuterium–tritium experiments (DTE1), and it is possible that double charge–exchange with helium–like ions of intrinsic plasma impurities could also produce a detectable flux of neutralized fusion alpha–particles. We assume that the neutralization probability in the NPA energy range (0.3–4.0 MeV) will be sufficiently large for the fusion alpha–particle energy distribution function to be determined.

2. Line–Integrated Alpha–Particle Distribution

The NPA measures the energy distribution of atoms whose velocity vectors lie inside a narrow cone [1]: if the velocity components parallel and perpendicular to the vertical direction are v_z and $v_\perp$, only atoms with $v_z/v_\perp \gtrsim 200$ are detected. It can be shown that f_α, the local alpha–particle velocity distribution, and F_α, the local energy distribution of alpha–particles which, if neutralized, would be detected, are related by [2]

$$F_\alpha(E,Z) = \frac{\pi v_z}{200^2 m_\alpha} f_\alpha(v_z,Z), \tag{1}$$

where $E = m_\alpha v_z^2/2$, Z is distance above the midplane, and m_α is alpha–particle mass. We define a line–integrated distribution by writing

$$\tilde{F}_\alpha(E) = \frac{\pi v_z}{200^2 m_\alpha} \int_{-b}^{b} f_\alpha(v_z,Z)dZ, \tag{2}$$

where b is plasma height. The NPA measures a line integral of the alpha–particle distribution, weighted by the neutralization probability per unit time $P_\nu(E,Z)$. The measured flux is proportional to the integral from $-b$ to b of $P_\nu(E,Z)F_\alpha(E,Z)$. An alpha–particle energy distribution $F_\alpha^{\rm NPA}(E)$ can be obtained by dividing the NPA flux by $P_\nu(E,0)$ [1]:

$$F_\alpha^{\rm NPA}(E) = \frac{1}{P_\nu(E,0)} \int_{-b}^{b} P_\nu(E,Z)F_\alpha(E,Z)dZ. \tag{3}$$

$F_\alpha^{\rm NPA}(E) \simeq \tilde{F}_\alpha(E)$ if $F_\alpha(E,Z)$ is more strongly-peaked in Z than $P_\nu(E,Z)$.

3. Local Alpha–Particle Distribution

We adopt the Fokker–Planck equation used by Sigmar [5]:

$$\frac{\partial f_\alpha}{\partial t} = S_\alpha(v,r,t) + \frac{1}{\tau_s}\frac{1}{v^2}\frac{\partial}{\partial v}\left[(v^3+v_c^3)f_\alpha\right], \tag{4}$$

where S_α is the rate of alpha–particle production per unit volume of phase space, τ_s is slowing–down time, $v = (v_z^2 + v_\perp^2)^{1/2}$, v_c is critical velocity, and r is minor radial distance. We neglect particle losses, quasi–linear diffusion resulting from velocity space instabilities, finite orbit width effects, and velocity space anisotropy.

Eq. (4) describes the evolution of f_α on a flux surface: S_α, τ_s and v_c do not vary over that surface. The assumed isotropy of f_α implies that it does not vary with poloidal angle, in which case we can replace r with Z. The equation has solution [6]

$$f_\alpha(v,Z,t) = e^{3t/\tau_s}\int_0^t e^{-3\eta/\tau_s} S_\alpha(v',Z,\eta)d\eta, \tag{5}$$

where $v' = \left[(v^3+v_c^3)e^{3(t-\eta)/\tau_s} - v_c^3\right]^{1/3}$. We have assumed that $\tau_s(Z)$ is time–independent: this is justified for the high fusion reactivity pulses in DTE1. The following profiles are adopted for electron temperature and density:

$$T_e = T_{e0}(1-Z^2/b^2)^{\nu_{Te}}, \quad n_e = n_{e0}(1-Z^2/b^2)^{\nu_{ne}}. \tag{6}$$

We assume the existence of ζ, ψ and H such that $S_\alpha = \zeta(Z)\psi(v)H(t)$. ζ and H can be obtained from tomographic analysis of neutron measurements [7]. We set $H = 1$ for $0 < t < \tau$ and $H = 0$ otherwise. The reacting species are assumed to have Maxwellian distributions at temperature $T_i = T_{i0}(1-Z^2/a^2)^{\nu_{Ti}}$, in which case [5,8]

$$\zeta(Z) = \zeta_0 \frac{n_i(Z)^2}{T_i(Z)^{2/3}} \exp\left[-20/T_i(Z)^{1/3}\right], \tag{7}$$

where $n_i = n_{i0}(1-Z^2/b^2)^{\nu_{ni}}$ is total ion density, T_i is in keV, and ζ_0 is determined by the requirement that the volume integral of ζ be equal to the alpha–particle production rate, S_n. An appropriate form for ψ is [8]

$$\psi(v) = \frac{\exp\left[-(v^2-v_\alpha^2)^2/\delta v^4\right]}{2\pi^{3/2}v_\alpha \delta v^2}, \tag{8}$$

where v_α is the mean alpha–particle birth speed and $\delta v = [8v_\alpha^2 T_i/(m_n+m_\alpha)]^{1/4}$, where m_n is neutron mass. To evaluate δv we set T_i equal to T_{i0}.

Fig. 1 shows $\tilde{F}_\alpha(E)$ (solid curves) and $F_\alpha(E,0)$ (broken curves) for: $\tau = 1.5\,\mathrm{s}$, $n_{e0} = n_{i0} = 5\times10^{19}\,\mathrm{m}^{-3}$, $\nu_{ne} = \nu_{ni} = 1$, $T_{e0} = 10\,\mathrm{keV}$, $T_{i0} = 20\,\mathrm{keV}$, $\nu_{Te} = \nu_{Ti} = 2$, major radius $R_0 = 3.1\,\mathrm{m}$, and $S_n = 4\times10^{18}\,\mathrm{s}^{-1}$. $F_\alpha(E,0)$ is normalized to have the same maximum value as $\tilde{F}_\alpha(E)$. The slowing–down time at $Z = 0$ is 0.74 s. In the NPA energy range a slowing–down distribution is established 1 s after alpha–particle production starts. After the end of alpha–particle production, the simulated NPA signal falls rapidly at high energy but not at low energy: the spectrum becomes progressively steeper at $t > \tau$.

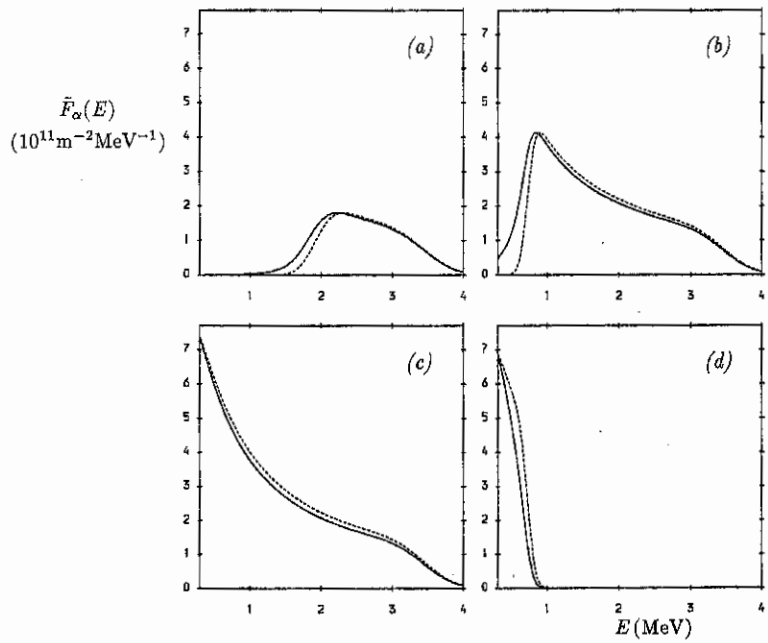

Fig. 1. Simulated alpha–particle energy distributions, integrated along a vertical chord (solid curves) and at $Z = 0$ (broken curves), for a JET–like tritium injection pulse ($\tau = 1.5\,s$) at (a) $t = 0.2\,s$, (b) $t = 0.5\,s$, (c) $t = 1.0\,s$, and (d) $t = 2.0\,s$.

4. Application to TFTR Data

Fig. 6 of Ref. [9] shows two alpha–particle spectra measured close to the centre of TFTR after tritium neutral beam injection (NBI) lasting for 1 s and 0.1 s. In the latter "beam blip" case (pulse 86299) the spectrum is narrow and peaks at 2.5 MeV. The measurements were obtained 0.12 s after the start of NBI, when $n_e(0) = 3 \times 10^{19}\,\mathrm{m}^{-3}$, $T_e(0) = 6\,\mathrm{keV}$, and hence $\tau_s(0) \simeq 0.58\,\mathrm{s}$. In this case the NPA gives the local alpha–particle energy distribution at $Z \simeq 0$ [4]. We have used Eq. (5) to evaluate $F_\alpha(E, 0)$, assuming that alpha–particle production occurred only during NBI, and setting $S_n = 2 \times 10^{14}\,\mathrm{s}^{-1}$, $T_{i0} = 30\,\mathrm{keV}$ [9]. F_α in Fig. 2(a) is the number of alpha–particles per unit volume per unit energy propagating in all directions: it is the distribution defined by Eq. (1), with the factor $\pi/200^2$ omitted. The data points have been normalized to have the same maximum value as the predicted distribution. The model agrees well with the measured distribution. The peak energy is a sensitive function of $\tau_s(0)$, and hence T_{e0}, n_{e0}. The peak energy differs from the mean birth energy E_α by $\Delta E \sim 2(t/\tau_s)E_\alpha \propto n_e/T_e^{3/2}$. In Fig. 2(b) the predicted alpha–particle energy distribution is plotted for three values of T_{e0}: the other parameters are identical to those used to obtain Fig. 2(a). Good agreement with the measured spectrum is only achieved if we set T_{e0} equal to the measured value 6 keV.

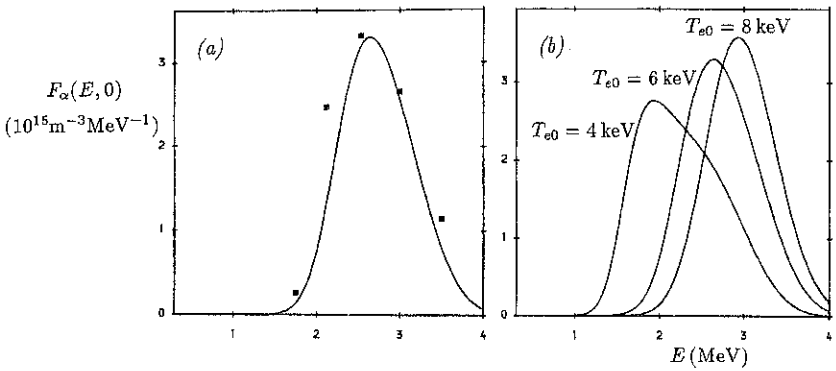

Fig. 2: (a) Measured alpha–particle energy distribution in the centre of TFTR after a short pulse ($\tau = 0.1\,s$) of tritium beam injection (data points) [9], *and the distribution predicted by the Sigmar model (curve). (b) Predicted distribution for three values of T_{e0}.*

5. Conclusions

We have used a simple slowing–down model to simulate alpha–particle energy spectra which could be measured using the JET NPA. At energies close to the birth energy and at times (after the onset of alpha–particle production) shorter than the slowing–down time, the NPA (line–integrated) spectrum closely resembles the spectrum at $Z = 0$. The model can account for the essential features of an alpha–particle spectrum measured on TFTR. Given measurements of fusion reactivity and the parameters needed to determine collisionality, the model can be used to predict the NPA measurement, if the physical processes in the Sigmar model (isotropic birth, confinement, classical slowing–down) are dominant. Substantial deviation of the NPA measurement from that predicted by the model would imply that other effects, for example collective effects or velocity space anisotropy, were playing a significant role in alpha–particle dynamics.

Acknowledgments

This work was funded by the UK Department of Trade and Industry and Euratom.

References

[1] AA Korotkov & A Gondhalekar, *Nucl. Fusion* **37** 35 (1997)
[2] KG McClements et al., *Nucl. Fusion* **37** 473 (1997)
[3] MP Petrov et al., Proc. 19th Eur. Conf. on Contr. Fusion and Plasma Physics, Innsbruck (1992), II, p.1031
[4] RK Fisher et al., *Phys. Rev. Lett.* **75** 846 (1995)
[5] DJ Sigmar, Proc. Varenna Course on Physics of Plasmas Close to Thermonuclear Conditions, Vol. 1 (1980)
[6] KG McClements et al., JET Report JET–R(97)02 (1997)
[7] FB Marcus et al., *Nucl. Fusion* **33** 1325 (1993)
[8] H Brysk, *Plasma Physics* **15** 611 (1973)
[9] SS Medley et al., *Plasma Phys. Control. Fusion* **38** 1779 (1996)

The influence of fast ions on the MHD stability of negative shear profiles

P. Helander, C.G. Gimblett, R.J. Hastie, and **K.G. McClements**

UKAEA Fusion, Culham, Abingdon, Oxon, OX14 3DB, U.K.
(UKAEA/Euratom Association)

Abstract: The influence of energetic ions on the stability of ideal double kink modes in a tokamak plasma with negative magnetic shear is investigated. It is found that the fast ions play a similar role as for the ordinary $m = n = 1$ internal kink. In particular, phenomena analogous to sawtooth stabilisation and fishbone excitation are possible.

1 The double kink mode

Several tokamaks have observed substantially improved confinement in discharges where the safety factor $q(r)$ is a non-monotonic function of the radius r, with a single off-axis minimum q_{min}. If q_{min} is less than, but close to, a rational number, $q_{min} \simeq m/n$, it has been shown that an ideal MHD mode with poloidal and toroidal mode numbers m and n may become unstable and limit the achievable β of the plasma [1]. The instability is driven by the combined action of the pressure gradient and unfavourable magnetic curvature. Mode-coupling to poloidal side bands plays a crucial role, and the mode structure is concentrated in the region where $q \simeq m/n$. Experimental evidence of the resistive analogue of this mode, the double tearing mode, with $m/n = 2/1$ has been observed in the form of off-axis sawteeth localised in the region around the $q = 2$ surface [2,3].

Here, we study the influence of fast ions on the double kink mode. Fast ions are well known to interact with the $m = n = 1$ internal kink in plasmas with $q(0) < 1$, being able to both stabilise sawteeth and to excite fishbone oscillations. We find that energetic ions may play a similar role for the stability of the double kink.

A difference between the internal $m = n = 1$ mode and the double kink is that the latter is more likely to have a narrow mode structure Δ_m, comparable to the banana orbit width Δ_b of the fast ions. Finite orbit-width effects are therefore important, and

accordingly, we carry out the analysis in both the limits $\Delta_m \ll \Delta_b \ll r$ and $\Delta_b \ll \Delta_m \ll r$, and allow the fast-ion Larmor radius to be comparable to the mode width.

The dispersion relation has the form

$$\delta I + \delta W_c + \delta W_f + \delta W_k = 0, \tag{1}$$

where δI is the kinetic energy, shown in Ref 3 to be equal to [see Eq (31) in that paper]

$$\delta I = -\frac{i\omega}{\omega_A}\frac{2\pi B^2}{\mu_0 m q R}\sqrt{1+2q^2}(r_1^2|s_1| + r_2^2|s_2|)\xi_0^2.$$

Here B is the magnetic field strength, R the major radius of the torus, r_1 and r_2 the minor radii of the rational surfaces where $q = m/n$, ξ_0 the jump in the radial component of the plasma displacement across these surfaces, s_1 and s_2 the magnetic shear, $rq'(r)/q(r)$, at these locations, ω the mode frequency, and $\omega_A = B/R(\mu_0\rho)^{1/2}$ with ρ the plasma density. The next term, δW_c, in the dispersion relation is the usual MHD potential energy of the bulk plasma, and the last two terms represent the energy associated with the "fluid" and "kinetic" response of the fast ions.

2 The role of fast ions

When fast ions are present in the plasma, the energy associated with their response to an ideal MHD displacement $\boldsymbol{\xi}_\perp = \boldsymbol{\xi}_0(r)e^{i(m\theta - n\varphi - \omega t)}$ in a circular, large-aspect-ratio tokamak, $\epsilon = r/R \ll 1$, can be shown to be [4,5]

$$\delta W_k = -\frac{\pi^2 M}{\Omega}\sum_\sigma \int v^3 dv \int dp_\varphi \int d\Lambda\, \tau_b \frac{\partial f}{\partial \mathcal{E}}\frac{\omega - n\omega_*}{\omega + n\langle\dot{\varphi}\rangle}\left\langle\left(\frac{v_\perp^2}{2} + v_\parallel^2\right)\frac{\bar{\xi}_{0r}}{R}\cos\theta\right\rangle^2, \tag{2}$$

$$\delta W_f = \frac{1}{2R}\int \xi_{0r}^2 \frac{d(p_\perp + p_\parallel)}{dr}\cos\theta\, d^3r, \tag{3}$$

where $\Omega = ZeB/M$ is the cyclotron frequency, τ_b the bounce time, and $p_\perp$ and $p_\parallel$ are the perpendicular and parallel pressures of the fast ions. Their distribution function f depends on the energy $\mathcal{E} = Mv^2/2$, the toroidal canonical momentum $p_\varphi = MRv_\varphi + Ze\psi$, $\sigma = v_\parallel/|v_\parallel|$, and the magnetic moment $\mu = Mv_\perp^2/2B$ through the variable $\Lambda \equiv \mu B_0/\mathcal{E}$ with B_0 the magnetic field strength on the magnetic axis. The bounce average along a guiding-centre orbit is indicated by $\langle\cdots\rangle$, and $\bar{\xi}_{0r}$ denotes the gyroaverage of ξ_{0r}. The stabilising or destabilising action of the fast ions is found by evaluating the integrals (2) and (3) in various cases.

Fast-ion stabilisation

If the fast ions are isotropic, it is natural to include their fluid response δW_f in the MHD potential energy of the background plasma by writing $\delta W_{MHD} \equiv \delta W_c + \delta W_f$. Instability then occurs if $\delta W_{MHD} + \mathrm{Re}\ \delta W_k < 0$, and if $\mathrm{Re}\ \delta W_k$ is positive the plasma is stable above the ideal MHD threshold. In the case of the double kink mode, the integral (2) becomes

$$\delta W_k = -\frac{2^{3/2}\pi}{R^{1/2}} \int_0^a \xi_{0r}^2 \frac{dp}{dr} r^{3/2} dr, \qquad (\Delta_b \ll \Delta_m) \tag{4}$$

$$\mathrm{Re}\ \delta W_k = -32.6\ \epsilon Z e B_\theta R X^2 \ln\vartheta \int_0^\infty \frac{\partial f}{\partial r} v^3 dv, \qquad (\Delta_m \ll \Delta_b) \tag{5}$$

in the limit of narrow and wide orbits, respectively. Here $\vartheta^2 \sim \Delta_b / \max(\rho, \Delta_m) \gg 1$, $X \equiv \int_0^a \bar{\xi}_{0r} dr$, and it has been assumed that the mode frequency is small in comparison with the toroidal precession frequency of the fast ions. In both the cases (4) and (5) the main contribution comes from the trapped ions, and their effect is stabilising. A phenomenon analogous to sawtooth stabilisation thus appears possible.

The ratio between the narrow (4) and wide (5) orbit limits is

$$\frac{\delta W_k^{tr}(\Delta_b \ll \Delta_m)}{\delta W_k^{tr}(\Delta_m \ll \Delta_b)} \sim \frac{\Delta_b}{\Delta_m \ln\vartheta} \tag{6}$$

for a slowing-down distribution $f \propto v^{-3}$. If the banana width and the mode width are comparable, which is likely in practice, the two limiting expressions (4) and (5) give fairly similar results. If the banana width exceeds the mode width, the fast ions spend only a fraction of their time in the region of the mode, and the customary small-banana-width approximation leads to an overestimate of their stabilising action.

Fishbone excitation

Neutral-beam injected ions are known not only to stabilise sawteeth, but also to excite finite-frequency fishbone oscillations. This occurs when the total hot-ion energy $\delta W_h = \delta W_f + \delta W_k$ has an imaginary part as well as a large negative real part. The real part of the dispersion relation (1) then indicates the existence of a mode with a growth rate $\gamma \propto -\delta W_c - \mathrm{Re}\ \delta W_h$ that can be positive in equilibria which are below the ideal MHD stability limit, while the imaginary part of the dispersion relation determines the real part of the mode frequency. Again, this is a well known feature of the usual $m = n = 1$ kink and we find that it carries over naturally to the double kink.

If, for simplicity $\Delta_b \ll \Delta_m$, the beam ions are injected perpendicular to the magnetic field and acquire a slowing-down distribution,

$$f(r,x,\Lambda) = N(r)\delta(\Lambda-1)\left(\frac{v_{max}}{v}\right)^3, \qquad v < v_{max}.$$

and the mode frequency is comparable to the fast-ion precession frequecy ω_φ, then

$$\delta W_k^{tr} = -\pi^2(2R)^{1/2}[2E(2^{-1/2}) - K(2^{-1/2})]Mv_{\max}^5 \int \xi_{0r}^2 N' r^{1/2} dr \;\; \hat{\omega} \;\ln(1-\hat{\omega}^{-1}), \quad (7)$$

with $\hat{\omega} \equiv \omega/n\omega_\varphi(v = v_{\max})$. When substituted in the dispersion relation (1), this result shows that instability may occur if the hot-ion beta exceeds a threshold

$$\beta_{\rm thres} \sim \epsilon(|s_1| + |s_2|)\frac{\sqrt{1+2q^2}}{q^2}\frac{\omega_\varphi(v_{max})}{\omega_A}.$$

Excitation of a fishbone-like instability then appears possible. In the case of large banana width, $\Delta_m \ll \Delta_b$, the fast-ion response is qualitatively similar,

$$\delta W_k^{tr} = M\Omega R X^2 v_{\max}^4 N'(r)\frac{2^{1/2}\pi^2\epsilon q^{-1}\ln\vartheta}{2E(2^{-1/2}) - K(2^{-1/2})}\left(\hat{\omega}^{1/2}\ln\frac{1+\hat{\omega}^{-1/2}}{1-\hat{\omega}^{-1/2}} - 1\right) \quad (8)$$

$$\delta W_f^{tr} = \pi^2\sqrt{2\epsilon}Mv_{\max}^5 N'(r)R\int_0^a \xi_{0r}^2 dr.$$

As in the case of narrow orbits, δW_k^{tr} has an imaginary part equal to πi if $\hat{\omega} < 1$, and a destabilising real part. The structurally necessary components for a fishbone instability are thus again present. Comparing the driving force of the instability in the narrow (7) and wide (8) orbit limits gives the same estimate (6) as obtained above.

This work was supported jointly by the UK Dept of Trade and Industry and Euratom.

[1] C.G. Gimblett, R.J. Hastie, and T.C. Hender, Phys. Plasmas **3**, 3369 (1996).

[2] Z. Chang et al., Phys. Rev. Lett. **77**, 3553 (1996).

[3] S. Turlur et al., in *Proc. 22nd EPS Conference on Controlled Fusion and Plasma Physics*, Bournemouth (1995), Vol IV, p. 73.

[4] F. Porcelli, R. Stankiewicz, W. Kerner, and H.L Berk, Phys. Plasmas **1**, 470 (1994).

[5] P. Helander, C.G. Gimblett, R.J. Hastie, and K.G. McClements, to appear in Phys. Plasmas (1997).

Experiments on Plasma Fuelling and ELM Control by Pellet Injection on JET

P. **Kupschus**, J.C.M. de Haas, M. Gadeberg, L. Horton, P.T. Lang*, J. Lingertat, A. Loarte, G. Saibene, B. Tubbing
JET Joint Undertaking, Abingdon OX14 3EA; *IPP Garching

First plasma injection experiments with the pellet centrifuge, which came into operation on JET during the last year, have been conducted. The centrifuge has been designed and built at JET, using a Garching type of rotor/stop cylinder arrangement, for injection of long-pulse pellet trains or sequences of order 1 minute at moderate pellet speeds and is therefore equipped for the appropriate gas handling requirements. Two pellet extruder units of novel design - with an ice reservoir of up to 150 cm^3 - are capable of launching cubic deuterium pellets of 2.7 and 4.0 mm at velocities ranging from 50 to 600 m/s with repetition rates so far up to 5 Hz. Problems with the acceptance of pellets in the rotor hub have lead to pellets missing from the sequence delivered to the plasma. Injection is performed from the plasma outboard side and along the curved pellet track horizontally about 300 mm below the midplane of the plasma, co-injecting at 15°. Pellets are characterised with regard to timing, speed and size when they traverse and de-tune two μ-wave cavities on the flight to the torus; the absolute size calibration has been checked against the highest achieved plasma content increase in ohmic plasmas. The arrival of pellets in the plasma is detected by a diode collecting light from the pellet plume (due to a marginal solid viewing angle this signal indicates a minimum penetration depth). For nominal 4 mm pellets the average particle flux to the plasma was up to 1.4×10^{22} deuterons/s and this fuelling rate can be sustained for up to 20 s (i.e. 100 pellets).

For reference and comparison to past pellet experiments with a pneumatic launcher, the centrifuge fuelled ohmic plasmas with pellets which showed very high fuelling efficiencies of up to 88 %, despite the shallow deposition to about 1/3 of the minor radius. Together with the build-up of the plasma density its profile peaked and this lasted for about 1 s after the termination of the pellet string: in so far the pellets acted like in the earlier JET experiments.

Various refuelling scenarios were probed with the aim to enhance the flexibility in density control, in particular, to increase the density over and above what has been achieved with strong gas puffing. Pellet trains, without and with additional gas puffing, were injected during quasi-stationary L- and H-mode phases of neutral beam and ICRH heated discharges up to a level of 12 MW in total. Generally, the commonly observed decrease in penetration with

increasing auxiliary heating power is accompanied by a decrease in fuelling efficiency. In particular, in the cases with 2.7 mm pellet trains into 12 MW ELMy H-mode plasmas the pellets can hardly be noticed in the noise of the ELM activity. With 4 mm pellets, in general, pure pellet fuelling acted faster and more efficiently than gas puffing in the density build-up but did in the end only marginally exceed the density obtained by gas fuelling. Combining both methods has shown advantages for fast density rises to maximum values of of 85% of the Greenwald limit so far. At these power levels, pellet induced particle losses do not seem to contribute significantly to the bulk plasma energy losses connected with ELM activity.

These main features can be seen in the following examples of 2.5 MA / 2.5 T high-triangularity (δ=0.3) type I ELMy H-mode discharges: 4 mm pellets of about 3.10^{21} deuterons each are injected at 240 m/s and 5 Hz into shots # 39988/91 without gas fuelling and # 39992 combined with gas fuelling (at a rate of about 5.10^{21} deuterons/s) during the phase of 8-9 MW of neutral injection (starting at 17 s). Fig.1 shows the torus outer divertor Dα-signal for the 3 pellet shots adjacently with their pellet train and those for the comparison shots # 39989/90 without pellets nor additional gas feed where "natural" ELMs do not start before 18.4 s. From the pellet Dα-light a penetration depth of 35 to 38 cm into the plasma is derived which is surprisingly deep (compared to code predictions) but otherwise in qualitative agreement with the plasma temperature profile development seen in fig. 2 below. Each pellet appears in the torus Dα-signal as a giant ELM of about 1.5 msec duration, starting with some delay of up to 1.5 msec after the pellet reaches the plasma, and a similar signature is found in the camera pictures of the divertor in the light of Bremsstrahlung, Carbon II (C II), and in the infra-red camera (measuring mainly the tile surface temperature), with the main activity showing up near the inner divertor strike zone as is typical for the ELMs on JET. We are unable to distinguish the pellet signature from that of a natural ELM, except for the fact that, expanded in time, a pellet

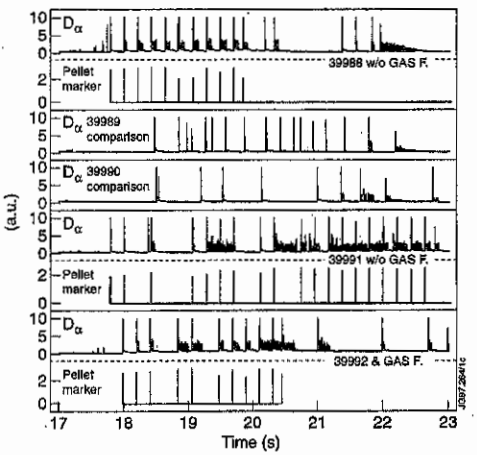

Fig.1: Dα and pellet marker traces for 3 JET pulses

ELM signal in comparison may have an initial small Dα-step on the time-scale of the pellet penetrating the outer plasma layers and that the outer plasma region is left after the induced ELM with an excess of particles rather than a deficiency as in the "natural" ELM case. The first pellet induced ELMs show a relatively clean signature whereas the later ones are successively followed by small or extended periods of small ELMs. Figure 2 shows on top 4 temperatures versus time at positions of 6, 13, and 36 cm into the plasma as well as on axis: The 3 outer traces clearly exhibit the direct pellet impact whereas the center is mildly affected but is also saw-toothing asynchronously. The lowest trace is from the central line density chord of the interferometer: The first three pellets show positive density steps followed later by positive short-lived excursions only, these usually accompanied by the small ELM activity. Smoothed line averaged density traces of the five pulses in Fig.3 indicate that the early regular pellet pattern of # 39988 and 39992 leads to a slightly faster density rise. However, the plasma particle content is on average already nearly constant 1.5 s into the heating pulse - approaching 85 % of the Greenwald limit marked on top of the diagram - although each pellet has sufficient particles to raise the entire plasma density instantaneously by at least 50 %. The radial density profile is for the first seconds very flat and the density reflectometer confirms that the outer indicating profile is hardly affected by the pellets on the time scale of >10 msec. Fig.4 shows the development of the radial temperature profile for the 3rd pellet in # 39988 as seen by the ECE which shows a dramatic temperature drop on the millisecond

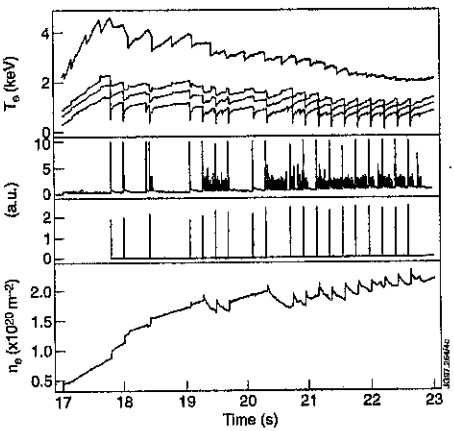

Fig. 2: Electron temperature and line density versus time in relation to the pellet sequence for # 39991

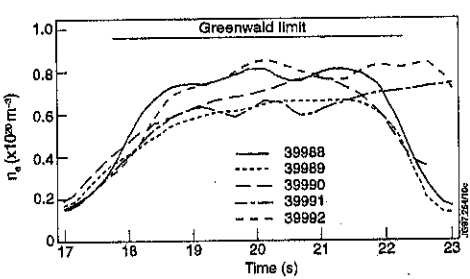

Fig. 3:Line averaged densities (smoothed) versus time

scale with comparatively slow re-heating. Apart from the astounding fact that the plasma tolerates so large disturbances at all the pellet induced ELM - ejecting roughly the equivalent of the particles injected with the pellet - the ITER H89 scaling factor is 1.8 ± 0.2 and the convective loss per pellet are in the order of 5-10 % of plasma energy (ca 4-5 MJ), both as inferred from the negative jump of diamagnetic loop signal and estimates from the drop in the electron temperature, and is therefore of the same order as that by giant ELMs. However, the CII camera signal from the divertor looks qualitatively much less dramatic. We presume that the energy transported into the divertor by a quantity of particles at least an order of magnitude larger than by natural ELMs may have a beneficial effect for the instant load onto the divertor plates. This is also supported by the observation that with larger gaps in the pellet train the subsequent pellet induced ELM creates a larger CII signal. Moreover, the size of the pellet induced ELM may depend on pellet size, penetration and repetition frequency and this leaves some room for further optimisation attempts. There is also good evidence that the high flow of pellet material towards the divertor does wash out Nickel impurities which otherwise will build up in the plasma.

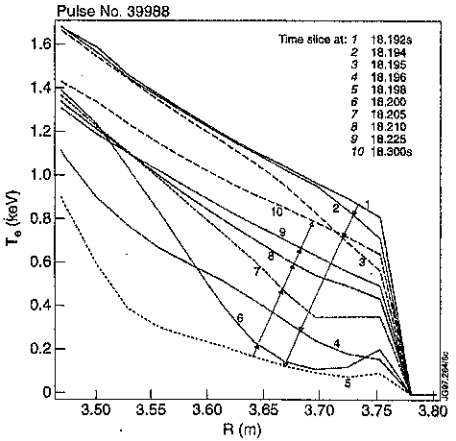

Fig. 4: Outer radial electron temperature profile of a pellet induced ELM for # 39988

In conclusion: First pellet injection experiments with the new centrifuge have demonstrated for these medium power type I ELMy H-mode discharges that ELMs can be triggered by large pellets without the plasma reverting to L-mode and with possible beneficial effects for the instant divertor power loading. If this can be shown also for higher performance discharges, possibly with more optimised pellet parameters, this would give some perspective for ELM control on ITER. Despite the launching of pellets clearly beyond the confinement barrier and the recycling zone the investigated plasmas resist the build-up of much higher densities than can be achieved with gas puffing.

Steady State H-modes at high plasma density in JET

G Saibene, B Balet, S Clement, B de Esch, G Fishpool, J C M de Haas, G Haas (*), L D Horton, J Lingertat, A Loarte, C G Lowry, R D Monk, M F Nave, R Sartori and K Thomsen

JET Joint Undertaking, Abingdon OX14 3EA, Oxfordshire, UK
(*) MPI for Plasma Physics, D-85748, Garching, Germany.

1. Introduction

One of the reference ITER operating scenarios [1] is a high confinement regime with H_{93} =0.9 to 1, $Z_{eff} \leq 1.8$ and plasma density at or above the Greenwald density limit (GDL) in steady state. However, as reported already by JET [2] and other Tokamaks [3], the plasma steady state density of ELMy H modes saturates at values below the GDL, due to a progressive loss of confinement (H mode density limit). Dedicated experiments have been carried out in the JET Mark II (MkII) divertor campaign to study the confinement of Type I ELMy H-modes at high density, under steady state conditions (t>4 τ_E).

The basic type of plasma studied is a 2.5MA/2.5T discharge (q_{95}=3.4) with 12 MW of Neutral Beam injected power, where D_2 gas fuelling scans were performed. The experiment studied the effects of the magnetic configuration and divertor plasma geometry, including low and high triangularity discharges (Δ = 0.2 and 0.3), and variation of the position of the separatrix (horizontal or vertical plates of the divertor).

Confinement data have been compared to the ITERH93-P ELM-free scaling for ELMy discharges (τ_{ELMy}=0.85 $\tau_{ELM\text{-}free}$). The plasma stored energy is corrected for the fast ion contributions, unless otherwise stated, and fast ion orbit losses are taken into account. For all the pulses analysed, the fast energy fraction is small and varies between 15% at low densities (≈4x10^{19} m^{-3}) to approximately 5% for densities above 7x10^{19} m^{-3}.

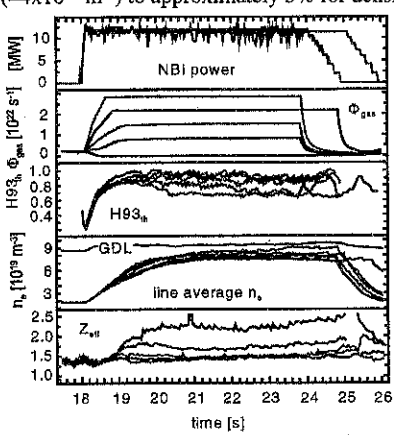

Figure 1: Typical D_2 gas scan for an high triangularity configuration. NBI power input, gas rates, H93, density (& Greenwald density) and Z_{eff}

2. General results

Fig. 1 shows the time traces for a series of discharges with high triangularity, where the gas input was varied from pulse to pulse from zero to 2.8x10^{22}s^{-1}. ELMs are produced during the whole heating phase, with a frequency increasing with fuelling from 12 to 46Hz. The energy and particle confinement deteriorate for the higher fuelling rates, and the line averaged density stays below the GDL. Similar results are observed in all configurations.

In general, the total fraction of radiated power varies with the plasma configuration, and is between 20-35% (no gas) and 50-60% (maximum fuelling). Increasing gas fuelling does not change the fraction of bulk radiation

(10-30%), while the X-point radiation increases steadily. Divertor MARFEs are not observed. The impurity content is low, with Z_{eff} usually around 1.3-1.4 with gas fuelling.

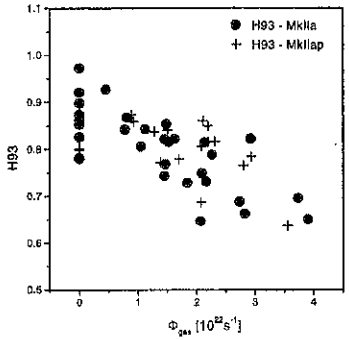

Figure 2: H93 before (MkIIa) and after (MkIIap) the closure of the by-pass leaks. Each point is a plasma discharge.

One effect of increasing the gas fuelling rate (and density) is an increase of the ELM frequency. We find that the total particle loss per ELM is a weak function of density and/or gas fuelling therefore as the fuelling is increased, the maximum achievable density saturates and then decreases. The high ELM frequency and loss of confinement result in a net loss of density. The maximum density achieved with gas fuelling saturates below the GDL and is determined by the balance between fuelling and confinement losses (see figs 3 and 4). The roll-over of n_e and H93 corresponds to a transition from Type I to Type III ELMs.

The effect of neutral pressure on the density limit and the confinement was studied before and after the closure of the by-pass leaks around the structure of the MkII divertor. The closure resulted in a decrease of the edge neutral pressure in the midplane (30%) while the divertor neutral pressure remained the same. However, the global confinement did not change appreciably (fig 2).

3. Effect of configuration on density and confinement

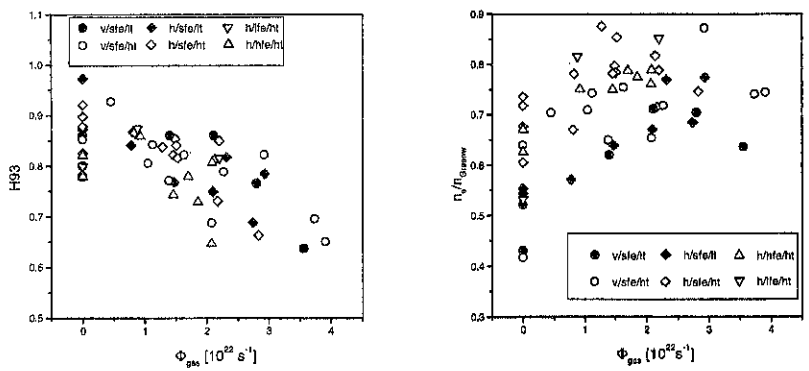

Figures 3 and 4: Thermal confinement degradation and maximum achieved density (expressed as a fraction of the GDL) for all the magnetic configurations studied (h-v = horizontal-vertical target, lt-ht = high-low Δ, lfe-sfe-hfe = low-standard-high flux expansion)

Fig 3 illustrates that the energy confinement does not depend on the magnetic configuration, whereas fig 4 shows that triangularity affects the maximum density achievable in steady state. In fact, for the same value of H93, the high triangularity discharges reach up to ≈ 90% of the GDL, while at low triangularity they achieve only 75%.

Most of the discharges analysed are characterised by an initial hollow density profile. This is also the case for no additional gas fuelling hence we conclude that edge recycling is responsible for the hollow profiles. The effect of recycling is evidenced by the fact that the initial density rise is about twice the beam fuelling, also in the absence of additional gas fuelling. Usually, the density profile fills up during the discharge and is flat in steady state. In some cases however, (medium gas fuelling, high Δ), the steady state n_e profile peaks. For these discharges, the GDL is exceeded locally in the central 10% of the plasma volume, while the edge density and the overall average density remain below the Greenwald density.

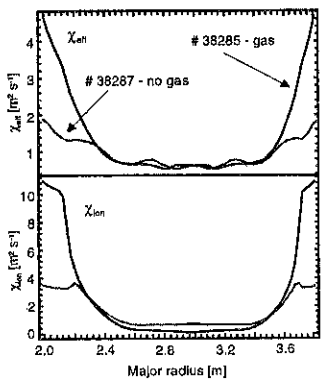

Figure 5: Radial profiles of χ_{eff} and χ_{ion} calculated by TRANSP.

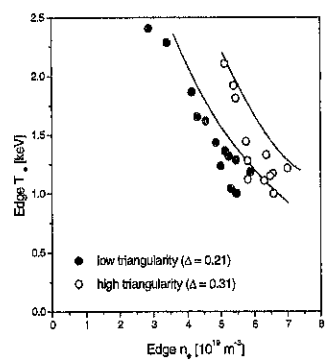

Figure 6: Empirical stability plot for Type I ELMs in low and high Δ discharges, in steady state.

4. TRANSP code analysis.

Figure 5 illustrates the results of TRANSP simulations of two discharges, on the horizontal plates and at low Δ, with zero and high gas fuelling (2.7×10^{22} s^{-1}), with H93(no gas)=0.83 and H93(gas)=0.69. The calculated profiles of the transport coefficients show that the lower confinement of the fuelled discharge is accounted for by enhanced energy transport in the edge (outermost 20% of the plasma radius), while the central confinement is not affected. This result seems to contradict the Kotschenreuther-Dorland model [4].

There are indications that the change in transport occurs mainly in the ion channel. Additional TRANSP runs were carried out to test the sensitivity of these results to the assumptions on particle recycling. These simulations, where the energy of the recycling particles or the particle confinement time were varied (fixed τ_P or $\tau_P \propto \tau_E$), confirm that the changes in the edge transport are relatively insensitive to the assumptions on the edge recycling in the code.

5. ELMs and edge parameters

The pedestal electron density and temperatures have been analysed for gas scans at low and high triangularity. In the edge n_e/T_e diagram [5,6], the experimental stability limit for type I ELMs is found to increase with plasma triangularity (i.e. shear), as expected (fig 6). Moreover, as shown in fig 7 for a gas scan (subset of fig 6), there is a correlation between the confinement of a discharge and its position in the stability diagram, with low confinement corresponding to a cool and dense edge. In fact, the increase of the gas fuelling results in the rise of the edge density at the expense of the edge temperature, at approximately constant pressure. The lower confinement point shown in the figure corresponds to a change from type I to type III ELMs. The crucial role of the edge temperature is confirmed by the analysis of the

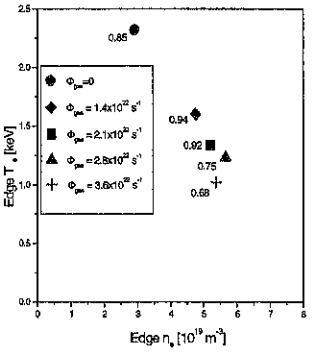

Figure 7: Variation of H93 for a gas scan at low Δ. H93 is calculated without subtraction of the fast ions energy.

time evolution of the edge n_e and T_e for low and high Δ discharges. This shows that for low Δ, n_e and T_e increase similarly between ELMs, until the stability limit is reached, whereas for high Δ, the pedestal temperature clamps after an initial rise, and the stability limit is reached due to the increase in n_e. The clamping of T_e is correlated with the occurrence of high frequency MHD modes (60-80 kHz), possibly located in the edge. The clamping of the edge temperature is consistent with the observation that high Δ plasmas have a lower energy confinement between ELMs than low Δ discharges.

In the high density ELMy H modes, partial detachment at the inner divertor is observed between ELMs. The degree of detachment [7,8] is quite low in all cases and there is no unique correlation between detachment and confinement degradation. At high triangularity, some detachment can be sustained without loss of confinement.

6. Summary

The H mode density limit is a confinement limit. The decrease in energy confinement at high density cannot be explained by the loss of fast ion contributions (typically around 10% or less). The maximum plasma density achieved in H mode is ≈ 90% of the GDL, with H93 ≈ 0.75 - 0.8. Discharges with high triangularity (edge shear) reach higher densities than low triangularity plasmas, for the same global confinement.

The core confinement of high density, low edge temperature pulses (H93=0.65) is comparable to the unfuelled reference case (H93>0.83), and the reduced confinement is accounted for by the enhancement of the edge transport (outer 20% of plasma radius).

Experimental data in steady state discharges confirm that the edge stability for type I ELMs increases with edge shear. The degradation of confinement is related to a trajectory in the n_e/T_e space toward low pedestal temperature, consistent with the existence of a minimum critical edge temperature for H mode confinement.

Clamping of the edge T_e between ELMs is observed in high triangularity discharges. In this case, the stability limit is determined by the density rise between ELMs, and not by re-heating. Divertor detachment and MARFE formation do not account for the observed loss of confinement.

References

[1] R Aymar and the ITER Team, IAEA -CN-64/O1-1, 16th IAEA Fusion Energy Conf., Montreal(Canada), 1996
[2] G Saibene et al, Journal of Nuclear. Materials, in press.
[3] M Kaufmann and the ASDEX Upgrade Team, IAEA-F1-CN-64/O1-5, as ref. [1]
[4] M Kotschenreuther and W Dorland, Communication to FESAC ITER Confinement reviewers, 14/02/1997
[5] H Zohm et al, IAEA-F1-CN-64/A5-1, as ref. [1]
[6] J Lingertat et al, these proceedings
[7] A Loarte et al, submitted to Nuclear Fusion.
[8] R D Monk et al, these proceedings.

Most of the discharges analysed are characterised by an initial hollow density profile. This is also the case for no additional gas fuelling hence we conclude that edge recycling is responsible for the hollow profiles. The effect of recycling is evidenced by the fact that the initial density rise is about twice the beam fuelling, also in the absence of additional gas fuelling. Usually, the density profile fills up during the discharge and is flat in steady state. In some cases however, (medium gas fuelling, high Δ), the steady state n_e profile peaks. For these discharges, the GDL is exceeded locally in the central 10% of the plasma volume, while the edge density and the overall average density remain below the Greenwald density.

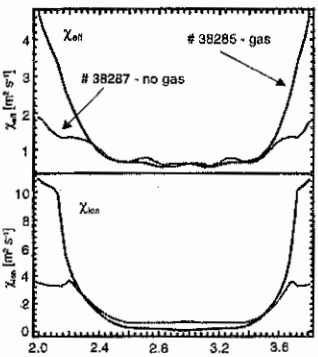

Figure 5: Radial profiles of χ_{eff} and χ_{ion} calculated by TRANSP.

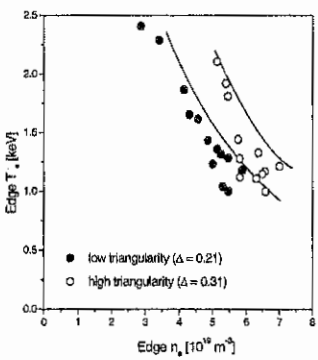

Figure 6: Empirical stability plot for Type I ELMs in low and high Δ discharges, in steady state.

4. TRANSP code analysis.

Figure 5 illustrates the results of TRANSP simulations of two discharges, on the horizontal plates and at low Δ, with zero and high gas fuelling (2.7×10^{22} s^{-1}), with H93(no gas)=0.83 and H93(gas)=0.69. The calculated profiles of the transport coefficients show that the lower confinement of the fuelled discharge is accounted for by enhanced energy transport in the edge (outermost 20% of the plasma radius), while the central confinement is not affected. This result seems to contradict the Kotschenreuther-Dorland model [4].

There are indications that the change in transport occurs mainly in the ion channel. Additional TRANSP runs were carried out to test the sensitivity of these results to the assumptions on particle recycling. These simulations, where the energy of the recycling particles or the particle confinement time were varied (fixed τ_P or $\tau_P \propto \tau_E$), confirm that the changes in the edge transport are relatively insensitive to the assumptions on the edge recycling in the code.

5. ELMs and edge parameters

The pedestal electron density and temperatures have been analysed for gas scans at low and high triangularity. In the edge n_e/T_e diagram [5,6], the experimental stability limit for type I ELMs is found to increase with plasma triangularity (i.e. shear), as expected (fig 6). Moreover, as shown in fig 7 for a gas scan (subset of fig 6), there is a correlation between the confinement of a discharge and its position in the stability diagram, with low confinement corresponding to a cool and dense edge. In fact, the increase of the gas fuelling results in the rise of the edge density at the expense of the edge temperature, at approximately constant pressure. The lower confinement point shown in the figure corresponds to a change from type I to type III ELMs. The crucial role of the edge temperature is confirmed by the analysis of the

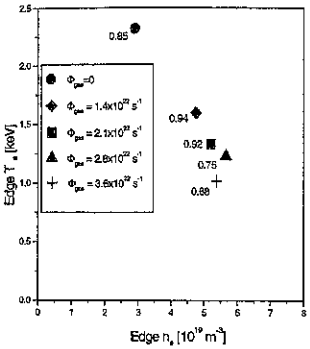

Figure 7: Variation of H93 for a gas scan at low Δ. H93 is calculated without subtraction of the fast ions energy.

time evolution of the edge n_e and T_e for low and high Δ discharges. This shows that for low Δ, n_e and T_e increase similarly between ELMs, until the stability limit is reached, whereas for high Δ, the pedestal temperature clamps after an initial rise, and the stability limit is reached due to the increase in n_e. The clamping of T_e is correlated with the occurrence of high frequency MHD modes (60-80 kHz), possibly located in the edge. The clamping of the edge temperature is consistent with the observation that high Δ plasmas have a lower energy confinement between ELMs than low Δ discharges.

In the high density ELMy H modes, partial detachment at the inner divertor is observed between ELMs. The degree of detachment [7,8] is quite low in all cases and there is no unique correlation between detachment and confinement degradation. At high triangularity, some detachment can be sustained without loss of confinement.

6. Summary

The H mode density limit is a confinement limit. The decrease in energy confinement at high density cannot be explained by the loss of fast ion contributions (typically around 10% or less). The maximum plasma density achieved in H mode is ≈ 90% of the GDL, with H93 ≈ 0.75 - 0.8. Discharges with high triangularity (edge shear) reach higher densities than low triangularity plasmas, for the same global confinement.

The core confinement of high density, low edge temperature pulses (H93=0.65) is comparable to the unfuelled reference case (H93>0.83), and the reduced confinement is accounted for by the enhancement of the edge transport (outer 20% of plasma radius).

Experimental data in steady state discharges confirm that the edge stability for type I ELMs increases with edge shear. The degradation of confinement is related to a trajectory in the n_e/T_e space toward low pedestal temperature, consistent with the existence of a minimum critical edge temperature for H mode confinement.

Clamping of the edge T_e between ELMs is observed in high triangularity discharges. In this case, the stability limit is determined by the density rise between ELMs, and not by re-heating. Divertor detachment and MARFE formation do not account for the observed loss of confinement.

References

[1] R Aymar and the ITER Team, IAEA -CN-64/O1-1, 16th IAEA Fusion Energy Conf., Montreal(Canada), 1996
[2] G Saibene et al, Journal of Nuclear. Materials, in press.
[3] M Kaufmann and the ASDEX Upgrade Team, IAEA-F1-CN-64/O1-5, as ref. [1]
[4] M Kotschenreuther and W Dorland, Communication to FESAC ITER Confinement reviewers, 14/02/1997
[5] H Zohm et al, IAEA-F1-CN-64/A5-1, as ref. [1]
[6] J Lingertat et al, these proceedings
[7] A Loarte et al, submitted to Nuclear Fusion.
[8] R D Monk et al, these proceedings.

Impurity transport studies for JET Hot-ion H-mode and Optimised Shear discharges

R. Giannella, H. Chen, B. Alper, I. Coffey[+], G.A. Cottrell, C. Gormezano, N.C. Hawkes[+], L.C. Ingesson, L. Lauro-Taroni, N.J. Peacock[+], A.C.C. Sips, F. Soldner, B. Tubbing, K-D. Zastrow*

JET Joint Undertaking, Abingdon, Oxfordshire, OX14 3EA, UK
**Imperial College, London, SW7 2BZ, UK*
[+]UKAEA/Euratom Fusion Association, Culham, Abingdon, OX14 3DB, UK

INTRODUCTION

The study of the relationship between fluxes and their conjugate gradients yields a direct test of *a)* the dependence of fluxes on gradients, *b)* the linearity of their relationship and *c)* the presence and relative importance of non-diffusive thermodynamic forces (convective effects). Using laser-injection of non recycling impurities, it was possible *in L-mode*, essentially unperturbed, steady discharges to confirm the validity of the diffusive hypothesis (i.e. points *a)* and *b)*) and to ascertain the dominant role of diffusion with respect to convection in those discharges[1,2].

This paper describes some initial interpretative analysis performed with laser-injection of non recycling impurities in enhanced confinement régimes. In the pulses described here, the plasma could not be kept in a stationary state but evolved considerably during the experiment.

HOT-ION H-MODE

Hot-ion H-mode discharges usually enjoy an extended (1-2s) ELM-free phase with high energy and particle confinement. During this phase, characterised by fast plasma energy and density rises, the impurity residence time in the discharge is much longer (typically > 1 s) than in L-mode discharges. Because of this the analysis can only be extended to the impurity ingress phase, as usually the high confinement is lost while the inward propagation of the injected impurities is still in progress. An important effect is the tendency of medium-Z impurities to assume a poloidally asymmetric distribution due to the centrifugal force [3,4] induced by the rapid toroidal rotation of these plasmas.

Tomographic reconstruction of the soft X-ray emissivity was obtained by further developing a technique earlier applied to bolometer data from ASDEX-U and JET [5]. In order to extract the incremental soft X-ray emissivity $\Delta\varepsilon$ induced by the injected impuritya linear extrapolation of the emissivity measured prior to the time of the injection t_0 is subtracted from the actual measured emissivity.

To analyse the *radial* transport we need the *flux-surface average* of the injected impurity density, $\langle n_{imp} \rangle$. The radial coordinate ρ, labelling the flux surface S, was chosen as the distance between the magnetic axis and the outer intersection of S with the magnetic axis' plane. This choice is relevant for the actual value of the diffusion coefficient D and of the *circular-equivalent diffusion coefficient* $\mathrm{D}=\langle|\nabla\rho|^2\rangle D$ used in this paper. We assume that the electron density, $n_e(\rho,t)$, and temperature, $T_e(\rho,t)$, of the plasma are constant on S and therefore $\Delta\varepsilon(\rho,l,t)$ is proportional to $n_e(\rho,t)\cdot n_{imp}(\rho,l,t)$ through a coefficient $Q_f(\rho,t)$ that doesn't depend on the poloidal coordinate l. $\langle n_{imp} \rangle$ is therefore simply obtained as $\langle\Delta\varepsilon\rangle/(Q_f(\rho,t)n_e(\rho,t))$.

The time dependence of Q_I is found by iteratively running simulations of the transport, alternated with iterated determinations of transport profiles based on the successive evaluations of $\langle n_{imp} \rangle$ using the equation above, as described in [2].

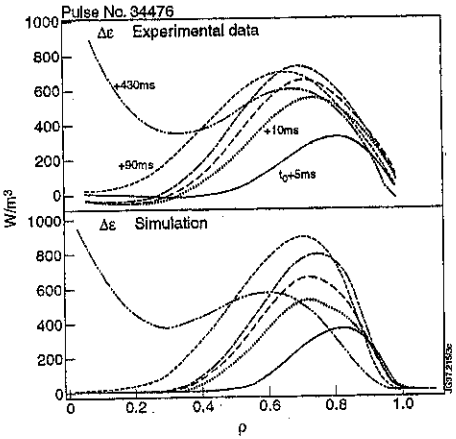

Fig. 1 Flux-surface averaged incremental soft X-ray emissivity from injected Ni for a hot-ion H-mode JET pulses.

During an initial short phase following the injection propagation across the plasma outer layers occurs on a very fast time scale. Fig. 1 illustrates the case of a pulse where an ELM is induced by the impurity injection. During the first 10 ms following the ELM injected Ni reaches $\rho \approx 0.7$: the diffusivity is very high (Fig. 2) ($D \sim 4$ m^2/s around $\rho \approx 0.7$-0.8) and the convection velocity appears directed outward. The duration of the enhanced transport phase, following the ELM instability is not longer than ~ 10 - 12 ms and the transition to the slow transport régime occurs within a few milliseconds.

Thereafter the propagation of impurity slows strongly The core region is only reached by the impurities after several hundreds of milliseconds. At these times any effects triggered by the injection itself are already extinguished throughout the discharge. The impurity propagation in this region is driven by convective effects and may in some cases lead to mild peaking of the Ni density profile in the centre of the discharge ($n_{Ni}(0)/\langle n_{Ni} \rangle < 2$). During the quiescent phase, the Ni diffusivity is small across the discharge ($D \leq 0.2$ m^2/s) and very low in the inner core ($D \sim 0.05$ m^2/s), where it is close to the neoclassical predicted values.

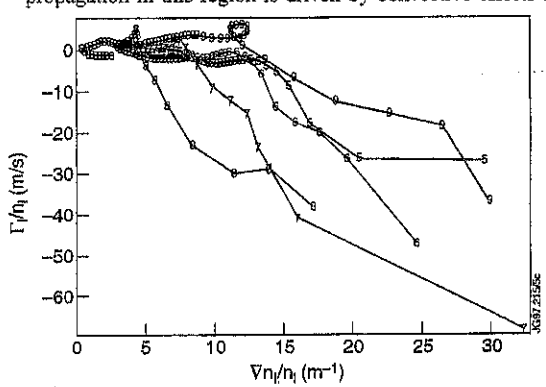

Fig. 2 Normalised Ni fluxes vs. the normalised Ni density gradients at five radial positions in a hot-ion H-mode pulse during the first 250 ms following Ni injection. Curve markers 5, 6 ... 9 indicate r=0.5, 0.6 ... 0.9. During a short initial phase (lasting ~12 ms after the ELM) the data are consistent with a strong diffusivity (i.e. strong slope of the curves). Thereafter the fluxes are strongly reduced.

The initial enhancement of the transport in the plasma outer layers is considerably smaller when no ELM is triggered by the injection.

OPTIMISED SHEAR PLASMAS

The Optimised Shear (OS) plasma is considered a good candidate for improving the tokamak concept [6]. JET experiments show that an Internal Transport Barrier (ITB) is formed in these cases at radii much further inside the plasma (up to $\rho \sim 0.5$ to 0.7) than in hot-ion H mode plasmas (about $\rho \geq 0.9$). The ion thermal diffusivity drops significantly inside the ITB and high fusion performance is obtained.

Two different OS discharges are discussed here in detail. The first discharge (38441) had a milder pressure gradient. Its ion temperature profile, that was still growing fast at the time of the Ni injection, reached a nearly-steady state within ~ 50 to 100 ms thereafter. We see that: a) The initial inward propagation of Ni is not hindered by the presence of an ITB. The tomographic reconstruction of SXR emission shows that, even in the presence of the ITB, Ni reaches the centre of plasma very quickly (within about 70 ms). The core concentration of Ni peaks at approximately $t_0 + 130$ ms (Fig. 3) and then decays exponentially with a time constant of ~300 ms. The line radiation of the highly ionised Ni ions (Ni^{24+}, Ni^{25+} and Ni^{26+}) shows very fast rise and decay features (Fig. 4). There are two different phases: a fast ingress phase with a strong (V = 20-30 m/s) inward convection localised outside the ITB (at $\rho \sim 0.5$); this convection drops rapidly to very low values and during the depletion phase, when the ion temperature growth has come to a halt, no important convection is acting on Ni any more. b) The C density profile $n_C(\rho)$ remains hollow and very slowly becomes less hollow; the greatest gradient of $n_C(\rho)$ practically coincides with the location of the ITB. The carbon diffusivity in the core is very low ($D \sim 0.1\ m^2/s$) and close to neoclassical.

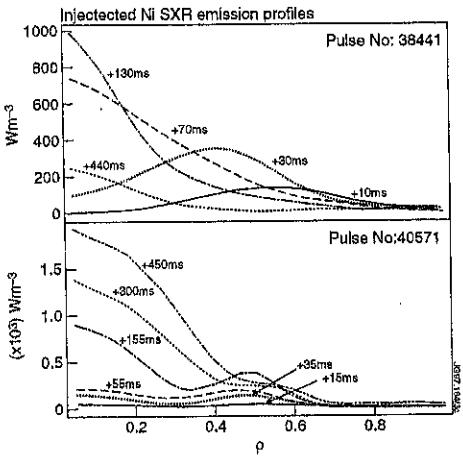

Fig. 3 Flux-surface averaged incremental soft X-ray emissivity from injected Ni for two optimised-shear JET pulses.

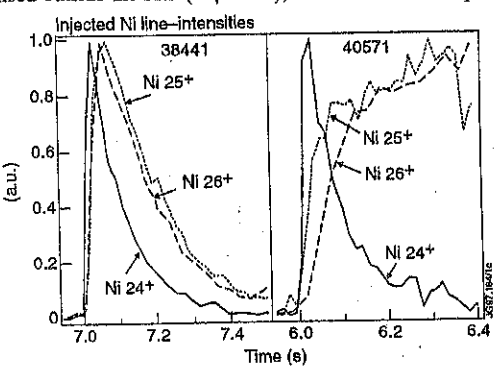

Fig. 4 Time evolution of line intensities from three highly ionised Ni ions for two JET pulses.

The other discharge (40571) has a stronger pressure gradient. We see that: a) The tomographic reconstruction of SXR emission shows that the injected Ni impurity progressively accumulates in the core (Fig. 3). This process is seen to continue until the confinement régime changes due to the onset of H-mode conditions at the plasma edge ~450 ms after the injection. A further confirmation of the convective nature of this process is given by the time evolution of the line radiation from Ni^{24+} and Ni^{25+} (Fig. 4). The line intensity from Ni^{24+} peaks at ~ t_0 + 30 ms and then rapidly decays while the signal from Ni^{25+} grows up to a nearly steady value on the same time scale and then does not decay but keeps increasing slightly. This is very surprising because the temperature dependence of the emission coefficients for these two ions is very close. The difference can only be explained by a strong modification of the Ni profile's shape at the radial position (ρ = 0.6-0.7) where the emission shells of these two ions are located. The required values of convection velocity are about 15 m/sec b) The intrinsic C impurity also shows a progressive peaking of n_{Ni} towards the centre with the n_C profile evolving over ~ 1s from a moderately hollow profile to a moderately peaked profile. Also for this pulse, the comparison of Ni (more pronounced and faster central density peaking) and C (slower and milder density peaking) indicates a marked Z dependence and therefore a possible electrostatic nature of the convective process.

A common feature to optimised-shear discharges is that no appreciable poloidal asymmetry is observed although the toroidal velocity is comparable to that measured in hot-ion H-mode discharges.

CONCLUSIONS

The transient nature of the pulses analysed made the interpretative transport analysis for injected impurities more complicated: a) signals from injected impurity are difficult to extract from the time-changing background; b) only the ingress phase is available for study; c) the impurity transport itself is often seen to change due to the changes of the main plasma.

ELM instabilities in hot-ion H-modes appear to be followed by a short lived (~10 ms) phase of high transport suggesting the presence of strong diffusion for the injected impurities in the outer regions of the discharge. The quiescent hot-ion H-mode phase is characterised by very low, but higher than neoclassical (by a factor of ~ 2 to 10), diffusion.

Strong poloidal asymmetries of the distribution of the injected Ni, induced by the fast plasma rotation, appear in hot-ion H-modes, but not in optimised-shear plasmas.

Strong inward convection is observed in OS plasmas for laser blow-off injected nickel.

Convective effects are much smaller on the intrinsic carbon impurity; this difference with Ni might be due to the different ion charge, if due to an electrostatic effect, but evidence on the radial electric field is so far inconclusive.

This work was partly funded by the UK Department of Trade and Industry.

1 R. Giannella, L. Lauro-Taroni, M. Mattioli et al. *Nucl. Fusion* 34 (1994) 1185.
2 R. Giannella and L. Lauro-Taroni Proc 21st EPS Conf. on Contr. Fus. and Pl. Phys., Montpellier 1994, Vol 3 p. 1260.
3 R. Giannella, M. Christensen, R. De Angelis et al. Proc. 19th EPS Conf. on Contr. Fus. and Pl. Phys. Innsbruck 1992, Vol 1 p. 279.
4 B. Alper, A.W. Edwards, R. Giannella et al. Proc 23rd EPS Conf. on Contr. Fus. and Pl. Phys., Kiev 1996, Vol 1 p. 163.
5 C. Fuchs, K.F. Mast, A. Hermann, K. Lackner Proc 21st EPS Conf. on Contr. Fus. and Pl. Phys, Montpellier 1994, Vol 3 p. 1308.
6 The JET Team (*presented by C. Gormezano*), 16th IAEA Fusion Energy Conference, Montreal 1996.

Studies of impurity production mechanisms in the JET divertors.

G McCracken, H Y Guo, R Barnsley, I Coffey, S J Davies, M von Hellerman, L D Horton, H Jäckel, J Lingertat, C Lowry, A Loarte, A C Maas, C F Maggi, A Meigs, G F Matthews, R D Monk, R Simonini, M F Stamp, P C Stangeby[1], A Tabasso, G Vlases, K-D Zastrow.
JET Joint Undertaking, Abingdon OX14 3EA, UK
[1]University of Toronto, Institute for Aerospace Studies, M3H 5T6, Canada

Introduction.

The JET programme has a series of divertors of increasingly closed geometry, from the open design first introduced in 1990 to the Mk IIGB (gas box) planned for 1998. In the present paper we have compared the impurity behaviour in the Mk I, MkIIA and Mk IIAP divertors. The Mk I divertor, with new divertor coils mounted inside the vacuum vessel, was installed in 1994. It had horizontal target plates and the flux surfaces were rather far from the vertical side plates. It was operated first with graphite target plates (Mk IC) and later with Be targets. Mark IIA was installed in 1995/6 and operated in the 1996 campaign. The graphite target plates are domed and the vertical side plates moved in to follow the flux surfaces and make the divertor more closed for horizontal target operation. The design allows the strike point to be on the vertical side plates, as in MkI. The Mk IIA had "bypass" leakage paths which allowed gas to flow from the subdivertor region back into the main chamber. In Oct 1996 these bypasses were blocked to prevent the neutral gas backflow. Operation with Mk IIAP (Plugged) started in Nov 1996 and is the present configuration. This paper reviews the results of the impurity measurements and presents some initial modelling using the DIVIMP/ NIMBUS suite of codes.

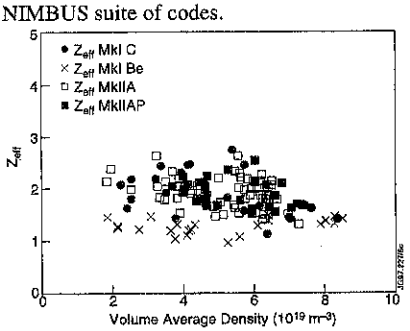

Fig 1. Variation of Zeff in an ELMy H-mode with 12 MW NBI, for different divertor configurations

Experimental Results.

Data are taken from a series of ELMy H-mode discharges with ~12 MW NBI heating, which are from the Divertor Task Force steady-state data base. The results for the global parameters, Z_{eff} and P_{rad}, as a function of density are shown in figs 1 and 2. Within the scatter of the data there is no difference in either Z_{eff} or P_{rad} between Mk IC, Mk IIA and Mk IIAP. However the results for the Mk I Be target show a decrease in Z_{eff} (ΔZ_{eff}~0.6) and a slight decrease in P_{rad} at higher densities. Z_{eff} does not depend much on n_e, implying that n_{imp}/n_e is ~ constant. $P_{rad} \propto n_e^2$, implying that $n_{imp}/n_e\, L(T_e)V$ =constant, where $L(T_e)$ is the radiation function and V is the radiating volume. Measurements of the intrinsic impurity concentrations have been made for carbon with the charge exchange diagnostic (KS4) and for nickel with the X-ray spectrometer (KX1). The carbon concentration is in the range 1 to 3% which usually accounts for all the observed Z_{eff}.

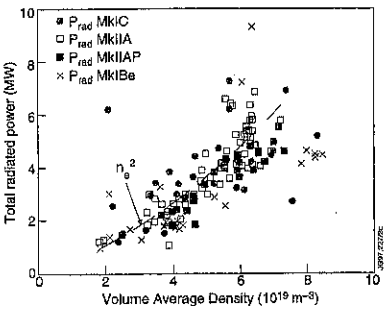

Fig 2. Dependence of the P_{rad} on density in ELMy H-modes for 4 different divertor xconfigurations

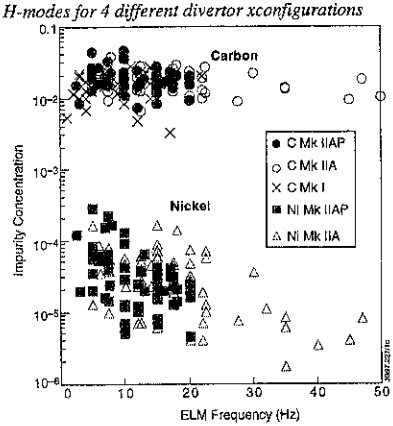

Fig 3. Intrinsic impurity dependence on ELM frequency in ELMy H-mode with 12 MW NBI.

The Ni concentration is normally less than 10^{-4} and thus makes an insignificant contribution to both Z_{eff} and P_{rad}. Generally both the carbon and the nickel densities increase with plasma density so that their concentrations are constant. As with the global parameters, Z_{eff} and P_{rad}, there is little difference between Mk I, Mk IIA and Mk IIAP. The Mk I campaign with the Be target had a significantly lower carbon concentration, consistent with the lower Z_{eff}, but the dominant impurity was still carbon. The Be concentration, measured by charge exchange, was $\leq 1\%$, which is near the limit of detection.

The effect of varying the triangularity, the flux expansion to the target and changing from the horizontal to the vertical target has been studied using a mid-plane CVI line (3.374 nm) during the Mk II campaign. There is no discernible effect (<50%) in changing from horizontal to vertical target or in changing the flux expansion. However there is typically an increase of a factor 2 in the CVI line intensity changing from low to high triangularity. This is correlated with the decrease in the ELM frequency and increase in ELM size observed in high triangularity discharges. The concentrations are plotted as a function of ELM frequency in fig 3. There is a decrease of more than an order of magnitude in the Ni concentration as the ELM frequency increases from 5 Hz to 40 Hz. This effect is independent of how the ELM frequency is changed: triangularity, gas puffing or change from H to D plasmas. The same effect is seen in the carbon concentration but to a lesser degree. In the case of nickel there are clear signs of accumulation in the core between ELMs which is enhanced by the longer period between ELMs. The low ionization states are enhanced during the larger low frequency ELMs, possibly due to more nickel influx from the larger ELMs.

DIVIMP/NIMBUS Modelling of JET Discharges

DIVIMP [1] is a Monte Carlo code which follows impurities in a specified background plasma. Impurity cross field and parallel transport, ionization and heating are all included. NIMBUS [2] is a linked Monte Carlo code which follows the neutral hydrogen species. In the present case the background plasma in the scrape-off layer is generated with

an Onion Skin Model (OSM) [3] using the experimental measurements of n_e and T_e taken at the target with Langmuir probes. Atomic data from the ADAS codes [4] has been used.

The present paper reports the modelling of a typical ohmic discharge (#38423) with I_p=2.5 MA, n_e= $2x10^{19}$ m^{-3}, B_T =2.5 T. Work on the ELMy H-modes described in the first section is in progress and will be reported later. A wide range of absolutely calibrated spectroscopic diagnostics have been modelled including a flux camera with optical filters (KL2) viewing across the divertor targets vertically from the top, two visible survey spectrometers looking at the inner and outer targets(KS3), two vuv spectrometers which scan poloidally across the divertor and the inner wall using a rotating mirror (KT1) and a visible

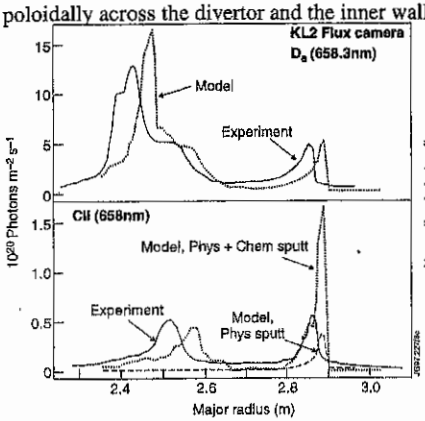

Fig4. Comparison of the radial profiles of $D\alpha$ and CII computed from DIVIMP/NIMBUS with experimental data (KL2), for an ohmically heated discharge (#38423)

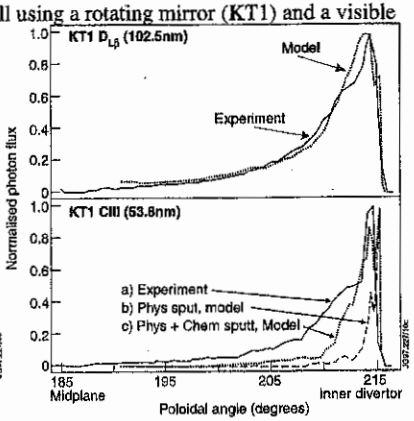

Fig 5. Comparison of poloidal distribution of $D_{L\beta}$ and CIII computed from DIVIMP/NIMBUS with experimental data from KT1 (#38423)

and UV spectrometer pair which monitor the outer target with high spatial resolution, covering the wavelengths from 200 to 700 nm (KT3A/B). The modelling has concentrated on reproducing the emission near the targets ie the low charge states of carbon (CII, CIII, CIV) and the D_α line . CII and D_α profiles from the Flux Camera are compared with the model in fig 4. The strong asymmetric D_α radiation observed at the inner target may be explained by recombination radiation. Due to uncertainties in the probe data at the inner target the T_e profile was adjusted approximately fit the D_α radiation. This T_e profile then was used to model the carbon radiation. The outer target signals are calculated using the measured T_e profiles. The CII model includes both physical and chemical sputtering [5]. The results from the upper horizontal KT1 spectrometer are compared with the code results in fig 5 using the same Te profiles as for fig 4. The D_α profile fits well, showing a large contribution to the D influx up the inner wall to the midplane. The corresponding CIII fluxes have been modelled with and without chemical sputtering. The physical sputtering alone underestimates the influx from the inner wall. With chemical sputtering the flux is higher though it still underestimates the experimental data. The photon fluxes from D_α and carbon charge states CII, CIII, CIV at the inner and outer targets have been modelled and compared to experiment,

Table I Comparison of the code result with the measured fluxes at the inner and outer target (KS3 spectrometer).

	D_α	CII	CIII	CIV
	10^{18} photons/m^2/s/ster			
Inner Target (Exp)	39	0.90	2.7	0.030
Inner Target (Model)	35	0.45	4.8	0.023
Outer Target (Exp)	17	1.03	4.1	0.04
Outer Target (Model)	7	0.84	6.2	0.15

as shown in Table I. There is agreement within a factor of 2 to 3, which is as good as can be expected given the uncertainties in the measured plasma parameters, the OSM modelling and the atomic data.

Summary

Carbon is the main impurity under most operating conditions, with a concentration in the range ~ 1 to 3%, depending slightly on input power, configuration and gas flow rate. Nickel (the main metal impurity) is normally negligible. There was no effect on the central impurity densities (C or Ni) due to plugging the divertor bypass leaks. Mk IC results are similar to Mk II. However the Mk IBe has lower Z_{eff} and P_{rad}. The dominant impurity with the MkI Be targets is still carbon [6], with Be being typically ≤1%. This may be due tothe Be targets becoming contaminated with carbon or that the main source of the carbon comes from the walls of the main chamber as illustrated by the observations and modelling in fig 5.

In high triangularity discharges, with ELM frequencies ~ 5Hz, the nickel concentration increases to ~2×10^{-4}. This appears to be due to metal injection by large ELMS and to impurity accumulation. The high confinement associated with low ELM frequency in long pulse discharges can result in carbon concentrations ~3%, equivalent to nearly 20% dilution

The spatial distribution of the radiation from deuterium and carbon (CII, CIII, CIV) at the target and the inner wall have been modelled for ohmic discharges. Good agreement is obtained at the outer target using the plasma n_e and T_e distribution derived from the target probe data. At the inner target it is necessary to tailor the T_e profile to obtain the correct D_α distribution. The model shows that, for this case, the chemical sputtering is dominant making a much larger contribution to the primary flux and to the core contamination than the physical sputtering. However the impurities are treated as 0.1 eV atoms rather than CD_4 and no allowance has been made for prompt redeposition due to breakup of the hydrocarbon molecules. The results from the KT1 spectrometer show that there is a large flux from the wall above the inner target. The DIVIMP/NIMBUS modelling reproduces this flux quite well but much more modelling is required for a wider range of discharges. The model shows that the flux from the inner wall is less well screened than that from the targets.

References

[1] P C Stangeby and D Elder, J Nucl. Mat., **196-198** (1992) 258

[2] E Cupini, A De Matteis and R Simonini, NET Report 9, EUR XII-324/9 (1983)

[3] P C Stangeby et al., 12th PSI, J Nucl. Mat., **241-243** (1997) to be published.

[4] H P Summers, Atomic Data and Analysis Structure Users Manual JET IR(94) 06

[5] B V Mech, A A Haasz and J W Davis, private communication, Mar 1997.

[6] C F Maggi, D Elder et al., 12th PSI, J Nucl. Mat., **241-243** (1997) to be published.

ELM Dynamics and Power Deposition in the JET divertor

E.Gauthier[1], A.Chankin, S.Clement, P. Coad, S. Davies, G.Fishpool, J.Lingertat, G. Mattews
JET Joint Undertaking, Abingdon, OX14 3EA, UK
[1]Association EURATOM-CEA sur la fusion contrôlée, CEA Cadarache, 13108 St Paul lez Durance, France

I. Introduction

Sublimation of the graphite tiles due to ELMs is expected to be the main limit to the lifetime of the ITER divertor. Multimachine scalings [1] show that type I ELM frequency decreases with the size of the machine while the product of the frequency and fraction of the stored energy lost per ELM increases with power. How this translates into surface heating depends on the duration of the heat pulse, the area of interaction and how much of the ELM energy is radiated. The dynamics of surface power deposition by type I ELMs are crucial for extrapolation to ITER.

II. Diagnostics.

For the first time, direct measurements of the power flux to the divertor during the ELM with high time resolution have been obtained in JET using a fast 2D infrared camera of 128x128 pixels, working in the 3-5 μm range. This camera looks at the divertor from the top of the torus, providing a space resolution of 3.7 mm/pixel or 7 mm/pixel, depending of the lens which was used. A full frame is acquired line by line and the exposure time can vary from 150 ns up to 16 ms. Due to the subscan capability and the high frame rate of this camera, time resolution of 15 μs has been achieved. More details about this diagnostics can be found elsewhere [2]. The power flux on the divertor tile is calculated from the surface temperature evolution by numerically solving the 2D heat conduction. The energy deposited on the divertor measured with this fast infrared camera has been compared with measurements of the plasma stored energy deduced from magnetic data.

III. Results and discussion.

A typical infrared image of the divertor, during an ELM in a NBI heated ELMy discharge is shown in figure 1, the increase of the temperature is unbalanced and much pronounced on the inner than on the outer part of the divertor. The inner and the outer strike zone can also be seen together with the shadowed area of about 10 cm in the toroidal direction, due to the height difference between tiles and the grazing angle of the magnetic field line with respect to the surface. During a type I ELM, a fast displacement of the plasma occurs [3], the power flux moves about 20 cm outward from the initial strike zone positions. The shift on the outer strike zone is not always observable as it is on the inner strike zone. Since no measurable increase of the temperature is observed in the scanned area during this displacement, the shift of the peak power must occur in a timescale shorter than 20 μs. A displacement of the power deposition takes place also on the toroidal direction, figure 2, and previously shadowed area may receive a large power flux during ELMs, due to the modification of the magnetic configuration.

Figure 3 shows the evolution of the peak temperature measured during type I ELMs with different time resolutions. Temperatures often exceed the experimental saturation level usually set at 1900°C but maximum temperature of 2250°C has been recorded in some occasions. The rise phase of the temperature is continuous and lasts about 130 μs. Independently of the resolution, the exposure time (in the range of 1 to 10 μs) is very small compared with the event

duration. As a consequence, the photon flux measurement is unaffected by the time resolution and the temperature deduced from it corresponds to an instantaneous temperature value.
From the surface temperature evolution, the power flux loading to the divertor is calculated, figure 4,assuming a toroidal symmetry but taking into account the shadowed area. The measured values of the thermo-physical properties of the carbon fibre composite tiles is used in the code. The peak power density exhibits a huge value of 4 GW/m2, which is a common value observed on type I ELM in JET with NBI heating but is several order of magnitude larger than peak power densities observed in Asdex-Up [4]. Although the ELM frequency is higher in Asdex Up (~50-160 Hz) than in JET (~10 Hz) and then, the lost energy per ELM is reduced[5], the large discrepancy between our results and the previous one requires some explanations. First of all, the power flux loading to the divertor is not directly measured but deduced from photon flux measurement and code calculation. So, either the ELM behaviour (and the photon flux) is drastically different in JET compared with Asdex-Up or the measurement and/or the code calculation induces the discrepancy. Looking at the experimental system and the code used in Garching [6], we believe that the deposited power during the fast transient events such as ELMs is underestimated in Asdex-Up, for three reasons: Most of the measurements have been done with a resolution and an exposure time of 256 μs which is twice the time required to reach the maximum temperature in JET, consequently, the temperature deduced from the average photon flux in Asdex is lower than the real maximum temperature. Then, the time resolution being larger than the ELM duration, the temperature evolution presents large jump from initial to maximum value within 1 frame, as we can see for similar conditions in JET (figure 3). The power flux calculated from such a temperature behaviour, plotted on figure 4, gives negative power when the time resolution is larger than the peak power duration.
To solve this problem, an infinity thin layer has been added to the top of the divertor tile in the code used at Garching. This modification in the structure of the material introduce an offset of the surface temperature during transient effect compared with the semi-infinite model. Thus, at a given surface temperature, the two layers model calculation provide a much smaller power flux (depending of the heat exchange coefficient between the two layers) than the semi infinite model.
The code used at JET gives exactly the same power deposition during ELM as the semi infinite model, as it is expected for such short events. A 3D plot of the power loading to the divertor as function of radial position and time is shown in figure 5 and a profile of the deposited energy, by integration of the power flux over time is plotted in figure 6, showing a peak energy density of 1 MJ/m^2 on the inner divertor. Then, space integration for both side of the divertor provide the total energy deposited on inner and outer divertor. Table I summarises the results obtained for several discharges. In all the cases, the total energy deposited on the divertor deduced from IR thermography is larger, by about a factor of three, than the drop of the stored energy deduced from the fast magnetic measurements. The origin of this discrepancy is not clear at the moment but some hypothesis can be given. The knowledge of the thermo-physical properties of the material is rather fair, in particular, the thermal conductivity is an average value over the two different components : the carbon fibre and the carbon matrix. How this composite material reacts on a very short heat pulse is unknown. We can expect a different surface temperature for each part. In such a case, due to the lack of space resolution and the non linear response of the photon flux with the surface temperature, the measured temperature will be governed by the low

thermal conductivity material. Such behaviour of the CFC tiles used in the Mk II divertor has been demonstrated in the JET Neutral Beam Test Bed [7], but extrapolation to the present situation in the tokamak would be very hazardous due to the number of unknown parameter.
Nevertheless, until further information is available, the "standard" thermo-physical properties of the CFC tiles are used in the code. The calculated power density deduced from IR measurements is in good agreement with the heat flux obtained by Borrass in his ELM model [8], moreover, the order of magnitude corresponds to what we would expected from other diagnostic measurements (drop of the stored energy ~ 0.3 MJ, timescale < 200 μs, wetted area ~$1m^2$: <P> ~ 1.5 GW/m^2).
Extrapolations to ITER based on our results and a multimachine scaling [1] give an energy deposition and an ELM frequency of about 30 MJ and 1 Hz, with a peak power flux in the range of 30 GW/m^2. This ELM behaviour implies an unacceptably high erosion rate for ITER divertor tiles. Since the ELM duration is about 100 μs, nearly all the incoming energy is used for sublimation and then, even a decrease of the ELM energy to 1% of the stored energy would not help significantly.

IV. Conclusions

A new 2D infrared camera developed at JET has been able to measure the surface temperature evolution of the divertor with a time resolution of 15 μs which has proved to be necessary for ELM analysis. The peak power deposition during a type I ELM lasts about 130 μs with a maximum value in the range of 5 GW/m^2, most of the ELM energy being deposited on the inner divertor. The power and energy deposited during ELMs is overestimated due to uncertainties in the CFC properties at the surface. Extrapolation based on this data suggest that ITER cannot be operated in a ELMy discharge with type I ELMs unless the energy per ELM, compared to the stored energy, can be reduced far below the minimum achieved in the present tokamaks.

V. References

[1] J. Lingertat et al, Proceedings of 4th Eur. Phys. Workshop, 11-13th dec. 1996, Stockholm.
[2] S. Clement, to be published.
[3] S. Ali-Arshad et al, Proceeding of 23 rd EPS conference, Kiev, (1996).
[4] A. Herrmann et al, J. Nucl. Mat.,220-222 (1995) 543.
[5] L. Horton et al, these proceedings.
[6] A. Herrman, private communication,3-4 feb. 1997.
[7] D. Ciric et al, Fusion Techn., (1994) 391.
[8] J. Lingertat et al, Proceeding of 12th PSI Conference, J. Nucl. Mat, to be published.

SHOT	Freq	Tmax	Pmax	Emax	W In	W out	W out	δW
elmy H-mode	(Hz)	(°C)	(GW/m2)	(MJ/m2)	(MJ)	(MJ)	(MJ)	(MJ)
40442	15	1280	2.7	0.6	0.93	0.53	1.47	0.3
	15	1340	2.7	0.46	0.66	0.31	0.97	0.3
40443	7	1630	3.4	0.87	1.18	0.45	1.63	0.45
	7	> 2000	4.1	0.72	1.18	0.5	1.69	0.4
40444	15	1480	3.4	0.39	0.81	0.56	1.38	0.3
	25	2070	3.7	0.81	1.24	0.63	1.88	0.55

Table 1. Summary of experimental values during ELMS with Freq : ELM's frequency, Tmax : max. temperature, Pmax : max. Power flux, Emax : max. energy flux, W in : energy deposited on inner divertor, W out : energy deposited on outer divertor, W tot : total energy deposited on divertor, δW : drop of the stored energy.

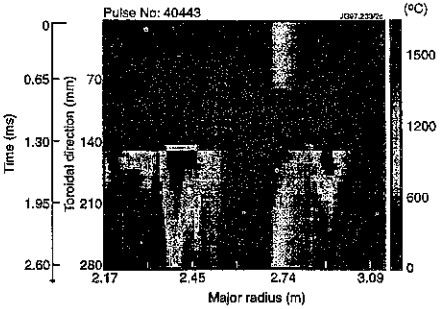

Fig. 1 Image of an elm; time goes from top to bottom due to the array scanning procedure.

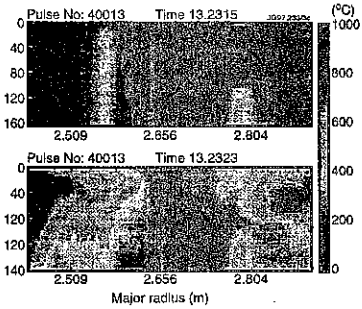

Fig. 2 "Ergodisation" of scrape off layer during an elm: power arrives to a normally shadowed area.

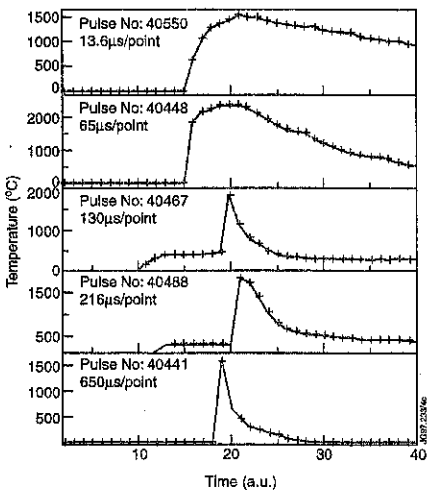

Fig. 3 Temperature evolution during elms with increasing time resolution

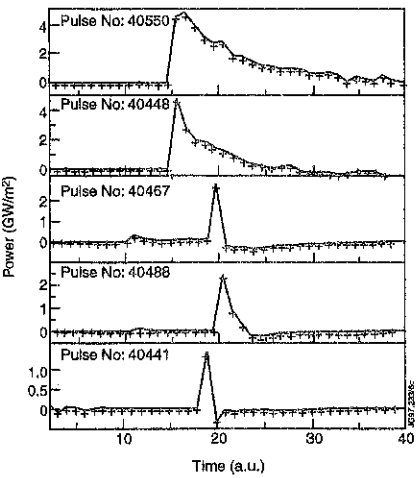

Fig. 4 Power deposition calculated from temperatue evolution in fig. 3.

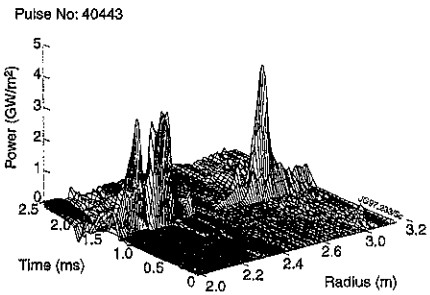

Fig. 5 3D plot of power deposited on the divertor during an ELM.

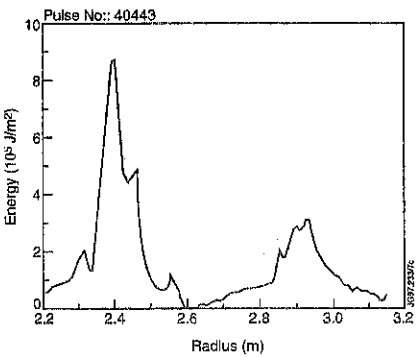

Fig. 6 Energy profile across the major radius.

Overview of JET Mark IIA divertor performance in ITER-relevant modes of operation

L.D. Horton for the JET Divertor Task Force and Divertor Physics Topic Group
JET Joint Undertaking, Abingdon OXON, U.K. OX14 3EA

Introduction

Over the last five years, the JET divertor programme has evaluated a series of different divertor geometries with increased closure to recycling neutrals. During 1994 and 1995 the first purpose-built divertor structure in JET was tested (Mark I). Mark I incorporated four in-vessel coils which provide flexible divertor configurations, carefully designed target tiles, and a cryopump in the volume beneath the divertor structure. In 1996/97 a more closed divertor structure was tested (Mark IIA). During a shutdown in October 1996, the leakage paths from the subdivertor volume back to the main plasma chamber were significantly reduced. We refer to the resulting divertor configuration as Mark IIAP (plugged).

The goal of our divertor programme is to define a scenario for combined divertor and core plasma performance acceptable for a reactor. Such a scenario must combine good core confinement ($H_{93}>0.9$), high core density (at or above the Greenwald value), and low core impurity content ($Z_{eff}<1.6$) with an acceptable power loading on divertor and other first wall components. In addition, helium exhaust rates must be sufficient to prevent poisoning the core plasma.

Two different lines of experiments have been followed: unseeded operation with large, separate ELMs, low impurity content, and good core confinement; and operation with a seed impurity which generates high radiant losses and low divertor power loading.

Performance without impurity seeding

With the flexibility provided by the four in-vessel divertor coils, it is possible to test a wide variety of magnetic configurations in JET. Variations in divertor flux expansion (and thus closure to neutrals), core triangularity, and target orientation (horizontal and vertical) have been tested systematically for ELMy H-mode plasmas at 2.5 MA, 2.5 T and with 12 MW of neutral beam heating. The principal influence of configuration is the effect of triangularity (or edge shear) on ELM frequency. Discharges with δ~0.2 and no fuelling other than by the neutral beams have an ELM frequency of about 15 Hz while discharges with δ~0.3 typically have an ELM frequency of 5-10 Hz. Despite this difference in ELM frequency the confinement of both low and high triangularity discharges with no additional gas fuelling is about 0.9 times the ITER93 ELM-free confinement scaling.

The density limit of ELMy H-mode discharges has been tested by adding gas fuelling to the fuelling provided by the neutral beams (Fig. 1). The density limit in H-mode is a particle confinement limit, as opposed to a radiative collapse such as that which sets the density limit in Ohmic and L-mode shots. The core confinement is degraded by the gas

fuelling to the point where the degradation in particle confinement outweighs the additional particle source and the effective fuelling efficiency becomes negative.

Measurements of the edge electron density and temperature [1] suggest that the addition of gas fuelling moves the discharge along a contour of constant pedestal pressure to lower temperatures and higher density until a minimum temperature is reached and the confinement is then strongly degraded. This is consistent with the idea that a minimum edge temperature is required to achieve and maintain an H-mode. Preliminary studies of edge parameters at higher plasma current [2] suggest that the operating space available between the lower, H-mode limit and the ELM limit narrows to the point where steady operation is difficult.

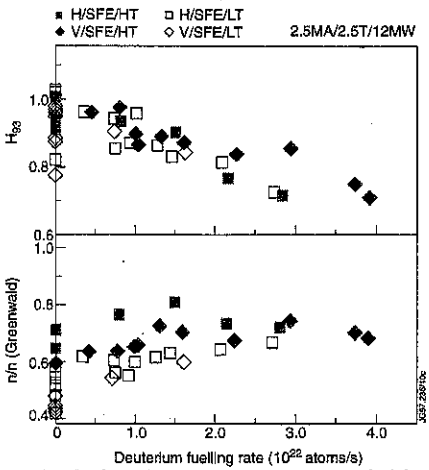

Fig. 1: The dependence of core confinement and of the line-averaged electron density on the gas fuelling rate for Mark IIA pulses at 2.5 MA, 2.5 T and with 12 MW of NB heating.

The Z_{eff} of JET ELMy H-mode discharges is typically about 1.6 and is dominated by carbon [3]. Surprisingly, the impurity content, which is believed to be predominantly a result of sputtering from surfaces not wetted by the divertor plasma, has not reduced with increased divertor closure and thus lower main chamber neutral CX sputtering. Three possible compensating factors have been suggested: (a) at the time of the plugging of the bypass leaks the carbon coverage of the inner wall of the vacuum vessel was increased, (b) the Mark IIA and IIAP divertors operate at a higher temperature than Mark I thus moving towards the peak in the chemical sputtering yield [4], and (c) the increased closure may have led to increased sputtering from the shoulders of the divertor by ELMs.

The main difficulty with unseeded operation is the high first wall and divertor power loading due to the large, Type I ELMs produced in NB heated discharges. The energy loss from the plasma scales with the ELM frequency (Fig. 2) and is typically 5-10% of the total energy content per ELM [5].

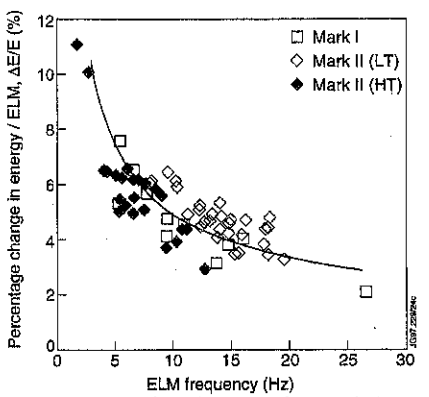

Fig. 2: Percentage loss of core stored energy during an ELM as a function of ELM frequency. The data are for pulses with NB heating and, for Mark II, are separated into low and high triangularity configurations.

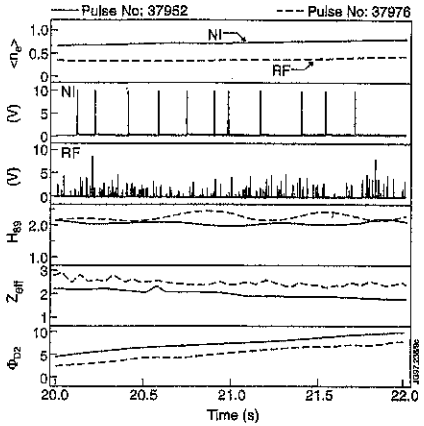

Fig. 3: Comparison of the ELM behaviour of two discharges, as measured by Dα emission (boxes 2 and 3), one heated by NI and one heated with RF.

This energy loss results in power loads on the divertor plates of several GW/m^2 and peak temperatures exceeding 2000°C [6].

ELMs in discharges heated by radio frequency waves have a much more benign character than those during NB heated shots [7]. The frequency of ELMs with RF heating is higher and more irregular than those in NB pulses (Fig. 3) and the peak power and integrated energy to the divertor target plates is a factor of 2-5 lower while the confinement quality remains high.

Performance with impurity seeding

The second line of experiments in the JET divertor programme has been to explore the possibility of reducing the power loading on the divertor by introducing a seed impurity to enhance the radiant losses from the plasma. This has proven to be successful in that up to 80% of the input power can be radiated in a stable, steady state discharge. The maximum radiated power fraction in this type of operation decreases with divertor closure from almost 80% in Mark I to 60% in Mark IIAP. This decrease in radiation is accompanied by an increase in charge exchange power losses such that the limit of the total volume losses is approximately constant from one divertor geometry to another [8].

The price which is paid for this improved divertor power loading is a significantly reduced core confinement. In Fig. 4 the confinement of radiative discharges both in JET and in other, smaller machines is plotted as a function of ρ^*. Also plotted in Fig. 4 is the data from a ρ^* experiment in JET for unseeded operation. The unseeded shots have approximately constant confinement on the ITER-93H scaling confirming the size scaling. In contrast, the radiative data have a very different size scaling than 93H, with lower confinement at low ρ^*. The range of confinement spanning the requirements from driven to fully ignited operation of ITER is also shown in Fig. 4 for comparison.

Local transport analysis has now been performed for JET radiative discharges and compared to unseeded pulses [9]. In Fig. 5, the effective heat diffusivity is shown for three pulses, one with beam fuelling alone, one with additional deuterium fuelling, and one with combined nitrogen and deuterium fuelling. In all three cases the central confinement is good, with the degradation in global confinement seen in Fig. 4 due to increased transport in outer plasma radii. In order to predict how radiative discharges scale to ITER such a local analysis is required including at least a model of the scaling of the width of the degraded region with machine size.

Implications for ITER

Two possible regimes of operation for ITER have been studied in the JET divertor programme. Operation without impurity seeding combines good core confinement with plasma purity but suffers from large, Type I ELMs which would limit the lifetime of actively cooled components in a reactor. The ELMs are significantly reduced in size in discharges heated with RF waves. Whether this better ELM behaviour would be typical of an ignited plasma depends on which physics is responsible. Experiments are planned to address this issue and will study the influence of central fuelling with the beam heating, beam momentum input and rotational shear, fast ion profiles in the two heating schemes, and the importance of RF-driven convective cells at the plasma edge.

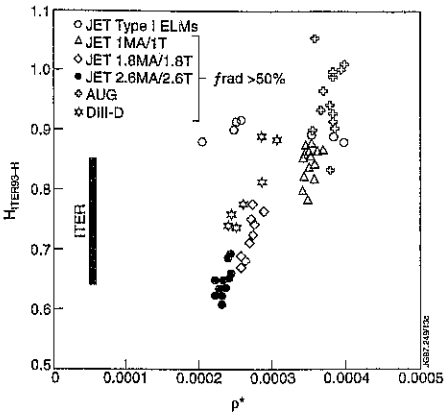

Fig. 4: Comparison of the confinement of radiative discharges from a variety of machines as a function of ρ. Unseeded JET discharges (open circles) are shown for comparison. The bar representing ITER spans the region from driven operation to the reference (ignited) point.*

Operation with an impurity seed so as to enhance radiant losses has been shown to be effective at reducing divertor power loads while maintaining plasma purity which scales at least reasonably to ITER. The confinement of such discharges appears to scale poorly with plasma size although definitive experiments such as those currently underway in the conventional ρ* studies have yet to be performed. Indeed, it is not possible in present tokamaks to simultaneously match the ITER parameters both in the plasma core and in the edge, so a local transport model will be required in order to predict the performance of radiative discharges in future machines.

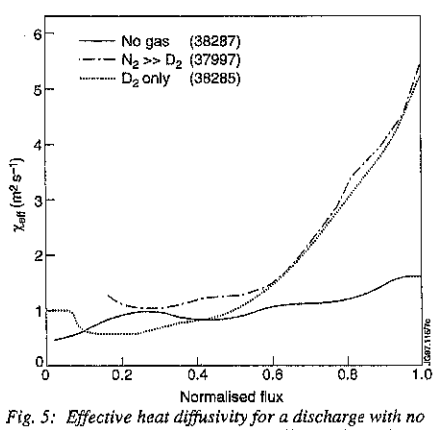

Fig. 5: Effective heat diffusivity for a discharge with no gas fuelling, one with deuterium fuelling only, and one with combined deuterium and nitrogen fuelling.

References

[1] G. Saibene, *et al.*, these proceedings.
[2] R. Sartori, *et al.*, these proceedings.
[3] G. McCracken, *et al.*, these proceedings.
[4] A. Haasz, private communication.
[5] R. Mohanti, *et al.*, these proceedings.
[6] E. Gauthier, *et al.*, these proceedings.
[7] V. Bhatnagar, *et al.*, these proceedings.
[8] C. Ingesson, *et al.*, these proceedings.
[9] G. Matthews, *et al.*, these proceedings.

Plasma-edge gradients and transport barrier widths in L- and H-mode JET plasmas

P.Breger, A.M.Cherubini, S.J.Davies, C.Flewin[1], N.C.Hawkes[2], R.W.T.König, V.Parail, Z.A.Pietrzyk[3], L.Porte, D.D.R.Summers, M.G.von Hellermann, K-D.Zastrow

JET Joint Undertaking, Abingdon, Oxfordshire, OX14 3EA, UK

[1] University College London, Gower St., Bloomsbury, London WC1E 6BT

[2] UKAEA Fusion/Euratom Association, Culham, Abingdon, Oxon OX14 3DB, UK

[3] CCRP, Lausanne, Switzerland

INTRODUCTION

The transition from L- to H mode confinement is accompanied by formation of a narrow region of reduced energy and particle transport near the plasma edge. In the H-mode regime, the operation space of a tokamak is limited to a finite edge pressure gradient by the ballooning mode stability. Experimental verification of the scaling behaviour of the barrier, the pedestal density and temperature, as well as the pressure gradient limits achieved before onset of loss of confinement require measurement of edge gradients with high spatial resolution and accuracy. Edge gradient, pedestal value and barrier width Δ were parameterised using a bi-linear fit of core and edge gradient, a non-linear fit of edge deviations from core gradient and a composite fit of the core and edge profile based on a tanh function.

THE ELECTRON DENSITY PROFILE $N_e(r)$

Edge $N_e(r)$ is measured using a 60 keV Li-beam and a reciprocating probe at the top of the vessel at the same poloidal coordinate, allowing direct data comparison. $N_e(r)$ are obtained by de-convolving the Li-emission over a length of 17 cm with resolution 0.7cm evaluating the beam excitation and ionisation balance. This requires beam current, edge temperature data and impurity concentration as input. A systematic three region model for temperature gradients in- and outside the separatrix based on ECE, CXRS, reciprocating probe and Lidar measurements has been used. $N_e(r)$ has an estimated error of <20% at peak density. A constant concentration of 3% C is used to match the bulk Z_{eff} of ~1.8-2.0 .

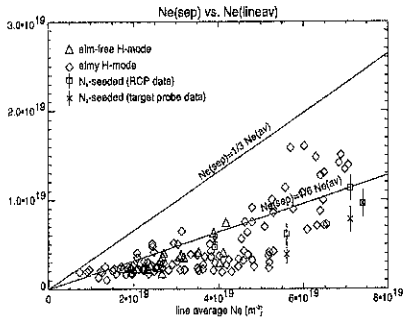

Fig. 1: Comparison of separatrix densities as function of line-average density during H-mode. Reciprocating probe and target probe results from N_2 seeded plasmas are shown for comparison.

Good agreement with RCP data and core Lidar data (corrected in absolute value using FIR interferometer results) is obtained. The error in midplane position is estimated to be of order ±1 cm. Separatrix densities are of order 15% of line average core density (fig. 1). Li-beam data for ELMy discharges is averaged over ELMs, but probe edge data is analysed between ELMs. $N_{e\text{-}sep}/N_{e\text{-}av}$ is larger for heavier gas puffing and higher ELM frequency.

The L- and H-mode edge

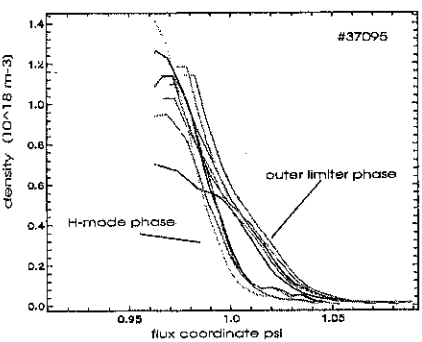

Fig.2 : Comparison of edge density profiles from an outer limiter plasma and the subsequent hot-ion H-mode.

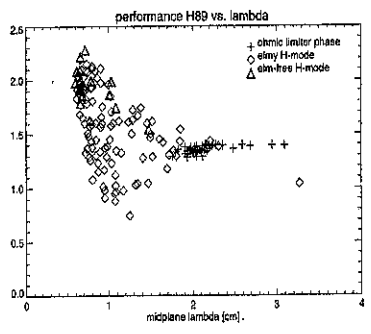

Fig. 3 : H-mode performance as function of density fall-off length (converted to cm at plasma midplane).

Data was obtained for similar discharges with an outer limiter period followed by a neutral beam heated Hot-ion H-mode phase. A steepening of $\nabla N_e(r)$ in H-mode is observed (fig.2). An exponential density fall-off length fitted over short sections of the profile around the separatrix reaches 0.8 cm (midplane) during the elm-free phase. The plasma performance (enhancement H-factor over the '89 L-mode scaling) is found to correlate with the fall-off length (fig.3). Scalings with respect to edge power loss, plasma energy, temperature, density, and connection length show no clear dependence, but a strong correlation with configuration-dependent local B_{pol} induced by plasma current and shaping coils.

THE ELECTRON TEMPERATURE PROFILE $T_e(r)$

Midplane $T_e(r)$ is measured using a ECE diagnostic. Due to large $\nabla T_e(r)$ at JET and the presence of a large fraction of relativistic electrons the spatial resolution is limited to about 1.5 cm. Measurements are taken at 250 kHz. For elm-free H-mode cases :

- pedestal temperature rises during elm-free H-mode from 2.5 - 3 keV ;
- the edge gradient builds up at start of elm-free phase in 0.2-0.3 s ;
- the barrier width is 3-4 cm in the elm-free phase, and 5-6 cm between elms ;

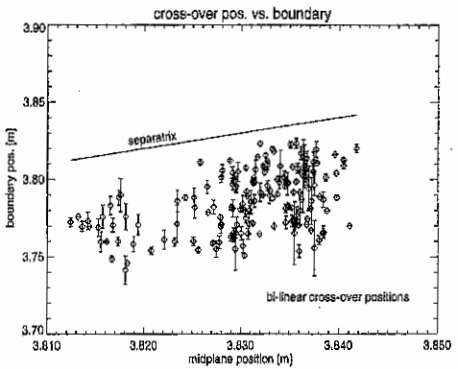

Fig. 4: Positioning of temperature barrier relative to EFIT separatrix position

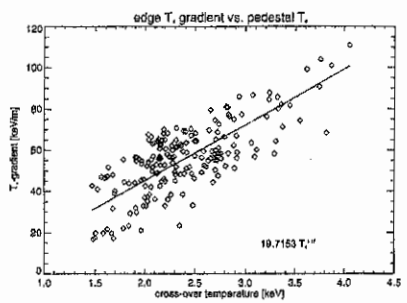

Fig. 5: Scaling of temperature gradient with pedestal temperature

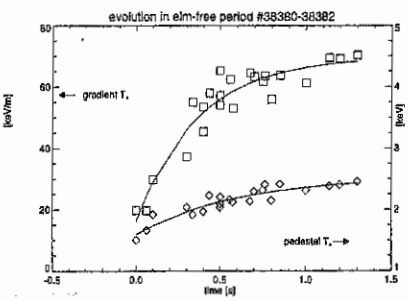

Fig. 6: Edge temperature (◊) and temperature gradient (□) evolution during elm-free H-mode

- the cross-over point lies at a position well inside EFIT separatrix position, at the latter the edge gradient intercepts zero temperature;
- gradient $\nabla T_e \sim T_e^{1.16\pm0.09} \cdot I_p^{0.01}$ and barrier width $\Delta \sim T_e^{-0.16\pm0.09}$.

THE ION TEMPERATURE AND DENSITY PROFILE

Ion temperatures and densities from active midplane CXRS (n=8-7, C^{5+}) have 1 cm radial

resolution. Temperature-time traces show a constant gradient between neighbouring chords during the elm-free period, the width varying linearly with the temperature. For elm-free H-mode discharges the edge gradient (bi-linear fit) does not scale with toroidal plasma current, giving a constant barrier gradient of 1.0±0.1 keV per cm. Density profile barrier widths are nearly always the same as those for temperature.

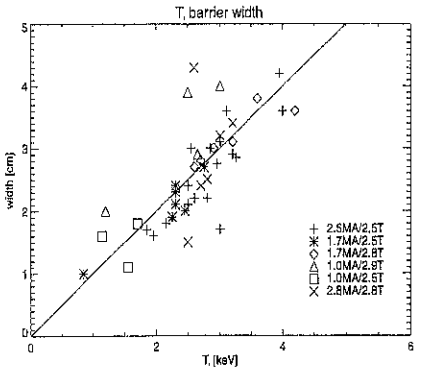

Fig. 7: Ion temperature barrier width as function of ion temperature (using a bi-linear profile fit).

THE ELECTRON PRESSURE PROFILE $P_e(r)$ AND BALLOONING LIMIT

$N_e(r)$ is mapped using EFIT equilibria to a midplane radius. The fitted $T_e(r)$ is extrapolated to zero temperature at the separatrix. The electron density edge width (tanh fit) is half the electron temperature edge width (fig. 8). $\nabla P_e(r)_{cr}$ is ~ 1/2 the critical ballooning mode gradient.

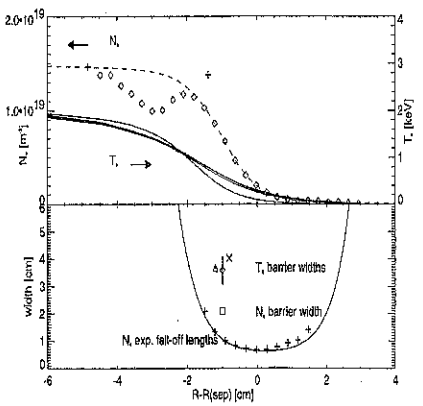

Fig. 8 : Combining electron density and temperature data to pressure profile: a) tanh fit to N_e , T_e in midplane coordinates, b) 1/e fall-off lengths (+ = exp. fit to N_e, line = tanh fit to N_e) and barrier widths (◊ =tanh T_e fit, Δ=linear T_e fit, x = core T_e deviation fit, □ = tanh N_e fit)

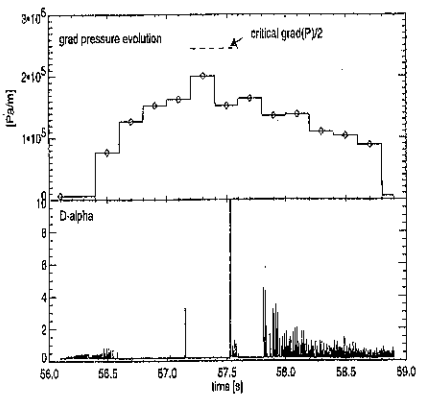

Fig. 9 : Computed electron pressure profile gradient (assuming coincident max. gradients) and D_α emission. The estimate of the marginal ballooning pressure gradient for electrons is given assuming $\nabla P_e = \nabla P_i$. The ∇P increases during elm-free phase until elms occur.

Confinement and performance of high current steady state ELMy H-modes with the JET Mark II divertor

R Sartori, B Balet, S Clement, G Conway, B de Esch, J C M de Haas, G Fishpool, L D Horton, J Lingertat, A Loarte, C G Lowry, C Maggi, M J Mantsinen(*), R D Monk, V Riccardo, E Righi, G Saibene, D Stork, K Thomsen, M G Von Hellermann
JET Joint Undertaking, Abingdon, OX14 3EA,Oxfordshire, UK
*Helsinki University of Technology, Association Euratom-Tekes, Espoo, Finland

1. Introduction. The confinement and performance of steady state ELMy H-modes with Type I ELMs have been studied in JET, with the Mark II divertor target, up to plasma currents of 5 MA and additional heating powers, by NB or combined NB and ICRF heating, of 25 MW. The discharges studied in this paper have neither impurity seeding nor additional deuterium gas fuelling in the heated phase. The main restriction in the choice of a plasma configuration for high plasma current operations, in particular when I_p is increased above 4 MA, is the need to limit both the shear stresses on the Toroidal Field (TF) coils, and the vertical forces on the vessel during disruptions. These requirements translate to a low triangularity (δ=0.22) configuration, which has a moderate flux expansion in the divertor and is relatively close to the vessel walls. Moreover, at high I_p, the condition of q_{95}>2 imposes operation at high toroidal field. The bulk of the discharges at 2.5 MA have a similar plasma configuration (with higher wall clearance), and also includes some discharges at higher triangularity (δ=0.3) and a wider range of flux expansion. Configurations with the strike points on the vertical plate of the divertor are also included. At 2.5 MA most of the discharges have q_{95} of 3.4 (2.5MA/2.5T). Discharges with q_{95} as low as 2.2 are also included. At 4 MA q_{95} varies from 2.5 to 3.1 and it is $\cong$ 2.4 at the maximum I_p/B_T of 5 MA/3.4T.

2. Confinement. The database analysed in this and the next paragraph contains data for each steady state discharges ($t>2\tau_E$.). At the q_{95} of the 5 MA/3.4T, an MHD n=2 mode is observed. The mode is triggered by a sawtooth crash and is non disruptive. The mode is avoidable by changing q_{95} and to this end the plasma current was limited to 4.7 MA. In Fig.1, the thermal stored energy W_{th} is plotted against the stored energy predicted by 0.85* ITERH93-P scaling (ELMy H-modes) . W_{th} was calculated from the diamagnetic measurements subtracting only the fast-ion energy due to NBI. The majority of the discharges are indeed heated only by NBI. For the few discharges at the highest ICRF powers ($\cong$8 MW), the error introduced in the W_{th} calculation by neglecting the ICRF fast ions is $\cong$ 10%. In the loss power calculation, NB shine-through and NB losses due to charge exchange and unconfined orbits were taken into account. The highest stored energies are achieved at 4.7 MA, with $W_{th} \cong$ 10 MJ in steady state for an input power $\cong$ 20 MW. At 2.5 MA there is good agreement with the scaling prediction, with an enhancement factor $H_{93}\cong$0.85, independent of plasma configuration or q_{95} (see also /1/,/2/). At higher plasma current H_{93} is lower, in fact at 3.5 MA $H_{93}\cong$0.8 and at 4 MA $H_{93}\cong$0.76. In agreement with what reported in /3/, the data shows a weaker β dependence than

predicted by the ITER93H-P scaling. Even though a better fit of the data is obtained with a scaling where the β dependence is $\beta^{-0.69}$ /3/, this does not fully remove the H factor degradation at high plasma current.

3. Performance. The aim of one of the experiments foreseen for the forthcoming DT experiment in JET is to maximise the fusion power in a steady state ELMy H-mode. Equivalent Q_{DT} of $\cong$ 0.2 is achieved in steady state ELMy H-modes. Overall, Q_{DT} improves with plasma current. The best fusion triple product are of 2.5-3 10^{20} $m^{-3}s$ keV for ion temperatures of $\cong$ 8 keV. Fig.2 shows the fusion power predicted by a TRANSP code simulation for a 4MA/3.4T discharge with 19 MW NBI heating. The simulation assumes a 50:50 D:T target plasma and 50:50 D:T mixture in the recycling from the walls. In the extrapolation to tritium operation, both the total NB power and the power fractions were maintained, with about 7.5 MW of tritium (at 150 keV) and 11.5 MW of deuterium (at 80 keV) injected. A total DT fusion power of 3.5-4.5 MW is predicted by the code of which about half is thermal. The tritium concentration in the discharge is about 45%. Similar levels of equivalent fusion power were obtained at 4.7 MA with 17 MW of NBI and at 3.5 MA with 24 MW combined heating. The main obstacle to the improvement of the fusion performance of an ELMy H-mode is that it has proven difficult to sustain a steady state discharge at high plasma current. In fact, most high current discharges suffered from a spontaneous H to L transition.

4. The spontaneous H-L transition. A temporary loss of confinement or/and a spontaneous H-L transition is observed in ELMy H-mode, in particular for plasma currents above 3 MA (Fig 3.). The H-L transition is often preceeded by a period of small ELMs (Type III ?) and decaying confinement. The back transition can occur early in the discharge, in a phase which is still transient, or after several energy confinement times. During the following L-mode phase, a slow rotating ($f \approx 100$Hz) n=1 MHD mode is observed. The mode is resonant at the plasma edge in the region of the H-mode pedestal, the poloidal m number being consistent with $m > q_{95}$. This mode has similar frequency and amplitude to the n=1 mode observed in the L-mode of optimised shear discharges /4/. In coincidence with the mode disappearance, the H-mode confinement can be recovered. Up to 3 cycles of H and L modes were observed in the same discharge, often with increasing performance. An H-L transition with the same characteristics of the spontaneous one can be induced with a plasma current ramp-up while a plasma current ramp-down restores the confinement.

4.1 Global parameters. Even when the H-mode confinement is maintained in steady state, high current discharges have an irregular ELM behaviour with bursts of high frequency, small ELMs. The typical input powers are of 15 to 19 MW, and high current discharges are close to the H-mode threshold at the lower end of this range due to their high steady state density ($6/7\times10^{19}m^{-3}$) and high B_T. The H-L transition is not only observed in discharges where the input power goes below the predicted L-H threshold power but also at input powers well

above the threshold. Nevertheless, a global parameter dependence similar to the H-mode power threshold scaling, which involve magnetic field, input power and density is observed. The lower the toroidal field, the easier it is to maintain the H-mode confinement. In fact, at fixed plasma current and input power, the duration of the H-mode phases increases if the toroidal field is decreased. Increasing the input power does also extend the duration of the high confinement phase. For example, at 4 MA/3.4T, the duration of the H-mode phase increases from 2s to > 4s when the NBI power is increased from 16 to 19 MW. Moreover, even though the H-L back transition is more frequently observed at high I_p, it is also observed at lower I_p (and lower B_T) if the input power is decreased but the Type I ELMs are maintained. Discharges with Type III ELMs (low density) seem to be more resilient to this phenomenon. In contrast with this favourable power dependence, when the ICRH power is increased above $\cong$ 3 MW an earlier confinement loss is observed. In Fig. 4, the data points immediately prior to the spontaneous H-L transition are compared to the 1996/97 L-H threshold data /5/. For the H-L data, the dW/dt in the ELM free period before the last ELM has been used to calculate the loss power. The H-L points are near to the line which separate L from H modes due to the increase of dW/dt with input power.

*4.2 **Local parameters.*** Fig. 5 shows the pedestal n_e/T_e (n_e from the FIR interferometer outermost channel, T_e from ECE heterodyne radiometer) trajectory for the discharge shown in Fig. 3 . The L-H transitions and the H-L transition at power switch off (1,6,9) are in the same region of the diagram /6/, but the spontaneous H-L transition occurs at higher T_e. This could be due to the presence of MHD. Compared to lower current steady state discharges /7/, the operating space for Type I ELMs (2,4,8) seems to be smaller at high current. Further analysis is in progress.

Summary. As expected the energy confinement time improves with plasma current, but the improvement is lower than predicted by 0.85ITERH93-P scaling and this cannot be completely explained with a weaker β dependence. Steady operation is difficult with high current discharges due to a spontaneous H-L transition, which is probably due to operation too close to the H-mode threshold. Nevertheless, an equivalent fusion power of 4 MW has been demonstrated in ELMy H-mode and an improvement could be possible in deuterium-tritium operation, if a favourable mass dependence of the H-mode threshold is observed.

/1/ L Horton et al., these proceedings
/2/ G Saibene et al., these proceedings
/3/ J G Cordey et al., these proceedings
/4/ B Alper al., these proceedings
/5/ E Righi, private communication
/6/ E Righi et al., these proceedings
/7/ H Lingertat et al., these proceedings

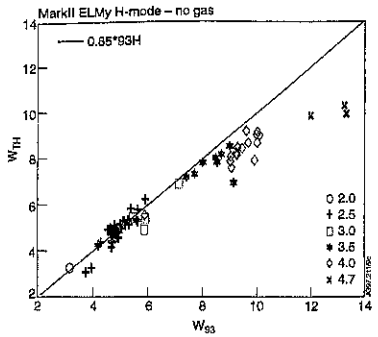

Figure 1 : Stored energy, as predicted by 0.85*ITERH93-P versus actual thermal stored energy [MJ].

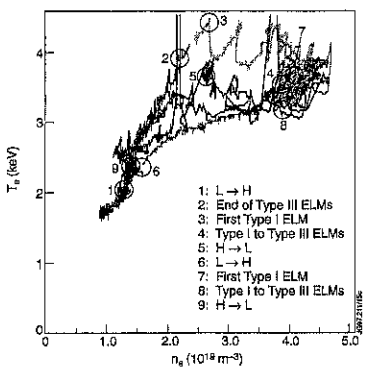

Figure 5 : Trajectory of discharge # 40973 in the pedestal n_e/T_e diagram.

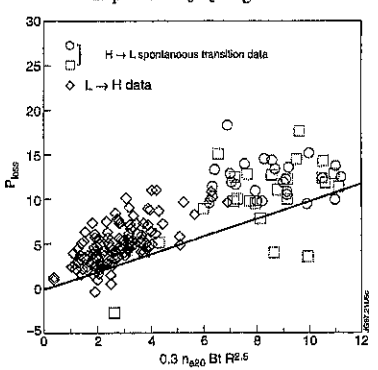

Figure 4 : Data for the L to H mode transition, compared to data for the spontaneous H to L transition.

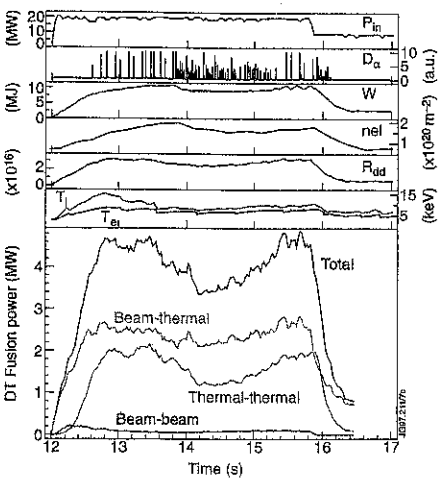

Figure 2 : Discharge # 40275, time evolution of main plasma parameters and TRANSP predictions for D-T fusion power.

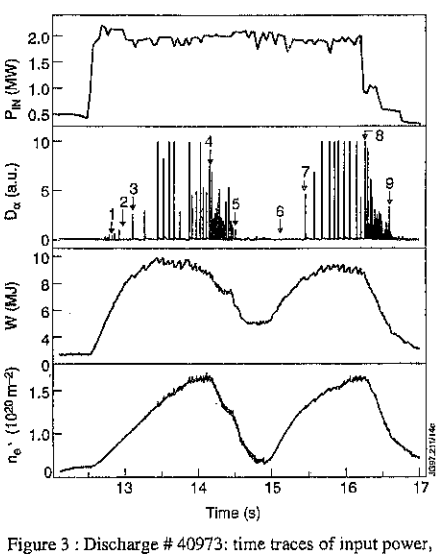

Figure 3 : Discharge # 40973: time traces of input power, D_α, stored energy and line integral plasma density

A COMPARISON OF ELMs CHARACTERISTICS BETWEEN ICRH AND NBI HEATED H-MODE DISCHARGES IN JET

V.P. Bhatnagar, D. Bartlett, S. Clement, J. De Haas, L. Eriksson, G. Fishpool, C. Gormezano, E. Gauthier, L.Horton, J. Jacquinot, J. Lingertat, A. Loarte, R. Monk, E. Righi, M. Stamp, D.F.H. Start, D. Stork, G. Vlases, , W. Zhang

JET Joint Undertaking, Abingdon, OXON, OX143EA, UK

1. INTRODUCTION

Edge localised modes (ELMs) are MHD-like instabilities which occur during H-modes and produce bursts of energy and particles that are ejected through the separatrix to the scrape-off layer and the divertor. For steady-state, it is desirable to operate next-step machines such as ITER in ELMy H-modes as they can provide appropriate confinement quality factor and they are likely to be beneficial in preventing the build up of density, impurity and helium ash. However, the energy delivered (and lost) to the divertor in discreet ELMs can be significant (1-10% of the thermal stored energy per ELM) leading to unacceptable erosion of the ITER target plate material. The peak heat loads that would occur during ELMs is a major issue in power and particle control in a reactor. In H-modes produced by ion cyclotron resonance heating (ICRH) in JET, physical characteristics of ELMs, such as their dominant power dumping on the inner divertor leg, a sudden decrease in edge plasma parameters and a decrease in stored energy, are the same as found with neutral beam injection (NBI) ELMs. However, for ELMs with ICRH, the perturbation of the above plasma parameters is typically 2-5 times smaller than that with beams although the confinement enhancement factor (subtracting energy of fast ions) is similar. In this paper, we study and compare in more detail the above characteristics of ELMs with ICRH and NBI.

2. EXPERIMENTAL RESULTS

2.1 Plasma Parameters and Configuration. The type of ELMs observed in a discharge depends on plasma shape, edge pressure profile, proximity to L-H / H-L transition, edge temperature and MHD stability limits at the edge. For the experimental results presented here, we have selected JET discharges that are amenable to producing type I ELMs. These discharges were obtained at toroidal field B_ϕ ~2.5-2.8 T, plasma current I_p ~ 2.5 MA and heated by D°-NB injection or central ICRF minority heating with hydrogen as the minority species in deuterium plasmas. The 4-strap A2 ICRH antennae were operated in dipole ($0\pi0\pi$ or $0\pi\pi0$) phasing. The configuration used was JET divertor Mark IIA, single-null X-point, "Standard-Fat", low triangularity (δ~0.2) plasma. Line averaged central densities ranged from 2.5-5x$10^{19}$$m^{-3}$. The H-mode threshold in such discharges is 4-6 MW. Additional heating (ICRH or NBI) power used was 10-12 MW. The separatrix position in these discharges is at about 3.86 m in the outer mid-plane.

2.2 General Characteristics of ELMy Discharges with ICRH and NBI. In Fig. 1, we show time traces of two consecutive discharges additionally heated by ICRH and NBI at a power level of about 10 MW each and having about the same plasma density and energy confinement time. Signals shown include line-averaged edge density (n_eL at 3.75m), D_α-

emission and confinement factor ITERH-93 (normalised to thermal, ELMy H-mode scaling). The ICRH fast-ion energy is estimated to be low (5-10%) at this high density. Note that the frequency of ELMs (D_α-signal) is much larger with ICRH as compared to that with NBI. On a detailed examination of ELMs with ICRH, it is found that in type I ELMs [1] with ICRH, not only the frequency is higher but also the repetition rate and amplitude of ELMs is relatively less steady. In addition, the amplitude of ELMs (D_α-signal) with ICRH is generally smaller by a factor of about 5-10 as observed in a single shot with successive NBI and ICRH heating. We note, however, that the D_α-behaviour, which is mainly governed by particle source rates, can be affected by wall conditioning and gas puffing. Therefore, in the following we will give less weight to the amplitude of D_α-signal for comparison of ELM characteristics with ICRH and NBI and put more accent on perturabation of edge plasma parameters, drop in stored energy, power loading of the divertor and rise in the tile temperature.

2.3 Ion-Saturation Current and Edge Electron-Temperature Perturbation. We illustrate the behaviour of ELMs produced by ICRH in a discharge (P_{RF}=9.5 MW, B_ϕ=2.6T and I_P=2.6 MA, "Standard Fat," low-triangularity, no additional gas-puff) shown in Fig. 2. The spikes on D_α-signal (box 1) represent the occurence of ELMs. Note that the amplitude and repetition rate is not steady. Correlated spikes are also observed on the ion saturation current (box 2) and electron density (box 3) measured by Langmuir probes mounted on the target plates on the inner divertor leg. However, the perturbation in the edge electron temperature (box 4) measured at 3.84m (outer plasma edge) shows correlation only with ELMs which are somewhat broader (larger area under ELMs). The reason for the spikes on T_e signal (electron cyclotron emission) is not clear and is possibly related to the occurrence of non Maxwellian (fast) electron population for some ELMs.

In Fig. 3 we compare the perturbation in edge electron temperature caused by ELMs with ICRH and NBI produced H-modes at a power level of about 10 MW. Generally, the ELMs produced by NBI are powerful and produce perturbation in the edge-T_e at each ELM as compared to the case of ICRH shown in Fig. 2. The decrease in edge-T_e is about 10% for stronger ICRH ELMs as compared to ELMs with NBI where it is about 35% at a radius slightly (9mm) closer to the centre.

2.4 Drop in Stored Energy due to an ELM and the Effect of Edge Density. At the occurrence of an ELM, plasma stored energy drops due to the loss of plasma particles from the edge. A comparison of such a drop due to ICRH and NBI ELMs at a power level of 10 MW is shown in Fig. 4 using fast diamagnetic stored energy measurements. After an investigation of a number of discharges, it was found that most of the ELMs with ICRH produce negligible drop in stored energy (0.5-1%) and the largest drop is about 4.5% whereas for ELMs with NBI, this drop in stored energy can be as high as 4-8% (see also Ref. 1). Based on an analysis of several ICRH and NBI discharges, a plot of ELM-amplitude as a function of line-averaged edge (3.75 m) density is shown in Fig. 5. Note that the amplitude (D_α) of ICRH ELMs does not rise significantly with edge density. Generally, the density reached in the case of NBI is higher (due to central fueling) as compared to the case of ICRH. Nevertheless, a considerable overlap can be achieved by appropriate gas feed.

2.5 Divertor-Tile Temperature and Power deposition by ELMs. A fast 2-D infra-red camera has been used to measure temperature of divertor tiles [2] during an ELM. Illustrative examples showing a comparison of tile temperature during ELMs with ICRH and NBI are given in [1]. Typically the peak tile temerature exceeds 1200°C with type I ELMs produced

by NBI whereas with ICRH ELMs, it is less than 500°C. In such examples, the power density falling on the tiles [2] in the case of beams is $P_{dm} \sim 3$ GW/m^2 and energy density $E_{dm} \sim 560$ kJ/m^2 whereas with ICRH, $P_{dm} \sim 0.9$ GW/m^2 and $E_{dm} \sim 45$ kJ/m^2.

2.6 Energy Release of an ICRH ELM Bit-by-Bit after a Sawtooth Crash. In ICRH H-mode discharges, we have found that the crash of a sawtooth often initiates an ELM-free period in an otherwise ELMy discharge. The heat-pulse generated by the crash of a sawtooth increases the edge temperature producing an ELM-free period. This 'charges-up' the ELM and when it crashes, it is accompanied by a decrease in the edge-T_e. But, this decrease in edge temperature occurs in small steps, each accompanying an ELM and an ELM-free period (see Fig. 6). At the 2nd sawtooth crash, only two steps are found. This is probably related to the magnitude of sawtooth crash which was about 2/3 smaller in the second case. Note also that the perturbation in the edge temperature after the crash of an ELM becomes progressively smaller as one moves further in towards the centre of plasma (see 2nd box in Fig. 6).

3. DISCUSSION AND CONCLUSIONS

It is believed that the effect of electric field shear and rotation stabilizes ballooning type of MHD instabilities leading to a build up of pressure gradient until the time that it can not be supported. The plasma then dumps the energy and particles in a repetitive way in the form of ELMs. The reasons for difference between NBI and ICRH ELMs are not clear. The plasma rotation with ICRH in JET measured [3] in the centre is found to be lower by a factor of 3-10 as compared to beams. There is no measurement of rotational shear with ICRH whereas the beams do indeed provide rotational shear. In the case of beams, the effect of central particle fueling and plasma rotation on ELMs can not be separated. Note that there is no central fueling with ICRH. However, the effect of the residual near-field of the ICRH antennae (which is higher in monopole phasing) influencing the plasma edge (and hence ELM behaviour) cannot be ruled out. The H-mode power threshold and H93 factor with dipole phasing are the same as with NBI but a study of ELMs with different phasing of ICRH antenna ($0\pi0\pi$ and $00\pi\pi$) in JET shows that the latter (monopole) phasing has higher threshold. A comparison [4] of dipole (0π) and monopole (00)-phasing of 2-strap A1 antenna in JET showed 30% degraded performance on confinement with monopole phasings which was ascribed to edge convective-cell effects. In **conclusion**, we have found that Type I ELMs produced by ICRH have higher frequency and lower amplitude. The repetition rate and amplitude of ELMs is relatively less steady as compared to beams but the energy confinement is about the same in the two cases. All effects studied at the occurrence of an ELM (decrease in edge electron temperature, drop in stored energy, rise in tile temperature) show that ICRH ELMs are milder by a factor 2-5 as compared to beams. Some examples presented show that ICRH ELMs produced after a sawtooth crash dump their energy in several steps rather than in one go making them even more benign.

ACKNOWLEDGEMENTS. We wish to thank the NBI and ICRH plant teams, the tokamak operation team and those operating the diagnostics used in the experiments reported here.

REFERENCES

[1] Bhatnagar, V.P. et al, in JET Posters to 24th EPS, Berchtesgaden, Report JET-IR(97)04.
[2] Gauthier, E. et al, this conference.
[3] Eriksson, L-G. et al., Plasma Phys Contr. Fusion **39** (1997) 27.
[4] Bhatnagar, V.P. et al, 18th EPS, Berlin (1991), Europhys. Conf. Abs. **15C**, I , 369.

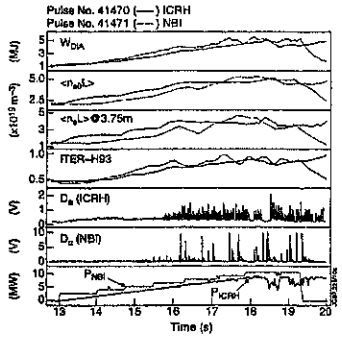

FIG. 1. Comparison of ELMs with ICRH and NBI at same density and thermal conf. time.

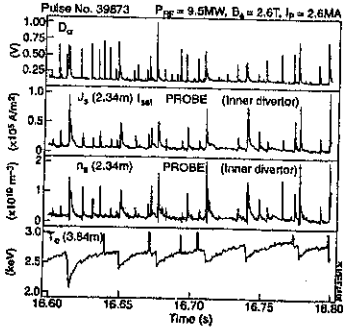

FIG. 2. Correlation of ELMs D_α with divertor probe ion saturation current, n_e and edge-T_e.

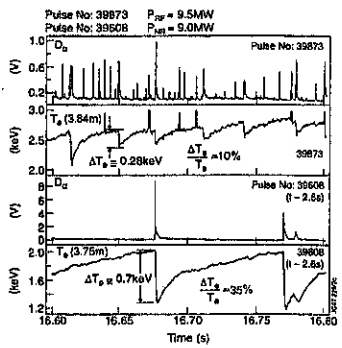

FIG. 3. A comparison of edge-Te perturbation during ICRH and NBI ELMs.

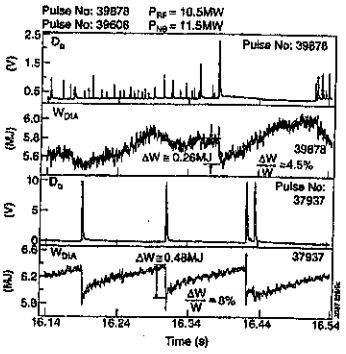

FIG. 4. A comparison of drop in stored energy during ICRH and NBI ELMs.

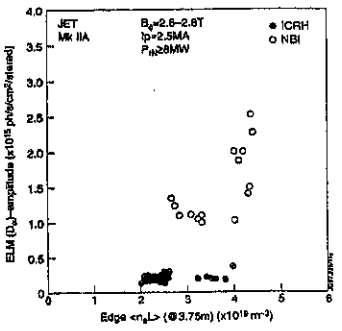

FIG. 5. ELM (D_α)-amplitude versus edge density for several ICRH and NBI discharges.

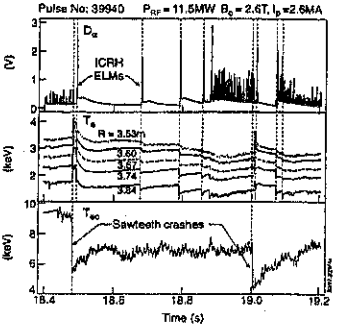

FIG. 6. Step-by-step release of energy of an ICRH ELM after a sawtooth crash.

Modelling of JET Optimised Shear Discharges

G.A.Cottrell, Y.Baranov, D.O'Brien, C.D.Challis, J.G.Cordey, J.C.M de Haas, L.-G. Eriksson, C.Gormezano, A.C.Howman, T.C.Luce*, M.Mantsinen†, G.J.Sadler, A.C.C.Sips, F.X.Söldner, D.F.H.Start, P.M.Stubberfield, B.J.T.Tubbing, D.J.Ward, M. von Hellermann, W.P.Zwingmann

JET Joint Undertaking, Abingdon, Oxon. OX14 3EA, UK

*General Atomics, San Diego, California, USA

†Also at Helsinki University of Technology, Association Euratom-TEKES, Espoo, Finland

Internal transport barriers (ITBs) have been produced in JET by heating during the current rise when the central shear is low or negative [1,2,3]. The optimised shear (OS) pulse shown in Fig.1, with both NBI and ICRF, produced the highest DD fusion yield so far in JET. The preheating phase included (1 - 2) MW of early LHCD at t = 0.5 s - 1.3 s and 1 MW of ICRH at t = 3 s - 5 s. Using TRANSP, the calculated neutron rate (Fig.2) lies within ± 10% of measurements, with thermonuclear neutron emission comprising approximately 2/3 of the total.

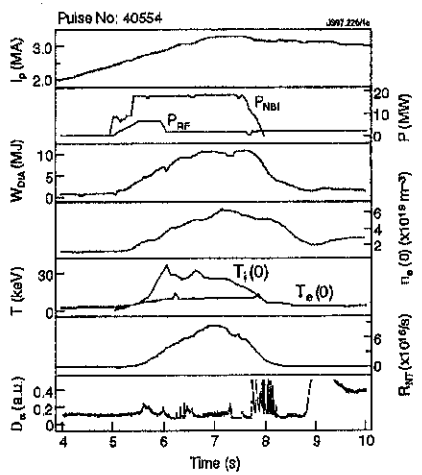

Fig 1. Evolution of plasma parameters

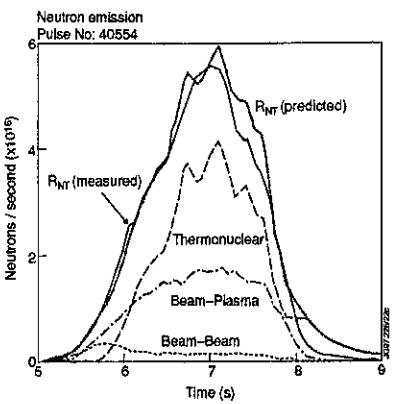

Fig 2. TRANSP code neutron emission modelling

The safety factor, $q(R)$, was derived from the EFIT code, constrained by magnetic and TRANSP kinetic plasma pressure data. To fix the axis position, ECE measurements from high and low field sides were compared and, in Fig.3(a), the minority fast ion pressure adjusted to reconcile all measurements. At t = 7 s the shear-reversed profile displayed is inconsistent with a monotonic one (within ± 5 % in the χ^2 statistic). The TRANSP q-profiles (Fig.3(b)), were

computed starting from a polarimetry-constrained EFIT profile at $t = 2.5$ s. At $t = 7$ s, the total bootstrap current was 1 MA and had a current density profile which peaked at radius $\rho = 0.26$.

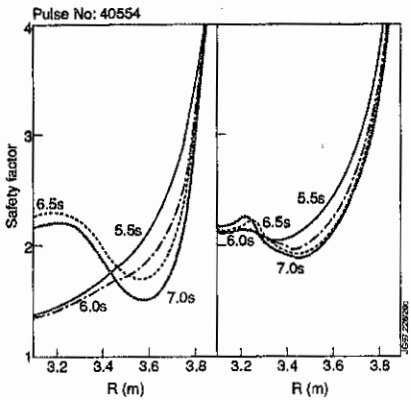

Fig. 3. Comparison of safety factor profiles: left (a) using kinetic EFIT and right (b) from TRANSP.

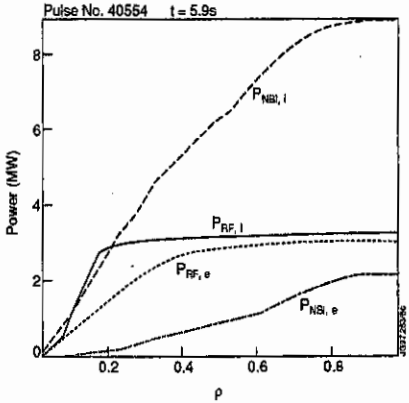

Fig 4. Volume-integrated deposition profiles. Subscripts i,e refer to ions or electrons.

Power Deposition and Heating Profiles

Central ICRF heating with $\pi/2$ phasing and frequency $\omega = \omega_{cH} = 2\omega_{cD}$ resulted in peaked RF power deposition (Fig.4). RF ion heating power in the region $\rho \leq 0.2$ was comparable

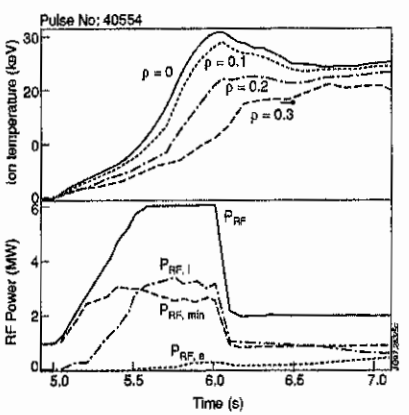

Fig. 5. Upper: response of the core ion temperatures at the RF power stepdown. Lower: RF Heating; Subscripts i, e, or min refer to D ions, electrons or H minority ions.

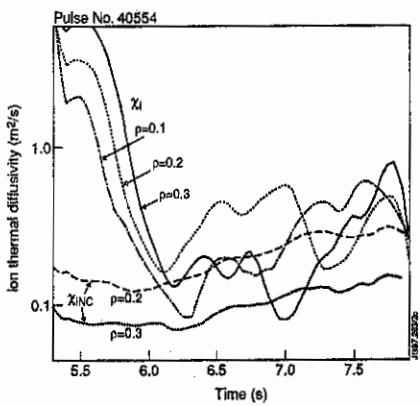

Fig. 6. Derived (χ_i) and neoclassical (χ_{iNC}) ion thermal diffusivities in the centre from TRANSP analysis.

with that of NBI, despite the difference in applied powers (P_{RF} = 6 MW, P_{NBI} = 18.6 MW). As P_{RF} was ramped up from 5 s to 5.5 s, the damping was predominantly on the H minority (Fig.5) which was assumed to have a fixed concentration of 1% of the electron density. At time $t \sim 5.5$ s, with the formation of an ITB, β_D (0) increased to a level where $2\omega_{cD}$ damping ($P_{RF,i}$) in the hot core became comparable with minority damping ($P_{RF,min}$). Any RF acceleration of resonant NBI deuterons above their injection energies (80 keV and 140 keV) to produce an energetic tail increases the beam-plasma DD reaction rate. No model of this effect was included in the version of TRANSP used; therefore the good agreement of Fig.2 indicates that any D tail was small. The RF power (Fig.5) was stepped down at t = 6 s to avoid unstable plasma pressure gradients [4]. After this time, the core D ions promptly cooled - from 31 keV to 24 keV - in a time of about 500 ms - reflecting the drop in central RF ion heating. In this time interval the equipartition loss from the core ions increased by only 250 kW. The ion thermal diffusivity was close to the neoclassical level (Fig.6) for $\rho \sim 0.2 - 0.3$. For the discharge as a whole, the main loss of heat was through the ion channel with convection and conduction comparable in the core but conduction dominating losses for $\rho \geq 0.4$. For electrons, conduction was the main loss and equipartition provided ~ 2 MW of heating.

The Region Of Enhanced Confinement

The ITB formed near the magnetic axis at time $t \approx 5.6$ s and then grew steadily to a maximum size of $\rho \approx 0.6$ at time $t \approx 6.5$ s (Fig.7). Similar behaviour was seen for the momentum diffusivity. At t = 6.52 s there was a drop in Dα emission and a 40% increase in

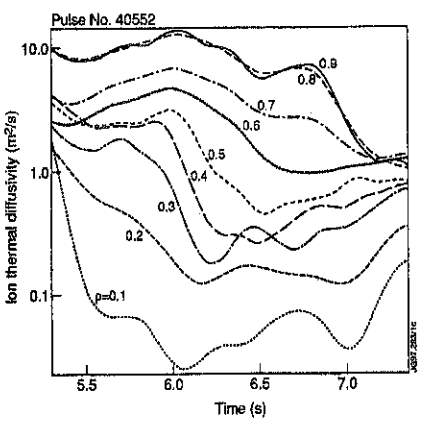

Fig. 7. Ion thermal diffusivities (χ_i) for pulse 40552 from TRANSP simulation.

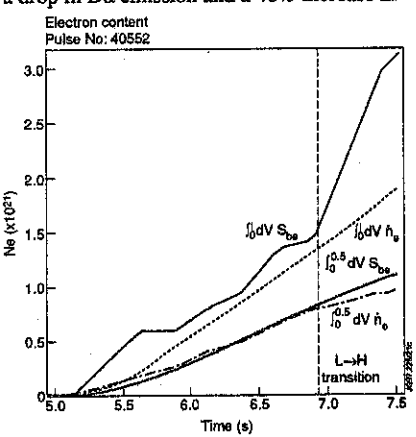

Fig. 8. Comparison of time-integrated total number of NBI electrons (S_{be}) with the measured total (n_e) taking volume integrals out to ρ = 0.5, and ρ = 1.0.

edge ion temperature showing an edge H-mode transport barrier. After t = 6.6 s the central χ_i increased and, at t = 6.95 s, there was a definite LH transition, shown by the rapid drop in χ_i (ρ > 0.6). In the H-mode, the core transport continued to degrade although, for a time, edge and internal transport barriers coexisted. Any causal relationship between edge and internal barriers is at present unclear although the H-mode may have been triggered by the increased edge power flux resulting from the loss of core confinement. The NBI particle accountability (Fig.8) shows that the NBI particles were well confined inside the barrier during the L-mode phase (t < 6.8 s) but, outside the barrier (ρ > 0.5), there was significant loss. After$t$ = 6.8 s particle confinement everywhere degraded.

Lower Hybrid Current Drive

Applying early LHCD at a power level of ~ 1MW increased T_{e0} to ~ 10 keV, increased the internal inductance, l_i, and sustained shear reversal with $q(0)$ ~ 4 - 5. During the LH phase, χ_e < χ_e (gyro-bohm) for $\rho \leq 0.4$ and calculations indicate a heat pinch for $\rho \leq 0.3$. MHD events resembling sawteeth have been observed when $q_{min} > 4$ with inversion radius $\rho \approx 0.2$. The n = 1 mode has been seen in the current flat-top when $q_{min} \approx 2$.

Conclusions

Optimised shear plasmas have so far produced the highest DD fusion reactivity in JET with typically 2/3 of the neutrons of thermonuclear origin. TRANSP and kinetic EFIT equilibria both indicate shear reversal with $q(0)$ ~ 2.1 and q_{min} ~ 1.5 - 1.9 at ρ (q_{min}) ≈ 0.4 - 0.5 with significant bootstrap current density peaking at ρ = 0.26. Analysis shows the formation and growth of a region of reduced ion thermal and momentum diffusivity reaching a radius ρ = 0.6 in a time of ~ 1 s. Inside the core, the ion thermal diffusivity is comparable with the neoclassical value and NBI particles are well confined inside the ITB for a time of about 2 s until it degrades. Edge and internal transport barriers can coexist transiently. 6 MW of applied ICRH is as effective in heating core D ions ($\omega \approx 2\omega_{cD}$) as is 18.6 MW of NBI. The application of early, low power LHCD increases T_{e0} and l_i and sustains shear reversal. Preparations are under way for DT experiments.

References

[1] Gormezano, C., et al. *Plasma Phys. and Controlled Nucl. Fusion Research* (Proc. 16th Int. Conf. Montreal, 1996) *to be published.*

[2] Sips, A.C.C. et al. *This Conference.*

[3] Söldner, F.X., et al. Topical Paper, *This Conference.*

[4] Huysmans, G.T.A. et al. *This Conference.*

High Fusion Performance with Combined Heating in ELM-free H-mode in JET

F.G.Rimini, P. Andrew, B. Balet, G. Cottrell, L-G. Eriksson, A. Gondhalekar, C. Gormezano, C. Gowers, T.T.C. Jones, R. König, P.J. Lomas, A. Maas, M. Mantsinen[1], F.B. Marcus, M.F. Nave, B. Schunke, D.F.H. Start, D. Testa[2], P.R. Thomas

JET, Joint Undertaking, Abingdon, OXON. OX14 3EA, United Kingdom
[1] also at : Helsinki Univ. of Technology, Ass. EURATOM-Tekes, FIN-02015 HUT, Finland
[2] also at Imperial College of Science, Technology and Medicine, London UK

Introduction High fusion performance has long been obtained in JET in ELM-free H-modes dominated by Neutral Beam Heating [1]. During the experimental campaign in the MKI divertor configuration limited but promising attempts were made to use ICRH in ELM-free Hot-Ion H-modes, which showed improved confinement and performance [2]. The properties of ELM-free Hot-Ion H-modes with combined NB+ICRF heating have been further explored in the MKII divertor campaign at high plasma current of 3 to 3.8 MA and high toroidal field of 3.4 T, with total power up to 25 MW.

The experiments described here have been carried out with ICRF tuned for fundamental hydrogen minority resonance in the central plasma region, either using a single frequency (monochrome) or up to 4 different frequencies (polychrome), with the resonance spread over a 30-40 cm region around the centre and on the low field side. A maximum ICRF power of 9.5 MW was coupled in dipole phasing at 51.2 MHz.

Overview of Combined Heating ELM-free Hot-Ion H-modes

Addition of ICRH to Hot-Ion H-modes (fig. 1) results in increased core electron temperature, from 10 keV up to 14 keV, and increased core ion temperature, or the same ion temperature for higher density. The observed relative increase in Ti(0) can be attributed to a combination of two factors : firstly direct input from ICRH to the ion power balance, as discussed below, and secondly the increased electron temperature, which produces decreased power loss via equipartition and increased slowing down time of the beam ions on the thermal bulk ions. To be noted that a continuous gas bleed is used in the ELM-free phase of combined heating discharges : this appears to be beneficial in controlling the impurity level and possibly the edge MHD activity [3], but it also results in slightly higher edge density and broader NB deposition profile than NB only discharges.

Stored energy is also increased, up to a record, for the Hot-Ion H-mode, of 14.5 MJ with 25 MW of total heating power. The contribution to the stored energy from fast ions is

estimated to be up to 2 MJ at the beginning of the ELM-free phase, and < 2 MJ around the peak of neutron emission. The thermal global confinement is similar to NB cases.

Statistically, the length of the high performance phase tends to decrease with increasing input power; the data suggest that NB+ICRH cases are comparable to NB cases at similar power level. There is some evidence that discharges with NB + modest ICRH (3-4 MW) reach the terminating ELM event at higher values of stored energy than with NB alone. One possible explanation could be the more peaked pressure profiles in the combined heating cases, but more analysis of the MHD stability of such discharges is needed. In the MKI divertor campaign it was found that Hot-Ion ELM-free H-modes with combined heating were terminated preferentially by core instabilities, mainly sawteeth. This is to some extent still true for NB + ICRH cases with $P_{RF} \geq 5$ MW and single central RF resonance. Discharges with modest RF polychrome power are less prone to large sawteeth during the high β phase.

Discharges with NB + ICRH are characterised by increased DD neutron yield (fig. 1) up to a record for the Hot-Ion scenario of 5.2×10^{16} neutrons/s, obtained with polychrome operation. The scaling of performance with total input power (fig. 2) and stored energy appears to be similar for NB and NB+ICRH discharges with $P_{RF} \leq 4$ MW. A deviation from the scaling is observed for discharges with ICRF power ≥ 5 MW, which are characterised by higher density, broader NB deposition, shorter ELM-free phase and lower ion temperature, approaching the electron temperature.

Data from the High Energy Neutral Particle Analyser (NPA) [4] show a presence of deuterons above the injection energy of the beam ions, 80 and 140 keV. This suggests that, at the very low hydrogen concentration, << 5 %, typical of these discharges, some of the ICRF power is coupled to deuterons at the 2^{ND} harmonic resonance, resulting in a non-thermal enhancement of the DD reactivity. The effect is more evident at high RF power density, i.e. high RF power and/or with monochrome operation (fig. 3) and it is also experienced in the NB+ICRH Optimised Shear scenario [5]. In the ELM-free discharges the data indicate that the deuterium tail driven by ICRH is not significant in the MeV range and that high energy tail formation is minimised by polychrome operation. In these pulses the critical energy at which deuterons heat electrons and bulk ions at equal rate is in the range of 200 keV, and when polychrome operation is used, collisional ion heating is maximised.

Numerical Simulations of NB+ICRH ELM-free Hot-Ion H-modes

Detailed simulations have been carried out using the PION code, which includes a self-

consistent treatment of RF damping and tail formation [6,7]. The full simulation, NB + ICRH, can be compared with a simulation of an artificial NB only case with the same plasma parameters of the actual discharge to identify any direct ICRH contribution to the ion power balance and the neutron yield. The code suggests that initially most of the power is absorbed by the hydrogen minority; with increasing ion pressure a larger power fraction, up to 40%, is absorbed by the deuteron population (fig. 4). Direct electron damping is typically responsible for ~ 10 % of the ICRF power absorption. Deuteron acceleration is greatest in the monochrome and high RF power cases and it is much reduced with polychrome operation, as observed in the experiments. However, most of the improvement in yield with ICRH is due to particles with relatively low energy, with only 15 -20 % of the neutron rate originating from energies above 200 keV. The ICRF power absorbed by bulk or collisionally transferred from deuteron tail is found to be ≅ 1 to 2 MW. Since the power deposition is peaked on-axis, ICRH provides a substantial, ≅ 30 - 35 %, contribution to the ion power balance in the plasma core.

Simulations have also been carried out with the TRANSP code for NB+ICRH Hot-Ion H-modes. It has to be noted that TRANSP does not have a self-consistent model for ICRH absorption and evolution of the deuterium distribution function ; hence, any enhancement of DD reactivity due to an RF driven deuterium tail is not taken into account. Nevertheless, TRANSP results for these cases show good agreement with the measured neutron yield and stored energy, again suggesting that contribution from a high energy deuteron tail is small.

Summary

An extensive series of Combined NB+ICRF Heating experiments in ELM-free Hot-Ion H-modes has been carried out during the JET MKII Divertor campaign.

The addition of ICRH results in increased core electron and ion temperature and stored energy, up to a record of 14.5 MJ. DD fusion yield is enhanced up to 30% by the addition of ICRH, resulting in a record for ELM-free Hot-Ion H-mode of 5.2×10^{16} neutrons/s.

Data from the High Energy NPA show presence of deuterons above the NB injection energy suggesting that ICRF power is absorbed by deuterons at the $2\omega_{CD}$ resonance. PION code simulations indicate that up to 40% of ICRF power is absorbed by bulk and NB ions, with tail formation minimised by polychrome operation.

Acknowledgements The authors gratefully acknowledge the support of the JET experimental Team and in particular of the RF Division and Task Force H personnel.

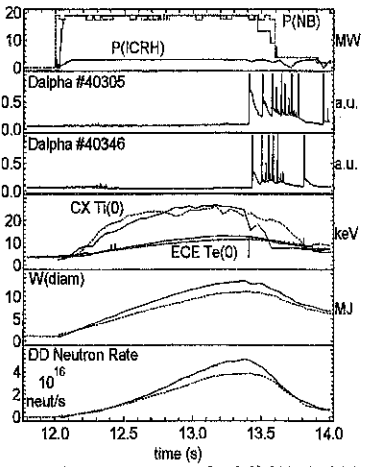

Fig 1 : plasma parameters for 3.8MA/3.4T ELM-free Hot-Ion H-modes with NB+ICRH (#40305 - solid) and NB only (#40346 - dashed)

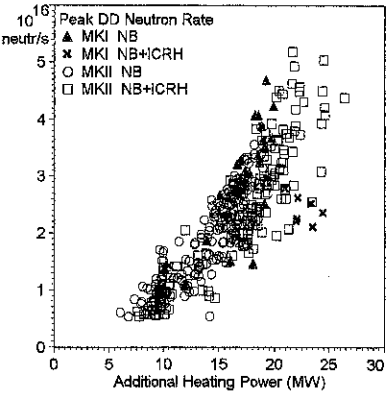

Fig. 2 : Peak DD Neutron Rate vs. Additional Heating Power for ELM-free Hot-Ion H-modes

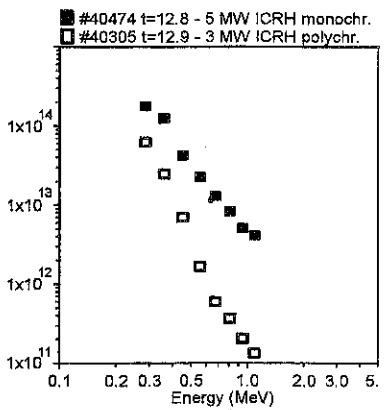

Fig. 3 : line integrated deuteron distribution function (NPA) for two ICRH schemes in ELM-fee Hot-Ion H-mode. Data taken at same values of electron density and temperature

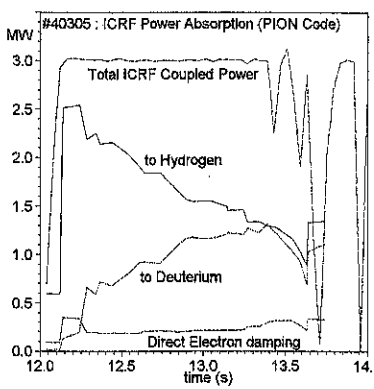

Fig. 4 : PION code - time evolution of ICRF Power absorption for NB+ICRH ELM-free Hot-Ion H-mode #40305

References

[1] T.T.C. Jones et al., Proc. of 38th Mtg. of APS Div. of Plasma Phys., Denver, USA 1996
[2] G.Cottrell et al. Proc. of 23rd EPS Conf. on Contr. Fusion and Plasma Phys., Kiev 1996
[3] M.F. Nave et al., these Proceedings
[4] A.A. Korothov et al., Nuclear Fusion **37** 35 (1997)
[5] G. Cottrell et al., these Proceedings
[6] L.-G. Eriksson et al., Nuclear Fusion **33** 1037 (1993)
[7] M. Mantsinen et al., these Proceedings

β scaling of confinement time

J.P. Christiansen, B. Balet, J.G. Cordey, C. Gormezano, L.-G. Eriksson, W. Kerner, E. Righi, D. Start, K. Thomsen
JET Joint Undertaking, Abingdon, Oxon, OX14 3EA, U.K.

1. Introduction

Extrapolations to future tokamaks from the multi-machine databases are subject to uncertainties depending on the direction and length of the extrapolation vector. Two approaches are traditionally employed. In the first approach empirical scaling laws for confinement, such as ITER93H, allow for extrapolations to be made in a multidimensional space: the step from JET to ITER involves changes to minor-major radius, current, field, density, mass number. In the second approach an extrapolation is made in only one variable i.e. in a specified direction: the step from a specific operating regime of JET to a similar one in ITER involves a "similarity scaling" of normalised Larmor radius ρ_*. In both approaches the scaling of confinement time τ_E with the relevant variables is assumed known, e.g. $\tau_E \sim \rho_*^{x_\rho}$. The uncertainty in an extrapolation can be assessed on the basis of statistical estimates for the uncertainties δx_ρ, $\delta\rho_*$ and/or experimental errors $\Delta\tau_E$; standard statistical procedures thus lead to a prediction for τ_E within some confidence interval [1, 2].

In this paper we examine results from similarity scaling experiments on JET. Section 2 describes how the experiments on ELMy steady H-mode plasmas confirm the scaling predicted by ITER93H of τ_E with ρ_* and with collisionality ν_*; the scaling of τ_E with β is however not established in β scaling experiments as well as by JET ELMy H-mode data [3]. In section 3 we explain how the β-scaling in empirical scaling law can arise from data artefacts: collinearities and spatial concentration of data. Early work by the authors pointed out that a large number of empirical-theoretical scalings could be "unified" into a collisional gyro-Bohm scaling and all differences could be accounted for by different β-scalings. As a consequence of this work we propose in section 4 a simple near-Neoclassical physics model as a physically meaningful description of the multi-machine H-mode data. This description like many others is based on the Connor-Taylor representation of the confinement scaling of a one-fluid plasma. The global confinement time is linked to a global average diffusivity

$$\tau_E = \frac{3}{4}\frac{a^2}{<\chi>} = \frac{3}{4}\frac{a^2}{\chi_B F(..,..)} = \frac{\tau_B}{F} \qquad (1)$$

The dimensionless function F is characterised by its dependence upon dimensionless plasma parameters like ρ_*, ν_*, β, ε, κ, M, q_* etc. As an example we quote the ITER 93H scaling law [2] which is the result of a linear regression on multi-machine data and it corresponds to

$$F_{93H} = C_{93}\, \rho_*^{0.78}\, \nu_*^{0.28}\, \beta^{1.24}\, \varepsilon^{5.05}\, \kappa^{-0.15}\, M^{-1.23}\, q^{-1.03} \qquad (2)$$

It has proved difficult to associate a plasma physics model with this empirical result for the following reasons:

1) gyro-Bohm scaling does not seem compatible with β-degradation.
2) The pronounced ε scaling should strongly favour Stellarators over Tokamaks.
3) The mass scaling is opposite to that of ion gyro-Bohm losses.
4) The q scaling is opposite to Neoclassical.

2. JET similarity scaling experiments

More than 50 JET pulses, NBI heated steady ELMy H-modes, with fixed geometry (ITER shape) have variations of F (2) arising from variations of one variable only, either ρ_*, ν_* or β; a subset of the "most similar" pulses is established by selecting global characteristics: pairs of pulses with matching ELM features and values of (ν_*, β_N), (ρ_*, ν_*), (ρ_*, β_N) respectively; ρ_*, ν_*, β are evaluated from the thermal energy content after the fast ion energy content W_f has been estimated. This estimate is based upon a fit to results from calculations by the TRANSP code

$$W_f = 7.5\, 10^{14} < T_e > P_{NBI} < n_e >^{-1} \qquad (3)$$

From (1) the global average of F (thermal) is calculated and the results from global similarity scans are

$$F \sim \rho_*^{1} \quad , \quad 2\,10^{-4} < \rho_* < 3\,10^{-4} \qquad (4a)$$

$$F \sim \nu_*^{0.3} \quad , \quad 10^{-3} < \nu_* < 7\,10^{-2} \qquad (4b)$$

$$F \neq F(\beta_N) \quad , \quad 1 < \beta_N < 2.3 \qquad (4c)$$

Some of the results have previously been reported [3]. Any residual or incorrect scaling can be examined by the data variation of $H_{93} = \tau_E/\tau_{93}$ against several parameters. It is found that

$H_{93} \sim \beta_N$ for $1 < \beta_N < 2$; thus the β scaling of ITER93H is not a good description of JET ELMy H-mode data.

3. β scaling of confinement

The ITER H-mode database [2] contain 858 ELM free and 769 ELMy data set values. Data collinearity problems amongst some of the variables used in (2) are well known [1, 2]. We have carried out a systematic study of the relationships between the variables in (2). A simple linear regression is made on the data of variables like e.g.

$$\{\beta\} = \beta_o + \gamma \{\varepsilon\} \tag{5}$$

In addition we carry out linear regression on residuals ratios such as e.g.

$$R_{\beta\varepsilon M} = \frac{\tau_E}{\tau_B} F_{93}\, \beta^{-1.24}\, \varepsilon^{-5.05}\, M^{1.23} \tag{6}$$

In a linear regression we assign the remaining variation of $R_{\beta\varepsilon M}$ to just β, say, via

$$\log R_{\beta\varepsilon M} = \log R^{o}_{\beta\varepsilon M} + x_\beta \log \beta \tag{7}$$

This procedure can demonstrate how x_β will vary when assumptions about the scalings with other variables are made. It is thus fundamentally different from studying the elements of the data correlation matrix which are formed on the presumption of definite dependencies through correlations. The representation (7) shows that the β scaling remains $x_\beta < 0$, until the assumption

$$\tau_E \sim \varepsilon^{x_\varepsilon} \tag{8}$$

is made; fitting to the 6 data values on ε yields $x_\beta = +1.24$ in (2). The main reason for the unphysical β scaling in (2) is the database collinearity (5) and the assumption (8).
Similar analysis is applied to other variables. The result of our analysis shows that

$$Y = \left(\beta^3\, \varepsilon^5\, \kappa^{1/3}\, M^{-1}\, q^{-2}\right)^{1/3} \approx \text{const.} \tag{9}$$

The representation of Y can be made with a data distribution yielding an RMS error of 18%. The scatter of data on Y is similar to that of H_{93} and is shown in Figure 1; the symbols in Figures 1 and 2 refer to the Tokamaks JET, DIII etc.

4. Near Neoclassical scaling

An examination of the ITER93 scaling expression (2) and the ITERDB2 data artefact Y given by (9) demonstrates that the scaling of F (or τ_E) with β, M, q, κ can be eliminated if we form F_{93}/Y. This procedure leaves us with a simple near-neoclassical model (subscript NN)

$$F_{NN} = C_{NN}\ \rho_*\ \nu_*^{1/3}\ \varepsilon^3\ C_{ELM} \qquad (10)$$

This model represents ELM free, ELMy and ELM free + ELMy data with a σ = 16-16.7%; Figure 2 shows the model representation of the ELMy data in DB2. The ELM free data determines the constant $C_{NN} = 7\ 10^{-3}$ and the ELMy data determines $C_{ELM} = 0.69$. The scaling (10) is nearly Neoclassical but it is degraded by collisionless (electrostatic) processes which cannot be determined from present data. Both C_{NN} and C_{ELM} may contain hidden physics. The remnant Neoclassical q_ψ^2 scaling can be represented by the global constant average $< q_\psi^2 > \ = \ 4-5$ which has been absorbed by C_{NN}.

Eq. (10) represents a physically meaningful and much simpler data representation than the 8 parameter form of ITER93H. However, the ε^3 scaling is not understood and may be due to other data artefacts.

[1] Nucl. Fusion 30 (1990) 1999. L-mode database working group

[2] Nucl. Fusion 32 (1992) 291, Nucl. Fusion 34 (1994) 131. H-mode database working group.

[3] JET Team, IAEA-CN-64/API-1, Montreal, 1996.

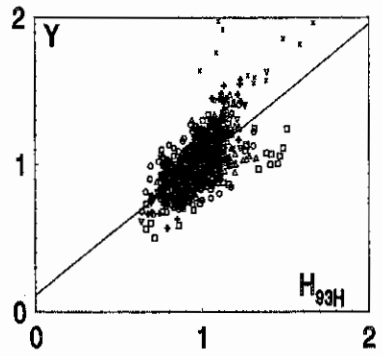

Fig.1 Data artefact Y (eq.9) correlates with H_{93}

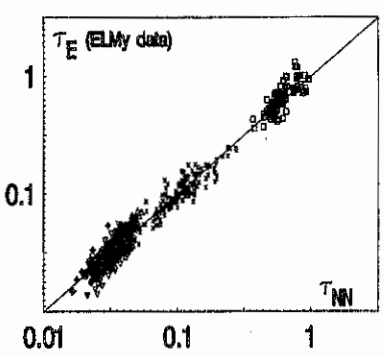

Fig.2 Near Neoclassical model (eq.10) description vs data

The Role of Edge Parameters in the H-mode Transition on JET

E Righi, D Bartlett, GD Conway, JG Cordey, JCM de Haas, L Horton, C Ingesson, L Porte*, R Sartori, ACC Sips, DFH Start

JET Joint Undertaking, Abingdon, OXON, OX14 3EA, England
*Present address: UCLA, Dept. of Electrical Engineering, USA

Introduction

Investigation of the edge conditions favourable to the transition to H-mode is of primary importance in order to understand the physics of the H-mode. Edge parameters have also been recognised as a key issue to extrapolate the operational space from present machines to ITER [1,2,3]. Results indicate that a necessary condition for the transition into H-mode is that the plasma edge exceeds a critical temperature, T_{crit}, which is weakly dependent on the edge density. However the scaling with the toroidal field B_t is not clear: while for ASDEX-U $T_{crit} \propto B_t$ [4], results from Alcator C-MOD give $T_{crit} \propto B_t^{1.46}$ [2] and for JET $T_{crit} \propto B_t^2$ [5].

In the first part of this paper experiments carried out on JET aimed at investigating the edge conditions in which the L-H and H-L transitions occur are presented. Good quality data at the top of the temperature pedestal have been obtained for Ion Cyclotron Resonance Frequency (ICRF) heated H-modes at two different combinations of toroidal field, and the evolution of the H-mode has been followed in the edge (T_e, n_e) operational space.

In the second part of the paper it is shown how the edge temperature can be influenced by phenomena occurring outside the separatrix. Excess radiation, produced in the divertor region and clearly outside the last closed flux surface, contributes to keep the plasma edge cool and delays the H-mode transition until the auxiliary power is increased sufficiently to compensate for the power lost through radiation. As a result the threshold power for the transition to H-mode is higher than expected.

Pedestal Temperature and Density at the L-H and H-L Transitions

The measurement of T_e and n_e near the plasma separatrix has been carried out in ICRF heated discharges at 1.7MA/1.7T and 2.6MA/2.6T with the main geometrical parameters similar to those predicted for ITER (average triangularity $<\delta>=0.2$, $q_{95}=3$, elongation $\kappa=1.7$). ICRF power was slowly ramped up to cross the threshold in order to minimise the contribution

of dW_{DIA}/dt in the expression of the threshold power. The gas fuelling rate was changed as much as possible from shot to shot to achieve the widest density range. The electron temperature at the plasma edge was measured using the ECE heterodyne radiometer. In the case of JET plasmas the measurement of the edge electron temperature, T_{ea}, is limited by the achievable spatial resolution, which is determined mainly by the plasma optical depth. For the data presented here, the plasma is in L-mode conditions or very early in the H-mode phase. This translates into a radial resolution of the order of 10mm, and a lowest measurable $T_{ea} \approx 100$ eV. The position of the separatrix, estimated from EFIT reconstruction of the magnetic equilibrium, is known with an uncertainty of ±2cm. Direct measurement of the electron density in this region is very difficult on JET with the present diagnostics. An indirect way to obtain the edge density consists in the use of the Abel inversion method by means of a series of polynomials fitted to the FIR interferometer data. The profile is mapped onto the EFIT equilibrium and a zero density at the last closed surface is assumed.

The results of the measurement of electron temperature and density at the top of the T_e pedestal ($R \cong 3.83$m) are summarised in Fig.1 for the two I_p/B_t combinations. The first transition into H-mode, from L-mode into a dithering H-mode, occurs at values of $T_{e,pedestal} \approx 300$ eV and is very weakly dependent on density. The plasma subsequently goes into ELMy H-mode at higher values of both T_{ea} and n_{ea}, when the transport barrier has already formed and the density dependence is stronger. The B_t dependence is however weaker than expected, with $T_{e,pedestal} \propto B_t^{0.4}$ for the transitions into dithering H-mode and $T_{e,pedestal} \propto B_t^{0.6}$ for the transitions into ELMy H-mode. This contrasts with results both from other tokamaks [1,2] and from JET MkI data [5]. The discrepancy could arise, for JET, from the different positions, along the T_e profile, where T_{ea} was measured (about 15cm from the separatrix for JET). The plasma evolution can be followed in Fig.2. The edge electron temperature needs first to reach a minimum value, T^1_{crit}, in order to go into H-mode. When the power (and the density) is further increased, $T_{e,pedestal}$ exceeds another critical value, T^2_{crit}, to go into ELMy H-mode. T_{ea} and n_{ea} evolve in parallel during the ELMy phase of the discharge until a saturation point seems to be reached, where n_{ea} continues to increase but T_{ea} remains roughly constant. The H-L transition occurs at values of T_{ea} roughly equal to T^2_{crit} (no hysteresis at the plasma edge).

Influence of X-Point Radiation on the H-Mode Transition

From the previous discussion it follows that conditions at the plasma edge for the H-mode transition must be such as to allow the temperature to exceed a critical value. Here an

example is presented where excessive radiation keeps T_{ea} below T_{crit} and, as a consequence, the plasma remains in H-mode. Two NBI heated discharges, one with the strike zones on the horizontal divertor target plates (Pulse No 38470 in Fig.3) and the other on the vertical target plates (Pulse No 38469 in Fig.4) are considered. For these two discharges power waveform, target density, plasma current and toroidal field are identical. In both figures the threshold power, calculated using the most recent multi-machine scaling expression [6] corrected to take into account radiation losses from the bulk plasma, is overlaid to the power traces. In the case of #38469 the strike zones were positioned on parts of the vertical target plates that were subsequently found not to be properly conditioned. As a consequence, the total radiation is about 50% higher, and the plasma remains in L-mode. Reconstruction of the radiation distribution in the divertor region shows that such excess radiation is produced outside the separatrix and near the inner divertor leg. In these circumstances calculation of the threshold power, even corrected for radiation losses from the bulk plasma, is not realistic. Calculation of the threshold power further corrected to take into account the total radiation gives a higher threshold and shows that only at the highest power step the transition is possible. The fundamental difference between the two discharges lies at the plasma edge. In fact for #38470 the L-H transition occurs at $T_{ea} \cong 400$ eV, a value in agreement with that of T_{crit} for the transition to dithering H-mode shown in Fig.1. However such temperature is reached only at the end of the high power phase in the case of #38469, in correspondence of which the D_α trace shows signs of dithering. Preliminary calculations indicate that such excess radiation, produced in the divertor region, can affect the upstream temperature.

Summary and Conclusions

Experiments confirm the existence of a critical temperature T_{crit} for each type of H-mode transition on JET. T^1_{crit} (L-mode to dithering H-mode) is weakly dependent on density, while $T^2_{crit} \propto 1/n_e$ (dithering to ELMy H-mode). Dependence on the toroidal field is weak ($T^{1,2}_{crit} \propto \sqrt{B_t}$) for both types of transition, in contrast with results from other tokamaks and from JET MkI. These results show that there is no hysteresis in the H-L transition at the plasma edge. Experimental evidence also suggests that excessive radiation losses, although originated *outside* the last closed flux surface, affect the edge temperature and can contribute to keep T_{ea} below T_{crit} and prevent the transition to H-mode. The result is that in these conditions the threshold power is effectively higher.

References

1. M Kaufmann et al., Proc. 16th IAEA Fusion Energy Conference, Montreal (Canada), IAEA-CN-64/O1 (1996).
2. J Snipes et al., Proc. 16th IAEA Fusion Energy Conference, Montreal (Canada), IAEA-CN-64/AP-2 (1996).
3. J Snipes et al., These Proceedings.
4. H Zohm et al., Proc. 16th IAEA Fusion Energy Conference, Montreal (Canada), IAEA-CN-64/AP-1 (1996).
5. E Righi et al., to be submitted for publication in Plasma Phys. and Controlled Fusion (1997).
6. T Takizuka et al., Proc. 16th IAEA Fusion Energy Conference, Montreal (Canada), IAEA-CN-64/F-5 (1996).

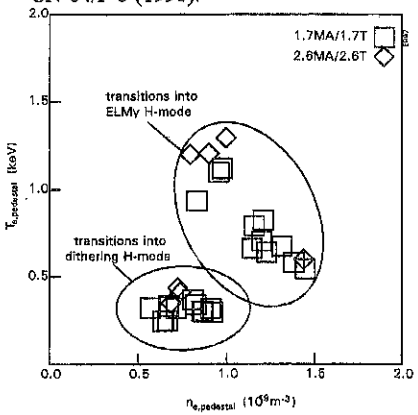

Figure 1.Measurement of pedestal temperature and density at the transition to dithering and ELMy H-mode for B_t=1.7T, 2.6T in ICRF heated plasmas.

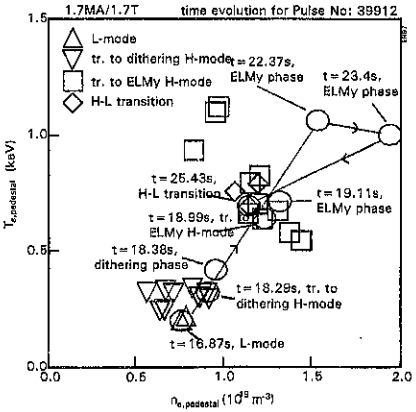

Figure 2. Evolution of T_{ea} n_{ea} in the edge operational space from L-mode to dithering and ELMy H-mode and back again to L-mode at the end of the discharge.

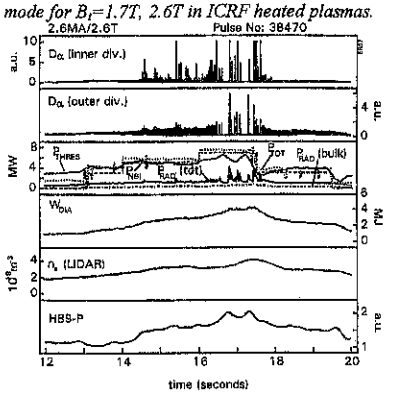

Figure 3. Time evolution of the main plasma parameters for the reference pulse #38470. The plasma goes into H-mode at $P_{TOT} \cong P_{THRES}$ [6], corrected for radiation losses from the bulk plasma.

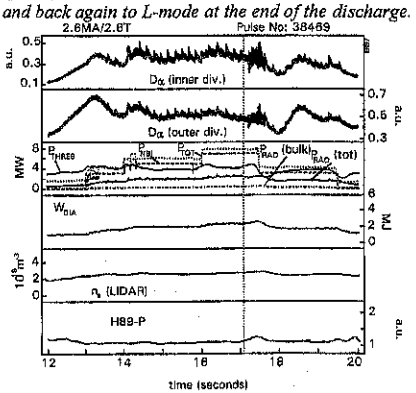

Figure 4. A discharge identical to that of Fig.3, but with the strike zones on unconditioned parts of the vertical target plates, shows no signs of H-mode. Due to the excess radiation $T_{ea} < T_{crit}$.

Operation at High Performance in Optimised Shear Plasmas in JET

A.C.C. Sips, C.D. Challis, G. Cottrell, L-G Eriksson, C. Gormezano, C. Gowers, C.M. Greenfield[1], J.C.M de Haas, M. von Hellerman, G.T.A. Huysmans, R. König, E.A. Lazarus[2], T. Luce[1], P. Nielsen, D. O'Brien, B.W. Rice[3], G. Sadler, F.X. Söldner, M. F. Stamp, E.J. Strait[1], B.J.D. Tubbing, M. Wade[2], and D.J. Ward.

JET Joint Undertaking, Abingdon, Oxon, OX14 3EA, United Kingdom.
[1]General Atomics, San Diego, USA, [2]Oak Ridge National Laboratory, Oak Ridge, Tennessee, USA, [3]Lawrence Livermore National Laboratory, Livermore, California, USA.

Introduction

In JET, internal transport barriers can be obtained when the main power is applied during the current ramp-up phase of the discharge, in conditions of low or negative central shear [1,2]. When central heating is applied, a regime with strongly peaked pressure profiles can be obtained which has improved confinement in the inner region of the plasma (Internal Transport Barrier). During the main heating, the central pressure continues to increase and needs to be controlled to avoid MHD instabilities (mainly disruptions). This can be achieved by controlling the input power, to allow the pressure profile to broaden, by using feedback on the D-D reaction rate. This regime has been optimised to D-D neutron rates in excess of 5×10^{16} n/s (with $n_{e0} \approx 6\times10^{19}m^{-3}$, $T_{e0} \approx 12$ keV and $T_{i0} \approx 26$ keV).

Current rise and barrier formation

A current rise in X-point and low density is used to provide the target for the high power heating phase. Low power LHCD and ICRH are used to modify the central q-values of the target plasma. However, when NBI is used for pre-heating, the power levels required to modify the q-profile trigger ELMy H-modes and deteriorate the target conditions required for the formation of the internal barrier (low target density for central power deposition). The scenario that provides the optimum target conditions in JET has LHCD in the first second after breakdown (Figure 1). After this, the X-point is formed and a low density Ohmic phase is followed by low power ICRH preheating (≈1 MW) to increase the electron temperature to 5 keV.

Both NBI (≤ 20 MW) and ICRH (≤ 10 MW) are applied to heat the centre of the discharge. Above a certain threshold power an internal transport barrier is formed with the plasma remaining in L-mode. The L-mode maintains the central power deposition of the neutral beams. The onset of the H-mode is delayed by: a) A very low target density: $0.6 \cdot 10^{19}$ m^{-3} with a low edge density, b) a continuation of the current ramp, and c) a low triangularity of the plasma cross-section at the start of the main heating. At this stage it is not clear if the formation of the Internal Transport Barrier prevents the plasma going to H-mode.

In Figure 2 the rapid increase of the ion temperature in the first second of the heating phase is shown. With the increase of the ion pressure the ICRH switches to bulk ion heating. This implies that NBI power is important to trigger the barrier, when ICRH still heats electrons and an increase in power can be detrimental (early H-mode). After the barrier is formed, the pressure peaking can be controlled with ICRH due to its narrow power deposition profile. The optimum ICRH power level is determined by the initial requirement to keep the electron temperature high, but to avoid the H-mode, and to control the ion pressure rise when the Internal Transport Barrier is formed.

In Figure 3 and Figure 4 the evolution of the q-profile and the Ion temperature are given. The heating is started at 5 seconds, which has given the best performance in JET. The timing of the heating has been varied to obtain different target q-profiles in the centre. For the later heating times the current rise can not be continued in the pre-heating phase due to low density error field modes at lower edge q. The low target density can be maintained by making a short flat top, however the subsequent current ramp needs to be increased to keep the plasma in L-mode.

Performance control

The evolution of the density profile is shown in Figure 5. The strike points are actively pumped by the divertor cryo-pump, keeping the edge density low. After the barrier formation, the plasma particle inventory in the centre rises by the number of NB particles deposited inside the barrier [3].

The MHD stability of the plasma is determined by the pressure peaking [4]. Just after the barrier formation the pressure peaking factor reaches its maximum. After this, the region of improved confinement expands, which broadens the pressure profile while the central density continues to increase. Important is not to 'overheat' the centre before the barrier has

moved out sufficiently (Figure 6). This implies controlling the input power to avoid disruptions, which can be achieved by controlling the rise of the D-D reaction rate (R_{DD}) with the input power. Typically, the ICRH power is stepped down when R_{DD} reaches $4x10^{16}$/s, and the NBI power is controlled by a R_{DD} waveform request. As shown in Figure 6, an initial lower rise of R_{DD} provides stability (and reproducibility) to obtain a high peak and overall neutron rate. For this regime, R_{DD} is related to the stored energy (W_{dia}) and the ratio of central (nel_{centre}) and edge (nel_{edge}) line averaged densities: $R_{DD} \propto (W_{dia})^2 \cdot (nel_{centre}/ nel_{edge})$.

Conclusions

In JET, heating a discharge with conditions of low or negative central shear has provided a regime with peaked pressure profiles and improved central confinement. By tailoring the target plasma and controlling the pressure peaking, MHD instabilities can be avoided. This 'Optimised Shear Regime' has provided the highest D-D neutron rates in JET, in excess of $5x10^{16}$ n/s (with $n_{e0} \approx 6 \cdot 10^{19} m^{-3}$, $T_{e0} \approx 12$ keV and $T_{i0} \approx 26$ keV). It provides, with the use of all of the heating methods of JET, a good basis for further physics studies and performance improvements in the next operational campaigns.

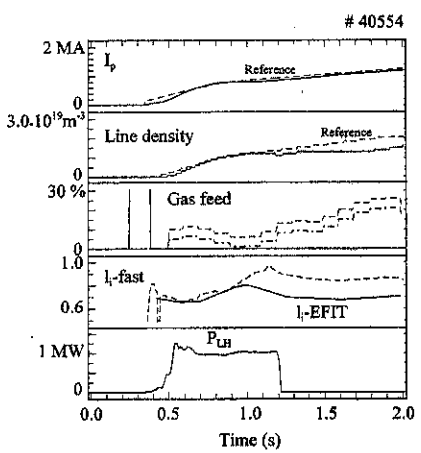

Fig. 1: Breakdown and initial current rise with LHCD assist. The X-point is formed at 1.3 seconds.

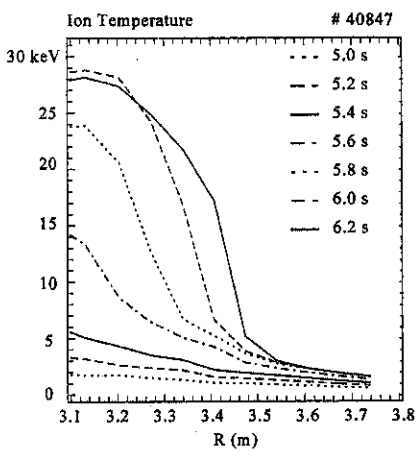

Fig. 2: Increase in central ion temperature in the first second of additional heating. Maximum NBI power starts at 5.4 seconds.

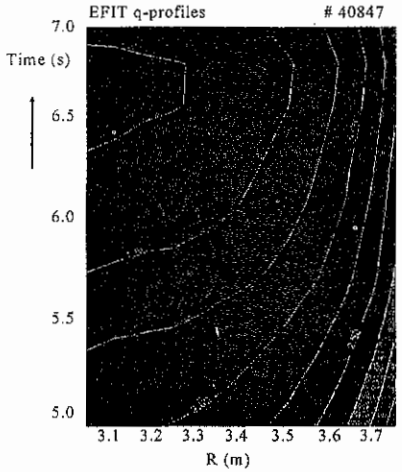

Fig. 3: Contour plot of q-profile evolution. Heating is started at 5.0 seconds.

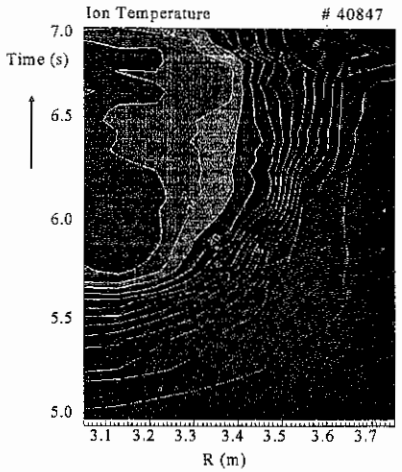

Fig. 4: With 17.5 MW NBI and 6 MW ICRH at 5.4 seconds the barrier is formed.

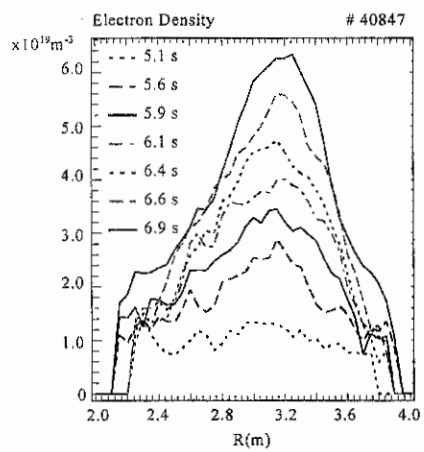

Fig. 5: Density profile evolution during the main heating phase.

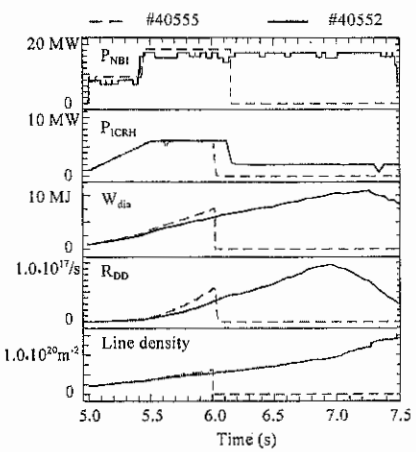

Fig. 6: NBI power is increased (# 40555), the pressure peaks too much and the plasma disrupts.

References [1] Gormezano C., 1997 Plasma Phys. and Contr. Nucl. Fusion Research (Proc. 16th Int. Conf., Montreal, 1996) to be published, [2] Söldner F.X., Topical Paper, This Conference, [3] Cottrell G., This Conference, [4] Huysmans G.T.A., This Conference.

Statistical Analysis of Type I ELMs at JET

R. Mohanti, C. Brickley, J.P. Christiansen, J.C.M. de Haas, J. J. Ellis, G. Fishpool, L.D. Horton, J. Lingertat, A. Loarte, C.G. Lowry, D. O'Brien, M.F. Stamp, K. Thomsen, G.C. Vlases, W. Zhang

JET Joint Undertaking, Abingdon, Oxon, OX14 3EA, UK

INTRODUCTION

Edge localised modes (ELMs), MHD phenomena observed at the plasma edge, in H-Mode discharges, are characterised by a sharp increase in the Balmer-alpha (Dα) emission. Steady-state H-Mode discharges at JET with neutral beam (NB) heating power well above the H-Mode threshold power have Type I ELMs. Type I ELMs are characterised by increasing ELM frequency with an increase in input power. Steady-state H-Mode experiments with different divertors , viz., MarkI, and MarkIIA, have been carried out at JET with variations in plasma current, toroidal field, plasma configuration, additional heating and D_2 gas fuelling rate. The results of ELM frequency and diamagnetic energy confinement are presented for Type I ELMs of NBI heated discharges, with and without gas fuelling. The results include percentage change in diamagnetic energy, and electron particle content per ELM. In addition, the time averaged power and density losses as functions of input power and injected particles, respectively, are presented.

DIAGNOSTICS AND CALCULATION OF STEP CHANGES

The divertors, MarkI and MarkIIA, are part of the JET programme designed to investigate the effect of divertor geometry on plasma performance. The present divertor under investigation is MarkIIA which is geometrically more closed than MarkI. The bypass leaks between the subdivertor volume and main chamber of the MarkIIA divertor were reduced at a later stage. MarkI discharges have low average separatrix triangularity, ($0.10<\delta<0.20$), whereas those of MarkIIA have low to high average separatrix triangularity ($0.20<\delta<0.35$). The average separatrix triangularity is taken as the average of the upper separatrix and lower separatrix triangularity. Furthermore, the MarkI discharges had low gas fuelling rate, relative to MarkIIA.

Three different types of diagnostics were used for the statistical analysis of Type I ELMs. The magnetic diagnostics include flux loops and pick up coils with the standard sampling frequency of about 90 Hz and a fast window of 5 kHz. Calibrated signals from flux loops and pick up coils are used to determine the changes in diamagnetic energy. The electron particle density is measured using a multichannel FIR (far infrared interferometer) with the standard sampling frequency of about 170 Hz and a fast window of 10 kHz (maximum). Results in this paper are reported for the central vertical chord at a major radius of 3.04m. The Balmer- alpha (Dα) monitor is a visible spectroscopy device and the channel used to estimate the ELM frequency is a vertical view at a major radius of 3.1m, which intersects the SOL outside the divertor. The standard sampling frequency of the Dα signal is 10 kHz.

A typical trace of particle and diamagnetic energy drops of a Type I ELM is shown in Fig. 1. The overshoot in energy drop is due to induced eddy currents, hence the calculation of energy drop due to ELMs is carried out as illustrated in Fig. 1. The diamagnetic energy increases following the drop until the next ELM.

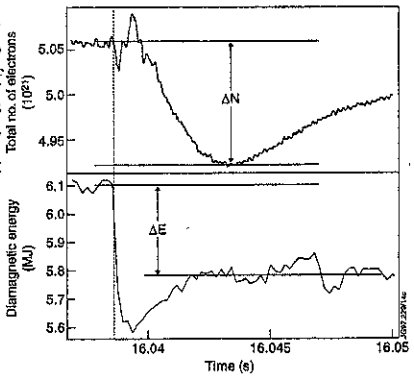

Figure 1 Typical trace of total electron particle and diamagnetic energy for a TYPE I ELM

ELM FREQUENCY AND DIAMAGNETIC ENERGY CONFINEMENT

It has been observed that ELM frequency is the controlling factor in steady-state ELMy H-Mode discharges. The ELM frequency, at fixed input power, magnetic field, and plasma current, depends primarily on triangularity, δ, and gas fuelling rate, as shown in Fig. 2(a) and Fig. 2(b). The variation of ELM frequency with gas fuelling rate on vertical and horizontal targets are different. Furthermore, the change of ELM frequency with gas fuelling rate differs with triangularity, for the same target orientation. The ELM frequency, at δ=0.2 is estimated to be f_{ELM} (Hz)=4.95(± 0.3)(Pin-1.5)$^{1.11\pm0.04}$ /Ip$^{1.79\pm0.084}$.The trends in ELM frequency with input power and plasma current are similar to those observed at ASDEX [1] and DIII-D [2].

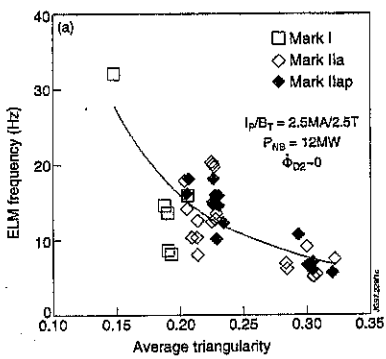

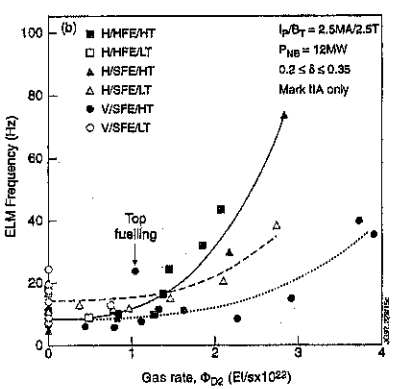

Figure 2 ELM Frequency versus :(a) Triangularity (b) Gas fuelling rate for Ip/Bt=2.5MA/2.5T at Pnb=12MW

The H89P enhancement factor between ELMs, is shown in Fig. 3(a). H89P between ELMs is about 2.5 for high triangularity (δ ~ 0.30) MarkIIA discharges, and increases with decreasing triangularity; for similar conditions in MkI it is about 2.2. H89P between ELMs reduces with increasing gas fuelling rate, relative to beam fuelling only. The time averaged H89P (averaged over several ELMs) is 65-85%, of H89P between ELMs, for discharges with beam fuelling

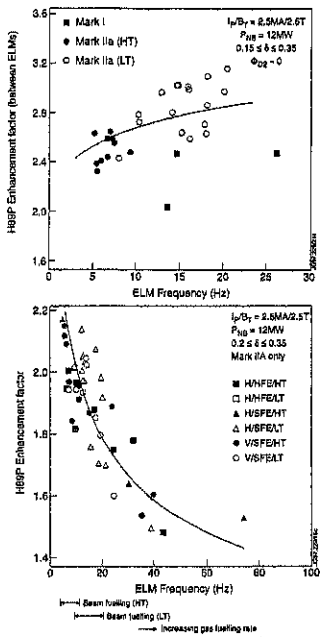

Figure 3(a) H89P between ELM; (b) Time averaged H89P (averaged over several ELMs) versus ELM frequency

only (Fig. 3(b)).

CHANGES IN DIAMAGNETIC ENERGY, AND DENSITY DUE TO ELMS

The percentage step change in diamagnetic energy per ELM, $\Delta E/E$, and step change in diamagnetic energy, ΔE, decrease approximately as the square root of ELM frequency, for a fixed plasma current (Figs. 4(a) & (b)). There are indications of a decrease in $\Delta E/E$ with increasing plasma current, however, there is no clear indication of any trend in ΔE with Ip. The $\Delta E/E$, in MarkI shows the same trend with ELM frequency, as that in MarkII [4]. The percentage step change in electron density, $\Delta N/N$, and the step change in electron density, ΔN, have similar trends as $\Delta E/E$ with ELM frequency, however do not indicate any current scaling (Figs. 5(a) & 5(b)).

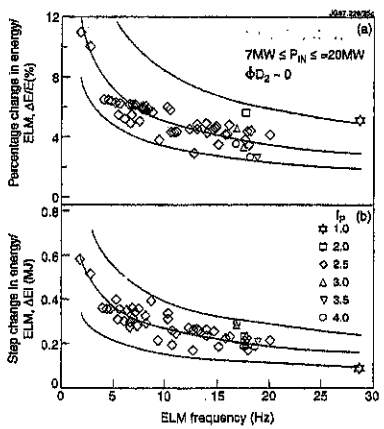

Figure 4(a) Percentage change in Energy/ELM, (b) Step change in Energy/ELM for MarkIIA

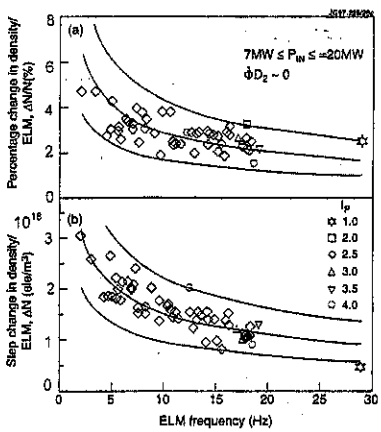

Figure 5(a) Percentage change in density/ELM (b) Step change in density/ELM for MarkIIA

The time average power loss due to ELMs, $\Delta E \times f_{ELM}$, is about 20% and 30% of the input power, for high and low triangularity, respectively for MarkIIA discharges (Fig. 6). The trend in average power loss due to ELMs is different in MarkI discharges ranging from about 0.2-0.25. The average power loss due to ELMs increases with gas fuelling for the same input power, as observed in discharges with Pin=12 MW and high triangularity configurations. The average density loss rate due to ELMs, $\Delta N \times f_{ELM}$, is approximately equal to the injected particle rate with NBI fuelling only.

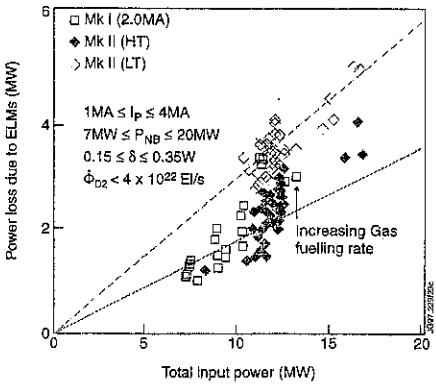

Figure 6 Time average power loss due to ELMs versus input power

ESTIMATED VALUES FOR ITER

The ITER design value for ELM frequency, f_{ELM}, is 3 Hz. For an input power of 300MW (alpha-heating power), plasma current of 21 MA, average separatrix triangularity of 0.3 and no gas fuelling, it is possible to obtain ITER's design f_{ELM} from JET data if it is assumed that $f_{ELM} \propto 1/R$ (where R is the major radius).

Table I gives a summary of some of the different methods used to predict the drop in energy/ELM and the corresponding temperature rise. The temperature rise is estimated for CFC (carbon fibre composite) as the target material, a total deposition area of 14 m^2 [6], and 200 μs deposition time.

Table I Estimated drop in energy/ELM and rise in temperature

	$\Delta E/E \propto f_{ELM}^{-0.51} Ip^{-0.5}$ Fig. 4(a)	$\Delta E \propto f_{ELM}^{-0.46}$ Fig. 4(b)	$\Delta E \propto Pin/f_{ELM}$ (Fig. 6 & Ref. [5])
ΔE(MJ/ELM)	30	0.5	25
ΔT(C)	8100	140	6750

It should be noted that the above estimated values may change with triangularity, gas fuelling rate and with machine size.

REFERENCES

[1] O. Vollmer et al, 18th EPS Conf., Vol. 15 C, Part I, I-385, 3-7 June 1991, Berlin.
[2] T. Osborne, Fourth Workshop of the ITER Expert Group on Divertor Modelling and Databases, San Diego, California, March 11-15, 1996.
[3] JET Divertor Task Force and Divertor Physics Topic Group (presented by L.D. Horton), these proceedings
[4] ITER DDR, December, 1996.
[5] J. Lingertat et al., 4th European Physics Workshop, Stockholm, 11-13 Dec., 1996.
[6] R. Tivey, private communication, June, 1997.

PLASMA RESPONSE TO EDGE COOLING IN JET AND RELATION TO PLASMA CONFINEMENT

P.Mantica[1], A.Cherubini, F.De Luca[1,2], M.Erba[3], P.Galli[1,2], R.Giannella, G.Gorini [1,2], A.Jacchia[1], H.J.Jäckel, V.V.Parail, L.Porte, A.Taroni

JET Joint Undertaking, Abingdon OX14 3EA, United Kingdom
[1]Istituto di Fisica del Plasma, EURATOM-ENEA-CNR Association, I-20133 Milano, Italy
[2] INFM and Physics Department, University of Milano, I-20133 Milano, Italy
[3]EURATOM-CEA Association , C.E. Cadarache, 13108 Saint Paul lez Durance France

Impurity injection by Laser Ablation (LA) causes a sudden local cooling of the electrons at plasma edge - the so called "cold pulse" (CP) - whose dynamics has been widely studied in JET [1]. The non local character of the plasma response to edge cooling is a well established fact; at JET it manifests itself in the form of a fast (Δt~1 ms) change in the time derivative of the electron temperature T_e occurring at the time of the impurity injection over a large fraction of the plasma volume. Such a discontinuity can be interpreted in terms of a sudden change of the electron thermal diffusivity similarly to some other transport transients, especially those originating from the plasma edge (e.g., L-H transition, ELMs) [2] [3]. In the case of CP events, the transport increase is generally short lived (a few ms) unless edge cooling triggers a type-I ELM spoiling the phase of good confinement.

A quantitative measure of the plasma response is obtained by determining the jump in electron diffusivity, $\Delta\chi_e$, at the Laser Ablation time, t_{LA}, across the plasma. Previous results [1] suggested that the $\Delta\chi_e$ profile can be strongly non-uniform depending on plasma conditions. Furthermore, the strength of the response seemed to be independent of the increase in radiated power, ΔP_{rad}, and related to the confinement state of the plasma; i.e.,the response was found to be stronger when the plasma approached the maximum energy content allowed by global stability constraints.

In order to provide a more direct test of this observation, a dedicated experiment was performed in which the impurities were ablated at five different times in a set of similar NBI heated, Hot Ion H mode plasma discharges (LA time scan). In all discharges, the NBI power is increased to its maximum level at about t_{NBI}=52 s and kept constant for a few seconds. After a short ELMy phase lasting about 0.4 s the plasma is in an ELM free, Hot Ion H mode state of confinement. The time evolution of T_e for one of the discharges (as measured by ECE heterodyne radiometer) is shown in Fig.1; T_e time traces at half normalised radius, ρ=0.5, for the five discharges are shown in Fig.2.

It can be seen that the plasma response to LA is progressively stronger. This leads us to conclude that indeed a relation exists between the strength of the plasma response to edge perturbations and some unknown physical parameter related to the plasma energy content. That the intensity of the radiation is not responsible for the strength of the plasma response is

confirmed (see Fig.2) by the fact that $\Delta P_{rad}/P_{rad}$ is much lower for the CP at t_{LA}=53.0069 s than it is for the previous event at t_{LA}=52.9098 s, whereas the enhancement of the electron transport coefficient increases monotonically with time.

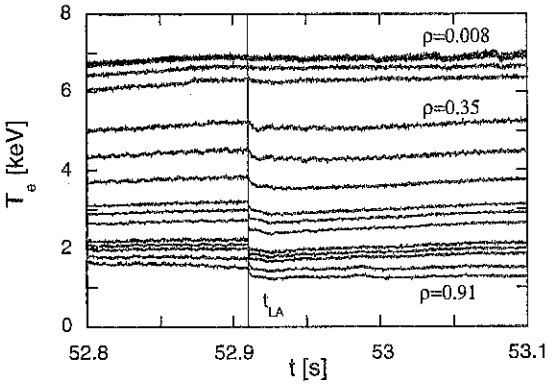

Fig.1 *Time evolution of the electron temperature following Laser Ablation in JET discharge #38385. The LA occurs at t_{LA}=52.9098 s when the plasma is well into an Hot Ion H-mode.*

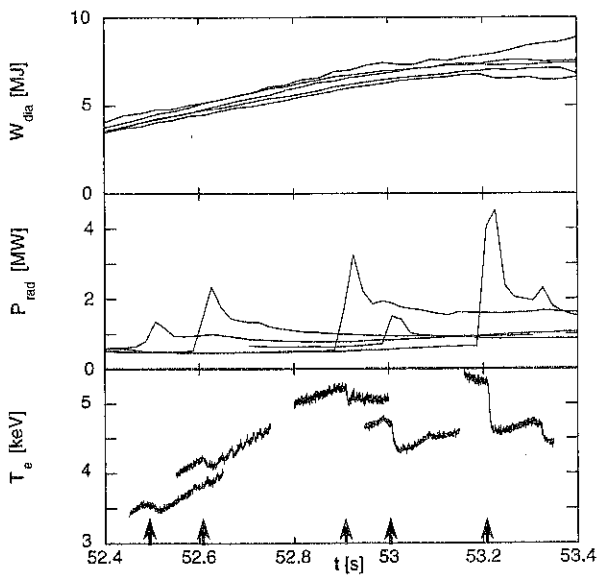

Fig.2 *Time traces of the stored energy (W_{dia}), total radiated power (P_{rad}) and electron temperature (T_e) at ρ≈0.5 for five (almost identical) Hot-ion H mode discharges where the LA time was varied as shown by arrows.*

A quantitative measure of the plasma response is obtained based on the assumption that a sudden change of the electron thermal diffusivity, $\Delta\chi_e$, occurs at t_{LA} [1].
Under this assumption, the time derivative of T_e, $\partial_t T_e$, exhibits a discontinuity at t_{LA}, $\Delta\left[\partial_t T_e\right]_{t_{LA}} = \lim_{\varepsilon\to 0^+}\left\{\left[\partial_t T_e\right]_{t_{LA}+\varepsilon} - \left[\partial_t T_e\right]_{t_{LA}-\varepsilon}\right\}$, in proportion to the changes in the diffusivity. The expression for $\Delta\chi_e$ is

$$\Delta\chi_e(\rho) = \frac{3}{2}a\frac{\int_0^\rho n_e \Delta\left[\partial_t T_e\right]_{t_{LA}} S_\rho d\rho}{n_e \nabla T_e S_\rho} \qquad (1)$$

where a is the plasma minor radius and S_ρ is the area of the flux surface of normalised radius ρ. This expression is used here to derive $\Delta\chi_e$ from the experimental density and temperature profiles. The same approach was used in [4] to determine the change in χ_e at the L-H transition in JET plasmas.

The $\Delta\chi_e$ profiles for the five CP events analysed here are shown in Fig.3. These diffusivity enhancements are short lived: typically, after 5-10 ms the plasma starts to relax back to pre-CP conditions. In the last two cases, the LA triggers a type-I ELM instability, but only the last ELM spoils the phase of improved confinement.

The relative variation of χ_e due to the CP is determined by dividing $\Delta\chi_e$ by the power balance diffusivity χ_e. The latter is determined from a transport simulation of a Hot Ion H mode discharge very similar to the ones of the CPs [5]; note that the χ_e profile does not change significantly during the Hot Ion H mode phase so the same χ_e profile is used for all CPs. The resulting $\Delta\chi_e/\chi_e$ profiles are shown in Fig.4. The increase of $\Delta\chi_e/\chi_e$ going from the plasma core to the edge is definitely beyond the uncertainties on $\Delta\chi_e/\chi_e$. Like $\Delta\chi_e$, $\Delta\chi_e/\chi_e$ is an increasing function of time.

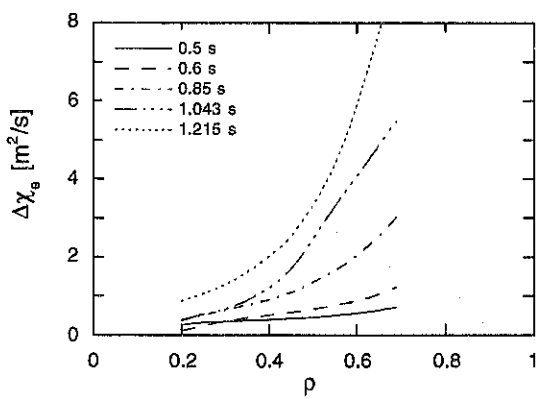

Fig.3 Profiles of the electron diffusivity enhancement, $\Delta\chi_e$, for the five CPs of Fig 2 (see text). For each discharge, the delay between the NBI switch-on time t_{NBI} and the ablation time t_{LA} is reported.

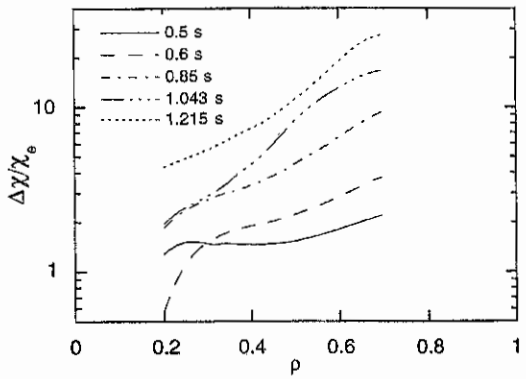

Fig.4 Relative variation of the electron diffusivity for the five CPs of Fig 2.

Several ideas have been proposed by various authors in order to explain the observed nonlocal transport features following a change of the plasma edge temperature. The strong coupling between edge and mid regions could be due, for instance, to long wavelenght turbulence originating at the edge [6] or to toroidal coupling of modes to form large radial structures [7, 8]. This nonlocality could be enhanced by the ITG turbulence destabilization caused by the cold pulse. More generally, the experimental observations reported here, establishing a quantitative relation between nonlocal changes of the electron thermal diffusivity and the attained energy content (independently of the T_e perturbation amplitude), provide a basis for testing theory based transport models aimed at reproducing the salient features of tokamak heat transport under both steady state and transient conditions.

This work was performed under the JET-ENEA-CNR task agreement on transient transport, with financial support from JET and CNR.

References

[1] *P.Galli et al., Control. Fusion and Plasma Phys. (Proc. 23rd Eur. Conf. Kiev, 1996), Vol. 20 C, Part 1, European Physical Society (1996) 135; R.Giannella et al., in Proc. 15th IAEA Conf. on Plasma Phys. and Contr. Nucl. Fusion Research (Seville, Spain, 1994), IAEA, Vienna, Vol.I, (1995) 289.*

[2] *J.G.Cordey et al., Plasma Phys. Contr. Fusion 36 (1994) A267.*

[3] *V.V.Parail et al., in Proc. 15th IAEA Conf. on Plasma Phys. and Contr. Nucl. Fusion Research (Seville, Spain, 1994), IAEA, Vienna, Vol.I, (1995) 255.*

[4] *J.G.Cordey et al., Nucl. Fusion 35 (1995) 505.*

[5] *M.Erba et al., Plasma Phys. Contr. Fusion 39 (1997) 261.*

[6] *B.B.Kadomtsev, Plasma Phys. Contr. Fusion 34 (1992) 1931.*

[7] *J.W.Connor.et al., Phys. Rev. Letters 70 (1993) 1803.*

[8] *F.Romanelli, F.Zonca, Phys. Fluids B 5 (1993) 4081.*

Turbulence Studies in the JET Scrape-off Layer Plasmas

I. García-Cortés[1], M. Endler[2], A. Loarte, S.J. Davies, S.K. Erents[3], H. Guo, C. Hidalgo[1], J. Lingertat, J.R. Martín-Solís[4], G.F. Matthews, B. van Milligen[1], R.D. Monk, R. Simonini and A. Taroni.

JET Joint Undertaking, Abingdon, Oxfordshire, OX14 3EA, UK.
1) Asociacion EURATOM-CIEMAT, 28040 Madrid, SPAIN.
2) Max-Planck-Intitut fur Plasmaphysik, EURATOM Association, 85740 Garching, GERMANY.
3) UKAEA Fusion, Culham (UKAEA/Euratom Fusion Association) Abingdon, Oxfordshire OX14 3DB, UK.
4) Universidad Carlos III de Madrid, 28911 Madrid, SPAIN.

1. Diagnostics

Turbulent particle transport and its radial correlation have been studied in the scrape-off layer (SOL) plasmas of the JET tokamak with Mark-II divertor by using a specially adapted Langmuir probe. The probe head is installed on a reciprocating probe drive at the top of the machine. The tips on the probe head have been arranged in two groups of three which are radially separated 1.3 cm (figure 1), and have a poloidal separation of 2.3 cm between both groups of tips. Simultaneous measurements of fluctuating poloidal electric fields and ion saturation current (I_s) have been used to evaluate the turbulent radial particle transport (Γ_{ExB}), neglecting temperature fluctuations, and its spatial correlation between the two radial positions. Radial profiles of fluctuation parameters and particle transport are obtained by several reciprocations into the plasma during each discharge. An additional probe is available for simultaneous measurement of the time averaged density, electron temperature and electric potential profiles at the same poloidal position but toroidally displaced.

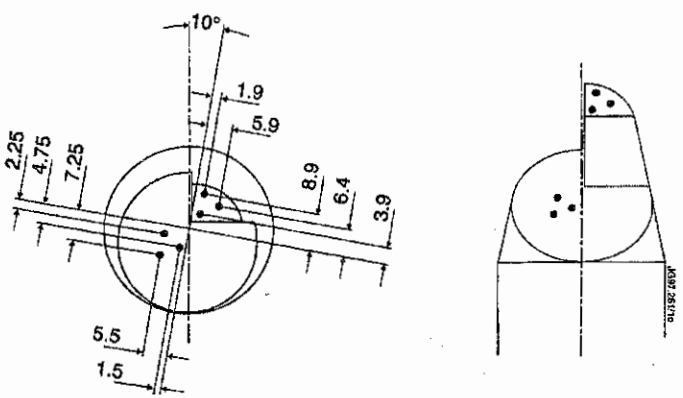

Figure 1. JET reciprocating Langmuir probe for fluctuation measurements.

2. Basic Characteristics of the Fluctuations

Measurements for JET (Mk-II) ohmic discharges (I_p= 2-2.6 MA, B_T= 2.6 T, $\bar{n}_e$= 1-2x10^{19} m^{-3}), both in limiter and divertor phases, with this reciprocating probe show that the electrostatic fluctuations and the induced radial particle transport have the same basic characteristics as observed in the SOL on other machines, i.e., normalised fluctuation levels

in the ion saturation current ($\tilde{I}_s/I_s$) decreasing from 40% far out in the SOL to 10% near the separatrix with broad frequency spectra dominated by frequencies below 50 kHz. The mean frequency of the fluctuations increases as the probe moves inside the plasma (figure 2) and there are non-gaussian distributions for I_s and, most prominently for transport signals.

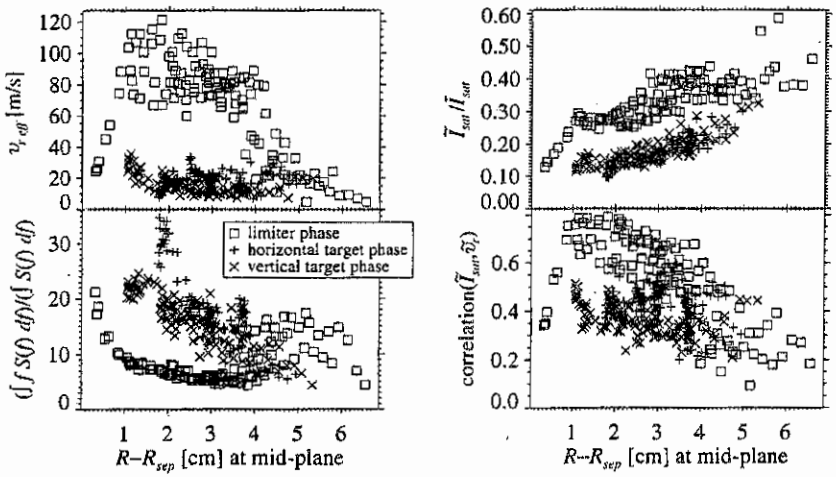

Figure 2. Radial profiles for limiter and divertor phases of the anomalous radial velocity, $\tilde{I}_s/I_s$, mean frequency spectra for floating potential fluctuations and the correlation between $\tilde{I}_s$ and $\tilde{v}_r$ signals.

3. Radial Particle Flux and its Comparison with Codes.

The derived anomalous particle fluxes have been used to estimate the anomalous outwards radial velocity, v_r = 10-20m/s, and, assuming a pure diffusive turbulent transport, the anomalous diffusion coefficient is $D_\perp$=0.15-0.3m^2/s, in horizontal divertor phases. There are two possibilities to obtain the experimental SOL decay length, of λ = 1 cm, with the 2-D EDGE2D/U-NIMBUS code simulations [1]. In the first case a $D_\perp$= 0.03 m^2/s and $\chi_\perp$= 0.625m^2/s were used, obtaining an outwards velocity of v_{diff} = 4m/s, in not good agreement with the experimental results. And in the second case the presence of an anomalous inward pinch [2] (v_{pinch} = 7.5 m/s) and a $D_\perp$ = 0.15m^2/s were assumed, resulting in a radial velocity of v_{diff} = 16m/s, comparable to v_r, and a λ = 1cm (figure 3), in good agreement with the experimental results.

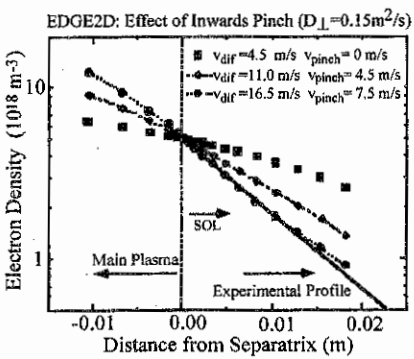

Figure 3. Outer mid-plane density profiles calculated by EDGE2D/NIMBUS code for different values of $D_\perp$ and an anomalous inward pinch term.

Future work will be directed towards comparing vertical and horizontal divertor results.

4. Differences between Divertor and Limiter Phases and the Radial Coherence

A notable change occurs in the characteristics of the turbulence between limiter and divertor phases, in ohmic discharges. The turbulent transport (figure 2) is larger in limiter phase than in X-point plasmas, due to larger fluctuation levels and to a higher correlation between density and poloidal electric field fluctuations. The anomalous radial velocity also shows differences between the two phases (see figure 2).

The level of radial coherence of the I_s fluctuations between the two groups of probes (separated 1.3 cm radially and 2.3 cm poloidally) is close to the statistical random noise, in the divertor phase (figure 4), which suggests that the radial correlation length of the turbulence is smaller than the typical dimensions of the SOL in those conditions. The pressure decay length in the shot shown is about 1.2 cm at the probe location.

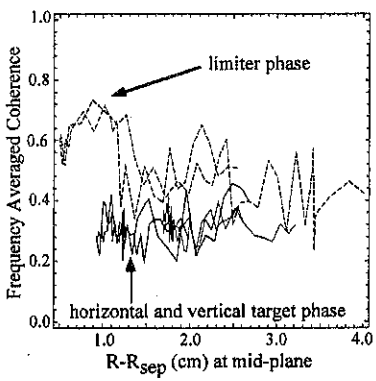

Figure 4. Frequency averaged coherence for $\tilde{I}_s$ signals between the two groups of probes versus the radial position and for the limiter and divertor phases.

However, a significant coherence is obtained in the limiter phases where the profiles are flatter and the SOL width (decay length 3.5 cm) is larger than in divertor cases. The frequency averaged radial coherence level between I_s signals increases as the probe is close to the separatrix position (figure 4). The feature in the coherence is located in the frequency range 0-40 kHz, and it is observed by the outermost tips before the innermost tips with a typical time delay of 30-40 μs. This could be explained by a poloidal velocity of the order of 1000 m/s in the ion diamagnetic direction, assuming structures in phase in the radial direction [3].

The coherence between the radially separated $\tilde{I}_s$ signals is always larger than for turbulent flux signals.

5. Double Peak Structure in Divertor Profiles

Measurements of broadband electrostatic fluctuations were also carried out in the JET Mk-I divertor plasmas [4] using a set of four Langmuir probes, two at the inner and the other two at the outer divertor, for high and low recycling conditions.

For low recycling regimes the radial profile of the relative fluctuation levels is almost constant in the SOL and increases in the private flux region [4].

In the evolution from low to high recycling regimes, by increasing the plasma density, a narrow peak in the ion saturation current appears near the separatrix creating a double peak structure [5] (figure 5). This peak grows further until it dominates the profile before detachment sets in. A significant reduction from earlier in the pulse, up to a factor of two, in the fluctuation level of ion saturation current (figure 6) is observed at the location of the peak nearest to the separatrix. This reduction has been measured in the I_s profiles at the outer divertor plates as well as at the inner.

Simulations with EDGE2D/U-NIMBUS are unable to reproduce this feature with a constant $D_\perp$ in the SOL plasmas and values similar to those used in section 3. Bohm

diffusion can produce a strong peaking at high recycling but not the double peak structure. It suggests that this phenomenon is due to a local change in transport and not to a localisation of ionisation sources near the separatrix. Sheared electric fields appear to be co-located with this feature and may be related to the reduction in $\tilde{I}_s/I_s$. Work is in progress to clarify if by a reduction in transport over a similar region of the EDGE2D/U-NIMBUS computational domain it is possible to reproduce some of these features.

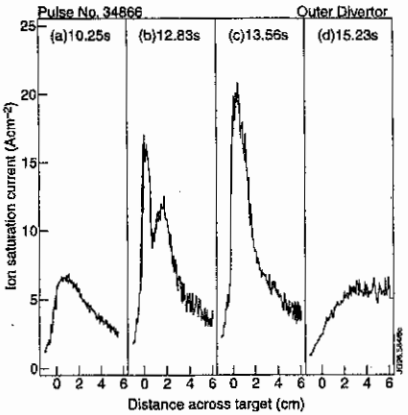

Figure 5.- Evolution of the I_s signal at the divertor plates going from low to high recycling conditions.

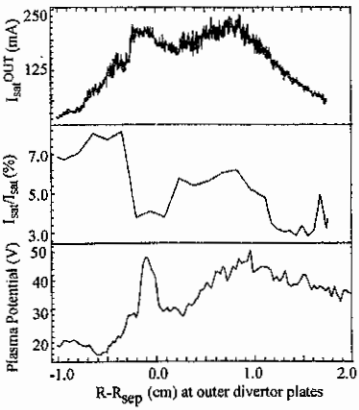

Figure 6.- Radial divertor profiles of I_s, $\tilde{I}_s/I_s$ and plasma potential (V_p) for high recycling plasmas.

6. Summary

- Turbulent particle transport and its radial correlation have been studied in the SOL plasmas of the JET Mk-II divertor by using a specially adapted movable Langmuir probe.
- The general properties of the fluctuations in the SOL plasmas exhibit the features similar to those observed in the SOL of other devices.
- Assuming a pure diffusive turbulent transport, an anomalous inward pinch is needed in EDGE2D/NIMBUS simulations in order to reproduce the profiles and the experimental value of $D_\perp$ and v_r.
- A significant radial coherence between the I_s fluctuations at the two radial positions has been observed with limiter operation but not for divertor operation. This coherence seems to be related to the plasma SOL width.
- The correlation between $\tilde{I}_s$ signals is larger than between turbulent flux signals.
- A reduction of the fluctuations near the separatrix position has been observed for high recycling plasma conditions. It suggests that this phenomenon is due to a local change in transport and not to a localisation of ionisation sources near the separatrix. This reduction coincides with strong radial electric fields. Further work is needed in the EDGE2D/NIMBUS computational domain to understand these features.

[1] R. Simonini et al. Contrib. Plasma Phys. 34 (1994) 448.
[2] A. Taroni et al. Proc. 22nd EPS Conf. on Control. Fusion and Plasma Physics Vol 19C Part IV, 297 (Bournemouth, 1995).
[3] J. Bleuel et al., this conference.
[4] I. García-Cortés et al. Plasma Phys. Control. Fusion 38 (1996) 2051-2062.
[5] A. Loarte et al. submitted to Nuclear Fusion (1997).

Radiation distribution and neutral-particle loss in the JET MkI and MkIIA divertors

L.C. Ingesson, R. Reichle, G.C. Fehmers,* H. Guo, L. Lauro-Taroni, A. Loarte, and R. Simonini

JET Joint Undertaking, Abingdon, Oxon. OX14 3EA, United Kingdom

* Technische Universiteit Eindhoven, Eindhoven, The Netherlands; present address: Shell Research, Rijswijk, The Netherlands

INTRODUCTION

The radiation distribution and neutral-particle loss in highly radiative discharges with impurity seeding in the JET MkI and MkIIA divertors have been studied by means of the bolometer diagnostics. This type of discharge in MkI has been discussed in Ref. 1; transport in similar discharges in MkIIA is presented in Ref. 2. The radiation distribution and neutral-particle loss are important quantities to study for ITER as they are related to the performance of radiative divertor plasmas and to the wall-loading. Furthermore, it is important to estimate the ratio of loss-power carried by electromagnetic radiation and that carried by neutrals.

The heat flux carried by neutral particles, which are assumed to be created by charge-exchange processes in the divertor, is measured by the bolometers in the divertor as an addition to the electromagnetic flux, whereas other bolometers are shielded by the bulk plasma and only measure the electromagnetic contribution. Comparison of these in and ex-divertor measurements can give estimates of the neutral particle flux [3]. Extensions to an existing tomographic reconstruction algorithm [4] were required to obtain the radiation distribution and neutral-particle loss. The results are compared with EDGE2D/NIMBUS [5] simulations of the edge plasma.

TOMOGRAPHY METHOD

The radiation distribution during highly radiative discharges in MkI could successfully be reconstructed by a tomographic method developed by Fuchs [4]. Despite the increased number of channels, the reconstructions in MkII proved more difficult. Several extensions to the method were required: a variable grid size, a non-negativity constraint, fully taking into account the geometric properties of the detection systems, and a way of dealing with neutral particles.

A series expansion method is used for the 2D tomographic inversion, in which the emission profile in a poloidal cross-section is discretized on a Cartesian grid by means of local basis functions. This can be written as:

$$f_i = \sum_j K_{ij} g_j + n_i \,, \qquad (1)$$

where f_i are the line-integrated measurements, g_j is the emission in the grid points, K_{ij} is the geometric matrix, and the summation is over all grid points.. The contribution of neutrals is taken care of in n_i, which is allowed to be non-zero only for bolometers in the divertor.

The underdetermined Eq. (1) is regularized by assuming smoothness, a zero or low level of radiation outside the plasma and an as small as possible neutral contribution. Anisotropic smoothness on the flux surfaces is expressed in a diffusion equation for emissivity [4]. These conditions are described in a quadratic functional that should be minimized:

$$\langle g|\Omega|g\rangle = \iint \left[\nabla \cdot \boldsymbol{D} \cdot \nabla g\right]^2 \mathrm{d}R\,\mathrm{d}Z + \langle g|C_1|g\rangle + \langle n|C_2|n\rangle, \tag{2}$$

where Ω is the resulting regularizing matrix, $\boldsymbol{D}$ is an anisotropic diffusion tensor, the integral is over the reconstruction region, C_1 and C_2 are parameter matrices to force edge points and the neutral contribution to small values, and the Dirac notation is used for scalar products.

The tomographic reconstruction is obtained by minimizing Eq. (2) with the constraint

$$\|f - Kg - n\| \approx \|\varepsilon\|, \tag{3}$$

where ε is the estimated measurement error and $\|..\|$ symbolizes the norm. Solving by the Lagrange multiplier method results in the linear system of equations

$$\left(\lambda K^{\mathrm{T}} W K + \Omega\right) g' = \lambda K^{\mathrm{T}} W f, \tag{4}$$

where λ is the Lagrange multiplier, g' contains both g and n, K and Ω are modified to include terms for n, and W is a matrix to weigh the measurements by the estimated errors: $W_{ii} = 1/\varepsilon_i^2$, and $W_{ij} = 0$ for $i \neq j$. Additional constraints can be added iteratively to make initially negative values in the resulting emission profile g zero or positive [6]. The free parameters in the method are: $D_{\perp}$ and $D_{//}$ in each grid point, C_1, C_2, and ε.

THE JET BOLOMETER SYSTEM

JET has two bolometer systems [3]: three fans of ex-vessel bolometers that cover the entire plasma, and miniature bolometers situated around the divertor and around the main plasma. Typically 49 channels were available in MkI and 85 in MkIIA (see Fig. 1). To collect sufficient radiation for a good signal-to-noise ratio the apertures of the detectors are relatively large, which leads to large beam widths. It is important to take these widths into account in the geometric matrix K in Eq. (1) because otherwise the reconstructions will be blurred.

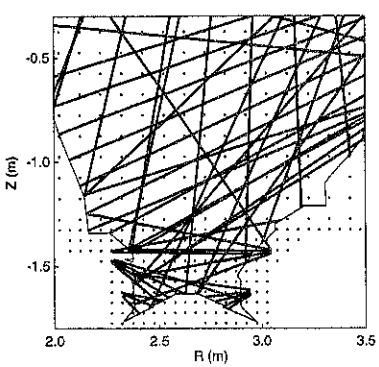

Figure 1: *Bolometer lines-of-sight in the divertor region typically available in MkIIA. The points indicate the grid used in the reconstruction. The variable grid size has been chosen to match the average distance between lines-of-sight.*

RADIATION AND NEUTRAL PARTICLE DISTRIBUTION

Tomography simulations have shown that, although the emission profiles may be smoothed due to the limited number of lines-of-sight and the beam widths, reliable results can be obtained, matching the location of peak emission and the total magnitude of radiation. In particular, in MkIIA it has been demonstrated that the method to estimate the neutral contribution is reliable. Figure 2(a) shows the radiation distribution reconstructed from the bolometer measurements at the radiation limit in an N_2 seeded discharge in ELMy H mode with 13 MW of NBI power. In this type of discharges, after detachment the main emission is found to come from inside the separatrix. Although this feature is not reproduced by EDGE2D/NIMBUS simulations [7,8] because the code has difficulties to find a stable solution with much radiation from inside the separatrix, the total radiated power is matched well. The location and amount of D_α emission is also reproduced by the code. Both the tomographic reconstructions and the EDGE2D/NIMBUS simulations were averaged over ELMs.

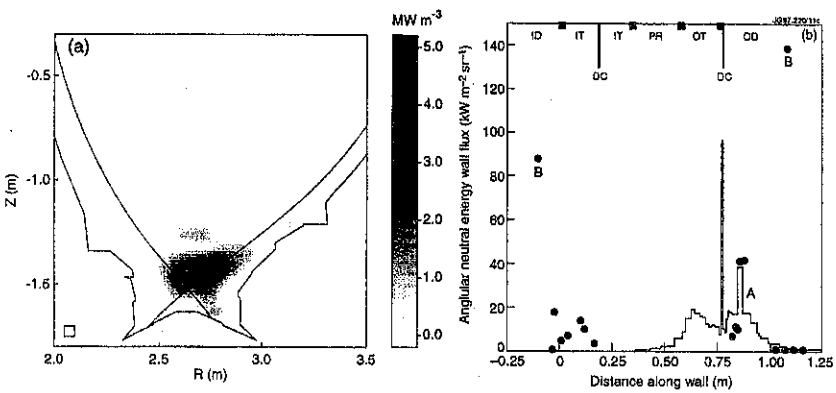

Figure 2: *(a) Tomographic reconstruction of the emitted radiation in MkIIA (#37991 at t = 17.7 s). The dashed line indicates the separatrix. (b) The energy wall flux carried by neutral particles, for the same discharge, as predicted by EDGE2D/NIMBUS (solid line) and derived from bolometer measurements (solid points). ID/OD: inner/outer divertor; IT/OT: inner/outer target; PR: private region; DC: divertor corner (The EDGE2D/NIMBUS solution in the inner corner was not reliable.)*

Figure 2(b) shows the energy flux carried by neutrals on the wall as simulated by EDGE2D/NIMBUS and as estimated from the bolometer measurements. The average energy of neutrals reaching the wall is of the order 10 eV in the MkIIA case, and five times higher in the MkI case. It has been assumed that the flux is uniformly spread over 2π sr and that all neutral power is absorbed by the detectors (in reality about 80% is absorbed [9]). Despite the approximations, the figure shows good agreement in the outer corner (marked A). The discrepancy for high divertor channels (marked B) that see the main radiating region above the X point, found in both MkI and MkIIA, may be related to a marked discrepancy between the signal level of these channels and a vertical line-of-sight viewing the same highly radiat-

ing region through the bulk plasma. The ratio between these vertical and horizontal channels at the radiation limit has been compared in several similar discharges as the one above in MkI and MkIIA, all with N_2 seeding and an NBI input power of 10–15 MW. This ratio shows an upward trend when the divertor becomes more closed (i.e. MkI to MkIIA), whereas the electromagnetic radiated fraction goes down. The temporal behaviour of the vertical and horizontal measurements is also markedly different. Furthermore, both the simulations and the derivation from the bolometer measurements show that the energy wall flux carried by neutrals increases with closure. The discrepancy in the ratio of vertical and horizontal channels and the discrepancy at the points marked B in Fig. 2(b) may be due to: (a) a very peaked radiating region which cannot be resolved by the present system, (b) a very directed flux of hydrogen neutrals from the highly radiating region, or (c) a neutral impurity flux (which is not yet available from the simulations). The fact that the electromagnetic power fraction goes down for more closed divertors supports the explanation by neutrals, when it is assumed that the total loss (neutral + electromagnetic losses) is similar.

CONCLUSIONS

Bolometer tomography gives reliable emission profiles during highly radiative discharges. Estimates of the neutral particle contribution to the signals are in reasonable agreement with EDGE2D/NIMBUS simulations. The total loss power due to neutrals in the divertor is more than 1 MW in the MkIIA case, but only 0.2 MW in a similar MkI case, to be compared with 9–10 MW of electromagnetic radiated power (of which about 70% comes from the X point and the divertor). During detachment the peak emission is measured to originate from inside the separatrix, which however is not reproduced by the simulations.

Going from open to more closed divertors, the power loss by neutral particles increases whereas the electromagnetic power fraction decreases.

These observations of neutral particles have consequences for the bolometer system planned for ITER, which has a very closed divertor. To be able to accurately distinguish between electromagnetic and particle loss a large number of lines-of-sight is required from both outside and inside the divertor.

ACKNOWLEDGEMENT: The authors would like to thank F.C. Fuchs of IPP-Garching for making available his tomography code, of which the present code is an extension.

[1] G.F. Matthews and the JET Team, Plasma Phys. Control. Fusion **37**, A227 (1995)
[2] G.F. Matthews *et al.*, this conference
[3] R. Reichle *et al.*, to appear in Proc. 12th PSI Conf. (St. Raphael, May 1996)
[4] J.C. Fuchs *et al.*, Proc. 21st EPS Conf. (Montpellier, June 1994), Part III, pp. 1308
[5] R. Simonini *et al.*, Contrib. Plasma Phys. **34**, 448 (1994)
[6] G.C. Fehmers, *Tomography of the ionosphere* (thesis Technische Universiteit Eindhoven, 1996)
[7] Loarte *et al.*, to appear in Proc. 12th PSI Conf. (St. Raphael, May 1996)
[8] Maggi *et al.*, to appear in Proc. 12th PSI Conf. (St. Raphael, May 1996)
[9] W.Eckstein and J.P Biersack, Appl. Phys. A **38**, 123 (1985)

The Effect of Divertor Closure on Detachment in JET

R.D. Monk, A. Loarte, S.J. Davies, J.K. Ehrenberg, H.Y. Guo,
L.D. Horton, J. Lingertat, C.G. Lowry, G.F. Matthews,
J.R. Martín-Solís[1], G. Saibene, R. Sartori and A. Tabasso[2].

JET Joint Undertaking, Abingdon, Oxfordshire, OX14 3EA, UK.
[1]Escuela Politécnica Superior, Universidad Carlos III de Madrid, Spain.
[2]Imperial College of Science, Technology and Medicine, London, SW7 2BZ, UK.

1. Introduction

JET has now investigated three divertor configurations of progressively increased geometric closure to the escape of recycling neutrals : Mark I (1994-95), Mark IIA (1996) and Mark IIAP (1996-97). Due to the reduced fraction of neutrals escaping from the divertor region, region models predict easier access to regimes of high divertor radiative losses and plasma detachment in closed divertors. This paper presents results from JET experiments designed to investigate the effect of divertor closure on plasma detachment in a variety of confinement regimes and magnetic configurations.

2. Ohmic and L-Mode Discharges

Using the simple "two-point" model [1] of the divertor scrape-off layer it can be shown that the ion flux (I_{div}) to the divertor should approximately scale according to :

$$I_{div} = n_{div} c_{div} = \left(\frac{7\gamma L_c}{8\kappa_0 m_i} \right) \frac{n_{mid}^2}{T_{mid}^{3/2}}$$

where γ is the sheath transmission coefficient, κ_0 the electron thermal conductivity coefficient, m_i the ion mass, L_c the connection length and the subscripts *div* and *mid* refer to the divertor and midplane respectively. Assuming that $n_{mid} \propto \langle n_e \rangle$ then the Degree of Detachment (D.O.D) [2] may be defined as follows :

$$D.O.D. = \frac{I_{div}^{scal}}{I_{div}^{measured}} = \frac{C\langle n_e^2 \rangle}{I_{div}^{measured}}$$

During ohmic and L-mode discharges, detachment (defined as D.O.D.>2) occurs in the Mk.IIA divertor at main plasma densities that are 20-30% lower than for comparable Mk. I discharges (fig. 1). In addition, the density limit is reduced by a larger factor of 30-40% and the degree of detachment is reduced particularly when compared with Mk. I standard flux expansion (SFE) discharges. Similar results are obtained with vertical plate configurations and L-mode discharges. In contrast to the Mk. I divertor, complete divertor detachment (i.e. D.O.D.>10) is not obtained in any Mk. IIA configuration prior to the density limit disruption. Plugging of the divertor by-pass leaks in Mk. IIAP increased the divertor compression by reducing the main chamber neutral pressure by ~30% but the detachment behaviour as a

function of main plasma density remained unchanged. Thus, in describing the following results "Mk. II" refers to both the Mk. IIA and Mk. IIAP configurations.

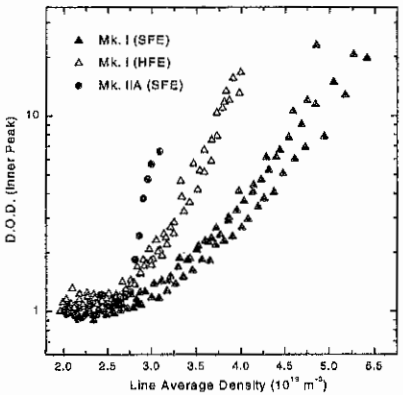

Figure 1 : Degree of detachment versus main plasma density for ohmic discharges in Mk. I and Mk. IIA.

Experiments with the separatrix located on the horizontal and vertical target plate of the Mark II divertor show significant differences with respect to detachment behaviour compared with Mk. I. For the horizontal plate, detachment begins in off-separatrix positions near the divertor corner (Fig. 2) as predicted by the numerical modelling of Borrass et al. [3]. In contrast, the vertical plate configurations show detachment beginning near the separatrix as observed previously in the Mk. I divertor [2]. The unusual detachment behaviour of horizontal plate discharges may be due to enhanced volume recombination occurring in the corner regions of the divertor as supported by a strong localised increase of D_α emission. Earlier onset of detachment is also observed when the inner strike point is moved near to the corner region of the inner divertor.

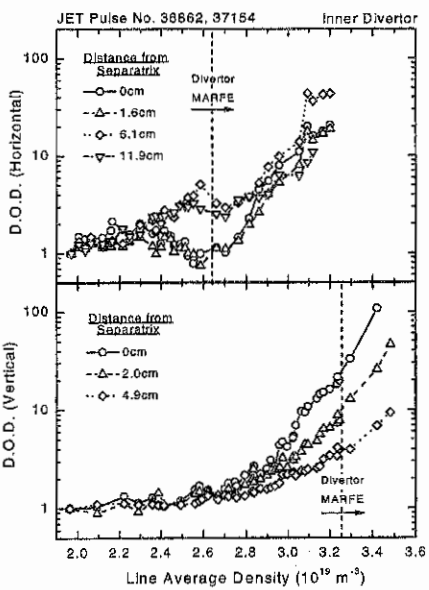

Figure 2 : Degree of detachment versus distance from the separatrix illustrating the difference between horizontal and vertical plate operation.

Comparing Mk. II and Mk. I, the measured D_α and CIII emission from the divertor are significantly higher over the whole density range for Mk. II (fig. 3). In terms of P_{rad}/P_{in} the Mk.II divertor closely follows the Mk. I high flux expansion (low wall clearance) discharges which have a higher proportion of carbon radiation in the divertor [4]. In all cases, detachment occurs at similar P_{rad}/P_{in} indicating that gas target physics determines detachment while the density limit (MARFE stability) may be more sensitive to the carbon concentration. More carbon may be present in the Mk. II divertor due to the proximity of the side-plates and enhanced chemical sputtering due to higher target temperature of Mk. II (200-250°C) compared with Mk. I (~40°C) [5]. An increased degree of detachment can

be sustained on the vertical plate before the divertor MARFE forms (fig. 3) but the density limit is still within ~10% of the horizontal plate discharges.

EDGE2D/NIMBUS numerical calculations were performed to simulate vertical target L-mode density ramps and compute the degree of detachment. The assumptions used were $P_e=P_i=1.0MW$, $n_{sep} = 0.25 \rightarrow 2.0 \times 10^{19} m^{-3}$, $D_\perp = 0.1 m^2 s^{-1}$ and $\chi_{e,i} = 1.5 m^2 s^{-1}$ for both pure plasma and impurities assuming $Y_{eff} = Y_{phys} + Y_{chem}$ where $Y_{chem}=2\%$. As shown in fig. 4, the general trend of the experimental results are reproduced by the simulations with ~25% lower separatrix density to achieve detachment in Mk. II compared with Mk. I. However, the larger reduction of the density limit threshold for Mk. II is not reproduced by the code which may depend sensitively on the impurity concentration in the divertor and therefore MARFE stability.

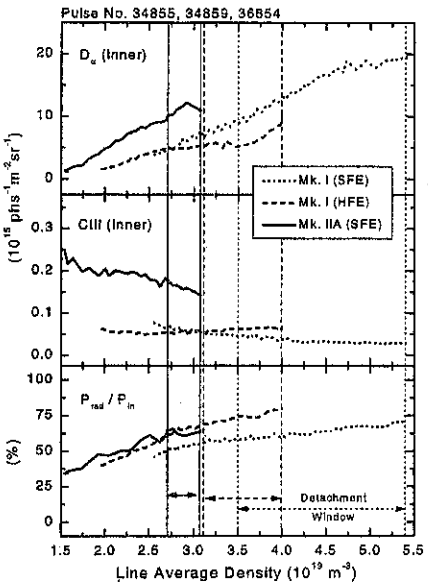

Figure 3 : Comparison of the inner divertor D_α, CIII and P_{rad}/P_{in} as a function of main plasma density for the Mk. I and Mk. IIA divertors.

4. H-Mode Discharges

An extensive series of experiments with steady-state ELMy H-modes have been carried out with the Mark II divertor [6]. With D_2 gas fuelling, partial detachment is observed in-between ELMs on the inner divertor although there is no MARFE formation. Above certain levels of D_2 gas fuelling the confinement degrades and the plasma density decreases resulting in a non-disruptive density limit. As shown in fig. 5, the onset of detachment is not uniquely correlated with the degradation of confinement and appears to be more dependent on the triangularity of the configuration. In high trangularity discharges

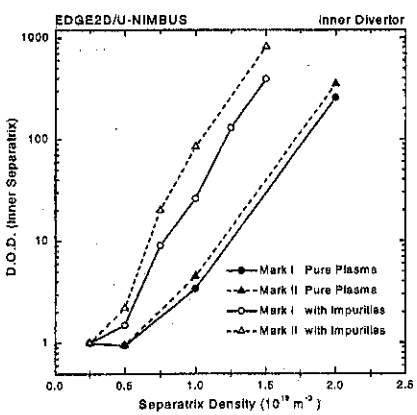

Figure 4 : EDGE2D/NIMBUS simulations of the degree of detachment for L-mode vertical target density ramps in Mk. I and Mk. IIA.

it is possible to access high edge densities and therefore detach with moderate levels of D_2 fuelling while maintaining good confinement. In contrast, for low triangularity discharges the increased level of D_2 fuelling necesary to produce the high edge densities and detachment result in a more severe degradation of confinement. Comparing Mk. I and Mk. II the degree of detachment reached for a given edge density appears to be lower which may highlight the influence of divertor closure.

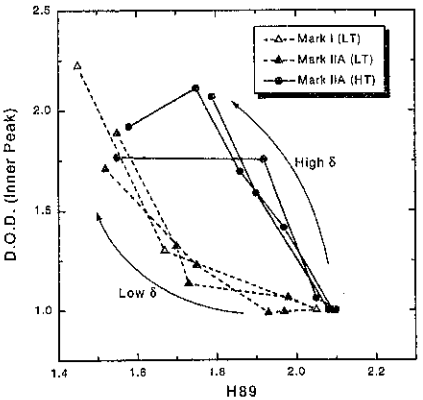

Figure 5 : Detachment behaviour as a function of the H89 confinement for ELMy H-modes in Mk. I and Mk. II with high (HT) and low triangularity (LT).

5. Conclusions

During ohmic and L-mode discharges, detachment and the density limit are achieved at lower main plasma densities in the more closed JET Mark. II divertor compared with Mark I. However, complete divertor detachment has not been observed with the Mark II divertor. The effects of divertor geometry are stronger in Mk. II than for Mk. I with detachment beginning in off-separatrix regions for horizontal plate configurations. The corner region appears to be associated with enhanced recycling and/or volume recombination. Numerical modelling (EDGE2D/NIMBUS) of the detachment for vertical plate L-mode discharges is in broad agreement with experiment. However, the approach to the density limit and MARFE formation is not well reproduced by the code and may depend sensitively on the (increased) impurity levels in the Mk. II divertor. In H-mode discharges with D_2 fuelling, detachment can be obtained on the inner divertor between ELMs. However, there is no unique correlation between detachment and the loss of confinement associated with the H-mode density limit and triangularity appears to be a more important parameter. With high triangularity configurations it is possible to access the high edge densities required for detachment with moderate levels of D_2 fuelling and little degradation of confinement. However, in the case of low triangularity discharges, the increased levels of D_2 fuelling required for the high edge densities associated with detachment result in a more severe degradation of confinement.

REFERENCES

[1] M. Keilhacker et al., Physica Scripta **T2/2** (1982) 443.
[2] A. Loarte et al., submitted to Nuclear Fusion JET-P(97) 03.
[3] K. Borass et al., these proceedings.
[4] C.F. Maggi et al., 12th PSI Conference, St. Raphael, France, (1997).
[5] G. M. McCracken et al., these proceedings.
[6] G. Saibene et al., these proceedings.

DIMENSIONAL SCALINGS FOR THE HEAT TRANSPORT IN THE SCRAPE-OFF LAYER OF JET AND ALCATOR C-MOD

S K Erents*, B LaBombard°, A V Chankin, S J Davies, R D Monk, G F Matthews and P C Stangeby+

JET Joint Undertaking, Abingdon, Oxon, OX14 3EA, United Kingdom

* UKAEA Fusion, Culham (UKAEA/Euratom Fusion Association), Abingdon, Oxon, OX14 3DB, U.K.

° Plasma Science and Fusion Centre, Massachusetts Institute of Technology, Cambridge, MA.

+ and Institute for Aerospace Studies, University of Toronto, Downsview, Ontario, M3H 5T6.

1. Introduction

Measurements of divertor target densities and temperatures have been used in the DIVIMP /NIMBUS Onion Skin Model (OSM), [1] to predict values for the average cross-field heat transport coefficient, $\chi_\perp$, in the scrape-off layer (SOL) of a number of JET ohmic, L -mode and H-mode (between ELM) discharges. These data are complemented with calculations of $\chi_\perp$ extracted from Alcator C-MOD upstream probe data [2]. The OSM uses particle and power balance along flux tubes, including particle ionisation, to arrive at a solution for $\chi_\perp$ (r) at any poloidal position in the SOL. Convection is neglected in the JET analysis (its inclusion reduces the magnitude of $\chi_\perp$), but included in the C-MOD analysis using $D_\perp = 0.4\ \chi_\perp$.

2. Radial profiles of $\chi_\perp$ across the SOL

A selection of $\chi_\perp$ (r) profiles is shown in figure 1 from a JET dataset of 25 Ohmic, L-mode and H-mode discharges, and a C-MOD dataset of > 60 discharges. Most radial profiles show $\chi_\perp$ increasing with radius (see also fluctuation studies, [5]). Some profiles reach a maximum value and show a subsequent fall far out in the SOL where the T_e scrape-off thicknesses are difficult to measure (hence possibly erroneous). Target probe data (JET) and upstream probe data (C-MOD) , as measured, were used to give the extracted $\chi_\perp$ values. In order to see the effect of the scatter in the JET probe data on the extracted $\chi_\perp$ values, two smooth curves have been drawn through the target probe radial profiles, one at each of the two extremes which just encompass the scatter. For most H-mode shots the extracted $\chi_\perp$ (r) still increases with r, even for the extreme fits to the input data. For some shots, where T_e (r) is flatter, the extracted $\chi_\perp$ (r) is flattened, or could even decline radially for one of the extreme fits to the probe data.

3. Scaling of $\chi_\perp$ with local plasma parameters

No clear scaling of $\chi_\perp$ with main plasma parameters (Ip, B_T, $\langle n_e \rangle$) is found, and indeed there seems to be no clear scaling with local plasma parameters with the exception of upstream temperature, T_{eu}, derived using the OSM.

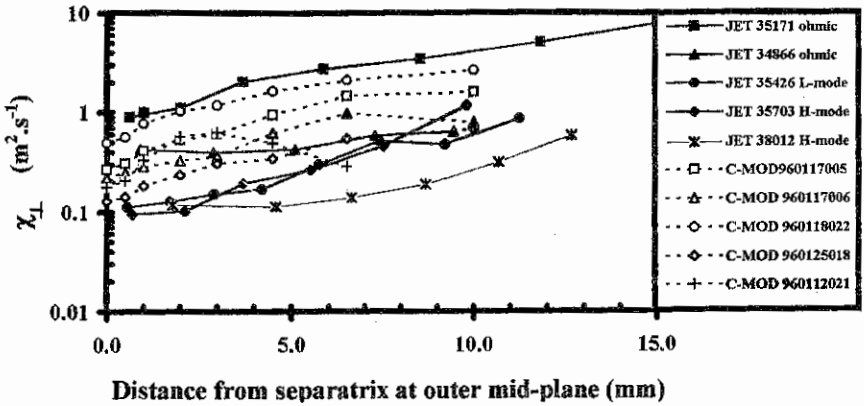

Figure 1. **Radial profiles of $\chi_\perp$ across the SOL from JET and C-MOD databases**

The scaling of $\chi_\perp$ with T_{eu} is shown in figure 2 for $\chi_{\perp s}$ (i.e. the value close to the separatrix) taken from the complete JET and C-MOD databases.

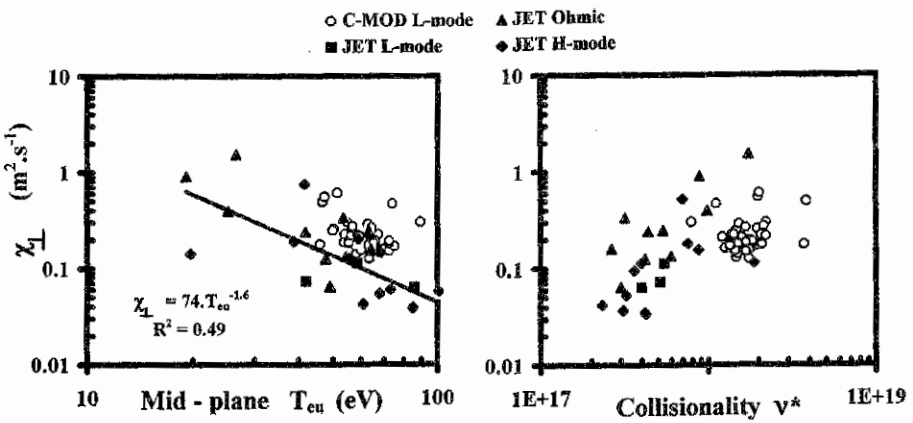

Figure 2. **$\chi_{\perp s}$ vs. T_{eu} close to the separatrix.**

Figure 3. **$\chi_{\perp s}$ vs. ν^* close to the separatrix**

Also shown in figure 2 is the best fit to the JET data. Clearly $\chi_{\perp s}$ falls with increasing T_{eu}, (as does $\chi_\perp(r)$), although there is considerable scatter in the data. Despite the large differences in main plasma parameters between JET and C-MOD (JET: Ip $\leq$ 4.7 MA, $\langle n_e \rangle$ = 1 - 8.10^{19} m^{-3}, B_T = 1 - 3.5 T ; C-MOD: Ip $\leq$ 1 MA, $\langle n_e \rangle$ = 1- 2.10^{20} m^{-3}, B_T = 2.8 - 7.9 T) there is a remarkable similarity in the predicted values of $\chi_\perp$.

4. Heat transport in a turbulent edge plasma

4.1 Skin effect

The collisional edges of JET and C-MOD contrast with the much less collisional edges of smaller lower density machines, such as COMPASS-D in which a Gyro-Bohm scaling for $\chi_\perp \propto (T^{3/2}/B^2)$ is found [3].

A random walk expression for $\chi_\perp$ due to turbulent fluctuations is:

$$\chi_\perp = \nu\Delta^2 \tag{1}$$

where ν is the frequency of the fluctuations and Δ is an associated scale length (e.g. the ion Larmor radius ρ_s for Gyro-Bohm transport). ν scales as the ratio of poloidal diamagnetic velocity, $\propto T_e/B\lambda_T$, to perpendicular wavelength, which scales as $\lambda_\perp \propto \sqrt{T_{eu}}/B$ for cold plasmas. Hence from (1): $\chi_\perp \propto T_e^{3/2}/B^2\lambda_T$ (2)

This is the Gyro-Bohm expression, which predicts $\chi_{\perp S}$ increases with T_e, and $\chi_\perp(r)$ decreases with radius across the SOL, both in contradiction to our results. In a collisional plasma, it is possible that conduction in a 'skin', due to the high frequency of fluctuations, can suppress turbulence, [4]. The skin thickness need not necessarily define the transverse amplitude of the fluctuations (like ρ_s in Gyro-Bohm), but simply restrict the amplitude of the fluctuations. Note that the perpendicular wavelength $\lambda_\perp \approx 30\rho_s$ for $K_\perp\rho_s \approx 0.2$.

Equation (2) can be modified to include the collisional skin-depth:

$$\chi_\perp \propto T_e^{3/2}/B^2\lambda_T.F(\lambda_\perp/\Delta_{skin}) \tag{3}$$

where F is a dimensionless function - which can be determined from our measurements.

The collisional skin depth is: $\Delta_{skin} = c/\sqrt{4\pi\sigma\nu}$, ($\sigma$ is Spitzer conductivity) where we assume the parallel conductivity, $\sigma = 1.2.10^{13}\ T_e^{3/2}\ s^{-1}$. Hence, $F(\lambda_\perp/\Delta_{skin}) = F(KT_e^{3/2}/B\sqrt{\lambda_T})$ where $K = 4\pi\varepsilon_0\mu_0^{1/2}/e^2$, and equation (3) can be written:

$$\chi_\perp B\sqrt{\lambda_T} = \frac{m_i^{1/2}T_e^{3/2}}{e^2B\sqrt{\lambda_T}}.F\left(\frac{KT_e^{3/2}}{B\sqrt{\lambda_T}}\right) \tag{4}$$

The term $KT_e^{3/2}/B\sqrt{\lambda_T}$ is dimensionless and appears on the RHS of (4) and in the argument of F, so we can define $G(x) = x\,F(x)$.

Then:

$$\chi_\perp B\sqrt{\lambda_T} = \frac{m_i^{1/2}}{Ke^2}G\left(\frac{KT_e^{3/2}}{B\sqrt{\lambda_T}}\right) \tag{5}$$

From our extracted values of $\chi_\perp$ we find $G(x) = 1/x$, i.e. $\chi_\perp \propto T_e^{-3/2}$, with *no* dependence on magnetic field, B_T. Since the argument of G was originally $\lambda_\perp/\Delta_{skin}$, the dependence of $\chi_\perp$ we extract is proportional to the square of the collisional skin-depth.

We expect that the collisional skin-depth might influence the scaling of cross-field transport when $\Delta_{skin}/\lambda_\perp \le 1$, which gives $T_e \ge 30$ eV and $\Delta_{skin} \le 18$ mm. (We have used $\nu \sim 10$ kHz, but fluctuations in JET have a wide bandwidth extending to > 50 KHz).

A change in the scaling of $\chi_\perp(T_e)$ with T_e would be expected for $T_e \leq 30$ eV. This is observed, but could be erroneous due to large scatter in data far out in the SOL. So an alternative explanation, that of an increase in collisionality with radius, is also proposed.

4.2 Collisionality

The collisionality is defined as the mean-free path between collisions divided by the connection length, i.e. $\nu^* = C.n_{eu}L_c / T_{eu}^2$, where C is a constant and ν^* is dimensionless.

Figure 3 shows $\chi_{\perp s}$ plotted as a function of collisionality, using values of n_{eu} and T_{eu} derived from the OSM. It is clear $\chi_{\perp s}$ increases with ν^* for both JET and C-MOD databases. This increase is difficult to quantify, but is stronger than linear. Note that the highest $\chi_\perp$ (and hence highest collisionality) is far out in the SOL, and it could be that turbulence from this region is controlling transport in the SOL right up to the separatrix.

5. Conclusions

From the combined JET and C-MOD databases it is found:

- $\chi_\perp(r)$ increases with radius, r, in the SOL.
- The absolute value of $\chi_{\perp s}$ (i.e. close to the separatrix) lies between 0.04 and 1 $m^2.s^{-1}$, with the lowest values occurring in H-mode discharges.
- Both $\chi_\perp(r)$ and $\chi_{\perp s}$ fall rapidly with increasing upstream electron temperature, T_{eu}, with $\chi_\perp \propto T_{eu}^{-3/2}$, in contradiction to Bohm or Gyro-Bohm scalings found on less collisional machines [3], but consistent with the collisional skin effect.
- No clear correlation of $\chi_\perp$ with B_T is found.

Two mechanisms have been proposed for this observation: (1) a skin-effect in the SOL near to the separatrix reducing the turbulence in this region, and (2) an increasing collisionality with radius from the separatrix. Extracted values of $\chi_\perp$ suggest the skin-effect is active even for low values of T_{eu}, i.e. far out in the SOL. This seems unlikely, as the skin thickness would be much larger here. So an alternative mechanism has been suggested which indicates $\chi_\perp$ increases with collisionality in the SOL. It is also suggested that the stronger turbulence far out in the SOL drives the transport close to the separatrix.

6. References

[1] P C Stangeby and J D Elder, Nucl. Fusion 35 (1995) 1391.

[2] B LaBombard, J A Goetz, I Hutchinson et al, 16th IAEA Fusion Energy Conf.,Montreal, 1996.

[3] M G Booth, J W Connor, G F Counsell, S K Erents, S J Fielding, D Gates and C Silva, APS Bull. 41, No.7 (1996), paper No. 6P.43

[4] A V Chankin and G F Matthews, This Conference.

[5] I Garcia-Cortes, M.Endler *et.al* ,This Conference.

**** This work is partly funded by the U.K. Department of Trade and Industry and Euratom***

Fluid Modelling with Drift Fluxes of Magnetic Field Reversal Experiments in JET

G.J.Radford[1], A.V.Chankin, G.Corrigan, R.Simonini, J.Spence, A.Taroni
JET Joint Undertaking, Abingdon, Oxon., OX14 3EA, UK.
[1] Theoretical Physics, University of Oxford, Oxford, OX1 3NP, UK.

Abstract
High-recycling L-mode JET plasmas, with normal and reversed magnetic fields, have been simulated with all particle drifts and currents and a range of different perpendicular anomalous transport coefficients. Many of the measured trends found with magnetic field reversal are reproduced by the code, but with smaller changes than seen experimentally.

Introduction

Classical cross field particle drifts have been of much recent interest in attempting to explain various divertor asymmetries. Much effort has therefore been put into the inclusion of these drifts into 2D scrape-off layer transport codes. At JET, the EDGE2D code has been upgraded to include all components of the ∇B and curvature drifts, and the $\mathbf{E}\times\mathbf{B}$ drifts for the main hydrogenic ions, electrons and impurity ions.

High-recycling L-mode JET plasmas, with normal and reversed magnetic fields, have been simulated with all particle drifts and currents and a range of different perpendicular anomalous transport coefficients. Recent analytical estimates [1], [2] have predicted the radial and poloidal $\mathbf{E}\times\mathbf{B}$ drifts to be dominant with the radial component more important for high density, high-recycling cases leading to increased plasma pressure and reduced temperatures at the inner divertor for normal magnetic field cases, and at the outer divertor for the reversed field. Results from modelling have been able to reproduce these trends.

The Drift Fluxes in EDGE2D

From standard fluid theory, the diamagnetic component of the particle drift flux consists of a divergence-free term (called the magnetisation flux [3]) and the ∇B and curvature drifts. The magnetisation fluxes have been shown [3] to make no contribution to the fluid equations and therefore have been omitted from the drift fluxes implemented into the code. This has resulted in a significant simplification and removed possible sources of numerical errors and instabilities. Target boundary conditions have been modified to take account of particle drifts as proposed in [4]. Magnetisation fluxes have not been included.

Full account is taken of radial currents arising from the drift terms. Outside the core plasma the electric field and parallel current density are determined fully from the electron momentum equation, divergence-free currents and target boundary conditions. In the core only the poloidal electric field and parallel current can be determined. The radial electric field is adjusted to maintain net ambipolarity of the radial current on closed magnetic surfaces.

Modelling Results and Comparison with Experiment

Two Mark I divertor JET shots with similar main plasma parameters but opposite directions for the toroidal magnetic field and plasma current were chosen for modelling. Discharges #31608 and #31485 are L mode plasmas with input power of the order of 5MW,

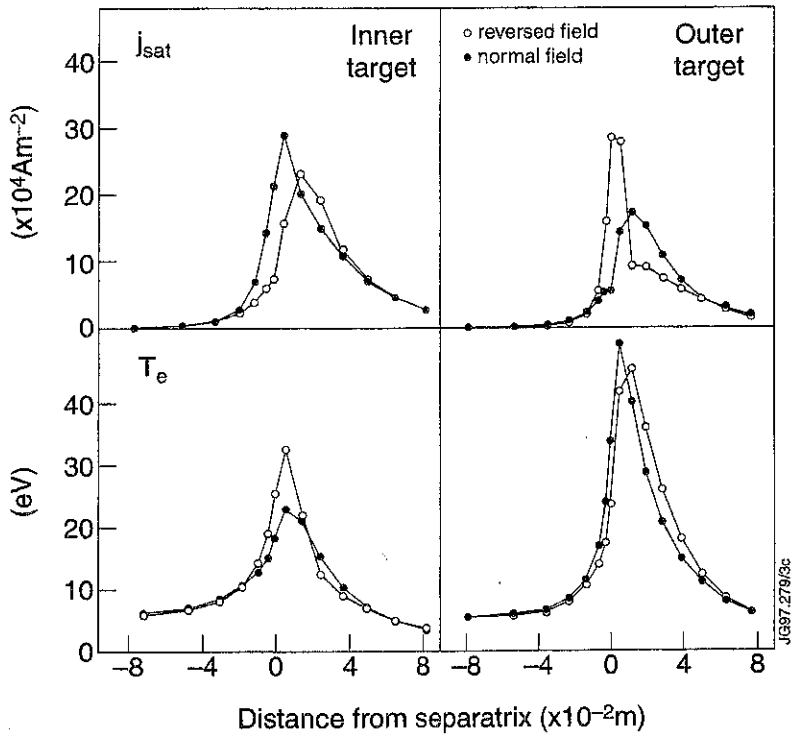

Fig. 1: Computed target ion saturation currents and electron temperatures

radiated power 1MW and line-averaged densities of 2.7-2.8×10^{19} m^{-3}, and with plasma currents of + and - 3MA and toroidal magnetic fields of + and - 3.3T respectively. Comparison of the experimental results for these discharges has been given in reference [2].

Code results have been obtained for pure plasmas with ion and electron input powers of 2.5MW and with modelled impurity radiation of 0.77MW, which with hydrogen radiation gives a total of about 1MW. Scans were made of the midplane separatrix density in the range 0.8-1.2×10^{19} m^{-3}, anomalous diffusion coefficient 0.2-1.0 m^2s^{-1}, pinch velocity 2.4-15 ms^{-1} outside the core plasma, and electron and ion thermal diffusivities 0.75-3.0 m^2s^{-1}. Anomalous diffusion coefficients are defined for particle and energy cross-field fluxes constant on a magnetic flux surface.

Results from modelling have shown that of the poloidal components, the **E×B** drift is dominant, while for radial components the **E×B** drift is larger near the divertor targets and the ∇B drift dominant everywhere else. The poloidal drift component is up to ten times larger in magnitude than the radial component. Both components of the drifts show a change in

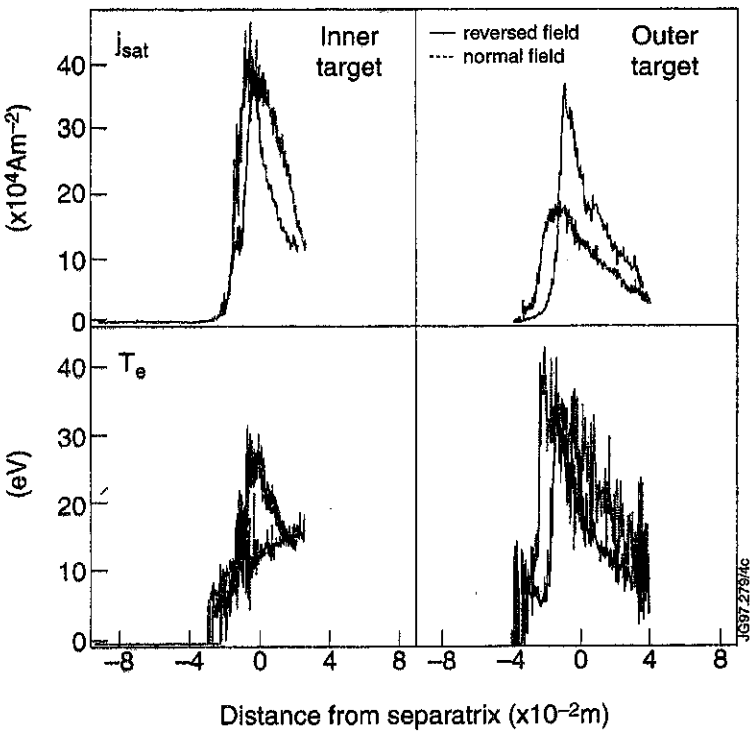

Fig. 2: Experimental target ion saturation currents and electron temperatures

direction with magnetic field reversal, excepting the radial drift in a small region near the separatrix at the outer target due to a reversal of the poloidal electric field in that region.

The effects of the poloidal drifts are masked by the target boundary conditions and particle sources and their effect on the parallel velocity. As a result, the total poloidal velocity near the targets changes by only 10-20% with magnetic field reversal. In the radial direction, the relative magnitudes of the total anomalous transport and the radial drift fluxes are such that the drifts are dominant near the divertor particle sources and in the core plasma. However the balance between the anomalous and drift fluxes, and thus the effects of B reversal, is strongly influenced by the magnitude of the anomalous transport coefficients, with better agreement with experiment for lower values of $D_\perp$ and pinch velocity.

In Fig. 1 are shown the modelling results for the target ion saturation currents and electron temperatures for the case with $n_s = 0.8\times10^{19}$ m^{-3}, $D_\perp = 0.3$ m^{2}s^{-1}, pinch velocity 4.5 ms^{-1} outside the core plasma, and $\chi_e = \chi_i = 1.5$ m^{2}s^{-1}. The experimental results from [2] are shown in Fig. 2. The peak ion saturation currents are lower than in experiment, but the combined results for j_{sat} and T_e do reproduce the trends seen experimentally. With B reversal

Table I: Comparison of target data for normal and reversed magnetic field cases and computed and experimental results.

Magnetic Field		Normal		Reverse	
Target		Inner	Outer	Inner	Outer
Particle Flux (10^{22} s^{-1})		6.6	6.5	5.9	6.8
P_{targ} (MW)	comp.	1.0	2.8	1.1	2.7
	expt.	<0.5	3.8	0.9	2.8
P_{rad} (MW m^{-2})	comp.	0.067	0.036	0.057	0.039
	expt.	0.1	0.056	0.068	0.096
H_α (10^{20} $m^{-2}str^{-1}s^{-1}$)	comp.	4.0	3.3	4.0	3.5
	expt.	5.3	2.9	2.0	2.5

the computed particle flux to the target plates does increase on the outer target and decrease on the inner target (Table I) although neither change is as large as may be inferred from the experimental j_{sat} signals. For the total power conducted to the targets, the computed results change only by 5-10% on B reversal and the asymmetry for the normal field case is not as large as found experimentally. The computed powers radiated in the divertors do not include core radiation but experimentally this only amounts to 10% of the total plasma radiation. The computed radiated powers do not show the large inversion of the asymmetry on B reversal but do follow the experimental trends. The simulated H_a signals have a smaller in/out asymmetry for the normal field case but again show only small changes on B reversal.

Conclusions

Overall, many of the measured trends found with magnetic field reversal have been reproduced by the code, but generally with smaller changes than seen experimentally. Variation of the magnitude of the anomalous transport coefficients has shown improved results for lower values of $D_\perp$ and pinch velocity, with the former having a greater effect at the inner target and the latter at the outer target. For the work presented here the standard model was used for the anomalous transport coefficients which defines the coefficients globally and with only a poloidal variation possible. The results obtained thus far indicate that the anomalous transport should be reduced to allow the drift fluxes to exert a greater influence, but with the model used this requires a global reduction which has resulted in some problems of numerical stability. Future work to complete the study of the relevance of drifts on divertor asymmetries will require the evaluation of different models for anomalous transport. This, and work on the effects of drifts on impurity transport, is in progress.

References

[1] Stangeby P.C. and Chankin A.V., *Nucl. Fusion* **36** 839 (1996)

[2] Chankin A.V. *et al*, *Plasma Phys. Cont. Fusion* **38** 1579 (1996)

[3] Radford G.J. *et al*, *Contrib. Plasma Phys.* **36** 187 (1996)

[4] Stangeby P.C. and Chankin A.V., *Phys. Plasmas* **2** 707 (1995)

MEASUREMENT OF INTERACTION OF MEV ENERGY PROTONS WITH LOWER HYBRID WAVES IN JET PLASMA

D.Testa[1], A.Gondhalekar, L.G.Eriksson, C.N.Lashmore-Davies[2], M.J.Mantsinen, T.J.Martin[2]
JET Joint Undertaking, Abingdon, OX14 3EA, United Kingdom
[1]Imperial College of Science, Technology and Medicine, London, SW7 2BZ, United Kingdom
[2]UKAEA Fusion, Abingdon, OX14 3DB, United Kingdom

ABSTRACT

Neutral particle analyser (NPA) measurements of ion cyclotron resonance frequency (ICRF) heated protons in the energy range $0.3 \leq E(MeV) \leq 1.1$ [1, 2] during Lower Hybrid (LH) current drive experiments in JET showed efficient coupling of LH power to the high energy protons. This behaviour has adverse implications for efficiency of LH current drive in plasmas containing high energy charged fusion products. Perpendicular Landau damping enables LH waves to interact with ions when the resonance condition $v_\perp \geq v_{RES} = c/n_{\perp MAX}$ is satisfied, where $n_{\perp MAX}$ is the maximum perpendicular refractive index in the LH wave spectrum. The observed coupling was unexpected in two respects: (i) taking place in the whole energy range of the measurement, it suggested that $n_{\perp MAX} \geq 40$, whereas model calculations of LH wave dispersion in JET plasmas give $n_{\perp MAX} \approx 20$, (ii) from the measurements, we deduced that approximately 30% of LH power intended for electron current drive was coupled to the protons, much exceeding the expectation of ≈ 5% - 10%, based on $n_{\perp MAX} \approx 20$ [3, 4]. We show that the presence of ICRF driven high energy protons modifies the LH wave spectrum in the way implied by the measurements. The LH wave dispersion relation is solved in slab geometry for a uniform plasma with JET parameters, including the ICRF driven anisotropic high energy proton population. For given ω_{LH} and $n_{||}$, corresponding to the experimental situation, we find that solutions exist with $n_{\perp MAX} \geq 40$ as required. For given ω_{LH}/Ω_p a discrete spectrum for magnitude of $n_\perp$ is found. For given background plasma and $n_{||}$, values of ω_{LH}/Ω_p are found for which no solutions exist with $n_\perp > 20$, indicating significant reduction of absorption of LH power by anisotropic fast protons. The latter result suggests a way of avoiding parasitic loss of LH electron current drive power to high energy protons.

I. EXPERIMENTAL EVIDENCE OF INTERACTION

Fig.1 and 2 show comparison of a pulse with on-axis first harmonic proton minority ICRF heating alone and another with combined (ICRF + LH) heating. NPA measurements show in

the latter case direct absorption of LH power by high energy protons, sustaining the minority population after termination of ICRF heating well above the slowing-down level.

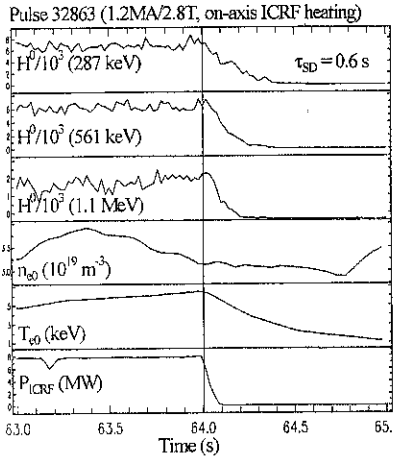

Fig.1. Evolution of hydrogen flux to NPA showing that the proton population decays within the slowing-down time τ_{SD} after termination of ICRF heating.

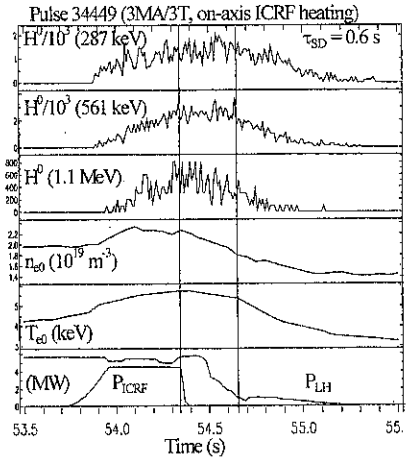

Fig.2. The hydrogen population is sustained by LH waves in the whole measurement range after termination of ICRF heating.

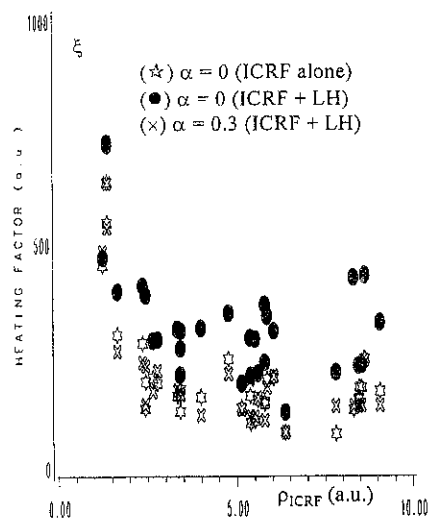

Fig.3. Comparison of ξ with different α for ICRF heating alone and combined (ICRF + LH) heating.

To deduce the fraction of LH power coupled to high energy protons, taking into account variations in the measured proton density n_p, slowing-down time τ_{SD} and applied power, we used as a figure-of-merit for proton heating the factor $\xi = n_p\ T_{p\perp} / \rho_{TOT}\ \tau_{SD}$, where $T_{p\perp}$ is the perpendicular proton tail temperature measured using the NPA. The power density coupled to fast protons is expressed as $\rho_{TOT} = \rho_{ICRF} + \alpha\ \rho_{LH}$, where an unknown fraction α of LH power goes to heating protons. We see in fig.3 that to reconcile the magnitude of ξ in pulses with (ICRF + LH) heating with that with ICRF heating alone, we need $\alpha \approx 0.3$.

II. NUMERICAL SIMULATIONS OF LH POWER ABSORPTION

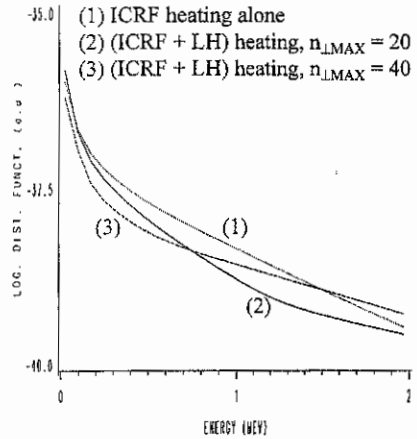

Fig.4. Simulated perpendicular proton distribution function for different heating schemes.

To simulate LH power absorption by an ICRF driven anisotropic fast proton population, a LH operator [5] was incorporated in the 1D Fokker-Plank code PION [6]. The LH operator for perpendicular diffusion in velocity space acts only upon ions satisfying the resonance condition $v_\perp \geq v_{RES} = c/n_{\perp MAX}$. In fig.4 are shown examples of simulated perpendicular proton distribution function for ICRF heating alone and for combined (ICRF + LH) heating with $n_{\perp MAX} = 20$ and $n_{\perp MAX} = 40$. The latter is in qualitative agreement with the measured distribution function.

III. MODIFICATION OF LH WAVE DISPERSION BY FAST PROTONS

Above simulations suggest that a LH wave spectrum with $n_{\perp MAX} \geq 40$ could give rise to absorption by protons as measured. We investigated the effect of a fast anisotropic minority proton population on dispersion of LH waves in a thermal deuterium plasma. The hot-plasma electromagnetic dispersion relation with $\omega_{LH} = 2\pi \times 3.7 \times 10^9$ rad/s, $n_{||} = 1.8$ and $B_\phi = 2.8$ T has been solved for a uniform plasma slab using a bi-Maxwellian distribution function for the minority proton population and including a 1% relativistic LH-driven electron population, with plasma and LH wave parameters corresponding to JET experimental situations for ICRF heating with LH current drive (fig.5). Usual simulations of LH current drive in JET [3, 4] omit the high energy anisotropic proton population and solve the warm plasma dispersion relation. We find that the presence of fast protons affects the dispersion of waves in the LH range of frequencies by introducing hot-plasma solutions. For a thermal deuterium plasma without the minority proton population, using either the cold or warm plasma approximation, slow and fast waves are found with $n_{\perp MAX} \leq 20$. For a thermal deuterium plasma containing a population of anisotropic high energy protons, solutions exist with $n_{\perp MAX} \geq 40$, as required by above simulations. These solutions show a discrete resonant structure in ω_{LH}/Ω_p. For given background plasma and $n_{||}$, values of ω_{LH}/Ω_p can be found for which such solutions do not exist, thus significantly reducing absorption of LH waves by anisotropic fast protons.

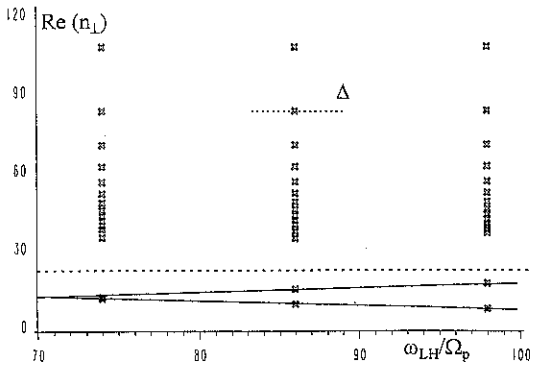

Fig.5. Solutions of dispersion relation in the LH range of frequencies for n_e = 3 x 10^{19} m^{-3}, n_D/n_e = 0.9, n_f/n_e = 0.11, $T_e = T_D$ = 5 keV, $T_{p\perp}$ = 300 keV, $T_{p//}/T_{p\perp}$ = 0.1, n_{er}/n_e = 0.01, $< E_{er//} >$ = 100 keV, $T_{er//}$ = 50 keV, $T_{er\perp}/T_{er//}$ = 0.2. Cold and warm plasma solutions have $n_{\perp MAX} < 20$ and are continuos in ω_{LH}/Ω_p. Hot plasma solutions have $n_{\perp MAX} > 35$ and exist only for discrete values of ω_{LH}/Ω_p with a width Δ increasing with $T_{p\perp}$ and n.

IV. CONCLUSION

We have shown evidence of coupling of LH waves to ICRF-heated MeV energy protons in JET using measurements made with a high energy NPA. From energy balance considerations we deduce that 30% of LH wave power is absorbed by anisotropic fast protons. We have tested, using 1D numerical Fokker-Planck modelling, a conjecture that this coupling is effected by modifications of LH wave dispersion in the plasma. Experimental observations are qualitatively reproduced with $n_{\perp MAX} \geq 40$. Solutions of dispersion relation in the LH range of frequencies with $n_{\perp MAX} \geq 40$ appear when high energy protons are added to a thermal deuterium plasma. These roots correspond to LH waves damping on fast protons and show a cyclotron-like resonant structure for given background plasma parameters and $n_{||}$. These solutions disappear by adjusting either the magnetic field or the LH frequency. This result is therefore promising for reducing the parasitic damping of LH power on high energy protons.

ACKNOWLEDGEMENTS

The authors would like to thank Professor Malcolm Haines of Imperial College of Science, Technology and Medicine, London, for support and encouragement of this work.

REFERENCES

[1] A.A.Korotkov, A.Gondhalekar and A.J.Stuart, *Nuclear Fusion* **37**, 35, 1997

[2] K.G.McClements, R.O.Dendy and A.Gondhalekar, *Nuclear Fusion* **37**, 473, 1997

[3] Y.F.Baranov, A.Ekedahl, P.Froissard, C.Gormezano et al., *Nuclear Fusion* **36**, 1031, 1996

[4] M.C.Ramos de Andrade et al., *Plasma Physics and Controlled Fusion* **36**, 1171, 1994

[5] E.Barbato and F.Santini, *Nuclear Fusion* **31**, 673, 1991

[6] L.G.Eriksson, T.Hellsten and U.Willén, *Nuclear Fusion* **33**, 1037, 1993

Analysis of a Wide Band Matching System for ICRH of ELMy JET plasmas

P U Lamalle[1], M Simon[2], V Bhatnagar[2], C Gormezano[2], J Jacquinot[2], A Kaye[2], M Schmid[2], A Sibley[2], D F H Start[2], M Timms[2], T J Wade[2] and A Whitehurst[2]
[1]Laboratoire de Physique des Plasmas - Laboratorium voor Plasmafysica,
EURATOM - Belgian State Association, Trilateral Euregio Cluster,
École Royale Militaire - Koninklijke Militaire School, B-1000 Brussels, Belgium.
[2]JET Joint Undertaking, Abingdon OX14 3EA, U.K.

Introduction

The rapid variations of the plasma boundary characteristic of edge-localized modes (ELMs, [1]) induce sudden and large increases of the load of the JET ICRH antennae (rise time: 50 to 100μs; decay: a few ms). These events are ubiquitous during the high combined power discharges, and occur at rates of up to 50-100Hz. The main impact of ELMs on the antenna properties is seen on the coupling resistance, the reactance being much less affected.

The JET ICRH plant [2] operates between 23 and 57MHz. Its existing automatic matching system (Fig.1, top) consists of variable stubs and line stretchers in each one of the 16 transmission lines, and adjustable generator frequency common to the four straps of each ICRH antenna module (Maximum ±200kHz in 1ms). The long main transmission lines (MTL, circa 80m) between each stub and antenna strap are the frequency-sensitive elements. Under slowly varying load conditions, this allows operation with negligible wave reflection at the generators. Conversely during ELMy discharges, the rapid variations of the coupling resistance of each antenna strap cannot be compensated due to the inertia of the matching stubs. The rf plant is then unable to deliver its nominal power because of unacceptable reflection at the generator tetrodes; in the presence of frequent ELMs, the average rf power coupled to the plasma is thereby significantly reduced. As ELMy operating regimes are highly relevant to ITER, it is crucial to remove this limitation. A wide band matching system is under development at JET to meet such demanding operating conditions [3-5]; the principle is as follows: A high characteristic impedance line section is inserted near the antenna in each transmission line; its length and position are adjustable (sliding impedance, in short 'SLIMP', lower part of Fig.1).

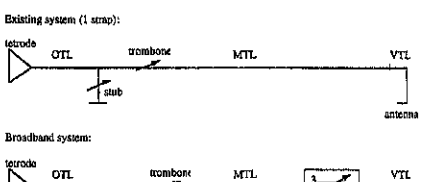

Fig.1: Suitable addition of a prematching sliding impedance in each line converts the JET ICRH transmission and matching system (top) into a broadband system (bottom). The indices at various points of the system are used for reference in the text.

To first approximation, this prematching element converts the fast coupling resistance variations on the antenna side into phase variations of the reflection coefficient on the main transmission

line. Variations of the rf frequency (at an increased rate of ±300kHz in 0.5ms) compensate these fast phase changes near the stub, and a low reflection is achieved at the generator over a much broader range of loads. With appropriate positioning of the SLIMP, operation over a wide load band takes place around four frequencies within the JET plant range; full power delivery is allowed during most of the ELM decay. (The abrupt load increase during the ELM rise is too fast to follow; however appropriate orientation of the tetrode anode load trajectory will avoid limiting the generator power during this very short time.) Moreover the prematching SLIMP greatly reduces the line power losses. A prototype will be installed at the end of 1997. We have studied this system using a simplified representation of the ELMy antenna load and a simple (but accurate) analytical model. This has allowed detailed understanding of the characteristics of the new plant configuration, calculation of design values - subject to technical constraints - and optimal settings for the circuit elements, and development of a control algorithm for automatic operation. In complement, a detailed numerical model of the rf transmission and matching system yields the sensitivity to changes in various parameters.

Modelling of the antenna: Given a reference operating frequency and an array phasing scenario, each strap of a JET A2 antenna can be represented [6] by an equivalent transmission line section with the standard characteristic impedance of the transmission system (30Ω), terminated on a lumped resistance equal to the experimental coupling resistance. The effects of an ELM are represented by phenomenological variations of the latter (typically from 2Ω before and after the ELM up to a safe maximum of 10Ω at the ELM peak), and variations of the phase of the strap reflection coefficient (typically increasing during the ELM rise, then decreasing by circa 8° during the ELM fall). Any delay between straps is neglected. Fig.2 shows these quantities as derived from fast acquisition of rf signals (sampling period 16μs) during a rather mild ELM.

Analytical model: The stub and the SLIMP sections are very short with respect to the long MTL, and can be assimilated to constant elements during the rapid frequency changes; conversely the line section between SLIMP and antenna short circuit (with electrical length l_{45}) is found to be a critical parameter. Analysis based on these observations yields strikingly simple results despite the number of parameters; detailed expressions will be reported elsewhere.

Detailed numerical model: Here each circuit element is represented by an equivalent transfer matrix. Several options are available for selecting the instantaneous frequency: e.g. the existing JET feedback, minimization of the OTL vswr, simple feedback proposed for practical automatic control (cf Figs.5-6). Characteristic curves of the new hardware are shown on Figs.3, 5 and results of a sensitivity study on Fig.4.

Results of the analysis: (1) The theoretical performance of the system increases with the SLIMP characteristic impedance; a value of 105Ω has been chosen in order to maintain an

acceptable rf current density on the sliding contacts. (2) Performance decreases as the SLIMP position recedes from the antenna, because the electrical angle θ_{45} of line section l_{45} becomes more sensitive to frequency variations. (3) The SLIMP must be connected circa $(2n+1)\lambda/4$ from the antenna short-circuit. A distance of order 18.75m allows 4 operating frequencies (28, 36, 44 and 52 MHz for n = 3, 4, 5, 6) within the plant range. It gives a good compromise with the previous point, and is anyway the practical position closest to the tokamak. As the 4 straps of each array are driven at a common frequency this distance is adjustable by 1m in order to compensate for the differences between strap equivalent lengths, be they intrinsic or due to a particular phasing scenario. The distance between 105-30Ω transition and antenna short must be set accurately, within 2cm, before the ELMy phase. (4) Best advantage is taken of the high impedance section making its length = $(2k+1)\lambda/4$. The $\lambda/4$ case will be implemented at JET, requiring a variable length for the 105Ω section to work at 4 frequencies. We find very similar theoretical performance for the alternate approach with k equal to the above n and a nearly fixed 18.75m SLIMP: this solution seems attractive as well. (5) There are two types of broadband configurations, respectively with frequency increasing or decreasing when the load increases. On the basis of the fast rf data (Fig.2), we prefer the second one: the antenna is electrically slightly longer during most of the ELM, partly compensating the adverse effect of point (2).

The control algorithm decomposes into two parts:

1. Preset including fine tuning of the mechanical elements during an ELM-free phase. A purely experimental assessment of the quality of configuration reached by the system would require e.g. data acquisition over a programmed frequency scan and their subsequent automatic analysis. Such a procedure would be extremely tedious and costly to implement, hence we adopt a control based on target parameters obtained from the above models. We have been able to formulate the control of the whole system in terms of electrical signals exclusively; this was not obvious since the distances between the two SLIMP 105-30Ω transitions and the measurement points are variable. Avoiding conversions from mechanical to electrical measurements is particularly welcome since accurate system preset is mandatory.
2. Fast frequency adjustment taking place during the ELMs. After numerical experiments with several complex error signals, we have found that a linear relationship between the instantaneous frequency and the antenna load gives good results, provided endstops are set on the frequency deviation (Fig.5). The coefficients are calculated from measurements of the ELM-free preset values reached by the system.

Conclusions

The new wide band matching system developed for JET will significantly increase the ability to couple ICRH power in presence of frequent ELMs; the reduction of power dissipation in the transmission lines will also improve the plant reliability thanks to a lower demand on the generator tetrodes. Applied to ITER, this system will give access to a broader range of interesting operational regimes at high auxiliary heating power.

References

[1] V Bhatnagar, these Proceedings.

[2] T J Wade *et al*, Fusion Engineering and Design **24** 23 (1994)

[3] T J Wade *et al*, 12th Symp. on Fusion Engineering (SOFE), Monterey, 1200 (1987)

[4] M Schmid *et al*, Proc.19th Symp. on Fusion Technology (SOFT), Lisbon, Portugal (1996)

[5] A Kaye *et al*, 12th Topical Conf. on RF Power in Plasmas, Savannah, Georgia (1997)

[6] P U Lamalle *et al*, Europhysics Conference Abstracts **19C** II 329 (1995)

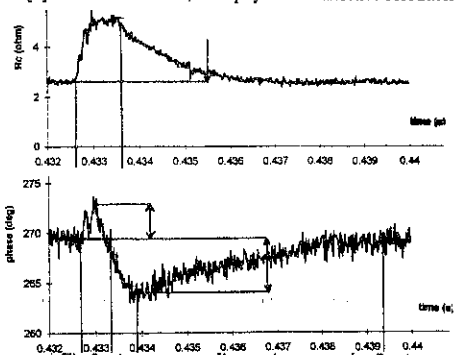

Fig.2 - Antenna coupling resistance and reflection phase during an ELM (from fast rf acquisition)

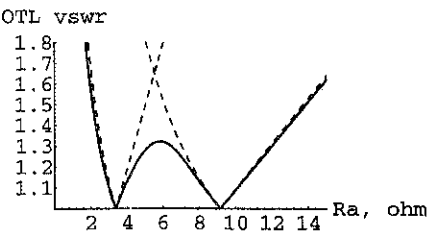

Fig.3 - Typical variations of OTL vswr vs antenna coupling resistance. Dashed lines: best performance of existing hardware for 2 different adapted loads; plain line: wide band matching system with frequency optimally controlled by the variable load.

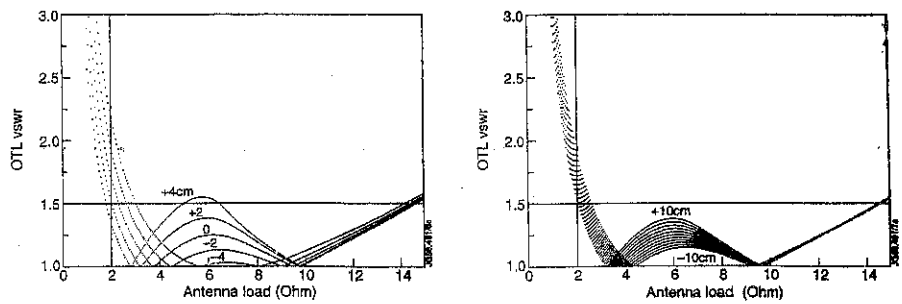

Fig.4 - Influence of a perturbation of the distance from SLIMP to antenna short (left, reference l_{45}=18.63m) and of the SLIMP length (right, reference length=1.39m) on the wideband system response at 52MHz.

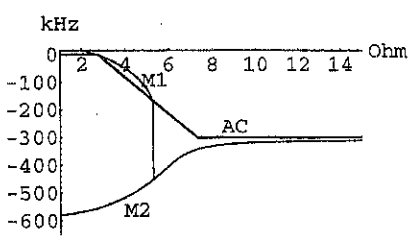

Fig.5 - Frequency deviations (near a 52MHz reference) M2: wide band matching, similar case to Fig.3 AC: simplified linear variation for automatic control; this branch allows a lower adapted load than M2, cf Fig.6.

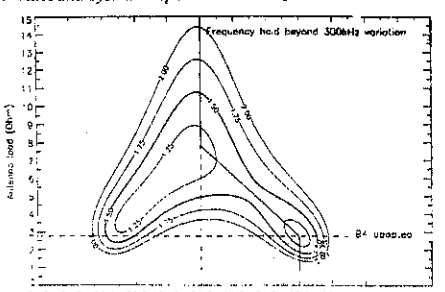

Fig.6 - Contours of constant OTL vswr vs frequency and antenna load. The 3 line segments indicate the zero of the error signal chosen for fast frequency control (The target frequency varies linearly with load between its endstops.)

Analysis of ICRF heating in JET at harmonics of the ion cyclotron frequency

M. Mantsinen[1], V. Bhatnagar, J. Carlsson[2], G. Cottrell, L.-G. Eriksson, A. Gondhalekar, C. Gormezano, T. Hellsten[2], R. König, P. Lomas, E. Righi, F. Rimini, G. Sips, D. Start, F.X. Söldner, B. Tubbing and K.-D. Zastrow

JET Joint Undertaking, Abingdon, OXON, OX14 3EA, UK

[1]Also at Helsinki University of Technology, Association Euratom-Tekes, Espoo, Finland

[2]Royal Institute of Technology, Association Euratom-NFR, Stockholm, Sweden

Introduction Second-harmonic heating of tritium ($\omega \approx 2\omega_{cT}$) is one of the major schemes for heating reactor-relevant plasmas with waves in the ion cyclotron range of frequencies (ICRF). Important aspects of the scheme have been explored on JET using second and higher harmonic heating in plasmas with ICRF heating alone, and in high-performance Hot-Ion H-modes and optimised shear plasmas with combined neutral beam injection (NBI) and ICRF heating. In high-performance discharges ICRF heating, tuned to $\omega \approx \omega_{cH} = 2\omega_{cD}$ near the plasma centre, leads to increased ion heating and DD-fusion reactivity, which is attributed to the second-harmonic damping of ICRF on deuterium beam ions. Since in higher harmonic heating the absorption strength, and thus the ICRF power partition among different absorbing species, depends strongly on the distribution function, such scenarios are particularly challenging to model.

Numerical tools ICRF heating in JET at harmonics of the ion cyclotron frequency ($\omega \approx n\omega_{ci}$, $n \geq 2$) has been analysed with PION [1] and FIDO [2] codes. PION is a self-consistent calculation of ICRF power deposition and velocity distribution of the resonating ions. In order to take into account the deuterium beam ion distribution function, which is important in analysing high-performance JET discharges, NBI source terms have been included in PION. Finite-orbit-width effects are taken into account in PION by noting that the fast ions have turning points close to the cyclotron resonance and by averaging the collision coefficients over those orbits.

Comparison with distribution functions measured by the high-energy neutral-particle analyser (NPA) [3] is facilitated by the Monte-Carlo code FIDO. The code calculates the fast-ion distribution function in the presence of ICRF waves, including radial transport and effects due to finite orbit widths. At present, the code does not include NBI source terms.

ICRH of high-performance discharges To illustrate the effects of ICRH heating in high-performance JET discharges, we concentrate here on a 3MA/3.45T optimised shear discharge with 16 MW of NBI and 6 MW of ICRF power (discharge 38437, Fig. 1). A single ICRF frequency of 51.2 MHz is used in the $0\pi0\pi$ phasing of the RF antennae (i.e. $k_{\parallel} \approx 9\ \mathrm{m}^{-1}$).

Comparison between the simulated and experimental DD-neutron yield R_{NT} is shown in Fig. 2. Simulations with PION, using measured plasma parameters as input, have been done both with and without taking ICRF heating into account. Without ICRH, the simulated R_{NT} is about 35% lower than the measured R_{NT}. With ICRH, reasonably good agreement is obtained assuming n_H/n_D = 2.5%, in rough agreement with experimental estimates (direct measurement of n_H/n_D in the ICRF heating region is lacking).

The sensitivity of the simulated R_{NT} to the hydrogen concentration is also shown in Fig. 2. The simulated R_{NT} depends rather strongly on n_H/n_D which determines the ICRF power partition between deuterons and hydrogen. When n_H/n_D decreases, the fraction of ICRF power absorbed by deuterons increases [Fig. 3(a)]. According to PION simulations, deuterons typically absorb 30–50% of the total ICRF power. The second-harmonic deuteron absorption gives rise to significantly greater bulk ion heating in the plasma centre as compared with NBI alone [Fig. 3(b)]. The increase in R_{NT} and bulk ion heating due to ICRH, observed both in Hot-Ion H-modes and optimised shear plasmas, depends on the level of applied ICRF power, phasing of the RF antennae, and spreading of the cyclotron resonance [4]. With 2–3 MW of ICRF power using either multiple frequencies (instead of 6 MW using single frequency as above) or $\pi/2$ phasing ($k_{\parallel} \approx 4\ \mathrm{m}^{-1}$), the high-energy deuteron tail is minimised (non-thermal contribution to R_{NT} is small) and more efficient bulk ion heating is obtained [4].

ICRH-only plasmas Good heating efficiency and transition into H-mode confinement have been obtained with ICRF heating alone at $\omega \approx 2\omega_{cH}$. PION simulations for discharge 39916 show good agreement between the simulated and experimental fast-ion energy content [Fig. 4(a)]. The experimental fast-ion energy content is obtained by calculating the difference between two different measures of the plasma stored energy [1]. The experiments were done shortly after a restart of the machine when the hydrogen concentration was still high. In our simulations we assume n_H/n_D = 10%, again in rough agreement with experimental estimates. The fast-ion energy content simulated with the FIDO code for discharge 39916 is also in agreement with the experiment. Furthermore, preliminary results from FIDO show reasonable agreement between the simulated and measured proton distribution functions [Figure 4(b)].

The simulated distribution function decreases sharply at $E \approx 1$ MeV because wave-particle interaction, which is proportional to $|E_+ J_1(k_\perp \rho) + E_- J_3(k_\perp \rho)|^2$, almost vanishes at this point. Here, $k_\perp$ is the component of the wave vector perpendicular to the background magnetic field, ρ is the Larmor radius, J_n is the Bessel function of first kind, and E_+ and E_- are the left-hand and right-hand components of the electric field, respectively.

According to PION simulations for ICRF heating at $\omega \approx 2\omega_{cH}$, hydrogen absorbs about 95% of the total ICRF power, and the rest goes to direct electron damping. Most (85–90%) of the power absorbed by hydrogen is transferred collisionally to electrons. Since the plasma current is low (1.6 MA) and very energetic ions are created, finite-orbit-width effects play an important role in the discharge. Due to these effects the profile of the collisional power transfer is broader than the power absorption profile (Fig. 5).

The importance of tail formation on the distribution function of the resonating ions for power partition is even more clearly demonstrated in ICRF heating experiments with $\omega \approx 3\omega_{cD}$. PION simulations for ICRF heating at $\omega \approx 3\omega_{cD}$ show reasonably good agreement between the measured and simulated R_{NT} (in these experiments the record R_{NT} of 9×10^{15} neutrons/s on JET for ICRH alone was obtained) and fast-ion energy content [5]. Due to tail formation, deuteron absorption is enhanced: in the beginning of the discharge damping on thermal deuterons is negligible as compared to competing absorption mechanisms, while in the high-power phase when the deuteron tail formation has taken place, deuterons absorb up to 80–85% of the total ICRF power.

Conclusions Analysis of JET discharges with ICRF heating at $\omega \approx n\omega_{ci}$, $n \geq 2$, shows that the theoretical picture of wave propagation and tail formation on which PION is based, is generally correct. This gives confidence in simulations of other experiments in JET and in modelling ICRF heating schemes for future reactor plasmas.

Acknowledgements The authors gratefully acknowledge the support of the JET experimental team and in particular of the RF Division and Task Force H and P personnel. The work carried out by one of the authors (MM) was done under a task agreement between JET Joint Undertaking and Association Euratom-TEKES.

References [1] L.-G. Eriksson, T. Hellsten and U. Willén, Nuclear Fusion **33** 1037 (1993). [2] J. Carlsson, T. Hellsten and L.-G. Eriksson, ALF-1996-104, Royal Institute of Technology, Stockholm, Sweden. [3] A.A. Korotkov, A. Gondhalekar and A.J. Stuart, Nuclear Fusion **37** 35 (1997). [4] C. Gormezano *et al.*, in Proc. of 12th Topical Conference on RF Power in Plasmas, Savannah, USA, 1997; see also F. Rimini *et al.* and G.A. Cottrell *et al.*, this conference. [5] L.-G. Eriksson *et al.*, submitted to Nuclear Fusion

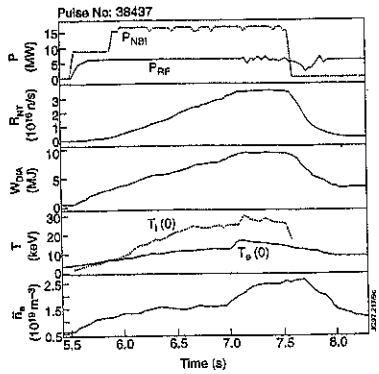

Fig. 1 Time evolution of main plasma parameters for optimised shear discharge 38437.

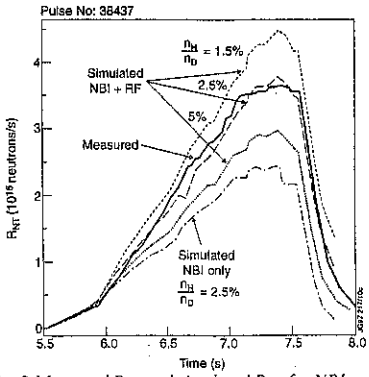

Fig. 2 Measured R_{NT} and simulated R_{NT} for NBI-only and for NBI+ICRF assuming different n_H/n_D.

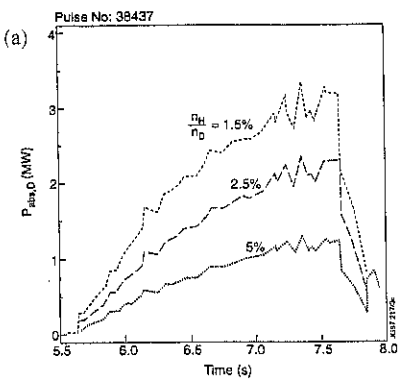

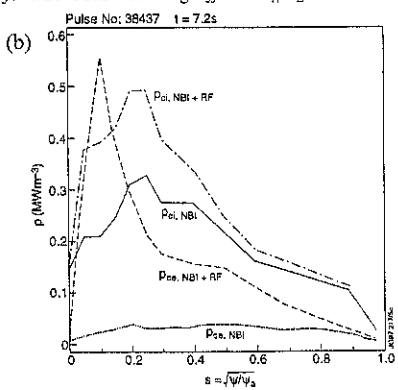

Fig. 3 (a) Power absorbed at the second harmonic deuterium resonance for different n_H/n_D. (b) Profile of the collisional power transfer to ions and to electrons for NBI-only and for NBI+ICRF with n_H/n_D=2.5%.

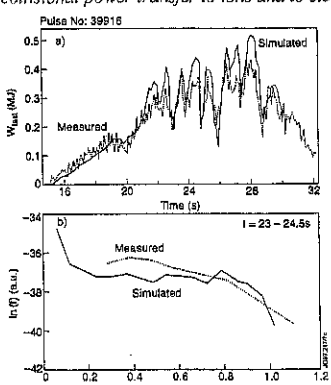

Fig. 4 Measured and simulated (a) fast-ion energy content and (b) proton distribution for $\omega \approx 2\omega_{cH}$.

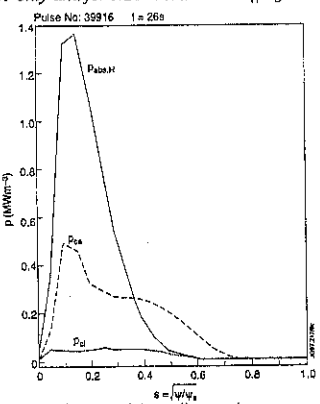

Fig. 5 Power density of the collisional power transfer to ions and electrons, and hydrogen absorption for $\omega \approx 2\omega_{cH}$.

BULK ION HEATING WITH ICRH ON THE ITER PATH TO IGNITION

D F H Start, V Bergeaud, L-G Eriksson, B Gayral*, C Gormezano, and M Mantsinen**

JET Joint Undertaking, Abingdon, OXON. OX14 3EA, United Kingdom.
* Ecole Polytechnique, Palaiseau, France.
**Also at Helsinki University of Technology, Ass. EURATOM-Tekes. 02150 Espoo, Finland.

INTRODUCTION. The auxiliary heating on ITER is likely to be a combination of neutral beams (NB), ion cyclotron heating (ICRH) and electron cyclotron heating (ECH). Of these, only ICRH is capable of predominantly heating the bulk ions in the plasma centre either on the route to ignition or during a driven-burn scenario. In the ITER Detailed Design Report (DDR) [1], simulations are made for equal ion and electron heating by the auxiliary power. The aim of this paper is to investigate the efficacy of bulk ion heating and to see how the ICRH scenario might be optimised, and the path to ignition best chosen, to achieve power equipartition.

ION CYCLOTRON HEATING SIMULATIONS. The PION code [2] is used to calculate the power absorption and the fast ion tail formation in a self-consistent way. In addition more than one resonance layer for a single ion species can be treated. A preliminary comparison of fundamental deiterium (ω_{CD}) and second harmonic tritium ($2\omega_{CT}$) ICRH scenarios showed the latter to be the more effective due to the stronger cyclotron damping compared to direct electron absorption. Consequently, only results for the $2\omega_{CT}$ scheme are given in this paper.

The ion heating is optimised by several methods. Two frequencies, 58MHz and 54MHz, are used to spread the power deposition and control the tail energy whilst maintaining central heating. The ratio of the input power levels at these frequencies is chosen to maximise the fraction of the input power, P_i/P_{RF}, transferred collisionally to the majority ions. A deuterium to tritium ratio, D:T = 30:70, is also used to reduce the triton energy whilst maintaining a high fusion rate. The parallel wavevector is chosen to be $k_{//} \sim 3m^{-1}$ to reduce direct damping of the fast wave on electrons by ELD and TTMP.

Typical heating profiles are shown in fig 1 for P_{RF} = 50MW, $n_{eo} = 6x10^{19}m^{-3}$ and T_{eo} = 17keV. The ion heating fraction for this case is 70% of the input power. Placing the two resonances at r/a = 0.05 (56.9MHz) and at r/a = 0.25 (53.8MHz) gives a central, flat-topped ion heating power density profile. The input power is divided in the ratio of 15MW at 56.9MHz and 35MW at 53.8MHz. The tritons absorb 70% of P_{RF} inside r/a = 0.5.

The inset to fig 1 shows the sensitivity of the direct electron damping to $k_{//}$. At $k_{//} = 3.1m^{-1}$ this process takes 10% of the power. The absorption rises with increasing $k_{//}$ to 30% at $5m^{-1}$. The results of many calculations for different values of n_{eo} and T_{eo} are plotted as contours of constant ion heating fraction to allow the effect of varying the path to ignition to be readily seen. Contours for 50MW of ICRH are shown in fig 2. The contour label is the ratio P_i/P_{RF}. Also shown in fig 2 are two routes to ignition. That labelled KWG is a calculation by Kinsey

using the Weiland/Guzdar-Drake transport model[3] and 50MW of neutral beams. The excursion of T_{eo} to a value exceeding that during the burn phase is characteristic of this path and can reach $1.5T_{eo}$(burn)[3]. This path is not good for ion heating.

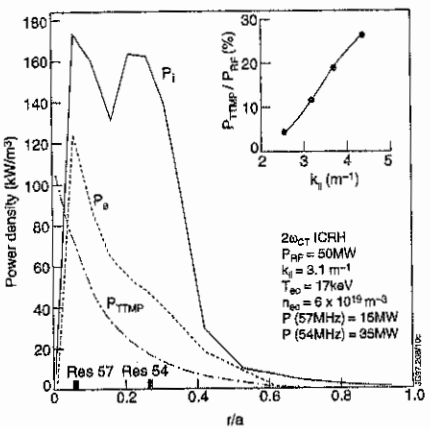

Fig 1 ICRF heating profiles for 50MW $2\omega_{CT}$.

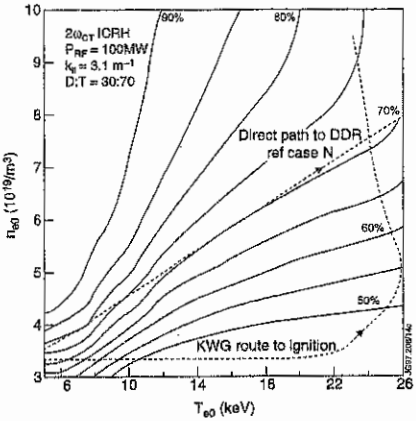

Fig 2 Contours of constant ion heating fraction for 50MW of $2\omega_{CT}$ ICRH.

The path labelled 'direct' is a straight line from ohmic heating, with $n_{eo} = 3.5x10^{19}m^{-3}$, T_{eo} = 5keV, to ignition with $n_{eo} \sim 1x10^{20}m^{-3}$ and $T_{eo} \sim$ 35keV, as in the ITER Nominal Ignited Scenario (case N). On such a path the fraction of ion heating from the ICRH is about 70% in the case of 50MW injection and around 40% when the power is raised to 100MW.

A transport code utilising the PION results is used to investigate paths closer to the 'direct' path and the results are presented in the following section..

OPTIMISING THE PATH TO IGNITION. The transport code used for this study includes ohmic heating, ICRH, NBI and α-particle heating and takes account of losses due to Bremstrahlung and synchrotron radiation. The 1-D heat diffusion equation is solved with $\chi_e = \chi_0(5 + 2(r/a)^2 + 10(r/a)^6)$ and $\chi_i = 2\chi_e$. The value χ_o is adjusted to give the required H89P factor, as in DDR. There is experimental evidence that the H-factor is related to the the power above threshold, at least for type 3 ELMs. An example from JET is shown in Fig 3 for H-minority ICRH in which the power is ramped slowly through the threshold value. The H-factor (without the fast ion content) rises to H89P = 1.7 at 20.5sec, At this time the power is about 20% above threshold.. A small jump to H89P = 1.8 occurs as type 1 ELMs appear and a further increase to 2.2 takes place in the ELM-free phase. Similar results are found with NBI.

In our calculations the H-factor and the density evolutions are prescribed. This fixes the net total power input, $P_{OH} + P_{aux} + P_{\alpha} - P_{rad}$, during the H-mode. The code runs with feeback on P_{aux} to follow the net total power waveform as the α-power and radiation losses evolve. The ion density and Z_{eff} are determined by 2% Be impurity and the production of He ash.

The prescribed density and H-factor waveforms are given in Fig. 4. The value of n_{eo} increases

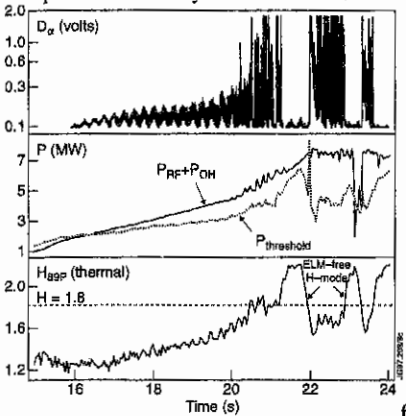

Fig 3 H-factor during ICRH power ramp

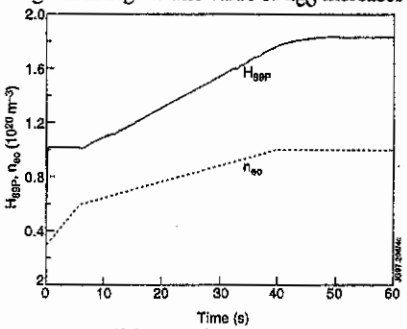

Fig 4 H-factor and n_{eo} waveforms.

from $3x10^{19}m^{-3}$ to $6x10^{19}m^{-3}$ in 6sec at which time the H-mode transiition is imposed. The H-factor rises to H89P = 1.8 as n_{eo} reaches $1x10^{20}m^{-3}$, approximately the Greenwald limit. The threshold and net total input power waveforms are shown in fig 5.

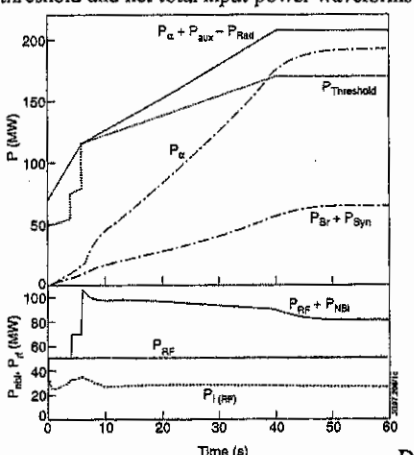

Fig 5 Evolution of P_{thresh} and heating levels

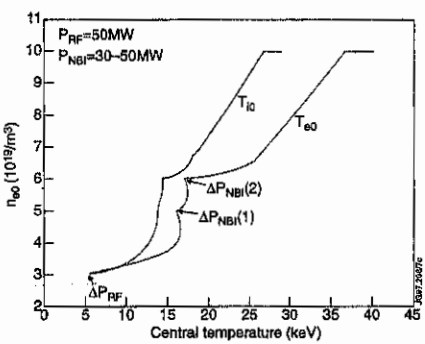

Fig 6 Trajectory for ICRF + NBI combined heating

During the L-mode, 50MW of ICRH is applied followed by a stepped waveform of beam power to produce the H-mode at 6sec with a total auxiliary power close to 100MW. The beam power is reduced to 30MW by the feedback as the α-power increases (see fig 5). At the H-mode the D:T ratio is changed from 30:70 to 50:50 over 4sec.

The path on the n_{eo}, T_{eo} plane is shown in fig 6 and proceeds as follows. With 50MW of ICRH , T_{eo} rises to 17keV and T_{io} to 14keV. As the density reaches $5x10^{19}m^{-3}$, just before the first NBI step, the ion heating power is 35MW (see fig 5). The first beam step maintains a constant temperature as n_{eo} rises to $6x10^{19}m^{-3}$. The second NBI step produces initially a fast

rise in T_{eo} and much a smaller increment in T_{io}. Thereafter the linear rise in net power and the linear increase in H-factor produce a straight -line path to the operating density of $1x10^{20}m^{-3}$. The ion heating in the driven steady state is 31MW (25MW RF + 6MW NBI) out of a total additional heating power of 84MW (P_i/P_{aux} = 37%).

The above is a simulation of a driven burn scenario and is used to assess the effect of ion heating in the steady state phase in the next section. The route to an ignited plasma is similar with the H-factor rising to 2.4 and the density to $1.3x10^{20}m^{-3}$.

ION HEATING IN DRIVEN BURN SCENARIOS. In this regime the above calculations show that 50MW of ICRH power will deliver around 25MW of power to the ions. The remaining power is predominantly absorbed directly by the electrons. The fusion power is 950MW, alpha power is 190MW, the radiation is 70MW and the Q-value is 11.7.

A sensitivity test was carried out by converting part of the ICRH ion heating to electron heating without changing the heating profile shape. This produced only minimal changes in χ_0 for a given H-factor.

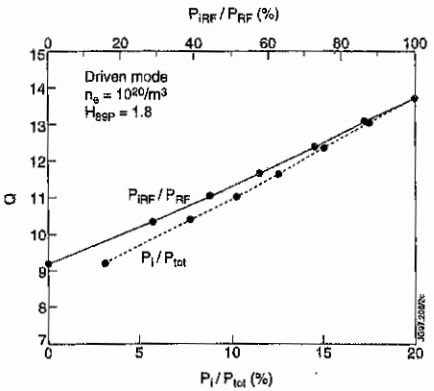

Fig 7 Q-value versus ion heating fraction.

The results are shown in fig 7 where the Q value is plotted against both the ratio P_{iRF}/P_{RF} and the ratio P_i/P_{tot} = $(P_{iRF} + P_{iNB})/(P_{RF} + P_{NB} + P_\alpha)$. From pure electron heating to pure ion heating by the ICRF the Q value increases by a factor of 1.5.

CONCLUSIONS As a by-product of the calculations we note that the central power deposition (fig.1), compared with a flat profile, as in fig 2.6-3 in DDR for NBI, enhances the H-factor by ~10% for the same transport coefficients. Such a flat profile with little bulk ion heating gives a Q value ~8.3 compared with Q = 11.7 for our case with combined heating.

The present calculations have shown that the fraction of the additional heating power deposited on the bulk ions is close to 40% with combined heating in driven-burn operation.

Optimisation of the ICRF parameters to maximise the power to the bulk ions and selecting appropriate density and power waveforms can bring the path to ignition close to the line of 70% ion heating by 50MW of ICRF power. The power needed for the direct route is ~10% higher than for the KWG-type path but a large swing in T_{eo} at low n_{eo} is avoided.

REFERENCES

[1] ITER Detailed Design Review; Physics Basis and Performance Assessment, Nov. 1996.

[2] L-G Eriksson, T Hellsten and U Willen, Nuclear Fusion 33 (1993) 1037.

[3] J Kinsey, to be published in Nuclear Fusion

Plasma viewing in JET using endoscopes and a detailed design for ITER

J P Coad, J Lingertat, *J-B Migozzi, P E Stott, **C I Walker and C H Wilson
JET Joint Undertaking, Abingdon, Oxon OX14 3EA, UK
*JBM Optique, F-91140 Villebon-sur-Yvette, France
**ITER Joint Work Site, D-85748 Garching, Germany

1. The new endoscope viewing system on JET

Video cameras were fitted to the JET tokamak in 1994 to provide detailed views of the newly-installed divertor and a wide-angle view of the inside of the torus in real time. Immediate visual information on the position of the plasma within the vessel (and possible regions of interaction with the wall), and on the strike-point positions in the divertor proved extremely useful for the operations staff. However, there were two limitations to the viewing. Firstly, the wide-angle view was limited by the location of the camera, which was within one of the horizontal ports approximately 1.5 metres from the first-wall: a computer-generated image of the torus seen through the port from the camera is shown in Figure 1(a). Secondly, the views of the divertor were obtained from ports at the top of the machine, which allowed complete views of the floor of the divertor used during 1994/5 (Mk I). However, the 1996/7 (Mk II) and planned future divertors have a more closed aspect and strike points may be on the side walls, so a complete view is not possible from the top ports.

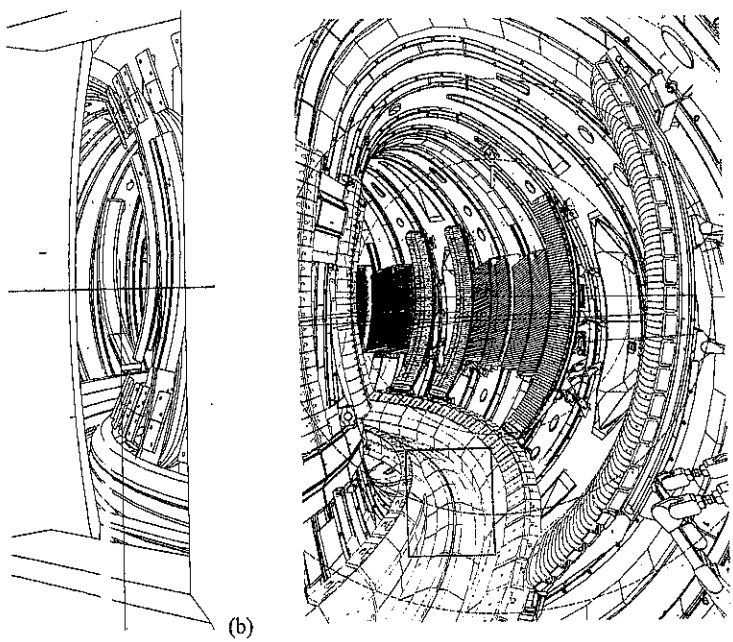

Figure 1 (a) CAD drawing of the wide-angle view of JET from 1994-6. (b) CAD drawing of the view obtained with the endoscope installed in June 1996.

The ideal position from which to obtain both wide-angle and divertor views is just inside the vessel near the outer midplane, however cameras cannot be placed at such points. Instead a re-entrant tube has been fitted to a flange which projects beyond the vessel support structure: the tube ends in a sapphire window at the ideal viewing point. An optical relay (endoscope) system has been constructed to allow cameras mounted outside this flange to view through the window. The window is in the shadow of an outer poloidal limiter which protects it from the plasma, and is covered by a shutter during vessel conditioning treatments such as glow discharge cleaning and Be evaporation. A sketch of the endoscope is shown in Figure 2.

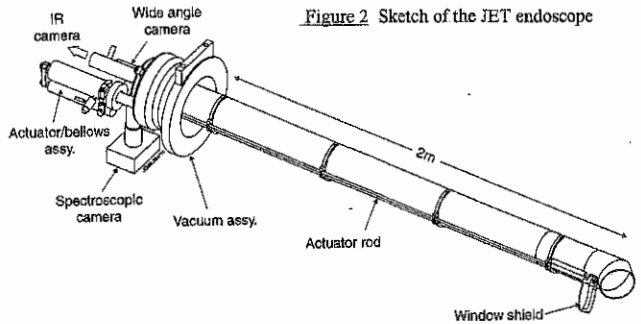

Figure 2 Sketch of the JET endoscope

The endoscope allows three different views into the torus; a wide-angle view and detailed views of the divertor in the visible and in the infra-red. Each of these views is accomplished via a separate set of relay lenses within the endoscope, and the assembly is water-cooled to maintain the mechanical stability required to give high resolution images. A computer-generated diagram of the wide-angle view is shown in Figure 1(b), and the improvement over the previous view (Figure 1(a)) is obvious: approximately one-third of the interior of the vessel is visible. The small rectangle towards the bottom of Figure 1(b) shows the field of view of the camera viewing the divertor in the visible range: this camera is fitted with a filter so that light of one specific wavelength is recorded (currently the CII line at 658 nm). The field of view in the infra-red is split into two halves, one giving a close-up of the inner half of the divertor floor, and one of the outer half, but at the present time the infrared camera is still viewing from the top of the torus whilst an improved image processing package is developed.

A colour wide-angle view and a close-up of the divertor in CII light are recorded for every pulse. From the wide-angle view one can

- verify plasma equilibrium and identify major hot-spots
- study qualitatively the location of ELM interactions outside the divertor
- monitor UFOs and look for first wall component failures
- detect high levels of visible bremstrahlung emission from the core associated with high performance discharges (e.g. optimised shear regime)
- diagnose density limits due to MARFE formation and disruptions

A typical frame from the divertor-viewing camera is shown in Figure 3. The strike points are clearly visible, and radiation can also be seen from the inner diveror leg extending to the X-point. The divertor view is used to study the positions of the strike points, the occurrence of detachment and ELM activity in the divertor.

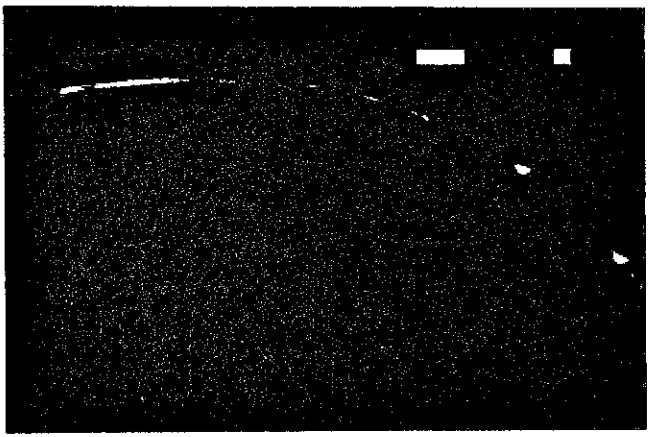

Figure 3
View of the divertor recorded in CII light during a JET pulse

2. A design of an endoscope system for ITER

The views provided by the endoscope system are invaluable for the team operating the JET tokamak, and it is equally important that there should be a real-time view of the plasma in ITER. However, the present JET endoscope is based solely on refractive optics, and the lenses would not survive for long in the high neutron (and γ-ray) fluxes close to the first-wall of ITER. An outline design for a system to view the interior of ITER from the outer midplane has been produced which uses reflective optics near the first-wall, changing to refractive optics at some distance into the shielding.

The design uses a concave aspheric mirror as the first element (Figure 4), and a catadioptric telescope (Figure 5) to produce a planar image to relay via conventional diffractive optics to the cameras which are located behind the shielding wall. A high resolution wide-angle view inside the vessel can be obtained for the assessment of the plasma, and the same optics can be used to examine closely any parts of the first-wall that appear to interact strongly with the plasma, and to view into the divertor. Figure 6(a) is a simulated image of the interior of ITER, and the approximately semi-circular lines show the view obtained at different included angles for the aspheric mirror. Figure 6(b) shows an expansion of the optimum angle for viewing the outer divertor leg, whilst the optimum view into the inner leg is shown in Figure 6(c).

Conclusions

A new endoscope system has been installed on JET which gives greatly improved wide-angle and divertor plasma viewing at high resolution. Similar real-time viewing of the ITER plasma may be possible using an aspheric mirror as the first optical component. The critical issues which control the resolution obtainable in ITER are the mechanical tolerances and stability that can be acheived on assembly and maintained long-term in the high radiation levels, and the thermal stability of the endoscope system. The next step is therefore to build a prototype system which is as close as feasible to the ITER configuration that can be tested in the laboratory and then installed on JET.

Figure 4 Concave aspheric mirror at the first-wall to provide a wide-angle view

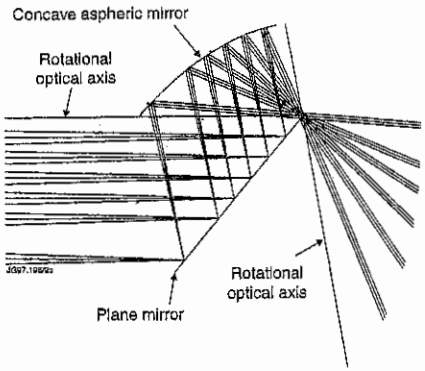

Figure 5 Catadioptric telescope stage to provide a suitable image for relaying

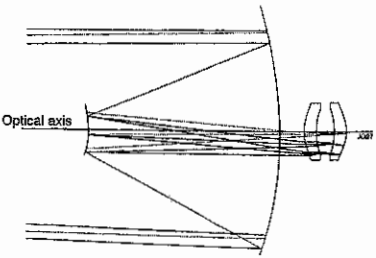

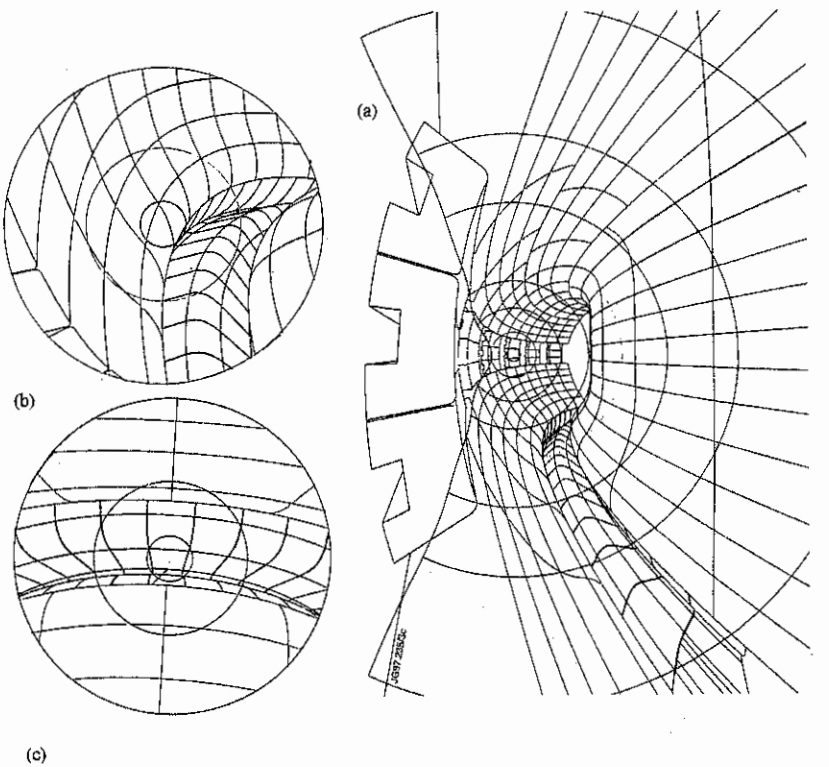

Figure 6 (a) Simulated wide-angle view inside the ITER vessel. (b) and (c) Views into the divertor.

Parallel electric resistivity in the Tore Supra Tokamak

R. Bregeon, V. Basiuk, E. Joffrin

Association Euratom-CEA, Département de Recherches sur la Fusion Controlée,
Centre d'Etudes de Cadarache
13108 Saint-Paul-lez-Durance, FRANCE.

1. Introduction.

The issue of determining precisely the parallel resisitivity in a tokamak discharge has recently become more crucial on devices equipped with a large number of current drive heatings such as Tore Supra [1]. The non-inductive current density profile determination is indeed essential for understanding current drive experiments and ultimately for implementing current profile control. The analysis of non-inductive current profiles generated by external (Lower Hybrid waves, Fast Wave Electron Heating, ...) or internal sources (i.e. bootstrap current) can be undertaken accurately only if the inductive current is predicted with a sufficient precision.

This paper focuses on the experimental validation of resisitivity analytic models using a complete data set of Tore Supra ohmic discharges. The first step is to validate for Tore Supra the analytical neoclassical corrections prescribed by Hirshman [2] and commonly used on present large devices [3, 4, 5]. However, this calculation is valid only in the limit of low collisionality ($\nu^* << 1$) for moderate inverse aspect ratio ($\varepsilon = a/R_0 < 0.3$). In a second step, the experimental conductivity profile is therefore compared to a more complete formula given in the original Hirshman theory [6] and to a more recent analytic formulation by Shaing [7] valid for arbitrary collisionality, aspect ratio and plasma β. Finally, the results of this analysis are discussed with regard to the neoclassical parallel transport theory.

2. Validity of the trapped particle corrections for the resistivity .

The question whether the Spitzer resistivity model alone or with trapped particle corrections [2] best describes the parallel electric field properties in a tokamak plasma has often been controversial. The trend given in the litterature is that the neoclassical corrections are necessary in large devices [3, 4, 5] to account for the measured ohmic current profiles. The validity of neoclassical conductivity on Tore Supra has been tested by computing the loop voltage for steady state ohmic discharges with the Spitzer and neoclassical conducvities σ by:

$$V(\text{calc}) = \frac{R.I_p}{\int_0^a \sigma.r.dr}$$

where Ip, a and R are the total current, the minor and major radii respectively.

The comparison with the measured loop voltage (fig 1) shows that the plasma resistivity is in fair agreement (within ±20%) with the prediction of neoclassical theory over a wide range of plasma parameters (Ip=0.4 to 1.7 MA; $\langle ne \rangle$=1.5 to 5.10^{19} m^{-3}; and B_T=1.3 to 4.0 T). This result underlines the importance of trapped particle corrections on Tore Supra like on other large devices such as DIII-D [3], JT-60 [4] or TFTR [5]. The lack of clear experimental observations of the trapped particle effect to the electrical conductivity in small tokamaks may be due to their larger aspect ratio (R/a) and to their higher collisionality.

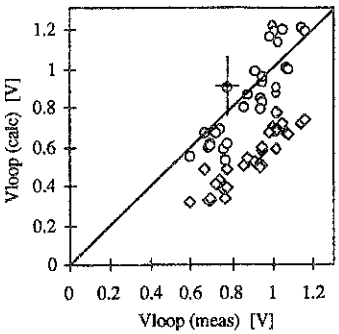

Fig 1: Comparison between the measured and the calculated loop voltage for neoclassical (circles) and Spitzer (squares) resistivities.

3. Comparison of the predicted and experimental conductivity profiles.

Even though the neoclassical conductivity is validated in section 2 using integrated quantites, a validation of the conductivity requires a systematic comparison of the predicted and experimental profiles at each radius.

The method for calculating the experimental conductivity profile is based on the determination of the ohmic parallel electric field profile E// deduced from the time derivative of the poloidal flux computed by a time sequence of equilibria reconstructions [8] from the IDENT-D code. These reconstructions are constrained by poloidal flux measurements from the magnetic and polarimetric diagnostics and by kinetic pressure measurements from Thomson scattering, interferometry and the line average $\overline{Z_{eff}}$ from the visible Bremsstrahlung diagnostic. The experimental resistivity is then determined by:

$$\sigma^{//}_{exp}(\rho) = \frac{\langle E.B \rangle}{\langle J.B \rangle}$$

where $\langle\ \rangle$ denotes the flux surface average operator and ρ the toroidal flux coordinate. The uncertainty in σ_{exp} arises mainly from the equilibrium reconstruction. Typical error bars on $\langle J.B \rangle$ (15%) and on $\langle E.B \rangle$ (10%) [9] lead to an uncertainty of about 25% on the experimental determination of the parallel conductivity.

The experimental conductivity profile is compared with three analytical formulations of the parallel conductivity. The first is the analytic expression from Hirshman-Hawyluk-Birge [2] used in the preceeding section. It uses one specy (the electron) and precise the dependance with the effective charge Z for all regimes of collisionality. However, except in the banana regime, it is restricted to small inverse aspect ratios and therefore to low collisionality. The second formulation is computed from the Hirshman and Sigmar theory [6]. This theory can accommodate to any number of species and give an expression of the viscous coefficients for each regime of collisionality. Then, it presents a prescription for the viscosity coefficients that is continuously valid throughout the three collisionality regimes. However, this expression is still restricted to low inverse aspect ratios and poloidal β. In the third analytic expression Shaing [7], the plasma viscosity coefficients are given for all regimes of

collisionality and can accommodate to any number of species, plasma shape and aspect ratio or poloidal β. It uses a Fourier harmonics expansion of the R and Z coordinates to express the magnetic field components for non axisymmetric plasmas. This model is otherwise still restricted to low poloidal rotation velocity (no orbit squeezing) and thin banana orbits compared to the gradient scale length. All three analytical formula use the full integral expression for the trapped particle fraction [9].

The predicted conductivities are determined using the temperature profiles from Thomson scattering and the $\overline{Z_{eff}}$ from the visible Bremsstrahlung diagnostic. Both are consistent with the total pressure profile (from T_e, $Z_{eff} = \sum_{i \neq e} n_i . Z_i^2 / n_e$ and T_i) and the diamagnetic energy content used for the equilibrium reconstruction. In addition, to prevent any spurious effects related to the internal relaxations, the data are averaged over a large number of sawtooth periods (typically 20) over a time slice of at least one second.

The data base used in this analysis gathers two density scan in deuterium and helium of ohmic discharges with B_T=3.9T and two current plateau of 1.6MA. The comparison between the measured and the predicted conductivities is undertaken in the steady state phase at least 2 second after the beginning of the current plateau.

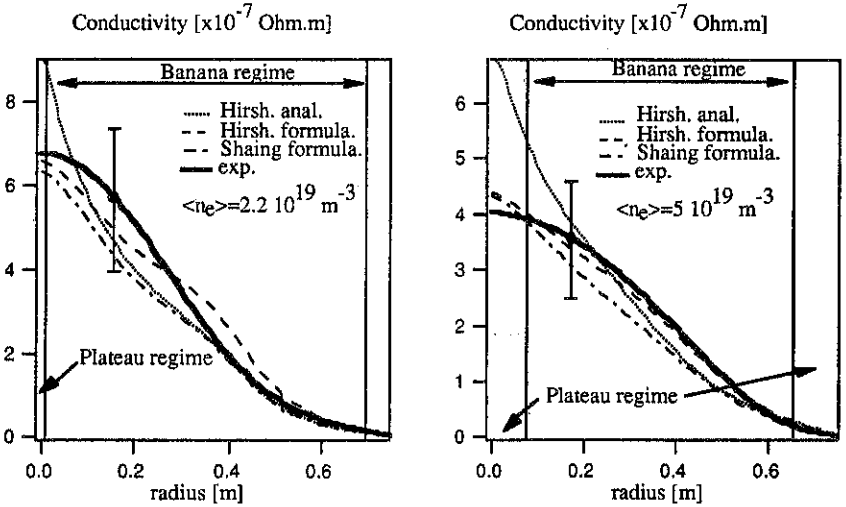

Fig 2a and 2b: Experimental conductivity profile (bold) compared with the three models described in the paper at low and high average density for two helium discharges. The analytical formula from Hirshman (dots) [2] does not match the experimental conductivity in the plateau regime (ν>1).*

Conductivity profiles are compared on figure 2a and 2b for two ohmic helium discharges at low and high density (<ne>=2.2.10^{19} and 5.10^{19} m-3) respectively and with an inverse aspect ratio of 0.33. Both measured and predicted conductivity have been computed with the same equilibrium data.

At low density (i.e. low collisionality) the simplified analytic conductivity of Hirshman is valid almost throughout the plasma. At higher density the electrons are becoming more collisional and this analytic conductivity model no longer holds. This is consistent with the fact that this model assumes low collisionality and is therefore restricted to the banana regime. On the other hands, both formulations from the Hirshman original model and Shaing correctly match the experimental conductivity profile within the error bars (of the order of ±25%) at any average density. Systematic diffrences are observed between these two models and the experimental conductivity. The two models under-estimate the experimental conductivity at mid-radius. These systematic discrepancies can be accounted for by the measurement of the Z_{eff} profile which is assumed constant and egal to the line integrated value $\overline{Z_{eff}}$ throughout the plasma radius. The same conclusions hold for deuterium discharges.

Systematic differences between the Shaing and Hirshman formula are also observed at mid-radius. In this region, the Shaing formula predicts smaller conductivity than the Hirshman formula. This could be explained by the low inverse aspect ratio approximation used in the Hirshman model for the calculation of the viscous coefficients whereas ε for the studied discharges is 0.33. However, more precise measurements of the current density profile are still required to distinguish experimentaly between these two models.

4. Conclusions

This systematic analysis of the conductivity shows that the analytical conductivity formula determined by Hirshman [2] cannot be used in general to predict the ohmic current profile in Tore Supra in particular in the center of the discharges. Due to the high inverse aspect ratio, high plasma β, and shape of the majority of today's devices, viscous coefficients must be predicted by more complete formula than those given in the Hirshman theory [6]. In addition, this study, together with other on the bootstrap current [8], supports that the generalized Ohm's law is valid along the field lines as predicted by the neoclassical transport theory.

References.

[1] X. Litaudon, E. Joffrin et al, to be published in Proceedings of the 12th Top. Conf. on Radio Frequency Power in Plasmas, Savannah, 1997.

[2] S. P. Hirshman, R.J Hawryluk and B. Birge, Nucl. Fus. 17 (3), 611 (1977).

[3] M. Kikuchi, ISPP-16 "Piero Caldirola", SIF, Bologna 1994.

[4] P. Politzer, Physics of Plasmas 1, p 1545, 1994.

[5] M.C. Zarnstorff, K. McGuire, et al, Phys. Fluid. B 2(8), 1852, (1990).

[6] S. P. Hirshman, Phys. Fluid. 21 (9), 3150 (1981).

[7] K.C. Shaing, M. Yokoyama, M. Wakatami, C.T. Hsu, Phys. Plasmas, Vol. 3, N°3, p 965, March 1996.

[8] E. Joffrin et al, 22th EPS Conference on Controlled Fusion and Plasma Physics, Bournemouth 1995, Vol 19C, Part IV, p 125- 129.

[9] Y.R. Lin-Liu and R.L. Miller, Phys. Plasma 2 (5), May 1995.

Pellet Fuelling Efficiency as a function of the Launching Location

B. Pégourié, L. Garzotti

Association EURATOM-CEA sur la Fusion Contrôlée,
C. E. Cadarache, 13108 Saint-Paul-lez-Durance, France

1 - Introduction

Pellet injection is promising for fuelling and density control. For this reason, it is planned to equip ITER with pellet injectors. However, with conventional technics, deep fuelling requires unrealistic velocities. Recently, a major break-through has been done in ASDEX-U by showing that the penetration increases by ≈1.6 (and the fuelling efficiency by ≈3) by launching the pellets from the High Field Side (HFS) [1]. This is because the ablatant, once ionized, drifts across the magnetic field (B) in the direction of the major radius (R). Indeed, due to the inhomogenous magnetic field, electrons and ions drift vertically in opposite directions. A charge separation results, thus a vertical electric field of the order of $C_s(t)^2 Bt/R$, where t is the time and C_s the ablatant sonic speed. The ablatant is then accelerated in the direction of the major radius, with an acceleration $C_s(t)^2/R$ [2]. The time available for incorporation to the background plasma is then $\approx \sqrt{2\lambda_p R}/< C_s >$ for pellets launched from the low field side (LFS) and $\approx \sqrt{2(2a-\lambda_p)R}/< C_s >$, where a is the discharge minor radius, for pellets launched from the HFS. The higher fuelling efficiency of HFS launched pellets is due to the longer time available for homogenization in this geometry.

2 - Calculation of the ablation profile and of the source of matter

To compute the source, one must account for: **1)** the existence of a poorly confined region at the plasma periphery. The particles deposited in this region have a high probability (the profile of which is $\pi(\rho)$, where ρ is the minor radius) to recycle on the wall. They are then re-injected with a profile $\eta(\rho)$ and a fuelling efficiency ε_{GP} equal to those of gas puff ($\varepsilon_{GP} = 5 \div 15\%$). Practically, we used a width $\Delta \approx 8$cm for $\pi(\rho)$ and the profile calculated by the recycling code [3] for $\eta(\rho)$. **2)** the outward displacement of the ablatant, which is estimated from the time τ_h required for incorporation to the plasma [4]. Indeed, the distance on which a plasmoid is spread is: $\Lambda \approx \tau_h^2 < C_s >^2 / 2R$, i.e. $\approx 10 \div 25$cm. The corresponding deposition profile $\gamma_\Lambda(R'-R)$ is deduced from the time history of the density increase of the plasma calculated in [4].

The instantaneous source of particles (in part./m) can then be written as: $S(\rho') = \int \delta\psi(\rho,\rho')d\rho$, where $\delta\psi(\rho,\rho') = \delta\psi_d + \delta\psi_r$ is the number of particles ablated at ρ and deposited at ρ' (see Figure 1). The number of particles deposited during the outward motion is $\delta\psi_d$. The part which has not been incorporated recycles on the wall. Its contribution to the source, which can be important, is $\delta\psi_r$. One has: $\delta\psi_d = \dot{N}_p[1-\pi(\rho)]\gamma_\Lambda(R'-R)/V_p$, where $\dot{N}_p$ is the ablation rate, and $\delta\psi_r = \{\dot{N}_p/V_p - \int \delta\psi_d d\rho)[1-\pi(\rho')]\eta(\rho')\,\varepsilon_{GP}$. The ablation rate is calculated with the NGPS ablation model

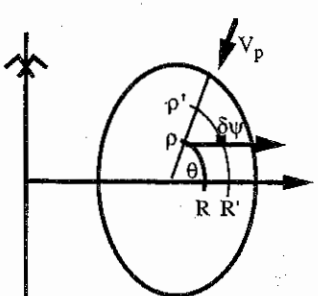

Figure 1: *Calculation of $\delta\psi$*

[5]: $\dot{N}_p = 4\pi n_s r_p^2 \dot{r}_{p_{NGPS}}$, where n_s is the density of solid deuterium and r_p and V_p the pellet radius and velocity. From the source profile $S(\rho')$, one has the pellet fuelling efficiency: $\varepsilon_P = 3\int S(\rho')d\rho' / 4\pi n_s r_p^3$.

When computing the ablation rate for pellets launched from the HFS, one must pay attention to the fact that the ablatant drifts in front of the pellet and cools the plasma. The cooling is estimated from the ablatant motions (radial and poloidal, see [4]) and from the typical temperature gradient length around the sheet of ablated material $\approx \sqrt{\pi \chi_\perp \tau_h}$, where $\chi_\perp$ is the plasma transverse diffusivity. This modification of the plasma characteristics in front of the pellet is the main phenomenon responsible for the increase of the penetration in the case of pellets launched from the HFS.

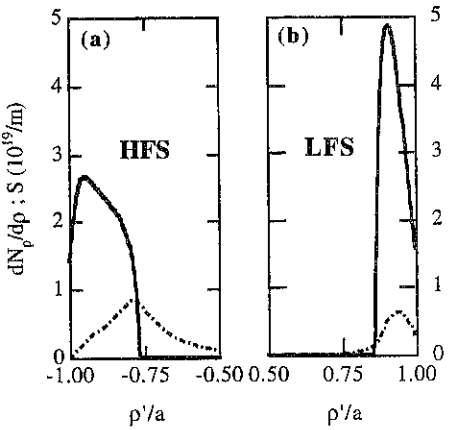

Figure 2: *Simulation of the ASDEX-U experiment: ablation rate (full line) and source of particles (dotted-dashed line).*
(a): *High Field Side;* **(b)**: *Low Field Side.*

3 - Comparison with experimental results

The simulation of the ASDEX–U experiment is displayed in Figure 2, where the ablation rate $\dot{N}_p/V_p$ and source S are plotted versus ρ'/a. The pellet and plasma parameters are: $r_p = 1\text{mm}$; $V_p = 130\text{m/s}$; $R_T = 1.65\text{m}$; a=0.5m.; elongation $\kappa = 1.7$; $n_e(0) = 10^{20}\text{m}^{-3}$ and $T_e(0) = 2.75\text{keV}$. For $\theta = 0$ (Fig.2b), the calculated penetration and fuelling efficiency are $\lambda_p = 7\text{cm}$ and $\varepsilon_P = 14\%$ (the measurements are $6 \div 9\text{cm}$ and $8 \div 18\%$, respectively). For the HFS (Fig.2a), one finds $\lambda_p = 12\text{cm}$ and $\varepsilon_P = 42\%$ (the measurements are $9 \div 14\text{cm}$ and $30 \div 55\%$). The cooling of the plasma is seen on the behaviour of $\dot{N}_p/V_p$ which is strongly lowered for $|\rho'/a| \leq 0.90$. The drift is also responsible for the deeper source location: the effective deposition depth, $<\lambda_p>$, is ≈13cm for the HFS (one has $<\lambda_p> \approx \lambda_p$), when it is only ≈4cm for the LFS ($<\lambda_p> \approx \lambda_p / 2$).

The importance of the plasma cooling and of the poloidal location of the launching point - θ - can be appreciated in Figure 3 where λ_p, $<\lambda_p>$ and ε_P are plotted versus θ. The vertical bars at $\theta \approx 0$ and $\theta \approx \pi$ are the ASDEX–U measurements [1]. In Fig.3a, the comparison of penetrations with and without plasma cooling - λ_p and $\lambda_{p;nc}$, respectively - shows that, for $\theta \approx \pi$, λ_p is almost twice what it would be in the absence of cooling ($\lambda_p/\lambda_{p;nc} \approx 2$). This effect depends on the ratio of the pellet and plasma contents and decreases with decreasing r_p. The effective deposition depth - $<\lambda_p>$ - increases smoothly with θ. As long as the penetration remains small ($\lambda_p \leq \Lambda$), the drift is efficient enough for $<\lambda_p>$ to be larger than λ_p. This effect depends on Λ/λ_p and decreases with increasing λ_p. The fuelling efficiencies with and without plasma cooling - ε_P and $\varepsilon_{P;nc}$ - are plotted versus θ

in Fig.3b. Here also, the plasma cooling plays a major role since one has $\varepsilon_P(\pi)/\varepsilon_P(0) \approx 3$ and $\varepsilon_{P;nc}(\pi)/\varepsilon_P(0) \approx 2$.

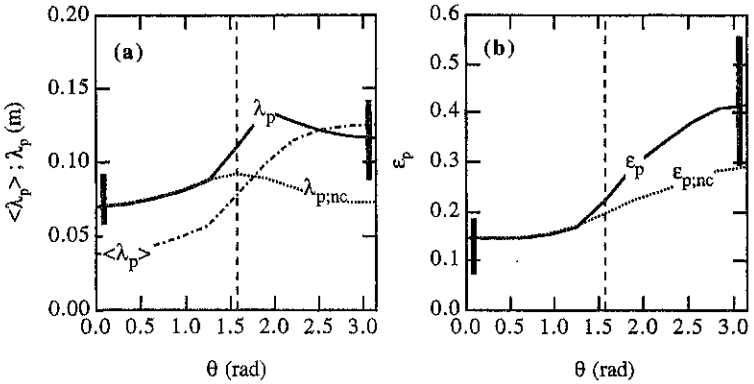

Figure 3: *Performances vs. location of the launching point for the ASDEX-U parameters.* (**a**): *penetration and source effective depth;* (**b**): *fuelling efficiency.*

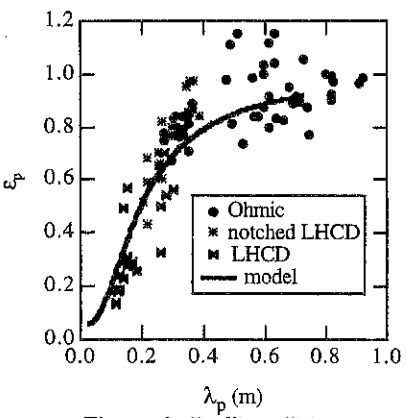

Figure 4: *Fuelling efficiency vs. penetration depth for Tore Supra.*

The drift is also responsible for the increase of ε_P with λ_p in the case of pellets launched from the LFS. This effect is well documented in ref.[6]. In Figure 4, ε_P is displayed versus λ_p for the Tore Supra database. The full line is the model prediction. It is found that ε_P depends essentially on λ_p and, to a lesser extent, on the peaking factors of the density and temperature profiles.

4 - Application to a reactor grade device

The influence of the drift on the fuelling of a reactor has been studied by running the model with parameters close to those planned for ITER. They are: $r_p = 4\text{mm}$; $V_p = 1.5\text{km/s}$; $R_T = 8\text{m}$; a=3m.; $\kappa = 1.6$; $n_e(0) = 1.4 \times 10^{20}\,\text{m}^{-3}$ and $T_e(0) = 22\text{keV}$. The results are displayed in Figure 5. The increase of the performances when launching the pellets from the HFS is less pronounced than for ASDEX–U. This is due to the lower values of both the ratio of the pellet and plasma contents and Λ/λ_p, which are ≈0.06 and $0.07 \div 0.10$ for ITER, and ≈0.15 and $0.15 \div 0.3$ for ASDEX–U. The benefit is nevertheless significant since, between $\theta \approx 0$ and $\theta = \pi$, λ_p and ε_P increase by ≈35%, and $<\lambda_p>$ by ≈2.5.

However, to launch a pellet from the HFS requires a strongly curved guide-tube and it is not sure that velocities in the range of 1km/s are allowed in such a geometry. Roughly, the innest location at which pellets can be launched at full velocity is $\theta \approx \pi/2$, for which one has $\varepsilon_P = 84\%$ and $<\lambda_p> = 20\text{cm}$. Advantage will be taken from launching pellets at $\theta = \pi$ only if these performances are improved. The required parameters are shown in Figure 6 where the

curves $\varepsilon_p = \varepsilon_p\left(1.5\text{km/s};\pi/2\right)$ and $<\lambda_p> = <\lambda_p>\left(1.5\text{km/s};\pi/2\right)$ are displayed in the $\{r_p \times V_p\}$ plane. As long as the plasma perturbation is kept at a constant level (i.e. for a given pellet radius), a minimum velocity of ≈800m/s is required to reach performances comparable to those obtained at $\theta \approx \pi/2$. To reach $\varepsilon_p \geq 90\%$ and $<\lambda_p> \approx 50\text{cm}$ would require, even at $V_p = 1.5\text{km/s}$, to increase r_p by 30% (i.e. to double the pellet mass, and thus the plasma perturbation). It must be noticed that, in this calculation, it has been introduced neither the influence of ELMs (which could increase Δ), nor the additionnal heating due to the presence of hot ions (ICRH or NBI, which could increase C_s).

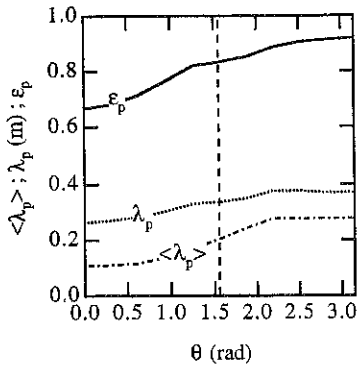

Figure 5: *Performances vs. location for reactor grade discharge.*

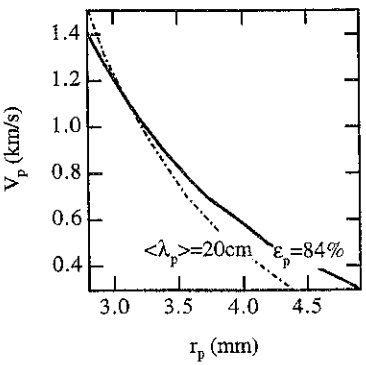

Figure 6: *Performances required for launching from the HFS.*

5 - Summary

A model has been built for the source due to pellet injection. The drift induced by the inhomogenous magnetic field is responsible for the differences in the fuelling efficiency and penetration between High Field Side and Low Field Side launched pellets. It explains also the behaviour of the fuelling efficiency with penetration for Low Field Side launched pellets. Main results are: **1)** The deeper penetration of High Field Side launched pellets is due to the cooling of the plasma by the ablated material. **2)** Due to the drift, the source of matter is shifted - in the direction of the tokamak major radius - by about 10 ÷ 25cm with respect to the H_α profile. **3)** When applied to reactor grade plasmas, one finds that fuelling efficiencies of ≈84% and effective deposition depths of ≈20cm can be obtained with pellets of radius 4mm (≈6% of the plasma content) and velocity 1.5km/s launched from the top of the plasma. To reach better performances with pellets launched from the High Field Side, a velocity of ≈800m/s is required.

References

[1] P.T. Lang *et al.*, IPP Report 1/304 (1996).
[2] L.L. Lengyel, NF **17** 805 (1977) ; V.A. Rozhanskii *et al.*, PPCF **37** 399 (1995).
[3] E. Tsitrone *et al.*, Proc. 22nd EPS Bournemouth, **Vol. 19C-IV** 301 (1995).
[4] B. Pégourié *et al.*, Phys. Plasmas **3** 4594 (1996).
[5] L. Garzotti *et al.*, to be published in NF (1997).
[6] A. Géraud *et al.*, Proc. 23rd EPS Kiev, **Vol. 20C-I** 460 (1996).

Nonlinear Evolution of Ballooning Modes in a Tokamak Plasma with Stochastic Field Lines

P. Beyer, X. Garbet, Ph. Ghendrih, M. Zabiégo
Association Euratom–CEA sur la Fusion,
CEA Cadarache, 13108 St–Paul–lez–Durance, France

Abstract: The results of three-dimensional numerical simulations of ballooning turbulence at the edge of a tokamak plasma are presented, for both L–H transitions and stochastization of magnetic field lines during ergodic divertor operations. The effects on turbulence levels and the structure of fluctuations are presented.

Introduction

In a tokamak plasma, anomalous transport and therefore confinement degradation can be attributed to turbulence generated by cross field pressure gradients. At the edge, the plasma is cold and therefore collisional, so that resistive ballooning instabilities are expected to be dominant. On Tore Supra, measurements of strong fluctuation levels at the plasma edge are compatible with such a picture of ballooning turbulence. Furthermore, full three-dimensional fluid simulations indicate that such fluctuations are driven by resistive ballooning modes [1]. On other machines, the turbulence level is often reduced commensurate with the generation of an edge transport barrier during a transition to an H–mode. At the transition, the self-generation of a sheared poloidal plasma rotation plays a crucial role in the suppression of fluctuations [2]. Recently, a comparable mechanism has been studied in the cylindrical approximation for ballooning turbulence [3].

In Tore Supra, a similar transport barrier can be generated by modification of the edge plasma with an "ergodic divertor" [4]. This divertor consists of magnetic coils whose principal effect on the topology of the magnetic field is the ergodization of field lines in a layer at the edge. This stochastic field creates two zones: a cold layer in contact with the wall with a low pressure gradient and an intermediate zone with a large gradient. The central pressure remains unchanged, in contrast to the H–mode where the central pressure is increased. An improved understanding of edge turbulence in the presence of stochastic field lines is expected to clarify the problem, if an H–mode is possible in this configuration. Turbulence measurements indicate that the fluctuation level can be actively controlled when running the ergodic divertor and that the wavenumber spectrum changes, i.e., large scale structures disappear [5]. In this paper, a model of the stabilization mechanism of these large convection cells is presented.

Model

The dissipative resistive MHD equations in the electrostatic approximation ($\partial\psi/\partial t \approx 0$) can be used to study resistive ballooning modes in a tokamak. These equations consist of

$$\eta j_\parallel = -\nabla_\parallel \phi - \frac{\partial \psi}{\partial t}\,, \qquad \text{(Ohm's law)}$$

$$\frac{d}{dt}(p_0 + p) = \kappa_\parallel \nabla_\parallel^2 (p_0 + p) + \kappa_\perp \nabla_\perp^2 p\,, \qquad \text{(pressure equation)}$$

$$m_i n_0 \frac{d}{dt}\nabla_\perp^2 \phi = B_0^2 \nabla_\parallel j_\parallel + 2\vec{B}_0 \cdot (\vec{g}_0 \times \nabla_\perp p) + \mu_\perp \nabla_\perp^4 \phi\,. \qquad \text{(vorticity equation)}$$

Here $d/dt = \partial/\partial t + \vec{v}\cdot\nabla_\perp$, where $\vec{v} = (\vec{B}_0 \times \nabla_\perp \phi)/B_0^2$ is the $\vec{E}\times\vec{B}$–flow, $\vec{B}_0 = B_\varphi[\hat{e}_\varphi + r/(Rq)\hat{e}_\vartheta] + \delta\vec{B}$ is the magnetic field in toroidal coordinates, and $\delta\vec{B}$ is the perturbation due to the ergodic divertor. The parallel operator is $\nabla_\parallel = \vec{B}_0/B_0 \cdot \nabla$, and the parallel current is $j_\parallel = \nabla_\perp^2 \psi/\mu_0$. The combination of the equilibrium pressure gradient ∇p_0 and the toroidal curvature of the field lines $\vec{g}_0$ drives the instability on the low field side.

Slab coordinates are introduced and a Fourier–mode representation is applied in the poloidal (m) and toroidal (n) directions. Since each mode $(p,\phi)_{mn}(r,t)$ is localized at a resonant surface $q(r) = m/n$, and the influence of the ergodic divertor is mainly at the $q = 3$ surface (decreases rapidly radially inwards), the simulation region can be restricted to lying between the $q = 2$ and $q = 3$ surfaces. In the numerical code, finite differences are used in the radial direction and all fluctuations are extrapolated to zero at a width Δ outside this interval. Furthermore, only those modes which are resonant in this interval are considered, up to mode number $n = 30$. The magnetic field perturbation from the ergodic divertor has a wavenumber of $n = 6$, therefore only toroidal wavenumbers of $n = 0, 6, 12, 18, \ldots$ are included in the code. The effect of local flattening of the mean pressure gradient due to turbulence is suppressed in the simulations.

Ballooning Turbulence

The toroidal curvature of field lines cause harmonics (m, n) to couple linearly to their neighbours $(m \pm 1, n)$ and to form global modes which have a large radial extent. The growth rate (to lowest order) and the radial envelope (to first order) of such modes can be calculated analytically in the ballooning approximation. Because the toroidal curvature is unfavourable on the low field side of a torus, the mode amplitudes are much larger in this region relative to the high field side. As illustrated in Fig. 1, such poloidal asymmetry is preserved even in highly unstable situations, when the modes nonlinearly couple and saturate to a strongly fluctuating state.

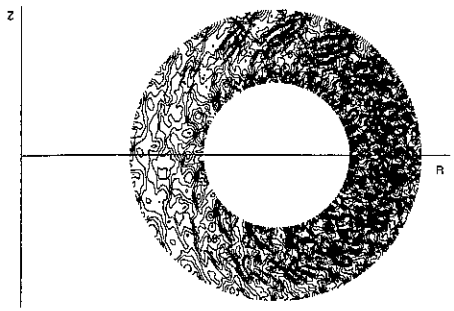

Fig. 1: Contour-plot of a snapshot of the plasma pressure in the poloidal plane $\varphi = 0$ for $r \in [r(q=2);\ r(q=3)]$.

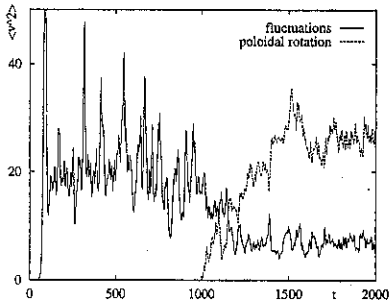

Fig. 2: Decrease of the turbulence level when allowing (from t=1000 on) the self-generated poloidal rotation to increase.

In the simulations shown in Fig. 1, two models of shear flow are considered: First, the growth of the ϕ_{00} component of the potential is explicitly suppressed, which then also eliminates the poloidal rotation $v_\theta = \partial\phi_{00}/\partial r$. Second, this same component is allowed to evolve, and the turbulence generates a sheared flow via a Reynolds stress. This second case leads to a significant reduction in the fluctuation level, as illustrated in Fig. 2, and is characteristic of an L–H transition.

Ergodic Divertor

Next the perturbation of the magnetic field due to the ergodic divertor is considered in the numerical simulations. Since $\delta B/B_0$ is small, the contribution to perpendicular terms can be neglected. However, the ergodic divertor has a strong influence on the topology of resonant surfaces which are characterized by vanishing $\nabla_\parallel$–terms. Therefore, the perturbation must be included in these terms. In order to test the additional contributions, the linear pressure equation with $\kappa_\parallel \gg \kappa_\perp$ is integrated and a steady-state, that represents the pressure distribution in the presence of the ergodic divertor, is sought. As expected, a flattening of the pressure gradient is observed at places where magnetic islands are formed. Finally, the full set of equations are used to simulate ballooning turbulence in the presence of stochastic field lines. First, as illustrated in Fig. 3, the level of fluctuations is significantly lower compared to the case without perturbing the magnetic field. Moreover the ballooning character of the fluctuation structures is preserved and the turbulence is "roughly" unchanged in the region between $q = 2$ and $q = 2.5$. Also, as illustrated in Fig. 4, the fluctuations are clearly reduced in the stochastic layer. Furthermore, Figs. 4 and 5 indicate that in the ergodic region, mainly the large scale structures are suppressed — a feature which is in agreement with turbulence measurements on Tore Supra.

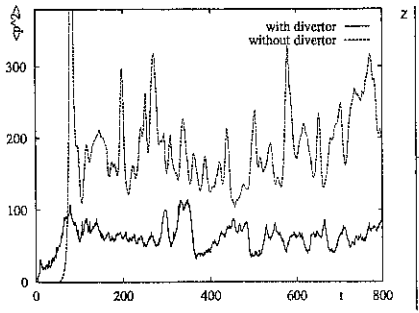

Fig. 3: The turbulence level with the ergodic divertor is decreased.

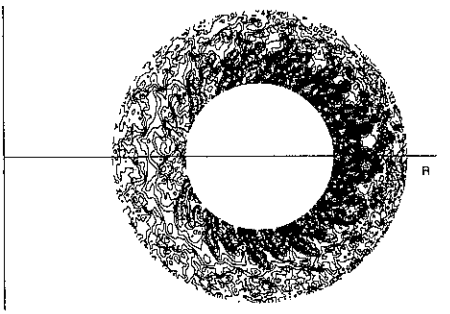

Fig. 4: Same as Fig. 1 but with the ergodic divertor turned on.

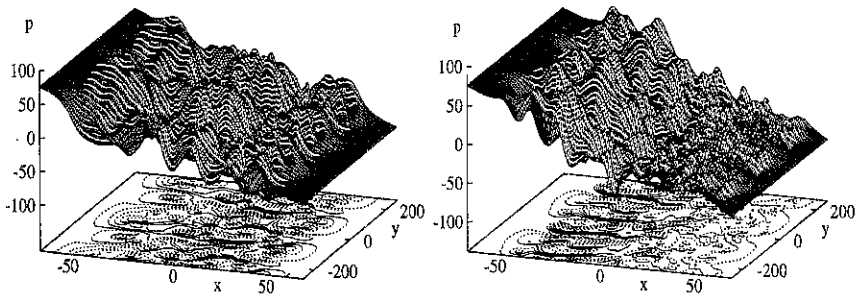

Fig. 5: Snapshot of plasma pressure without (left) and with ergodic divertor (right) in a sector $(x, y) \triangleq (r, \theta) \in ([r(q=2)-\Delta;\ r(q=3)+\Delta],\ [-\pi/6;\ \pi/6])$ *of the plane* $\varphi = 0$.

Conclusions

Three-dimensional numerical simulations of ballooning-turbulence show strong fluctuations at the plasma edge which are mainly located on the low field side. Basic experimental features that are in agreement with measurements on Tore Supra during ergodic divertor operations are reproduced, i.e., a decrease of the level of fluctuations and a suppression of large scale structures. Such simulations also have the potential to explain the dynamics of the L–H transition with a generation of shear flow. The possibility of an H-mode with the ergodic divertor is presently under investigation.

References:

[1] P. N. Guzdar et al., Phys. Fluids B **5**, 3712 (1993).

[2] H. Biglari, P. H. Diamond, and P. W. Terry, Phys. Fluids B **2**, 1 (1990).

[3] P. Beyer and K. H. Spatschek, Phys. Plasmas **3**, 995 (1996).

[4] P. Ghendrih, A. Grosman, H. Capes, Plasma Phys. Control. Fusion **38**, 1653 (1996).

[5] J. Payan et al., Nucl. Fusion **35**, 1357 (1995).

Plasma feedback control for stationary enhanced performance operation of Tore Supra

T. Wijnands[1] , G. Martin, D. van Houtte, P. Froissard, X. Litaudon

Association Euratom-CEA, CEA-Cadarache F 13108 Saint-Paul-lez-Durance, France

Feedback control of a non-inductive current drive source has been used to sustain specific current profiles in a Tokamak plasma which lead to high thermal electron energy confinement. In fully non-inductive driven regimes, pre-shaping of the current profile in combination with real time control of the launched RF wave spectrum is used. Improved confinement is observed in steady state discharges with high or vanishing central magnetic shear ($s_{center}>0$ or $s_{center}\approx 0$).

Plasma Feedback Control

There is a tendency in present day Tokamaks to vary plasma current, density and heating power in an attempt to control particular physics parameters related to the plasma performance and stability. In this field, feedback control of the current profile is of particular interest since a large number of experiments have demonstrated that current profile shaping leads to stable plasmas with improved energy confinement. However, most Tokamaks operate mainly with inductively driven current and transient techniques have to be used to change the current profile shape. The current profile modifications disappear with the current diffusion. Stationary modifications of the current profile can only be obtained with non-inductive current drive. Therefore, an important part of the physics programme of Tore Supra is devoted to the study of long pulses (> 30s) with stationary improved confinement using current profile control.

Lower Hybrid Current Drive

The Lower Hybrid system on Tore Supra (6MW, 3.7 GHz) is used for non inductive current drive. Partially, fully and overdriven non-inductive regimes are routinely produced when operating at standard toroidal field and reduced current and density (B_T = 3.8 T, Ip = 0.8-1 MA and n_e = 1.5-2 10^{19} m^{-3}).

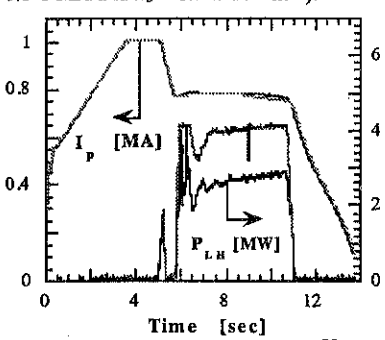

Fig 1 : Full current drive at I_p=0,8 MA. (V_l=0 from 5s) using 4MW of LHCD at $n_{//}^{peak}$ =2.1 and 3 MW at $n_{//}^{peak}$ =1.6 ($\bar{n}_e$=1.5x10^{19} m^{-3}).

The associated flux savings have recently allowed to extend the maximum pulse length on Tore Supra to more then 2 minutes [1]. In such long pulses, the effects of a change of the current profile can be studied on a time scale much longer then the current diffusion time. In particular, some plasma instabilities with a small growth rate are likely to be detected. An initial difficulty in achieving long pulses is the absence of a control over the amount of non-inductively driven current. At constant LH power, the loop voltage (V_l) varies as function of the current drive efficiency which depends on many plasma parameters. The total available flux is thus consumed at an uncontrolled pace and if the LH power is not fixed exactly at the

[1] *Present address : UKAEA Fusion, Culham Laboratory, Abingdon, OX14 3DB, U.K.*

right level, the discharge will terminate prematurely

This motivated the development of the new long pulse operating scenario in which V_l is feedback controlled by the main poloidal field power supply and the plasma current by the total LH power (figure 1) [2]. Successful long pulse steady state discharges (V_l =0 for 70 s at I_p = 0.8 MA and n_e =1.5x10^{19} m^{-3}) in an improved confinement mode have been achieved using this mode of operation.

Global improved confinement

In the presence of LH driven current, the current profile changes shape and the thermal electron energy confinement can increase up to 1.4-1.8 times the value predicted by the Rebut-Lallia-Watkins scaling law. Early work has shown that the improvement in confinement is strongly related to the modifications of the magnetic shear at mid radius [3].

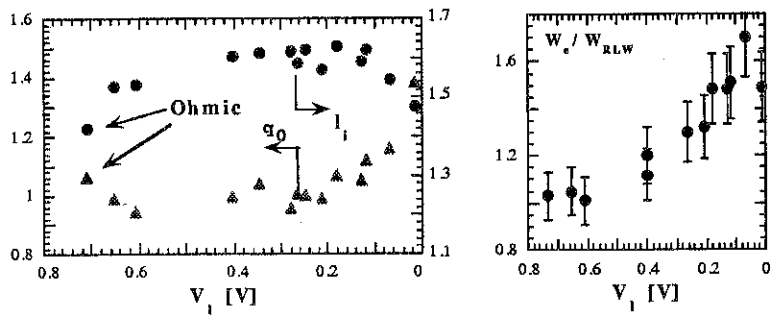

Fig 2 : Modification of the current profile and the thermal electron energy confinement as a function of the loop voltage during LHCD experiments. Individual shots, V_l cst..(0<P_{LH}<5 MW, $n_{//}^{peak}$=1.9, B_T=3.8 T, I_p=0.8-1 MA and $\bar{n}_e$=1.5-1.7x10^{19} m^{-3})

Figure 2 shows the evolution of the internal inductance (V_l) and the central value of the safety factor (q_0) as a function of the loop voltage when LH power (0-5 MW) is coupled to an Ohmic target plasma (B_T = 3.8 T, I_p = 0.8-1 MA and n_e = 1.5-1.7x10^{19} m^{-3}). Each point represents one shot in a stationary state.

At low power (1-2 MW) loop voltage V_l falls from 0.8 to 0.2 Volt but no significant change in l_i or q_0 is observed. The current profile remains nearly identical to that of an Ohmic equilibrium and the strong residual electrical field is constraining its shape (figure 2, left). As a consequence, when V_l >0.2, there is no significant variation of the central magnetic shear and the thermal electron energy contents remains close to the prediction given by the RLW scaling (figure 2, right).

At higher LH power (3-5 MW), $V_l \rightarrow 0$ and the previously mentioned resistive and inductive effects gradually disappear. The amount of non-inductive driven current becomes significant and the shape of the current profile is increasingly dominated by the LH power deposition profile. In this regime, the central value of the safety factor q_0 and the magnetic shear at mid radius increase and the electron energy confinement is improving with the total LH power (figure 2, right).

In fully driven regimes (V_l = 0) a wide range of different current density profiles can be obtained. The current profile is now entirely determined by the domain in which the LH waves can propagate. At constant current and density, the boundary of the domain accessible to the LH waves varies as a function of $n_{//}^{peak}$ and the shape of the current profile.

In steady state, an increase of the LH power does not necessarily improve the confinement any further. On the contrary, it can make the plasma MHD unstable. A statistical analyses of a large number of discharges showed that either high or vanishing central magnetic shear ($s_{center} > 0$ or $s_{center} \approx 0$) is correlated to an increase of the electron energy confinement up to values 1.6-1.8 times above the RLW prediction [4]. High central shear discharges have $l_i > 1.5$ and $1.1 < q_0 < 1.4$. The low central shear is obtained in discharges with $l_i < 1.5$ and $q_0 > 1.5$.

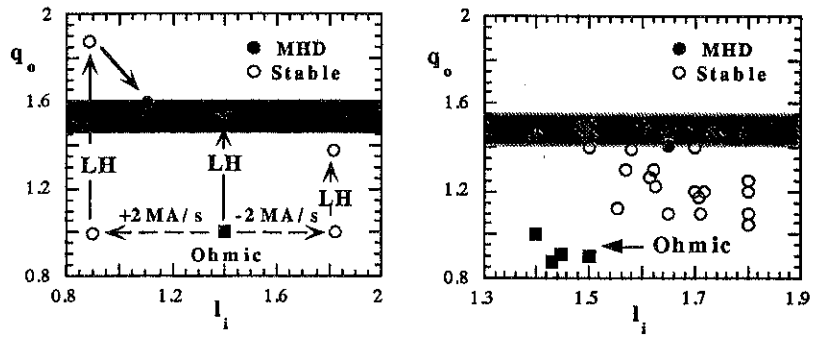

Fig 3 : (left) Time traces in (l_i, q_o)-space of the start-up phase of steady state discharges (V_l=0). (right) l_i and q_o of various shots (Ohmic and LHCD at V_l=0). Open circles : stable long pulses (>30 s) closed circles : (l_i, q_o) of shots just before MHD activity is observed.

Feedback control of the current profile

The influence of the current profile shape on the plasma stability and confinement in steady state discharges has been studied in a new and efficient manner by extending the previously mentioned long pulse operating scenario with a feedback control of l_i. LH power and the feedback control of V_l=0. In other words, the shape of the current profile in a fully driven discharge depends on the initial conditions. During the pulse, the current profile can be controlled by injecting the LH power at different values of $n_{//}^{peak}$.

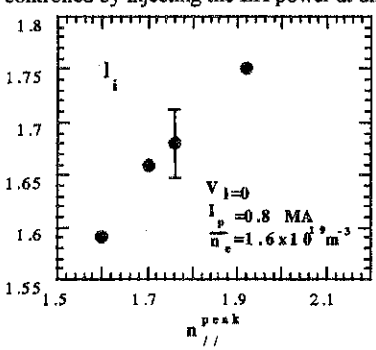

Fig 4 : Variation of l_i as a function of $n_{//}^{peak}$ in steady state when applying LHCD just after a current ramp down (high l_i).

Under the previously mentioned experimental conditions (B_T = 3.8 T, I_p = 0.8-1 MA and n_e = 1.5-1.7x10^{19} m^{-3}). LH power at various $n_{//}^{peak}$ has been applied to hollow current profiles (after a current ramp up, $l_i << 1$), to peaked current profiles (after a current ramp down, $l_i >> 1.8$) and to stationary ohmic equilibrium (no current ramp, $l_i \approx 1.4$) (broken lines, figures 3, left). For each target profile, the LH waves initially tend to drive current off-axis and in the startup phase q_0 increases at constant l_i. (solid lines, figure 3, left).

When any toroidal electric field has disappeared, only plasmas with high l_i and high central shear have been sustained on timescales much longer then the current diffusion time (figure 3, right).

The current profiles with low l_i and low central magnetic shear are likely to develop (m,n)=(2,1) dominated MHD mode activity when the current is diffusing.

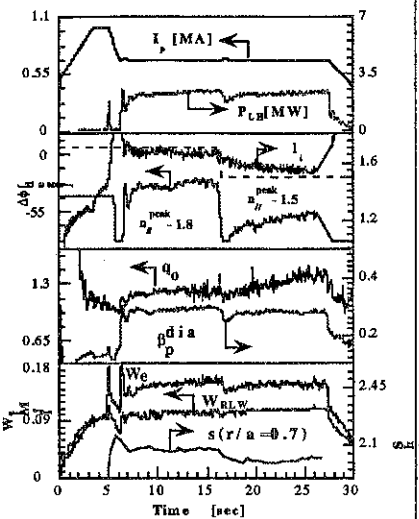

Fig 5 : Feedback control of l_i with $n_{//}^{peak}$ in steady state (V_l and plasma current feedback controlled).

For the steady state plasmas with high l_i, a significant influence of the $n_{//}^{peak}$ on the global shape of the current profile is observed. Figure 4 shows the result on l_i when power is injected at different values of $n_{//}^{peak}$. For this particular regime, this was obtained by a feedback control of l_i by adapating $n_{//}^{peak}$ during the pulse [5].

Figure 5 shows a steady state discharge with feedback control of V_l, I_P and l_i. In this example, l_i is required to change at 16 seconds from 1.7 to 1.5. At this instant, the feedback loop on $n_{//}^{peak}$ temporarily saturates but then the flattening of the current profile is clearly observed on both l_i and q_0. Due to the previously mentioned MHD instability, the range of current profile shapes that can be achieved with this operating scenario is limited. In particular, it is difficult to obtain significant modifications of the magnetic shear at mid radius. In the case of figure 5, a minor variation in the thermal electron energy contents is observed during the variation of the current profile.

Stability of steady state discharges

In figure 3 (right), it is tempting to define a stability criterion for steady state discharges in terms of global profile parameters like q_0 and l_i. Just before the onset of strong MHD activity, the discharges are situated in a narrow zone with q_0 between 1.4 and 1.5. The trapped particle instability and the associated turbulence is a possible candidate for explaining the observed phenomenon [6]. The growth rate of this instability is reduced when the magnetic shear is either high (s_{center}>3) or very low ($s_{center} \approx 0$). But when the radial excursion of the particles is large enough, the shear of the plasma rotation can play a stabilising role when the particles encounter a change in velocity of the order of the growth rate of the plasma instability.

Conclusion

New plasma feedback control scenarios on Tore Supra combine poloidal field and non-inductive current drive power and allow for studying the correlation between the current profile, the plasma stability and the thermal electron energy confinement. Preliminary experiments with feedback control of l_i in fully non-inductive regimes show enhanced performance when the magnetic shear.

[1] Equipe Tore Supa *(presented by B. Saoutic)*., IAEA Montreal, 1997, IAEA-CN-04/02-2.
[2] Wijnands, T. *et al.*, Nuclear Fusion 36, No. 9 (1996) 1201
[3] Hoang, G.T. *et al.*, 23rd EPS Conference 24-28 June 1996, Kiev, Part I p 24.
[4] Equipe Tore Supra *(presented by X. Litaudon)*, Pl. Ph. and Contr. Fusion, No.12 A (1996) A 256
[5] Wijnands, T. *et al.*, Nuclear Fusion 37, No.13 (1997)
[6] Maget, P. *et al.*, this conference.

Contribution of electrostatic fluctuations to heat transport during L mode additional heating in Tore Supra

P. Devynck, X. Garbet, C. Laviron, C. Fenzi

Centre d'études de Cadarache, Association Euratom-CEA sur la fusion

F-13108 Saint Paul-lez-Durance, France

ABSTRACT

In this paper, experimental results on density fluctuations obtained in Tore Supra in L mode with ICRH additional heating are used to estimate the contribution of electrostatic fluctuations to the total heat flux in the plasma bulk. The low wavenumber density fluctuations are measured with an homodyne reflectometer at several distinct radii and the evolution of the k_θ spectrum between 5 and 15 cm^{-1} of density fluctuations is obtained with a CO2 laser scattering diagnostic. We then make predictions on the generic parametric dependencies of the turbulent thermal flux which is dominant in the plasma bulk. We finally incorporate the results of the density fluctuation measurements in the calculation of the heat flux ratios and compare them to experimental values. It is found that the ratios of heat fluxes associated to electrostatic fluctuations are compatible with most of the experimental heat flux ratios in the plasma core ($0.4<r/a<0.6$). This property does not seem to hold at the edge of the plasma ($r/a=0.7$). The calculated level of density fluctuation necessary to account for the heat transport at mid radius is also found to be compatible with values measured in other tokamaks.

DISCUSSION

In the plasma bulk, the heat flux carried by electrostatic fluctuations can be written for each species (e=electrons, i=ions) as:

$$Q_{es,s} = \frac{3}{2}\frac{T_s}{B}\langle \delta n_s \delta E_\theta \rangle + \frac{3}{2}\frac{n_s}{B}\langle \delta T_s \, \delta E_\theta \rangle \qquad s=e,i \qquad (1)$$

Where δE_θ is the fluctuating poloidal electric field. The first term in the rhs of Eq.(1) is the heat flux associated to the particle flux. In absence of core particle source, this term vanishes. This is the case in Tore Supra where no particles are deposited by the additional heatings in the plasma core (electromagnetic waves). We will evaluate here only the second term of Eq.(1) which is the contribution of electrostatic fluctuations to the conductive heat transport in the plasma bulk. By writing the fluctuation terms in the Fourier space, we get

$$Q_{es} = Q_{es,e} + Q_{es,i} = \frac{3}{2} n_e \frac{T_e^2}{eB} \bar{k}_\theta \left(\frac{\delta n_e}{n_e} \right)^2 C \qquad (2)$$

where

$$\frac{\bar{k}_{\theta,f}}{\bar{k}_{\theta,oh}} = \left(\frac{T_{e,oh}}{T_{e,f}}\right)^{1/2}$$ and expression (3) becomes

$$R = \frac{T_{e,f}^{1.5}}{T_{e,oh}^{1.5}} \frac{C_f}{C_{oh}} \frac{\delta n_{e,f}^2}{\delta n_{e,oh}^2} \qquad (4)$$

Expression 4 only depends on the form factor and on the density fluctuation level. To calculate the parametric changes of the form factor, we suppose that the heat is advected by electrostatic eddies. A fluid equation for the temperature has been solved with the following hypotheses: The radial electric field is proportional to the ion density gradient (banana plateau regime), the mean frequency of the fluctuation spectrum is proportional to the density diamagnetic frequency. The latter hypothesis implies that the fluctuations are of drift wave type, but allows any type of drift wave. The hypotheses above lead to:

$$C\alpha \frac{L_n}{L_{Te}}[f_1(\delta_e) + \frac{n_i}{n_e}\frac{\tau}{Z} f_2(\delta_i)].$$

where δ_e and δ_i are respectively the electron and ion collision widths, $\tau = T_i/T_e$ and Z is the charge number. The functions $f_1(\delta_e)$ and $f_2(\delta_i)$ contain the information about the phase angle between $\delta T_e, \delta T_i$ and $\delta\phi$. If we evaluate the term in front of $f_2(\delta_i)$ for the selected series of shots, we obtain a mean Z= 1.8, $n_i/n_e \approx 0.5$, so that $\frac{n_i}{n_e}\frac{\tau}{Z} \approx 0.28\,\tau$. In these discharges, $\tau<1$ and the ion contribution to the transport is small. We then suppose that the phase angles are weakly modified during additional heating (weak dependence on collision), so that the ratio of form factors in expression (4) can be written as:

$$C_f/C_{oh} = L_{Te_{oh}}/L_{Te_f}\ L_{n_f}/L_{n_{oh}}$$

If we input this dependency in expression (4), we get at constant density:

$$R = \frac{\sqrt{T_{e,f}}}{\sqrt{T_{e,oh}}} \frac{\nabla T_{e,f}}{\nabla T_{e,oh}} \frac{\delta n_{e,f}^2}{\delta n_{e,oh}^2} \qquad (5)$$

This ratio has been estimated for three radii (r/a=0.4, 0.55 and 0.7) during the ICRH additional heating and is represented in figure 2 as a function of P_{tot} (ICRH)/ P_{tot} (OH). It can be shown that the ratio of total plasma powers is equivalent to the ratio of local heat fluxes (ion +electrons) as long as the radius considered for the estimation of expression (5) is outside the region where the additional heating power is deposited (for ICRH waves, the power is deposited inside r/a<0.3). Figure 2 shows that within this simple quasi linear approach , the changes of density fluctuations level are consistent with the experimental heat flux changes at r/a=0.4 and r/a=0.55. At r/a=0.7 these ratios are not sufficient to account for the experimental heat flux ratios unless there is a large change in the phase angles.

$$\bar{k}_\theta = \frac{\sum_{k,\omega} k_\theta \left|\frac{\delta n_{k\omega}}{n_e}\right|^2}{\sum_{k,\omega} \left|\frac{\delta n_{k\omega}}{n_e}\right|^2}$$ is an average poloidal wave number, $C = \sum_{s=e,i} C_s \frac{n_s}{n_e}$, the sum of the ion and electron contributions where

$$C_s = \frac{\sum_{k,\omega} \frac{\delta T^*_{s,k\omega}}{T_e}(-ik_\theta)\frac{e\delta\phi_{k\omega}}{T_e}}{\sum_{k,\omega} k_\theta \left|\frac{\delta n_{k\omega}}{n_e}\right|^2}$$

is a form factor which contains information about phase angle difference as well as absolute values of $\delta T_{e,i}/T_e$ and $e\delta\phi/T_e$.

$$\left(\frac{\delta n_e}{n_e}\right)^2 = \sum_{k,\omega}\left|\frac{\delta n_{k\omega}}{n_e}\right|^2$$

is the level of density fluctuations squared. It is obtained by taking the fluctuation data from the reflectometer, which measures the density fluctuation level integrated over the wavenumbers with a ponderation on low values of k_r.

Equation 2 shows that the heat flux carried by electrostatic fluctuations is a function of the square of the density fluctuation level, of the mean value of the k spectrum and of the phase between potential and temperature fluctuations. We propose here to evaluate the relative change of ICRH to ohmic electrostatic heat fluxes at constant density, i.e.

$$R = \frac{Q_{ES,f}}{Q_{ES,oh}} = \frac{T^2_{e,f}}{T^2_{e,oh}} \frac{\bar{k}_{\theta,f}}{\bar{k}_{\theta,oh}} \frac{C_f}{C_{oh}} \frac{\delta n^2_{e,f}}{\delta n^2_{e,oh}} \qquad (3)$$

where (f) stands for the ICRH case and (oh) for the ohmic one.

First, we take into account the k spectrum shift monitored by the CO_2 laser scattering diagnostic during the additional heating phase. The shift of the k spectrum towards low k values observed in figure 1 can only be attributed to the change of the electron and ion temperature , it does indicate that a relationship of the type $k_\theta \rho_s$=cst (ρ_s is the ion Larmor radius where the ion temperature is replaced by the electron one) often predicted for drift waves may indeed apply for the bulk density fluctuations. In that case

It can also be shown that relation (2) requires a reasonable level of density fluctuations to account for the heat flux in the plasma core. From relation (2), we can deduce:

$$\chi_e = \frac{3}{2}\frac{Te}{eB}\ \overline{k\theta}\ L_{T_e}\left(\frac{\delta n}{n}\right)^2 C$$

Using the same plasma conditions as above, at mid-radius, $\chi_e \approx 1.5\ m^2/s$, Te≈3keV, B≈3.78 T, LTe≈0.25 m, $k_\theta \approx 200 m^{-1}$, and C≈1 give $\delta n/n \approx 5\ 10^{-3}$. Such a value is in the range of values measured in a tokamak like TFTR in L mode [1]. So electrostatic fluctuations have also the correct order of magnitude to account for the bulk heat flux.

[1] Paul S F , Bretz N , Durst R D , Fonck R J , Kim Y J , Mazzucato E , Nazikian R 1992 Phys Fluids B **4** (9) 2922

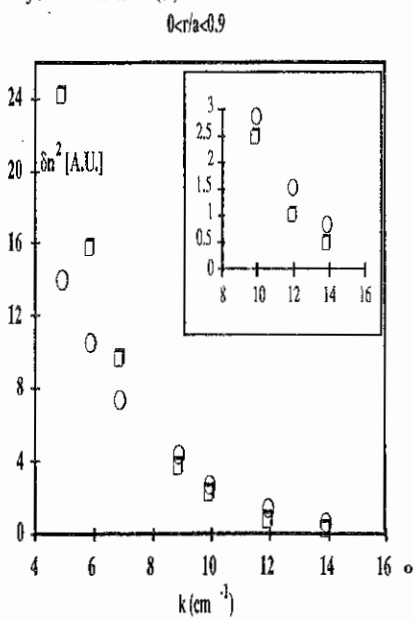

Fig. 1

Plot of the kθ power spectrum measured by the CO2 laser scattering diagnostic. Comparison between ohmic case (circles) and 2.8 MW ICRH phase (squares). The graph is enlarged for the three hihgest kθ values.

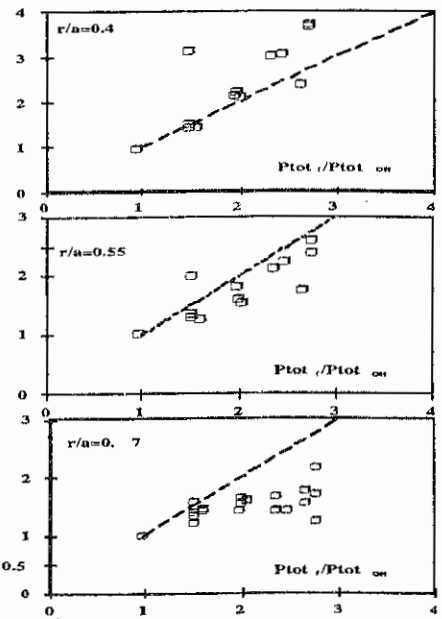

Fig. 2

Increase of the estimated heat flux relative to the ohmic level, carried by electrostatic fluctuations at r/a=0.4 (top), 0.55 (centre), 0.7 (bottom) as a function of total plasma powers normalised to ohmic level, during ICRH phase. The dashed line corresponds to the situation where all the heat flux is transported by electrostatic fluctuations.

Dimensional Analysis of Transport and Turbulence in Tore Supra

Zou X.L., Clairet F., Devynck P., Fenzi C., Garbet X., Laviron C,
Leclert G.*, Misguich J., Moreau P., Paume M., Seak T.F., Voitsekhovitch I.

Association Euratom-CEA sur la fusion contrôlée, C.E.Cadarache,
13108 Saint Paul lez Durance France
* Laboratoire de Physique des Milieux Ionisés, URA CNRS 835,
Université Henri Poincaré, Nancy I, BP 239, 54506 Vandœuvre Cedex, France

1) Introduction

Dimensional analysis is a convenient tool for the comparison of transport in different tokamaks, and for its extrapolation to future machines. It has been observed that the tokamak plasma is governed by a small number of dimensionless parameters, such as the normalized Larmor radius ρ^* ($=\sqrt{2m_eT_e}/(q_eBa)$), the beta number β ($=nT/(B^2/2\mu_o)$), and the collisionality ν^* ($=$ const $(R/a)^{3/2}q_aRn_e/T_e^2$). The combination of these parameters allows to conclude about the local thermal diffusivity and global confinement. In the dimensionless representation, the heat transport coefficient normalised to the Bohm coefficient χ^B ($=T/(eB)$) is given by :

$$\chi/\chi^B = K\,(\rho^*)^{x_\rho}\,(\beta)^{x_\beta}\,(\nu^*)^{x_\nu} \qquad (1)$$

Recently, similarity experiments have been performed in Tore Supra for the investigation of the ρ^*-scaling relation with transport [1]. It has been shown that the electron transport is close to the gyro-Bohm scaling *i.e.* $x_\rho = 1$ in the low confinement regime (L mode), while the ion transport is rather Goldston-like. The dimensional analysis is now completed with the new experiments to investigate the scaling in β and ν^* for transport.

2) Transport scaling in L regimes

To investigate the ν^*-scaling and β-scaling in Tore Supra, two series of experiments have been performed, corresponding to two magnetic field regimes: (1) B = 3.76 T, I_p = 1.30 MA; (2) B = 1.72 T, I_p = 0.60 MA. For all considered discharges, the plasma species is Helium and the geometry remains unchanged : the minor radius a is 0.76 m, and the major radius R is 2.32 m. The electron temperature is controlled by two heating methods : ICRH which is only efficient in a high magnetic field range (high density in this case), and lower hybrid (LH) wave heating which is more efficient in low density regimes. In both heating cases, the additional power deposition are estimated to be in the central region $\rho < 0.3$. The local transport analysis is then performed from profile analysis with a numerical code LOCO as in [1]. In the first experiment, β remains fixed while ν^* is varied. From equ.(1), a representation of $(\rho^*)^{-x_\rho}\,\chi/\chi^B$ will give the β and ν^* scaling. Figure 1a displays the ratio of radial variation of $(\rho^*)^{-x_\rho}\,\chi/\chi^B$ for two limit cases $x_\rho = 1$ (gyro-Bohm) and $x_\rho = 0$ (Bohm). From this figure, one can see that this function scales as $(\nu^*)^{x_\nu}$ with $0 < x_\nu < 0.5$. In the

second experiment, ρ^* is fixed while β is changed. Figure 1b displays the ratio of the radial variation of $(\nu^*)^{-x_\nu}\,\chi/\chi^B$ which scales as $(\beta)^{x_\beta}$ with $0 < x_\beta < 2$ for $x_\nu = 0$ and $x_\nu = 0.5$.

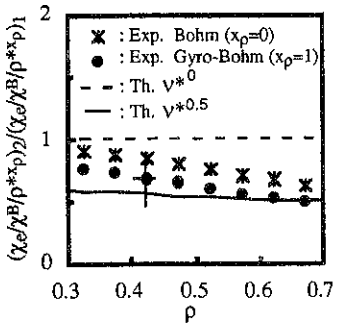

Fig.1a Radial profile of the transport ratio for β constant.

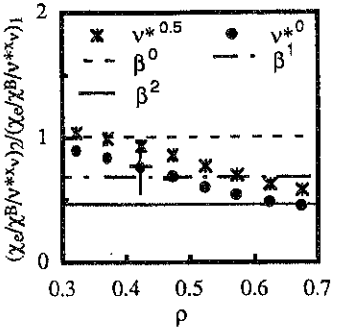

Fig.1b Radial profile of the transport ratio for ρ^* constant.

A global analysis has also been made where the average heat diffusivity $<\chi>$ is evaluated from the energy confinement time τ_{Dia} (diamagnetic measurement) with $<\chi> \approx a^2/\tau_{Dia}$, and the average temperature $<T>$ and average line density $\bar{n}$ are used in the expression of the global parameters ρ^*, β and ν^*. From the above experiments, a simple dimensionless scaling of the transport is then obtained :

$$<\chi>/\chi^B = K\,(\rho^*)^{0.4\pm0.2}\,(\beta)^{1.3\pm0.2}\,(\nu^*)^{0.1\pm0.2} \qquad (2)$$

In figure 2, this scaling is plotted versus the experimental values, showing a very good agreement. This global scaling given by equ.(2) is consistent with the one obtained above from local analysis (Fig.1a & b). It should be noted that $<\chi>$ includes both electron and ion contributions, which may explain the global scaling in $(\rho^*)^{0.4}$.

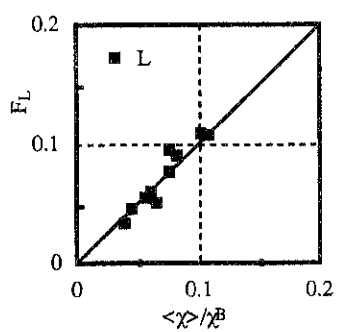

Fig.2 Dimensionless scaling of transport F_L versus the experimental values of χ_e/χ^B in L regimes with $F_L = K\,(\rho^*)^{0.4}\,(\beta)^{1.3}\,(\nu^*)^{0.1}$.

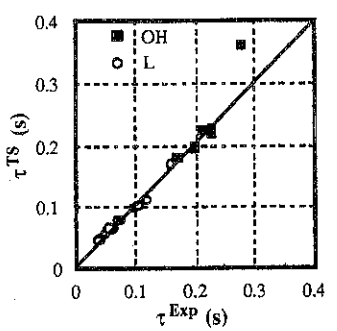

Fig.3 Confinement time scaling of Tore Supra τ^{TS} versus experimental values.
$\tau^{TS} = 0.02\,R^{2.04}I_p^{0.98}\bar{n}^{0.43}B^{0.2}P^{-0.75}$.

Scaling (2) is also compatible with that previously established for the confinement time in Tore Supra [2] :

$$\tau_E^{TS} = 0.02\ R^{2.04}\ I_p^{0.98}\ \bar{n}^{0.43}\ B^{0.2}\ P^{-0.75} \qquad (3)$$

Indeed, the equivalent dimensionless representation of this scaling is

$$<\chi>/\chi^B = K\ (\rho^*)^{1.02}\ (\beta)^{1.35}\ (\nu^*)^{-0.07} \qquad (4)$$

In figure 3, τ_E^{TS} is plotted versus the experimental values, the agreement is excellent except may be one point which corresponds to the high density and high magnetic field OH plasma. The dimensionless scaling of transport in ohmic regimes will be discussed in the next section.

To summarise, local transport analysis, confirmed by global analysis, show that the electron transport in L regimes is strongly β-dependent and weakly ν*-dependent. This means that the turbulence causing the anomalous transport is electromagnetic [3], and that the collision effect is weak in the transport process in the L regimes.

3) Transport scaling in OH regimes

In ohmic regimes, a simple expression of the dimensionless scaling for electron transport has been obtained by dimensional analysis [4] as :

$$\chi_e/\chi^B = K\ (\rho^*)^1\ (\beta)^{-2}\ (\nu^*)^1 \qquad (5)$$

In Fig.4 this scaling is plotted versus the experimental values, and a good agreement is found. Compared to the L regimes, the ρ*-scaling is consistent (gyro-Bohm), but the ν*-scaling and β-scaling are quite different. In ohmic regimes the electron transport is clearly collisional and the transport coefficient decreases with β. The result in ρ* seems in contradiction with that previously reported [1] where it has been shown that the electron transport is Bohm like. In fact, in the previous work we have omitted the β effect in the OH similarity experiments (ν* = const, β ≠ const). The reason is that one can never keep simultaneously constant β and ν* in the ohmic case, because the temperature is not an independent parameter. It rather depends on other parameters as the density, the plasma current and the magnetic field. When the β-dependency is corrected, we can show that the electron transport follows the gyro-Bohm scaling.

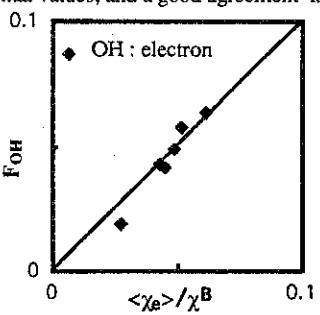

Fig.4 Dimensionless scaling of ohmic electron transport F_{OH} versus χ_e/χ^B.
$F_{OH} = K\ (\rho^*)^1\ (\beta)^{-2}\ (\nu^*)^1$.

4) Fluctuation scaling

In the similarity experiments, the density fluctuations are measured by CO2 laser scattering. To investigate the ρ*-scaling of fluctuations, two shots are considered and described in Tab.I & II. The probed poloidal wavenumber is chosen to maintain $k_\theta\ \rho_e$ = const (see

Tab.II). The scattering volume is located in a region from $\rho \approx 0.6$ to $\rho \approx 0.9$. From the generalised mixing length theory, $\tilde{n}/n$ is directly linked to ρ^* at ν^* and β constant as

$$\tilde{n}/n(\theta,r,z,t) = \rho^* F(\theta r/L_\theta, r/L_r, z/L_{/\!/}, t/\tau_c) \quad (6)$$

where L_θ, L_r, L_z are respectively the fluctuation correlation length in the poloidal, radial and toroidal direction, and τ_c is the correlation time defined as $\tau_c = L_n/c_s$ (L_n is the density gradient length, c_s is the ion acoustic velocity). The structure of fluctuations are typically $L_\theta = \rho_s$ (Larmor radius), $L_{/\!/} = q\,R$, $L_r/a = (\rho_s^*)^\alpha$. $\alpha = 1$ corresponds to a short radial correlation scale fluctuation leading to a gyro-Bohm transport, and $\alpha = 0$ corresponds to a large radial correlation scale fluctuation leading to a Bohm transport. For one measured k_θ-component of fluctuation and due to the Fourier transform, it yields :

$$(\tilde{n}/n|_{k_\theta})^2 = (\rho^*)^{4+2\alpha} f(k_\theta \rho^*) \quad (7)$$

From Tab.I and Tab.II, we obtain : $\alpha = 0.40$. For these experiments the measurement of density fluctuations seems to confirm the results on core transport from profile analysis.

Shot	B (T)	Ip (MA)	n_{e0} ($10^{19}m^{-3}$)	$\langle T_e \rangle$ (keV)	k_θ (cm^{-1})	$(\tilde{n}/n\|_{k_\theta})^2$ (a.u.)
20641	3.7	1.3	6.25	1.65	8.2	3.1×10^{-4}
20631	1.7	0.6	2.25	1.08	5	5.0×10^{-3}
Ratio	2.18	2.17	2.78	1.53	1.64	6.2×10^{-2}

Table I. Engineer parameters of shots 20641 and 20631 in their L phase.

Shot	R/a	q_a	β (10^{-3})	ν^*	ρ^* (10^{-5})	$k_\theta \rho^*$
20641	3.04	3.57	1.64	0.17	4.8	3.94×10^{-4}
20631	3.08	3.50	1.72	0.15	8.5	4.25×10^{-4}
Ratio	1.01	0.99	0.95	1.13	0.56	0.93

Table II. Non dimensional parameters of shots 20641 and 20631 in their L phase.

5) Conclusions

Similarity experiments have been made in Tore Supra to investigate the dimensionless scaling of local transport in ρ^*, β and ν^*. Local and global analyses have shown that in L regimes the electron transport is nearly gyro-Bohm ($x_\rho \approx 1$), electromagnetic ($x_\beta \approx 1$ - 2) and weakly collisional ($x_\nu \approx 0$), while in ohmic regimes it is gyro-Bohm ($x_\rho = 1$), electromagnetic ($x_\beta = -2$), and strongly collisional ($x_\nu = 1$). For these experiments, when using a generalised mixing length model by dimensional analysis, the measurement of density fluctuation seems to confirm the ρ^*-scaling of internal transport obtained from local transport analysis.

[1] Zou X. L., Laviron C., Colas L., *et al., 23th EPS Conf. on Contr. Fusion and Plasma Phys.*, Kiev, Vol.20C, I-130 (1996)
[2] Hoang G.T., Saoutic B., Guiziou L., *et al.*, Report EUR-CEA-FC-1582 (1996)
[3] Connor J.W., Plasma phys. Controll. Fusion, 30 (1988) 619
[4] Zou X.L., Hoang G.T., Moreau P., Report EUR-CEA-FC-1603 (1997), submitted for publication.

A model for improved confinement in PEP discharges

P. Maget, X. Garbet, A. Géraud, E. Joffrin
Département de recherches sur la fusion contrôlée
Association Euratom-CEA sur la fusion
Centre d'études de Cadarache
St Paul-lez-Durance, France

1. Introduction

Pellet injection in the centre of Tokamak plasmas, combined with core additional heating, leads to an improved confinement, the PEP (Pellet Enhanced Performance) mode. The goal of our study is to identify and to compare the mechanisms that can reduce the turbulence during this regime.

Since low wave number instabilities are expected to play a dominant role in the anomalous transport, we focus on Trapped Electron Drift and Ion Temperature Gradient modes. The contribution of trapped particles in the growth rate is of interchange type : $\gamma_l^2 \propto \omega_n^* \omega_D$, where ω_n^* is the electron diamagnetic drift frequency and ω_D is the toroidal drift frequency of trapped electrons. It is known since Kadomtsev [1] that ω_D changes its sign for barely trapped particles, and that the point of drift reversal moves towards deeply trapped particles domain when the magnetic shear is lowered. In other words, there are less and less destabilising trapped particles when going towards reversed shear configuration. In addition to the magnetic shear effect, **ExB** shear increases the radial decorrelation, bringing a stabilising contribution. A criterion deduced from numerical simulations of ion turbulence [2] says that when $\gamma_E > \gamma_l$, the turbulence is suppressed, γ_l being the maximum linear growth rate, and $\gamma_E = E_r'/B$.

We present here a simple linear approach of drift waves driven turbulence, integrating these two shear effects. An application to a Tore Supra PEP mode is described.

2. Basic model

Our model is based on a kinetic approach, in the approximation of large growth rate. The collisionless formulation of the dispersion equation involves trapped particles and circulating ions. In the case of large trapped electron collisionality, which is relevant in PEP mode conditions, the instability is sustained by ions only.

We use a ballooning decomposition of the fluctuating quantities in the limits $k\delta \ll 1$ and $|k_{//} v_{//}/\omega| \ll 1$, where δ is the ion banana width, k is the radial wave vector, and $k_{//} v_{//}$ is the parallel transit frequency of passing ions. This model yields an equation of the form :

$$-\delta^2 \phi'' + \left[U_{nm}(\omega) + x V_{nm}(\omega) - x^2 W_{nm}(\omega)\right]\phi = 0 \qquad \text{(E)}$$

where ϕ is the fluctuating electrostatic potential, U_{nm} , V_{nm} and W_{nm} are the particle response to an (n,m) perturbation, and x is the radial co-ordinate relative to the $q=-m/n$ surface.

At lowest order, the radial structure of the mode is neglected, and equation (E) reduces to $U_{nm}(\omega)=0$. The wave frequency is then $\omega_o = \omega_n^*/2 + i\gamma_o$, where $\gamma_o/n = \sqrt{\gamma_I^2 - \omega_n^{*2}/4}$. The complete solution of the differential equation yields a gaussian ϕ ($\phi \propto \exp(-\alpha(x-a)^2/2)$), and the pulsation is treated as a correction to ω_0. This calculation of the radial structure of the mode gives the linear approach of shear stabilisation.

We have derived an analytical estimate of the growth rate in the collisionless limit, which gives :

$$\gamma \approx \gamma_I(s) - \gamma_n^* - \gamma_{ExB} - \delta\alpha^{1/2}\gamma_I$$

where $\gamma_n^* \approx \omega_n^{*2}/8\gamma_I$ and $\gamma_{ExB} \approx (L_S\,\gamma_E/V_{Ti})^2\,\gamma_I$, $\delta\alpha^{1/2} \propto \frac{s}{\sqrt{\varepsilon}}\sqrt{1+(L_S\,\gamma_E/V_{Ti})^2}$, $L_S = qR/s$, and V_{Ti} is the thermal velocity of ions. The two latest terms come from the shear correction. The magnetic shear influence is due to the interchange nature of the instability, and appears in the local growth rate term. A clear stabilising contribution from density gradient and **ExB** shear is explicitly shown in this expression. A simple estimate of density gradient influence shows that the correction γ_n^*/γ_I is of order RL_p/L_n^2, where L_p and L_n are the pressure and density gradient lengths, and R is the major radius of the plasma.

3. Study of a PEP mode

The strong density and pressure gradients expected in PEP modes lead to a favourable variation of all stabilising terms : (i) the magnetic shear is lowered, due to the bootstrap current, (ii) the steep density profile increases the γ_n^* stabilisation, and (iii) the **ExB** shear is increased ($E_r \approx \nabla p_i/e_i n_i$).

The determination of experimental **ExB** shear has been obtained indirectly, since we have no direct measurement of the radial electric field in Tore Supra. A code (NeoClass) solves neoclassical equilibrium in the Hirshman and Sigmar formulation [3], assuming that the toroidal balance is given by the charge exchange friction with neutrals. This hypothesis allows the determination of the radial electric field, consistently with neoclassical flows.

We take as an example a PEP mode obtained on Tore Supra. This shot was performed with a modest additional power (ICRH) of 3 MW, and a pellet velocity of 2 km/s. For this discharge, the Tore Supra record of neutron production was obtained, with a value of 1.6 10^{14} s^{-1}.

In figure 1, we plot the local growth rate (γ_o), whereas γ_o-γ_E is plotted in figure 2, during and after the PEP mode. The linear treatment of shear stabilisation is plotted in figure 3. The toroidal mode number for these calculations was determined from the relation $k_\theta\rho_i = 0.1$, which is expected to be in the domain of the saturated regime of turbulence, as indicated by recent numerical simulations [4].

Density gradient plays a major role in the reduction of the local growth rate. The ratio RL_p/L_n^2, which gives an estimate of the density gradient induced stabilisation (γ_n^* term), is increased by a factor of 3 during the PEP mode (from 1 to 3). The magnetic shear also

contributes, but in a minor way, since the current profile was taken to be flat, as indicated by Ident-D magnetic equilibrium for this particular PEP mode. The uncertainty on this quantity is quite large in the central part of the plasma, and it is not excluded that a hollow profile was obtained. This eventuality has been considered, and leads to a strongly reduced growth rate in the negative magnetic shear region. Our final choice corresponds to the more realistic and pessimistic case, which highlights the alternative stabilising terms.

The shear induced stabilisation in the linear approach is important, as indicated by comparison between fig.1 and fig.3. The $\gamma_{\mathbf{ExB}}$ component is dominant in the very central part of the plasma, whereas the radial width of the mode ($\alpha^{-1/2}$) is strongly reduced in the half outer part, due to the combination of magnetic shear and **ExB** shear. The non-linear analysis (fig.2) indicates also a strong stabilisation by this mechanism.

The validity of our method falls for high value of $n.s$ product, where n is the toroidal mode number and s is the magnetic shear. In this case, the radial extension of the mode becomes of the same order of magnitude as the banana width of ions, that is to say $k\delta \sim 1$. This constraint limits the analysis to approximately the region $0 \le \overline{\rho} \le 0.8$ for $k_\theta \rho_i \approx 0.1$.

4. Conclusion

A model for improved confinement in PEP discharges, based on drift waves analysis, has been developed and tested on a Tore Supra experiment. It yields a linear approach of shear stabilisation due to the banana excursion of trapped ions. From an analytical estimate of the growth rate, we find that magnetic shear, density gradient, as well as **ExB** shear can contribute favourably to the reduction of turbulence. The analysis of a Tore Supra experiment shows that the main stabilising terms come from density gradient and **ExB** shear. But a more negative magnetic shear would strongly reduce the growth rate, thanks to the stabilisation of trapped particles contribution. The linear approach of shear influence on the structure of the mode indicates a shift of the region of main instability, towards the outer part of the plasma. The use of a non-linear criterion ($\gamma_E > \gamma_l$) gives a similar change, keeping the idea that drift waves are stabilised in the plasma core.

These results are in good agreement with current ideas on improved confinement origins. They suggest that the PEP mode is similar to the ERS mode. Note however that the ERS is a spontaneous transition whereas the PEP mode is triggered by a pellet. The fact that negative magnetic shear is not a necessary ingredient in PEP modes, as seems to show our example on Tore Supra, has also been pointed out in a TFTR paper [5]. However, a lower magnetic shear should lead to a better confinement, and PEP experiments on JET [6] are supporting this expectation.

Figures :

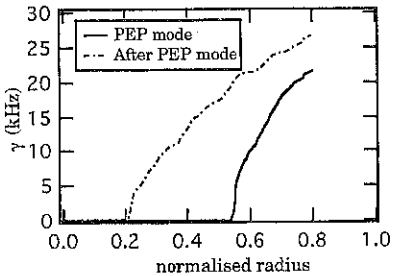

Fig 1 : Local growth rate (γ_o) during and after the PEP mode ($k_\theta \rho_i$=0.1).

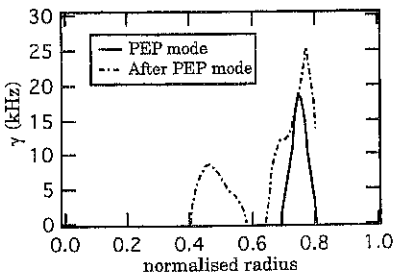

Fig 2 : Growth rate γ_o-γ_E, during and after the PEP mode ($k_\theta \rho_i$=0.1).

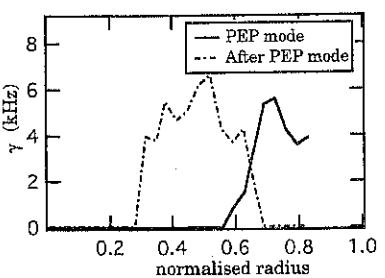

Fig 3 : Growth rate calculated in the linear approach, ($k_\theta \rho_i$=0.1).

References :

[1]KADOMTSEV B.B., POGUTSE O.P., Rev. of Plasma Phys., 5, *249-400*, 1970
[2]WALTZ R.E., KERBEL G.D., MILOVICH J. , Phys. Plasmas 1 (7), *2229-2244*, 1994
[3]HIRSHMAN S.P., SIGMAR D.J., Nuclear Fusion **21**, *1079-1201*, 1981.
[4]SYDORA R.D., DECYK V.K., DAWSON J.M., Plasma Phys. Control. Fusion, **38**, *A281-A294*, 1996.
[5]L.R. BAYLOR et al., Nucl. Fus., **37** (1), 1997.
[6]HUGON M., Nuclear Fusion, **32** (1), 1992

Predictive Simulations of Tore Supra Discharges in stationary and transient regimes

M.Erba, M.Mattioli, T.Aniel, V.Basiuk, A. Bécoulet, X. Litaudon, A.L. Pecquet, J.L. Segui, T. Dudok de Wit *.

Association Euratom-CEA, Département de Recherches sur la Fusion Contrôlée

Centre d'Etudes de Cadarache, 13108 Saint Paul lez Durance Cedex

* Centre de Physique Théorique, Luminy, case 907 F-13288 Marseille cedex 9

Heat Transport Models for L-mode

In the development of simple empirical expressions for the L-mode heat conductivity using dimensionless analysis [1] it has been found that it is difficult to distinguish between pure Bohm or pure gyro-Bohm models within a single experiment and both can approximately describe data. However, in order to simulate a wider database it has been necessary to use a combination of Bohm and gyro-Bohm terms, as it is done in the mixed model [2].

None of these models is completely in agreement with the ITER96 scaling law for L-mode thermal confinement [3]: in fact the Bohm model gives a negative dependence on the toroidal field $\tau_{Eth} \propto Bt^{-1/2}$ and a too weak power degradation $\tau_{Eth} \propto P^{-1/2}$. Hence we introduce a new mixed model where the gyro-Bohm-like term for electrons contains a dependence on $\beta=8\pi p/B_t^2$:

$$\chi^{M}_{e} = \chi^{B}_{e} + \chi_{GB}^{*} \quad , \quad \chi_{GB}^{*} = \alpha_{GB}^{*} \cdot \chi^{B}_{e} \cdot \rho^{*} \cdot \beta^{1/2} \cdot \frac{q}{L_{pe}^{*}} \qquad (1)$$

where $\chi^{B}_{e} = \alpha_B\, c\, a\, q^2\, |\nabla p_e| / (e\, n_e\, B_t)$, the normalization constants α_B and α_{GB}^* are chosen so that the Bohm and gyro-Bohm part are similar in large machines, the dependence on β is introduced in order to increase power degradation and the additional dependencies on q and $L_{pe}^* = p_e/r\nabla p_e$ are necessary to have a radially increasing shape of the diffusivity. The scaling law corresponding to the χ_{GB}^* term alone is very close to the ITER 96 scaling law.

Predictive Simulations of Tore Supra and ITER-database discharges

Using the Astra transport code [4] we have carried out predictive simulations of a number of discharges both from the ITER database [5] (JET, TFTR, DIIID, Alcator C-MOD) and from the local databases of Tore Supra (TS). The normalized radius ρ^* varies by an order of magnitude in the chosen database, which could not have been achieved using discharges from a single machine. Simulations of Tore Supra discharges where Fast Wave Electron Heating is varied from 3 to 9 MW show that the new mixed model with β dependence does give enough power degradation to account for experimental measurements of the Te profile (Fig. (1)). The simulation of an ohmic discharge from START [6] shows the Bohm model and mixed

model [2] to be in strong disagreement with data, while good results are obtained with the pure gyro-Bohm-like model and the new mixed model (Fig. (2)).

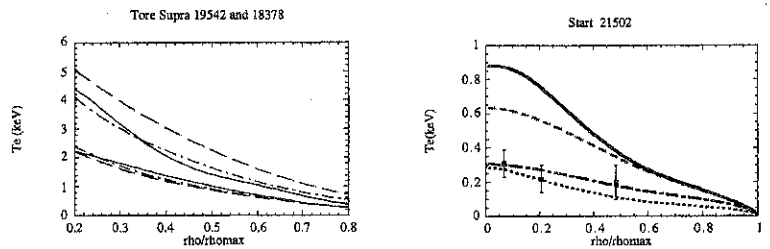

Left : Fig.1: simulations of the experimental electron temperature profile (solid lines) of two Tore Supra shots with different input power using the mixed model [2] (dashed lines) and the new mixed model of eq.(1) (dashed -dotted lines). The 3 higher curves correspond to 9MW of input power, the 3 lower curves to 3 MW.

Right: Fig.2: simulation of the electron temperature in a START discharge (error bars) using the pure Bohm-like model (solid line), the mixed model [2] (dashed line), the pure gyro-Bohm-like model (dashed -dotted line) and the new mixed model of eq.(1) (dotted line).

The statistical analysis of the simulations results is carried out by computing the quantity m defined as the relative deviation of the predicted profile T with respect to the experimental profile Texp averaged over the minor radius. As the product $\rho^*\beta^{1/2}$ (which characterizes the new gyro-Bohm term in eq.(1)) increases, the Bohm-like model and the mixed model [2] predictions deviate from experimental Te by ~ 100% (Fig.(3)).

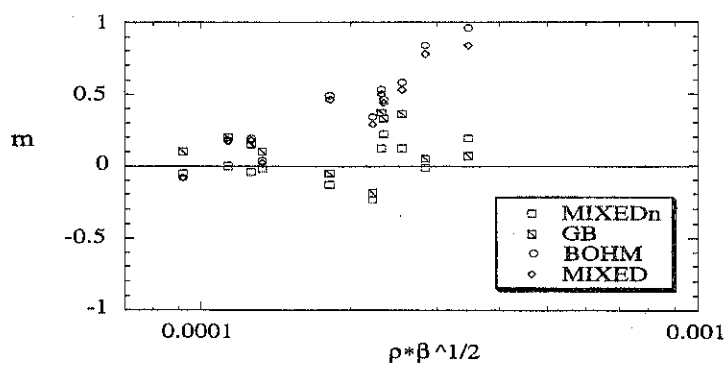

Fig.3: Deviation of the Te profiles predicted with different models with respect to the measured profiles as a function of $\rho^*\beta^{1/2}$ computed at x=1/2.

For ion heat transport on the other hand we find that the mixed model [2] gives good results in all simulated discharges.

Simulations of Laser Blow-off experiments (impurity transport)

Nickel is injected during the current plateau of two ohmic TS discharges (20792,20601), one of which had the Ergodic Divertor (ED) activated (20601). The Ni ion transport is studied by means of an impurity transport code and the radial profiles of the diffusion coefficient D and of the inward convection velocity V(r)=(r/a) VA(r) = 2 S D(r) r/a^2, with peaking factor S~1.5 everywhere, are obtained by simulating soft X-ray brightness and emissivity time evolutions. To simulate satisfactorily in both experimental conditions the initial phase of the Ni ion inflow before the first inverted sawtooth, it is necessary to increase transiently the transport parameters (by one order of magnitude or more) during the first milliseconds after the injection (Fig. (4)). The simulations confirm the previously reported presence of a central core with reduced transport parameters inside the surface q=1 or s=1/2 (Figs (4)-(5)). In the simulation of the discharge with ED activated # 20601 it is necessary to introduce a peripheral transport barrier (with increased inward convection and/or reduced diffusion).

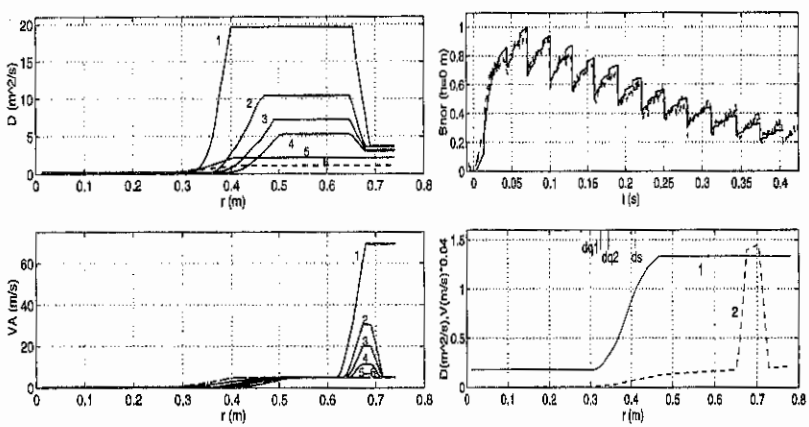

Left: Fig.4: D(r) and VA(r) profiles for 20792 during the initial phase following the laser blow-off injection at t=0, prior to the inverted sawtooth . Curves 1 to 6 show the profiles at t=0, 5ms, 7.5ms, 10.5ms, 13.5ms, 17.5ms.

Right: Fig. 5: Above : The solid and dashed lines show respectively the simulated and experimental soft X-ray signals from a central line for shot 20601. Below: Radial profiles of D (solid line) and V (dashed) for 20601. The position of the q=1 surface as indicated by temperature (dq1) or soft X-ray signal (dq2) together with the position of the s=1/2 surface (ds) are also shown.

Simulations of Laser Blow-off experiments (heat transport)

The evolution of Te(r,t) is obtained solving the heat diffusion equation with the transport code Astra, and the radiated power profiles are taken from the previous analysis and imposed in the simulations. The results are compared with the heterodyne radiometer measurements of Te with good time (1 ms) and space (4 cm) resolution. The raw data are smoothed using the Generalized Singular Value Decomposition technique that allows to reduce the effect of sawtooth modulation in the cold pulse propagation. For the thermal electron conductivities we use a model previously tested in several different transient events [7] which is essentialy the mixed model [2] where the Bohm part is multiplied by a term containing a non-local dependence on the edge temperature. The transport model is completed by the prescription of the edge temperature Teb(t) made in accordance with the outermost measurement of Te.

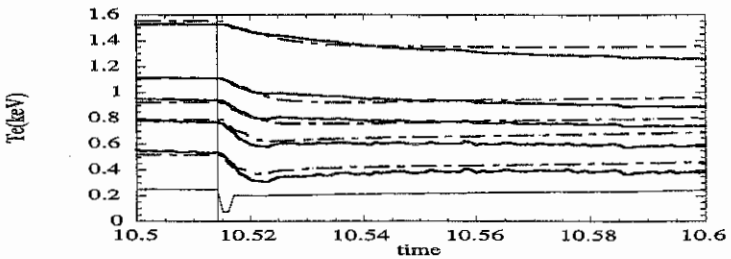

Fig.6:Time evolution of Te for shot 20792 at x=0.56, x=0.65, x=0.70, x=0.74, x=0.78 from simulation (dashed-dotted lines) and experiment (solid lines). The lowest solid line represents the prescribed time evolution of Te at the edge, the vertical line indicates the injection time.

Te begins to drop immediately after the pulse at several radial positions (Fig.6) and this is reproduced in the model by a sudden, non-local increase in the electron heat diffusivity all over the plasma column. The radiated power cannot explain this effect because impurities are carried to the plasma centre only at the inverted sawtooth 21.5 ms after the injection. The model describes well also the data for the impurity injection in shot 20601 with ED if the region of ergodized magnetic surfaces near the edge is excluded from the simulated domain.

[1] Taroni A., Erba M.,Tibone F., Plasma Phys. and Control. Fusion **36** (1994) 1874.

[2] Erba M., Cherubini A., Parail V.V., et al., JET-R(96)07.

[3] T.Takizuka et al., Montreal , Canada, 1996, IAEA-CN-64/FP-20.

[4] Pereverzev G.V., Soldner F.X., Bartiromo R., et al., Nucl. Fusion **32** (1992) 1023.

[5] Connor J. et al., Montreal, Canada, 1996, IAEA-CN-64/FP-21.

[6] Roach C.M., Plasma Phys. Control. Fusion **38** (1996) 2187.

[7] Erba M., Cherubini A., Parail V.V., et al. Plasma Phys. Control. Fusion **39** (1997) 261.

Analysis of up-down poloidal asymmetries of density fluctuations in Tore Supra

C. Fenzi, C. Laviron, A. Truc*, P. Devynck, F. Gervais*, P. Hennequin*, A. Quéméneur *
Association Euratom-CEA sur la fusion contrôlée, CEA/Cadarache,
13108 Saint Paul lez Durance Cedex, France
(*)PMI-CNRS (UPR287), Ecole Polytechnique, 91128 Palaiseau Cedex, France

1-Introduction

Anomalous transport in fusion devices is a major problem to plasma confinement, and is known to be mainly due to microfluctuations, either electrostatic or magnetic. In present day large tokamaks, measurements on density fluctuations have shown that this turbulence can be separated into two constituents, a bulk turbulence and a larger magnitude turbulence at the edge: in this last external region, electrostatic fluctuations play an important rôle for particle and energy transport.

Most of previous investigations have focused on the relation between turbulence and global parameters and, in few cases, local parameters through the radial component. Only small effort has been put on the analysis of poloidal asymmetries, although qualitative observations have been made in some tokamaks (TEXT, ALCATOR, CCT, ASDEX).

In the circular cross-section tokamak Tore Supra, where heat and particle control is based on the use of a set of modular limiters but also on ergodic divertor, up-down asymmetries of the density fluctuations have regularly been observed [1] by the CO2 laser scattering diagnostic ALTAIR [2]. So, an investigation has been engaged to understand them and find their origin. Depending on the configuration of the machine and plasma conditions, a thorough analysis may help to understand the origin and the development of the edge turbulence as well as some of the plasma wall interaction mechanisms. We present hereafter a first analysis of these asymmetries.

2-Experimental set-up

This first analysis of density fluctuations asymmetries on Tore Supra has been made using plasma discharges for which the scattering diagnostic was configured to observe them, but it was not a specific experience, and it happened on statistically different plasmas, not covering the full range of operating parameters.

The experimental set-up of the infra-red laser scattering diagnostic ALTAIR has been described in details in Ref. [2], and only the features necessary for the understanding of this specific analysis are summarised hereafter. ALTAIR measures density fluctuations through the collective scattering of a CO2 laser probing beam. It has an excellent resolution in

wavevector **k** (which can be adjusted between 3 and 15 cm-1 in any direction perpendicular to the vertical probing beam in the plasma) at the expense of a poor spatial resolution. It is known that fluctuations are locally perpendicular to the magnetic field lines, and taking into account the helicity of these embedded field lines, some resolution is obtained along the vertical probing chord by selecting the proper direction of the probed wavevector [2]. In addition, the use of an heterodyne detection (allowing the determination of the direction of propagation of the plasma turbulence) and two intermediate frequencies allows to observe simultaneously two independent wave vectors within this chord.
In order to compare the turbulence coming from the upper part of the probing chord to the lower one on a same plasma and at the same instant, we used a configuration based on the simultaneous measurements of two wave vectors **k1** and **k2**, adjusted with the same wave number but different orientation.

3-Analysis of asymmetries

No correlation has been found with different plasma parameters such as the density, the safety factor at the edge qa, the feeding gas (D2, He or H2) or the range of values of k probed (k = 5, 6 and 12 cm-1). But, taking into account local parameters such as the device used for the edge control (limiter(s) defining the plasma edge), a tendency appears. In fact, the level and the location of observed asymmetries depend on the limiter(s) facing the plasma, and this level can be high as 5 dB (corresponding to a factor of 3).
The strongest ones appear when the plasma is leaning on the lower limiters, with a higher level of turbulence originating from the lower part of the plasma. Conversely, when the plasma is leaning on the outboard limiter, the asymmetry is opposite with a maximum towards the upper part. In a third configuration, when the inner wall is used as a limiter, these asymmetries are not so pronounced and do not exceed 2 dB (but generally towards the upper probed volume). Other configurations, with multi-limiters (such as for an example, first inner wall and lower limiters or outboard limiter altogether) give intermediate results and are more difficult to interpret.

4-Connections with limiters

An analysis has been made for the connection of the magnetic field lines (of the last closed flux surface, LCFS) between the limiter(s) and the probing chord. It seems that all variations about the location and the amplitude of the asymmetry can be attributed to the connection of the edge magnetic lines with the probed fluctuations volume. Depending on their poloidal and toroidal locations, the limiters are magnetically connected either to the upper or lower parts of the fluctuation probing chord. It is necessary to specify that the analysis of these magnetic field lines connections is only valid for the LCFS, while the turbulence is measured in a

volume extending to (r/a)~0.5. Nevertheless, the apparent correlation found between the limiter(s) controlling the plasma and the asymmetry tends to show that the limiters are an additional source of turbulence: they could locally induce specific fluctuations which propagate along the magnetic field lines.

5-Frequency spectra

Additional information has been obtained by an analysis of the frequency spectra. They present two peaks corresponding to two regions of the plasma, differentiated by a shift frequency due to Doppler effect [3]. One component, for positive frequencies, presents a Gaussian shape in our configuration (k1 probing the lower part of the plasma and k2 the upper one), corresponds to the inner part of the plasma inside the radial electric shear layer [3], and the propagation is in the electron diamagnetic direction (figures 1, 2). The second component, roughly presenting a Lorentzian shape [4], corresponds to the outer part of the plasma and the scrape of layer (SOL), with a propagation in the ion diamagnetic direction.

In figure 3, a comparison is made between two configurations, with and without asymmetry. In case of strong asymmetry of the fluctuation level (figure 3a), turbulence develops mainly towards negative frequencies i.e. in the outer part of the plasma, the extreme edge and the SOL. Although of a lower amplitude, the asymmetry is also observed for the positive frequencies (corresponding to r/a<~0.9). Moreover, without asymmetry (figure 3b), the turbulence propagates mainly in the electron diamagnetic direction in a poloidal plane: less turbulence is observed in the outer part.

All this tends to show that the local turbulence induced by the limiters seems to extend radially towards the plasma core.

6-Conclusion, discussion

These preliminary results show that strong correlations exist between up-down poloidal asymmetries of density fluctuations and the plasma configuration, the limiters probably inducing specific fluctuations which propagate along the magnetic field lines. The analysis of frequency spectra give precious radial informations: asymmetries develop mainly towards the extreme edge of the plasma beyond the radial electric shear layer. Because an effect is also observed towards the core whith a lower amplitude, a radial propagation of this turbulence can be considered. Four different mechanisms of instability can be proposed for this edge turbulence linked to the limiters, for which investigations will be made: ionisation, interchange, thermal and sheath instabilities.

New specific experiments will now be realized on Tore Supra to complete these first qualitative observations. Then, it will become possible to be more quantitative, with a

rigorous study of the asymmetry evolution for stationary and ohmic plasmas, taking into account all possible geometric configurations and various physic parameters.

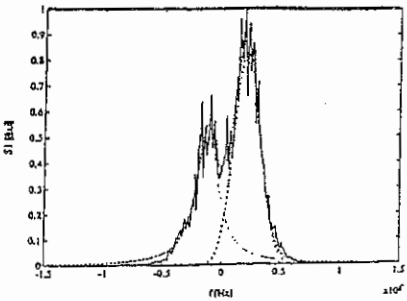

Figure 1. *Frequency spectrum channel 1, for k = 6 cm^{-1}, probing the lower part of the plasma*
left: Lorentzian shape (external region) rigth: Gaussian shape (inner region)

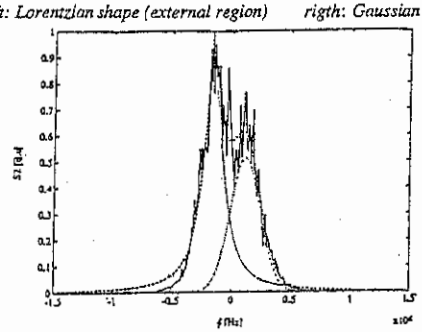

Figure 2. *Frequency spectrum channel 2, for k = 6 cm^{-1}, probing the upper part of the plasma*
left: Lorentzian shape (external region) rigth: Gaussian shape (inner region)

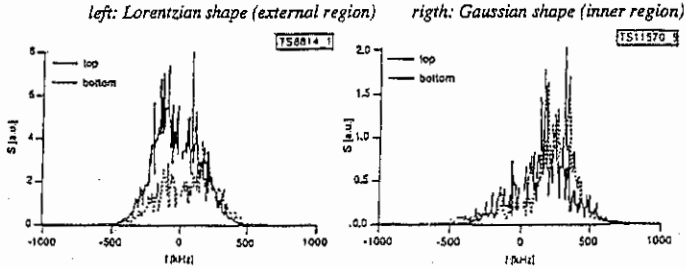

Figure 3a. *Frequency spectrum with strong asymmetry* **Figure 3b.** *Frequency spectrum without asymmetry*

References:

[1] P.Devynck & al., Plasma Phys. Control. Fusion 35 (1993) 63

[2] A. Truc & al., Rev. Sci. Instrum. 63 (1992) 7

[3] X. Garbet & al., Nucl. Fusion, vol. 32, 12 (1992) 2147

[4] F. Gervais & al., Proc. of 21 st. E.P.S. Conf. on Control. Fusion and Plasma Phys. vol 1 (1994) 118

Boundary temperature profile and core energy confinement in Ergodic Divertor configuration

Samuel Féron and Philippe Ghendrih
Association Euratom-CEA, DRFC, CEA Cadarache
13108 St Paul-lez-Durance, Cedex, France

1 Introduction

During Ergodic Divertor operation, strong steady state poloidal and radial modulations of the temperature field are observed in stochastic boundaries [1]. In the plasma core, the temperature is not affected, while the temperature in stochastic boundaries is very low. This experimental evidence indicates that an energy transport barrier must build-up in the vicinity of the separatrix. These results are in contrast with the standard theory which predicts a low temperature throughout the divertor volume and an unchanged temperature gradient in the core, which implies therefore a core temperature drop. The transport barrier formation in a stochastic boundary is investigated with a 2D mapping transport code which exhibits the basic features of the ergodic divertor of Tore Supra [1], see section 2. The turbulent transport is assumed constant throughout the divertor volume and cannot explain therefore the observed transport barrier at the separatrix. Analytical and numerical evidence of the formation of the transport barrier are presented in section 3.

2 Transport model

Energy transport in a stochastic field is a 3D transport process since the axisymmetry is destroyed by the helical perturbation. In particular the parallel transport combines the standard rotational transform at constant radius superimposed to radial steps induced by the magnetic perturbation of the coil system. Given the large mode numbers of the Tore Supra ergodic divertor, $\overline{n} = 6$ and $\overline{m} = 18$, the perturbing field remains located to the vicinity of the coils. The 6 octopolar coils, equally spaced toroidally, are thus modelled by a magnetic perturbation with a $\cos(\overline{m}\theta)$ poloidal dependence extending from $-\pi / 4$ to $\pi / 4$. This is the poloidal extent of the coil in magnetic coordinate for typical ohmic shots [2]. The radial decay of the perturbation is governed by the poloidal wave number in cylindrical coordinate, hence r^{-m_c} with $m_c \sim 10$. The toroidal extent of the perturbation is taken to be vanishing in contrast to the effective coil extent of 14°. This localisation in a Dirac distribution allows one to generate a 2D mapping similar to the standard map (Chirikov-Taylor map) after integration along the toroidal angle. In order to avoid the spurious loss of symmetry of time inversion which characterizes the standard map, i.e. the loss of symmetry with respect to the horizontal axis, the Dirac distribution is split into two "half Dirac" apart from the poloidal plane of reference and at a vanishing distance from the latter. The issue of inversion with time of this mapping has been carefully investigated. Indeed, upon integration along the toroidal coordinate, the magnitude of the perturbation is multivalued due to the radial dependence of the perturbation. Neglecting this

dependence leads to an inward pinch which could induce other misleading artefacts. To evaluate this effect 3D calculation have been performed with toroidal dependencies of the perturbation tending to the Dirac distribution. It is then found that this error leads to negligible effects in all the divertor volume.

The magnetic configuration generated by this 2D mapping is very close to that of the ergodic divertor. The perturbation is maximum at the plasma boundary and the Chirikov parameter [1] which evaluates the level of stochasticity, decreases towards the plasma core. The global diffusion of field lines terminates at $q(\rho_{sep}) \sim 2$, which defines the location of the separatrix, $\rho_{sep} \sim 0.8$. Transport analysis with such a mapping is investigated with test particles. The turbulent transverse transport is then modelled by a noise superimposed to the parallel motion. The energy transfer which is thus computed can be compared to the temperature field insofar as the plasma density is a monotonous decreasing function of radius. Using the quasilinear field line diffusion [1] one can estimate the parallel transport, typically $D_{FL}\, v_{the}$, v_{the} being the parallel velocity of the test particles and $D_{FL} \sim \pi\, q\, R_0\, (\delta B / B)^2$. This naturally introduces the time lag between two successive radial perturbations $\tau_{//} = (R_0\, 2\pi / 6) / v_{the}$, $R_0 \sim 2.4$ m and $2\pi / 6$ is the toroidal angle between 2 successive coils. The transverse transport is defined by the transverse diffusion $D_\perp = \delta^2 / \tau_{//}$ which thus determines δ, the random step of the noise. The balance between parallel and transverse transport is characterized by $D_\perp / D_{FL} \sim (\delta / (\pi\, R_0\, \delta B / B))^2$, roughly the ratio of the random walk step to the width of the magnetic island. Since the transverse transport is assumed constant in the divertor volume, the only change in the parallel and transverse transport balance is due to the modification of the stochastic transport.

2 Analytical & numerical results

For given values of the transverse diffusion coefficient $D_\perp$, the temperature profile is compared to the limiter case, where transport only results from the transverse diffusion. Several regimes are expected depending on the magnitude of $D_\perp / D_{FL}$. When transverse transport dominates, $D_\perp >> D_{FL}$, limiter features prevail. As transverse transport is reduced, one should recover the regime predicted by the standard theory, namely a lowered temperature in the boundary associated to a reduced core temperature. This is indeed observed, for $D_\perp / D_{FL} \sim 1.4\ 10^{-2}$, fig.(1). However, as the ratio $D_\perp / D_{FL}$ is further decreased the build-up of the transport barrier is observed, fig.(1). The increase of the gradient extends from $\rho = 0.65$ to $\rho = 0.85$, where the Chirikov parameter is close to the chaos threshold value. We emphasize that the transverse diffusion coefficient is assumed to be constant in all the plasma. The transport barrier does not result from a local reduction of the turbulent diffusion coefficient. Simultaneously to the formation of the transport barrier steady state modulations of the test particle density are observed.

The underlying mechanism of the transport barrier can be related to a varying trapping probability, i.e. the probability for a field line to experience a radial step larger than δ vanishes towards the separatrix. A simple energy flux balance with a varying stochastic diffusion step Δ,

then yields the energy flux $q = -d(D_{eff}\, nT) / dr$, with $D_{eff} \sim D_\perp + D_{FL}$. At given energy flux from the core and constant density, the temperature profile in the divertor volume is a function of the limiter temperature profile, $T_{ED}(r) \sim T_{Lim}(r)\, D_\perp / D_{eff}$. The temperature is thus depressed in the divertor volume where $D_{eff} \sim D_{FL} >> D_\perp$, and strongly increases in the vicinity of the separatrix, $D_{eff} \sim D_\perp$ to reach the temperature profile of the limiter configuration, fig.(2). This analytical description of the transport barrier is in agreement with experimental observations [1].

As the ratio $D_\perp / D_{FL}$ decreases below $1.7\ 10^{-3}$, the transport barrier is such that the core ED energy profile exceeds the limiter profile, fig.(1). This result cannot be recovered in the frame of the first order expansion in terms of the radial dependence of $D_\perp / D_{FL}$ which leads to the hereabove analytical result. Our present conjunction is that trapping mechanisms of stochastic field lines in the vicinity of remnant islands is a major mechanism. In the case $D_\perp = 0$, a radial profile of the poloidally averaged transit times to the boundary is plotted on fig.(3). Furthermore the 2D plot of this transit time indicates that poloidal structures of these trapping times occur. The non monotonic variation of the trapping time shows that two transport process coexist as assumed in the model of two coupled networks [3]. In this model, the small scale network stands for the transverse transport while the large scale network stands for the stochastic radial transport. A transport barrier at the separatrix is achieved when crossing the separatrix from the core to the boundary can only be achieved on the small scale network while the stochastic network allows for a radial step through the separatrix from the boundary to the core. Along the lines of this result, it seems that parallel transport from the stochastic region to the separatrix is probable but that the trapping mechanism at the separatrix associated to the small level of transverse transport reduce the probability for particles to flow back to the stochastic region along the field lines.

3 Conclusion

As a consequence, little change of the pressure profile within the core plasma is found for standard transport cases so that one readily expects a moderate, ~ 10 %, decrease of the energy content of the discharge despite the large volume dedicated to open field lines, typically 36 % of the volume of the limiter configuration. The numerical check of this analysis indicates that the intrinsic transport barrier strongly depends on the magnitude of the turbulent transport compared to the stochastic transport, $D_\perp / D_{eff}$. In contrast to typical axisymmetric divertor configurations in L-mode, the Ergodic Divertor can thus combine a reduced volume of confined plasma and an unchanged core temperature with respect to a configuration making full use of the magnetic volume. Such results are not specific to Tore Supra but concern stochastic boundary configurations as achieved in stellarators.

References

[1] Ph. Ghendrih et al., Plasma Phys. Control. Fusion, **38**(1996)1653.
[2] Ph. Ghendrih, A. Grosman and A. Kaleck, this conference.
[3] S. Féron and Ph. Ghendrih, 12th PSI to be published in J. Nucl. Mat.

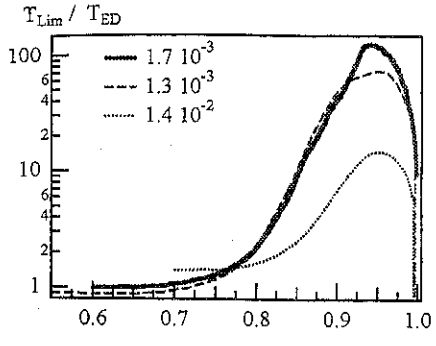

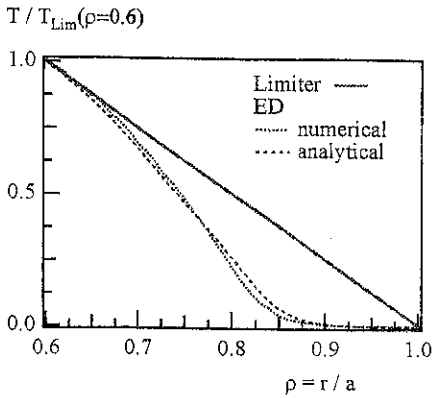

Figure 1 : numerical energy profiles, Limiter normalized to ED, versus radius for 3 values of $D_\perp$ / D_{eff}

Figure 2 : numerical energy profiles, Limiter and ED and analytical energy profile versus radius.

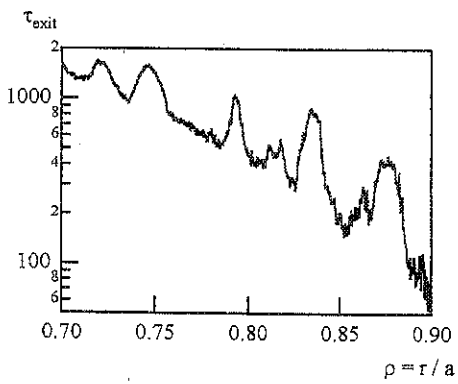

Figure 3 : poloidally averaged exit time versus radius indicating localized trapping regions.

Investigation of particle and energy transport in RF heated and ergodic divertor discharges on Tore Supra, using CXRS

W.R.Hess, W.Mandl*, J.L.Farjon, S. Böddeker, C.DeMichelis, M.Druetta*, I.Voitsekhovitch°

Association EURATOM-CEA sur la Fusion Contrôlée
CEA-Cadarache, 13108 Saint-Paul-Lez-Durance Cedex, France
*Lab. TSI, UMR CNRS 5516, Univ. J. Monnet, 42023 St. Etienne Cedex 2, France
°permanent address: "Kurchatov Institute", Moscow, Russia

Active beam spectroscopy is a powerful tool to measure ion temperature and impurity density radial profiles. First results have been obtained in Tore Supra ohmic and rf heated discharges, and are used to improve our impurity particle and energy transport analysis. We investigate the transport for different plasma scenarios, including different additional heating schemes and the activation of the Ergodic Divertor (ED) in D- and in He-plasmas.

A vertical diagnostic injector is used to generate charge exchange reactions between injected beam neutrals and fully stripped light impurity ions (fig 1). Carbon spectra before and during the beam injection are used to extract the active, beam induced charge exchange recombination spectrum (CXRS) by background subtraction. The resulting active component is then further analysed using a least square line fitting procedure. The Doppler shifted emission spectrum of the impact excited Hα transition of fast beam particles on the outermost viewing line is used to characterise the diagnostic injector. Based on the experimentally determined power distribution into full, half and third energy components of the neutral injector and using a neutral particle penetration code, the local densities of the three different energy components can be determined.
The active spectra of the CVI transition at 5291Å are used to deduce ion temperature profiles from their Doppler broadened line shapes, while the absolute brightness is exploited for ion density measurements. Additional line broadening effects (fine structure and Zeeman effect) are neglected here; temperatures from the outermost viewing lines ($r/a > 0.9$) are therefore overestimated by about 10% [2]. Since the absolute neutral beam power is poorly known and variable during this initial period of operation, absolute densities are normalised to the Zeff value deduced from visible bremsstrahlung, carbon being by far the dominant impurity.

Both, Ti and carbon density profiles are used in the impurity transport code to deduce transport parameters. Assuming a neo-classical pinch velocity $v_d(r)$, the particle diffusivity profile D(r) can be modelled. This produces low D values compared to results from transport analysis based on the penetration of injected impurities [1]. In addition, the dimensionless convective parameter $S(r)=a^2v_d/(2rD)$ (a=minor radius), which gives a measure of the peaking of the radial impurity profile in the confinement region of the plasma, is found to be higher than previously inferred. It turns out that the S(r) profile is characteristic of the specific plasma scenario (fig 2).

Whereas ohmic limiter discharges tend to be associated with radially flat S profiles (fig 2a), LH discharges feature a central increase of S, indicating a central accumulation of light impurities during LH heating (fig 2c). C^{6+} concentration profiles are generally observed to be fairly flat in ohmic discharges. Increasing the fast wave electron heating power increases Zeff with little change in the C^{6+} density profile shape (fig 6b). Central peaking of these profiles at high power levels is observed for LH electron heating (fig 6a). The C^{6+} profile shape is found unchanged if the working gas is changed from D to He (fig 4a,b).

Ohmic ergodic divertor discharges show, on the other hand, a radially outward increasing convective parameter (fig 2b), concomitant to a steeper carbon concentration gradient towards the plasma edge (fig 3a,b). At the plasma periphery ($r/a > 0.8$) the concentration of C^{6+} ions is reduced during activation of the ED compared to limiter discharges. This is due to the increased heat conductivity in the ergodic zone, which modifies the Te profile, and therefore diminishes the higher ionisation states at the plasma edge. No change of the Ti profile between $0<r/a<0.9$ is observed during ED operation.

Zeff profiles are deduced from the C^{6+} density profiles under the assumption that carbon is the dominant impurity. In the periphery ($r/a > 0.8$), the lower ionisation states are taken into account via impurity transport simulation. Contrary to results from Abel inverted measurements of bremsstrahlung, a flat Zeff profile is found in the vicinity of the plasma edge (fig 4c).

For pertinent energy transport analysis [3] knowledge of the Te *and* Ti profiles is indispensable. The ratio Ti/Te varies from 0.4 to 1, depending mainly on the plasma density (fig 7a,b). In purely ohmic heated plasmas the thermal diffusivities of electrons and ions are found to be very close (fig 7e). Indeed, we observe similar characteristic scale lengths ($a \cdot \mathrm{grad}T/T$) for Te and Ti which leads to similar driving terms for ionic and electronic turbulences (fig 7c). Electron-ion equipartition is low, due to both low plasma density and high electron temperature in LH heated discharges (fig 5c,d). Good electron-ion coupling is observed during high density fast wave electron heating (fig 5a,b).

The evolution of T_i with additional electron heating depends on the plasma density and is determined by both electron-ion equipartition and ion heat transport. FWEH at high density increases both, T_e and T_i (fig 5a,b). Strong electron heating at low density, on the other hand, does not affect T_i whereas T_e still increases (fig 5c,d). Both, electron and ion heat transport increase with auxiliary electron heating. Whereas the ion heat diffusivity changes only by a factor of 2-3, similar to the particle transport, the electron heat diffusivity is raised more strongly (fig 7e,f). With additional heating the characteristic T_e scale length in the gradient region is higher than the characteristic scale length of T_i. This indicates that electron heating destabilises preferentially electron modes but affects, however, not only the electrons but also the ion thermal transport.

References: [1] M.Mattioli et al, Nucl.Fus., 35, p. 807 (1995)
[2] R.P.Shorn et al, Nucl.Fus., 32, p. 351 (1992)
[3] G.Pereverzev, P.Yushmanov et al., ASTRA an automatic system for transport analysis in a tokamak, report IPP 5/42, August, 1991

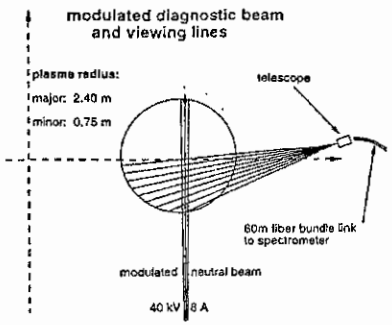

Fig.1

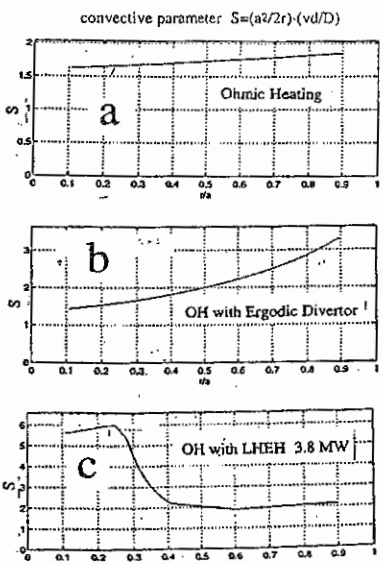

Fig.2

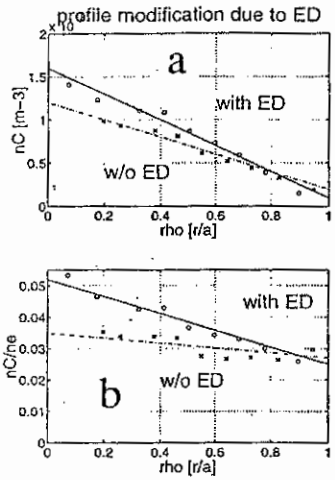

Fig.3

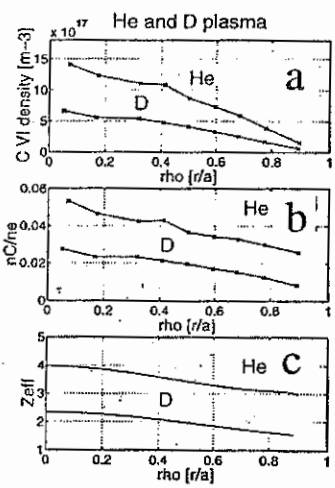

Fig.4

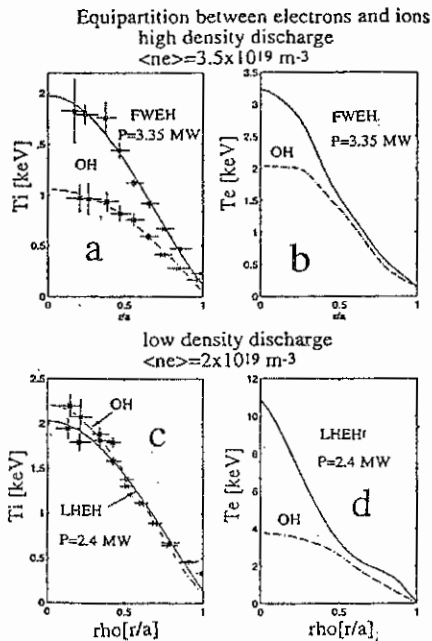

Fig.5

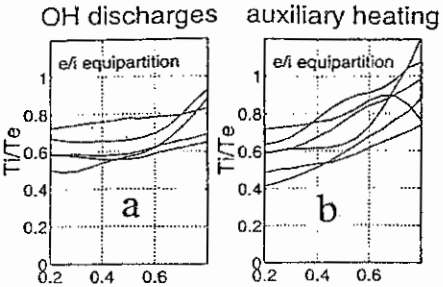

Fig.7

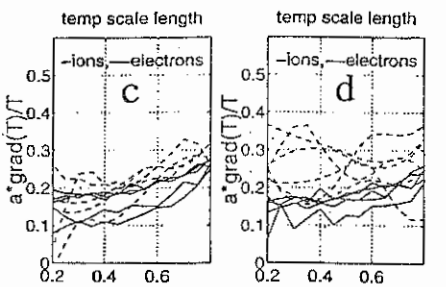

Fig.7

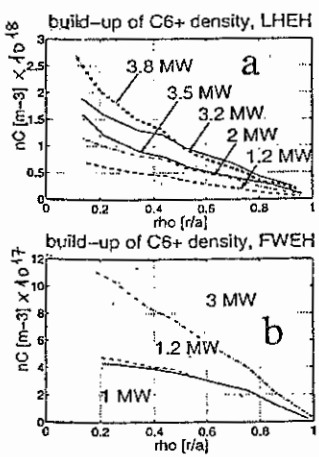

Fig.6

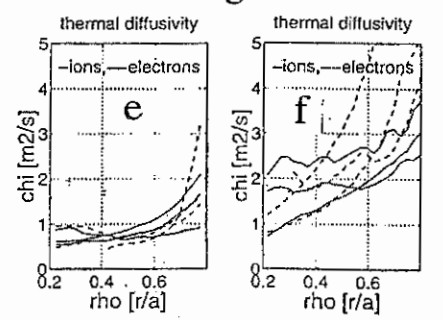

Fig.7

Intermittent Transport due to Particle Flux Drive of SOL Turbulence.

Y. Sarazin, Ph. Ghendrih and X. Garbet
Association Euratom-CEA, DRFC, CEA Cadarache,
F-13108 St Paul lez Durance, Cédex, France.

Introduction.

Control of SOL turbulence is characterized by two conflicting issues. On the one hand, it governs heat deposition on target plates and limiters which is among the most important challenges in ITER. The beneficial high turbulence level increases the wetted area hence lowering the power flux and reducing the thermal constraints. On the other hand, a reduced edge turbulence level, which is very likely coupled to SOL turbulence, is required to generate an edge transport barrier, H-mode transition. Recent works indicate a possible SOC, Self-Organized Criticality, behavior of turbulence models when driven by a volumic source [1]. Our new results, dealing with the interchange instability in the SOL, clearly show an avalanche-like behavior of the system when driven by a constant particle flux.

Models for the non-linear study of a given instability mechanism.

The interchange instability is the analogous of the Rayleigh-Bénard instability where the temperature gradient is replaced by a pressure gradient. In the low field side of tokamaks, the curvature $\mathbf{g}$ of the magnetic field lines, in the opposite direction to the plasma density gradient $\nabla_{\perp} n$, destabilises electrostatic modes. Parallel current losses have then to be reduced to allow the fluctuations to grow. In the SOL, radially limited by the separatrix at $r = a$ and the first external wall, this crucial point is ensured by the very low value of the sheath parallel conductivity σ, which has a destabilising effect [2]. The flute hypothesis, consisting in a field line average, reduces the problem to two dimensions, giving in a slab geometry $x = (r-a) / \rho_s$ and $y = r\theta / \rho_s$. This assumption is legitimated by the experimental parallel wave number of the fluctuations $k_{/\!/} \approx 0$ [3]. All lengths are normalized to an average ionic Larmor radius $\rho_s = m_i c_s / eB$, where m_i is the ionic mass, e the proton charge, B the average magnetic field in the SOL, and $c_s = [T_e(1+\tau) / m_i]^{1/2}$ the sound velocity. τ is the ratio between the ionic and the electronic temperatures T_e, which is supposed to be constant in the SOL. Taking into account a temperature gradient would add an other instability mechanism, the negative resistivity instability [4]. The essential linear characteristic of interchange instability lies in the existence of an instability threshold, proportional to $(g \nabla n)^{1/2}$. Thus, taking g constant, there is a critical density gradient over which interchange modes become unstable. This threshold results both from the sheath conductivity, which stabilises the large scale modes, and from the collisional diffusivity D and the viscosity ν which dissipate the energy on small scales structures. Finite ionic Larmor radius effects also induce a dissipation for small modes.

In a general manner, there are two different ways to study the non-linear evolution of a given instability mechanism. In the standard approach, the constant average thermodynamical force, here the density gradient, is the driving term of turbulence : the driven fluctuations are super-imposed to this average gradient without modifying it. The implicit assumption is that the

characteristic size of the fluctuations is much smaller than the equilibrium typical scale. This yields a system involving the normalized fluctuating quantities $\tilde{N} = \tilde{n}/\bar{n}$ and $\tilde{U} = e\,\tilde{u}/T_e$, with periodic radial conditions. The basic fluid equations are the electron and the current conservation laws, where the zero order terms, corresponding to the equilibrium, have been subtracted. The driving term, namely the density gradient appears in the electric drift velocity of the electron conservation law. The non-linear contribution of this drift determines the turbulent transverse transport, responsible for the dynamics of the system. The current conservation law contains the curvature term, and the non-linearities induced by the polarization current [5].
In our more realistic approach, the scale separability hypothesis is no longer assumed, and equations for the normalized global variables $N = n/n_0$ and $U = e\,u/T_e$ are derived. The driving of the turbulence is then ensured by a volumic source, ionization of the neutral influx coming from the wall [6] or core particle outflux as in the present paper. This naturally breaks the periodicity of the radial boundary conditions. In the present case $\tau = 0$. The non-linear expression of the sheath conductivity is used : $\sigma \exp(\Lambda - U)$, where $\Lambda = \ln\{2m_i/(\pi m_e(1+\tau))\}^{1/2}$ is the floating potential. The divergence of the constant particle influx from the core is modeled by the source $S(x) = S_0 \exp\{-(x/\lambda_s)^2\}$ of normalized width $\lambda_s \approx 10$. The equations for the flux driven system are :

$$\left(\partial_t - D\nabla_\perp^2\right) N = [N,\, U] - \sigma N \exp(\Lambda - U) + S(x) \qquad (1)$$

$$g\partial_y N + \partial_t \nabla_\perp^2 U - \nu\nabla_\perp^4 U = \left[\nabla_\perp^2 U,\, U\right] + \sigma\left\{1 - \exp(\Lambda - U)\right\} \qquad (2)$$

$[N, U]$ and $[\nabla_\perp{}^2 U, U]$ are the Poisson brackets related to the electric drift velocity and the polarization current respectively. The non-linear treatment is performed with a bidimensionnal code similar to that of [5].

Results and discussion.

The average gradient driven turbulence is studied for $\tau = 0$, which implies enstrophy conservation of the system. However, no inverse energy cascade, which would result in energy transfer to large spatial structures, is seen. The radial particle flux is an advection by the radial component of the electric drift velocity $\Gamma_r = \langle \tilde{n}\, \tilde{v}_r^{Elec} \rangle_\theta \simeq -\bar{n} c_s \langle \tilde{N}\, \partial_y \tilde{U} \rangle_y$. $\Gamma_r(x, t)$ exhibits a rather homogeneous shape, without any temporal or spatial structures when considered on a measurement time scale. This allows a diffusive description of the transport. The probability density function (PDF) of Γ_r, fig. (1), is a Gaussian centered on a few $\bar{n} c_s$. For the case with a very strong drive, the amplitude of the transport exceeds the one given by the Bohm criterion $D_B \approx T_e/eB$.

Fig. (2) represents the radial flux evolution for particle flux driven turbulence, eqs. (1-2). Its evolution has dramatically changed, showing an intermittent behavior, and thus recovering recent experimental results [7]. It is also characterized by bursty events which induce a variability of almost a factor ten in the radial outflux amplitude, and a non-Gaussian PDF, fig. (1). The explanation of these bursts, also called avalanches, is as follows : the turbulence driving source locally stiffens the density gradient, which then reaches the critical one. Fluctuations are thus excited, generating transverse transport. This results in a local relaxation and in the outward propagation of a super-critical state of the system, an avalanche.

Fig. (3) is a plot of the cross-correlation functions of the poloidally averaged profile of the density fluctuations at different times. The linearity of these contours, which represent the propagation of the avalanches as a function of time, indicates the ballistic nature of this transport. An avalanche outflux is thus the advected quantity $\Gamma_r^{avalanche} = \tilde{n}\, v$. The characteristic velocity v is found to increase with the driving thermodynamical source $\int_0^\infty S(x)\, dx$, and is close to c_s. The confinement is completely destroyed during these fast events since $\Gamma_r^{avalanche} \approx \Gamma_{//}$. The temporal transform of the radial flux at a given location is presented in fig. (4). In the low frequencies range, where avalanches are expected to interact, the dynamics exhibits a shape close to $1/f$, characteristic of avalanche-like phenomena [8] and which is also observed experimentally [9-10]. This $1/f$ noise means that the most efficient avalanches in terms of particle exhaust also have the smallest frequencies. In the regime where avalanches do not interact, one recovers the $1/f^4$ decrease of [1]. As expected, the transition frequency between these two regimes, associated with the duration of a single avalanche [11], increases with the driving intensity. The poloidally averaged equilibrium density profiles in both low and high field sides are presented in fig. (5), together with the source. In the simulation, the high field side stands for the case with no turbulent transport and thus characterizes the smoothing diffusion terms of eqs. (1-2). The reduced density gradient of the low field side profile is therefore the signature of the turbulent transport. The averaged profile can be described in terms of an exponential decay as would be expected from the standard analysis of the transport with well defined diffusion and convection terms [6]. As such, the averaging process does not allow one to capture the proper signature of turbulent transport allowing for misleading transport analysis. However, the e-folding length λ_{SOL} of the average profile is meaningful reaching $\lambda_{SOL} \approx 16\ \rho_s$. Interestingly enough, and similarly to experimental observations [12], the SOL width appears to be independent of the magnitude of the driving term. Finally, the equilibrium profile is super-critical with regard to the most unstable linear modes, $k_r = 0$.

Conclusion.

Our simulations, based on the same threshold instability mechanism, demonstrate the outstanding difference which results from the change from a gradient drive to a volumic source drive. In the general case of a threshold instability driven by a volumic source, any diffusive description of turbulence is no longer valid because of the high spatial and temporal heterogeneity of the transport. Transport events look like ballistic propagations of super-critical states of the system, called avalanches. The exponential decay of the average density profile is recovered despite the intermittent behavior of the underlying transport mechanism.

References. **[1]** D.E. Newman et al., *Phys. Plasmas 3* **5** (1996) 1858.
[2] X. Garbet et al., *Nucl. Fus.* **31** (1991) 967.
[3] A.J. Wootton, *J. Nucl. Mat.* **176-177** (1990) 77.
[4] H.L. Berket al., *Nucl. Fus.* **33** (1993) 263.
[5] S. Benkadda et al., *Phys. Rev. L.* **73** (1994) 3403.
[6] Y. Sarazin et al., to appear in *J. Nucl. Mat.* (1997).
[7] C. Hidalgo et al., *16th IAEA Fusion Energy Conf.*, Montreal, Canada (1996).
[8] P. Bak et al., *Phys. Rev. L.* **59** (1987) 381.
[9] A.J. Wootton et al., *Phys. Fluids B* **2** (1990) 2879.
[10] Zhai Kan et al., *Phys. Rev. E* **55** (1997) 3431.
[11] T. Hwa et al., *Phys. Rev. A* **45** (1992) 7002.
[12] P.C. Stangeby et al., *Nucl. Fus.* **30** (1990) 1225.

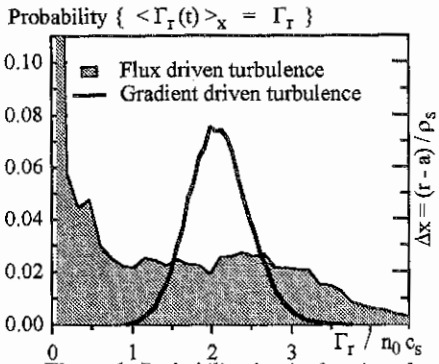

Figure 1: *Probability density function of the radial flux in the flux & gradient driven turbulence models.*

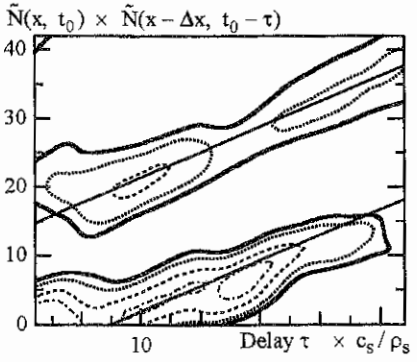

Figure 3: *Cross-correlation of the density fluctuations profiles. Straight lines are avalanches of velocity 3/4 c_s.*

Figure 2: *Evolution of the radial flux in the flux driven turbulence model.*

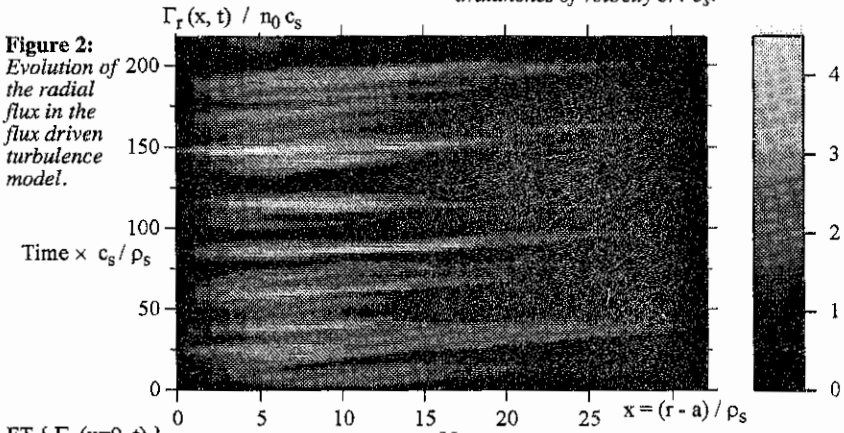

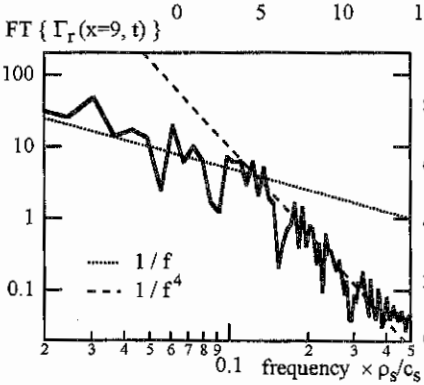

Figure 4: *Temporal Fourier transform of the normalised radial flux at a given radial location.*

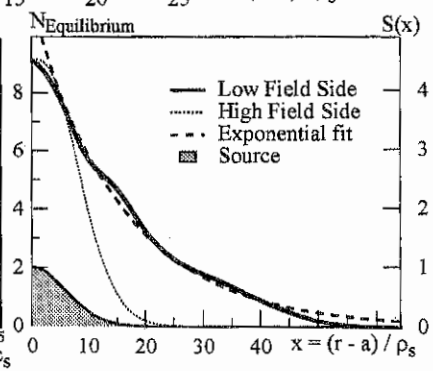

Figure 5: *Normalised equilibrium density profiles in the low & high field sides (left axes), and particle source S (right axes).*

Heat and particle deposition on the new neutraliser plates of the improved ergodic divertor in Tore Supra

B. Meslin, Ph. Ghendrih, **A. Grosman**, M. Chantant, L. Gargiulo, T. Loarer, J.Y. Pascal
Association Euratom-CEA sur la Fusion Contrôlée
CEA- Cadarache, 13108 Saint-Paul-Lez-Durance, France.

1) Introduction :

The 6 ergodic divertor (ED) modules of Tore Supra have been equipped with 42 new vented neutraliser plates. They consist of actively cooled copper tubes designed to sustain average power fluxes up to 7.5 $MW.m^{-2}$ and covered with a thin boron carbide coating. The front face of the modules are totally covered with 0.02m CFC tiles : the overall module power exhaust capability will approach 10 MW for 30 s [1]. An improved set of diagnostics allows to study the heat and particle deposition onto the plates. Three infrared cameras yield the divertor modules surface temperature and consequently the power flux onto them. A new and dedicated internal calorimetric measurement gives access to the energy loading onto many neutraliser plates with an increased geometrical accuracy. Special efforts have been directed towards electron density and temperature measurements close to the neutralisers plates where 14 fixed Langmuir probes characterise the particle and power fluxes among the 6 ED modules.

The new scheme was experimentally studied for a short but intensive probation period in Autumn 1996 with auxiliary heating by RF waves (lower hybrid and/or ion cyclotron) up to 8 MW although the following studies are essentially done with ohmic plasmas. The radiative fraction was maintained generally below 50%, leading to a heat deposition on the plates very close to the nominal value.

This paper will address the major findings of the campaign. Heat and particle flux deposition onto the neutraliser plates and the modules are shown to meet the design requirements ; some deposition patterns affect mainly the heat flux. Parallel transport will be shown to exhibit regimes similar to those observed with X-point divertors. A more comprehensive survey of the experiments will be found in [2].

2) Heat and particle flux deposition onto the neutraliser plates and the modules

The resonant effect which allows the creation of an ergodised edge zone, results also in an alignment of the field lines to the current bars of the modules [3]. Hence, the heat flux is maximised when the adequate edge safety factor is reached. Otherwise, a shadowing effect takes place. Infrared images give evidence of such shadowing as the area wetted by the plasma on the equatorial neutraliser decreases linearly from its maximal value for $q = 2.9$. Calorimetric measurements indicate that the whole heat deposition on all neutraliser plates decreases exponentially with Δq (the deviation from the resonant safety factor) with an exponential factor $\Delta q=0.5$. Such factor characterise generally other divertor effects such as the radiation enhancement [2] and meets theoretical understanding [3]. This in fact restricts the experimental domain in a range similar to the one involving the overall ergodic divertor capabilities when optimal performances are requested. Generally, the wetted part of the neutraliser plate agrees well with that expected with parallel dominated heat transport, deduced from the field-line tracing MASTOC code calculations [4]. In that line, the total heat deposition varies linearly with the relative perturbation from the divertor.

The former ED of Tore Supra exhibited a strong resilience to misalignment of the modules [4]. This is confirmed in its new configuration. The toroidal variation of the heat flux towards the neutraliser plates between the six modules remains in a window of ±20%, very similar to the estimated error bar on the internal calorimetric measurement involved. The deposition on the front face stems from both the remnants of the convective flux, not sufficiently channelled to reach the plates, but also from the « radiative fraction ». The rather systematic distribution between the 5 modules (for which reliable position measurements were achieved), which is displayed in figure 1, is in agreement with a heat flux e-folding length of about 0.011m if one assumes that the radiative fraction amounts to about 10% of the total power received, a sound hypothesis in these ohmic shots, when radiation stays below 25% of the plasma output. Noticeably, the particle flux does not exhibit variations at the same level as the radial variation does not show any particular trend in a domain of ±25% to the average value.

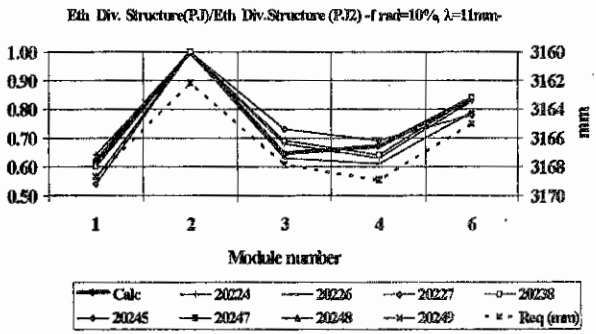

Figure 1 : Power deposition normalised to the maximum, on the various divertor module front faces for many shots (qedge is varied from 3.7 to 2.9). Expected distribution with a power e-folding length of 11mm for a radiative input equal to 10 %. Major radius of each front face in the equatorial plane is also displayed.

But, the heat deposition on the front face is far from homogeneous. A part of the flux is due to radiation and charge exchange. For the shots achieved up to now, the radiative fraction remains low and its contribution to the front face heating should remain negligible (about 0.005MW/m² if it is homogeneous). The IR camera resolution is unfortunately larger (about 0.1 MW/m²). Consequently, one cannot drive an accurate statement about the likely inhomogeneity of the radiation deposition which, in any case appears to stay small in these cases. Nevertheless, the conductive power reaching the modules front face instead of the imbedded neutraliser plates can be estimated by its location on their edges. It amounts on average to 0.2 MW/m² on areas spreading on about 50% of the front face (3 m²). Much higher values are reached for q values far from resonance : a maximum of 1 MW/m² at location close to the equatorial plane is recorded for q=3.3 and, for this value, other strong deposition (<2 MW/m²) are noticed in the top and bottom part of the ED where, the poloidal width of the bars cannot decrease along with the flux tube shrinking.

This heat deposition overview allows to confirm that the improved ergodic divertor of Tore Supra should reach its nominal capability as far as power injection is concerned; the neutraliser plates may extract up to 3 MW as foreseen if no hot spots are to be coped with [5]. The front face receives about 50% of the conductive flux. This may alter somewhat the possibility to reach long discharges (30s) because of the strong deposition on poloidally extreme parts of the modules : 4 MW should then be extracted in this case, taking into account extrapolated fluxes of 6-8 MW/m² at most. Configurational changes should nevertheless alleviate the problem.

3) Heat and particle deposition patterns

The heat deposition patterns onto the neutraliser plates have been already studied and a simple model relating them to the complex structure of the field lines and more specifically to their radial penetration for a correlation length (about 1 toroidal turn) [4,6]. This is essentially correct for cases where the parallel heat conduction is dominant, i.e. for sufficiently high edge electron temperatures (>30 eV). The new diagnostics allowed to derive the heat flux for each type of neutraliser. The ones facing a flux from the electron side are characterised by probes and dedicated calorimetric measurements. As a direct consequence of the simple model quoted above, the heat flux is shown to increase from bottom to top as, due to the module configuration on the low-field side, the radial penetration of the field lines increases with the number of modules it has to experience before leaving to the high field side. Figure 2 displays the linearity between the heat flux and the corresponding field line penetration. On the same figure, the particle flux is shown to follow a similar trend.

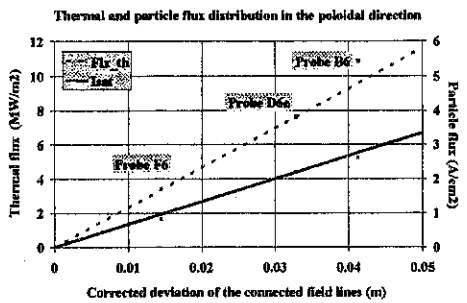

Figure 2 : The thermal flux received by different neutralizer and the particle flux deduced from Langmuir probe saturation current is plotted against the radial penetration of corresponding field lines as they cross different nearby modules.

The latter coherence is not so obvious when the specific patterns on one neutraliser plate are considered. Generally, the particle flux is much less modulated than the heat flux. Such behaviour is confirmed by the homogeneous recycling pattern deduced from D_α imaging [7]. The experimental study was here undertaken by slowly varying the plasma current so to affect the edge q ; this in turn induces the movement of the heat pattern on the neutraliser plates. As such patterns are displaced across the Langmuir probes, they may be recorded for the relevant parameters and compared to the heat flux deduced from the infrared measurements. Figure 3 displays the outputs for an experiment for which, in addition, the density was varied. This in turn has an effect on edge temperature and density. It appears that in the high temperature case (here for the larger q values), the heat flux is strongly modulated and essentially due to temperature variations. The strong heat flux dependence on electron temperature T ($T^{3/2}$) does not result in a significant particle flux dependence ($T^{1/2}$). For lower temperature regimes, a more clear particle flux variation also appears.

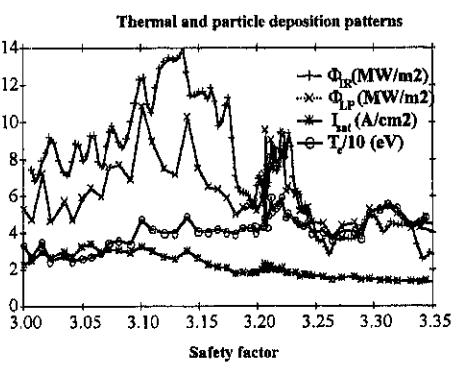

Figure 3 : During a plasma current ramp-up, the heat flux to a the neutraliser close to the Langmuir probe is recorded by IR thermography. The probe saturation current, the electron temperature and the deduced heat flux are displayed. Modulations are noticeable. For q<3.1, the density was increased.

4) Parallel transport regimes

The transport regimes within the edge region still deserve a comprehensive studies. The « stochastic region » was already reviewed in [3]. The laminar region, in which the flux tubes are connected to the wall along one correlation length, is relevant of the X-point divertor physics. In particular three regimes are expected for the perpendicular transport. At high enough temperature, it remains constant, for lower temperature, the heat parallel transport is strongly reduced like $T^{5/2}$. If in addition, the neutral density is sufficient, a pressure drop may appear, due to the momentum loss exerted through charge exchange processes. These regimes are measured with the ED, see figure 4 where the edge density at the plate is plotted against the volume averaged density, the data being taken from different shots. It yields first a linear , then a $<n_e>^3$ dependence, specific to each of the first two regimes. The transition from one to the other is accompanied by an abrupt temperature drop below 20 eV. Then, detachment occurs for T_e=10eV, characterised by a decrease of the particle flux by a factor of 4 and of the energy flux by a factor of 6, and is discussed in [2]. It should be stressed that all transitions occur simultaneously for every Langmuir probes in the modules.

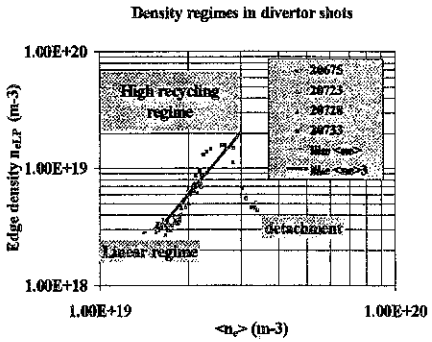

Figure 4 : Variation of density at the equatorial neutraliser plate, measured by a Langmuir probe against volume average density showing the three parallel transport regimes.

5) Conclusion

The improved ergodic divertor of Tore Supra proved to efficiently exhaust heat. The neutraliser plates are wetted as expected and this furthermore confirms that parallel transport dominates as long as Te>30 eV. The only present limitation will be due to conductive power impinging on the font face areas neighbouring the neutraliser plates, for very high power discharges. At sufficiently high densities, the parallel transport regime changes ; this allows to obtain high recycling and detachment regimes very similar to the one encountered in X point-divertor. Generally, the heat flux patterns, characteristic of the complex magnetic edge structure are more peaked than the particle flux ones.

Acknowledgements : The help of Hélène Roche in analysing IR data was appreciated.

References :

[1] L. Doceul et al., Proceedings of SOFT (Lisboa, Sept.1996)
[2] Equipe Tore Supra (presented by Ph. Ghendrih), this conference, to be submitted to Plasm. Phys. and cont. Fus..
[3] Ph. Ghendrih et al, Plasm. Phys. And Cont. Fus., 38(1996)1653.
[4] Ph. Ghendrih and A. Grosman, J. Nucl. Mat., 241-243(1997)517.
[5] M. Goniche et al., this conference.
[6] A. Grosman et al., J. Nucl. Mat., 241-243(1997)532.
[7] L. Cherigier et al., this conference.

Impurity penetration in ergodic divertor experiments in Tore Supra

L. Chérigier[1], P. Monier-Garbet, R. Guirlet, C. DeMichelis, J. Hogan[2]
Ass. EURATOM-CEA, DRFC, CEN Cadarache, 13108 Saint Paul lez Durance (France)
[1]Equipe Turbulence Plasma, UMR 6633 CNRS/U. de Provence,
IMT Château-Gombert, 13451 Marseille (France)
[2]Fusion Energy Division, OakRidge National Laboratory, OakRidge, TN, 37830 (U.S.A.)

1. Introduction : The ergodic divertor (ED) of Tore Supra has been equipped with new vented neutraliser plates [1]. They have been designed to sustain large power fluxes while allowing for deuterium pumping. They consist in four actively cooled, B_4C coated 30 cm long copper tubes separated by three 10 mm wide pumping slots. The new target plates have been equipped with a set of dedicated diagnostics including four in-situ optical fibers connected to a visible spectrometer, fixed Langmuir probes localised in the gap between two tubes, and a visible imaging system consisting of an endoscope equipped with a CCD camera and a set of interference filters to visualise the recycling pattern on the ED neutraliser plates and coils. Preliminary experiments with this improved ED have been aimed at assessing its overall properties, among which the plasma core decontamination effect observed with the old ED design [2, 3]. The new set of diagnostics have been used to measure the impurity penetration in the plasma edge. In order to get further insight into the physics issues controlling neutral penetration, a simple 2-D model has been developed and the results are in agreement with both experimental data and calculations from the BBQ 3-D impurity transport code.

2. Plasma core decontamination effect for intrinsic impurities : We have already reported the core decontamination effect obtained with the old ED design [2]. This beneficial effect might have been changed in the new design, due to the larger surface of the neutraliser plates, their new orientation (towards the plasma), and the larger surface of carbon covering the ED coils. However it has been found again for intrinsic C, O, and Cl. Fig. 1 shows the carbon concentration normalised to the total input power as a function of the volume averaged electron density, for limiter and ED plasmas. The absolute value of the carbon density in the plasma core is obtained from the CVI Lyα line brightness combined with soft X-ray and visible bremsstrahlung measurements. The total input power ranges here from 1MW (ohmic) to 6.5MW (ICRH). The results of the 1996 experimental campaign with the new target plates (triangles) are compared to the data base obtained with the old ED design (circles, gas puff fuelling, and squares, pellet fuelling). The new series of points aligns well with the old one, the carbon content decreasing by the same factor 3 to 5 (depending on $\langle n_e \rangle$) in ED plasmas. As already observed in the past, the situation for oxygen is less clear. A decrease of the oxygen content is found only when normalised to Dα measurements[2]. Chlorine is present in small quantities only in high density plasmas ; it is very efficiently screened. To further

understand this impurity screening effect, the impurity penetration in the plasma edge has been analysed, taking advantage of the new diagnostics installed in the target plates.

3. Penetration of the impurity neutrals produced at a target plate.

3.1 Experimental data and 2-D model : The absolute brightnesses of CII (658.0 nm), CIII (464.7 nm) and CIV (465.8 nm) are measured in front of the neutraliser plate by four in-situ optical fibers. The lines of sight in the equatorial plane are shown on Fig. 2. On Fig. 3a the brightness of the CII line recorded on the four fibers is plotted versus the distance from the neutraliser surface (symbols), for a series of experiments in which the total ED current I_{ED} was scanned between 18 kA and 45 kA. The volume averaged electron density was roughly constant, $\langle n_e \rangle \approx 1.8$ to 2.0×10^{19} m^{-3}. At the edge, n_e measured with the fixed Langmuir probe increased with I_{ED}, from 1.8×10^{18} to 4.0×10^{18} m^{-3}, and T_e was between 45 and 70 eV. Fig. 3a shows that, when increasing the magnetic perturbation, the maximum emission is shifted toward the neutraliser, and the radial decay length of the line brightness decreases. In order to better understand these experimental results, we have developed a simple 2-D model describing the ionisation of impurity neutrals in the vicinity of the neutraliser plates. The geometry of the neutraliser included in the model is shown on Fig. 2. The magnetic field lines striking the neutraliser under an angle $\phi \approx 1°$ are represented by straight lines parallel to the x-axis. The impurity neutral density in each point M is $n_I(M) = \sum_P n_I(P)\sin\theta\, e^{-L}$, where $n_I(P)$ is the neutral density in a point P of the surface. Neutral atoms are assumed to be homogeneously produced at the target plate ($n_I(P)$=1 a.u.) and to be emitted according to the Lambert law ($\sin\theta$). The e^{-L} term represents the attenuation due to ionisation, $L = \int_0^y (S_I(y')n_e(y')/v_0)\, dy'$, where $S_I(y)$ is the ionisation rate coefficient of the impurity neutrals, function of the electron temperature. y is the radial coordinate, and v_0 is the velocity of the neutrals entering the plasma. The determination of the electron temperature $T_e(x,y)$ and density $n_e(x,y)$ fields in the laminar region in front of the neutraliser plate is not a simple problem. Calculations from the MASTOC code [4] show that two classes of flux tubes exist : hot field lines with large radial exploration and cold field lines with shorter connexion lengths. Indeed, modulations of the electron temperature field have been observed in some cases [5]. These density and temperature fields are not included in the 2-D model. In the present stage of development of the model, the boundary conditions are given by the n_e and T_e values on the surface of the neutraliser as measured by the fixed Langmuir probe, and constant $T_e(y)$ and $n_e(y)$ gradients are extrapolated from a reciprocating Langmuir probe. The CII ion density distribution is calculated assuming ionisation equilibrium with the carbon neutrals, $n_{II}(M) = (S_I(y)/S_{II}(y))n_I(M)$. The brightness of the observed CII line is then calculated, for comparison with the experiment, by a numerical integration along the lines of sight of the 4 optical fibres. The only free parameter of the model is v_0 which value is indicative of the impurity production mechanism. It is adjusted so that the computed brightness profile fits the experimental one. The lines in Fig. 3a represent the best fit to the

experimental data. The neutral velocity v_0 has been set close to 10 eV for the three shots. This value is indicative of a physical sputtering process, previously observed in Tore Supra inertial limiter plasmas [6]. Fig. 3a shows that the variation of the experimental brightness profiles with I_{ED} is well reproduced by the model. The difference between the electron temperatures given by the fixed probe for the three shots is compensated by different gradients, leading to an electron temperature of the same order of magnitude in the first centimeters for the three cases. Fig. 3b shows the CII ion density radial profiles for the three I_{ED} values, indicating that the carbon penetration decreases with increasing I_{ED}. This is due, in our model, to the increasing electron density at the neutraliser surface (from 1.8×10^{18} to 4.0×10^{18} m^{-3}). However, this result could also be linked to the variation of the angle of incidence of the magnetic field lines along the neutraliser surface with I_{ED} which is not included in our model.

3.2. Results from the BBQ 3-D transport code : The carbon impurity production at the neutraliser plate has also been modeled with the BBQ 3D scrape-off layer impurity transport code [6]. For a given D^+ deposition profile, BBQ follows the evolution of CI, CII, CIII, etc., near the plate. Using the measured plate electron density and temperature for the I_{ED} scan (Fig. 3), the Monte-Carlo BBQ code shows the same trends as those seen in the 2D ionisation model. However, the BBQ atomic physics description is more complex, including recombination, particle radial and parallel transport and parallel friction, and MASTOC-generated fields near the plate. The BBQ calculations support the idea of emitted CI energies in the 10eV range with a high energy tail up to 50 eV in the distribution (Fig4a). The power deposition on the neutraliser, computed [4] or from IR imaging, is not homogeneous : significant sources from the gaps between the tubes of the plate as well as a broad poloidal pattern are oberved, consistent with views of D_α recycling. The influence on the carbon sources of adding a non uniform, progressively larger, D^+ particle source is shown in Fig 4b.

4. Conclusion : We have shown that (1) during ED operation on Tore-Supra, the plasma core intrinsic impurity content is reduced compared to the case with no magnetic perturbation (I_{ED}=0) and (2) the penetration of the carbon neutrals reduces with increasing I_{ED}. This last result has been obtained from the analysis of edge spectroscopy data using both a simple 2D ionisation model and the BBQ 3D code. Indeed, a detailed study of the impurity production mechanism requires a 3D spatially resolved modelling. Nevertheless, using a simple 2D model allows to identify the relevant physics parameters (neutral velocity, edge electron density).

References :

[1] A. Grosman et al., J. Nucl. Mat., **241-243** (1997).

[2] C. DeMichelis et al., J. Nucl. Mat. **196-198** (1992) 485-488.

[3] W. R. Hess et al., 23rd EPS Conference, Kiev, 24-28 June, 1996.

[4] Ph. Ghendrih et al., J. Nucl. Mat., **241-243** (1997).

[5] S. Féron, Ph. Ghendrih, J. Nucl. Mat., **241-243** (1997).

[6] S.J. Tobin et al., Plasma Phys. Control. Fusion **38** (1996) 251-263.

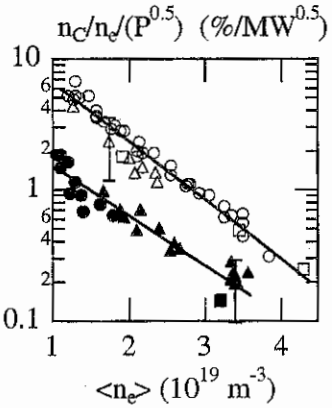

Figure 1 : Normalised carbon concentration
- open symbols, limiter shots
- closed symbols, ED shots.

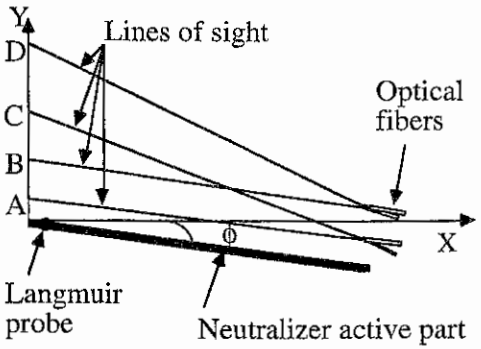

Figure 2 :Schematic view of the neutraliser in the equatorial plane

Figure 3 : (a) Experimental brightness and (b) computed CII density profiles, for three I_{ED} values,

** and - - - - 45 kA*
+ and —— 34 kA
o and .-.-.- 18 kA

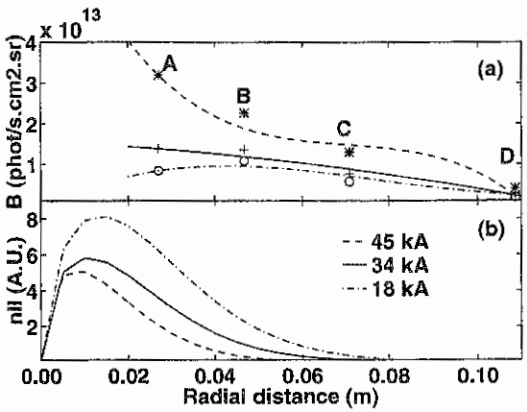

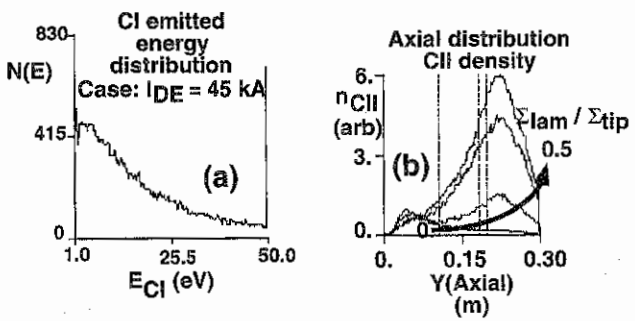

Figure 4 (a) BBQ calculated (Thomson) energy distribution of C neutrals emitted from the neutraliser plate, for the case I_{ED}= 45 kA. (b) Calculated distribution of CII density (BBQ) along the neutraliser for an additional laminar particle source with strength 0, 12.5, 37.5, and 50% of the source at the neutraliser tip.

EXPERIMENTAL INVESTIGATION and MODELLING of HEAT LOADS on LIMITERS.

D. Guilhem, J. Hogan*, G.T. Hoang, B. Meslin, S. Boddeker, J.C. Vallet, E. Joffrin, M. Lipa, J. Schlosser, P. Ghendrih.

Ass. EURATOM-CEA, DRFC, CEA - Cadarache, 13108 Saint Paul lez Durance (France)

* Fusion Energy Division, Oak-Ridge National Laboratory, Oak-Ridge, TN 37830 (U.S.A.)

I) INTRODUCTION:

The increase in auxiliary heating power in present day machines has led to the use of large plasma wall interaction. For exemple the present ITER divertor design is such that the field lines are weakly inclined with respect to the landing surface. The particle and heat load on nearly tangent surfaces are still difficult to model, especially on surfaces having a large poloidal extension, as the inner wall limiters in TORE-SUPRA [1] and TFTR [2]. Usually, one uses the « standard » analytical expression : $Q(x)= Qo//\ \exp(-x/\lambda q)\ \mathbf{B.n}$ Eq. (1)

where Qo// is the parallel heat flux at the Last Closed Flux Surface (LCFS) , **B.n** is the dot product of the normalized magnetic field vector **B** with the vector normal to the surface **n** (**B.n** proportional to $\sin(\theta)$, θ being the angle of incidence of the field line on the surface), and finally λq is the e-folding length for power deposition. However, for toroidal limiters having a *large poloidal extension* with almost *grazing angle of incidence*, Eq. (1) must be modified to include a local perpendicular heat flux term, Qoperp, which can be as large as Qo// over 3, to get the right power balance. A sequence of shots have been used to understand the consequences of additional power (up to 9MW) and particle deposition and their effects on the main plasma parameters, especially the implications in terms of Z-effective and total plasma radiation, with the plasma leaning on the large ($10m^2$) inner-wall or on the outboard limiter ($0.3m^2$). It is a « conventional » roof type pump limiter with two leading edges at the throats entrances on the ion and electron sides. These leading edges are close (0.015m) to the LCFS, since the distance has been optimized for particle pumping. A large variety of plasma parameters have been analyzed: $1 < Ptot < 9MW$, $2 < Zeff < 5$; $0.3MW < Prad < 1.7MW$, $1.5x10^{19}m^{-3} < \langle ne \rangle < 3.5x\ 10^{19}m^{-3}$, $0.75m < r < 0.78m$.

II) EXPERIMENT and RESULTS

We present results from a new set of diagnostics dedicated to evaluate the power flow to the large inner wall. This set includes *4 fixed Langmuir probes* located poloidally on the front face of the inner wall at 10°, 15°, 25° and 45° with respect to the equatorial plane, *infrared thermographic temperature maps* of the inner wall surface and a *tomographic bolometer array* located at the outboard mid-plane [J.C. Vallet this conf.]. These measurements suggest again [1] a value of $\lambda q > 0.03m$, larger than the value found when the plasma is leaning on the outboard limiter, $\lambda q = 0.01m$, as observed also on TFTR [2].

Figure 1 shows the Langmuir probes data, indicating a flat electron temperature profile at 12-16eV even during a 7.6MW ICRH pulse. On the other hand, the shape and absolute values of the density profile do change during the heating pulse. The effect of additional power (up to 9MW) is to increase locally the recycling of particles, as indicated by a large increase of the density profile, while no significant modification of the electron temperature profile is observed. The general profile has its maximum peaked below the equatorial plane but depends on the real plasma geometry. The flatness of these profiles indicates the surprisingly long e-folding length for power deposition which was already deduced [1] from a reciprocating Langmuir probe located at the top of the machine, and from a fixed Langmuir probe located at the LHCD grill mouth.

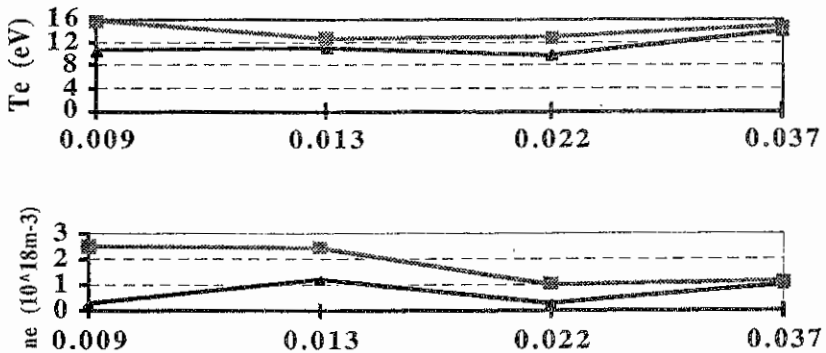

Figure1: Density and Temperature profiles (inner wall) as a function of the distance in the SOL. Lower curves for ohmic heating and upper curves with 7.6MW of ICRH in the plasma.

The infrared surface temperatures (below 350°C) and also the power load are relatively homogeneous. The surface temperature of the inner wall indicates a broad poloidal profile with a maximum temperature below 350°C at the end of a 3s ICRH pulse (except on a few defectuous tiles). This is also indicated by the Langmuir probe flat electron density and temperature poloidal profiles, figure 1. From the time evolution of the surface temperature and since the ICRH pulse length power (<5s) is << inner wall time constant (>15s), one can deduce the time evolution of the power flux density from the semi-infinite wall model. For shot 20540 where the ICRH power is 7MW, we find a power heat flux of 0.6MW/m^2.

Zeff and the radiated power (Prad) have been compared for two plasma configurations. Figure 2 shows that in the inner wall limiter case, a weak variation of Zeff and Prad is observed (Zeff is almost constant around 2, Prad = 0.5 - 1MW in the range of total power 1 - 9 MW). On the contrary, in the outboard limiter case, Zeff and the radiated power increased strongly with the total power ($2.5 \leq Zeff \leq 4.5$, and $0.5 \leq Prad\ (MW) \leq 1.5$ for total powers from 1.5

MW to 5 MW). A new bolometer array [4] is used to make tomographic reconstruction of the radiated power. It can be shown that the maximum absolute value goes from 0.2MW/m^3 in the ohmic phase to 0.4MW/m^3 during a 9MW ICRH pulse. The poloidal profiles are rather flat or eventually slightly peaked and depends on the real plasma geometry along the inner wall (ellipticity or oblatness).

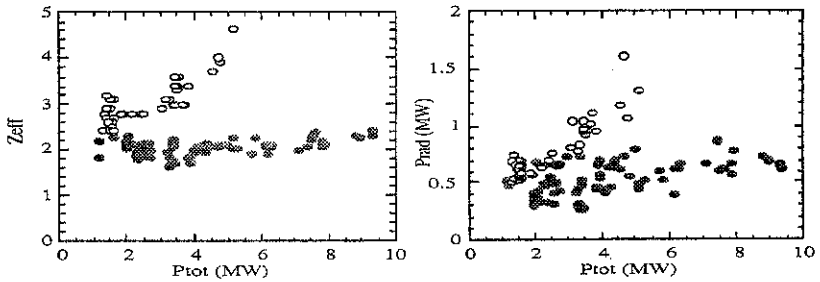

Figure 2: Zeff (left) and total radiated power (rigth) variations as a function of ICRH power for the limiter case (open circles) and for the inner-wall case (full circles).

III) MODELLING:

A 3D Monte-Carlo code THOR has already [1] been used to describe the diffusion of heat and hydrogenic particles across the LCFS to the limiters located in the SOL. It indicated that D_{perp} has to be assumed to be large in te range of 10m^2/s to reproduce satisfactorily the power heat flux poloidal profile.

The BBQ code [3] has been used to model impurity production at the inner wall which drives the central Zeff. BBQ is a 3D, Monte Carlo impurity scrape-off layer (SOL) transport code. The code uses a detailed description of the wall geometry, resolving individual tiles, and magnetic reconstructions [4] of the last closed flux surface. Although Tore Supra has nominally a circular plasma, deviations in circularity from +15% (ellipticity) to -5% (oblateness) are observed, and these have a very important effect in spreading the distribution of power on the inner wall. Starting with the D^+ incident flux (poloidal profile shapes given by the Langmuir probe measurements), the code calculates C_0 atom emission by physical and chemical sputtering, then tracks C_0, C^+, C^{++} etc. in the SOL to determine the penetration efficiency into the core plasma. Table I shows the results of BBQ calculations for several cases with varying LCFS shape and incident power. In the Table, k is the effective plasma elongation (which is different for upper and lower segments of the LCFS), Π is the penetration efficiency (the fraction of generated impurities which reach the core plasma), Y_{eff} is the sputtering yield averaged over the wall, and Γ_Z is the global impurity source for the considered wall segment.

Table I: BBQ calculations

Shot N°	Time (s)	Padd MW	Wall segment	κ	Π	Y_{clr} (%)	Γ_Z (10^{20} pt/s)
20556	3.1	0	Upper	0.97	0.20	0.02	0.45
	3.1	0	Lower	1.07	0.25	0.04	0.52
	5.2	7	Upper	0.97	0.21	0.02	0.46
	5.2	7	Lower	1.07	0.25	0.03	0.50
20559	3.2	0	Upper	1.05	0.23	0.03	0.51
	3.2	0	Lower	1.15	0.22	0.03	0.53

These results show that there can be significant impurity screening for the inner wall. This is especially true for impurities generated at high poloidal latitudes (above the equator). Because of the noncircularity of the LCFS (in the Table I the elongation, k, varies from 0.97-1.15) the incident power is distributed more uniformly than for the circular case, and impurity production is shifted from the midplane (where the screening efficiency is minimum) to higher poloidal latitudes, where the screening efficiency is higher.

VI) CONCLUSIONS:

We have presented new measurements available on TORE-SUPRA to diagnose the inner wall, namely Langmuir probes and infrared imaging. They help to understand the power deposition on such large poloidal (and toroidal) inner wall. These measurements confirm the hypothesis that on such an element the 'exponential' model for the heat and particle can ONLY give a *good representation* of the TORE-SUPRA observations *only if* several conditions are fulfilled: 1) a large perpendicular heat flux must be included, Qoperp = Qo// / 3 ;

2) the detailed plasma and wall geometry must be taken into account,

3) the actual large (> 0.03m) SOL decay length (which includes the effect of sources due to localized recycling at the inner wall) must be used.

The heat flux can then be computed by the following expression:

$Q(x) = Qo//_{LCFS} \sin\theta \exp(-dx/\lambda_q) + Qoperp_{LCFS} \cos\theta \exp(-dx/\lambda_q)$,

where $\theta = 0°$ when the flux surface is exactly tangential to the limiting surface, dx is the distance measured from the last closed flux surface (LCFS), λq is the SOL heat flux decay length, Qo// and Qoperp are the parallel and perpendicular heat fluxes density at the last closed surface.

[1] A.Seigneur, D.Guilhem, J.Hogan, et al. in Proc. 20th European Conf. Controlled Fusion and Plasma Physics, Lisbon, Portugal, July 26-30, 1993, Vol.2, P.603, European Physical Society (1993).

[2] C.S.Pitcher, P.C.Stangeby, J.N.M. 196-198 (192) 241-247.

[3] J. Hogan, C.Klepper and al. IAEA-CN-64/DP-15, 1996

[4] E. Joffrin et al., EPS Lisbonne 93. Volume 17C part I p 107

[5] J.C. Vallet , this Conférence.

Thanks to H.Roche, K.Mony and J.Y.Pascal for their help in data collection and analysis

Particle balance in ergodic divertor experiments with auxiliary heating on Tore Supra

T Loarer, B Meslin, A Grosman, Ph Ghendrih, S Böddeker, C Grisolia,
R Guirlet and P Monier-Garbet
Association EURATOM-CEA sur la fusion contrôlée
CEA Cadarache, F-13108 Saint-Paul-Lez-Durance Cédex, FRANCE.

The ergodic divertor of Tore Supra has evolved towards a larger energy extraction capability with advanced neutraliser plates. Associated to the enhanced radiating capability demonstrated in the ergodic divertor (ED) configuration [1], this new structure will allow one to operate at input power of the order of 12 MW and towards 30 seconds pulse length [2]. The boundary density of both the working gas and of the injected radiator, and hence the pumping and injection capability, are among the main control parameters for the operation of the foreseen high power scenarios.

In the present paper, experiments of the short 1996 probation period are reported. The active density control is obtained by combining the ergodic divertor configuration and the pumping capability the outboard pump limiter (OPL) equipped with a set of turbomolecular ensuring a pumping speed of $6m^3s^{-1}$. A typical shot is described with 3.5 MW of ICRH auxiliary heating which exhibit an increase of the radiated fraction from 30 to 50 % from the ohmic phase to the ICRH phase. The strong D_2 injection of ~2.5 Pa m^3s^{-1} required to maintain the plasma density is compensated by active pumping. During the ICRH phase, neon is injected and an enhancement of the radiated fraction from 50 to 60% is observed. The effectiveness of neon pumping by the turbomolecular pumps with the outboard limiter is also demonstrated. Finally, and as previously reported, active pumping of the outboard limiter is shown to remain efficient only as long as plasmas stay attached.

Experiments

The reported experiment describes a plasma discharge with I_p=1.45MA, a toroidal fiel of 3T in order to satisfy the ED resonance conditions (q_{edge}~3), while the feature of this shot included a feedback control of the gas injection (D_2) in order to maintain the plasma density $<n_e>$ constant over the discharge duration. The active pumping was ensured by the turbo pumps of the OPL which was introduced 0.04 m ahead of the front face of the ergodic divertor without modifying the global properties of the divertor configuration [3]. Figure 1 displays the general characteristics of the shot. The ED was energized from the beginning of the shot at its maximum current (I_{ED}=45kA), while 3.5MW of auxiliary heating (ICRH) was applied from 5 to 9 s. During the ICRH pulse, the radiated rate γ (γ=Total input power/Radiated power) increases from 35% to about 40%, while the Z_{eff} increases from 1.5 to 1.8. The active pumping by the OPL allows one to compensate the strong gas injection required to maintain the plasma density constant. It can be noted that with active pumping the

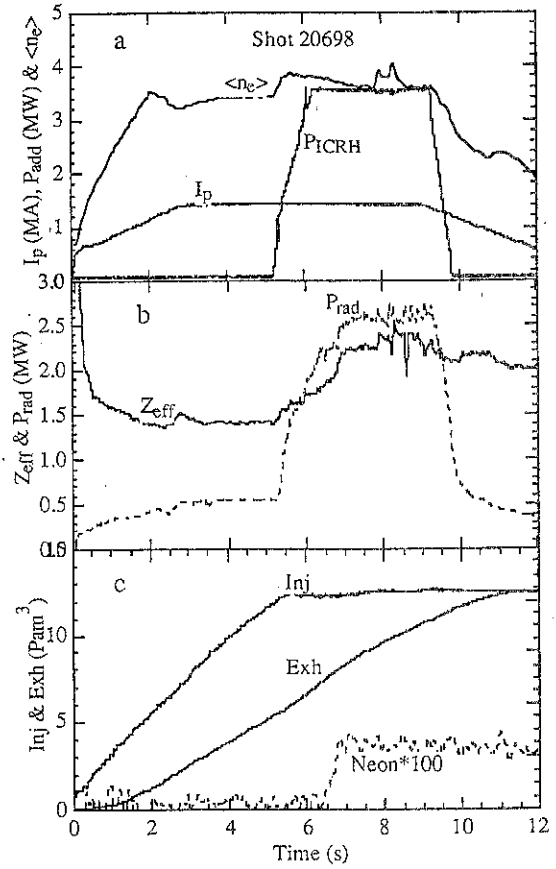

Figure 1 : *General characteristics of an ED shot versus time*
a) Plasma current Ip, averaged density <ne> and ICRH power.
b) Z_{eff} and radiated power Prad.
c) D2 (Inj), Neon injection and total particle exhausted Exh

usual density increase observed when the ICRH is applied is strongly reduced and also ensures a density decrease during the ICRH pulse. Finally, just before the end of the shot, the global particle balance exhibits an equilibrium between the injection and the exhaust. This clearly indicates that the active pumping ensures an equilibrium particularly in the wall particle balance and therefore prevent this latter from saturation while the plasma density is actively controlled. The edge plasma characteristics on the neutraliser plates of the ED are rather uniform (toroidally as well as poloidaly) and exhibit tyical ne of $10^{19}m^{-3}$ while the electronic temperature does not exceed 20eV [4] during the ICRH pulse.

Neon injection is used in order to enhance the radiated fraction, while the turbo pumps of the OPL allows one for the exhaust. The time evolution NeVII/<ne> ('edge emission') exhibit an increase during the neon puff and a deacrease of both these ratio with a time constant of 2.8s. This shows that active pumping by the turbomolecular pumps of the OPL in the ergodized layer allows one to control the plasma density as well as the extrinsic impurity content. The radiated fraction increases by about 15% due to the neon while the Z_{eff}

increase is estimated to be about 20% (from 1.8 to 2.2) which correspond to the screening efficiency of the ED already obtained with the previous ED configuration [5].

In spite of a medium plasma density, as well as a rather large total input power (~5MW), the resulting neutral pressure behind the vented structure of the ED neutraliser plates is modest for the attached plasma (typically 2-3 10^{-2} Pa of D_2 pressure), compared to the previous neutral pressure obtained with throat ED neutraliser plate (typically 2-3 10^{-1} Pa [6]) in similar plasma discharges. Since the surface of the vented neutraliser plates of the ED is typically ten times larger than the previous throat structure, the neutral pressure is in agreement with the surface ratio assuming the same neutralised particle flux. However, in these plasma conditions, the surface temperature of the throat neutraliser plates was

Plasma detachment : density and impurity control

A shot, similar to #20698 (fig 1) has been performed with the same plasma except for the Neon injection which was 2.5 larger. In this case, a plasma detachement occured nearly simultaneously to the injection while the radiated fraction increases abruptly. As a consequence, the coupling of the ICRH waves was lost and the auxiliary power was cutoff. In these conditions, the edge plasma became too cold (Te <10eV) in order to keep the plasma attached. The saturation current on the Langmuir probes in the OPL throats, as well as on the ED neutraliser plates dramatically decreases. In these plasma edge conditions, the exhaust efficiency of the OPL decreases since the particle influx (parallel flux) in the OPL throats is divided by about ten (see fig.2). The particle balance performed for this shot clearly shows that the total number of particles injected for the attached case (shot 20698) is pumped during the shot while for the detached case (shot 20699) only 70% of the injected particles are recovered. Moreover, it is worth noting that these particles are exhausted during the attached phase of the plasma discharge. This scenario is the same for the impurity as it can be clearly observed on NeVII/<ne> which exhibits a decrease during the attached phase with a characteristic time of 2.8s, while this signal remain constant when the detachment occurs (t=8s, Fig. 3). Finally, partial pressure measurements (RGA) of the neon in the OPL plenum clearly show that

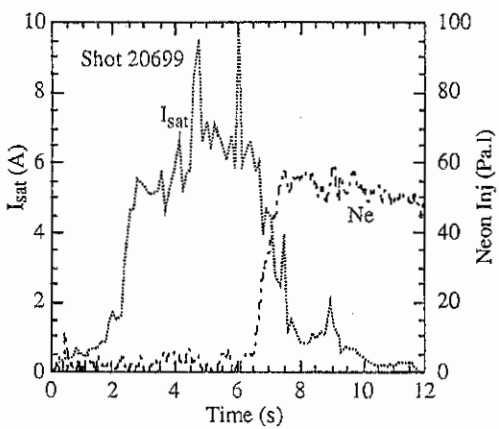

Figure 2 : *Saturation current on a Langmuir probe as a function of time for a neon injection leading to a plasma detachment at about t=8s.*

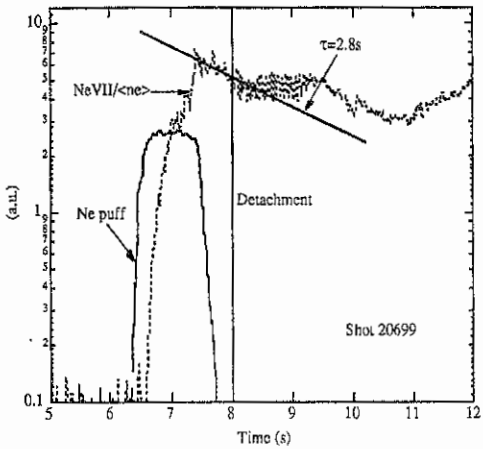

Figure 3 : *Neon injection and resulting NeVII and NeX as a function of time. As far as the plasma is attached the neon can be pumped (τ=2.8s).*

neon is exhausted by the pumps as far as the plasma is attached. The screening efficiency is obviously affected even in this ED configuration and consequently the Z_{eff} increases to values close to 3. Even if the pumping efficiency is strongly reduced during the detachment phase it appears clearly the Z_{eff} profile is more peacked in the one hand and that the edge plasma is more contaminated as soon as the detachment occurs. Finally, while the D_α signal is peacked close to the neutraliser plates i.e; the recycling surface, the detachment leads to a global decrease of the D_α signals as well as a uniformisation all around the plasma surface. This experience clearly shows that a throat structure cannot ensure a plasma density control for detached plasma.

Summary

Active density control as well as neon exhaust are obtained by combining the ergodic divertor configuration and the pumping capability the outboard pump limiter as far as the plasma is attached. Indeed, as soon as the plasma detaches, the pumped flux is strongly reduced and does not allows one for the density control. In these plasma conditions, the vented structure may deliver a better exhaust efficiency.

References :

[1] Ghendrih Ph, this conference

[2] Doceul L et al, Proceedings of SOFT XX (1996).

[3] Ghendrih Ph, Grosman A and Capes H, Plasma Phys. Control. Fusion, **38** (1996) 1653.

[4] Meslin B, Ghendrih Ph, Grosman A et al., this conference.

[5] Monier-Garbet P, et al., J. Nucl. Mater, 241-243, pp 92-104, 1997.

[6] Loarer T, Chatelier M, Grosman A et al, Plasma Phys. Control. Fusion **37 (11)** (1995) A203.

Aknowledgements

The authors are grateful to JC Hatchressian, MH Mathieu, JY Pascal, SJ Vartanian and JL Violet for providing excellent experimental conditions and valuable data.

Plasma Enhanced RF Power Deposition on ICRF Antennas in Tore Supra

R. H. Goulding, J. H. Harris, M. D. Carter, D. J. Hoffman, J. T. Hogan, P. M. Ryan
Oak Ridge National Laboratory, Oak Ridge, Tennessee, USA
B. Beaumont, S. Bremond, T. Hutter, Équipe Tore Supra
Centre d'Études de Cadarache, Association EURATOM-CEA sur la Fusion
St. Paul lez Durance, France

INTRODUCTION

The Tore Supra ion cyclotron range of frequencies (ICRF) system consists of three dual-element, radially moveable antennas designed to launch 12 MW power in the range 35-80 MHz. Both dipole (antenna current relative phase $\phi = \pi$) and phased operation ($\phi = \pi/2$) have been employed in experiments including fast wave electron heating with high bootstrap fraction and improved confinement, and fast wave current drive (FWCD) [1-2]. An important consideration in experiments utilizing ICRF is the power handling capability of the system, and it has been seen in particular during phased (and monopole, ϕ=0) operation that the limiting factor is usually surface heating of the antenna plasma facing components. This is caused by interactions between the local plasma and the launched power, resulting in highly localized heat fluxes [3]. The power may be coupled through inductive fields [4], and/or potentials on the antenna "box" caused by surface currents [3,5]. The inductive fields furthermore may be influenced by asymmetries in coupling sensitive to the direction of wave propagation [6]. The relative importance of these mechanisms has not been fully determined, and depends on specifics of antenna geometry and plasma conditions. In this paper we discuss recent experimental observations and modeling results which are relevant to this question.

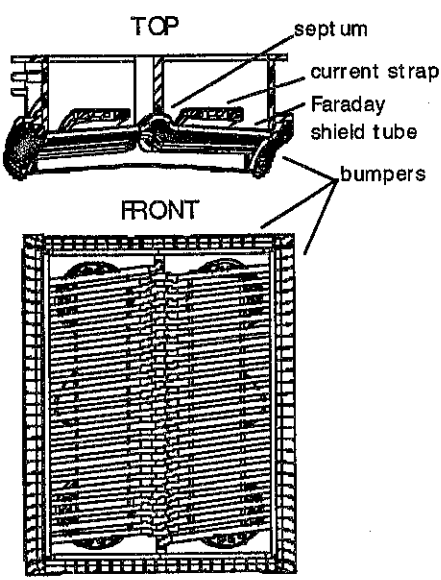

Figure 1. ORNL antenna at Tore Supra with improved Faraday shield

ANTENNA DESCRIPTION

Figure 1 is a drawing of a Tore Supra ICRF antenna with a recently upgraded Faraday shield. The design uses bent shield tubes and a recessed center septum, resulting in lower surface temperatures in this region than the previous straight-tube design. The recess also reduces central poloidal image

currents, generating a parallel wave spectrum with increased directivity for FWCD experiments. At present one antenna at Tore Supra utilizes this design while three use the previous design (including 1 "spare"). The antenna is surrounded by water cooled bumpers with graphite tiles, and the Inconel shield elements are coated with boron carbide.

ANTENNA SURFACE HEATING

Figure 2. shows some of the commonly observed dependencies of surface heating on antenna power level, antenna-plasma gap, and phasing for this antenna. The data was taken during a discharge with B_t = 2.15 T, I_p = 0.68 MA, and $\langle n_e \rangle \sim 3 \times 10^{19}$ m^{-3}, with ICRF antenna parameters f = 48 MHz and $\phi = \pi$. The top graph shows the maximum bumper surface temperature T_{max} as a function of time for two shots with differing power and plasma gap time histories. It can be seen that a 600 °C temperature spike is produced when the antenna-plasma gap shrinks as the power is being raised. If a large gap (~3 cm) is maintained during this time, T_{max} is reduced by 200 °C. Larger effects are seen during phased operation. The bottom graph shows the plasma loading on the antenna for the temperature spike shot (19708) only. The rapid loading increase at t = 4.6 s is due to the decreased gap, which results in a higher local plasma density in front of the antenna. This higher density during the power ramp is in turn responsible for the elevated temperature observed.

The strong dependence of T_{max} on phasing is shown in fig 3. Figure 3a. is a temperature profile along the bottom bumper for two shots taken eight months apart, with π antenna phasing. Figure 3b. is a profile for corresponding shots with $\pi/2$ antenna phasing. The profiles correspond to a time ~ 2s after rf turn-on, at which point the regions of maximum temperature have reached equilibrium. There is a 550 °C increase in T_{ma} in going from $\phi = \pi$ to $\phi = \pi/2$ phasing. For all shots except 20554, the rf power level is 1.5 MW, while for 20554 P_{rf} = 2.7 MW. The similarity of the profile shapes for shots having the same phasing indicate the robust nature of the phase dependency. Shots 19708 and 19710 were made under the conditions specified above, while for shots 20371 and 20554 the corresponding values are B_t = 3.7 T, I_p = 1.3 MA, $\langle n_e \rangle = 3 \times 10^{19}$ m^{-3}, and f = 57 MHz. In all cases, the plasma gap is 2-3 cm.

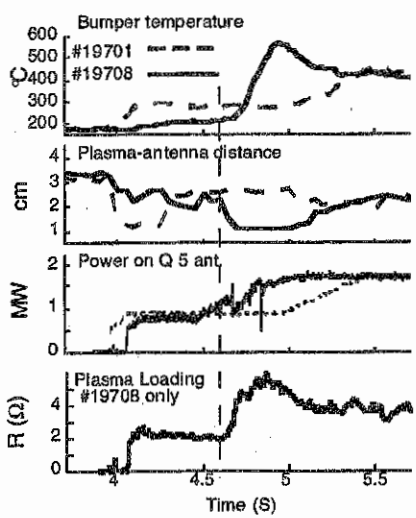

Fig. 2. Surface heating dependency on plasma gap and power. Loading also shows an effect of plasma gap.

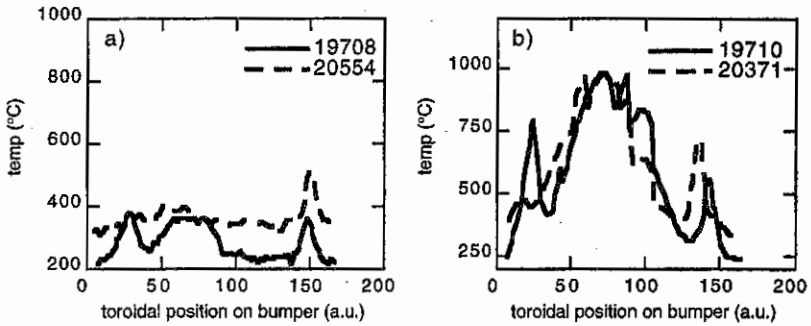

Fig. 3. Temperature profiles on the bottom antenna bumper for a) , and b) for differing plasma conditions

Not shown in the figures are the profiles for the top bumpers. There is a strong up/down asymmetry in the $\phi = +\pi/2$ cases, with the top bumper temperature ≤ 350 °C near the center.

An interesting result was the observation of a dependency on the direction of the antenna phasing. Figures 4a. and b. show time profiles for temperatures on the bottom left and right corner bumper tiles with a) $\phi = +\pi/2$, and b) $\phi = -\pi/2$. In these cases, the higher temperature corner is the one in the direction of the wave propagation. This is a localized effect. In both cases the maximum temperature actually occurs near the center of the bumpers and is ~ 1000 °C.

DISCUSSION

The main surface heating characteristics evidenced by this antenna and Faraday shield are: 1) substantially increased temperature on the center bottom bumper for non-dipole phasing, 2) increased temperature on the side bumpers for non-dipole phasing and 3) elevated temperatures (600 °C) at the midplane to the left and right of the septum. In addition, with phased operation, the bottom corner bumper tile in the direction of wave toroidal propagation heats up more than the tile at the opposite corner. The chief mechanical differences of the older shield design are the use of straight shield elements, a septum which extends radially 1 cm beyond the shield tube surface instead of being recessed, and triangular covers between the top and bottom-most tubes and the antenna box. These areas are left open in the newer design (fig. 1). The old shield evidences behaviors 2) and 3) above strongly and 1) weakly. In this case the midplane heating is directly on the septum instead of to either side.

In evaluating explanations for this behavior, we note that all three mechanisms - near field, surface voltages, and traveling wave effects predict the observed phase dependence. All three can also cause at least some up/down asymmetry. The traveling wave mechanism predicts an up/down asymmetry in plasma loading due to Hall currents [7] which can in turn result in corresponding asymmetries in near-field amplitudes and antenna surface heating, as has been

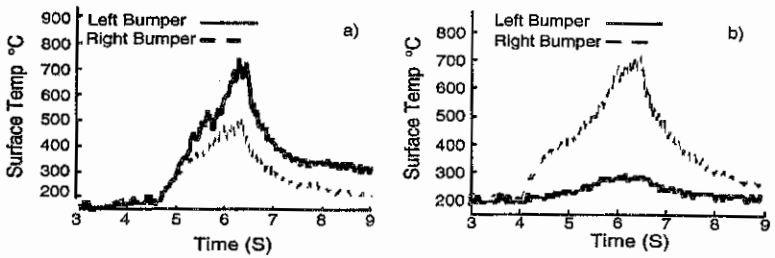

Fig. 4 Time profiles of corner bumper tile temperature for a) $\phi=+\pi/2$, and b) $\phi=-\pi/2$.

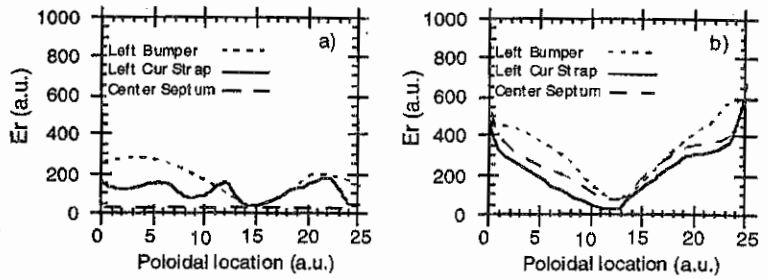

Figure 5. Radial electric field measurements in air 1 cm in front of antenna for a) $\phi=\pi$, and b) $\phi=\pi/2$

shown in RANT code modeling [6]. Small up/down asymmetries have been seen in radial electric fields measured in air in front of the antenna. These arise from asymmetries in surface potentials caused by the antenna resonant circuit geometry. For the $\phi = \pi/2$ case, the difference from the bottom (Poloidal location = 25) to the top (Poloidal location = 0) is ~20%. In addition, convective cells [8] can produce an up down asymmetry due to potentials created by any of these mechanisms. There is considerably less up down asymmetry seen in heating patterns on the older shields. This could be explained by reduced potentials due to the presence of the protruding center septum intercepting static magnetic field lines in the case of the inductive field mechanism. Finally, the local effect of $\pm\pi/2$ phasing on corner bumper tile heating can only be explained by propagating wave effects. This work was supported in part by US DOE Contract DE-AC05-96OR22464.

REFERENCES

1. G.T. Hoang et al., 23rd EPS (Kiev), **20C**, Pt. 1, June 1996, pp. 19-22
2. X. Litaudon et al.,11th Top. Conf. Rf Power in Plasmas,AIP Conf. Proc. 355, pp. 90-101, 1995
3. J. H. Harris et al.,12th Int. Conf. on Plasma-Surcface Interactions, St. Raphael, France, May 20-24,1996
4. J.R. Myra and D. A. D'Ippolito, 11th Top. Conf. Rf Power in Plasmas,AIP Conf. Proc. No. 355, pp. 405-408
5. D. J. Hoffman et al., 11th Top. Conf. Rf Power in Plasmas,AIP Conf. Proc. 355, pp. 368-371
6. M. D. Carter et al., Bul. Am. Phys. Soc., 41, November 1996, p. 1510
7. E. F. Jaeger,"Co-counter Asymmetry in Fast Wave Heating and Current Drive and Profile Control in NSTX, this conference
8. J. R. Myra and D. A. D'Ippolito, Phys. Plasmas, 3,February 1996, pp. 699-701

High power lower hybrid wave coupling to ergodic divertor plasmas

M.Goniche, P.Ghendrih, A.Grosman, P.Froissard, P.Bibet, D.Guilhem, X.Litaudon, G.Rey

Centre d' études de Cadarache
Association Euratom-CEA
F-13108 Saint Paul-lez-Durance, France

1) Introduction

Previous experiments have shown that lower hybrid (LH) current drive can be achieved with the ergodic divertor configuration [1]. In particular, the specific magnetic configuration does not prevent good LH coupling and the current drive efficiency is not significantly affected in most cases. A good impurity screening was also reported. However strongly localized heat fluxes, mainly on the neutralizers of the divertor connected to the LH grills, yielded a limitation of the coupled LH power. Recently, the neutralizers of the divertor have been improved in order to provide a much higher effective area [2,3] and current drive experiments have been carried out at low density ($\bar{n}_e$ = 2.2-2.5 $10^{19}m^{-3}$) and higher RF power (P_{LH} = 4.5 MW) with the LH grills located 1 to 2 cm radially behind the ergodic divertor coils. These experiments are reported here with emphasis on wave coupling, current drive efficiency and heat loads on the components.

2) LH wave coupling

In the ergodic divertor configuration, the pertubed edge magnetic configuration induces modification of the electronic density at the LH grills aperture. When the LH grills are radially in front of the ergodic divertor coils, it was shown that wave coupling was modified according with the flux tubes connexion but the global reflection coefficient $R = \Sigma(P_{ref.})/\Sigma(P_{for.})$ remains low [4]. In the new experiments, the plasma was leaning on the divertor modules and the LH grills were located 1 or 2 cm behind the ergodic divertor coils.-Coupling was first evaluated at low LH power (200 kW). The reflection measured for the 16 RF modules of one antenna is rather uniformally increased compared to a limiter discharge and, for the standard 0° phasing of the modules, the average reflection increases from 4.3 to 6.9 % (figure1). Consistently, the density at the grill averaged on 3 Langmuir probes measurements decreases from 5.6 to 3.8

10^{17} m^{-3}. For the other module phasing (from -90° to +90° allowing the $N//_0$ to be varied between 1.4 and 2.4), a moderate increase by 2-3% of the average reflection is also measured.

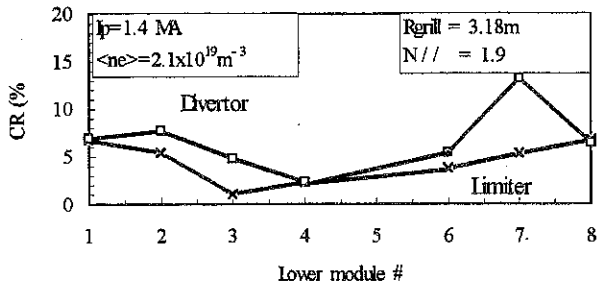

Fig.1 Reflection coefficient for the lower modules in the limiter and ergodic divertor configurations

When the power is increased, a different trend is observed for the 2 rows of 8 modules. The upper modules coupling deteriorates whereas the lower modules coupling improves. For slightly different plasma conditions (Ip=1.3/1.4 MA), the 2 rows show just the opposite behaviour. Globally, with 3.9 MW, the average reflection is almost unchanged (6.6 %) with respect to the low power case. The edge density governing the coupling is measured locally and because of its inhomogeneity in front of the grill, a good correlation between this measurement by probes and the LH coupling is not always found. This density is mainly built up by the rather high recycling which occurs in the edge. The vacuum gauge located in the LH vessel was used to evaluate this recycling (pulses for which breakdowns occur where discarded). A good correlation between the neutral gas pressure in the LH vessel and the coupling is found (figure2). When this pressure is high (above $2x10^{-3}$ Pa), the average coupling can be as low as 3-4 %.

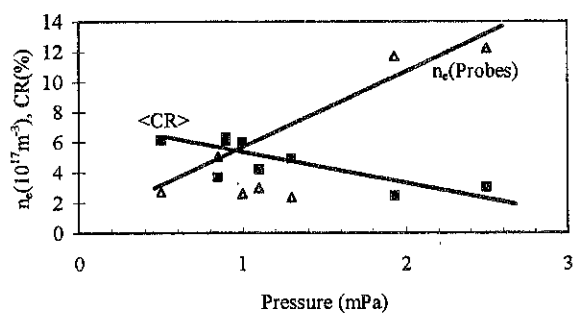

Figure 2 . Average reflection coefficient and edge density vs neutral pressure

No direct effect of the LH power on the pressure and in particular the higher pressure case of figure 2 was obtained at medium power (2.4 MW).

3) Current drive efficiency

Current drive experiments were carried out with the following range of parameters Bt = 2.8-2.9 T, Ip=1.3-1.4 MA, $\bar{n}_e$ = 2.1-2.75 $10^{19}m^{-3}$ in deuterium, P_{LH} = 3.3-4.5 MW (1-2s flat top). The standard phasing of the RF modules was used ($N//_0$ = 1.9). For all these discharges the radiated power was low ($P_{rad}/P_{tot} \approx 20$ %) and the Zeff in the range of 1.9-2.4 (1.9-2.1 for the 1.3 MA series). Spectroscopic measurements indicate that contamination by metallic impurites, from the grills was low ([Cu] < 10^{-3}) and did not increase, in most cases, during the LH power injection. From the loop voltage drop, it is deduced that up to ~ 65 % of the plasma current is driven by the LH waves. In these discharges, the current drive efficiency was evaluated by plotting the relative loop voltage drop $(V-V_0)/V_0$ versus the inverse of the efficiency parameter $P_{LH}/\bar{n}_e.R.Ip$ (Figue 3). Comparison with limiter discharges (performed at higher plasma current) indicates that the current drive efficiency is reduced by 25 % at most. Extrapolations indicate that a 30 s discharge should be achievable at similar densities.

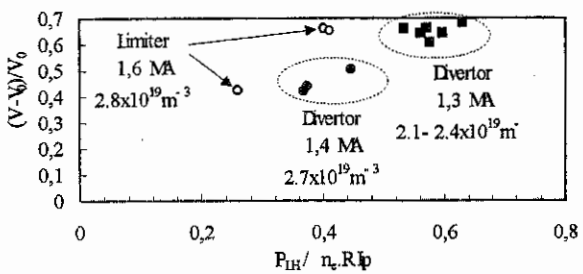

Figure 3 Relative loop voltage drop vs current drive efficiency parameter $P_{LH} / n_e R Ip$

4) Heat load on the grills and the neutralizers of the divertor

In the near-field of the grills, Landau damping of the very high N// components of the excited spectrum ($N_{//}$ > 25) occurs and electrons are accelerated up to a few keV [5,6]. It results high heat flux on plasma facing components which are magnetically connected to the grills. On TdeV, it was established that the heat flux on the connected plates of the divertor scales with the rf power but also with the convective flux in front of the grills Φ_{edge} [7]. The heat flux on one of the neutralizer of the the closest ergodic divertor module to the grill 1 (L//= 1.2 m) was calculated from the surface temperature measured by infra-red imaging. The neutralizer is only connected to the lower row of waveguides of this grill. This heat flux varies linearly with the rf power (P = 0.15-1.7 MW) when normalized to the edge flux (Φ_{edge}=0.6-1.6 MW/m^2) deduced

from the Langmuir probes attached to the grill. The same analysis was performed on the guard limiter of the grill at the point connected to the same row of waveguides. Despite the higher grazing angle of the field line with respect of the surface, the heat flux for the same normalized power is lower, demonsrating that, in this high magnetic ripple zone, the accelerated electrons are marginally intercepted by the guard limiter of the grills (figure 4). For the divertor module located on the opposite side, one neutralizer is connected to both grills and consistently, higher heat flux are measured, in the range of 3 to 8 MW/m^2 (P_{LH}= 2.6-4.5 MW).

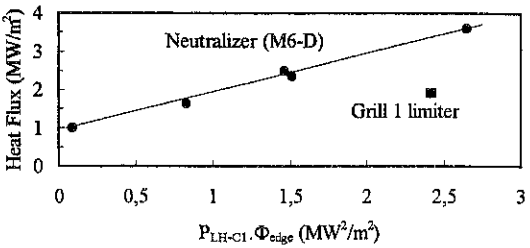

Figure 4. Heat flux on connected neutralizer and grill limiter vs normalized LH power (grill 1).

5) Conclusion

The modification of the ergodic divertor allowed the coupling of large LH power, up to 4.5 MW, with the LH antennas behind the divertor coils. In this configuration low reflection coefficients can be obtained (<R> = 5-6%) and ~65 % of a 1.3 MA discharge was driven by the LH waves. In order to perform long pulse operation, it is needed to optimize the density (or equivantly the convective flux) in front of the grill in order to maitain the heat flux below 7 MW/m^2 on the neutralizers magnetically connected to the grills.

References [1] M.Goniche et al., Proc. of 21st EPS Conf. Monpellier, III, 1042(1994)

[2] B. Meslin et al., this conference

[3] Equipe Tore Supra (presented by P.Ghendrih), this conference

[4] M.Goniche et al., Proc. of 20th EPS Conf., Lisbon, II, 615(1993)

[5] V.Fuchs et al., Phys.Plasmas 3 (11), 4023 (1996)

[6] M.Goniche et al, Rapport EUR-CEA-FC-1598 (1997)

[7] J.Mailloux et al, Nucl. Mat. 241-243 (1997) 745

Competition between electron and ion damping in FWCD scenarios in the JET and Tore Supra experiments.

F. Nguyen, V. Basiuk, P. Zerlauth, B. Beaumont, A. Bécoulet,
V. Bergeaud[1], D. Fraboulet, T. Hutter, L. Ladurelle, Ph. Lotte, B. Saoutic

Association Euratom-CEA, Centre d'Etudes de Cadarache, France.
[1] present affiliation: JET Joint Undertaking, Abingdon, Oxon, OX14 3EA, UK

Introduction

Fast Wave Current Drive (FWCD) scenarios where only the 3rd harmonic D (or He) cyclotron layer is present at the plasma centre have been studied in Tore Supra and JET giving different results concerning the ion damping. The FWCD scenario on ITER is similar to the above configuration in the sense that a 2nd harmonic ion cyclotron resonance is present in the plasma. The understanding of the competition between electron and ion absorptions in FWCD experiment then becomes a crucial element.

Experimental results

Initial experiments in Helium plasmas on Tore Supra have demonstrated efficient direct electron heating [1] whereas the experiments performed at JET in Deuterium plasmas have shown both electron and ion absorption with creation of suprathermal ions (particles with energy > 1.1 MeV detected by Neutral Particle Analyser or deutons with E_d>1.8 MeV due to γ emission, high DD rate and giant sawteeth [2,3]). On Tore Supra, no giant sawtooth or fast particle trapped in the toroidal magnetic ripple (with however a detection threshold around 100 keV for fast ions at centre) has been seen in He (e.g. #17883) or in D (e.g. #19095) plasmas. In the TS shot #17883, a perpendicular (20°) neutral beam injection (0.6 MW with an energy of 70 keV) has been performed overlapping the ICRF pulse (cf fig. 1a). Due to the high density of the plasma (n_l = 6 10^{19} m^{-2}), the power deposition of the beam is mainly at mid radius and the fast ions concentration at the centre is of the order of 5 10^{13} m^{-3}. The figure 1c displays the experimental neutron rate and the neutron rate calculated with plasma-plasma and beam-plasma contributions. The discrepancy between the experiment and the simulation means that fast deutons accelerated by 3rd harmonic cyclotron resonance at centre are present in the ICRF only phase as well as in the combined heating phase. At the switch off of the NBI (t=41.25 s), the decrease of the neutrons rate is very fast with characteristic time ~10 ms. When the ICRF power is switched off (t=39.92 s), the neutron rate has an exponential decrease with a characteristic time ~95 ms. Exponential decreases are also measured on the differents channels of the probe collecting the particles trapped in the magnetic ripple at the ICRF power switch off and NBI switch off (cf. fig. 1b for total ripple loss). For the latter, the characteristic times (5-13 ms) reflect the particle drift from the unconfined edge region to the probe. However, at

the ICRF power stop, the characteristic times are much larger (~ 60 ms) and are compatible with a diffusion from the centre where fast particles are created to the edge where the ripple trapping occurs.

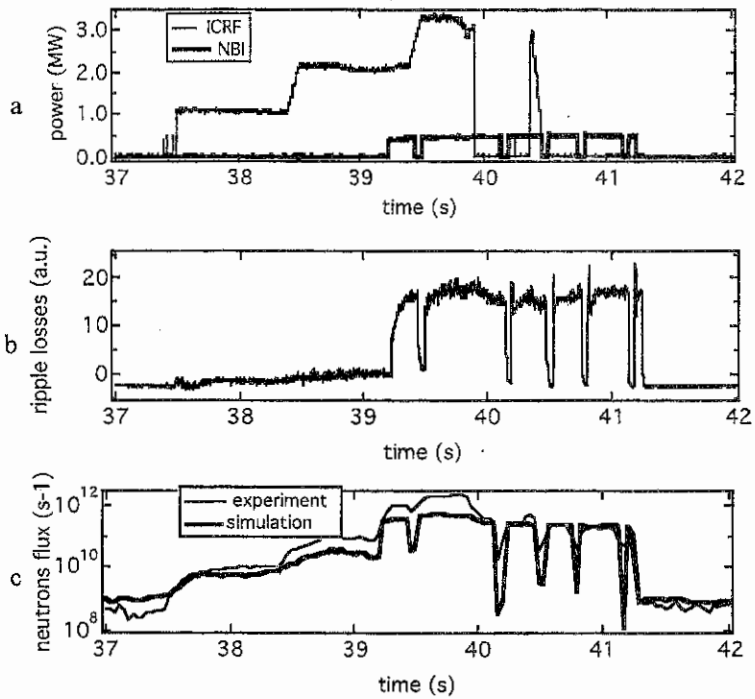

Figs 1: *TS # 17883, He plasma, I_p=750 kA, B_0=2.1 T, f_{ICRF}=48 MHz, dipole phasing.*

Power partitioning with the ABSOR code

The crucial point to understand is the trigger to ion damping in the plasma. Indeed, in steady state RF heated plasmas, ion damping may have two components: one from the bulk ions and an additional one from the fast ions (if created). As the latter contribution increases with the Larmor radius ρ_i of the fast ions (the ion cyclotron n harmonic damping is proportional to $(k_\perp \rho_i)^{n-1}$), the fast ions tail could be self sustained once created [2, 4, 5]. The plasmas of JET (e.g. JET #35320 in He with $0\pi\pi0$ phasing) and Tore Supra (e.g. TS #17883 in He and #19095 in D with dipole phasing) have been carefully studied. A precise analysis taking into account the entire spectrum has been achieved by using the ABSOR code (multipasses approach based on single pass absorption (SPA) calculated with 1D fluid like model [6]) which provides power partitioning and deposition profile for experimental temperature and density profiles [7]. The exponential decrease in the non propagative zone due to the low density of the SOL region

is taken into account. The influence of the parasitic edge losses is also considered since the SPA on bulk ions are low (< 5%). The results are displayed on the tables 1-4. The parasitic damping per reflection at the edge is the second column and the third column is the total percentage of the launched power lost at the edge. The power finally coupled to plasma is then distributed in columns 3, 4 and 5 (the sum of columns 3, 4 and 5 is then 100%). Without parasitic edge absorption, the power deposition on bulk ions is much more favorable on JET (81.8 % on electrons and 18.2 % on ions) than on Tore Supra (# 19095 in D: 95 % on electrons and 5 % on ions; # 17883 in He: 98.9 % on electrons and 1.1 % on ions) due to the difference in the launched spectra between the JET 4-strap and Tore Supra 2-strap ICRF antennae (cf. fig. 2) and the differences in the SPA on electrons and ions (cf fig. 3). These partitionings are probably overestimated on ions due to the 1D geometry that prevents the poloidal effects to occur [7]. The influence of hot ions (0.1% of the bulk ions in concentration) on the power partitioning is also given. Again, the coupling on the fast ions is larger on JET plasmas than on the Tore Supra plasmas. For JET in $0\pi0\pi$ phasing (that provides the same results than $0\pi\pi0$ phasing [2]), the damping on bulk ions is reduced without hot ions (9.6% with no parasitic damping) but recovers the figures of $0\pi\pi0$ phasing on high energy ions (23 % on 1 MeV ions to compare with 26%). This is coherent with a partitioning strongly influenced by the fast ions in JET plasmas. The parasitic edge damping between 0 and 5% per reflection does not modify the partitioning between ions and electrons but leads to a larger total edge absorption on JET due to the lower electron SPA.

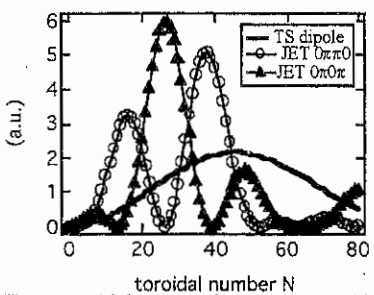

Fig.2: *toroidal spectra for Tore Supra (dipole phasing) and JET ($0\pi\pi0$ and $0\pi0\pi$ phasings)*

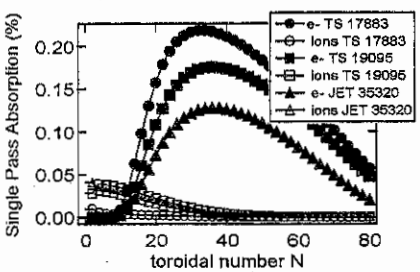

Fig. 3: *single pass absorptions on electrons and bulk ions in the RF phase*

Ripple loss simulations

Simulations of the ripple losses on Tore Supra have been performed with a Monte Carlo code taking into account the collisions [8]. For a distribution function with E_{max}=0.6 MeV, the influence of the plasma current is low: 7% of losses at I_{plasma}=2 MA and 9.2 % of losses at I_{plasma}=0.6 MA. Indeed, a fast particles distribution function is possible at moderated plasma current as minority heating has been achieved at 1 MA (TS # 19766 in D plasma). This value is to be compared with the 0.9 MA current of the TS deuterium pulse #19095 in FWCD scenario. Concerning the ripple loss, the main effect lies in the the absolute value of the magnetic ripple.

A simulation with a ripple reduced by a factor 10 (close to the JET value) shows a drastic reduction of fast particles losses (1.4%).

Conclusion

In Tore Supra, some Fast Wave damping on bulk ions at the 3rd harmonic layer cyclotron resonance has been seen in FWCD scenario but does not lead to a fast particle distribution function with energy in the MeV range as it is the case in JET. There is also evidence of FW3DH on the fast particles produced by NBI in Tore Supra. The power depositions calculated with the ABSOR code reflect the gross tendancy of a much larger ion damping on JET plasmas (especially if the fast ion tail is preponderant) compared to Tore Supra plasmas.

References

[1] Equipe Tore Supra, 15th IAEA Conference, Séville. IAEA-CN-60/A-3-I-6 (1994).

[2] F. Nguyen *et al.*, 22nd EPS Conference, Bournemouth (UK), **19C-II**, 353 (1995).

[3] The JET Team, 16th IAEA Conference, Montréal. IAEA-CN-64/O1-4 (1996).

[4] The JET Team, 16th IAEA Conference, Montréal. IAEA-CN-64/A2-6 (1996).

[5] L.-G. Ericksson *et al.*, to be submitted to *Nucl. Fusion* (1997).

[6] D. Fraboulet *et al.*, 21st EPS Conference, Montpellier (France), **18B-II**, 660 (1994).

[7] F. Nguyen *et al.*, 12th Top. Conf. on RF Power in Plasmas, Savannah (Georgia) (1997).

[8] V. Basiuk *et al.*, 23rd EPS Conference, Kiev, **20C-III**, 1092 (1996).

edge losses (%)	total edge absorption (%)	electron (%)	bulk ions (%)	hot ions (%)	T_{hot} ions (keV)
0	0	81.8	18.2	0	2.7
1	10	83.5	16.5	0	2.7
5	33.8	86.6	13.4	0	2.7
0	0	77.9	13.9	8.2	100
1	8.9	79	13.2	7.8	100
5	31.6	81.5	11.6	6.9	100
0	0	63.4	10.1	26.5	1000
1	7	64	9.8	26.2	1000
5	26.6	65.6	9	25.4	1000

Table 1: *JET #35320 dipole phasing (0π0)*

edge losses (%)	total edge absorption (%)	electron (%)	bulk ions (%)	hot ions (%)	T_{hot} ions (keV)
0	0	98.9	1.1	0	0.9
1	5.8	99.3	0.7	0	0.9
5	21.8	99.6	0.4	0	0.9
0	0	95.7	0.5	3.8	100
1	5.3	96	0.4	3.6	100
5	21	96.4	0.4	3.2	100
0	0	85	0.4	14.6	1000
1	4.6	85.1	0.4	14.5	1000
5	18.9	85.5	0.3	13.3	1000

Table 2: *TS#17883 dipole phasing (the hot ion is He)*

0	0	90.4	9.6	0	2.7
1	9.2	90.8	9.2	0	2.7
5	31.8	91.5	8.5	0	2.7
0	0	86.8	8.2	5	100
1	8.8	87	8.1	4.9	100
5	30.7	87.5	7.8	4.7	100
0	0	70.6	6.3	23.1	1000
1	7.3	70.6	6.3	23.1	1000
5	26.4	70.7	6.1	23.2	1000

Table 3: *JET #35320 dipole phasing (0π0π)*

0	0	95	5	0	1.8
1	6.4	95.2	4.8	0	1.8
5	24.8	95.7	4.3	0	1.8
0	0	90.2	3.6	6.2	100
1	6	90.2	3.6	6.2	100
5	23.5	90.2	3.6	6.2	100
0	0	79.4	3.6	17	1000
1	5.3	79.5	6.6	14.5	1000
5	21.3	79.8	3.4	16.8	1000

Table 4: *TS #19095 dipole phasing*

Full wave simulation of lower hybrid current drive in tokamaks

Yves Peysson, Eric Sébelin, Xavier Litaudon, Didier Moreau, Jean-Claude Miellou*
Magdi Shoucri**, Issie Shkarofsky**

Département de Recherches sur la Fusion Contrôlée, Association Euratom-CEA,
Centre d'Etudes de Cadarache, 13108 St. Paul lez Durance Cedex, France
**Université de Mathématiques Appliquées de Franche-Comté, Besançon, France*
***Centre Canadien de Fusion Magnétique, Varennes, Québec, Canada J3X 1S1*

Abstract. Full wave calculations based on the use of eikonal trial functions which are locally solutions of the homogeneous problem are carried out for the lower hybrid current drive problem in tokamaks. The lower hybrid power deposition profile as well as the non-inductive driven current are determined self-consistently with a two-dimensional relativistic Fokker-Planck solver. Simulations for the high aspect ratio tokamak TRIAM-1M are presented.

1. Introduction

Up to now, the modeling of lower-hybrid (LH) current drive experiments in tokamaks has largely relied on ray tracing to describe the propagation and absorption of the LH wave [1]. Though numerous features of the LH dynamics may be explained by ray tracing, in particular the broadening of the LH power spectrum launched into the plasma as an inherent consequence of the toroidal geometry [2], it turns out that for most parameter regimes of practical interest, geometrical optics fails to hold [3]. Indeed, LH rays suffer usually multiple reflections between the low density cut-off layer at the edge and the "whispering gallery" layer in the plasma core before being significantly damped. For the highest phase velocity part of the launched spectrum, such a multireflexion process lead to electromagnetic chaos, for which geometrical optics assumptions are no more valid, and a large uncertainty in the predictions of the radial and spectral absorption of the LH wave may take place. In this stochastic regime, a more appropriate description of the wave dynamics corresponds to a quasilinear exchange of electromagnetic energy between a large number of LH modes in the bounded geometry [4]. However, because of the very small wavelength of the electromagnetic field at the LH frequency, a conventional full wave analysis represents a extremely difficult numerical task, far beyond computer capabilities [5]. If the phase information of the wave field is ignored, it is nevertheless possible to study the propagation of these short-wavelength modes in weakly inhomogeneous and slowly time-varying medium by solving the wave kinetic equation [6]. Since the Hamiltonian structure of the ray equation gives rise to an incompressible flow in six-dimensional phase space, this approach allows to remove singularities at turning points which are usually encountered in the traditional ray tracing techniques. It is then possible to make an explicit statistical treatment of the wave propagation physics, which is valid in the multipass regime when the stochastic nature of the wave dynamics comes fully into play.

Though the wave diffusion model is equivalent to the normal mode master equation based on an expansion of the toroidal wave equation in terms of cylindrical eigenmodes, the lack of description of all node structures due to interferences between ingoing and outgoing waves which may develop especially in the vicinity of turning points in the weak absorption regime, may significantly modify the self-consistent wave spectrum and the radial profile of the absorbed power density. Indeed, phase correlations may give rise to large local variations of the wave electric field around the averaged solution given by the wave kinetic equation, even if the interference pattern lies on a small scale length [6]. This problem is adressed in the present work, by full wave calculations based on a variational technique [4], which provides an efficient scheme to describe in a global manner both the propagation and absorption of electromagnetic waves in plasmas. The resulting solution, with self-consistent coupling to the two-dimensional relativistic Fokker-Planck equation is restricted to the current drive application of the LH wave [7]. Though calculations are carried out for a cylindrical equilibrium, they may be applied for experiments on large aspect ratio tokamaks like TRIAM-1M [8], for which both toroidal and magnetic ripple corrections in the LH wave dynamics are negligible [9,10] .

2. LH wave propagation and absorption

The variational scheme that is used for LH current drive calculations is based upon the use of eikonal trial functions, which are local solutions of the homogeneous problem. It allows to describe the electromagnetic field over a scale length which can be larger than the wavelength [4]. This approach greatly reduces the number of unknowns of the problem as compared to a conventional finite element method, in which each spatial oscillation of the field must take place over several much smaller elementary cells. The plasma volume is therefore divided non-uniformly into concentric ring shaped cells, so that plasma parameters may be considered as homogeneous over their radial sizes, with respect to the gradient scale length.

As this study is restricted to current drive application of the LH wave, the wave frequency is well above the LH resonance frequency, so that mode conversion to hot electrostatic plasma waves or ion Bernstein waves can be completely avoided. In these conditions, the wave dynamics may be accurately described in the cold plasma approximation, which supports two independent modes of propagation, the slow wave which corresponds to a cold electrostatic plasma wave, and the fast wave, namely the whistler wave. Because of the simultaneous presence of the slow and fast propagation branches, a vectorial wave equation must be solved, which incorporates mode conversion usually occuring in such experiments. The plasma current $\mathbf{j}(\mathbf{r})$ linear response to the oscillating electric field $\mathbf{E}(\mathbf{r})$ is given by $\nabla\times\nabla\times\mathbf{E}(\mathbf{r}) = \omega^2\varepsilon_0\mu_0\mathbf{E}(\mathbf{r}) + i\omega\mu_0(\mathbf{j}(\mathbf{r}) + \mathbf{j}_a(\mathbf{r}))$, where $\mathbf{j}_a(\mathbf{r})$ is a current source equivalent to the electric field excited at the antenna, and ω the pulsation of the radiofrequency field. Here $\mathbf{j}(\mathbf{r})$ is related to $\mathbf{E}(\mathbf{r})$ through the cold local conductivity tensor. By performing an appropriate integration of the above equation over the volume of interest V previously multiplied by $\delta\mathbf{E}^*(\mathbf{r})$, which characterizes any wave field perturbation, it may be shown that the variational scheme reduces to find the stationary point of the bilinear form with respect to all possible variations of $\mathbf{E}^*(\mathbf{r})$, $L(\mathbf{E},\mathbf{E}^*) = \int_V dV\left[(\nabla\times\mathbf{E}).(\nabla\times\mathbf{E}^*) - \omega^2\varepsilon_0\mu_0\mathbf{E}^*.\overline{\overline{\mathbf{K}}}.\mathbf{E} - i\omega\mu_0(\mathbf{E}^*.\mathbf{j}_a)\right]$ subject to the condition $\mathbf{n}\times\delta\mathbf{E}^* = 0$ on the volume boundary, together with the principal condition $\mathbf{n}\times\mathbf{E} = 0$ on the same boundary. Here $\overline{\overline{\mathbf{K}}}$ represents the cold electromagnetic dielectric tensor. Provided some dissipation is assumed to take place at every point within the volume V, it can be shown that the field inside this volume is uniquely determined whenever $\mathbf{n}\times\mathbf{E}$ is given at each point of the boundary. Therefore, the boundary condition $\mathbf{n}\times\mathbf{E} = 0$ corresponding to a perfectly conducting wall which is assumed here, is sufficient to ensure uniqueness of the solution.

For a cylindrical equilibrium, eikonal trial functions are determined in each plasma cell labelled by an index ℓ varying from 1 to L, by solving Maxwell's equations in the local frame of reference. They can be expressed as $\mathbf{E}(r,\theta,\phi) = \exp(in\phi + im\theta)\sum_{\ell=1}^{L} H_\ell(r)\sum_{i=1}^{4}\alpha_{i,\ell}\mathbf{E}_{i,\ell}r^{\lambda_{i,\ell}}$, where $\lambda_{i,\ell}$ are eigenvalues of the system of equations, which correspond physically to the slow and fast waves propagating both inward and outward. The polarization vector for the electric field $\mathbf{E}_{i,\ell}$ is nothing but the associated eigenvector, $H_\ell(r)$ is a step function the value of which is one in the ℓ-th cell and zero everywhere else, and n and m are respectively the toroidal and poloidal mode numbers. The set of scalar unknowns $\alpha_{i,\ell}$ is determined by the variational principle, so that local conditions $\mathbf{n}_\ell\times\mathbf{E}_\ell = -\mathbf{n}_{\ell+1}\times\mathbf{E}_{\ell+1}$ may be satisfied at boundaries of each plasma cell.

Both collisional absorption and resonant Landau damping of the LH wave are taken into account, by including the corresponding anti-hermitian contribution in the dielectric tensor. For an accurate determination of the non-inductive driven current, a two-dimensional relativistic Fokker-Planck equation is solved [7], and the electron distribution function f_e is determined self-consistently with the quasi-linear diffusion coefficient as for convential ray-tracing

simulations. Because of the global treatment of both the wave propagation and absorption in the full wave analysis, an additional iteration process is carried out, until the parallel component of the wave electric field, with respect to the local equilibrium magnetic field direction, can be also estimated in a self-consistent manner with the distribution function. The resonant wave absorption rate γ by Landau damping is thus given by $\gamma = -\frac{e^2\pi\omega}{k_{//}^2 m_e}\mathrm{sgn}(k_{//})\left[\frac{\partial F_e}{\partial v_{//}}\right]_{v_{//}=\omega/k_{//}}$ for all values of n and in each cell, where $F_e(v_{//}) = \pi\int_0^{+\infty} f_e(v_{//},v_\perp)dv_\perp^2$, and $f_e(v_{//},v_\perp)$ is determined from the Fokker-Planck equation. Here $k_{//}$ is the wave vector component parallel to the local magnetic field direction. For a set of n values, the quasi-linear diffusion coefficient is $D_{ql} = \sum_n \frac{\pi}{2}\frac{e^2}{m_e^2}\delta(\omega - k_{//}^n v_{//})\left|E_{//}^n\right|^2$.

3. Full wave simulation of a current drive experiment

Simulations are carried out for a straight cylindrical equilibrium, which includes a rotational transform as a result of the current flow in the plasma. Flux surfaces are circular and concentric. Calculations are carried out for the high aspect ratio tokamak TRIAM-1M, which is dedicated to steady state operation studies [8]. With a plasma major radius of R = 83 cm, and a minor radius of a = 11 cm, the traditional toroidal parallel refractive index upshift which is invoked to bridge the spectral gap is quite negligible, and therefore, the underlying mechanism to explain how the LH wave may be damped in the plasma remains to a large extent unclear [9]. Recently, it has been pointed out that the toroidal magnetic ripple due to the reduced number of coils (16) is not able to offer a plausible alternative to the lack of toroidal $n_{//}$-upshift [10]. Hence, as both poloidal and toroidal inhomogeneities fail to account for experimental observations without streching too much the ray-tracing picture, it is a unique opportunity to investigate the LH wave dynamics without the WKB approximation.

Central main plasma parameters used for simulations are: T_{e0} = 1keV, $n_{e0} = 1.0\times10^{+19}$ m^{-3}, while central and edge safety factors are respectively q_0 = 1 and q_a = 3. All radial dependences are considered to be parabolic. The magnetic field on axis is 5T, the LH frequency f_{LH} = 2.45 GHz, and 30 kW of LH power are coupled to the plasma. The number of radial cells is set to 113 for accurate calculations, and for the Fokker-Planck solver, the computational domain is divided into $n_\mu \times n_p$ = 120×150 grid points, where n_μ and n_p are respectively the number of angular and momentum points. Simulations are carried out for a phase shift $\Delta\phi$ = 130° between adjacent waveguides [8]. In this case, the positive part of the launched power spectrum peaks at $n_{//}$ = 2.2 and extends up to $n_{//} \approx 4$. The negative part which lies between $n_{//}$ = -2.4 and -6 represents 30% of the LH power launched in the plasma (Fig. 1). For calculations, the spectrum is divided into 75 slices. Because of the low electron temperature, the damping rate of the LH wave is very weak, leading to large numerical instabilities when only the positive part of the power spectrum is considered. Indeed, in this case, the electric field level becomes very high, and the normalized quasilinear diffusion coefficient exceeds usual values (1-20) for which the numerical scheme to solve the Fokker-Planck equation is stable. This result indicates that node structures of the electric field do not contribute significantly to a modification of the LH wave absorption process in the plasma. However, if the full launched power spectrum is taken into account, an effective absorption of the LH wave occurs, as a result of the strong damping of the negative part. Because of pitch-angle scattering, a significant amount of fast electrons are scattered towards the positive direction, and the low-$n_{//}$ positive part of the power spectrum may be absorbed. Such a process is intimately linked to the bidimensional nature of the fast electron dynamics in momentum space (Fig. 2). Nevertheless, even if an efficient damping is observed, it turns out that the resulting current level remains very low and fairly negligible as compared to the experimental observation, I_p = 28 kA, (Fig. 3). As only a very

weak non-inductive current level is predicted, it has been checked that the LH power is mainly carried by the slow wave branch, for the accessible part of the launched power spectrum. In Fig. 4, it is shown that the slow wave branch is effectively excited at the antenna, and that the contribution of the fast wave remains almost negligible everywhere in the plasma. To recover the experimental level of the non-inductive driven current, it is necessary to introduce a large ad-hoc spectral broadening of the launched power spectrum. Hence, for a boxcar power spectrum lying between $n_{//} = 1.4$ to 7.8, a non-inductive current of 28 kA is found, for 30 kW of LH power. Such a result indicates that interferences do not contribute to an enhancement of the power absorption process, even when the LH damping rate is weak. However, the exact treatment of the wave dynamics which is here presented allows to investigate accurately other potential mechanisms to bridge the spectral gap, when toroidal corrections are negligible.

4. References

[1] Y. Peysson, R. Arslanbekov, V. Basiuk, J. Carrasco, X. Litaudon and J. P. Bizarro, Phys. Plasmas **3**, 3668 (1996).
[2] J. P. Bizarro, Nucl. Fusion **32**, 1845 (1992).
[3] M. Brambilla and A. Cardinali, Plasma Phys. **24**, 1187 (1982).
[4] D. Moreau, Y. Peysson, J. M. Rax, A. Samain and J. C. Dumas, Nucl. Fusion **30**, 97 (1990).
[5] K. Kupfer, D. Moreau and X. Litaudon, Phys. Fluids B **5**, 4391 (1993).
[6] D. Moreau, J. M. Rax, A. Samain, Plasma Phys. Controlled Fusion **31**, 1895 (1989).
[7] M. Shoucri and I. Shkarofsky, Comp. Phys. Commun. 82, 287 (1994).
[8] S. Moriyama, Y. Nakamura, A. Nagao, E. Jotaki, K. Nakamura, N. Hiraki and S. Itoh, Nucl. Fusion **30**, 47 (1990).
[9] H. Takahashi, Phys. Plasmas, **1**, 2254 (1994).
[10] J. P. Bizarro and R. Nakach, to be published.

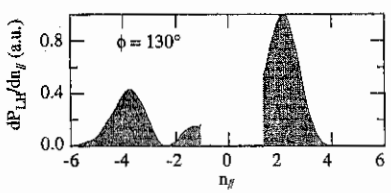

Fig. 1: Launched LH power spectrum

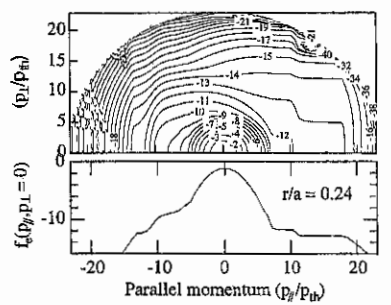

Fig. 2: Electron momentum dynamics

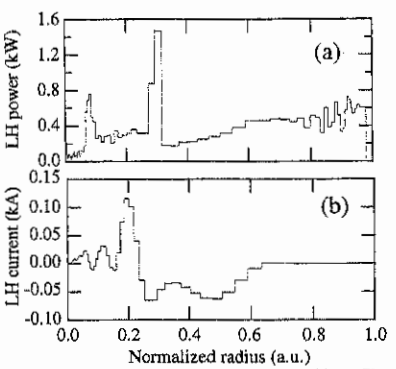

Fig. 3: Power deposition (a) and current (b) profiles

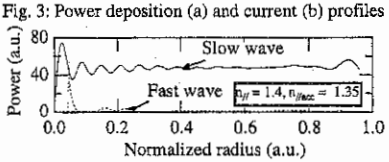

Fig. 4: Power deposition profiles for each mode

Fast Electron Bremsstrahlung Tomography on TORE SUPRA

Yves Peysson, Léna Delpech, Frédéric Imbeaux, X. Litaudon, E.Sébelin

Département de Recherches sur la Fusion Contrôlée, Association Euratom-CEA, Centre d'Etudes de Cadarache, 13108 St. Paul lez Durance Cedex, France

Abstract. Experimental validations of the instrumental design of the new fast electron bremsstrahlung camera installed on TORE SUPRA are presented, as well as first results of power deposition profiles during lower hybrid current drive experiments.

1. Introduction

The control of the non-inductive current density profile is a critical issue to increase performances of tokamak plasmas, and to achieve steady-state discharges in reactor-like conditions. During the last past years, such studies have been carried out in detail on the TORE SUPRA tokamak, by an extensive use of the lower hybrid (LH) wave to sustain a fast current carrying electron tail. Besides the discharge where the ohmic current has been fully replaced during more than 75 s with 3 MW of LH power, stationary states with magnetic shear reversal have been also successfully obtained, leading to enhanced plasma performances, so-called LHEP regimes [1]. These regimes, which are now routinely obtained on TORE SUPRA, are characterized by a rapid increase of the central electron temperature, few seconds after the LH power has been switched on. This sudden rise of the core electron temperature is usually ascribed to the onset of an internal thermal transport barrier, though no clear direct evidence of such a process has been yet demonstrated [2]. However, even if off-axis LH power deposition profiles have been observed experimentally from the fast electron bremsstrahlung emission at high energy when operating conditions correspond to a poor accessibility of the LH wave [2], it is a critical issue to determine wether the radial dependence of LH power absorption remains similar for resonant electrons whose energy is much lower, but well above the thermal bulk. Though their contribution to current drive is likely negligible and may be therefore not identified by time evolution of plasma parameters, they can lead to a direct and efficient core plasma heating and an apparent thermal transport barrier. Such an analysis is supported by recent measurements of the non-thermal bremsstrahlung emission on the TdeV tokamak during similar current drive experiments. Indeed, the non-thermal bremsstrahlung emission profile which is hollow at high energy, in agreement with ray-tracing simulations, becomes peaked and broad at energies much lower than expected as compared to the launched power spectrum, but well above thermal energies [3]. However, the coarse spatial resolution of all x-ray diagnostics used for experiments either on TdeV or TORE SUPRA tokamaks prevents from having a precise insight on the fast electron dynamics in momentum space as a function of radial position [3,4]. For this purpose, a new fast electron tomographic system has been designed for TORE SUPRA [5,6]. Experimental assessment of diagnostic performances for various operating conditions is presented, as well as first results obtained with the full tomographic system.

2. Experimental set-up and performances of the diagnostic

The fast electron tomographic system is designed to record the hard x-ray emission between 20 and 200 keV, with requirements of high time and space resolutions [5]. In order to fulfill severe additional constraints that result from a high ambiant magnetic field, high neutron and γ ray fluxes with deuterium plasmas and the lack of place in the near vicinity of the tokamak, it is based on the use of room-temperature semiconductor CdTe detectors which exhibit, besides their high x-ray stopping efficiency, several nice properties for this purpose [5,6]. The tomographic system is made of a horizontal and a vertical camera with respect to the

equatorial mid-plane, each with 21 and 38 detectors respectively. At present time both cameras are installed on TORE SUPRA. They have been designed to be very compact as shown in Fig. 1, in order to save place and reduce the amount of matter in the near vicinity of the detectors. In such a way, the number of interactions between neutrons and the shielding is expected to be low. The large redundancy in spatial measurements in the inner half of the plasma volume allows to get accurate details of the non-thermal bremsstrahlung emission in the core of the plasma, even if the radial profile is hollow like in usual magnetic shear reversal experiments sustained by the LH wave. By an appropriate filtering of raw data using the well known bi-orthogonal decomposition method [7], it is possible to estimate consistently from both time and space evolutions all averaged signal levels an corresponding error bars, according to the Poisson statistic.

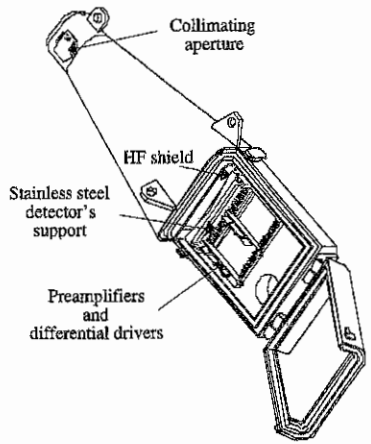

Fig. 1: Fast Electron Bremsstralung tomographic system, horizontal camera (21 CdTe detectors).

For each chord, a spectral analysis of 8 energy channels of width 20 keV is carried out. Even if only a coarse spectrometry is performed, it is possible to estimate accurately the photon temperature, a critical parameter for synergy experiments between the LH and ion Berstein waves in view to improve current drive efficiency. In Fig. 2, recorded hard x-ray energy spectra for a central chord at different plasma electron temperatures are presented. Within a large energy range, a quasi-exponential decrease of the non-thermal bremsstrahlung emission is observed as shown in previous experiments [4], and the related photon temperature increases with the bulk electron temperature, a well known and expected behavior. Departures from the exponential-like dependence at low energy may be ascribed to the contribution of thermal electrons to the bremsstrahlung emission, while at high energy, the count rate becomes low and as a result the dispersion of the data is large.

With 2 mm thick detectors, high counting rates up to 150 kHz may be achieved without significant distortion of the energy spectrum because of carrier mobility [8], and a time resolution of 4 ms has been obtained successfully. In Fig. 3 a typical time evolution of the non-thermal bremsstrahlung emission is displayed for a central chord, with a time sampling of 16 ms. It should be emphasized that a time resolution down to 1 ms may be foreseen without any difficulty during burst acquisitions, on the basis of observed performances of the diagnostic.

The ability to measure the non-thermal bremsstrahlung emission in presence of a high thermonuclear neutron flux has been adressed during realistic combined heating experiments. As shown in Fig. 4, the noise level induced for photon energies larger than 40 keV remains fairly negligible as compared to the bremsstrahlung signal, though the ion cyclotron power reaches 4 times the launched LH power level, and the neutron rate exceeds $4.0\times10^{+12}$ s^{-1}. This result confirms that operating conditions of the diagnostic with deuterium plasmas have been

greatly enhanced as compared to the previous system installed on TORE SUPRA [4]. It can be inferred from the use of thin detectors and an appropriate design of the X/γ shielding, made of a thick layer of lead (20 mm) in between two thin layers of stainless steel (5 mm). In the photon energy range 20-40 keV, the large signal which is observed without any fast electron tail results from electron heating of the plasma bulk.

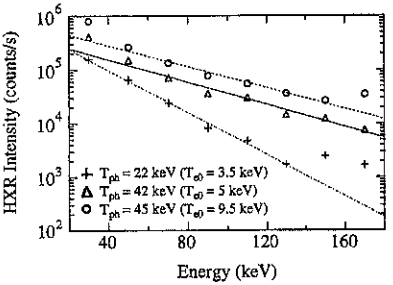

Fig. 2: X-ray energy spectra

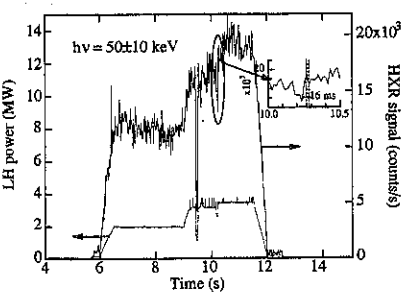

Fig. 3: Time evolution of the hard x-ray signal for a central ch

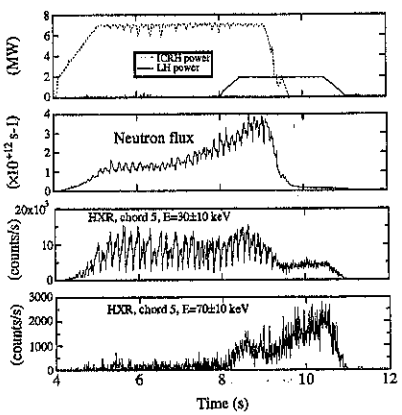

Fig. 4: HXR measurements with high neutron flux

3. Results

Profile reconstruction capabilities of the tomographic system have been investigated by performing LH wave accessibility experiments. Electron density scans for line averaged values ranging between 2.0 and $6.0\times10^{+19}$ m^{-2} have been carried out for two toroidal magnetic field values, 2.2 and 3.9 T. The plasma current is kept constant at I_p = 0.8 MA, as well as the LH power, which is set at a low level of 0.8 MW. Profile reconstruction are carried out using the Fischer's information technique for the photon energy range between 60 and 80 keV. The plasma emissivity is considered to be constant on flux surfaces and its number is set to 30. As shown in Fig.5a, a significant modification of the x-ray emission profile is observed when the electron density is increased, at high toroidal magnetic field. Though x-ray emission profiles remain roughly peaked, they become progressively narrow when the electron plasma density increases. This result is in agreement with previous analysis obtained with the former hard x-ray diagnostic [4], and confirms that the magnetic ripple may affect significantly the LH power deposition profile [9]. When the density exceeds $4.0\times10^{+19}$ m^{-2}, the signal level becomes very

low, but the high data redundancy enables to have nevertheless an accurate estimate of the local profile. At a lower toroidal field value, the non-thermal bremsstrahlung emission is much broader, and sharp structures in the profiles may be clearly observed (Fig. 5b). These structures are more pronounced at high density, but remain at the same plasma radius. Detailed analysis will be carried out to assess the origin of such complex radial dependence of the x-ray emission. It must be emphasized that the consistency between data obtained with both cameras clearly indicates that wall contribution is negligible, as compared to plasma emissivity. However, when the LH input power level becomes high, Abel inversion of line integrated data is often difficult, because of the occurrence of very large poloidal inhomogeneities of the non-thermal bremsstrahlung emission. This is likely due to fast electron hot spots on first inner wall of the tokamak.

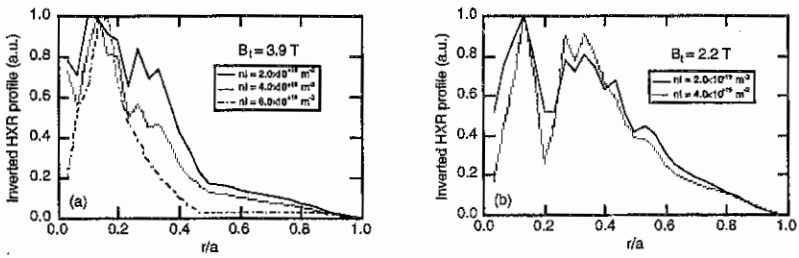

Fig.5: X ray emission profile between 60 and 80 keV

4. Conclusion

A powerful tomographic has been installed succesfully on TORE SUPRA to study the non-thermal bremsstrahlung emission during LH current drive experiments. All results show that CdTe technology is appropriate for accurate measurements performed in a severe environment like a tokamak, with high time varying magnetic fields and large neutron rate. Profile reconstructions of the local non-thermal bremsstrahlung emission have shown the high sensitivity of the diagnostic as a consequence of the large data redundancy, even if the signal level is low.

5. References

[1] Equipe Tore Supra, Plasma Phys. Control. Fusion 38 A251 (1996).

[2] X. Litaudon, R. Arslanbekov, G.T. Hoang, E. Joffrin, F. Kazarian-Vibert, D.Moreau, Y. Peysson, P. Bibet, P. Froissard, M. Goniche, G. Rey, J. Ferron and K. Kupfer, Plasma Phys. Control. Fusion 38 1603 (1996).

[3] Y. Peysson, P. Brooker, R. Arslanbekov, M. Shoucri, I. P. Shkarofsky, X. Litaudon, A. Côté, C. Côté and Y. Demers, 37th APS-DPP Conference, Louisville, USA (1995).

[4] J.P. Bizarro, Y. Peysson, P.T. Bonoli, J. Carrasco, T. Dudok de Wit, W. Fuchs, G.T. Hoang, X. Litaudon, D. Moreau, C. Pocheau and I.P. Shkarofsky, Phys. Fluids B 5, 3276 (1993).

[5] Y. Peysson and R. Arslanbekov, Nucl. Instr. Methods A, 380, 423 (1996).

[6] Y.Peysson, 23th EPS Conf. Controlled Fusion and Plasma Physics, Kiev, Ukrain, Vol. 20C, 1096 (1996).

[7] T. Dudok de Wit, A. L. Pecquet, J. C. Vallet and R. Lima, Phys. Plasmas 1, 3288 (1994).

[8] G. Knoll, Radiation Detection and Measurements, 2nd Edition (John Wiley & Sons, 1989).

[9] Y. Peysson, R. Arslanbekov, V.Basiuk, J. Carrasco, X. Litaudon, D.Moreau and J.P. Bizarro, Phys. Plasmas 3, 3668 (1996).

THE NEW BOLOMETRIC DIAGNOSTIC ON TORE SUPRA

J.-C.Vallet, C.Balorin, M.Jouve, M.Mattioli, A.-L.Pecquet, D.Guilhem.
DRFC Association CEA-EURATOM sur la Fusion
CE Cadarache F13108 Saint-Paul-Lez-Durance

Introduction: Given the important role of radiation, in present scenarios, for the control of the thermal flux in a thermonuclear reactor, it appears that both the absolute measurement of the total radiated power and its spatial structure are crucial parameters which have to be accurately determined[1].

On TORE SUPRA , correlatively with the increasing effort made to produce, control and analyse edge radiating layers in both Ergodic Divertor and limiter experiments, a project of improvement of the bolometric diagnostic has been conducted these two last years. Two guidelines have been followed in its definition : i) allowing a check of the toroidal symmetry assumption usually made in the estimated total radiated power; ii) in case of weak toroidal asymmetry, the possibility of performing tomographic reconstruction of the plasma emissivity. To reach this goal the number of bolometer has been brought from 16 to 48, mounted in six bolometric cameras located at three different toroidal angles, allowing us to record three full plasma profiles: two from a top port and one from an equatorial port.

After a description of the diagnostic itself , first results obtained with the full system in the last campaign, mainly devoted to ''non highly radiative experiments'' will be reported in this paper.

Detectors, cameras and electronics. The detectors used are those developed for AUG and TS[2,3]. Detectors of the same type are used on JET, ALCATOR-C-M, W7AS....These detectors are assembled in four channel module. Each channel is made of two bolometers for differential measurements. A bolometer is composed of a gold absorber $2x3x0.004mm^3$ and of two 1.2kΩ electrical resistors. Absorber and resistors are deposited on the two sides of a 7.5μm thick Kapton foil. Kapton limits the temperature range of use of these bolometer modules below 100°C. TS being currently operated at wall temperature up to 200°C, cameras have been installed outside the vacuum vessel and are connected to the torus by a valve. The new cameras are movable and can be operated at wide opening poloidal angle (21°) corresponding to the observation of a full plasma radius or at small opening poloidal angle (10.5°) for better spatial resolution.

The electronic part of the diagnostic has been rebuilt. Three objectives have been pursued: i) cost minimizing ii) low maintenance, iii) no degradation of the inherent quality of bolometer signals. In the previous version of the electronics (coupled power supply for 4 channel 40Vpp 50kHz) [2, 3], the measurements were made after an external balancing of the a.c. Wheatstone bridge, such that both zero signal and zero a.c. bridge voltage merged. This had three major effects: i) signals of very low amplitude have to be carried in a noisy environment: costly cabling, ii) near the zero voltage of the a.c. Wheatstone bridge the phase is strongly varying: need for frequent or automatic adjustments, iii) low amplitude signal implies powerful and costly detection technique: synchronous demodulator.

In the new version of the TS bolometer electronics, these three problems have been removed by superimposing to the bridge voltage signal an a.c. offset voltage of about .5% of the bridge generator voltage. The phase of the offset voltage is such that irradiation of the measuring bolometer causes an increase of the bridge voltage. At this voltage level a simple amplitude demodulator and offset subtraction is enough to extract the signal. The control of the phase is no longer necessary: the offset voltage being chosen high enough to be in phase with the generator voltage. The offset voltage provides a carrier for signal and cheap conventional cable can be used. No effect, neither on the sensitivity nor on signal to noise ratio nor on the linearity have been found associated with the use of the new electronic. On TS the offset voltage is produced by a set of additional resistors which can be connected in parallel with one reference bolometer resistor. One may envisage for future detectors to generate directly this offset voltage in the bolometer head by increasing the measuring resistors of about 1% with respect to the reference resistors.

Toroidal asymmetries in TS : The last campaign devoted to low radiative regime has been a good test to analyse the sources of toroidal asymmetries of the plasma emissivity. It has been found that they are mainly due to a break of the toroidal symmetry of the plasma facing

components produced either by the introduction in the scrape off layer of modular elements such as modular limiters or rf antennas or by the appearance of hot spots on the inner first wall which is fully covered with graphite tiles. Concerning modular pfc the situation on TS is quite complicated : the machine is composed of six toroidal modules quoted Q1 to Q6, each being made of two parts QnA and QnB, each having three access ports to the plasma chamber : one top, one bottom and one centred in the mid plane. Bolometric cameras are installed in Q2Am, Q3Bt and Q5Bt. Modular limiters equip ports Q1Bb, Q2Ab, Q2Bm, Q4Ab, Q5Ab, Q6Bt and Q6Bb. ICRH antennas are located in ports Q1Bm, Q4Am and Q5Bm ; LH grills are installed in Q6Am and Q6Bm. The six modular ED coils overlap the junction plane between two adjacent modules in the low field side of the machine such that direct view of the ED coils is not accessible from the outside of the vacuum vessel.

Usually bottom limiters have few influence on the estimate of the Total Radiated Power (typically less than 20%) because only few lines of sight intercept them. The main problem is that perturbations induced on profiles make more uncertain tomographic reconstructions. This is the case for Q2Am profiles where two or three lines of sight at the bottom edge intercept directly the Q2Ab limiter and for the Q5Bt profiles where two or three inner central chords (with respect to magnetic connection of line of sight and limiter) are perturbed by the Q5Ab limiter. The use of the Q2Am outboard limiter perturbs more the Q2Am profiles because almost all the horizontal lines of sight intercept the over emissive cloud produced by this limiter in the low field side region and may cause a discrepancy with the two other estimates of the TRP of the order of 20 to 50%. The use of ICRH antennas, especially the Q5Bm one, with a short gap to the last closed magnetic surface (of about 1cm), has a strong influence on the vertical profiles both in Q5Bt for which several lines of sight intercept directly the antenna, but also in Q3Bt profiles, up to which the emissive cloud seems to propagate, such that frequently the TRP estimates from each of this two vertical systems, with the toroidal symmetry assumption overcome the total input power while the TRP estimate from Q2Am remain well below. The over estimate of the TRP with ICRH seems to be related to the outgasing of the antennas induced by an increase of the antenna temperature as it may be inferred from the time evolution of the bolometer signal compatible with the heating of massive structures on a time scale of a few seconds. However this particular point has still to be documented. Usually the turning on of the ED perturbation reduces very much the toroidal anisotropy of the plasma emissivity caused by modular limiters while it has only few effects on the anisotropy caused by ICRH antennas. This may be explained by the different mechanisms causing the anisotropy. While the ED perturbation is efficient to spread out the conductive power flux escaping from the plasma, it is less efficient in spreading out neutral clouds due to the outgasing caused by a self heating of ICRH antennas.

The inner first wall is an actively cooled structure made of 8600 graphite tiles (2x7x1cm3) brazed on stainless steel water pipes, which is used as a toroidally symmetric limiter. It covers 120° of the poloidal section in the high field side region. It has been observed, especially in high power experiments or in long pulse discharges, that local thermal overloading may appear either due to defaults propagating within the graphite tile or to the heat deposition pattern. Locally, the temperature of a given tile may rise and increase the local impurity sources. Usually this phenomena leads gradually to the break of the faulty tile and then get off the wall. This has been observed in a series of LH (3MW few seconds) shot TS20493 to TS20520 where a graphite tile in the neighbouring of the Q3Bt cameras has experienced the above mentioned phenomena. For this series of shots the TRP estimate from Q3Bt cameras deviates significantly in time from the two others. Deviation being mainly due to few line of sight intercepting the inner wall below the mid plane.

The field of sight of the horizontal cameras Q2Am intercepts the inner first wall in a region covered by the field of sight of an IR camera. In some discharges, asymmetries appearing on horizontal bolometer profiles have been correlated to asymmetries of the heat distribution on the inner wall. This point will be more largely documented in further analysis.

All these results confirm the fact that local emissivity sources may lead to large over estimates of the TRP and that a cross check is absolutely necessary.

Tomography: In the case of weak toroidal asymmetries, as expected in high radiating regimes or in Ergordic Divertor experiments, it is possible to combine 16 vertical and 16 horizontal lines of sight to perform a tomographic reconstruction of the local plasma emissivity.

For this purpose an Iterative Least Square Positive algorithm has been implemented. For each tomography the 32 measurements are linearly interpolated to define 184 lines of sight, which will allow us to determine the average emissivity of the 191 pixels defined on a simplified magnetic equilibrium roughly corresponding to the observed plasma magnetic geometry. This simplified equilibrium is made of 16 shifted circular magnetic surfaces with $<\Delta\rho>\sim 1/16$. The shift being estimated from magnetic and polarimetric measurements. The 191 pixels are defined as follow: the 11 central rings are the 11 first pixels and the 5 outer rings, where poloidal structures are expected, are divided in 36 poloidal sectors (10° each). A geometric matrix 184x191 is built where each element Mij is the length of the ith interpolated line of sight crossing the jth pixel. The χ^2 is minimised in two steps: first the m=0 mode verifying $(B_i\text{-}B_i{}^{m=0})>$-Bnoise for each i, Bi and Bnoise being the integrated plasma emissivity and noise level respectively, is extracted. This leads to a maximisation of the contrast for the asymmetric part of the profiles which are then treated subject to constraints on the curvature and amplitude of the emissive regions. An example of tomographic reconstruction is given on Fig.1, which shows the tomographic reconstruction of a marfe observed in the predisruptive phase of an ohmic density limit disruption. The average $\chi^2/184$ is of the order of 4%. From top to bottom Fig.1 shows i) the 3D plot of the plasma emissivity, ii) the experimental and reconstructed interpolated profiles and iii) the emissivity of each of 191 pixels. In this particular case the m=0 mode amplitude is practically negligible. The TRP estimates is about 1.25MW from both the vertical and horizontal cameras. The ratio of the TRP to the ohmic power is larger than 90%. The emissivity inside the marfe is of the order of .8MW/m^3.

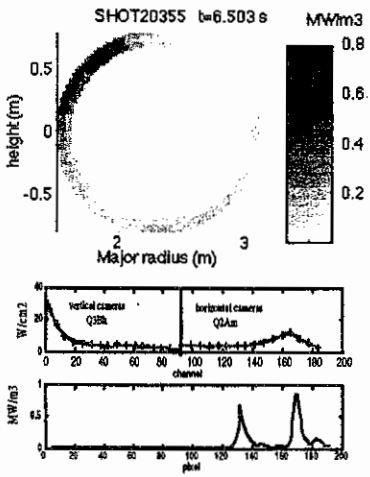

Fig.1 tomographic reconstruction of a marfe in a density limit disruption.

Simulations: The horizontal cameras Q2Am have been installed on the same port as a spectrometer recording impurity line emissions along an horizontal diameter of the plasma. Central lines of sight of the Q2Am cameras, having more or less the same geometry, provide for the first time on TS the possibility of a direct comparison between impurity measurements and radiated power without uncertainties due to geometrical effects. For a first, attempt Ni injection using a laser blow-off technic, has been analysed. The transport code has been modified to simulate the bolometer brightness of a central chord. The radiative losses for Ni are obtained by interpolation of tables of Ref. [4], where radiation power loss coefficients are given for all isoelectronic sequences starting from the Ar-like for several elements from C to Mo. These tables are the only ones available in the literature not at the Ionisation Equilibrium. For less ionised sequences, estimations are obtained guided by atomic physics data of ref.[5]. The simulated central brightness of the bolometric signal shows an initial peak in

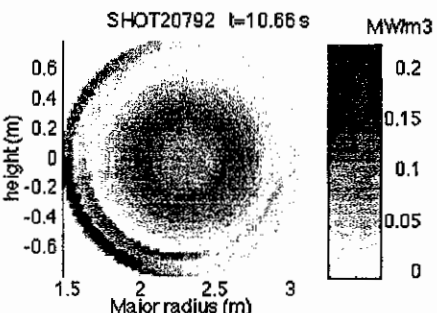

Fig.2 Tomographic reconstruction of plasma emissivity during Ni injection ($\chi^2/184$ ~5%).

the range of 10^5W/m2 (the total power radiated in a peripheral layer being in the 1-2MW range), followed by a slowly decreasing tail, very weakly modulated by sawtooth activity. The simulated brightness peak occurs at the end of the Ni pulse, but due to the finite time resolution of few tens of ms of the bolometric data, this short initial phase (less than 10ms) is not observed on bolometer signals. Subsequently, when the impurity ions move towards the center, radiation is emitted from the plasma core, but the emissivity profile of the radiated power remain slightly hollow, since in the 1-3keV Te range the radiated power density is a decreasing function of Te. It peaks, after the inflow phase at r/a~0.3-0.4, as experimentally found in tomographic reconstruction of the plasma emissivity (Fig.2).

In Fig.3 the experimental and simulated increase of bolometer brightness due to Ni injection in shot TS20792 are plotted (dotted and solid lines respectively). Note that for comparing experimental and simulated data with respect to the finite time resolution of the bolometers the simulated data have been low pass filtered with a cut-off frequency of about 20Hz. Doing this, time evolution of both traces compare satisfactorily, but a discrepancy of a factor of about two appears on the amplitude (in Fig.3 the simulated data are multiplied by 2). A few remarks are needed about this discrepancy, which seems to be related to the atomic data available. First, to the best of our knowledge, no simulation of bolometric data following laser blow-off injection has been reported and second, quite surprisingly, even quantitative comparison of bolometric signals with simulations from intrinsic impurity emission are very scarce.

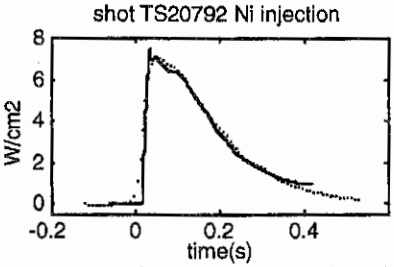

Fig.3 measured (doted) and simulated multiplied by 2 (solid) time evolutions of the increase -due to Ni injection- of bolometer signal

Comparison between the tables [4] used for these laser blow-off experiments and the data of the tables [6] for instance for Fe shows rather large discrepancies especially between 0.5 and 1keV, better agreement being found around 3keV. Consequently in the Ni laser blow-off experiment reported here, where the maximum emission during the decay phase is localised in a region where Te~1-1.5keV, it appears that the radiative power losses proposed in Ref.[4] underestimates clearly the experimental data. Those proposed in Ref. [6] seem better and probably satisfactory, taking into account the usual uncertainties of plasma experiments.

Conclusions: A new simplified and very cheap bolometer electronic has been successfully developed. This has been a prerequisite to realise an extended version of the TS bolometer diagnostic which is now fully available. It provides three full plasma profiles each of 16 chords -two verticals and one horizontal - taken at three different toroidal locations, allowing us to check,when needed, the assumption of toroidal symmetry of the plasma emissivity usually made to estimate the total radiated power. The high conductive loss regime performed during the last campaign has constituted a good opportunity to observe the various sources of toroidal inhomogeneity and their impact on the total radiated power estimates. In case of good enough toroidal symmetry, as expected in high radiating regimes, horizontal and vertical chords can be combined to perform tomographic reconstruction of the plasma emissivity. For this purpose a simple algorithm based on an ILSP method has been implemented and provides us good quality 3D images. Horizontal cameras has been installed at the same toroidal location as an IR camera imaging the inner first wall and as a spectrometer, allowing direct comparison of bolometer signals with impurity sources and plasma impurity containt respectively. For the first time simulation of Ni injection using the laser blow-off technique has been presented.

References

[1]R.Reichle & al. JET Report P (95)51
[2]E.R.Muller,G.Weber,& al. IPP Report 1/224 (1985)
[3]Mast K.F.,Vallet J.C. & al. RSI 62 (1991) p.744
[4]Summers H.P. & McWhirter R.W.P. J.Phys B:Atom. Molec. Phys. 12 (1979) p.2387
[5]Post D.E.,Jensen R.V. & al. Atom. Data Nucl. Data Tables 20 (1977) p.397
[6]Post D.E., Abdallah J. & al. Phys. Plasmas 2 (1995) p. 2329

Dual frequency O-mode heterodyne reflectometer on Tore Supra

F. Clairet, P. Moreau, M. Paume and J.M. Chareau
Association EURATOM-CEA sur la Fusion Controlée
Centre d'Etudes de Cadarache, 13108 St Paul Lez Durance, FRANCE

Introduction

A new heterodyne dual frequency reflectometer has been installed on Tore Supra. It combines high dynamic sensitivity and fast frequency sweeping potentiality (down to 10μs). Its performances can be compare with the actual three O-mode homodyne reflectometers and provide more valuable informations for understanding the role of the plasma turbulence upon the reflected signal.

Experimental system

Recently, a new dual frequency O-mode heterodyne reflectometer has been installed on Tore Supra tokamak (figure 1). The frequency band covered is 26-36 GHz providing edge density measurements from 0.8 to 1.5 10^{19} m^{-3}. The frequency source used is a Hyperabrupt Tuned Oscillator (HTO 12000, 12-18GHz). A linear frequency versus time sweeping is provided with a synthetised arbitrary waveform voltage generator (Wavetek 395). A quartz local oscillator provides a modulation signal at fm=80 MHz. Modulation of the frequency is achieved with a mixer providing identical side bands. Power is launched into the plasma through 4m of fundamental waveguides and using separate emitter and receiver rectangular antennas. The reference signal is extracted from the source with a 3dB power divider, and a delay line is used to compensate the phase differences of the probing wave due to the propagation into the emitter and receiver waveguides. Detection is performed through an I/Q mixer providing in-phase and 90°-phase signals and allowing absolute phase and amplitude detection for both frequencies. The demodulation is performed with the same quartz oscillator providing no need of phase locking system. The dynamic range of such heterodyne detection typically lies around 60 dB.

Detected signal

Since two frequencies are simultaneously launched into the plasma, the reflected signal carries information from both cut-off layers with different beat frequencies (figure 2). The detected signal can then be written:

$$S = A_{(2F+2fm)}.e^{i\Phi_{(2F+2fm)}} + A_{(2F-2fm)}.e^{i\Phi_{(2F-2fm)}}$$

A and Φ are the amplitude and the phase for the reflected signals.

The phase reference is conveniently taken from the reflection coming out the antenna coupling which as been calculated to represent 5 cm of propagation length.

Comparison homodyne versus heterodyne technique

Figure (3) shows a comparison of the reflected group delay between the actual homodyne reflectometer and the new heterodyne device. The features observed between both type of detection is mainly due to the sensitivity difference : while the homodyne reflectometer (sensitivity: 20 to 30dB) do not give a clear representation of the time delay evolution, the heterodyne reflectometer clearly detects the cut-off layer.

Moreover, heterodyne I/Q detection allows direct extraction of the phase and separation from the amplitude (contrary to homodyne technique whose signal is S=A.cosΦ). It is then possible to calculate the intantaneous group delay $\tau = \frac{1}{2\pi}\frac{\partial\phi}{\partial F}$ and compare to the usual sliding FFT analysis. Figure (4) shows how FFT analysis can conveniently average out the group delay, and how the instantaneous group delay calculation points out the effect of the plasma fluctuations (backscattering or oscillating mirror effect) over the exact location of the cut-off layer. So, the question of the resolution is mostly a matter of how these fluctuations disturb the measurement.

Ultra fast sweeping

We have studied the effect of the decrease of the sweeping time for identical plasma discharges from 1ms to 10μs (figure 5). It has been observed that the decrease of the sweeping time leads to an important improvement of the density profile determination. In fact, the number of the phase jumps are less numerous and the amplitude of these jumps is less important.

Effect of the plasma turbulence

Each time a jump occur in the group delay, the amplitude of the signal decreases (figure 6). These jumps are of very short duration as they can occur in less than 0.1μs. Moreover, it is noted that most of the time the group delay jumps occur in the negative direction and at such value that the plasma would be out of the torus. Such behaviour might be interpreted [1] as a Doppler effect of a wave reflected upon a rotating grating like cut-of layer. So, two phases in these jumps are clearly seen (figure 7): a rapid and a slow events. Each events would be due to a difference in the slopes in the reflecting layer that would also explain the simultaneous change in the amplitude signal. This turbulence would look like inclined rotating (poloidally and toroidally) structures (figure 8) as simulated by numerical codes performed to investigate the role of the plasma shear rotation upon transport [2].

[1] V.V. Bulanin and D.O. Korneyev : Proceedings of the 1st IAEA Technical Metting on Microwave Reflectometry for Fusion Plasma Diagnostics Abingdon (1992).

[2] Y. Kishimoto, J.Y. Kim, T. Tajima, W. Horton and G. Furnish : Theory of Fusion Plasmas Proc. of the Joint Varenna-Lausanne international workshop. Varenna (1996) Italy.

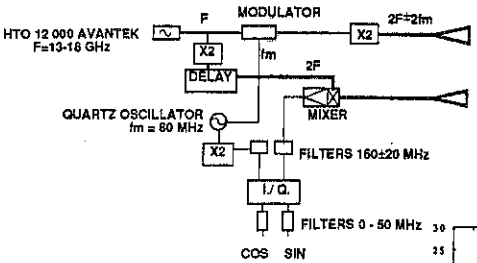

Figure 1 : Schematic diagram of the dual frequency heterodyne reflectometer

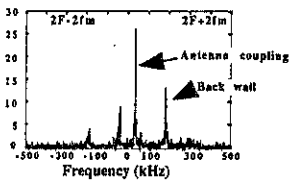

Figure 2 : Beat frequency spectrum of the reflected waves (F+fm) and (F-fm) for 1ms sweeping time.

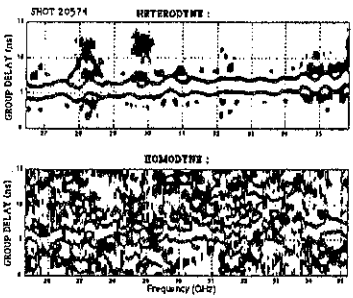

Figure 3 : Group delay mesured with the homodyne and the heterodyne reflectometer (sliding FFT analysis signal: 1024 pts, width:64pts, sliding 4pts) at the same time.

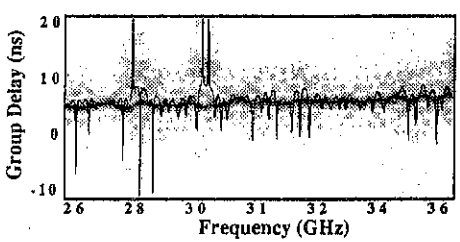

Figure 4 : Comparison between sliding FFT analysis (broad curve) (signal: 1024 pts, width:64pts, sliding 4pts) and instantaneous group delay measurement (thin curve).

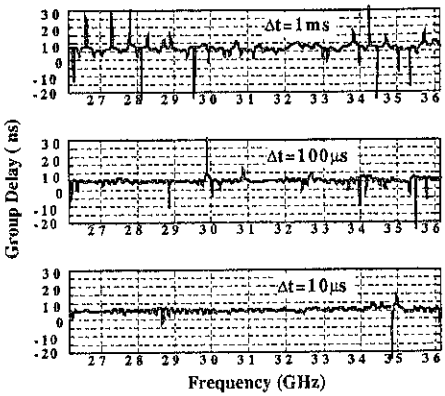

Figure 5 : Group delay measurement for three identical plasma discharges. The decrease from 1ms to 100μs and 10μs sweeping time shows an improvement of the cutoff localisation.

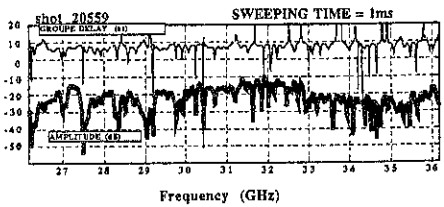

Figure 6 : Group delay (thin line) and amplitude signal (thick line) variations.

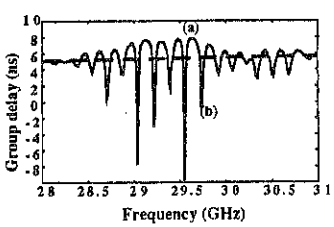

Figure 7 : Group delay variation (solid line) and average cutoff position (dash line) (sweeping=1GHz/μs). (a) and (b) refer to slow and rapid variation of the cut-off position as indicated figure 7.

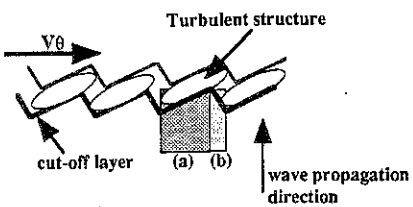

Figure 8 : Modelisation of the Doppler shifted reflected wave : (a) Strong negative shift, and, (b) small positive shift.

Ion heating and confinement in NBI heated START plasmas.

P. G. Carolan, N. J. Conway[1], M. R. Tournianski[2], R. J. Akers, C. A. Bunting, M. P. Gryaznevich, I. Jenkins, R. Martin[3], M. P. S. Nightingale, C. M. Roach and M. J. Walsh.

UKAEA Fusion, Culham, Abingdon, Oxon, OX14 3DB, UK
(UKAEA/EURATOM Fusion Association)

[1] University College Dublin, Republic of Ireland
[2] University of Essex, Wivenhoe Park, Colchester, UK
[3] UMIST, Manchester, UK

Introduction

The novel use of neutral beam injection (NBI) in tight aspect ratio tokamaks with relatively low edge magnetic fields is being investigated in the START [1] tokamak. The heating of the plasma ions and electrons, as well as the generation of plasma momentum, are studied by monitoring the particle kinetics. The $T_e(r)$ and $n_e(r)$ distributions are obtained from a 30 point Thomson scattering and the T_i and V_ϕ from a 20–chord Doppler spectrometer [2] using both passive and charge–exchange emission. From these results ion energy confinement are studied using the ASTRA transport code [3] and, for the treatment of the fast–ions from the NBI, a Monte–Carlo code [4] that includes tight aspect ratio and finite Larmor radius effects.

General ion behaviour

The ion temperature and toroidal plasma rotation have been obtained from measurements of the Doppler broadening and shift of the C^{5+} line (n=7–8, 529.05nm). This line radiates relatively strongly both with and without beam injection allowing for continuous monitoring of the ion behaviour (e.g. with beam switch–off during a discharge). To interpret the line–of–sight averaged spectra from the Doppler multichord diagnostic it is necessary to calculate the beam attenuation, arising primarily from charge exchange with the plasma ions. This involves measuring the fractions of the beam energy components and the $n_e(r)$ results from the Thomson scattering (TS) diagnostic. In Fig. 1 are shown emissivity contour plots of the charge exchange radiation

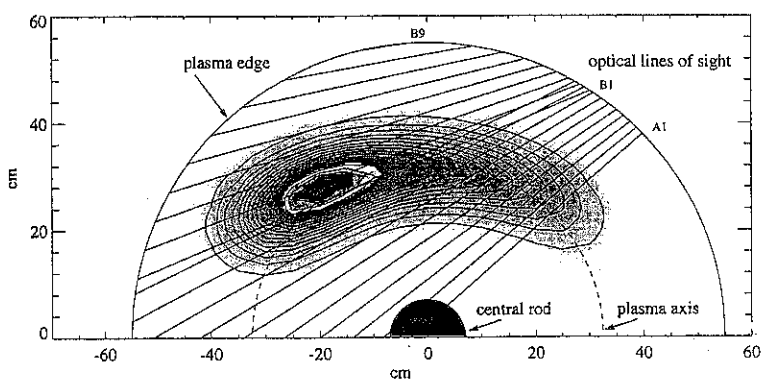

Figure 1: *Contours of the product $n_b n_{C^{6+}}$ which is proportional to the flux of the emitted photons ($n_{C^{6+}}$ and n_b are the C^{6+} and the beam hydrogen densities. In this case E_0=30keV.) The viewing chords A1→A10 and B1→B9 are also indicated.*

The ion temperatures, in this example, reach peak values of up to $T_i \sim$350eV for the central chords (shown here: A9, B1 and B3) but with lower values for other chords further out from the plasma centre (*e.g.* A5 and B7). The A1 radially viewing chord shows only a modest increase in temperatures although it views the central regions but this is because it sees little of the core radiation due to the beam attenuation (cf. Fig. 1). The sudden increase in T_i as viewed by a relatively outer chord after the Internal Reconnection Event (IRE) signifies a broadening of the T_i profile similar to that observed for the electrons from the Thomson scattering. Indeed, in both Ohmic and NBI heated discharges the shape of the $T_e(r)$ and $T_i(r)$ profiles are very similar but with the peak vales of T_e much higher for pure Ohmic cases as for conventional tokamaks. In principle, a time slice through all the recorded spectra can only be unfolded when the $T_e(r)$ and $n_e(r)$ profiles are available (at present, only once during a discharge from the single pulse Thomson scattering system) since the beam attenuation across all the lines of sight is required.

Much the same behaviour is seen for the ion toroidal velocity behaviour, shown in Fig. 4, as exemplified in the increase during the discharge, the broadening of the profile after the IRE and the reduction in temperatures after the beam switch–off. The beam–induced rotation has reached values in excess of 60km.s^{-1} (here up to ~50km.s^{-1}) in the toroidal direction with the usual co–injection. Absolute velocity fixes are obtained from the A1 and A2 chords which have near radial views and thus see little toroidal rotation (cf. Fig. 4).

Confinement

In selected Ohmically heated plasmas, where there is a sufficient period free of MHD activity and sawteeth, predictions of the ASTRA transport code [3], which includes tight aspect ratio effects [5], and observations of ion temperature profiles and using measured $T_e(r)$ and $n_e(r)$ distributions from Thomson scattering for the collisional ion heating are in good agreement, given the preliminary stage of this investigation (*e.g.* more modelling on the edge transport is required). Central ion and electron temperatures are compared in Fig. 5 for a wide range of plasma densities and currents for both Ohmic and NBI–assisted plasmas. The calculated curves include electron–ion collisional heating and, additionally, fast–ion heating, for the NBI–assisted plasmas. The heating is derived from the beam power, the measured $T_e(r)$ and $n_e(r)$ and the Monte–Carlo code. The ion energy confinement time, calculated from axial power balance using a simple 0D model, is typically 3ms→4ms and similar to that for the ion momentum confinement time, during NBI, extracted from the velocity measurements and estimates of the momentum injection from the fast ions.

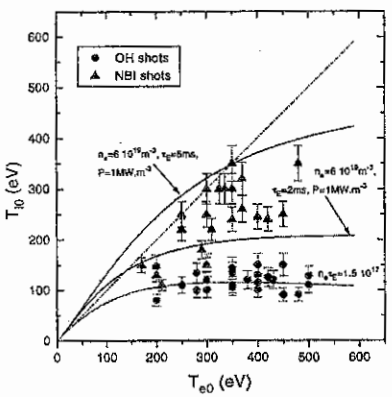

Figure 5: *Measurements of T_{io} and T_{eo} in Ohmic and NBI assisted plasmas. Calculated ion temperatures are shown for comparison, assuming electron–ion collisional heating for pure Ohmic shots and, additionally, heating from fast ions during NBI. A simple 0D model is used to calculate T_{io}*

At times when the $T_e(r)$ and $n_e(r)$ profiles are available we can compare 1D predictions, from the ASTRA code, with observations. Assuming neoclassical confinement of the ions is also valid for the NBI cases then the observed $T_e(r)$, $T_i(r)$ and $n_e(r)$ distributions during NBI can be used to assess the fast ion heating *vis a vis* the Monte–Carlo code simulations. Radially unfolded ion temperature profiles are shown in Fig. 6 and compared with the TS $T_e(r)$. (The two curves for the $T_i(r)$ derive from different extreme assumptions on the character of the passive emissivity of the spectral line used for the Doppler profile.) The information for the beam neutral density, required to separate passive and active emissivities, is obtained from the beam attenuation code, incorporating the Thomson scattering data on $T_e(r)$ and $n_e(r)$ and the beam energy fractions. The T_e and T_i profiles are similar in shape and magnitude for this particular plasma and beam power so that the ions are heated predominantly by the fast ions.

resulting from H_0+C^{6+} $\rightarrow$ $H^+ + C^{5+*}$. (Here C^{5+*} is the carbon ion in the excited $n = 8$ quantum state.) The emissivities are derived for a typical plasma using the measured chord intensities and includes the beam attenuation modelling in the data unfolding procedure. In this case a Gaussian distribution is used to represent the fully ionized impurity density radial profile and has here a $1/e$ half-width of C^{6+} of 10cm, which is fairly typical from the full unfolding of the intensities. The radiation is highest from the central regions of the plasma and chords viewing this region (*e.g.* B1, B2 and B3) will predominantly register central ion temperatures and velocities.

Observations of ion temperatures from a central-chord are compared in Fig. 2 for an Ohmic discharge and two levels of NBI power, ~150kW and ~300kW. Whereas the peak electron temperature, T_{eo}, does not generally show a significant increase with NBI, although there is a broadening of the profile and an increase in $\overline{n}_e$, there is a considerable increase in ion temperature during beam injection as seen, for example, in Fig. 2, taking ~10ms to reach an apparent maximum equilibrium value. The ion temperature continues to increase with beam power up to about the peak electron temperature, in these case ~300eV. The decrease in T_{io} with beam switch-off is often complicated by the frequent accompaniment of increased MHD activity making it difficult to extract energy and momentum confinement times from the decay times of T_i and V_ϕ. The decay is also affected by the presence of the fast ions which have an e-folding decay time of a few ms after beam switch-off.

The time evolution of ion temperature and toroidal velocity behaviour from the line-of-sight-integrated measurements of various chords are shown in Figs. 3 and 4.

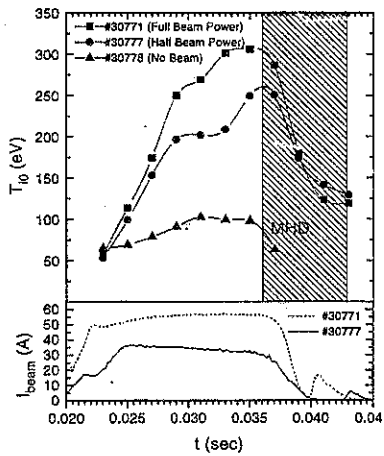

Figure 2: *The ion temperature for different neutral beam powers (T_e ~300eV, n_e ~ $5 \times 10^{19} m^{-3}$, I_p ~200kA, E_0=30keV, P_{beam} ~150kW and ~300kW).(Shots #30771, #30777 and #30778)*

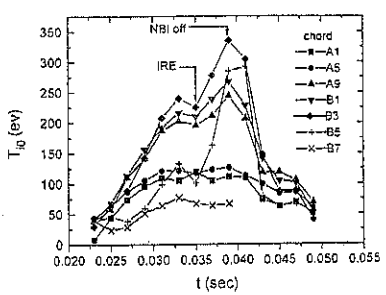

Figure 3: *Line-of-sight intensity-weighted ion temperatures obtained from various of the viewing chords. The occurance of an Internal Reconnection Event (IRE) and beam switch-off are indicated, both showing decreases in T_i, especially for the central viewing chords, here: A9, B1 and B3. (Shot #31663)*

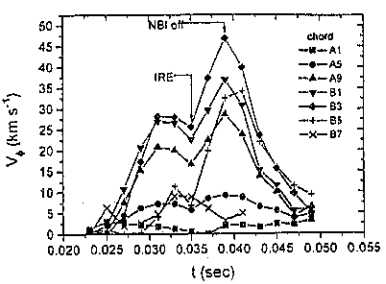

Figure 4: *Temporal behaviour of the ion toroidal velocity from the same data as in Fig. 3.(Shot #31663)*

The steady-state solution for the T_i distribution has been computed using the ASTRA transport code [3], assuming the Chang-Hinton ion neoclassical heat conductivity with corrections for tight aspect ratio [5]. Ion heating from electron–ion collisions was computed using the Thomson scattering profiles of $T_e(r)$ and $n_e(r)$. Uniform Z_{eff} and ion depletion profiles are assumed (2 and 80%, respectively). The NBI heating (total input power ~500kW), *via* the fast ions, is obtained from *ab initio* calculations in the Monte-Carlo code using measured beam energy component fractions. The resulting $T_i(r)$ profile is compared with the measured $T_i(r)$ profile in Fig. 6. The ion heating profile obtained from the Monte-Carlo code is almost Gaussian in shape with a 1/e width of ~6cm, a peak value on axis of ~1.2MW m^{-3} and a total power of ~85kW.

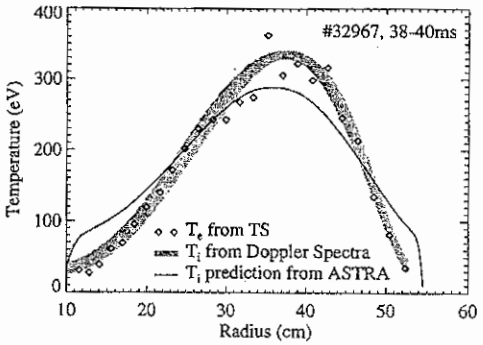

Figure 6: *Ion temperature distributions (unfolded from the Doppler spectra) during NBI, (#32967; $n_e \sim 6 \times 10^{19} m^{-3}$, I_p ~200kA, E_0=30keV, P_{beam} ~500kW). Also included, for comparison, are the electron temperature measurements from Thomson scattering and the ion temperature distribution predicted using the ASTRA transport code and the Monte-Carlo fast ion code.*

Given the preliminary nature of this exercise in comparing measuements with theory and codes the agreement is quite satisfactory and gives confidence in our treatment of the fast ion heat deposition in the START plasma.

Conclusions

Predictions from the ASTRA transport code, which includes tight aspect ratio effects, are in good agreement with observations of ion confinement in START Ohmic plasmas. NBI heating of the START tokamak is most evident in the ion temperature which typically increases from ~100eV to ~300eV. Assuming ion neoclassical confinement during NBI the required heating from the fast ions to account for the observations is consistent with that predicted from a Monte-Carlo fast ion transport code. Similar $T_e(r)$ and $T_i(r)$ profiles are found and at the highest NBI heating to date (500kW) the magnitudes are also similar. High toroidal velocities are seen with NBI and similar ion momentum and energy confinement times are found.

This work is funded by the UK Department of Trade and Industry and EURATOM.
The Neutral Beam system is on loan from the US Department of Energy.

References

[1] A.Sykes *et al.*, "High β performance of the START spherical tokamak", review talk this conference, to be publ. in Plasma Phys. and Contr. Fusion.

[2] P. G. Carolan, N. J. Conway, C. A. Bunting *et al.*, Rev. Sci. Instrum., **68** 1015 (1997).

[3] G. V. Pereverzev*et al.*, IV Kurchatov Institute of Atomic Energy, IAE-5358 (1992).

[4] R. J. Akers, paper in preparation

[5] C. M. Roach, Plasma Phys. and Contr. Fusion, **38**, 2187 (1996).

Profile optimization and MHD-activity in high-β NBH discharges on START

M Gryaznevich, T C Hender, M P S Nightingale, S Sharapov*,
A Sykes, M J Walsh** & START team
UKAEA, Fusion, Culham, Abingdon, Oxfordshire, OX14 3DB, UK
(UKAEA/EURATOM Fusion Association)
* JET, Abingdon, Oxfordshire, OX14 3EA, UK
** Walsh Scientific Ltd, Abingdon, Oxfordshire, OX14 2RT, UK

Introduction.

High beta values[1] of $\beta_T \sim 30\%$ at $\beta_N \sim 4$ have been achieved in the START spherical tokamak using additional heating provided by a neutral beam injector on loan from ORNL. These high β values have been obtained through optimising secondary current ramp and gas puff during the discharge and improving the plasma purity with the help of boronisation, glow discharge cleaning and Ti gettering. Details of the regime optimization procedure on START are presented. The stability of these high β shots and their MHD behaviour is discussed.

An advantage of the low aspect ratio tokamak is its potential for stable operation at high normalised current $I_N = I_p/aB_T$ before a q_ψ-limit is encountered; this feature allows the achievement of high β values. The possibility of operation at I_N and shaping factor $S = I_N \times q_{95}$ significantly higher than that obtainable in conventional tokamaks has been already demonstrated on START [1]. In the recent experiments, a combination of hardware improvements, wall conditioning and regime optimization has yielded $\beta_T \geq 30\%$ at $I_N \geq 8$ [2], Fig.1. In this figure the recent high β data, trajectories for two typical shots with different scenarios and the high β DIII-D results [3] are shown.

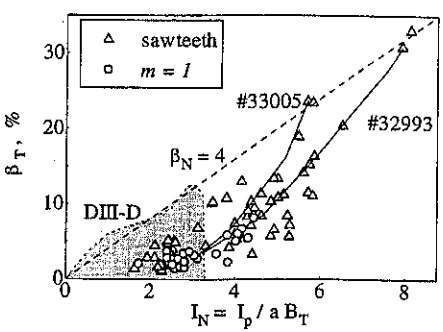

Fig.1 Experimental high β results in START (lines indicate trajectories during a shot).

Regime optimization.

As in other high β experiments on DIII-D [3], JT60-U [4] and TFTR [5], regime optimisation is very important on START. Optimisation of the current ramp and density ramp scenario is believed to be a key feature of the increase in shaping factor and normalised current as it implies a broad current profile which produces plasmas of high elongation and triangularity. The value of normalised current of $I_N > 8$ achieved is substantially greater than the value $I_N \sim 3$ previously achieved in optimised conventional aspect ratio tokamaks [6]. The optimisation is preformed by pre-programming the applied loop voltage (which controls the speed of additional current rise), and controlling the pre-programmed additional gas puffing to control the density rise speed in order to avoid the density limit. The current ramp also

[1] $\beta_T = 2\mu_0 \int pdV / VB_T^2$, where B_T - vacuum toroidal field at the geometric center; $\beta_N = \beta_T / (I_p/aB_T)$

supports the formation of a broad pressure profile (by making T_e profile broad), which is favourable for ballooning stability in the plasma core.

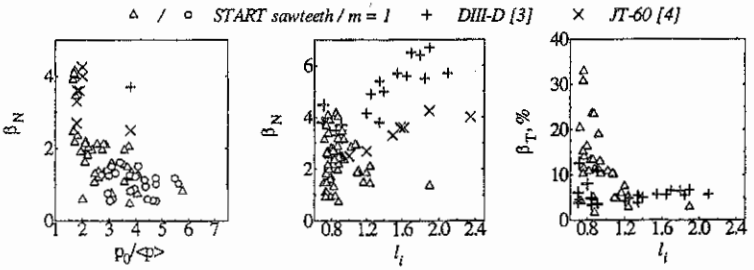

Fig.2. Normalised and total β vs pressure profile peakedness and l_i in START

Results of the pressure and current profile scans are shown in Fig.2. Some high β_N DIII-D and JT60-U shots [3,4] are shown for comparison. The pressure profile peakedness factor $p_0/\langle p\rangle$ was ≤ 2 in the best shots, which, as shown later, satisfies the requirements on the pressure profile optimisation for ballooning and low-n pressure driven modes. The optimum values of l_i ($l_i = l_i(2) = 1/\langle B_p\rangle_s^2 \int B_p^2 dV$) to achieve the highest β values were found to be in the range of 0.7 - 1.0, a further decrease in l_i leading to a reduction in the beta value. Unlike DIII-D and JT60-U, the highest β_N value of 4.2 in shot #32998 on START (which corresponds to the higest β_T value of ~ 34%) has been obtained using current ramp-up; the fast ramp-down technique has not been tested so far.

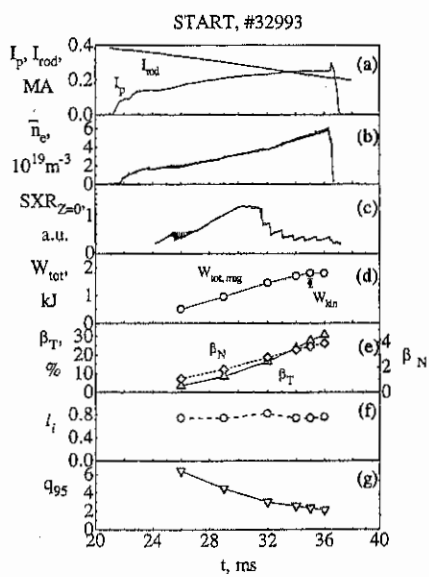

Fig.3. Traces for a typical high β shot.

Typical high β shot traces are shown in Fig.3. To keep the optimum value of l_i the plasma current was ramped up with a speed dI_p/dt ~ 10 MA/s (a) and programmed gas puffing was used to prevent the plasma current profile becoming hollow, which is adverse for neutral beam power absorption. As a result, the l_i value was kept ~ 0.7 - 0.8 through the shot, (f). Toroidal field was decreased by decreasing the central rod current, I_{rod} (a), (on a timescale slow compared to the particle and resistive diffusion times), which allows the β value to rise. In these shots the value of I_p/I_{rod} = 1.2 has been achieved representing an important result in itself, as ST power plant designs require $I_p \geq I_{rod}$.

The density rose throughout the shot (b); however density and temperature profiles (measured by 30 point Thomson

scattering) became flat after the beginning of the sawteeth (time 31 ms in (c)) and $q = 1$ radius increased (measured from the sawteeth inversion). This suggests that the sawteeth have prevented further peaking of the current profile, and so this remains broad enough to provide high plasma elongation which allows the normalised current to reach $I_N \sim 8$ whilst q_{95} remains above 2 (g).

The total energy W_{tot} (d) (from free-boundary equilibrium reconstruction with two independent codes, TOPEOL and EFIT) continued to rise during the sawteething phase and shows signs of reaching steady state shortly before the discharge terminated. This behaviour was typical of the low q high β shots, but at higher TF the energy continues to rise until the end of the shot. The broadening of the profiles, however, was typical for all high β shots and could by accompanied by different types of MHD activity.

MHD activity and stability.

The analysis of Mirnov coil and SXR data shows that the MHD activity during profile redistribution can be either an *m/n=1/1* slowly rotating mode, or coupled low-*n* Mirnov activity with *m/n = 2/1, 3/1* and, probably, other harmonics. In the highest β shots sawtooth activity usually replaces the low *m, n* rotating modes and the sawteething stage continues until the current rapidly terminates due to contact with the X-point coils during the IRE (Internal Reconnection Event), Fig.3a. In some cases when the current ramp produces much broader current profiles, no preliminary MHD-activity was seen. However, the β_T value was lower than in a case with sawteeth, probably because of the lower neutral beam power absorption.

A high frequency "chirping" mode, similar to that observed on DIII-D [7], is often seen in the high-β NBH shots. This mode is likely to be an energetic particle mode (EPM) driven by fast beam particles ($\nu_{b\|}$ is typically ~ ν_A in START). Modes with frequencies and spectrum typical for Toroidal Alfven Eigenmodes (TAE) [8] are also sometimes seen early in the discharge and at lower beam power.

High normalised β values $\beta_N \geq 4$ have been achieved at different I_N values of ~ 8 and 6, Fig.1, corresponding to minimum $q_{95} \sim 2$ - 2.3 and 2.7 - 2.8. Ideal stability analysis shows that in both cases the pressure profile was close to marginal stability to the high n ballooning modes, Fig.4a. Low n stability calculations using CHEASE and ERATO [9,10] codes show that while the low q shots such as #32993 were close to an external kink limit, the higher q

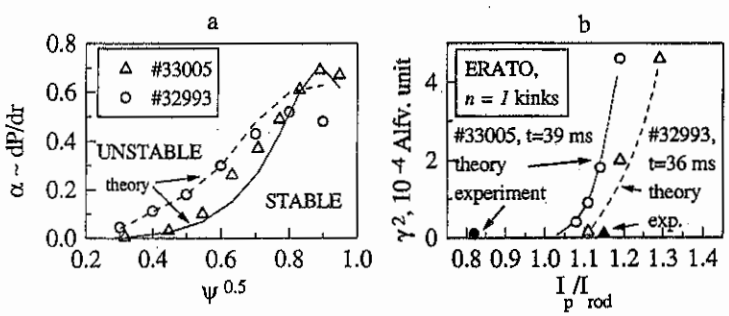

Fig.4. Ideal ballooning and external kink stability of high β shots on START.
#33005: $q_{95} = 2.8$, $\beta_T = 23.6\%$, $\beta_N = 4.14$; #32993: $q_{95} = 2.28$, $\beta_T = 30.8\%$, $\beta_N = 3.89$

shots like # 33005 were clearly stable to the external kink, Fig.4b. In the simulations, both cases become unstable to low n pressure driven internal modes for pressure profiles more highly peaked than the experimental value. In all $\beta_N \sim 4$ shots high frequency MHD activity accompanying a low frequency internal mode has been observed preceeding an IRE and discharge termination, Fig.5. It is possible that the core outward displacement due to the growing internal $m = 1$ mode destabilises localised ballooning modes [11]. It is also observed on START that discharge terminations earlier in the shot can occur at high β in a case of a high amplitude internal $m = 1$ growing mode (circles in Fig.1, 2). These cases correspond to initially more peaked SXR and pressure profiles. However, when in some shots the sawteeth replaced the $m = 1$ rotating mode, it was possible to avoid the IRE at this stage and achieve higher β values. It is found so far that all high β shots on START terminate through an IRE with no evidence of a growing external mode. These high β regimes on START appear so far to be limited by internal low n modes.

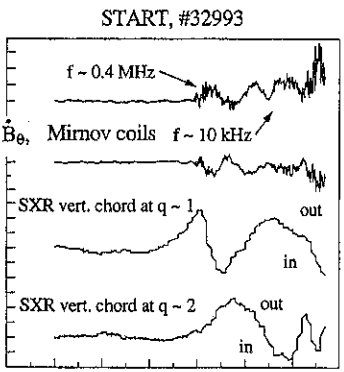

Fig.5. Mirnov coil and outer vertical SXR chord signals preceeding the IRE in high β shot #32993 on START

More flexibility in the discharge scenario provided by recent improvements in the central OH solenoid power supply system may allow further increases in β_N, for example by permitting operation at higher q_{95} and higher elongation (giving higher shaping factor $S = I_N \times q_{95}$) to provide stability of the external modes, or by increasing l_i. However, as in other features of the spherical tokamak, the requirements of ballooning stability, internal mode stability and external kink stability may lead to entirely different scenarios for β optimisation. The good agreement with the stability code predictions demonstrated so far on START is very encouraging.

Acknowledgement. *This work is funded by the UK Department of Trade and Industry and EURATOM and supported by a collaboration with ORNL and the US DOE. We thank the Lausanne group for providing us with ERATO and CHEASE and General Atomics for supplying EFIT.*

[1] R Akers et al., 16th IAEA Fus. En. Conf., Monteal, (1996), IAEA-CN-64/C2-1
[2] A Sykes et al, this conference, M Gryaznevich at al., subm. to Phys. Rev. Let., (1997)
[3] E Lazarus et al, Phys. Fl., B 4 (1992) 11; T Taylor, ISPP-16, SIF, Bologna, (1994) 111
[4] Y Kamada et al., Nucl. Fus., 34 (1994) 1605; T Ozeki et al, ibid, 35 (1995) 861
[5] M Mauel et al, Pl. Phys.d Contr. Nucl. Fus. Res., 1992 (IAEA, Vienna, 1993) Vol.1, p.205
[6] E J Strait, Phys. Plasmas, 1 (1994) 1415
[7] W W Heidbrink, Pl.Ph.Contr.Fus., 37 (1995) 937
[8] A Fasoli et al, Nuclear Fusion, 35 (1995) 1485
[9] H Lutjens et al, Comp. Phys. Comm., 69 (1992) 242
[10] R Gruber et al, ibid, 21 (1981) 323
[11] W Park et al, Phys. Rev. Lett., 75 (1995) 1763

The density and q limits in START

C.Ribeiro, T.C.Hender, I.Jenkins, R.Martin, M.P.S.Nightingale, D.C.Robinson, A.Sykes, T.N.Todd, M.J.Walsh

UKAEA, Fusion, Culham, Abingdon, Oxon OX14 3DB, UK
UKAEA/EURATOM Fusion Association

Introduction

Limits on plasma density and edge safety factor q operation have been studied in the low aspect ratio tokamak START (Small Tight Aspect Ratio Tokamak). The main characteristics of this device are: low-aspect ratio plasmas with high plasma current [$I_p \leq 300kA$] at low toroidal field [$B_\phi \geq 0.1T$, $I_p/I_{B_\phi} \leq 1.2$]; compact volumes [$R_\circ \leq 0.34m$, $a \leq 0.27m$, aspect ratio $R_\circ/a \geq 1.23$, elongation $\kappa \simeq 1.2-3.0$, and triangularity $\delta \leq 1.0$]; Ohmic and NBI (0.4MW, 30keV, H/D species, 2.5×10^{20} particles/second, Co-injection) heating; high energy confinement times [eg $\tau_E^{Ohmic} \sim 4ms$ ($\tau_E \sim 2 \times \tau_{ITER93-H\,mode}$)]; hot plasmas [$T_e(0) \sim 0.5keV$]; and very high β [eg with NBI: $\beta_\phi(magnetic\ axis) \simeq 50\%$, $\beta_T \simeq 30\%$ (both are world records), $\beta_N \simeq 4$]. The vessel and the plasma-facing components are regularly boronised using deuterated tri-methyl boron in helium glow discharges and sometimes the Ti gettering technique is also applied. Naturally exhausted/limiter (NED), single (SND) or double-null (DND) X-point plasmas are currently produced.

The edge q limit has been approached by means of ramping down the toroidal field current, I_{B_ϕ}, during the discharge, obtaining with the world record volumetric beta ($\beta_T \equiv \frac{2\mu_\circ}{VB_\phi^2}\int pdV \simeq 30\%$[1], where B_ϕ is the vacuum toroidal magnetic field at the geometric centre).

Recently, a short campaign on the density limit studies has been carried out by using a combination of NBI and extra gas puff in DND plasmas. Helium glow discharge and titanium gettering techniques have been systematically applied between the discharges.

Edge-q limit

Figure 1 shows the dependence of $q_\psi(95\%)$ as a function of the aspect ratio $R_\circ/a$. It is clear that the expected benefits of higher $q_\psi(95\%)$ relative to the conventional tokamaks start at approximately $R_\circ/a \simeq 1.6$. For example, in the shot 32993, the minimum $q_\psi(95\%)$ (from the equilibrium reconstruction) is around 2.3 at $R_\circ/a \simeq 1.37$, which was obtained simultaneously with the world record volumetric β, ie, $\beta_T \simeq 30\%$. Analysis with the ERATO code for such a low-q value indicate that both external and internal n=1 kink modes could be the cause of this limit although only internal modes are observed to date at high β[2]. In addition, ratios of I_p/I_{B_ϕ} above unity, ie, $\simeq 1.2$ have been observed for the first time. Further q_ψ reduction is usually limited by internal reconnection events (IREs).

This regime of neutral beam injection into a DND configuration achieves very low $q_\psi(95\%)$, possibly by obtaining plasma current profiles favourable to MHD stability. In-

deed, on other ST devices with no NBI or DND configuration, like CDX-U and TS-3, a limit of $q_\psi(95\%) \simeq 3$ is observed.

Density limit

Density limit studies have been carried out by using a combined NBI-extra gas puff method in DND plasmas. Gas pre-filling plus NBI are used to set up the discharge in the early phases, with strong extra gas puff refuelling the plasma even further. Helium glow discharge and titanium gettering techniques have been systematically applied between the discharges and high reproducibility of discharges has been observed.

The highest value of line average density achieved in START was obtained in this campaign: in the shot 33543, $\overline{n}_e \simeq 9.4 \times 10^{19} m^{-3}$ with a symmetric parabolic-like profile centered at $n_e(0) \simeq 1.5 \times 10^{20} m^{-3}$ in a relatively cold plasma ($T_e(0) \simeq 170eV$) have been measured by the 30 point Thomson scattering. In addition, a more favourable density per plasma current density scaling has been approached at this limit. With $B_\phi \simeq 0.36T$: $\overline{n}_e \simeq 9.4 \times 10^{19} m^{-3}$; $I_p \simeq 100kA$; $a \simeq 0.17m$; therefore $N^G \equiv \overline{n}_e \frac{\pi a^2}{I_p(MA)} \simeq 0.81$, where N^G is the Greenwald number[3]. This result can be seen in figure 2 in which $\overline{n}_e$ is plotted against the plasma current density. The temporal evolution of the shot 33543 and the Greenwald limit are also shown.

The proximity to the Greenwald limit at higher $I_p/\pi a^2$ is an important feature for MAST since this device is planned to operate at least at $I_p/\pi a^2 \geq 1.3 MA/m^2$ ($I_p \geq 1MA$ and $a = 0.50m$ yield $\overline{n}_e^{max} = 1.3 \times 10^{20} m^{-3}$ from the Greenwald scale).

No sign of plasma detachment from the divertor has been observed. During the continuous density rise, H_α radiation from the top divertor and also the ion saturation current level (Langmuir probes in the same divertor) are also rising. No sign of MARFEs has been observed. IREs limit further density increase, as observed in previous density limit studies on START.

Unlikely previous observations of the edge radiative losses at the bottom divertor (the ion ∇B_ϕ drift direction) during the density rise, in the present experiment the edge radiation seems uniformly distributed poloidally. These may be due to the observed reduction of the level of impurities added to the systematic use of glow and Ti gettering techniques.

Finally, the START operating diagram is shown in figure 3. The improvement with the NBI are clearly seen by comparing the pure Ohmic with NBI heated discharges: the parameter $\overline{n}_e R_o/B_\phi$ increases from 0.8 to $1.5 \times 10^{20}/m^2 T$.

From this figure, a remarkable time evolution from the shots 32993/32998 is also observed. They move to the limit of the two regions: the highest normalized density and current, both by $\overline{n}_e R_o/B_\phi$ and $1/q_{cyl}$, respectively. Since these shots overcame the highest value of $\overline{n}_e R_o/B_\phi$, ie, $1.35 \times 10^{20}/m^2 T$ but not the $1/q_{cyl}$ maximum ($\simeq 1.0$), this might be an indication of a q limit, or a limit due to a combination of effects including pressure-driven instabilities[2].

Conclusion

Experimental results of density and edge safety factor limits of START have been presented. Very low q-edge [$q_\psi(95\%) \simeq 2.3$] at aspect ratio $R_o/a \simeq 1.37$ in high β ($\beta_T \simeq 30\%$) shots have been observed. In high density regimes, an integral line density of $\overline{n}_e \simeq 9.4 \times 10^{19} m^{-3}$, the highest yet, has been obtained by means of a combination NBI and strong extra puff. High reproducibility of discharges due to the inter-shot helium glow and Ti gettering has been observed in a scenario in which the density approaches the Greenwald limit ($N^G \simeq 0.81$). No sign of MARFEs, or plasma-divertor detachment have been observed.

Studies of the density dependence as a function of toroidal field, magnetic configuration (limiter/DND), input power heating, gas species, plus deuterium/hydrogen pellet injection are planned for the coming months.

Acknowledgement. This work is funded jointly by the UK Department of Trade and Industry, and EURATOM and supported by a collaboration with ORNL and the US DOE.

[1] A. Sykes et al., "High β performance of the START Spherical Tokamak", topical talk in this Conference (to be published in Plasma Phys. and Contr. Fusion).

[2] M. Gryaznevich, et al. "Profile optimization and MHD-activity in high-β NBI discharges on START", in this Conference.

[3] M. Greenwald et al., Nucl. Fusion, 28 (1988), 2199.

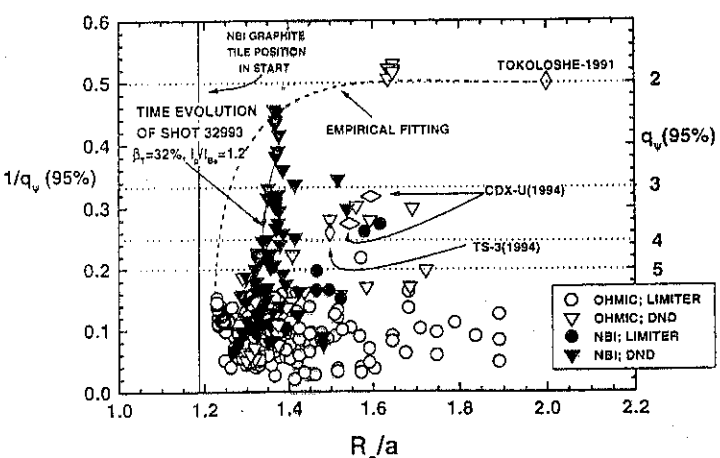

fig.1 - Experimental results of the edge safety factor, $q_\phi(95\%)$, as a function of the aspect ratio R_o/a.

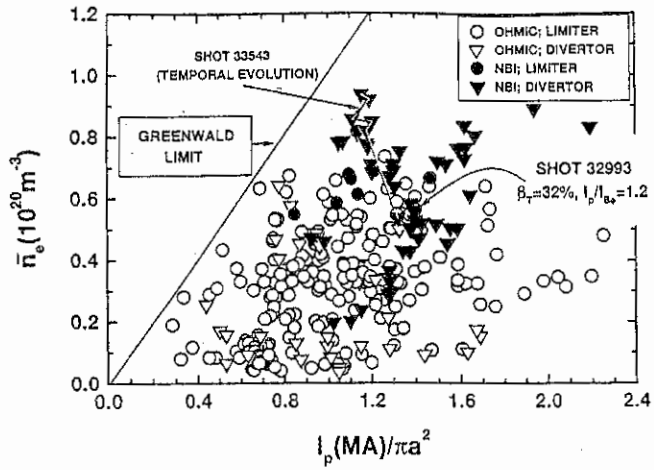

fig.2 - Integral line density, $\bar{n}_e$, as function of the plasma current density.

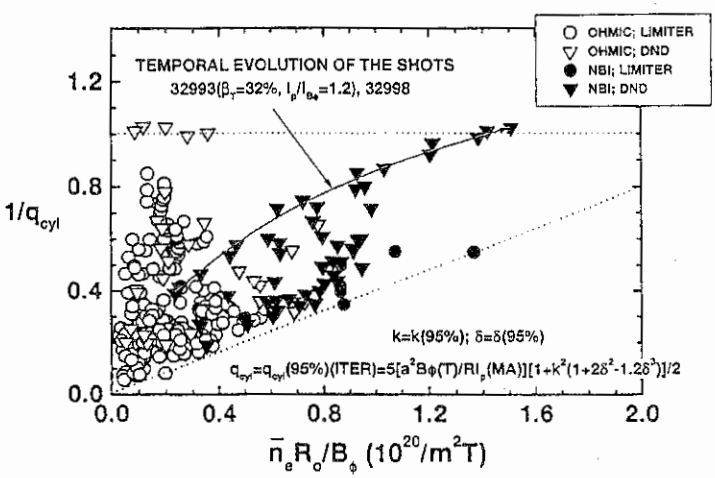

fig.3 - START operating diagram

Edge Scalings on COMPASS-D and START

GF Counsell, MG Booth, JW Connor, SJ Fielding, KM Morel† and C Silva‡

UKAEA Fusion, Culham Science Centre, Abingdon, Oxfordshire, OX14 3DB
(UKAEA Fusion/Euratom Association)
†Imperial College of Science, Technology and Medicine, London, SW7 2BZ
‡Associação EURATOM/IST, 1096 Lisboa Codex - Portugal

Introduction

A firm theoretical understanding of the tokamak scrape off layer (SOL) remains elusive and even empirically based scalings for the SOL properties are rare. This paper reports the development of a database of SOL parameters for the conventional aspect ratio tokamak COMPASS-D and the tight aspect ratio tokamak START at Culham, both of which exhibit a collisionless SOL. A simple empirical scaling for the power scale length, Δ, is developed and compared to a variety of theoretical scalings derived from a balance of perpendicular and parallel heat flows in the SOL. A collisional form of one of the theoretical scalings, which gives the best fit to available data, is used to estimate a SOL power scale-length for ITER.

Theory

Simple models for the tokamak SOL are often based on a balance of parallel heat transfer against perpendicular diffusion. In the most common 2-point model (Figure 1), all power flow into the SOL is taken to occur at a single point, the stagnation point, at a distance L_c from the nearest material surface.

Since the parallel diffusivity is normally assumed to be classical, the models are essentially determined only by the collisionality of the SOL and the choice of cross-field transport coefficient, $\chi_\perp$. Several models for $\chi_\perp$, including Bohm and Gyro-Bohm diffusion, have been integrated into models for the SOL by Itoh and Itoh [1] to develop scalings for the SOL width (Δ) in terms of key operating parameters, such as the safety factor. This work has been extended at Culham to include a greater range of parameters in the scaling and to investigate other models for $\chi_\perp$.

Power flow from the plasma into the SOL must be balanced by // and $\perp$ flows -
// heat flow $\Rightarrow$ $P = -A_{//} n \chi_{//} \nabla_{//} T$, $\perp$ heat flow $\Rightarrow$ $P = -A_\perp n_i \chi_\perp \nabla_\perp T$. Taking $A_\perp \sim aR$, $A_{//} \sim \Delta B_p / B_t$ (allowing for the field line angle) and approximating $\nabla_{//} T \sim T/L_c$, $\nabla_\perp \sim T/\Delta$ yields

$$\left.\begin{array}{ll} \text{// heat flow} & n\chi_{//}\dfrac{T}{L_c} \sim \dfrac{P}{\Delta R}\dfrac{B_t}{B_p} \\ \perp \text{ heat flow} & n\chi_\perp \dfrac{T}{\Delta} \sim \dfrac{P}{aR} \end{array}\right\} \quad \Rightarrow \quad \Delta^2 \sim L_c^2 \frac{\chi_\perp}{\chi_{//}}$$

$$\text{assuming, } B_p \sim \frac{a}{Rq} B_t,\ L_c \sim Rq$$

Generalised classical heat transfer for the // case $\Rightarrow$ $\chi_{//} \sim T^\beta \chi_{//_0}$, where $\beta = 1/2$ and $\chi_{//_0} \sim L_c$ for collisionless SOLs and $\beta = 5/2$ and $\chi_{//_0} \sim 1/n$ for collisional SOLs. For the $\perp$ case, let $\chi_\perp \sim \chi_{\perp_0} T^\alpha \nabla T^\gamma$ (from micro-turbulence arguments), where $\chi_{\perp_0} \sim n^\delta q^\mu R^\nu a^\sigma B^\lambda$ then gives

$$\Delta \sim R^{\frac{(\nu+1)(\beta+1)+\eta\varepsilon}{\omega}} q^{\frac{\mu(\beta+1)+(\eta+1)\varepsilon}{\omega}} B^{\frac{\lambda(\beta+1)}{\omega}} a^{\frac{(\sigma+1)(\beta+1)-\varepsilon}{\omega}} P^{\frac{\varepsilon-(\beta+1)}{\omega}} n^{\frac{(\delta+1)(\beta+1)+(\eta-1)\varepsilon}{\omega}}$$

where $\omega = \alpha + (\beta+2)(\gamma+1)$, $\varepsilon = \alpha + \gamma + 1$ and $\eta = 0 \Rightarrow$ Collisionless, $\eta = 1 \Rightarrow$ Collisional

Models for $\chi_\perp$ can then be expressed in terms of the six parameters, yielding a scaling law for the SOL width. For instance the Bohm model, $\chi_\perp \sim T/B$ $\Rightarrow$ α=1, γ=0, δ=μ=ν=σ=0, λ=-1 $\Rightarrow$

$\Delta \propto Rq^{8/11}B^{-7/11}a^{3/11}P^{-3/11}n^{7/11}$. For comparison with experiment, q was taken as q_{95}, B as the axial magnetic field B_0, n as the electron density at the separatrix n_{es} and P as (P_{in}-P_{rad}). This choice is, to a certain extent, arbitrary and scalings developed elsewhere (for instance [2],[3]) have been expressed in terms of other local and global quantities.

Experiment

The theoretical SOL width scalings involve 6 parameters, some of which have small exponents. These models can only be adequately validated against data covering a broad parameter regime, not usually available on a single machine. UKAEA Fusion has two tokamaks, COMPASS-D - with a conventional ITER-like aspect ratio and START - a tight aspect ratio device. A database of SOL parameters has now been established for both devices. Only L-mode shots have so far been considered but these include shots with auxiliary ECRH on COMPASS-D and with NBI on START.

Data have been obtained using arrays of swept Langmuir probes across the strike point region and (in the case of COMPASS-D), from a fast reciprocating triple probe at the top of the plasma. Calculated SOL power scale lengths were mapped back to the mid-plane using reconstructions of the magnetic flux surfaces, by assuming pressure conservation along flux tubes. Table 1 indicates the range of parameters and observed scale lengths in the two devices.

Care has to be taken when comparing data from different tokamaks. Most importantly, the collisionality of their SOLs should lie in the same regime. A measure of the collisionality is $\nu^* \sim n(10^{18})L_c(m)/850T^2(keV)$. For COMPASS-D, ν^* <1.6 and for START, ν^* <0.6 indicating that both devices exhibit an essentially collisionless SOL.

Analysis

Figure 2a presents a multivariate least squares fit to the COMPASS-D database (excluding the R and a parameters, which are nearly constant between shots). This yields $\Delta \sim q_{95}^{0.448}P^{0.139}n_{es}^{-0.438}B_0^{-0.172}$. The P and n_{es} exponents have the strongest correlation coefficients and sensitivity analysis reveals n_{es} to be the most important parameter in determining the quality of fit. Indeed, formulating a best-fit scaling in terms of n_{es} alone yields $\Delta \sim n_{es}^{-0.405}$ with only a marginally worse quality of fit (Figure 2b).

Figure 3a shows the combined COMPASS-D and START data against the empirical scaling, $\Delta \sim n_{es}^{-0.405}$. Although the START data also seem to be reasonably well fitted by this simple single-variable scaling, it does not provide a good fit to the coupled data set. This may indicate the need to include other parameters, such as B_0 or R, to account for tight aspect ratio effects and Figure 3b presents a multivariate best-fit to the coupled data set using the full set of six parameters, n_{es}, B_0, q_{95}, P, R and a - $\Delta \sim q_{95}^{-0.019}P^{0.106}n_{es}^{-0.694}B_0^{-0.399}R^{-1.66}a^{4.08}$. The exponents for P and n_{es} are similar to the COMPASS-D only fit, giving enhanced confidence in the scaling with these parameters.

Eight theoretical scalings for the SOL power width were tested against the COMPASS-D and START databases. Five of the collisionless scalings appear to fit the COMPASS-D data reasonably well, however the fit provided by the collisionless skin depth model ($\chi_\perp \sim T^{1/2}/Rqn$) is significantly better than the rest (Figure 4). None of the models fit both the COMPASS-D and START data simultaneously but the collisionless skin depth model provides a reasonable fit to both data sets individually. This model produces a simple scaling for collisionless SOLs - $\Delta \sim n_{es}^{-1/2}$, in good agreement with the empirical scaling observed for the COMPASS-D data.

Since both COMPASS-D and START exhibit a collisionless SOL, only the collisionless models have been tested in detail. However, a preliminary set of data from Alcator C-MOD [2], ASDEX [4] and JET [5] (each of which exhibits a collisional SOL) was assembled. This was used to examine whether the collisional scaling derived from the assumption of a collisionless skin depth model for $\chi_\perp$ (but with

collisional parallel transport) may also provide a good model for the collisional SOLs found in the majority of large devices,

The collisionless skin depth model, for a collisional SOL, yields $\Delta \propto R^{3/10} q^{-1/10} B^{0} a^{4/10} P^{-4/10} n^{0}$. This can also be expressed in terms of the power density at the separatrix P_{surf} (~P/aR), yielding $\Delta \propto (qR)^{-1/10} P_{surf}^{-4/10}$. Figure 5 shows data from the collisional SOLs against this scaling, which seems to provide a reasonable fit.

Clearly, testing against a comprehensive multi-machine database will be required before stronger conclusions can be drawn. However, the collisionless skin depth scaling would yield a mid-plane SOL power width for ITER (P_{SOL}~100MW, R~8m, a~3m, q_{95}~3.0) of order 6-9mm, somewhat narrower than that predicted by other scalings.

Conclusions

- A database of SOL parameters has been established on both COMPASS-D and START, both of which exhibit an essentially collisionless SOL. The COMPASS-D database has been incorporated into the ITER multi-machine divertor database of SOL parameters.

- Best-fit analysis of the COMPASS-D data shows that the SOL power scale length in that device is well fitted by a very simple scaling law, $\Delta \sim n_{es}^{-0.405}$. Inclusion of the START data indicates that machine size or toroidal field may need to be included in order for the scaling law to be valid at tight aspect ratio.

- Theoretically based scaling laws have been developed and validated using the COMPASS-D and START databases, as well as data from tokamaks exhibiting a collisional SOL. Of those tested, the collisionless skin depth model for $\chi_{\perp}$, which generates a simple scaling based only on the separatrix density $\Delta \sim n_{es}^{-1/2}$, provides the best fit and is in good agreement with empirical scalings derived from the database.

- A preliminary set of SOL power width data for a range of tokamaks exhibiting collisional SOLs has been tested against a collisional scaling derived with the assumption of collisional parallel transport and a collisionless skin depth model for $\chi_{\perp}$. This model yields $\Delta \propto (qR)^{-1/10} P_{surf}^{-4/10}$. The data does not appear inconsistent with this scaling, although a much more comprehensive database will be required to properly test the scaling. The collisionless skin depth model scaling indicates a SOL power width for ITER of order 6-9mm

References

[1] 'On scaling laws in scrape of layer plasmas', S-I Itoh and K Itoh, Plasma Phys. Control. Fusion 36 (1994) 1845-1851

[2] 'Experimental investigation of transport phenomena in the scrape of layer and divertor', Invited Paper, B LaBombard *et al*, 12th PSI Conference, San Raphael, May 1996

[3] GK McCormick *et al*, Journal of Nuclear Materials 196-198 (1992) 264-270

[4] GK McCormick *et al*, Journal of Nuclear Materials 162-164 (1989) 264-269

[5] JA Tagle *et al*, Journal of Nuclear Materials 196-198 (1992) 409-414

Acknowledgements

This work has been funded by the UK Department of Trade and Industry and EURATOM. KM Morel would like to acknowledge joint support by UKAEA Fusion and the EPSRC. C Silva would like to thank EURATOM for a fellowship.

	COMPASS-D (SND)	START (DND)
R (m)	0.56	0.22-0.29
a (m)	0.18	0.15-0.22
P (edge, MW)	0.06-0.48	0.23-0.49
q_{95}	3.0-6.2	4.0-8.3
B_0 (T)	0.8-1.9	0.21-0.29
n (edge, $10^{18}m^{-3}$)	1.5-15	0.4-1.8
T (edge, eV)	30-50	40-100
ν^* (edge)	0.2-1.6	0.03-0.6
ν^* (edge) - Typ	1.2	0.1
Δ (power, cm)	0.4-1.1	0.4-1.3

Table 1 COMPASS-D/START operating parameters

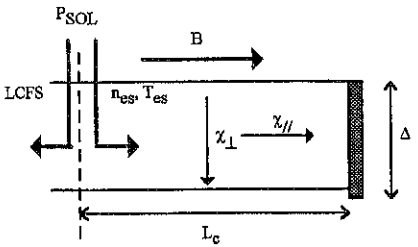

Figure 1 Simple model for the SOL - width determined by balance of parallel and perpendicular flows

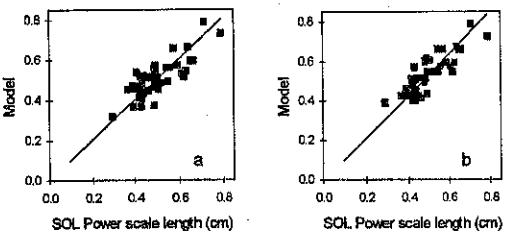

Figure 2a Multivariate least squares fit and 2b single variable only fit ($\Delta \sim n_{es}^{-0.405}$) to COMPASS-D data

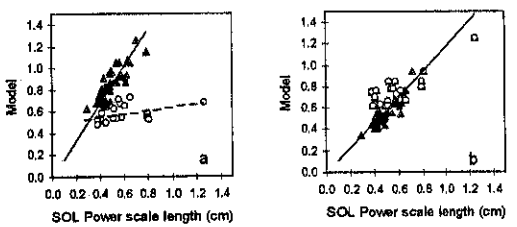

Figure 3a Single variable only fit ($\Delta \sim n_{es}^{-0.405}$) and 3b multivariate fit to combined COMPASS-D and START data

▲ COMPASS-D
○ START

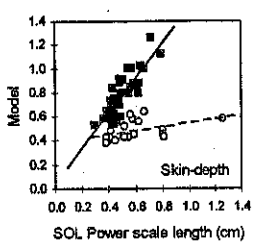

Figure 4 Collisionless skin-depth model against combined COMPASS-D and START data

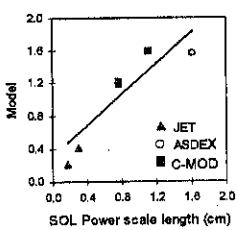

Figure 5 Collisional SOL scaling based on collisionless skin-depth model for $\chi_\perp$ against measured power scale lengths from variety of collisional SOL tokamaks

Analysis of Halo Current Results on COMPASS–D and START

G.G. Castle, A.W. Morris, L.C. Appel, A. Caloutsis, C.G. Gimblett, P.J. Knight, R. Martin

UKAEA Fusion, Culham, Abingdon, Oxon. OX14 3DB.

(UKAEA/EURATOM Fusion Association)

Introduction The study of both toroidally symmetric and asymmetric halo currents during disruptions is of interest due to the mechanical and thermal stresses produced on the containment vessel and its interior structures. Of particular importance for the design of ITER is understanding the scaling of the halo currents. In this paper halo current data from COMPASS–D ($a < 0.232\ m$, $b < 0.385\ m$, $R = 0.557\ m$, single null divertor) vertical displacement event (VDE) experiments are compared to theory, using both analytical models and numerical codes. New data from START (spherical tokamak, $a = 0.13 - 0.34\ m$, $R = 0.2 - 0.4$, double null divertor) is also presented.

Symmetric halo currents Data from both COMPASS–D and Alcator C-MOD [1, 2, 3] exhibit maximum symmetric poloidal halo current bounded by the curves of the form $I_\theta < C_o I_{po}/q_{95}$ (I_{po} is the pre-disruption plasma current; for COMPASS–D $C_o = 1.2$, for Alcator C-MOD, $C_o = 1.6$). Upper limits of this form may be derived either from requiring the halo region to be force-free or from imposing a constant toroidal flux condition. As the plasma disrupts, both the plasma pressure and current are lost, causing a net change in the toroidal flux. Poloidal currents will be induced to attempt to conserve this flux. In the cylindrical zero pressure case ($\beta_\theta = 0$) (experimentally the largest halo currents are paramagnetic) one can show that if the plasma and vessel cross-sectional areas are A (pre-disruption) and A_v, then the largest poloidal halo current I_θ which can be driven due to the loss of the plasma current is

$$I_\theta = \frac{A_v}{A}\frac{1}{2q_v} I_{po} \tag{1}$$

(here we use $q_v = (a_v/R_v)B_\phi/B_\theta(a)$ where the subscript 'v' refers to vessel quantities). For COMPASS–D plasmas, typically $A_v/A \simeq 2.5$ so that one would expect $I_\theta = 1.3 I_{po}/q_v$ to be a representative value of the maximum halo current driven by a loss of I_p alone. The force-free constraint also provides a mechanism for deriving a scaling for the maximum poloidal halo current. We consider a simplified model of the plasma-halo system consisting of an inner 'core' plasma (of minor radius r_o) carrying a current of $I_{core} = \alpha I_p$ (I_p is the instantaneous total toroidal current and $0 \le \alpha \le 1$) and a surrounding cylindrical shell of thickness Δ carrying the remaining current of $(1-\alpha)I_p$. Calculation of B_θ and q as a function of minor radius yields the relation

$$\frac{I_\theta}{I_p} = \frac{2}{q_*}\frac{1-\alpha}{2\delta+\delta^2}\left[\alpha\log(1+\delta) + \frac{1-\alpha}{2\delta+\delta^2}\left(\delta + \frac{1}{2}\delta^2 - \log(1+\delta)\right)\right] \tag{2}$$

where $\delta = \Delta/r_o$ and $q_* = 2\pi r_o^2 B_\phi/(\mu_o R I_p)$. It can be shown that the maximum poloidal halo current occurs for a thin halo region ($\delta \to 0$) carrying all of the plasma current

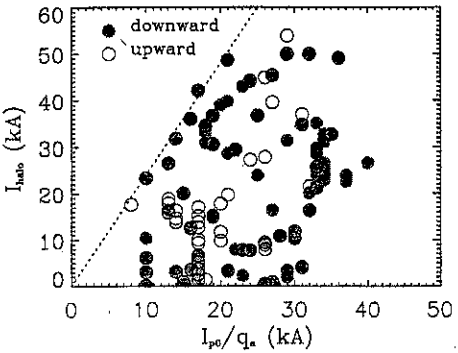

Figure 1: *The maximum poloidal halo current I_θ as a function of I_{po}/q_v. The dashed line indicates the upper limit of $I_\theta^{max} \sim 2.2 I_{po}/q_v$.*

($\alpha \rightarrow 0$). In this limit we find that

$$\frac{I_\theta}{I_{po}} = \frac{1}{2q_v}\frac{r_o^2}{a^2}. \tag{3}$$

Thus it appears that the experimental scaling $I_\theta/I_{po}|_{max} \sim q_v^{-1}$ is predicted by both the force-free and the flux conservation constraints, although the leading coefficients from both theories are smaller than those observed experimentally.

Asymmetric halo currents On COMPASS–D (as on other machines) toroidal asymmetries in the poloidal halo currents have been observed; these typically have peak-to-average ratios of $\sim$ 2. This asymmetric component exhibits varying behaviour from machine to machine, rotating toroidally on some while remaining stationary on others (on COMPASS–D and START it is fixed). The cause of the asymmetry has not yet been determined, although there are a few possible explanations. One explanation is that the asymmetry is an $m = 1$, $n = 1$ kink mode which grows as the halo $q \sim 1$. However, on COMPASS–D the maximum growth rate of the asymmetric halo current component $\gamma_1 = d/dt(I_{asy})/I_{asy}|_{max}$ was compared to the Alfvén frequencies $\gamma_A = v_A/a$ (spanning a factor of two) and no obvious correlation was found (the Alfvén frequencies ranging from 10-20 MHz while the maximum asymmetry growth rates ranging from 30-80 kHz, see Figure 2). A similar result obtained from comparison of the maximum amplitudes of the asymmetry to the Alfvén times. One expects a correlation of $\tau_{asymmetry}$ with $\tau_{Alfvén}$ for kink modes, but none is observed. This suggests that kink modes are unlikely to be the cause of the asymmetry. However, $\tau_{asymmetry}$ is correlated with I_θ^{max}/I_{po}, which is suggestive of the halo current entering the wall through a sheath. A second mechanism for the development of a toroidal asymmetry has been advanced in the form of the 'moving-contact instability' [4]. The idea is that the plasma acts like a series of coupled inductive loops, each of which may evolve in cross-sectional area and whose 'contact points' (the points at which the annular halo region intersect the vessel wall) may move. The dispersion relation for such an instability has been evaluated in an idealised cylindrical geometry.

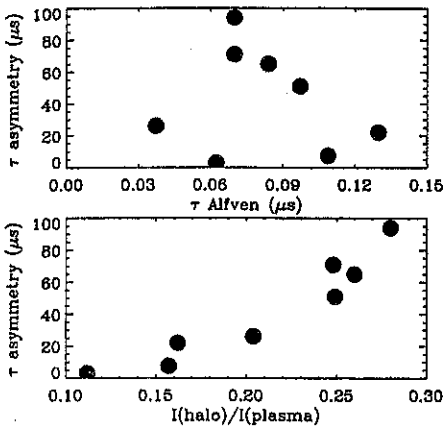

Figure 2: Minimum asymmetry growth time $\tau_{\text{asymmetry}}$ as a function of I_θ^{max}/I_{po} (bottom plot) and $\tau_{\text{Alfvén}}$ (top plot) for SND COMPASS–D discharges with $q_{95} = 3.4 - 3.7$, $I_{po} = 171 - 175\,kA$. The magnetic field and density vary from $B_\phi = 1.12 - 1.42\,T$ and $\overline{n}_e = 1.9 - 5.2 \times 10^{19}\,m^{-3}$. The Alfven velocity was calculated via $v_A = B\mu_o^{-1/2}\rho_m^{-1/2}$, $\rho_m = Zm_p\overline{n}_e$, and $Z = 2$.

While the model in its present form is not quantitatively applicable to realistic tokamak geometries, several qualitative features have emerged. One feature is that the 'effective q' of the lines of current density, given by

$$q_{\text{eff}} = \lambda q_w + (1 - \lambda)q_* \tag{4}$$

(where λ is the angular fraction of the halo region occupied by the wall path and $q_w = \epsilon j_\phi^{\text{wall}}/j_\theta^{\text{wall}}$), should be a rational number for maximum growth rate. Preliminary estimates of q_{eff} near the time of peak halo asymmetry in COMPASS–D data range from $q_{\text{eff}} \sim 1 - 2$ or so. Whether these values of q_{eff} are sufficiently resonant cannot be answered until the width of the resonance is known.

START results START is a low aspect ratio ($1.2 \leq A \leq 1.5$) spherical tokamak usually run in a double null divertor configuration. New halo current diagnostics were installed recently on START, including six partial Rogowskii coil segments spaced evenly in toroidal angle around the centre column (each samples nearly 60 toroidal degrees) located at $Z = +60.3\,cm$ above the vessel midplane, and at a major radius of $R = 0.059\,cm$. Six other Rogowskii coils were fitted to measure the currents flowing in one coil feed, four coil supports, and the TF centre column (all located at $Z \simeq +60cm$). Normally, START plasmas are vertically stable and immune to VDEs. We counteracted the intrinsic vertical stability by applying a B_R bias to vertically destabilise the plasma and produce a VDE. Typically the plasma current decays in $50-200\,\mu s$, during which time poloidal currents are driven in the plasma (and perhaps external conducting structures), producing changes in B_ϕ which are detected by the partial Rogowskii segments (see Figure 3). For the START discharges studied thus far, the B_ϕ structure produced during VDEs appear to be a mixture of $n = 2$ and $n = 1$ components (n is the toroidal mode number), with the $n = 2$ amplitude predominating. This structure is nearly stationary in phase, and is reproducible from shot to shot for the discharges studied. The interpretation of the signals from the halo Rogowskiis is complicated in this case by several facts. One problem is that the lower surface of the top graphite limiter is located at $Z = +45\,cm$, 15 cm away from the halo segments. This precludes measuring the symmetric halo current flowing anywhere

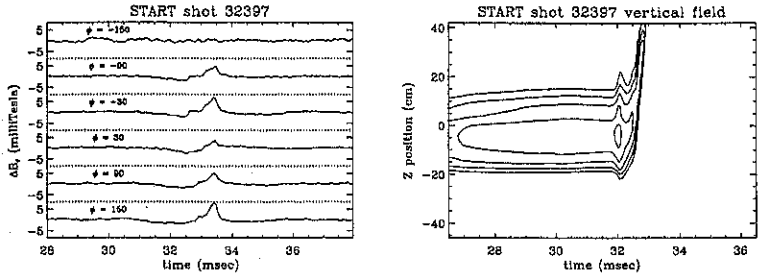

Figure 3: *The left figure indicates the temporal evolution of $\Delta B_\phi = B_\phi - B_{\phi o}$ during a VDE at the six toroidal locations of the new partial halo Rogowskiis on START for shot 32397. The toroidal angles are marked in degrees. The right figure is a contour plot of the vertical magnetic field distribution along the centre column, and clearly shows the vertical plasma motion.*

except along the TF centre column (through the plane of the coils). Some axial current is detected, albeit at a low level ($I_{\text{axial}}/I_{po} \sim 1\,\%$ or less). However, within the context of a suitable model it is possible to determine the toroidally asymmetric poloidal halo current distribution. If one assumes that the poloidal halo current flows on the plasma surface with a spatial dependence like $I_{mn}(\theta,\phi) = I_{mn}\sin(m\theta - n\phi)$, then for $m = 1$ one obtains estimates $I_{1n}/I_{po} \sim 10\,\%$ ($n = 1$, $n = 2$). Analysis of the currents flowing in the various coil feeds shows that as much as 30 % of the asymmetric signal could be due to pickup from the currents induced in the feeds.

Conclusions The form of the scaling for the maximum symmetric poloidal halo currents can be derived from both flux conservation and magnetic geometry constraints, lending credibility to the experimental scaling as a predictive indicator. The current ITER design point falls on the boundary of the COMPASS-D data ($I_\theta^{max}/I_{po} = 0.4$, $q_{95} = 3$). The toroidal asymmetry in the poloidal halo currents on COMPASS-D is unlikely to be due to a kink mode, as the Alfvén times are around 2-3 orders of magnitude smaller than, and uncorrelated with, the experimental asymmetry growth times. The 'moving-contact' model is however a possible mechanism for the asymmetry.

This work was funded by the UK Department of Trade and Industry and Euratom

References

[1] G.G. Castle, A.W. Morris, et al., 23^{rd} EPS, Kiev, **20C** part I, pp. 420-423, 1996

[2] G.G. Castle, A.W. Morris, et al., Proc. Montreal IAEA Conf., 1996

[3] R.S. Granetz, et al., Nuc. Fus., **36**, No. 5, pp. 545-556, 1996

[4] A. Caloutsis, C.G. Gimblett, Int. Sherwood Fusion Theory Conference, Madison, Wisconsin, poster 1D44, 1997

Neoclassical Islands on COMPASS-D

D. A. Gates, B. Lloyd, A. W. Morris, G. McArdle, M. Valovic, C. D. Warrick, H. R. Wilson, and the COMPASS-D and ECRH teams
UKAEA, Fusion, Culham Science Centre, Abingdon, Oxon, OX14 3DB, UK.
(UKAEA/EURATOM Fusion Association)

Introduction

Neoclassical magnetic islands are observed to limit the achievable β ($\beta \equiv 2\mu_0 \langle p \rangle / B^2$, where $\langle p \rangle$ is the volume averaged pressure) in COMPASS-D low collisionality, single-null divertor plasmas with ITER-like geometry(R_0=0.56m, B_0 =1.2T, I_p=120-180kA, κ=1.6, ε=0.3). The limiting β is well below that expected from ideal instabilities with the maximum achievable normalised β ($\beta_N \equiv \beta a B / I_p$) in the range of 1.6-2.2. The plasma is heated with up to 1.8MW of 60GHz ECRH at 2nd harmonic with X-mode polarisation. The deviation from the ideal β-limit ($\beta_N \sim 3.0$) is an important issue for ITER since ITER will operate at low collisionality for longer than most high β tokamak experiments to date and has a nominal design point with a normalised β of ~2.2.

Initial calculations of the stability of bootstrap driven islands [1], which preceded the initial observations, indicated that neoclassical tearing modes were unstable for all values of β_p at collisionalities sufficiently low for a significant fraction of bootstrap current to flow. More recent calculations [2,3], motivated by the initial observation of a critical island width on TFTR [4], suggest that other stabilising mechanisms are important in determining the onset of these modes. At present, there are two proposed mechanisms for stabilisation: one based on a model of the transport through the island [2], called the $\chi_\perp / \chi_\parallel$ model, the other on the effect of ion polarisation currents [3]. The measured islands on COMPASS-D have a threshold island width below which the mode will not grow, in accordance with [4]. The density scaling of the point of onset of the measured instabilities is compared to the predictions of [1,2] and [2] is shown to be consistent with observation.

Island Dynamics

The basic mechanism that drives neoclassical tearing modes is relatively simple. If a magnetic island exists, the radial pressure gradient inside that island is removed (assuming the transport along field lines dominates the transport across field lines). The loss of this pressure gradient removes the drive for the bootstrap current (in the helical region inside the island separatrix). The loss of the bootstrap current further increases the size of the island, which removes the pressure gradient over a wider region. This process continues until the drive from the bootstrap current is balanced by the (potentially) stabilising effects of the equilibrium current gradient.

The full equation that governs the dynamics of neoclassical tearing modes can be written:

$$\frac{dw}{dt} = \left(\frac{1.22\eta_{nc}}{\mu_0}\right)\left[\Delta' + a_1 \varepsilon^{1/2} \beta_p \frac{L_q}{L_p}\left(\frac{w}{w^2 + w_c^2}\right) - a_2 \frac{\rho_{\theta i}^2 \beta_p g(\varepsilon)}{w^3}\left(\frac{L_q}{L_p}\right)^2\right] \qquad (1)$$

where w = island width, η_{nc} = the neoclassical resistivity, Δ' = the jump in logarithmic derivative of the perturbed magnetic flux, β_p = the local poloidal β, L_p and L_q are, respectively, the scale lengths of the pressure and q, and m and n are the poloidal and toroidal mode numbers,respectively (all quantities to be evaluated at the rational surface of interest, $r=r_s$ where $m = nq(r_s)$). Here a_1 and a_2 are coefficients which depend on the details of the equilibrium parameters. The second term on the right is a combination of Glasser-Green-Johnson (stabilising) and bootstrap island (destabilising) terms modified to include the stabilising effects of transport, with w_c parameterising the magnitude of the effect of the $\chi_\perp/\chi_\parallel$ model and given by the relation:

$$w_c = 1.8 r_s \sqrt{\frac{8R_0L_q}{r_s^2 n}} \left(\frac{\chi_\perp}{\chi_\parallel}\right)^{1/4} \qquad (2)$$

The third term in Equation (1) is the contribution due to ion polarisation currents, with $\rho_{\theta i}$= the poloidal ion Larmor radius, and $g(\varepsilon)$ defined by:

$$g(\varepsilon) = \begin{cases} \varepsilon^{3/2} & for\ \nu_i/\varepsilon\omega_{*e} << 1 \\ 1 & for\ \nu_i/\varepsilon\omega_{*e} >> 1 \end{cases}$$

The ratio L_p/L_q is unmeasured, so it is assumed fixed and equal to 1.0 during the discharge. $\Delta' = -2/r_s$ also by assumption. The coefficients are taken to be $a_1 = a_2 = 7$ (for discussion of coefficients see Refs. [1] and [3]).

This equation has been fitted to measured mode amplitudes on several experiments. An example for COMPASS-D is shown in Figure 1.

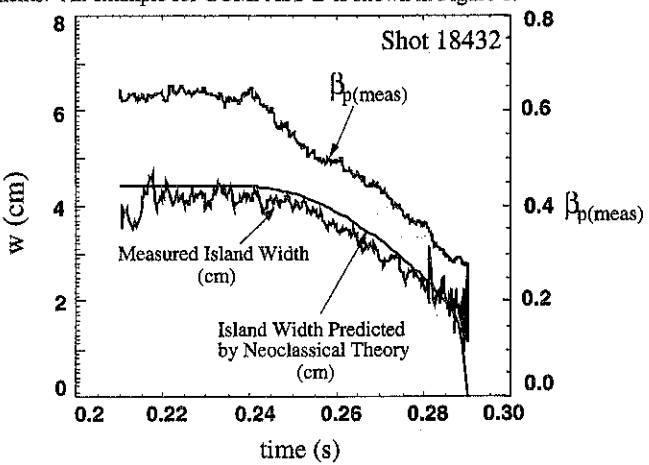

Figure 1 *Comparison between the predicted and measured island width (from $B_{r(n=1)}$) during a power rampdown for a neoclassical island on COMPASS-D.*

Thresholds

Figure 2a shows the Mirnov activity as measured by a Mirnov coil on the outboard midplane for four of the shots in a density scan. The values of density and β_p at the onset of MHD (or at maximum if no MHD) are also shown. As the density is raised the onset of the MHD is delayed progressively until it ceases to appear.

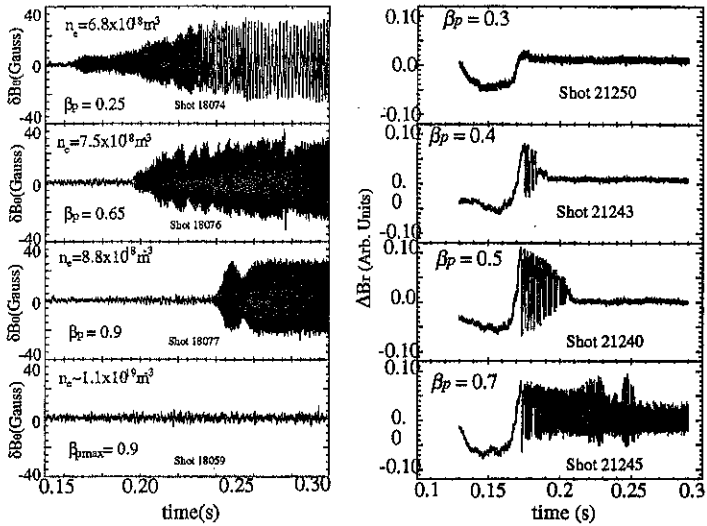

Figure 2 a)Magnetic fluctuation data from a shot to shot density scan showing the progressive delay of the onset of a neoclassical island as the density is raised. The ECRH power was ramped similarly in each discharge. b) An error field induced mode, which at low β_p decays after the error field is turned off, decays more slowly as the pressure is raised, finally persisting. This indicates a critical β for instability.

The cause of the delayed onset of the mode in Figure 2a is a change in the critical island threshold width with plasma density (and hence plasma collisionality). The physical mechanism that determines the size of the island threshold width is an important issue under current examination by all the experiments on which neoclassical tearing modes have been observed. Also crucial is the scaling of the perturbations that "kick" the neoclassical mode over this threshold, since the onset of neoclassical modes is always correlated with another "benign" MHD event (e.g. error fields [as in Figure 2b], sawteeth [as in Figure 2a], ELMs, and fishbones). The critical island threshold and the seed island are the key to understanding the likely impact of neoclassical tearing modes on ITER, since they determine the onset of the mode and which modes are unstable. Unfortunately, there is still considerable uncertainty in the theoretical calculations (see reference [5], for example) of the threshold mechanisms as well as in the experimental data. An ITER database [6] of critical plasma parameters at the point of onset of neoclassical tearing modes has been assembled in order to help determine the physical mechanisms responsible for the neoclassical island threshold. Shown in Figure 3 are comparisons between the data from ITER database for MHD mode onset and the scalings predicted by the threshold mechanisms espoused in References [2] and [3].

Critical β

Figure 2b shows a series of discharges for which the power was quickly ramped to a set value and then held fixed. An error field was then applied to induce a mode. Following this, the error field was turned off and the behaviour of the mode

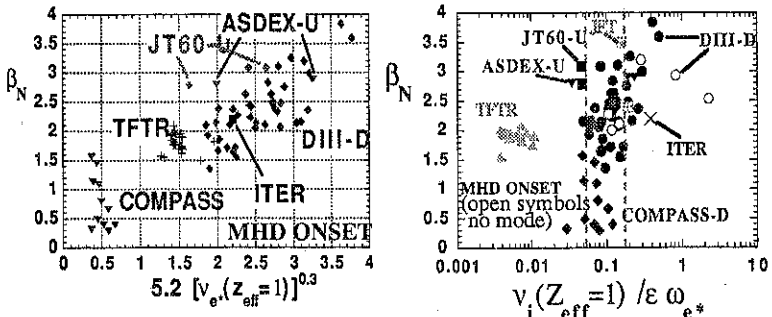

Figure 3 *Figure showing the scaling of the measured onset of MHD against the scalings predicted by the threshold theories in* [2] (left) *and* [3] (right).

observed. There is a clear indication of a critical β_p for instability. For low values of β_p, the mode either never appears or decays. As β_p is raised, the decay of the mode slows. Eventually, when the critical β_p is exceeded ($\beta_{pcrit} \sim 0.6$), the mode persists. The density in all these shots was set to ~1.1×10^{19}m^{-3} which, as can be seen from Figure 2a, is naturally stable to neoclassical islands. By operating with a density of 5.5×10^{18}m^{-3}, neoclassical islands can be observed with $\beta_p \sim 0.2$. This indicates that the critical β_p is a strong function of the plasma density [7]. This agrees with the polarisation current model which predicts a rapid change (due to the function $g(\varepsilon)$), but disagrees with the $\chi_\perp/\chi_{//}$ model which varies only slowly with collisionality (since $w_d \sim (\chi_\perp/\chi_{//})^{1/4}$).

Summary

Neoclassical islands have been observed to limit the achievable β in COMPASS-D long pulse, low-collisionality ITER-like plasmas. This effect has also been observed in ASDEX-U, TFTR, DIII-D, and JT-60U. The onset of the modes is determined by the collisionality scaling of the threshold island width. The threshold width is large at high collisionality, thus preventing naturally occurring MHD "seeds" from triggering the modes. An ITER database for the onset of neoclassical islands has been compared to the predictions of two threshold theories. As well as a critical island width, there is also a critical β_p. On COMPASS-D this critical β_p is shown to be a strong function of density, hence collisionality, in agreement with the polarisation current model. Understanding the mechanism that controls the onset of these modes is an important issue for ITER so that, if possible, they can be avoided.

This work is jointly funded by the UK Department of Trade and Industry and EURATOM.

[1]Callen, J. D., et al., in the *Proc. 11th International Conference on Plasma Physics and Cont. Nucl. Fusion Research* (Kyoto, 1986) 1987 vol. 2, 157
[2] Fitzpatrick, R., Phys. Plasmas **2**, 825 (1995)
[3] Wilson, H. R., et al., Phys. Plasmas **3**, 248 (1996)
[4] Chang, Z. et al., Phys. Rev. Lett., **74** (1995) 4663
[5] Waelbroek, F., and Fitzpatrick, R., Phys. Rev. Lett. **78** (1997) 1703
[6] Sauter, O., et al., Phys. Plasmas, **4** (1997)
[7] Gates, D. A., et al., to be published in Nucl. Fusion

Error Field Mode Thresholds, Harmonics and Scaling Studies on JET and COMPASS-D, and Implications for ITER

R. J. Buttery, D. J. Campbell[#], M. De Benedetti[*], D. Gates, T. C. Hender, P Leahy, A. W. Morris, A. Santagiustina[†], B. Tubbing[†], and the JET[†] and COMPASS-D teams.

UKAEA Fusion, Oxon, UK. [†]*JET Joint Undertaking, Oxon, UK.* [*]*Imperial College, London, UK.* [#]*NET Team, Garching , Germany.* (UKAEA/EURATOM Association)

Abstract

Error field modes remain a significant concern for ITER. Experiments on COMPASS-D and JET confirm a scaling towards very low tolerance of intrinsic error ($\delta B/B \sim 10^{-4}$- 10^{-5}) for ITER. Thresholds are lowest at low density, a regime necessary for H mode access on ITER. COMPASS-D results show strong scaling with toroidal field (TF) and q, consistent with JET experiments. These suggests a very low error field threshold for ITER of 1 in 10^{5}, although further experiments at higher TF are necessary to confirm this scaling. Further scans demonstrate a strong drag effect of (3,1) harmonics on (2,1) penetration thresholds, indicated by recent DIII-D. This suggests a correction system, with flexibility to correct sidebands, preferably assisted by beam rotation, will be essential for ITER.

1. Introduction

Error fields are a major cause of concern for ITER. They can drive the formation and growth of a locked modes in otherwise MHD stable plasmas, leading to a disruption. This could lead to serious damage in a large tokamak, such as ITER, particularly since it is likely to trigger a vertical displacement event. These modes limit operation in low density Ohmic plasmas, a regime necessary for access to H mode on ITER. Experiments on error field locked modes in Ohmic plasmas - most notably COMPASS-C [1], DIII-D [2] and JET[3] - have shown error field sensitivity increases with size and magnetic field. This places crucial design and operational constraints on ITER, for which some form of error field correction, together probably with additional rotation from neutral beam injection, is considered essential.

Error fields inevitably arise in any tokamak from sources such as coil positioning errors, feeds, connections, etc. Experimentally the resonant (2,1) (denoted as m,n) error field component has been observed to induce dominantly (2,1) locked modes in a range of tokamaks [1,2,3]. This is understood [1,4] to occur when magnetic torque exerted by the error field in the vicinity of the q=2 surface, which slow plasma rotation, overcomes inertial and viscous torques, stopping the MHD fluid and driving island growth - 'penetration'. From torque balance considerations [6], the criteria for mode penetration can be obtained in terms of viscous and resistive time constants, which can in turn be related to various confinement scalings to obtain the predicted scaling for Ohmic heating as (where fixed ITER aspect ratio is assumed),

$$B_{pen}/B_T \propto n^{7/12} B^{-13/15} R^{-11/10} \qquad (1)$$

(neglecting q dependence) . This indicates magnetic field and radius scaling are key issues for ITER, suggesting a low threshold to induce locked modes .

Recent work on DIII-D [2,5] also suggests that sideband ((3,1) and (1,1)) components have a strong influence on island formation at the q=2. Here the coupled torque is assumed to result from viscous drag, with weightings between the various components fitted to discharges with q_{95}=3.3 and 4.6 to obtain a form for critical density for a locked mode as:

$$\bar{n}_e(10^{19}m^{-3}) = 2.7x10^4 I_p(MA)\left(\frac{3.3}{q_{95}}\right)^2\left[\frac{0.3B_{r1,1}^2 + B_{r2,1}^2 + 0.8B_{r3,1}^2}{B_T^2}\right] \quad (2)$$

Thus to determine experimentally the likely locked mode thresholds in ITER, and the requirements for error field correction, there are 2 basics issues which must be studied: the dependence of the threshold on the harmonic (in m,n) of the error field and the scaling of the threshold with machine parameters, eg: q_{95}, B_T, n_e, R, etc. With the JET internal lower saddle coils, or COMPASS toroidal bars, it is possible to simulate intrinsic error fields, and thus directly measure penetration thresholds. On COMPASS-D, arrays of 8 or 10 external toroidal bars in each quadrant allow much flexibility to examine the effects of other harmonics and mode mixing models.

2. Effect of Sideband Harmonics

The torque applied directly by the error field at a given resonant surface (r_j) is [7]

$$T(r_j) = \left|\sum_m I_m C_m^j\right|^2 \quad (3)$$

where I_m are complex numbers arising from the Fourier coefficients of the error field current, which in Ref 7 are decomposed into toroidal ring functions. The C_m^j are real numbers representing the toroidal coupling of the component resonant at r_j to the edge of the plasma. In addition to this, torques applied at neighbouring resonant surfaces act by viscous coupling to apply a torque at r_j, so total torque at r_j has the form $T_{tot}(r_j) = T(r_j) + \sum_{k\neq j} A_k^j T(r_k)$.

Experiments have been performed on COMPASS-D to investigate the form of this torque: By using different combinations of toroidal bars, the mixture of Fourier harmonics may be varied. In particular, coil combinations with different dominant (m,n) can be independently powered to scan variation in threshold. Figure 1 shows two such scans where (3,1) current is fixed while (2,1) current is ramped to determine threshold.

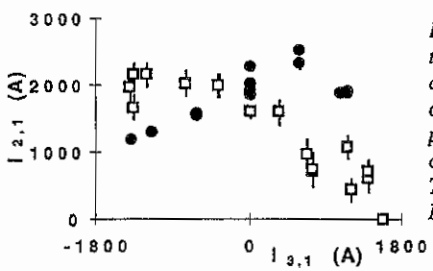

Fig 1: Dependence of penetration threshold current in dominantly (2,1) combination ($I_{2,1}$) on current in (3,1) combination ($I_{3,1}$). Two scans were performed with different phase (2,1) combinations (squares and filled circles). The plasma conditions were invariant with I_p=133kA, B_T=1.1T, n_e~2.3x10^{19}m^{-3}

It can be seen that there is strong interaction between the (2,1) and (3,1) combinations. The locked mode formed remains dominantly (2,1) throughout. Similar results are obtained from the interaction of dominantly (1,1) and (2,1) combinations. The Fourier components of the error field current (see Eq(3) and Ref 7) have been evaluated to obtain a general form for the torque fitted to the data. The dominant terms are: $T_{tot}(q=2) \propto I_{2,1}^2 + 0.6I_{3,1}^2$ which are the force that the (2,1) applies at q=2 and the drag from q=3, respectively (using vacuum toroidal co-ordinates [7]). Resonant toroidal coupling (as defined in Eq(3)) is relatively small.

These results are important for 2 reasons. Firstly they show that to understand the locked mode physics in a machine where the mode mix varies, harmonic coupling effects must be taken into account. Secondly, these results show that it is desirable to be able to correct at least the (2,1) and (3,1) error field components independently.

3. Scaling Behaviour and Implications for ITER

Turning to the scaling behaviour of the penetration threshold. A form $B_{pen} \propto n^{\alpha_n} B_t^{\alpha_B} q_{95}^{\alpha_q} R^{\alpha_R}$ is assumed, in line with the power law form seen in the penetration models (based on Eq(1)). On JET scans have been performed in density and in B_t at fixed I_p, with the result that a regression fit gives α_n=0.97 and $\alpha_B+\alpha_q$=0.5 (shown in Fig 2). These thresholds are substantially higher than those obtained for previous limiter experiments [3] possibly due to the lower TF used here. Further investigations into this, and other factors, are planned.

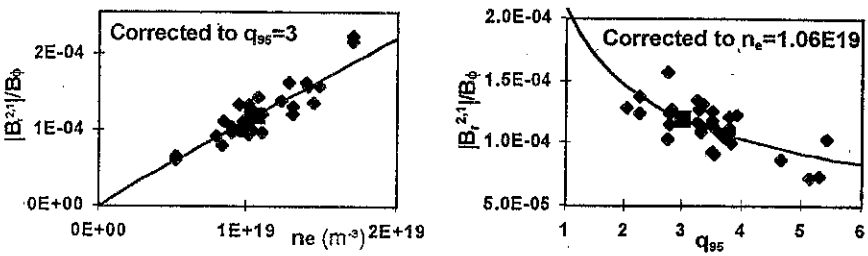

Figure 2: Regression fit to JET penetration thresholds (corrected for intrinsic error) for scans in density and q (at constant I_p) yields $B_{2,1}/B_t \propto n^{0.97}\, q^{-0.51}$. Data plotted vs line average density and q, using the fit to scale points to constant q and density respectively.

On COMPASS-D scans have been performed in density, at fixed q (I_p and B_t varied in proportion) and in I_p at fixed B_t. The fit to density in COMPASS-D is complicated by the fact that higher density points access a different confinement regime where a toroidal velocity fall occurs, discarding these points gives α_n=1.0. The I_p scan gives α_q=1.7, and the constant q-scan (shown in Fig 3) gives α_B=-1.34. The dominant effect causing the q and B_T scaling is a change in ω_0 (determined by Doppler spectroscopy measurements) before locking. It is this latter TF scan that is crucial for ITER, suggesting much higher sensitivity at higher TF. A scan in I_p for circular limiter plasmas in COMPASS-C gave α_q in the range 0.8-1.2 [1] while density scans gave α_n=0.67. The COMPASS-D scans are consistent with the JET results, but less so with the circular limiter plasma COMPASS-C results.

To minimise the parametric uncertainties in scaling to ITER, ITER-like shape (single null X-point), q and density discharges on JET, DIII-D and COMPASS-D are used. It is not possible to obtain the same error field spectrum on these machines so the harmonics are combined according to the weightings in Eq(2). The resulting scaling is shown in Figure 4 with extrapolations to ITER: a simple extrapolation in radius (disregarding TF variation) from COMPASS-D, DIII-D and JET gives an Ohmic locked mode threshold in ITER of $B_{r2,1}/B_t \sim 1$ to 2×10^{-4}. However, incorporating the B-dependence of COMPASS-D (α_B=-1.3) suggests a much lower threshold of $B_{r2,1}/B_t \sim 10^{-5}$ for 5.7T Ohmic operation in ITER. This would represent a considerable challenge for a correction and NBI system on ITER and further

experiments are necessary to test this scaling at higher TF and examine further other dependencies.

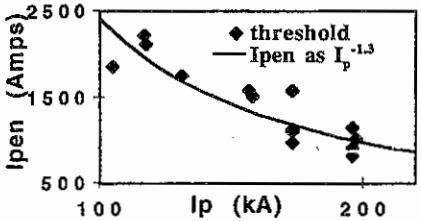

Figure 3: Scaling of penetration threshold with TF and I_p at constant q on COMP-D.

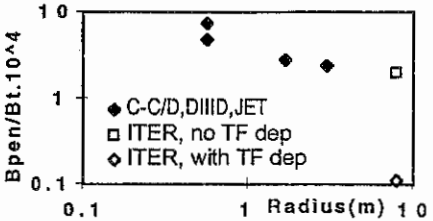

Figure 4: Cross machine scaling from COMPASS-C, -D, DIII-D, JET to ITER.

Given that error fields can impose operational limits, then detection and correction methods need to be examined for ITER. Both COMPASS-C and DIII-D [8] used in-situ coil arrays to determine error fields, as have recent JET saddle experiments (though not measuring sideband structure). Correction of error fields using coils external to the plasma is routinely used on DIII-D. On COMPASS-D error field correction can be achieved without detailed matching between the spectrum of the error field and correction coil [9] (though ITER may be more sensitive). Experiments on COMPASS-D also showed that ECRH resonant near q=2 can remove error field locked modes [10]. Another possibility is to raise the error field threshold using neutral beam injection to spin the plasma: counter injection is most efficient since this adds to the intrinsic Ohmic mode rotation (electron drift direction). The increase in threshold with NBI has been demonstrated in TF ripple experiments on JET, and also on DIII-D [11].

4. Conclusions

There is a reasonable physics understanding of the processes underlying error field locked modes. Best current extrapolations to ITER indicate a considerable uncertainty in the locked mode threshold of $B_{r2,1}/B_t \sim 10^{-5}$ to 10^{-4}. Further work, soon to be undertaken, will answer some key questions remaining and help resolve these uncertainties. Given expected construction tolerances error field correction is desirable over this entire range, and the sideband coupling observed indicates partial correction of 1,1 and 3,1 is also desirable.

References

[1] Hender T C et al, Nucl Fusion **28** (1992) 2091
[2] LaHaye R J et al, Phys Fluids **B4** (1992) 2098
[3] Fishpool G and Haynes P S, Nucl Fusion **34** (1994) 109
[4] Fitzpatrick and Hender T C, Phys Fluids **B3** (1991) 644.
[5] LaHaye R J et al, proc's 37th APS (1996) Louisville, General Atomics report GA-A22468.
[6] Fitzpatrick R, Nucl Fusion **33** (1993) 1049
[7] Fitzpatrick R and Hender T C, Phys of Plasmas **2** (1994) 3337
[8] LaHaye R J and Scoville J T, Rev Sci Instrum **62** (1991) 2146
[9] Carolan P G et al, in Contr Fus and Plas Phys **18B** (1994) 214.
[10] Morris A W et al, Plas Phys and Contr Nucl Fus Res (IAEA, Seville) (1994) 365.
[11] LaHaye R J, Hyatt A W and Scoville J T, Nucl Fusion **32** (1992) 2119.

(The UKAEA work is jointly funded by the UK Dept of Trade and Industry and Euratom)

Energy Confinement of High-β Plasmas on COMPASS-D with ECRH

M Valovič, D A Gates, B Lloyd, A W Morris, M O'Brien, C M Roach,
C D Warrick, H R Wilson and the COMPASS-D and ECRH Teams
UKAEA, Fusion, Culham, Abingdon, Oxon OX14 3DB, U.K.
(UKAEA/Euratom Fusion Association)

Introduction

In order to predict the energy confinement on ITER it is important to study tokamak plasmas in stationary regimes and with dimensionless plasma physics parameters close to those expected on ITER. None of the present day tokamaks, however, can match all these parameters simultaneously so that uncertainty will always exist in the prediction of plasma performance. In this situation the only practical approach is to match at least a few of such parameters. Even so, such plasmas produce highly relevant information about the plasma physics expected on ITER.

The objective of this work is to reach ITER-like beta on COMPASS-D in a stationary regime, at relevant safety factor and plasma geometry, without sources of external momentum and without central fuelling. We report on factors limiting the duration and confinement of such plasmas. High power ECRH is used with P≤1.3 MW and f=60 GHz. Therefore the energy confinement is determined by electron transport. Experiments are performed with a single null divertor, inverse aspect ratio a/R=0.31, elongation κ=1.6 and edge safety factor q_{95}=3.3-4.2, i.e. close to ITER. Waves are launched from both low and high field side, and for most of the data reported here, antenna angles are set to drive zero non-inductive current. High beta can be presently achieved only at low values of toroidal magnetic field due to the power limitation so that heating at 2nd harmonic frequency is used. For on-axis heating, the toroidal field is B_T=1.1 T and the line-averaged electron density is kept at $\bar{n}_e \approx 1\times10^{19}$ m^{-3} (below the cut-off). At these low densities H-mode is not observed. In order to achieve ITER-like beta, β_N=2, the electron energy content should be $W \approx W_e \approx 5.5$ kJ. At maximum heating power this would require an energy confinement time of $\tau_E \approx 4.2$ ms. This is anomalously high compared to recent ITER L-mode scaling, $\tau_E/\tau_{ITERthL}$=2-2.4 for q_{95}=3.3-4.2 respectively [1]. The volume averaged electron temperature of these plasmas is high, $\langle T_e \rangle \approx$ 4keV, leading to a collisionality about 10-times lower than on ITER.

The perpendicular beta $\beta_{p,dia}=\beta_{p\perp}$ is measured using the diamagnetic signal including corrections from Shafranov integrals. These are determined from reconstruction of the poloidal magnetic field outside the plasma using 33 magnetic coils and 5 flux loops. In addition, the equilibrium beta $\beta_{p,eq}=(\beta_{p//}+\beta_{p\perp})/2$ can be deduced from poloidal field reconstruction (i.e. ℓ_i can be separated from $\beta_p+\ell_i/2$).

Quasi-stationary $\beta_N \approx 2$ Plasmas

In order to achieve a quasi-stationary high beta plasma, careful optimisation is required. Firstly the X-point is formed at an early phase of current ramp-up leading to low MHD activity during this phase and hence slower current diffusion. Further optimisation has been done with respect to the timing of the heating pulse. Figure 1 summarises the results. At q_{95}=4.2 optimum timing of ECRH pulse can be found. When heating is applied early, during the current ramp up, the fast increase of beta is terminated at β_N=1.3, followed by a phase with slow beta rise, occasionally terminated by a disruption (trace a). When the heating is applied late (trace b), then the high beta is reached transiently but a stationary, slowly rotating m/n=2/1 mode develops, energy confinement deteriorates and beta gradually decreases. There are also cases when this timing of ECRH leads to a disruption. However, an optimum time window exists during which the beta can be raised above β_N=2 and consequently sustained at this value for a long time (trace c). No disruptions have been encountered in this regime. When the ECRH is switched off, a slowly rotating mode appears, leading occasionally to a disruption. For q_{95}=3.3, high beta plasma can be sustained only transiently even with optimum timing. The discharge terminates with a disruption caused by a slowly rotating mode (see $\tilde{b}_r$ signal of trace d). The simplest explanation of the effect of the timing of ECRH on the discharge is in terms of different target q-profiles. Immediately after the current ramp the q-profile is presumably flat. If such a plasma is suddenly heated, then substantial bootstrap current is generated and the q-profile profile can be 'frozen'. Simulations by the ASTRA [2] and SCENE [3] codes indicate that plasmas represented by shot 22374 (case c Fig. 1) could have a significant fraction of bootstrap current (~50%), leading to a current density profile such that q≥2. There is, however, presently no measurement of the q-profile on COMPASS-D, so that other mechanisms of mode stabilisation cannot be excluded.

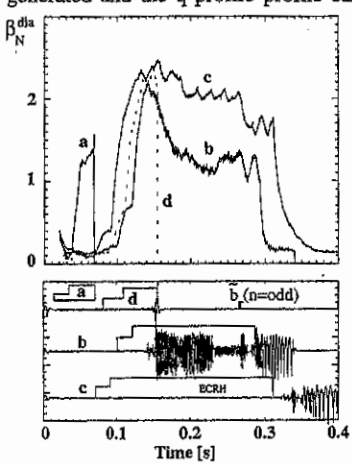

Figure 1. Effect of timing of ECRH on temporal evolutions of normalised beta. Cases a-c have q_{95}=4.2, case d has q_{95}=3.3. $\tilde{b}_r$ is measured by saddle coils outside the vessel.

Figure 2 shows other temporal characteristics of beta-optimised discharge 'c'. The duration of the phase with $\beta_N \geq 2$ is Δt=150 ms. Normalised to the current diffusion time scale $t_\sigma \propto \mu_0 \sigma_{Sp} a^2$, it represents about 13% of $\Delta t/t_\sigma$ expected for a nominal ITER discharge (volume averaged electron temperature is used in the Spitzer conductivity σ_{Sp}). The internal inductance and loop voltage are approximately constant during the high beta phase, indicating

that the current density profile is not evolving substantially. The time-averaged loop voltage is relatively high ≈0.10V. Including trapped electron effects and the bootstrap current, SCENE predicts a loop voltage of 0.06V for Z_{eff}=3. Other global characteristics indicate progressive degradation of performance. Beta decreases gradually and falls below β_N≈2 before the end of the flat top of ECRH. The amplitude of the Mirnov signals increases with increasing beta. These oscillations are coherent with frequency f~24-34 kHz, toroidal mode mumber n=1 and poloidal mode number m~3-4. Similar beta dependent Mirnov signals, however using different timing of ECRH, have previously been identified as neo-classical tearing modes with m,n=2,1 and f~7 kHz [5]. Degradation of beta occurs in steps. Up to 10 % of the plasma energy can be lost, as shown in detail in Fig 3. In some cases such a large energy loss is followed by onset of a slowly rotating mode and then beta irreversibly decreases to β_N~1. No pressure asymmetry is observed during the event (Fig. 3). MHD activity is immediately reduced after the beta drop (Fig. 2). Both ECE and SXR signals show sawtooth-like behaviour. SXR signals reveal an inversion radius at r/a~0.25. These observations indicate that the physics of the process is related to MHD and not to kinetic effects related with the electron distribution function. A possible interpretation is the q-relaxation process due to a pressure driven ideal mode occurring between two q=2 resonant flux surfaces [6].

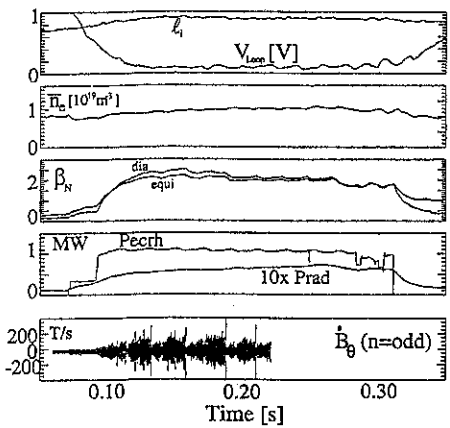

Figure 2 . Temporal evolution of quasi-stationary high beta discharge #22374 (case c from Fig. 1)

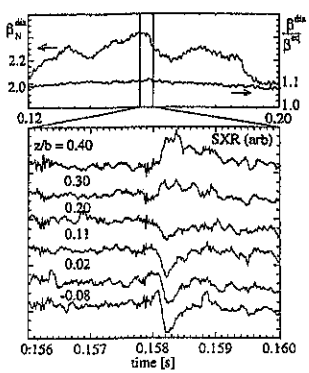

Figure 3 Detail of energy loss during MHD relaxation for #22374 and SXR signals from horizontal camera. Inversion is also observed at lower half plasma.

Beta degradation is however not always accompanied by MHD relaxation events and a continuous decrease of beta with time may be observed. In such cases the density increases. Radiation losses measured by a bolometer reach ~100 kW and thus start to contribute to the energy balance. The averaged power density at the divertor reaches ~1MW/($2\pi R \times 2\lambda$) ≈ 7 MW/m^2, where λ=2cm is the typical width of strike points as measured by

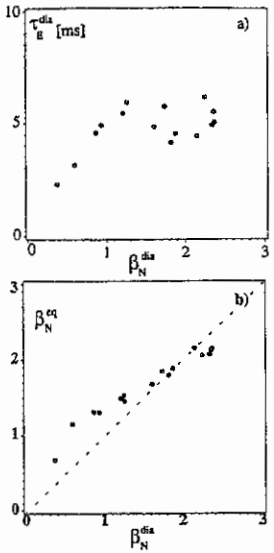

Figure 4. Energy confinement time (a) and pressure asymmetry (b) as a function of normalised beta. Data from 9 shots with parameters as for shot #22374 and n_e=(0.8-1.3)×10^{19} m^{-3}.

Langmuir probes [4]. An infrared camera reveals hot spots on the divertor with temperatures of more than 600°C.

Figure 4a shows the energy confinement time τ_E as a function of β_N. It is seen that for β_N≈1-2, τ_E is approximately constant and ~5ms. This is anomalously high (>2.4×) if compared with ITER L-mode 'thermal' scaling [1]. Another anomaly is the independence of τ_E on beta for $\beta_N \geq 1$. There is no obvious correlation between τ_E and n_e in this narrow density range and therefore $\tau_E \propto \beta^0$ implies $\tau_E \propto T_e^0$. This is a very weak power dependence in comparison with ITER L-mode 'thermal' scaling [1], which gives $\tau_E \propto \rho_*^{-2}\beta^{-1.34}\nu_*^{0.18} \propto T_e^{-2.7}$ (with $\rho^* \sim T_e^{1/2}$). A possible explanation for such an anomaly might be the low values of ν* which are outside the ITER L-mode database. Another possibility is the deviation of the electron distribution from Maxwellian as indicated by Fokker-Planck calculations using the BANDIT-3D code [7]. Nevertheless a comparison of diamagnetic and equilibrium betas shows no significant pressure anisotropy (Fig. 4b), indicating that anomalous scattering processes might be present.

Conclusions

Quasi-stationary discharges with $\beta_N \approx 2$ have been developed on COMPASS-D using ECRH at $q_{95} \approx 4$ and in ITER like geometry. These regimes last for more than 10% of the duration of an ITER discharge, normalised to a resistive time scale. If optimised, the duration of the high beta phase is limited by a progressive degradation of energy confinement and not by disruptions. The energy confinement time is independent of beta at constant density.

This work was jointly funded by the UK Department of Trade of Industry and Euratom

[1] T Takizuka et al, 16th IAEA Conf. Montreal, 1996, IAEA-CN-64/F-5
[2] G V Pereverzev, 'ASTRA-An Automatic System for Transport Analysis in a Tokamak, Rep. IPP 5/42, Max-Planck-Institut fur Plasmaphysik, Garching (1991)
[3] H R Wilson, 'SCENE-Simulation of Self-Consistent Equilibria with Neoclassical Effects', Rep.UKAEA FUS 271 (1994)
[4] C Silva, private communication (1997)
[5] D A Gates et al, submitted to Nucl. Fusion
[6] C G Gimblett *et al*, Phys. Plasmas 3 (1996) 3369
[7] M R O'Brien *et al*, Proc. IAEA Technical Committee Meeting on Advances in Simulation & Modelling of Thermonuclear Plasmas, Montreal (1992) 527

Rotation and mode locking in Compass–D H-mode plasmas

R. O'Connell, P. G. Carolan, C. A. Bunting, N. J. Conway[1], P. Leahy[2] and T.N. Todd.

UKAEA Fusion, Culham, Abingdon,Oxon, OX14 3DB, UK
(UKAEA/EURATOM Fusion Association)
[1]University College Dublin, Republic of Ireland
[2]University College Cork, Republic of Ireland

Introduction

Characteristics of the toroidal rotation are explored in single null divertor plasmas with ITER-like geometry. This study is important in understanding the creation of magnetic islands by error fields during H-mode plasmas. Multichord Doppler spectrometers are used to measure both poloidal and toroidal velocities.

General description of COMPASS–D rotation

We summarise the rotation observations as shown in figure 1, listing them in order from the edge inwards: (i) at the very edge where the CIII($\lambda = 464.7nm$) emits strongly: The toroidal velocity (v_ϕ) is low ($< 2km/s$) and the poloidal velocity (v_θ) is also low ($< 5km/s$) except during ELM-free H-mode where $\Delta v_\phi \approx 5km/s$ and $\Delta v_\theta \approx 25km/s$; (ii) at $\sim 3-5cm$ further in the BIV($\lambda = 282.1nm$) emits strongly v_ϕ can be up to $10-15km/s$ and $v_\theta < 2km/s$, during H-mode $v_\phi \sim 30km/s$ and v_θ ranges from $0km/s$ to $10km/s$ depending on various plasma paramaters such as shaping possibly affecting the radial electric field E_r and its overlap with the BIV emission shell; (iii) core ClXVI toroidal velocities ($r/a < 0.3$) as measured by a high resolution CCD X-ray spectrometer show $\Delta v_\phi \sim 60km/s$.

We also avail here of toroidal behaviour observations extending from the edge to the core as above during ECRH and mode locking (naturally occurring and induced using resonant magnetic perturbations, RMP's) during ELM-free H-modes.

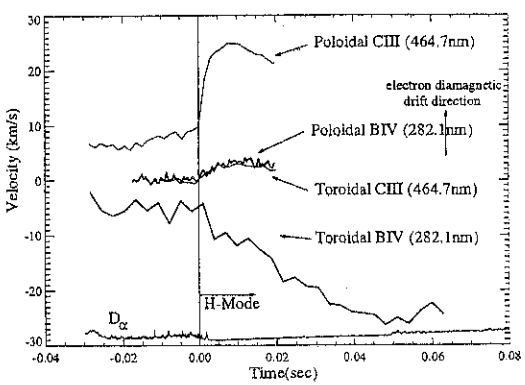

Figure 1: *v_ϕ and v_θ from L-mode to H-mode showing the contrasting behaviour between CIII at the edge and BIV further in.*

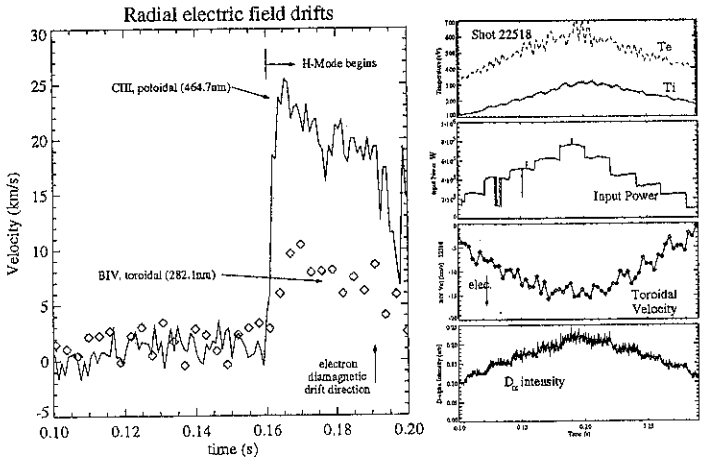

Figure 2: *Edge and core changes in velocity.*

Toroidal rotation and ELMs

The two component picture of the BIV emission shell, seen above, helps explain the effects of ELMs on the observed Doppler shifts in the toroidal direction, as shown in figure 3.
This graph shows a small time window around an ELM during a H-mode. During the H-mode the BIV toroidal velocity has increased in the plasma current direction but during the ELM the velocity increases further still in this direction. This is perhaps surprising until one notes that the CIII experiences velocity changes in the same direction during an ELM although it undergoes a velocity change opposite to BIV velocity during the L-H transition. Measurements of poloidal CIII rotation (which are a good measure of the radial electric field) show that an ELM only briefly reduces the radial electric field. Since the radial electric field causes a drift in a direction opposite to the drift in the plasma current direction that characterises the toroidal BIV flow, and since the toroidal line of sight from these discharges samples both components BIV emission shell, the brief reduction of the radial electric field during the ELM causes the integrated line of sight spectrum to be less shifted in the electron drift direction.

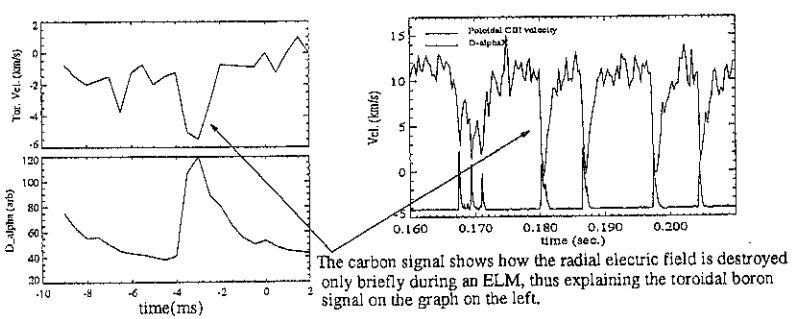

Figure 3: *Change in toroidal velocity during an ELM.*

Explications of the rotation observations

We pursue three elements of the physics to explain these rotations.

- If we look to the equation of radial force balance for each species:

$$\underline{E} + (\underline{v_z} \times \underline{B}) = \frac{\nabla p_z}{n_z Z e} \tag{1}$$

  where E is the electric field, B the magnetic field and, for each species, Z: v_z is the velocity, p_z the pressure, n_z the density and Ze the charge of the species. We note that the diamagnetic drift term $\nabla P \times B$ is small ($< 2km/s$), this implies that the plasma edge rotation is governed by E_r. The edge rotation is relatively insensitive to magnetic modes as seen particularly in RMP experiments. The E_r overlaps the CIII emission shell very well. It should further be noted that the rotation observations at the edge do not suffer from poloidal damping with $v_\phi/v_\theta \sim B_\theta(0.17T)/B_\phi(1.1T)$.

- the E_r may partly overlap the BIV emission shell and this is reflected by its v_θ. Unfolding of the velocity across the emission shell shows a toroidal component due to $E_r \times B$ drift, as shown in figure 2.

- Extending approximately from the region of the high BIV emission to the plasma core (the ClXVI emission shell) the rotation behaviour is different in character to the edge rotation, in particular the dominance of toroidal velocity requiring at least different underlying physics. Surprisingly the toroidal rotation of the BIV emission shell, which is quite close to the plasma edge, is very similar in character to the Cl rotation, which is measured in the core. Since we have established that the impurities can rotate poloidally, consistent with a simple radial force drift, the absence of poloidal rotation further in suggests a toroidal or force-free source term.

According to Hazeltine[1] the toroidal rotation of the plasma ions may be described by:

$$V_T \approx -\frac{c}{enB_P}(p' + en\Phi' + \kappa n T_i') \tag{2}$$

where p is the pressure, Φ is the electric potential, $\kappa \approx 1$ and T_i is the ion temperature ($'$ denotes the gradient in the radial direction).
Equation 2 suggests an explanation of the boron impurity toroidal rotation (figure 1) *viz* the fuel ions are driven toroidally, by the temperature/pressure gradients. The impurities rotate similarly by frictional coupling with the fuel ions. The friction coupling is reduced by increases in the electron and ion temperatures which is not included here.
In experiments on Compass–D where the electron and ion temperatures are ramped up and down by ramping the ECRH input power we find that the toroidal rotation is approximately consistent with this prediction. This can be seen in figure 2. Estimating the terms of equation 2 and using typical COMPASS–D values:$n \approx 2e19$, $B_P \approx 0.17T$, $T_1 \approx 100eV$, $T_2 \approx 250eV$, $\Phi' \approx 0kV/m$, $a \approx 0.2m$ and $\kappa \approx 1$, and setting $p' \approx (n\Delta T + T\Delta n)/a \approx 2nT/a$ and $T' \approx T/a$, we then find for the change in ion temperatures $T_2 - T_1$ a change in velocity $\Delta V_T \approx 15km/s$. The ion temperature used here is derived assuming equipartition with the electrons and assuming in a 0-D representation $\tau_{Ei} = 10ms$, the electon temperature is derived from the resistivity.
The origin of the toroidal flow is of significant interest since during ELM-free H-mode large toroidal rotations are observed. This toroidal rotation can be accompanied by natural locked modes during ELM-free H-mode discharges. This may be associated with the large changes in the toroidal velocity that are always observed during H-mode.

Relationship between toroidal rotation and locked modes.

In theories of the threshold for production of a magnetic island by an external non-axisymmetric (e.g. m=2,n=1) error field, the toroidal rotation of the MHD frame of reference is crucial. Error fields are an important but still unresolved problem for ITER[3] It has been experimentally observed that it is easier for a mode to lock both naturally and through applied error fields during a H-mode: locked modes occur at higher densities in H-modes than for L-mode[2]. Figure 4 shows the toroidal rotation and the mode rotation as a natural slowly rotating m=2 mode occurs during an ELM-free H-mode leading eventually to a locked mode. This behaviour suggests at least an interplay between the toroidal rotation and mode locking. COMPASS–D experiments using external windings to apply static m=2,n=1 error fields showed a clear association between error field threshold and the inital toroidal BTV velocity. The identification of the underlying physics of the source of toroidal rotation will help the understanding of error field and natural magnetic islands in ELM-free H-modes.

Conclusions

The velocity behaviour in COMPASS–D can be undertood in terms of a radial electric field at the edge, activated during ELM-free H-modes, and a neoclassically driven toroidal rotation, which depends on gradients of ion pressure and temperature, for the bulk of the plasma. Toroidal rotation is seen to play a key role in mode locking underlying the importance of its understanding, particularly in extrapolating present results to ITER.

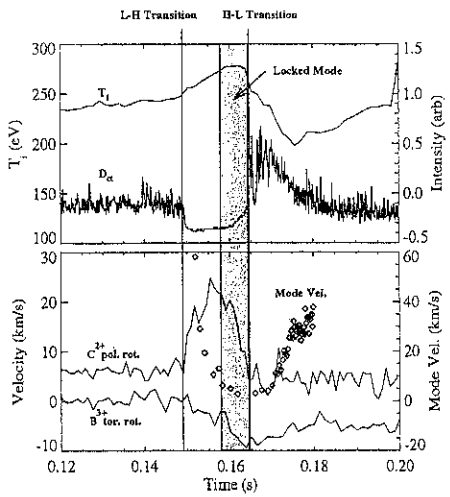

Figure 4: *Toroidal rotation versus mode rotation velocity (Shot 15615).*

References

[1] Hazeltine R.D. and Meiss J.D., Plasma Confinement (1992).

[2] Morris A.W. et al., IAEA 1994, Vol.1, p365..

[3] Buttery, R.J. et al., this conference.

Effects of Electromagnetic Turbulence on Tokamak Stability and Transport

A. Thyagaraja, C. Lashmore-Davies, W. Han and W-H. Yang*
UKAEA, Fusion, Culham, Abingdon, OX14 3DB, UK.
*University of Science & Technology of China, Hefei, Anhui, 230027, P.R. China.
(UKAEA/Euratom Fusion Association)

Introduction and Two-Fluid Model: This paper presents results obtained using the recently enhanced version of the nonlinear, electromagnetic, global, large eddy simulation code CUTIE [1] modelling tokamak turbulence and associated transport. This code has already been shown to be in qualitative agreement with transport in COMPASS-D[1]. The interaction of drift and Alfvén turbulence is described within a fluid model relevant to turbulence ranging from macroscales (ie from system size) to mesoscales (approaching the ion gyroradius ρ_i). CUTIE results pertinent to electromagnetic effects on ITG modes(not generally negligible for $\beta > \frac{m_e}{m_i}$), nonlinear saturation of TAE modes and calculations of edge turbulence in COMPASS-D are presented in brief.

The present version of the CUTIE code solves the well-known[1] two-fluid quasi-neutral plasma equations of motion for the seven variables, $n_e, T_e, T_i, V_{\|}, \phi, \psi, \Theta \equiv \nabla.(n\nabla_{\perp}\phi)$. The equilibrium geometry is taken to be a periodic cylinder but the fluctuating parts include linear mode-coupling and destabilizing curvature effects. Appropriate sources and neoclassical transport coefficients are included as are low collisionality(ie 'Knudsen corrected') forms for parallel diffusivities. The typical forms of the vorticity and Ohm's law equations are:

$$\frac{\partial \Theta^*_{m,n}}{\partial t} + i\mathbf{k}.\mathbf{V}_0\Theta^*_{m,n} + i\bar{k}_{\|}\bar{V}_A\rho_s^2\nabla_{\perp}^2\Psi^*_{m,n} = ik_{\theta}\bar{V}_A\rho_s^2(\frac{4\pi}{cB_0}\frac{dj_0}{dr})\Psi^*_{m,n} + \nabla.(D^{\Theta}\nabla_{\perp}\Theta^*_{m,n}) + \Sigma^{\Theta}_{m,n} \quad (1)$$

$$\frac{\partial \Psi^*_{m,n}}{\partial t} + i\mathbf{k}.\mathbf{V}_{e0}\Psi^*_{m,n} + i\bar{k}_{\|}\bar{V}_A\Phi^*_{m,n} = D^{\Psi}\nabla_{\perp}^2\Psi^*_{m,n} + \Sigma^{\Psi}_{m,n} \quad (2)$$

These are complemented by electron continuity, ion parallel momentum and the two energy equations. The following conventions apply: $\bar{V}_A^2 = B_0^2/4\pi n_0(0)m_i$, $\bar{V}_{th}^2 = (T_{e0}(0) + T_{i0}(0))/m_i = \bar{T}/m_i, \Omega_{ci} = eB_0/m_ic, \rho_s = \bar{V}_{th}/\Omega_{ci}, \bar{\beta} = (\frac{\bar{V}_{th}}{\bar{V}_A})^2, k_{\theta} = m/r, \bar{k}_{\|} = \frac{(m+nq)}{qR_0}$, $\Theta^*_{m,n} \equiv \rho_s^2\nabla.(\frac{n_0(r,t)}{n_0(0,t)}\nabla_{\perp}\Phi^*_{m,n})$. The potentials $\delta\phi, \delta\psi$ are in Gaussian units with nondimensional forms: $\Phi^* = \frac{e\delta\phi}{\bar{T}}, \Psi^* = \frac{\delta\psi}{B_0\rho_s\bar{\beta}^{1/2}}$. The source terms include curvature effects(ie linear toroidal coupling terms linking different poloidal mode numbers) and all the nonlinear terms.

A novel solution scheme has been developed wherein the equations are split into mean(ie,surface averaged) and fluctuating components interacting nonlinearly with each other. The linear terms in describing shear Alfvén waves, drift waves, sound

waves, tearing and ballooning modes are written in a 5×5 matrix form for each m, n Fourier component of $\delta n_e, \delta V_\parallel, \delta\phi, \delta\psi, \delta\Theta$. Nonlinear sources involving Jacobeans are finite-differenced using a conservative Arakawa scheme and evaluated in position-space and then transformed into Fourier space. The resulting implicit, unconditionally stable, matrix tridiagonal system is inverted by a Gaussian direct solver with provision for iterative improvement at a time-step. Curvature and toroidal effects are included in the fluctuation dynamics. The two temperature equations are solved by standard implicit tridiagonal matrix solvers. Typical radial mesh size, $\Delta r \simeq 2\rho_s$; upto 32 poloidal and 16 toroidal modes are employed. Time-steps resolve shear Alfvén frequencies ($\Delta t \simeq 5 \times 10^{-2}\mu$s).

Electromagnetic effects on fluid η_i modes: It is well-known that when $\beta > m_e/m_i$, electrostatic approximations are inaccurate, especially close to $k_\parallel \simeq 0$. It is necessary to include electromagnetic coupling terms which link the drift and the Alfvénic modes of low frequency oscillations. Simple considerations indicate that near mode rational surfaces, in a layer of width $\Delta r \simeq \beta_{\rm pol}^{1/2}(\frac{L_s}{L_n})\rho_s$, electromagnetic effects are important in altering the phase relation (via linear and nonlinear mode coupling) between the electrostatic potential and density perturbations. We have run CUTIE in a purely *linear* mode for identical conditions both electrostatically ($\delta\psi$ is a 'passive' variable) and electromagnetically using the fluid (dissipationless) η_i mode as a bench mark. The electrostatic run closely matches simple linear theory predictions of instability growth rate when $\eta_i > 2/3$, as well as the real frequency. The electron response is adiabatic. Using the full Ohm's law, a simple local dispersion relation shows that the instability is removed due to shear Alfvén waves provided $\eta_e > 0$. The code results confirm that electromagnetic effects greatly reduce the growth rate of $k_\parallel \simeq 0$ modes and alter the mode structure considerably. Fig. 1 shows the radial profiles of RMS current density of a (3,2) η_i mode with and without electromagnetic effects; the amplitude in the electromagnetic case is multiplied by 10 to show the radial profiles on the same scale. When $k_\parallel$ is nonzero within the plasma, the differences between electrostatic and electromagnetic calculations are negligible, although in practice such 'nonresonant' modes are strongly ion Landau damped. Code simulations of finite-β electromagnetic effects in fully nonlinear toroidal situations suggest that under JET-like conditions ($T_{i,e} \simeq 10$keV, $n_e \simeq 10^{20}$m^{-3}, $B \simeq 2$T, $I_p \simeq 2$MA, $R = 3$m, $a = 1$m, $\beta \simeq 10\%$) the energy confinement time attributable to these modes is of the order of 1 sec. These preliminary calculations of nonlinear saturation and spatial mode-structure are being extended to address these and other scaling issues with reference to ITER.

TAE saturation via nonlinear mode-coupling: We have studied the nonlinear saturation of Toroidal Alfvén Eigenmodes in tokamaks. These modes are thought to be important[2] in reacting plasmas as they can be driven unstable by fusion α particles, and could redistribute them leading to their possible loss from the plasma. In our model, we specifically investigate the possibility that the TAE modes could saturate by nonlinear mode coupling effects[3], complementing work on other modes of saturation (eg. quasilinear flattening and velocity space nonlinearities) [2]. We represent the

drive due to α particles by a term on the RHS of the vorticity equation of the form[4] $\Gamma_{\alpha m}\nabla_\perp^2\phi^*_{m,n}$, where, $\Gamma_{\alpha m} = \frac{\beta_\alpha}{2R^2}\frac{V_A^2}{\omega_0}(\frac{\omega_{*\alpha m}}{\omega_0} - 1)(R_{m+1} + R_{m-1}), \zeta_{m\pm1} = \frac{\omega}{V_\alpha|k_{\parallel m\pm1}|}, R_{m\pm1} = \pi^{1/2}\exp(-\zeta^2_{m\pm1})\zeta_{m\pm1}(\zeta^4_{m\pm1} + \zeta^2_{m\pm1} + 1/2), V_\alpha^2 = \frac{2T_\alpha}{m_\alpha}$. A simple local dispersion relation gives the growth rate[4], $\frac{\gamma}{\omega_0} = -(\beta_\alpha/4k_\parallel^2R^2)(1 - \frac{\omega_{*\alpha}}{\omega_0})(R_{m+1} + R_{m-1})$. Since the R's are positive, instability occurs for $\frac{\omega_{*\alpha}}{\omega_0} > 1$. Linear code results support the simple picture and also lead to quantitative estimates for the growth rate and linear eigenfunctions in agreement with the literature[2]. Typically, for $T_i \simeq 10$keV, $V_A \simeq 3000$km/s,$R = 3$m, $B \simeq 2$T, $T_\alpha \simeq 1$MeV, and $L_{n\alpha} \simeq a/2$, the instability condition is readily satisfied. For experimental $\beta_\alpha \simeq 0.1\%$ we expect $\frac{\gamma}{\omega_0} \simeq 10^{-3}$. In actual fact, we obtain a value around 3.5×10^{-2} for the $n = 1, m = -1, -2$ mode, corresponding to an e-folding time of about 100μs. It is interesting to note that in the strongest drive region there is evidence for highly oscillatory radial modes associated with vanishing parallel wave number. We have continued the linear solution with the full nonlinear code using $-8 \le m \le 8, -2 \le n \le 2$, $\Delta t = 12.5$ nanosecs and $\Delta r = a/200$. As in the linear case, $\beta_\alpha = 0.003$. The nonlinear terms do not affect the solution until $\frac{\delta B}{B} \simeq 7.5 \times 10^{-6}$ at around 2.5 ms. The mode appears saturated at 3 ms with an amplitude level similar to observations in TFTR[5]. Fig. 2 shows the nonlinear evolution of the RMS current density in the final stages of evolution. We conclude that this mechanism for mode saturation via position-space nonlinear mode coupling to stable branches (essentially a form of nonlinear radiation damping) is viable in existing devices such as JET, supporting earlier studies[3].

Edge turbulence simulations:We have also applied the CUTIE code to modelling edge turbulence in COMPASS-D. At present the code essentially has no scrape-off layer model and simulates ELM-free periods. Figs. 3 shows the comparison between CUTIE simulations and experiment (wavelet transforms of magnetic fluctuations at outboard midplane) of edge turbulence. The simulation exhibits intermittency and broad band turbulence above 100kHz. A coherent mode of nearly the correct($\simeq$ 100) frequency and spatial location is predicted, although there is less turbulence below 100kHz than is evident in experiment. It was already shown that the code obtains results for global transport in qualitative agreement with COMPASS-D data[1].

Conclusions: We have presented recent results obtained using the **global, electromagnetic** code CUTIE which has been developed during the last few years for the purpose of simulating tokamak turbulence and transport in a realistic fashion taking account of nonlinearities, sources and toroidal effects. The code suggests, in accordance with linear theory that 1) for $\beta > \frac{m_e}{m_i}$, electromagnetic effects have an important stabilising influence on ITG-like modes with $k_\parallel \simeq 0$ in a layer of width $\rho_s\beta^{1/2}(\frac{qR}{a})(\frac{d\ln n_e}{d\ln q})$, 2) predicts nonlinear mode coupling as a possible saturation mechanism for TAE's and 3) simulates features (quasi coherent modes and intermittency) seen in edge turbulence in COMPASS-D in ELM-free periods. Deeper study of these issues is in progress.

Acknowledgements: This work was funded jointly by the UK Dept. of Trade and Industry and Euratom. Dr. Yang was a Royal Society Visiting Fellow.

References

[1] A. Thyagaraja, Journal de Physique, IV, Colloque C6-105, **5**, (1995) and the invited paper in *Proceedings of the Joint Varenna-Lausanne International Workshop on Fusion Plasmas*, Villa Monastero, Varenna, August, (1996). Also available as UKAEA FUS 339, (1996).

[2] G.Y. Fu *et al*, Sixteenth IAEA Fusion Energy Conference, Montréal, Canada, IAEA-CN-64/F1-CN-64/D2-6, (1996). Also, G.Y. Fu and J.W. Van Dam, Phys. Fluids B **1**, 1949, (1989).

[3] G. Vlad, C. Kar, F. Zonca and F. Romanelli, Phys. Plasmas, **2**,418, (1995).

[4] Y.M. Li, S.M. Mahajan, and D.W. Ross, Phys. Fluids, **30**, 1466, (1987).

[5] R. Nazikian *et al*, Phys. Rev. Letts. **78**, 2976, (1997).

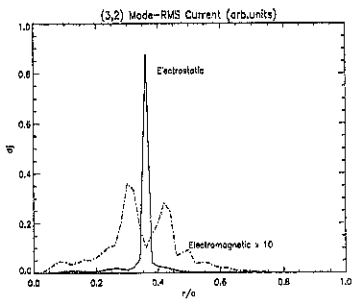

Figure 1 δj(ES and EM) radial profiles in (3,2) η_i mode

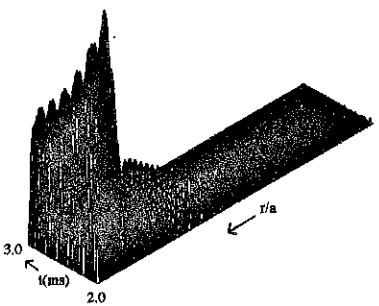

Figure 2 RMS Current in nonlinearly saturated TAE

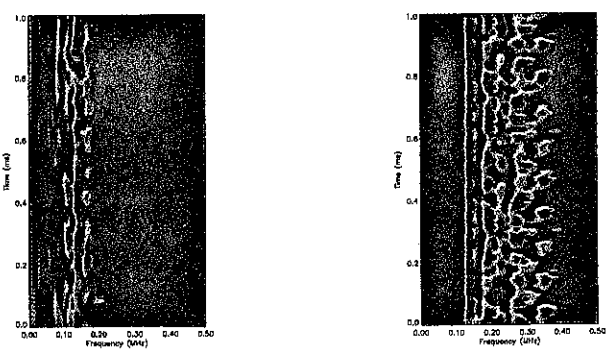

Figure 3 Wavelet transforms of (left) a magnetic signal from COMPASS-D shot 18206 during an ELM-free period, and (right) radial magnetic fluctuations, $\frac{\delta B_r}{B_{pol}}$, from a CUTIE simulation.

ELMs and asymmetries at the COMPASS-D boundary

C. G. Silva*, S. J. Fielding, K. B. Axon and M. G. Booth
UKAEA Fusion, Culham, Abingdon, Oxon OX14 3DB, UK
UKAEA/Euratom Fusion Association
* Associação Euratom/IST, Centro de Fusão Nuclear, Instituto Superior Técnico
1096 Lisboa Codex - Portugal

1 Introduction

Transient increases and/or asymmetries in the heat flux into the divertor of a tokamak directly affect the peak heat load at the target and, for example, are crucial considerations in the ITER divertor design. ELMs, a prime example of such transients, seem to be unavoidable in steady H-mode and have beneficial effects in impurity control. We report here edge measurements on COMPASS-D during L- and ELMy H-mode discharges in single null divertor plasmas, using a fast reciprocating Langmuir probe poloidally remote from the X-point, and a high spatial resolution (5mm) array of embedded probes in the divertor target which provide detailed information on the effect of ELMs at the boundary.

Asymmetries in the heat flux to the inner and outer target, reported on many devices, can occur in all discharge phases. On COMPASS-D the asymmetry shows strong variations with the discharge parameters and in particular with the direction of the magnetic field, B_T. Analysis of the effect of the B_T reversal can help in establishing the underlying physical mechanisms responsible for the in/out asymmetries.

2 ELMs

We use as a reference discharge an Ohmic H-mode in lower single-null divertor geometry ($R = 0.56$m, $a_{sep} = 0.175$m, $\kappa = 1.6$, $I_p = 180$kA, $B_T = 1.1$T, $q_{95} = 3.3$), which can be repeatedly reproduced provided that the boronisation is still active. These discharges evolve with increasing density into H-mode with type III ELMs, an ELM-free period and then regular large amplitude ELMs with typical repetition frequency of 500Hz, where discharge conditions reach an equilibrium. Observations reported here refer to these latter large ELMs.

The divertor probe array gives high resolution divertor plasma T_e and n_e profiles during ELMs. These single probes are swept at 100Hz and an average characteristic is built up over a series of ELMs. Typically, the power e-folding width at the target broadens from 16mm in the ELM-free H-mode to 32mm during an ELM to be compared with 26mm in the L-mode. The average power loss per ELM has been estimated by toroidal integration of the divertor heat flux profile, as measured by the probe array. For large ELMs $\sim 4\%$ of the plasma energy is lost (Langmuir probe estimates agree with diamagnetic-based measurements of this) together with $\sim 3\%$ of the particles [1].

Time development of the target floating potential and particle flux during an ELM is shown in fig.1. The results have been obtained by a box-car average over an ELMy period, synchronised by the D_α peak (t=0). Large negative spikes in V_f are observed during the fast increase in the D_α emission, particularly at the outer strike point, probably corresponding to the prompt arrival of energetic electrons as the ELM event destroys the confinement barrier. Simultaneously, a rapid broadening of the particle flux profile is

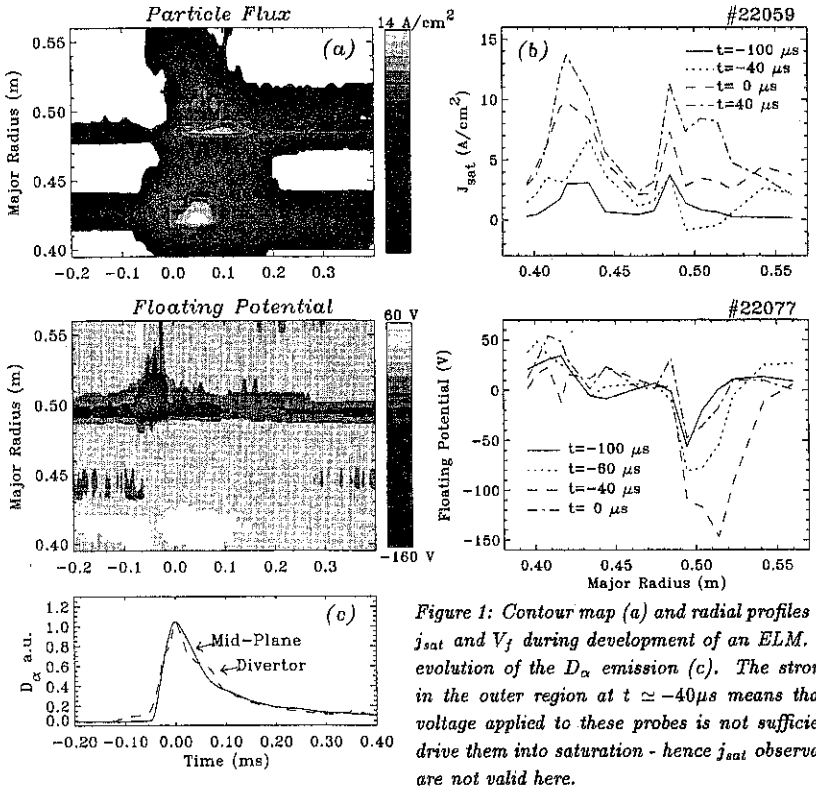

Figure 1: Contour map (a) and radial profiles (b) of j_{sat} and V_f during development of an ELM. Time evolution of the D_α emission (c). The strong V_f in the outer region at $t \simeq -40\mu s$ means that the voltage applied to these probes is not sufficient to drive them into saturation - hence j_{sat} observations are not valid here.

observed, followed by an increase in amplitude, mainly close to the strike-points. As shown in fig. 1, on COMPASS-D no significant movement of the strike point position is seen, contrary to JET observations [2].

3 Divertor asymmetries

The effect of the field direction on in/out asymmetries in parameters at the divertor has been investigated on COMPASS-D in L-mode discharges, by reversing the magnetic field and plasma current direction simultaneously, so that the sign of the helicity of the field lines is unchanged. The toroidal magnetic field direction corresponding to ∇B ion drift down towards the X-point is defined as negative, the configuration favourable to H-mode.

The B_T direction has a substantial effect on the target density, fig 2. The density profile is approximately symmetric for $B_T < 0$ (I_p clock-wise), while for $B_T > 0$ a large density imbalance is observed. As a result of changes in the n_e and T_e distributions in opposite directions when the magnetic field is reversed, the heat flux distribution is similar for both directions, with higher power flowing to the outer target, as observed on other devices.

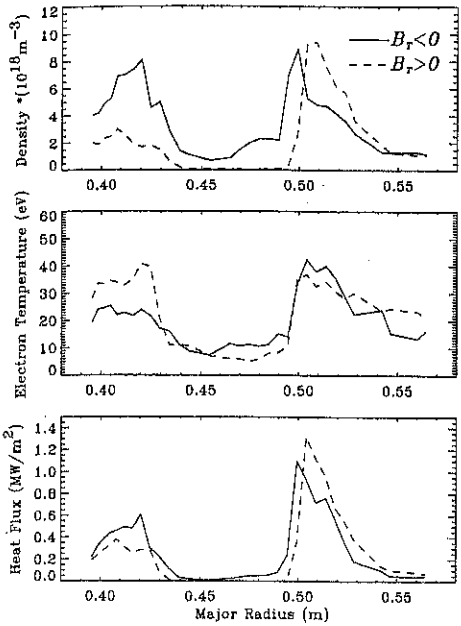

Figure 2: Profiles of n_e, T_e and q ($8j_{sat}T_e/e$, assuming $T_i = T_e$) for $B_T < 0$ (#21432) and $B_T > 0$ (#21495). The ion drift side is located at the outboard region for $B_T > 0$

3.1 Asymmetry dependence on $\bar{n}_e$ and P_{in}

In/out asymmetries were found to depend on the plasma average density ($\bar{n}_e$) and input power (P_{in}). For $B_T > 0$ the asymmetry in the target density (n_{out}/n_{in}) is observed to increase with the average plasma density and to decrease with the input power. Because the temperature imbalance is small for $B_T > 0$, the out/in power asymmetry (integrating over the inner and outer divertor regions) is mainly determined by the density profile, varying between 2:1 and 4:1.

For $B_T < 0$ no dependence of the density asymmetry with other plasma parameters has been found. The out/in power asymmetry is approximately 2:1 and although the heat flux profile changes in the L-H transition (narrowing) and during an ELM (broadening), the asymmetry does not change significantly (contrary to other devices where ELMs are observed to deposit most of the power in the inboard side, e.g. [2]).

3.2 Drift effects at the divertor

The direction of the toroidal field determines the direction of particle drifts. Therefore, imbalances that are sensitive to the field direction are almost certainly a reflection of the drifts. The convective heat flux carried by the $\mathbf{E} \times \mathbf{B}$ drift is suggested as a possible mechanism causing the asymmetry. Radial and poloidal electric fields exist naturally in the scrape-off layer (SOL) and can change the density redistribution between the in/out targets [3].

Figure 3 shows the density, temperature, pressure and plasma potential measured by the reciprocating probe at the top of the plasma, and by divertor probes. A temperature gradient along the SOL is observed, particularly near the separatrix; however, the pressure is approximately conserved ($p_e^{probe} \simeq 2p_e^{target}$ averaged between inner and outer regions). By comparing the upstream and target potentials, the poloidal electric field is derived. Radial fluxes, caused by the poloidal electric field, will increase the density in the outer divertor region for $B_T > 0$. The parallel T_e gradient and E_θ are observed to increase with increase in edge collisionality, so that the density asymmetry would be expected to increase. This is in agreement with the experimental results, which show an increase in the density asymmetry with $\bar{n}$ (increasing collisionality) and a decrease of the asymmetry with P_{in} (decreasing electron collisionality).

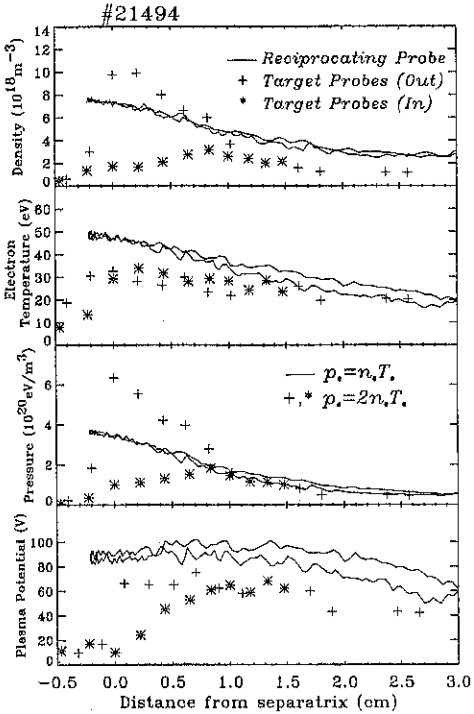

Figure 3: Radial profiles measured by the reciprocating probe and target probes for $B_T > 0$

In addition to the poloidal electric field, there is a radial electric field at the divertor target. The magnitude of this electric field is larger in the inboard region where the direction of the poloidal $\mathbf{E_r} \times \mathbf{B}$ drift is again towards the outer region, increasing the asymmetry. The direction of the $\mathbf{E_r}$ is opposite to that expected for an ambipolar sheath [3], due to the existence of currents in the SOL which relax the sheath potential from its ambipolar value. Large negative currents are indeed observed in the inner divertor region, particularly near the strike-point.

4 Summary

High resolution probe array measurements in the divertor show that about 3% of the plasma particle content is transferred across the separatrix to the SOL, and about 4% of the plasma energy content, leading to high power transients $3MW/m^2$ for Ohmic plasmas, a factor of 6 increase on the ELM-free values. The time evolution of the divertor parameters is consistent with the ELM being associated with a fast collapse of the transport barrier and no significant movement of the strike point position is seen.

Strong outboard/inboard imbalances (up to a factor of 4) in the divertor target parameters, which reverse with the sign of the toroidal field, have been measured on COMPASS-D in L-mode plasmas. Furthermore, for $B_T > 0$ the asymmetry in the target density depends on the main plasma parameters, increasing with the average plasma density ($3 < \bar{n} < 12 \times 10^{19}m^{-3}$) and decreasing with input power ($175 < P_{in} < 600$kW).

On COMPASS-D, drifts can significantly influence the divertor profiles, offering possible explanations for the observed asymmetries.

5 References

[1] S. J. Fielding, et. al., Proc. 12^{th} PSI Conference, St Raphael France, 1996
[2] J. Lingertat, et. al., Proc. 12^{th} PSI Conference, St Raphael France, 1996
[3] P. C. Stangeby and A. V. Chankin, Nucl. Fusion **36** 839 1996

Acknowledgements: This work is jointly funded by the UK Department of Trade and Industry and Euratom. C. Silva was supported by a EURATOM fellowship.

Extensions to fluid models of tokamak edge plasma transport

G P Maddison & P Helander

UKAEA Fusion, Culham Science Centre, Abingdon, Oxon. OX14 3DB, UK.
(UKAEA/Euratom Fusion Association)

1. Introduction

Computational fluid models of tokamak edge plasma transport now commonly in use are based typically on a reduced form of the Braginskii representation[1] for near-thermalized distributions in a strong magnetic field limit. It is recognized, though, that important corrections could apply even for basic processes. A novel instance recently described by Helander *et al*[2] is that conventional fluid theories do not properly include strong coupling of cross-field and parallel fluxes which actually defines the scrape-off layer (SOL), and that amending them accordingly reveals new parallel forces acting between different ion species. A preliminary test of their influence is made using an adaptation of the Braams "B2" code[3] for minority helium efflux[4] in COMPASS-D.

This revision further recalls the potential effect of Onsager constraints on 2-D fluid treatments, plus a need for generalization of multiple ion species interactions for arbitrary relative abundances.

2. Coupled transport corrections

Within the SOL of a limiter or poloidal divertor, plasma profiles and fluxes are determined by a close balance between parallel and cross-field transport. Proceeding from a drift-kinetic equation properly accounting for this coupling, Helander *et al* have shown it in fact modifies ion dynamics already on a kinetic level[2]. In a weak turbulence, short mean-free path (fluid) approximation, extra *parallel* forces on ions emerge, driven by *cross-field* gradients. Significantly this means that if cross-field diffusion is anomalous, then parallel SOL transport *cannot* be entirely classical[2]; ie, traditional combination of these mechanisms in edge modelling is actually physically *inconsistent.*

2.1 THERMAL FORCES

One example of such an established 2-D collisional edge plasma model is the Braams "B2" code[3]. Its normal treatment of parallel inter-species friction $R_\parallel^{ab}$ and thermal forces $\mathcal{T}_\parallel^a$ experienced by separate ion species $a\,(b)$ with number densities n_a, masses m_a and a common temperature T_i employs a simplification appropriate for low concentrations everywhere of all impurities[3]. This leads to an estimate[3] :-

$$\mathcal{T}_\parallel^a + \sum_b R_\parallel^{ab} \;\approx\; \left(\frac{Z_a}{Z_{\rm EFF}} - 1\right) Z_a\, n_a \left(c_e\, \nabla_\parallel T_e + c_i\, \nabla_\parallel T_i\right) + \sum_b R_\parallel^{ab} \qquad \left(\frac{\rm N}{\rm m^3}\right) \quad , \quad (1)$$

where effective ionic charge $Z_{\rm EFF} \equiv \sum_a n_a Z_a^2 / n_e$ for quasi-neutral electron density $n_e = \sum_a n_a Z_a$. Correction for strong orthogonal coupling reveals[2] these thermal terms become :-

$$\mathcal{T}_\parallel^a \;\longmapsto\; \left(\frac{Z_a}{Z_{\rm EFF}} - 1\right) Z_a\, n_a \left(c_e\, \nabla_\parallel T_e + c_i \left[\nabla_\parallel T_i - \frac{2\, m_a\, D_\perp}{T_i}\, \nabla_\perp v_\parallel^a\, \nabla_\perp T_i\right]\right) \quad , \quad (2)$$

with $D_\perp$ the particle (anomalous) diffusivity, assumed species-independent. Another along-field drive is therefore seen, proportional to a product of *cross-field* gradients of ion

parallel velocity ($v_\parallel^a$) and temperature. Hence if these are both of the same sign, they can oppose the conventional $\nabla_\parallel T_i$ force, eg helping to improve retention of higher-charge impurities within a divertor, whereas if they have opposite signs, converse divertor leakage can even be compounded.

2.2 ONSAGER RELATIONS

Onsager symmetry of the complete transport matrix implies a counterpart to the foregoing new force, pointing in turn to replacement of the ion energy (anomalous) diffusion :-

$$- \chi_\perp^i \nabla_\perp T_i \sum_a n_a \;\longmapsto\; - \chi_\perp^i \nabla_\perp T_i \sum_a n_a + D_\perp T_i \sum_a \nabla_\perp n_a \quad \left(\frac{\mathrm{W}}{\mathrm{m}^2}\right) \quad . \qquad (3)$$

Generally, Onsager symmetry is not wholly preserved in approximate fluid edge models, although consequent discrepancies in thermodynamic laws are probably small. It is evident from (3), however, that associated contributions indeed can be significant. Here, depending on relative temperature and density gradients, the additional flux may be similar in magnitude to usual Fick-type diffusion, and if $\nabla_\perp \sum_a n_a$; $\nabla_\perp T_i$ have the same sign, it too could oppose the latter, acting like an inward ion energy "pinch".

2.3 ARBITRARY IMPURITY ABUNDANCES

Even when not contravened globally, the prescription of small impurity fractions underlying (1) generally tends to be invalid in some localities. Resolution of ion forces for arbitrary plasma compositions is consequently a priority for reliable modelling of impurity flows, with or without correction for coupling of transport components. A complete generalization of (uncorrected) parallel momentum balance has recently been given by Bergmann *et al*[5]. For small viscous fluxes, on the other hand, the alternative formulation of Hirshman[6] and Hinton[7] can equally be applied, and moreover becomes especially concise with the Braams assumption of equal temperature ions[3]. A detailed account will be given elsewhere[8], but identification of parallel ion forces per unit volume $F_\parallel^a$ for arbitrary species abundances then reduces to solution of the linear equations :-

$$F_\parallel^a = \sum_b \left(A^{ab} u_0^b + B^{ab} u_1^b \right) \quad ; \quad \frac{5}{2} n_a \nabla_\parallel T_i = \sum_b \left(C^{ab} u_0^b + D^{ab} u_1^b \right) \quad , \qquad (4)$$

where $u_0^a \equiv v_\parallel^a \sqrt{\{m_a/(2T_i)\}}$, $u_1^a \equiv -\{2q_{\parallel\mathrm{cond}}^a/(5n_a T_i)\}\sqrt{\{m_a/(2T_i)\}}$ with $q_{\parallel\mathrm{cond}}^a$ the parallel conductive power density for species a , and matrices $\underline{\underline{A}}$; $\underline{\underline{B}}$; $\underline{\underline{C}}$; $\underline{\underline{D}}$ are determined from the Hirshman-Hinton quantities[6,7] and by local concentrations.

3. Trial calculations for COMPASS-D

Amended parallel forces (2) have been introduced into the "B2" code, retaining at first its restriction to low impurity abundances. Note that in its control-volume discretization scheme[3], the altered ion term is approximated :-

$$\int dV \, T_\parallel^a \;\approx\; \left(\frac{Z_a}{Z_{\mathrm{EFF}}} - 1 \right) Z_a \, n_a \, c_i \left(\mathcal{A}_\parallel \Delta_\parallel T_i - \left[\frac{2 m_a D_\perp}{T_i} \nabla_\perp v_\parallel^a \right] \mathcal{A}_\perp \Delta_\perp T_i \right) \quad , \qquad (5)$$

for temperature increments ΔT_i across a discrete cell having facial areas $\mathcal{A}$ in its respective coordinate directions.

The dimensionless factors c_e ; c_i in (2) must be chosen as constants[3] to preserve $\sum_a T_\parallel^a = 0$ ($\sum_a (\sum_b R_\parallel^{ab}) \equiv 0$ also). Another adjustment made is to change their original

values[3] in "B2", viz $c_e = 0.71$; $c_i = 4.05$, to a smaller ion number $c_i = 2.2$, consistent[2] with a formulation by Rutherford. Thus ion thermal forces are at once lowered by a half. In addition, Helander's drift-kinetic derivation implies certain fixed relations[2] between all ion anomalous cross-field coefficients (thermal diffusivity $\chi_\perp^i$, viscosity $\eta_\perp^a$, see Table 1 below), which are inserted as input specifications.

Except as next explained, other aspects of calculations are kept as in earlier cases[4] modelling efflux of a helium minority from single-null diverted plasmas in COMPASS-D, and reference 4 should be seen (with Table 1 below) for details. Breaks, or "cuts", incurred in the computational grid to separate[4] closed interior and divertor private flux-surfaces have approximately been rendered continuous using an indirect mapping technique[9]. Furthermore, present trials have been expedited using certain analytic estimates of neutral-particle recycling. The so-called "minimal" treatment[3] of Braams for helium ions has been combined with a more elaborate one for majority deuterium, developed by Hotston[10]. An important connotation is that recycling levels are then no longer solved for, but instead imposed, by assignment of a reflection coefficient $0 \leq \mathcal{R} \leq 1$ for ions to target surfaces. Consistent evaluation of sources with the EIRENE neutral gas transport code, as before[4], would eventually be needed for more quantitative results.

3.1 Results

Incorporation of corrected parallel forces (2) $\mapsto$ (5) in fact is found severely to degrade stability of the "B2" solution method[3], so that the added cross-field gradients term can only be included when multiplied by a factor α, incremented gradually from 0. In practice, progress still could not be made beyond $\alpha = 0.75$. Notably, though, the disturbances met thereafter are not physical in origin, as confirmed by fluctuations staying the same versus iteration number, rather than cumulative time, as time-steps are made either smaller or larger. Indeed, time-stepping can be removed altogether from "B2", and a similar development still followed in effect over a single time-step of infinite size.

Chief parameters of test calculations are summarized in Table 1. A moderately high level of helium is set, to accentuate alterations in impurity properties, but note that even a 50% abundance of He^{++} ions locally gives $Z_{EFF} = 1.5$ only, so (2) remains reasonable. One crucial measure of helium behaviour in a divertor SOL is its "compression"[4], or the change in its fractional abundance between upstream and near-target vicinities, eg :-

$$C \equiv \frac{\left(\int_{\text{divertor}} \left(n_{He^+} + n_{He^{++}} \right) dV \right) / \left(\int_{\text{divertor}} n_{D^+} dV\right)}{< n_{He^+}^{\text{inner}} + n_{He^{++}}^{\text{inner}} > / < n_{D^+}^{\text{inner}} >} \quad . \tag{6}$$

Here averages in the denominator are evaluated around the inner boundary[4] magnetic surface. In an ignited device, C ought to be as high as possible to optimize proportional pumping of ash. Results also listed in Table 1 demonstrate that from $\alpha = 0$ to $\alpha = 0.75$, helium compression *increases*, consistent with a dominant effect of coupled transport corrections being opposition of the expulsive classical thermal force for highest-charge He^{++} ions.

Table 1. Main details of COMPASS-D trial calculations

$R_0 = 0.56$ m; $I_p = 0.15$ MA; $B_0 = 1$ T	$Q^{\text{SOL}} = P^{\text{inp}} - P^{\text{rad}} \approx 0.13$ MW
inner $Q_e/Q_i = 2$; Bohm target sheaths ; $\mathcal{R} = 0.74$; exterior pedestals	
$\chi_\perp^a = \chi_\perp^i = 1.5\,\eta_\perp^a/(m_a\,n_a) = 1.5\,D_\perp = 1.5\,D_{\text{Bohm}}$	$n_{D^+}^{\text{inner}} = 5\,n_{He^{++}}^{\text{inner}} = 7\times10^{18}$ m^{-3}
Results	$C(\alpha = 0) = 0.846$; $C(\alpha = 0.75) = 0.959$ (see equation (6))

Fig. 1 Ion densities (10^{18} m^{-3}) v poloidal co-ord (m)
solid – classical forces broken – + correction × 0.75

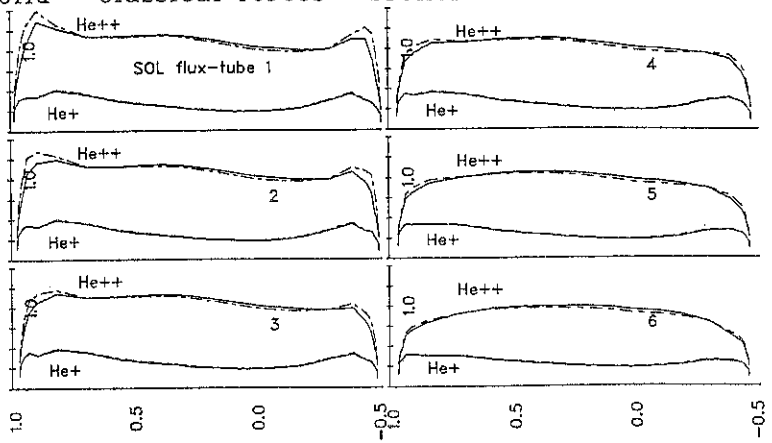

More detailed profiles of species densities are plotted in Fig.1 for the first few SOL flux-tubes (grid rows), against a poloidal distance along the separatrix (0 outboard magnetic axis level, + towards inboard target, – towards outboard). The principal difference from $\alpha = 0$ to $\alpha = 0.75$ is clearly seen to be an increase in divertor accumulation of He^{++}, as commented. There is a smaller, counter increase in upstream density of He^{+}, consistent with its constraining ($Z_{He^+} < Z_{EFF}$) classical thermal force being opposed too. Reactions of deuterium properties are small for moderate impurity fractions.

4. Conclusions

Properly accounting for strongly coupled cross-field and parallel transport in SOL plasmas discovers non-classical, along-field fluid forces acting between different ion species. Trial calculations with an adapted "B2" code for minority helium efflux in COMPASS-D show these effects, even reduced by a factor of 0.75 , can oppose classical thermal forces and imply better divertor retention of impurities. Their impact is likely to be greater at full magnitude, and importantly for heavier impurities or at higher recycling, when their driving shear in SOL flow is naturally more variable. Potential contributions to transport due to Onsager symmetry are also reemphasized. Generalization of ion forces in edge modelling for arbitrary impurity levels is essential, though, and will be addressed next.

This work is funded jointly by the UK Department of Trade & Industry and Euratom.

References

1. S I Braginskii *in* "Reviews of Plasma Physics" Vol 1, *ed* M A Leontovich ('65)
2. P Helander *et al* Phys Rev Lett 77 ('96) 2479
3. B J Braams NET report EUR-FU/XII-80/87/68 (Jan '87)
4. G P Maddison & M Baelmans 22nd EPS CCFPP, Bournemouth (July '95) IV-309
5. A Bergmann *et al* Contrib Plasma Phys 36 ('96) 192
6. S P Hirshman Phys Fluids 20 ('77) 589
7. F L Hinton *in* "Handbook of Plasma Physics", Vol 1, *eds* A Galeev & R Sudan ('83)
8. G P Maddison & P Helander *in preparation*
9. R Schneider *et al* Contrib Plasma Phys 32 ('92) 450
10. H D Pacher *et al* Nuc Fus 32 ('92) 1373

Ballooning Instabilities, Poloidal Flow and the Temperature Pedestal at the Tokamak Edge

H R Wilson and J W Connor
UKAEA, Fusion, Culham, Abingdon, Oxon OX14 3DB, UK
(UKAEA/Euratom Fusion Association)

1 INTRODUCTION A formalism for high toroidal mode number ($n \gg 1$) ballooning mode stability was originally derived by expanding about the radial position where the mode was most unstable: the 'conventional' ballooning modes [1]. In drift wave theory it was realised that this approach is not so useful, as one is then often interested in the transport caused by the drift instability across the full plasma radius. This led to the development of a new type of 'general' ballooning mode theory to address instabilities which exist away from a radial position where the growth rate is maximised [2,3]. The 'conventional' and 'general' ballooning mode properties were found to be described by the same 1-D differential equation (known as the ballooning equation) along a field line to leading order in n. The result of solving this ballooning equation is a local eigenvalue which varies slowly with minor radius (linearly for the general mode, and quadratically for the conventional mode) but with a stronger (periodic) dependence on the 'ballooning angle', k (also often referred to as θ_0). At higher order one finds that for the conventional mode k must be chosen so that the eigenvalue is stationary and the radial structure is a Gaussian coupling $\sim n^{1/2}$ rational surfaces, while for the general mode the eigenvalue is averaged over a period in k and the radial structure is extended, spanning $\sim \epsilon n$ rational surfaces (ϵ is a measure of the toroidal coupling). Often this higher order theory is neglected, but this is an example when the higher order theory has a dramatic effect on the mode stability and structure.

A weakness in ballooning mode theory is its application at the tokamak plasma edge. It is important to overcome this for two reasons. First, in H-mode plasmas the steepest pressure gradient exists at the edge and this appears to drive edge localised modes (ELMs) which are important to understand for ITER. Indeed the onset of type I ELMs has been associated with the stability boundary for the conventional ideal MHD ballooning mode, though clearly the conventional ballooning mode theory cannot be applied at the edge of an H-mode, where the variation of the local growth rate is essentially linear with r. Second, several confinement models are sensitive to the value of the 'temperature pedestal' at the top of the edge steep gradient region (the H-mode transport barrier). Both the width of the transport barrier and the maximum pressure gradient within it may be determined by the structure of edge ballooning modes. This provides the motivation for the present work: to develop a theory for edge ballooning modes, use this to consider the consequences for ideal MHD stability and the radial extent of flow generation from Reynolds stress due to drift wave turbulence and then combine these to give a model for the temperature pedestal.

2 IDEAL MHD BALLOONING Previous work has concentrated on the analysis of a

simple model equation for ideal MHD stability [4] and the insight gained from analysing that model system led to the present formalism for a more realistic description of MHD ballooning modes at the plasma edge. In particular, the model calculation demonstrated the existence of a class of ballooning modes localised at the plasma edge which have the same stability properties as the conventional ballooning mode, but a different radial mode structure. It was found to span $\sim n^{1/3}$ rational surfaces and the shape of the radial envelope is the tail of an Airy function; this radial envelope was identified as the rapidly decaying tail (beyond the WKB turning point) of the general internal mode. The model calculation also included the possibility of coupling to a high n external kink mode; we do not treat this coupling here.

We start with the Euler equation for the displacement ξ which minimises the change in energy (eg see [1]): this is the eigenvalue equation. We apply the ballooning transformation, which maps the poloidal angle χ (in which ξ must be periodic) onto the ballooning coordinate η in which the ballooning transform of ξ, denoted by F, tends to zero as $\eta \to \pm\infty$. There is an issue here: the ballooning transformation is only useful if there is approximate translational invariance across rational surfaces. This breaks down as one crosses the plasma-vacuum interface, but as the eigenfunction is zero there (we impose the boundary condition that the radial envelope of $F = 0$ at the interface) this is not important: 2-D numerical calculations using the above simplified model have supported this picture. The formalism now deviates from that of conventional ballooning theory. To take proper account of the different radial mode structure of the edge ballooning mode, a radial variable $x = n^{2/3}(\psi - \psi_a)$ is defined, where we expect the envelope $A(x)$ to vary on the scale x. Here $\psi = \psi_a$ is the poloidal flux at the plasma boundary. This allows the full 2-D eigenvalue equation to be expanded in powers of $n^{-1/3}$. Thus

$$\begin{aligned} &\{L_0 + n^{-1/3}L_1 + n^{-2/3}L_2 + \cdots + [\omega^2(\psi,k) + (\Omega^2 - \omega^2(\psi,k))] \\ \times\ &[M_0 + n^{-1/3}M_1 + n^{-2/3}M_2 + \cdots]\}[F_0 + n^{-1/3}F_1 + n^{-2/3}F_2 + \cdots] = 0 \end{aligned} \tag{1}$$

L_0 and M_0 are the same operators as those in the conventional theory (defined in [1]) and

$$P_1 = -\frac{i}{\nu'(k)}\frac{\partial P_0}{\partial k}\frac{\partial}{\partial x} \qquad P_2 = -\frac{1}{2\nu'(k)}\frac{\partial}{\partial k}\left(\frac{1}{\nu'(k)}\frac{\partial P_0}{\partial k}\right)\frac{\partial^2}{\partial x^2} \tag{2}$$

$P_j = L_j$ or M_j, ν' is the local magnetic shear, prime denotes derivative with respect to ψ, Ω^2 is the mode frequency and $\omega^2(\psi,k) = \Omega^2 + O(n^{-2/3})$ is a 'local' eigenvalue determined from the leading order standard ballooning equation to be solved for all k $[0, 2\pi]$:

$$L_0F_0 + \omega^2(\psi,k)M_0F_0 = 0 \tag{3}$$

Thus L_0 involves only differential operators in η and we may write the general solution as $F_0 = A(x)f_0(\eta)$, where f_0 satisfies eqn (3) and the envelope $A(x)$, ballooning angle k and the relationship between the true eigenvalue Ω^2 and the local one ω^2 are all determined at higher order. In fact k is determined from a solubility condition at $O(n^{-1/3})$, ie

$$\frac{\partial\omega^2}{\partial k} = 0 \tag{4}$$

which is the same condition as that derived for the conventional ballooning mode. Finally, at $O(n^{-2/3})$ we derive a solubility condition which provides the envelope equation:

$$\frac{\partial^2\omega^2}{\partial k^2}\frac{d^2A}{dx^2} + 2[\nu'(k)]^2\left[n^{2/3}(\Omega^2-\omega^2(\psi_a)) - \left.\frac{\partial\omega^2}{\partial\psi}\right|_{\psi=\psi_a} x\right]A = 0 \qquad (5)$$

where we have Taylor expanded ω^2 about $\psi = \psi_a$. Applying the boundary conditions that $A(x)$ decays sufficiently rapidly as $x \to \infty$ (ie into the plasma) and $A(0) = 0$, we find that k must be chosen to *minimise* ω^2 and the eigenvalue condition yields

$$\Omega^2 = \omega^2 + \left[\frac{9\pi}{8n\nu'(k)}\frac{\partial\omega^2}{\partial\psi}\right]^{2/3}\left[\frac{1}{2}\frac{\partial^2\omega^2}{\partial k^2}\right]^{1/3} \qquad (6)$$

In summary, the edge MHD ballooning mode has the same growth rate as the conventional ballooning mode to leading order in n and this provides the justification for its use in the interpretation of ELMs. However, the edge ballooning mode has a quite different radial structure, spanning $\sim n^{1/3}$ rational surfaces, and its shape is the tail of an Airy function, while the conventional mode spans $\sim n^{1/2}$ surfaces with a Gaussian envelope.

3 DRIFT BALLOONING AND TEMPERATURE PEDESTAL The formalism for analysing MHD ballooning modes can also be used to analyse edge drift ballooning modes, and we find there is a Reynolds stress associated with these edge modes. To illustrate the essential features we adopt a simple model of drift waves in a large aspect ratio, circular cross-section tokamak:

$$\left[\frac{1}{(nq')^2}\frac{\partial^2}{\partial y^2} - \frac{\sigma^2}{\Omega^2}\left(\frac{\partial}{\partial\theta} - inq'y\right)^2 - \frac{\alpha}{\Omega}\left(\cos\theta - \frac{is}{nq'}\sin\theta\frac{\partial}{\partial y}\right) - \Lambda\right]\phi = 0 \qquad (7)$$

where ϕ is the perturbed electrostatic potential, the radial coordinate $y = a - r$ is redefined relative to the edge at $r = a$, θ is the poloidal angle, a prime denotes radial derivative, $\alpha = 2\epsilon/bs^2$, $\sigma = \epsilon/bqs$, $\epsilon = L_n/R\tau$, $\tau = T_e/T_i$, $b = (k_\vartheta\rho_i)^2/2$, $\Omega = \omega/\omega_{*e}$, with L_n the density scale length, R the major radius, T_j the temperature of species j, k_ϑ the poloidal mode number, ρ_i the ion Larmor radius, q the safety factor, $s = rq'/q$ the magnetic shear, ω the complex mode frequency and ω_{*e} the electron diamagnetic frequency. The eigenvalue

$$\Lambda = \frac{1}{bs^2}\left[\frac{\Omega-1}{1+\tau+\eta_i} - b\right] \qquad (8)$$

Proceeding in an analagous way to the ideal MHD problem, we define a local eigenvalue λ which is found to be identical to that in conventional ballooning theory. The mode envelope $A(x)$ ($x = n^{2/3}y$) is again found to be an Airy function spanning $n^{1/3}$ rational surfaces. It is useful to obtain an analytic solution to the leading order drift ballooning equation and this is possible in the limits $\sigma/\Omega \ll 1$, $\alpha/\Omega \ll 1$ and $\eta_i \gg 1$. In this case the eigenvalue condition $\Lambda \simeq \lambda$ yields

$$\lambda = -\frac{i\sigma}{\Omega} - \frac{\alpha}{\Omega}\cos k \qquad \Omega = 3^{1/4}ic\sqrt{\frac{\epsilon s\eta_i}{q}} \qquad f_0(\eta) = \exp[-cs^2\eta^2] \qquad (9)$$

for the slab-like η_i mode branch (assuming $s \gg q$, which may represent a feature of separatrix geometry) where $k = 0$ must be chosen and $c = [1 - i(\sqrt{2} - \sqrt{3})]/\sqrt{6}$. The instability growth rate has been maximised with respect to b.

This edge drift ballooning mode can be shown to generate a Reynolds stress:

$$R_y = \frac{1}{2\pi r} \oint \left[\frac{\partial \phi^*}{\partial \theta} \frac{\partial \phi}{\partial r} + \frac{\partial \phi}{\partial \theta} \frac{\partial \phi^*}{\partial r} \right] d\theta \tag{10}$$

which, using the above result for f_0 and assuming a single dominant k_θ (that which maximises the linear growth rate as above), reduces to

$$R_y = \frac{k_\theta}{r} n^{2/3} s |A|^2 \qquad r k_\theta = \frac{\sqrt{2b}}{\rho_{*i}} = \frac{2}{3^{1/8} \rho_{*i}} \left[\frac{\epsilon s}{\eta_i q} \right]^{1/4} \tag{11}$$

where $\rho_{*i} = \rho_i / r$. This result implies that the Reynolds stress acts over the radial width of the edge drift ballooning mode and, provided the resulting torque is sufficient to overcome damping processes (eg neoclassical viscosity), it will generate a sheared flow. The precise magnitude of this flow depends on the non-linear saturation of ϕ (ie $|A|$), which we do not address here. Instead we *assume* the flow to be sufficiently large that turbulent transport is suppressed where the Reynolds stress acts, leading to an H-mode transport barrier width of

$$\Delta = L \left(\frac{q^2 \rho_{*i}^2}{4b} \right)^{1/3} \qquad \text{where} \qquad L = \left(\frac{\lambda_{kk}}{q'^2 \lambda_x} \right)^{1/3} \sim a \,, \qquad b = \frac{2}{3^{1/4}} \left[\frac{\epsilon s}{\eta_i q} \right]^{1/2} \tag{12}$$

If we further assume that the pressure gradient can rise to the ideal MHD limit as a result of transport suppression, then we find that the pressure at the top of the pedestal is

$$p_{\text{ped}} = \frac{B^2 \alpha_c(s)}{2\mu_0 R q^2} L \left(\frac{3^{1/4}}{8} \sqrt{\frac{\eta_i q}{\epsilon s}} q^2 \rho_{*i}^2 \right)^{1/3} \tag{13}$$

where $\alpha_c(s)$ is an $O(1)$ number characterising the MHD ballooning limit. For fixed q and B, this can be expressed as a relationship between the pedestal temperature and density: $T_{\text{ped}} \propto n_{\text{ped}}^{-3/2}$.

In summary a new edge ballooning mode structure has been identified, which has the same stability properties as the conventional ballooning mode, but has an Airy function radial structure, spanning $\sim n^{1/3}$ rational surfaces (cf a Gaussian spanning $\sim n^{1/2}$ surfaces). Applied to a drift wave model, it suggests that η_i modes can drive sheared flow at the edge which would lead to a temperature pedestal width scaling as $\rho_{*i}^{2/3} a$.

REFERENCES

[1] J W Connor, R J Hastie and J B Taylor, Proc Roy Soc London Ser A **365** 1 (1979)

[2] F Romanelli and F Zonca, Phys Fluids B**5** 4081 (1993)

[3] J W Connor, J B Taylor and H R Wilson, Phys Rev Lett **70** 1803 (1993)

[4] J W Connor and H R Wilson, *Theory of Fusion Plasmas* (eds J W Connor, E Sindoni and J Vaclavik), Editrice Compositori Bologna 1997, p 441

This work was funded jointly by the UK Dept. of Trade and Industry and Euratom.

CT Fuelling of TdeV

R. Raman[1], F. Martin, G. Pacher, B. Stansfield, D. Michaud, P. Gierszewski[1], C.S. Pitcher[1], J-L. Lachambre, C. Côté, G. Abel, C. Xiao[2], D.Q. Hwang[3], A. Hirose[2], H.S. McLean[3], B-J. Leblanc, J-L. Gauvreau, N. Richard, B. Quirion, M. St-Onge

Centre Canadien de Fusion Magnétique, Varennes, Québec, Canada, J3X 1S1
[1]Canadian Fusion Fuels Technology Project, Mississauga, Ontario, Canada, L5J 1K3
[2]University of Saskatchewan, Saskatoon, Saskatchewn, Canada, S7N 0W0
[3]University of California - Davis, Livermore, California, USA 96550

The CT fuelling program at TdeV has been concerned with the technological development of the CT injector as well as the understanding of the physics of CT injection as a means of tokamak fuelling. We have constructed a new injector (CTF-II) that incorporates several technological improvements. CT injection into a toroidal field shows that penetration is greater for lower fields with a broad density deposition profile. This broad deposition profile could be due to a lower velocity ion population that trails the high velocity component which has maximum penetration. CT injection into a tokamak plasma has produced significant fuelling (~15%) without impurity cooling. An increase in density and reduction in divertor H_α emission have also been observed following CT injection, indicative of transition in confinement regime.

Introduction

On-line particle fuelling is needed for long-pulse or steady state operation of a tokamak. Present fuelling schemes such as gas puffing and pellet injection are not expected to deep fuel reactor grade plasmas. A large portion of the fuel will not penetrate to the center and will be lost before burnup. With future use of tritium, deep fuelling of the injected fuel is more important in order to maximize tritium burn up, reduce tritium accumulation in the vessel walls and possibly for density profile control of the tokamak. Deep fuelling a tokamak plasma can improve several tokamak parameters by providing density profile control, including improved confinement, increased bootstrap current fraction, and greater fusion power with central densities higher than the edge Greenwald limit. Peaked density profiles can also reduce the ignition margin for a reactor.[1]

In 1988, deep fuelling of tokamaks by CT-spheromaks was first proposed by Perkins[2] et al. and Parks.[3] The spheromak is a compact toroid (CT) plasma configuration with approximately equal amounts of toroidal and poloidal magnetic fields. The spheromak can be formed in a magnetized Marshall gun and efficiently accelerated to high velocities in a coaxial rail gun in which the plasmoid forms the sliding armature.[4,5]

The CTF Device

In 1993, the CTF device was used to demonstrate the first non-disruptive fuelling of a tokamak on TdeV.[6,7] TdeV has a major/minor radius of 86 and 26 cm respectively. For CT injection experiments the tokamak was operated with a toroidal field of 1.4 T and a plasma current of 160 kA corresponding to an edge q of about 4 in a single null plasma configuration. Due to plasma contamination, there was rapid cooling of the tokamak plasma and CT fuelling was generally accompanied by extensive MHD activity. In 1995, reduction in plasma contamination allowed fuelling without any adverse perturbation to the tokamak.[8] In these experiments, some fuel possibly reaches the center (r/a = 0.), but due to the long length of these CTs (comparable to the TdeV minor radius), the maximum in the density change after CT injection occurred at r/a ~ 0.6 with an overall particle inventory perturbation of 16%. Some discharges also show indications of improvement in confinement as shown in Figure 1. In this discharge, the increase in energy confinement and diamagnetic energy is accompanied by a reduction in the divertor H_α signal and a reduction in the magnetic fluctuations, features

associated with H-mode transition.[9,10] However, our diagnostics are not capable of ascertaining if the edge density gradient is steeper for these discharges.

The CTF-II device

We have now begun operation of a second generation CT injector (CTF-II) that incorporates improvements in CT injector technology. A dense W coating is plasma sprayed on all plasma facing surfaces to reduce electrode erosion and minimize the high Z impurity content of the CT plasma; the amount of W injected into the tokamak plasma is negligible. The CT electrodes are maintained at 115°C with a hot oil circulating system to condition the wall surfaces and minimize outgassing. Fast pulsed gas valves have been developed to minimize the amount of injected gas and improve the gas coupling to the CT. The injector has been operated up to an accelerator bank voltage of 20 kV (~ 40% of full bank energy). Initial experiments were performed in a pure vacuum toroidal field to determine the extent of CT penetration. The TdeV SMM interferometer which is located in the adjacent bay (22.5 degrees toroidal azimuthal separation with respect to the CT injector) was used to determine the depth of CT penetration. We find that at a nominal 1T field (r/a = 0.), the CT can penetrate to the innermost interferometer location (r/a = -0.7). This is shown in Figure 2. We note that the interferometer chords at r/a = +0.8, 0.5, 0.2 and -0.1 show about the same increase in signal but the innermost chords at r/a = - 0.5 and -0.7 show less of a signal increase. This may be related to the axial density distribution within the CT. At higher toroidal fields (1.35 to 1.5 T) the CT penetrates up to about r/a -0.1 at about the 40% accelerator bank voltage.

The broad density deposition profile could be a consequence of a spread in ion velocity within the CT. Figure 3 shows the temporal evolution of the linear integrated CT density and the CT B_z (poloidal) field, both measured at the same axial location on the CT, just before final compression. The CT B_z field is associated with the magnetic structure of the CT and gives an indication of its extent. The poloidal field is narrower in time than the density and is strongest in the ascending part of the CT density trace. Correlation between two B_z magnetic probes situated 10.5 cm apart indicate a CT velocity before compression of 45 cm/μsec. This is probably the velocity of the leading part of the density distribution, the rest following at a lower velocity. Correlation between two density measurements separated by the same 10.5 cm indicates a velocity of about 15 cm/μsec for the "bulk" of the CT plasma. This lower velocity portion will probably be slowed down more by the final compressor than the initial higher velocity portion, essentially stretching out the former. A visible bremsstrahlung detector (signal ~ n_e^2) situated at the exit of the CT focus cone shows a short high density pulse (~0.3 μsec, ~15 cm) followed by a longer low density component [fig. 4]. These lower velocity ions will have less penetration and provide fuelling at higher r/a and exterior of the tokamak plasma. These CT characteristics have also been observed by the RACE and the CTIX groups at LLNL and is believed to be due to improper coupling of the injected gas to the CT.[11] Fast gas valves and high gun voltage operation are proposed as solutions to increase gas coupling in order to minimize the trailing plasma.

Initial plasma injection experiments have been performed with a toroidal field in the 1.35 to 1.5 T range. As in the past, we have observed indications of increased energy confinement on some shots [fig 5]. We have also observed signature of change in confinement regime. Figure 6 shows the time evolution of the divertor H_α signal and the central interferometer chord signal for two different shots. On the first shot [fig. 6a], the interferometer shows an increase in density for as long as the divertor H_α signal stays depressed. The drop in the divertor H_α signal occurs within about 1ms after CT injection. One can also observe a burst of MHD activity initiating an ELM accompanied by a momentary loss of particles. After the H_α signal returns to the pre-CT injection value, the interferometer signal starts to decrease indicating that confinement is reverting to the pre-CT level. For the second shot [fig. 6b], the H_α signal returns to a value slightly below the pre-CT injection level. In such shots, the central interferometer signal attains a flattop which is sustained for nearly 100ms, much longer that the 20 ms particle confinement time on TdeV. There is no ELM activity on this shot.

In summary, we have confirmed that CT injection can be used for fuelling of a tokamak. In our experiments, the CT length is of the same order as the minor radius, preventing local fuelling. There is evidence that CT injection affects the confinement of the tokamak plasma, producing several of the features associated with H mode transition. Projections of the CT length to the minor radius of large tokamaks (ITER) puts this ratio at about 10-15%[12] compared to ~100% in TdeV experiments. In addition, the particle inventory perturbation (as a percent of fuelling) is < 1% for an ITER class device whereas non-perturbative deep fuelling of more than 15% has been demonstrated on TdeV.

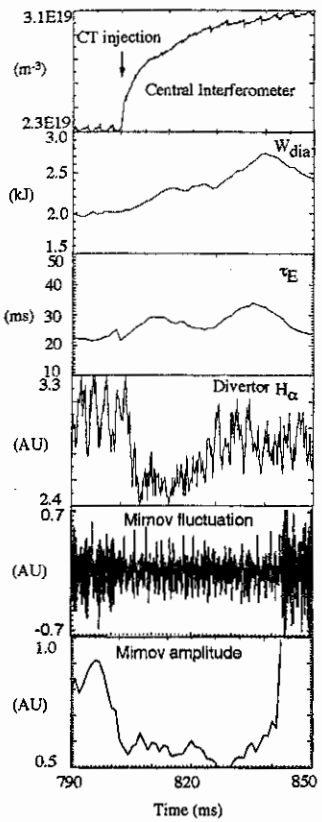

Figure 1: The improvement in τ_E is accompanied by a reduction in the divertor H_α signal and a reduction in the amplitude of the magnetic fluctuations.

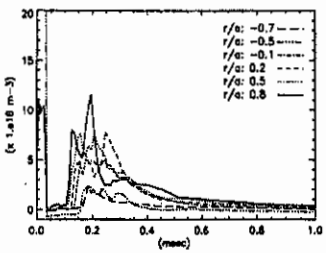

Figure 2: TdeV multi chord interferometer signals for the case of CT injection into a IT vacuum magnetic field.

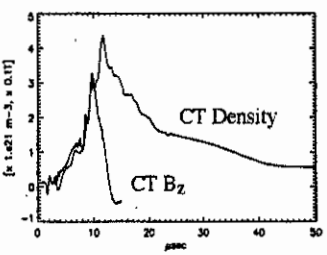

Figure 3: CT poloidal magnetic field and interferometer signal at the same axial location in the accelerator.

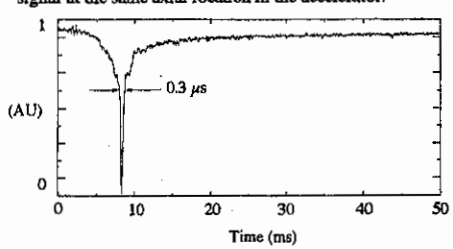

Figure 4: Visible Bremsstrahlung signal (proportional to n_e^2) measured a few cm outside the CT injector focus cone.

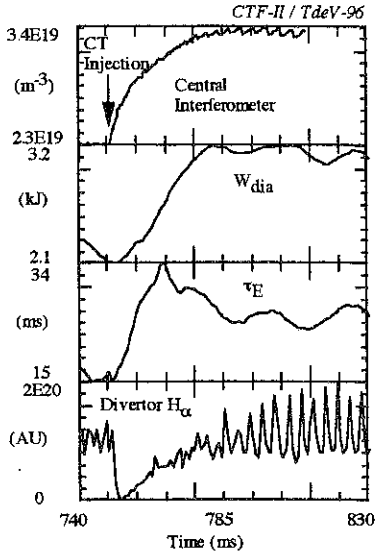

Figure 5: Example of improved confinement discharge from the CTF-II/TdeV96 run. B_T = 1.5 T, Ip = 170 kA, Te(0) = 900 eV, single null discharge. Beyond t = 785 ms, the oscillation amplitude in the divertor H_α signal increases.

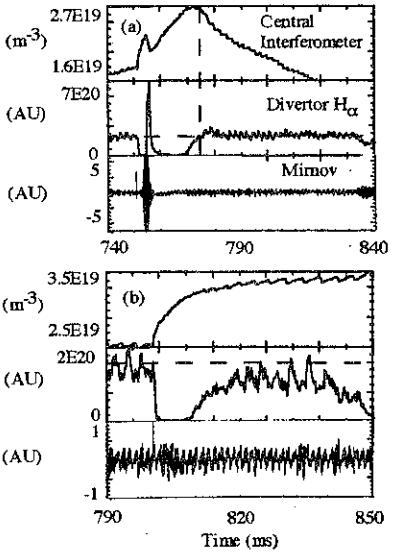

Figure 6: (a) The density signal continues to rise for as long as the H_α signal stays depressed. A single ELM is observed. (b) In this case, the H_α signal never quite reaches the pre-CT injection level while the density signal continues to gradually increase. No ELM feature is seen in this and in most CT injection discharges.

ACKNOWLEDGMENTS

The CTF project is funded and managed by the Canadian Fusion Fuels Technology Project. The Centre canadien de fusion magnétique is funded by the Government of Canada, Hydro-Québec and the Institut National de la Recherche Scientifique.

REFERENCE

[1] Perkins, L.J., Spears,W.R., et al.,"ITER parametric analysis and operational performance report," ITER documentation series,No.**22**, IAEA,Vienna, Austria (1991)
[2] Perkins, L.J., Ho, S.K., Hammer, J.H., *Nucl. Fusion* **28**, 1365 (1988)
[3] Parks, P.B., *Phys. Rev. Lett.*, **61**, 1364 (1988)
[4] Hartman, C.W., Hammer, J.H., *Phys. Rev. Lett.*, **48**, 929 (1982)
[5] Molvik, A.W., Eddleman, J.L., et al., *Phys Rev. Lett.*, **66**, 165 (1991)
[6] Raman, R., Thomas, J., Hwang, D., et al., *Fusion Tech.*, **24**, 239 (1993)
[7] Raman, R., Martin, F., Quirion, B., et al., *Phys. Rev. Lett.*, **73**, 3101 (1994)
[8] Raman, R., Martin, F., St-Onge, M., et al., *Proc. 23rd EPS Conf. on Controlled Fusion & Plasma Physics*, Kiev (1996)
[9] Wagner, F., et al., *Plasma Phys. Control. Fusion*, **36**, A61-A74 (1994)
[10] Toi, K., et al., *Plasma Phys. Control. Fusion*, **36**, A117-A122 (1994)
[11] Hwang, D.Q., et al., in "Development of Innovative Fuelling Schemes for Fusion Energy Science," *Proc. 16th IAEA Fusion Energy Conf.*, Montreal (1996)
[12] Gierszewski, P., Raman, R., Hwang, D., *Fusion Tech.*, **28**, 619 (1995)

Effect of Divertor Geometry and Plasma Density on Helium Enrichment on TdeV-96

G.W. Pacher, J.-L. Gauvreau, R. Décoste, R. Marchand, M.M. Shoucri, G. Abel, J.P. Gunn, J.-L. Lachambre, N. Richard, B.L. Stansfield, and the TdeV Team
Centre canadien de fusion magnétique, 1804 boul. Lionel Boulet,
Varennes, Québec, Canada, J3X 1S1

Introduction

The divertor of the TdeV-96 tokamak (I<250 kA, B<2T) allows the separatrix to be incident on a quasi-horizontal target plate with outboard pumping (OB), or on a quasi-vertical plate with pumping through the private (PR) flux region [1] while divertor entrance baffling and overall plasma shape remain unchanged. All experiments reported here were carried out for these two configurations with ohmic heating alone in single-null geometry. As the density was varied, detachment was characterized in terms of the position of the maximum of D_α emission and of the power reduction to the target plates. Divertor pressure and helium enrichment were obtained from a puff-and-pump experiment. The results are compared with simulations.

Experiment

Pumping is performed only in the active divertor using a cryo-sorption technique to pump helium. Helium is puffed in the main chamber early in the discharge and its decay constant (τ^*_p) is measured from a HeII monitor in the main plasma. The walls are reset with glow discharge cleaning followed by a low density shot. The same sequence is repeated without helium injection in order to subtract the helium background. With this sequence, the pumping of the tiles on helium is negligible at medium and high densities, but must nevertheless be taken into account for the low density shots.

Using a two-reservoir model, τ^*_p is related to He compression (C_{He}) from which we obtain the enrichment (η):

$$C_{He}=\frac{n_{d,He}}{\langle n_{p,He}\rangle}=\frac{V_p}{V_d}\left(\frac{\tau^*_p}{\tau_{ex}}-1\right)^{-1}, \qquad \eta=\frac{C_{He}}{n_{He}/n_e}$$

where $n_{d,He}$ and $n_{p,He}$ are the helium densities in divertor plenum and main plasma, V_d and V_p are the divertor plenum and main plasma volumes, and τ_{ex} is the pumping time constant of the vessel including divertor plenum.

The plasma mean electronic density is obtained from a 7-chord interferometer and the partial pressures of He and deuterium in the divertor were measured with a modified Penning gauge [2]. The quantity of He puffed is adjusted to have 5-7% helium content in the main plasma.

Experimental values of enrichment and divertor pressures are shown in fig. 5. It is observed that geometry has a strong effect on enrichment at low density and that increasing density decreases enrichment, especially in the PR configuration. Divertor fuelling increases the

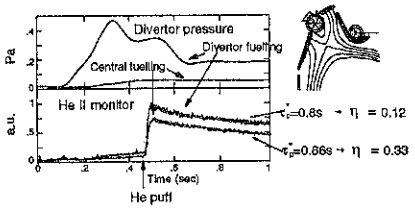

Fig. 1 - Effect of fuelling from the divertor plenum on divertor pressure and helium enrichment

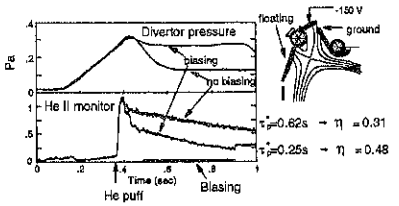

Fig. 2 -Effect of negative biasing on divertor plenum pressure and helium enrichment

deuterium partial pressure in the plenum but does not affect He pumping significantly (fig. 1). With negative biasing, such that **ExB** points toward the outer divertor, at high density the divertor plenum pressure and helium exhaust are increased by almost a factor 3 (fig. 2), while the enrichment increases by about 50%, rising from 0.31 to 0.48.

Simulations

The simulations were performed with the B2-Eirene code package [3] for three densities (0.5, 0.9, and $1.6\text{x}10^{19}\text{m}^{-3}$) at the core-SOL boundary. The temperature at the core-SOL boundary was adjusted to give a power input of approximately 100 kW into the scrape-off layer for transport coefficients of D=0.4 m^2/s and χ = 3 D. The carbon (2%) and helium (5%) concentrations were imposed at the same boundary. Both configurations, outboard and private region pumping, were investigated.

The experimental situation, in which the quasi-horizontal and the quasi-vertical divertor plates are separated by the pumping slot, could not be simulated in the coupled B2-Eirene runs. Instead, the pumping slot constituted a part of the quasi-vertical divertor plate, with a sheath boundary condition imposed on the whole target for the plasma calculation (B2 - fluid model), and a uniform reflection model for neutrals in the Eirene Monte Carlo calculation. The coupled simulation was run to a stationary solution for both plasma and neutrals. The neutral flux on the pumping slot was then determined from a stand-alone Eirene calculation in the real geometry, with the plasma background as determined from the coupled run.

The calculated ion flux incident on the pumping slot region Γ_i is not negligible compared to the calculated neutral flux Γ_n (up to 0.8 Γ_n for the outboard pumping geometry) and must be accounted for when comparing code to experimental results. This is especially important for determining helium enrichment, as the helium concentrations in the calculated ion and neutral fluxes are different (generally larger in the ion flux). In reality, the ion flux would traverse the pumping slot and be neutralized on the continuation of the divertor plate. Assuming a re-emission of neutrals in a cosine distribution, approximately half of the incident flux would return to the calculation grid, and the other half would enter the divertor plenum. For the comparison, we therefore define the total particle flux entering the divertor plenum $\Gamma_T = \Gamma_n + \frac{1}{2}\Gamma_i$, and the helium enrichment $\eta = (\Gamma_{n,He} + \frac{1}{2}\Gamma_{i,He})/\Gamma_T \times (n_e/n_{He})$. To evaluate the pressure, we assume that the

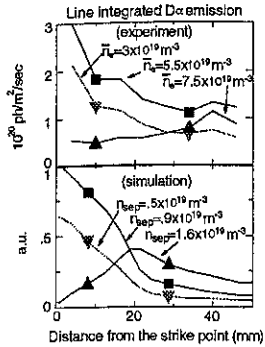

Fig. 3 - Comparion of emission of Dα in experiment and simulation

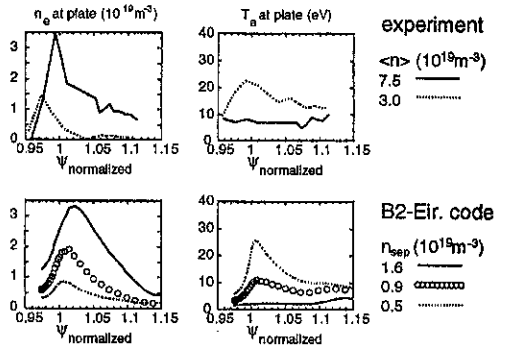

Fig. 4 - Comparison of experiment (top) and simulation (bottom) for electron densities (left) and temperatures at the divertor plate

neutral flux entering the divertor plenum is thermalized on the plenum walls. Then, by conservation of particles in the plenum $p = \Gamma_T/(S_P+S_S)$ where S_P and S_S are the pumping speeds of external pumps and the pumping slot respectively.

Comparison of simulations and experiment

Both in experiment and simulation, as the density is raised, the D_α emission first increases near the plate and then decreases (fig. 3). This behaviour had been observed in the previous divertor configuration [1] and corresponds to a transition from attached to semi-detached state. However, the maximum is nearer the plate in the simulations than in the experiment. At the lowest densities, simulated values at the plate are lower for density and higher for temperature and profiles are wider for density and narrower for temperature than the measured ones. Conversely, at the high densities, simulated values are comparable for density, but lower for temperature than in the experiment (fig. 4). For processes in which the value of electron temperature near the plate is important, the high density simulations may therefore correspond to higher densities than experimentally investigated. The divertor plenum pressure and helium enrichment deduced from the code are compared with the experimental values on figure 5.

Conclusions

Experiments have been performed with outboard (OB) and private region (PR) pumping in attached and semi-detached conditions. The helium enrichment tends to decrease from the attached to the semi-detached condition, but a large effect is only observed in the PR configuration, with η = 0.6 at low density (attached), and η = 0.25 at high density (semi-detached). Enrichment in the OB configuration is around 0.3 for the highest densities investigated. Negative biasing of the divertor plate in that configuration increases both divertor plenum pressure and helium exhaust - the enrichment increases by 50 % to η = 0.48. Fuelling of the main plasma from the divertor plenum does not change the helium exhaust.

In experiment and in simulation, the divertor plenum pressure rises faster than the core plasma density (as $\langle n \rangle^{1.7}$ in experiment, as $n_{sep}^{1.3}$ in simulation), and is lower for pumping in the private region than for outboard pumping (~2/3). Helium enrichment does not vary appreciably with density for the outboard pumping geometry in the experiment nor in the simulation. For private region pumping, as the density is raised from low to medium values, the helium enrichment drops in both experiment and simulation. However, the simulation predicts an increase of enrichment at the highest density, a tendency that is not observed in the experiment. The numerical values for pressure and helium enrichment obtained in the simulation are respectively twice and one-half those experimentally observed. These discrepancies may be due in part to the imperfect treatment of the pumping slot in the simulation. In addition, adjustment of the transport coefficients and of the radiated power are surely required to better reproduce the profile shapes and temperature values near the plate.

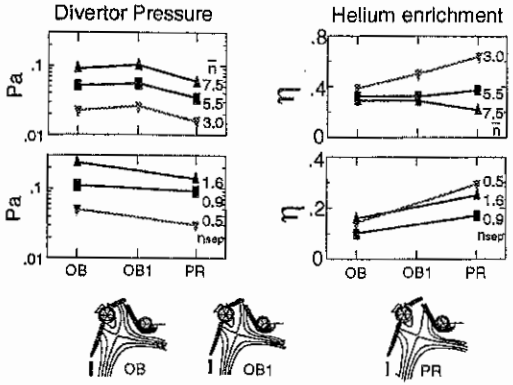

Fig. 5 - Comparison of experiment (top) and simulation (bottom) for divertor plenum pressure (left) and helium enrichment (right). Densities are in 10^{19} m^{-3}

Overall, the tendencies observed in the experiment are well reproduced by the simulation, especially for low and medium densities.

Acknowledgements

This work was funded by the Government of Canada, Hydro-Québec, and INRS. We wish to thank IPP-Garching, KfK Juelich, and B. Braams for the B2-Eirene code package, and especially D. Coster, A. Kukushkin, H.D. Pacher, D. Reiter, and R. Schneider for their help in its use.

References

[1] R. Décoste et al., 1996, *Plasma Phys. Control. Fusion* **38** A121-A133

[2] K.H. Finken et al., *Rev. Sci. Instrum.* **63** (1), 1 (1992)

[3] R. Schneider, D. Reiter, D. Coster, J. Neuhauser, K. Lackner, and B. Braams, *J. Nuc. Mat.* **220-222**, 1076 (1995) and references therein

Measurement and simulation of the sheath expansion in front of a flush-mounted probe

J. P. Gunn, Centre canadien de fusion magnétique, Varennes, Québec, Canada

THE PROBLEM WITH FLUSH-MOUNTED PROBES

The tokamak edge plasma is strongly magnetized and sufficiently dense so that the dimensions of a Langmuir probe are typically very much larger than both the ion Larmor radius r_{Li} and the Debye length λ_D. This facilitates the interpretation of the probe's *I-V* characteristic because its effective collection area A_{EFF} is equal to its geometrical projection along the magnetic field, so the ion current saturates at large negative biasing voltage. With the temperature T_e obtained from the diode part of the characteristic near floating potential V_f the density is calculated from the expression

$$I_{sat} = n_e e A_{EFF} c_s \qquad (1)$$

where c_s is the ion sound speed. The situation is different, though, for a probe which is flush-mounted into a divertor plate. There, the angle of attack α between $\boldsymbol{B}$ and the surface is only a few degrees, so then the geometric projection of the probe will be comparable to r_{Li} and λ_D. The standard analysis is useless because the ion branch of the characteristic exhibits strong nonsaturation [1] due to the expansion of the sheath above the probe [2]. This does not pose a problem if $V_f \geq V_{plate}$ because the short circuit ion current I_o^i gives an exact measure of n_e using Eq. (1) [3]. One only has to fit a reasonable function, such as a straight line, to the ion current in order to correctly subtract off the electron current for the exponential fit (Fig. 1).

There has been recent theoretical work aimed at understanding the nonsaturation. Weinlich [4] has proposed a simple model which has been validated by the two dimensional particle-in-cell (PIC) simulations of Bergmann [5]. The idea is that the increase in effective collection area is given by sheath thickness itself, which is a function of the local plasma parameters: $A_{EFF}=A_{pr}\sin\alpha+2r_{pr}k\lambda_D V_{pr}^{3/4}$ where $k=0.5(\sin\alpha)^{-1/2}$ is the sheath expansion parameter, describing the sheath thickness in numbers of Deybe lengths. The angle dependence is a result of current continuity. The ion flux arrives at the entrance of the magnetic presheath with speed c_s parallel to $\boldsymbol{B}$ (the parallel Bohm criterion), and is turned towards the surface normal under the action of the electric field gradient so that it enters the sheath at the sound speed (normal Bohm criterion). The corresponding density drop is proportional to the angle, so the

local Debye length at the sheath entrance is longer.

This model will not be valid when the ion trajectories in the sheath are very strongly magnetized. In that case, the magnetic presheath does not exist at all, and there is no focusing of ions onto the edges of the probe. The effective collection area will equal the probe projected area, and the sheath expansion parameter k will tend towards zero. The degree of sheath magnetization is characterized by the parameter $\zeta=c_e\omega_{ci}^{-1}\lambda_D^{-1}=(m_i n_e \varepsilon_o^{-1}B^{-2})^{1/2}$, that is, the ratio of the Larmor radius at the cold ion sound speed ($c_e^2=T_e/m_i$) to the Debye length. We have run one dimensional PIC simulations of the sheath over the entire range of sheath magnetization, and we have measured $k(\zeta)$ in the TdeV divertor for an order of magnitude variation of ζ. The results indicate that the nonsaturation is probably not useful for diagnostic purposes in most tokamaks.

MEASUREMENT OF SHEATH EXPANSION PARAMETER

Since we measure the density using the short circuit ion current I_o^i, we have an immediate check on whether the predicted sheath expansion k is correct. On shot #30383, we programmed the strike point to sweep over the entire outboard divertor plate in which are embedded 2 mm wide flush probes every 6 mm. At each probe position, and as a function of time, we calculated the magnetic field and its angle using the equilibrium code, and k using the measured electron density and sheath expansion current. The results in Fig. 2 clearly show that the nonsaturation becomes very weak for low ζ; it has a dependence on the density, the very parameter one would like to measure.

ONE DIMENSIONAL PIC SIMULATION

The coordinate system is illustrated in Fig. 3. The three components of the equation of ion motion are

$$m\frac{du_{xi}}{dt} = qBu_{yi}, \quad m\frac{du_{yi}}{dt} = -qBu_{xi} + qE\cos\alpha, \quad \text{and} \quad m\frac{du_{zi}}{dt} = qE\sin\alpha. \tag{2}$$

The system evolves until a self-consistent, steady state is attained with the potential profile given by Poisson's equation $d^2\phi/ds^2=-e/\varepsilon_o(n_i-n_e)$ with $s = y\cos\alpha + z\sin\alpha$ being antiparallel to the surface normal. The equations are rendered more intuitive by a convenient normalization which highlights the two scale nature of the problem: $t\rightarrow\omega_{ci}t$; $x\rightarrow x/\lambda_D$; $u\rightarrow u/\omega_{ci}\lambda_D$; $\phi\rightarrow\phi/T_e$, $E\rightarrow E\lambda_D/T_e$; $n\rightarrow n/n_o$. We also introduce the nondimensional parameters $\tau=T_i/T_e$, $\mu=m_i/m_e$, and the magnetization parameter ζ, defined above. The equation of motion for the ions becomes

$$\frac{du_{xi}}{dt} = u_{yi}, \quad \frac{du_{yi}}{dt} = -u_{xi} + \zeta^2 E\cos\alpha, \quad \textit{and} \quad \frac{du_{zi}}{dt} = \zeta^2 E\sin\alpha\,. \tag{3}$$

The electrons' motion is adiabatic, so we only need the parallel equation $du_{ze}/dt=-\mu\zeta^2 E\sin\alpha$. Poisson's equation is written $d^2\phi/ds^2=-(n_i-n_e)$. The injected Maxwellian flux is adjusted so that $n_i=n_e=1$ just outside the source sheath. The results presented below are for equal ion and electron temperatures ($\tau=1$), and the wall potential is $\phi=-10$. The Bohm criterion in our notation is $\langle u^{-2}\rangle^{-1/2}\geq\zeta$.

The role of sheath magnetization is obvious from an examination of Eqs. (3). When ζ is small, the perpendicular and parallel equations are decoupled: the ion motion is adiabatic, so there is no mechanism available for the formation of a magnetic presheath, and only the parallel Bohm criterion need be satisfied at the sheath edge [Fig. 4(a)]. The velocities in the figure are normalized by c_s. The solution is identical to the $\alpha=90°$ case, except that the normal velocities are reduced by $\sin\alpha$. As ζ increases, the MPS forms, and the sheath broadens due to the quasineutral density drop before the sheath edge [Fig. 4(b)]. The ion focusing which results in the lack of ion current saturation is due to the polarization drift in the y direction. The flow streamlines which terminate on the probe deviate further from their original $\boldsymbol{B}$-aligned trajectories than do the streamlines which terminate on the wall (Fig. 5). The flux tube expansion Δy reduces to zero as the sheath becomes very strongly magnetized ($\zeta\rightarrow 0$), and so therefore must the nonsaturation, in qualitative agreement with the measurements (Fig.2). A plot of the magnetization parameter regimes reveals that most tokamaks, like TdeV, will have partially magnetized sheaths (Fig. 6). The electron density cannot be reliably measured using the nonsaturation of the ion current, so analyses must be restricted to measuring the short-circuit ion current.

REFERENCES

[1] G. F. Matthews, et al., Plasma Phys. Cont. Fusion **32**, 1301 (1990).

[2] A. Carlson, et al., Proc. 20th Europ. Conf., Lisbon, III-1103 (1993).

[3] J. P. Gunn, et al., Rev. Sci. Instrum **68**, 404 (1997).

[4] M. Weinlich, PhD Thesis, IPP Report No. 5/64, Dez. 95 (1995).

[5] A. Bergmann, Phys. Plasmas **1**,3598 (1994).

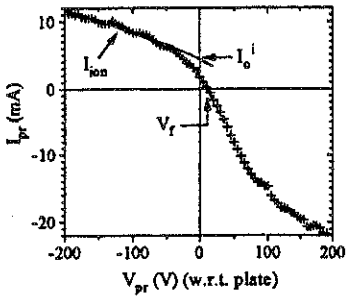

Fig. 1. A typical flush probe *I-V* characteristic showing nonsaturation of the ion current. I_o^i is the short-circuit ion current.

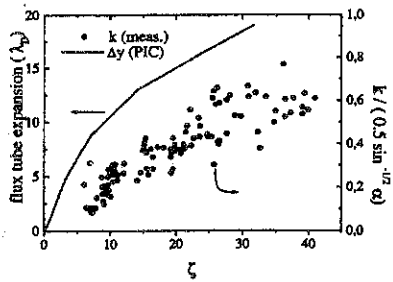

Fig. 2. Sheath expansion parameter k normalized by theoretical expression, and "flux tube expansion" (deviation of flux streamline from $\boldsymbol{B}$) calculated with PIC code.

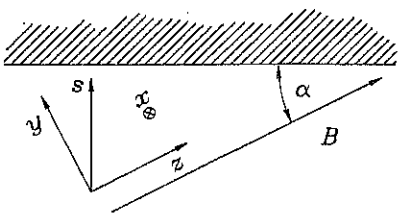

Fig. 3. Coordinate system used in PIC code: x is the $\boldsymbol{E}\times\boldsymbol{B}$ direction, y is the polarization drift direction, and z is the parallel direction. s points in the direction of the electric field, normal to the surface.

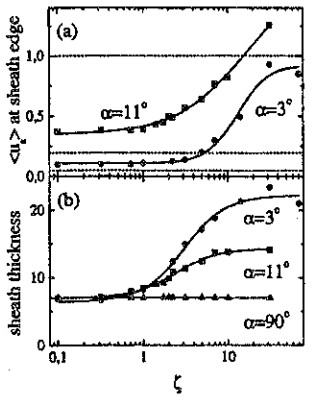

Fig. 4. PIC code results: (a) sheath edge velocity, and (b) sheath thickness in Debye lengths versus sheath magnetization for different $\boldsymbol{B}$-field angles.

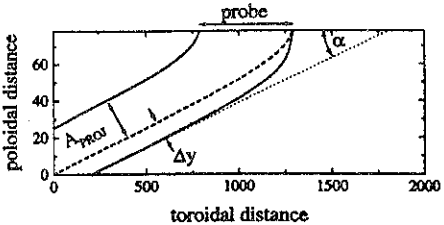

Fig. 5. Schematic of flux tube expansion Δy due to polarization drift. A_{PROJ} is the geometric projection of the probe.

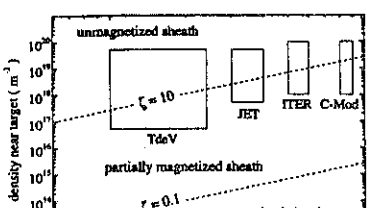

Fig. 6. Sheath magnetization for typical divertor plasmas.

Finite element modelling of plasma and impurity transport in the TdeV divertor

R. Marchand, M. Simard, G. Pacher, J.-L. Gauvreau, R. Décoste, N. Richard, and J. Mailloux
Centre Canadien de Fusion Magnétique[1]
1804 boul. Lionel Boulet Varennes Qc, Canada, J3X 1S1

Introduction

Computer modelling of edge and tokamak plasmas has matured into a well established activity used to support experimental programmes. The most advanced models to date are used routinely to make detailed comparisons with experiment and to extrapolate to the next generation of fusion experiments [1-4]. All these models are based on a finite volume discretisation of the transport equations, on a structured quasi-orthogonal mesh. This approach, however, is known to have a number of intrinsic difficulties or limitations such as the impossibility of performing local mesh refinement, the necessity of introducing unphysical cuts when considering a multiply connected geometry, and the difficulty of representing domains with boundaries of arbitrary shapes. These considerations have recently motivated efforts to develop models based on a different approach. One promising avenue is to use a finite element discretisation of the fluid transport equations on an unstructured triangular mesh [5-7]. In this paper, we present results obtained with such an approach, applied to the edge and divertor plasma of TdeV. The multi-fluid computer code TOPO is used to model the transport of a D-He plasma in the new divertor configuration of TdeV and to make some preliminary comparisons with experiment. Specifically, we calculate ion temperature profiles at two locations. The helium pumping enrichment and powers deposited on the divertor plates are also calculated and compared with experimental measurements.

Model description

The transport model is based on a Braginskii fluid description of the plasma [8]. A brief description is given here for completeness. For every ion species, we solve conservation equations for the particles, the parallel momentum, and energy. A distinctive feature of this work is that it can account for as many ion temperatures as there are ion species. It is indeed commonly assumed that all charged species have the same temperature, and a single ion energy conservation equation is solved for all ion species. As illustrated below, this assumption is not necessarily valid, particularly for the heavier low ionisation stages in the presence of recycling. An equation is also solved for the electron energy conservation equation. For simplicity, D (atomic) and He neutral transport is described in the diffusion approximation. That is, for every neutral species, a conservation equation is solved for the neutral density and energy, assuming the particle and energy fluxes to be purely diffusive. Also, for simplicity, all terms involving drift velocities are neglected. The atomic rates used in the calculation of source terms associated with ionisation, recombination, and inelastic collisions with electrons are obtained from a collisional radiative atomic model [9]. Charge exchange rates, on the other hand, are calculated in the coronal approximation.

Standard sheath boundary conditions are imposed at the plates. At the boundary with the central plasma, the species densities and temperatures are specified. At the outer flux boundaries (in the private region and in the SOL), a decay length of 1cm is imposed on all profiles. The anomalous transport coefficients which govern particle density, parallel

---

1 This work was funded by the Government of Canada, Hydro-Québec, and the Institut National de la Recherche Scientifique.

momentum, and energy in the radial direction are chosen for best agreement with
experimentally measured density and temperature profiles, and the power entering the SOL.

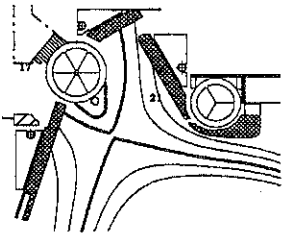

Figure 1. Illustration of the new TdeV divertor geometry.

Results

The new TdeV geometry is illustrated in Fig. 1. It is characterised by an outer divertor composed of two annular plates EA (inner) and EB (outer). We distinguish between two broad classes of equilibria depending on which of the outer diverter plates is intercepted by the separatrix. One important distinction between the two is that when the point of impact (the intersection between the plate and the separatrix) is on EA, the entrance to the pumping plenum is on the outer side of the SOL. With the point of impact on plate EB, however, pumping is through the private flux region [10]. In the following, results are presented for two equilibria corresponding to these two possibilities.

The first case considered is for a point of impact on plate EA. The triangular mesh used in the calculation is shown in Fig. 2. The advantage of using an unstructured triangular mesh is readily visible from the figure. In particular, it is straightforward to have fine spatial resolution in the vicinity of the X point, where conventional structured meshes would typically give very coarse resolution. It is also possible to extend the simulation domain into the shadow region, between plates EA and EB and, thus, better represent the entrance to the pumping plenum. It should be noted that, because of the strong anisotropy of diffusive (particularly thermal electron) transport, it is necessary to have an *aligned* triangular mesh; that is, most triangles must have two nodes on the same flux surface. This constraint is not excessively restrictive, however, and considerable advantage can still be taken of the unstructured nature of the mesh along field lines. This is the case, in particular, with the representation of the region near plate EB. With a conventional structured quadrilateral mesh, the representation of that region would required very strong distortions in the mesh, probably accompanied by serious inaccuracies in the numerical discretisation schemes.

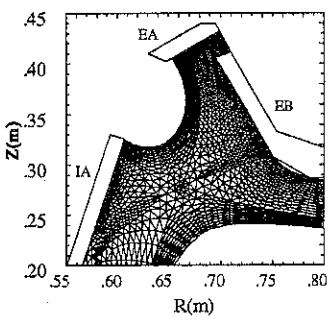

Figure 2. Triangular mesh used in a simulation with the point of impact on plate EA.

The first case considered is for a medium density discharge; $\langle n_e \rangle \sim 3\times10^{19}m^{-3}$. The species densities in the discharge are determined by the densities of the ions imposed at the inner boundary. In this paper, the density ratio of HeIII to DII is fixed at 1:20 at that boundary. In the comparisons with experiment, it assumed that the line average density is three times larger than the density imposed at the inner boundary. Figure 3 shows profiles of the ion temperature for the three ion species DII, HeII, and HeIII, calculated along the plate EA (a) and across the outer midplane (b). This comparison of the various ion temperatures is of interest in view of the assumption made in all other 2D edge simulation models, that all ion temperatures are equal. The temperature profiles calculated here are indeed similar. There is, however, an appreciable difference in the numerical values, particularly for HeII, which has a

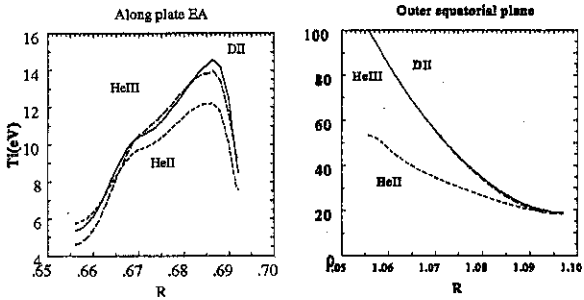

Figure 3. Ion temperature profiles calculated along plate EA and across the outer midplane. In this calculation, the point of impact was on plate EA. The temperatures are plotted as a function of the major radius R.

temperature significantly lower than the other ion species. This difference is attributed to the larger mass of helium - hence, for the same ion charge, to a longer energy equipartition time.

We now turn to a quantity which is of relevance to reactor design; that of helium enrichment at the entrance of the pumping plenum. In an ideal reactor, most of the D-T fuel should be recycled at the plates and returned back to the plasma, while most of the helium ash should be pumped away. This brings the definition of the theoretical and experimental enrichment factors,

$$\eta_{th}=\left(\frac{\Gamma_{p\,He}}{\Gamma_{p\,D}}\right)/\left(\frac{n_{0\,He}}{n_{0\,D}}\right), \qquad \eta_{exp}=\left(\frac{P_{p\,He}}{2P_{p\,D_2}}\right)/\left(\frac{n_{0\,He}}{n_{0\,D}}\right),$$

where n represents the total density (atomic + ions) associated with a given atomic number, Γ is the total particle flux entering the pumping plenum, and P is the neutral pressure in the plenum. Subscripts p and 0 refer to the pump entrance and the centre of the discharge respectively. Efficient evacuation of helium ash requires that η be as large as possible. Experimentally on TdeV, the strongest variations in η are observed when the line average density $\langle n_e \rangle$ is varied, with the point of impact on plate EB. Figure 4 shows a comparison between the experimental and calculated enrichments as a function of $\langle n_e \rangle$. In both cases, the enrichment is seen to decrease as the line average density increases. Quantitatively, however, the calculated values of η are systematically larger than the ones inferred from the experiment, especially at the higher densities. Also, the experimental values decrease much more rapidly with density than those obtained from the simulation. These differences may be caused by a number of factors. First, the definitions of the experimental and calculated enrichments are different. The helium measurements are made indirectly, and are based on a determination of helium global confinement time in the main plasma. Also, the transport model used here is only approximate. In particular, drift and current effects are ignored and neutral transport is calculated with a diffusive approximation. It is likely that a more accurate and

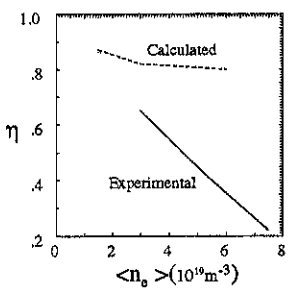

Figure 4. Comparison between the calculated and experimental enrichments for an equilibrium with the point of impact on plate EB.

complete model would yield better agreement with experiment. Considering the sensitivity of this diagnostic to neutral gas dynamics, it appears that the most critical gain should be made by improving the neutral transport model.

Finally, the ratio of the power deposited on plate EA to that deposited on plate EB is considered. Figure 5 shows a comparison of this ratio measured experimentally to that determined from the simulations, for an equilibrium where the point of impact is on plate EA. This geometry is considered here because it exhibits the strongest dependence on density. The agreement between simulation and experiment is excellent. Both ratios show the same tendency with density, and quantitatively, they agree within approximately 20%.

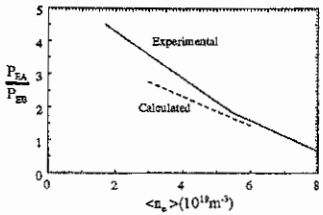

Figure 5. Comparison between the ratio of powers deposited on plate EB to that deposited on EA as a function of the line average density. The equilibria considered here correspond to a point of impact on plate EA.

Conclusions

In summary, a new multi-fluid finite element 2D simulation code has been applied to model transport in the edge and divertor of TdeV. This new approach offers some important advantages compared with conventional codes based on a finite volume discretisation of the transport equations on structured quadrilateral meshes. In particular, it allows local grid refinement and a straightforward representation of divertor plates of arbitrary shapes, without additional complexities in the discretisation scheme. Another interesting aspect is that it accounts for as many ion temperatures as there are ion species. Calculations made for representative TdeV discharges reveal appreciable differences in the temperatures of different ion species. This contrasts with the assumption made in other simulation codes, that all ion species have the same temperature. Code predictions are in good qualitative agreement with experiment. Quantitative differences suggest, however, that the physical model needs to be completed and made more accurate.

References

[1] R. Schneider, D. Reiter, D. Coster, J. Neuhauser, K. Lackner, and B. Braams, J. Nuc. Mat. 220-222, 1076 (1995).

[2] A. Taroni, G. Corrigan, R. Simonini, J. Spence, and S. Weber, J. Nuc. Mat. 220-222, 1086 (1995).

[3] S. Tsuji, K. Shimizu, T. Takizuka, N. Asakura, K. Itami, M. Shimada, Y. Suzuki, and N. Ueda, J. Nuc. Mat. 220-222, 400 (1995).

[4] G.R. Smith, P.N. Brown, R.B. Campbell, D.A. Knoll, P.R. McHugh, M.E. Rensink, and T.D. Rognlien, J. Nuc. Mat. 220-222, 1024 (1995).

[5] R. Zanino, J. Nuc. Mat. 196-198, 326 (1992).

[6] Th. Pütz, "Entwicklung eines Finite Elemente Verfahrens zur Modellierung der Plasmaströmung in der Randshicht von Tokamaks", Ph. D. Dissertation, University of Düsseldorf (1993).

[7] R.A. Vesey and D. Steiner, J. Comp. Phys. 116, 300 (1994).

[8] S.I. Braginskii in Reviews of Plasma Physics, Vol. 1, M. Leontovich, Ed., Consultants Bureau, New York, p. 205 (1965).

[9] R. Marchand, C. Illescas, X. Bonnin and J. Botero. International Atomic Energy Report INDC (NDS)-309 (1995).

[10] R. Décoste et al., Plasma Phys. Control. Fusion 38 A121 (1996).

Proposal of a quasi-optical grill operating at 3.7GHz for TdeV tokamak.

J. Preinhaelter†, A. Côté‡, Y. Demers‡, V. Fuchs‡, L. Vahala*, G. Vahala**

† *Institute of Plasma Physics, Czech Academy of Sciences, 182 11 Prague, Czech Republic*

‡ *Centre canadien de fusion magnétique, Varennes, Qc, J3X 1S1, Canada*

* *Old Dominion University, Norfolk, VA 23529, USA*

** *College of William & Mary, Williamsburg, VA 23185, USA*

The new type of LHCD launchers so called quasi-optical grills [1] underwent a large theoretical development in the last five years but there is no direct experimental verification of this concept. The medium size TdeV tokamak [2] is well suited for an eventual proof of principle experiment.

A simulation with the ACCOME [3] code on the absorption of the lower hybrid waves shoved that for the TdeV operating frequency 3.7 GHz, electron central density $n_o = 2.5 \times 10^{19}\mathrm{m}^{-3}$ and main magnetic field B_t=1.96T we could reach 150kA of current drive for an injected power 650kW with a peak absorption at r/a=0.25 at $N_{||} = 2.0$. On the basis of our theory of bounded quasi-optical grills with rods of the resonant cross-section [4] and its enlargement for large structures [5] we optimized two structures having the main peaks of power spectra at $N_{||}$=-2.03 and at $N_{||}$=-2.35.

In this contribution we are concentrated on the solution of a very important problem of good coupling of the quasi-optical grills to plasma and, at the same time, reaching an acceptable directivity of the outgoing waves. One peculiarity of quasi-optical launchers is that the good directivity may reached only if some region of well defined thickness exists in front of structure, where the electron plasma density is below critical. Here the waves with $N_{||} > 1$ are evanescent and the short wavelength parasitic peaks, which are present in the power spectra of QOG, are highly damped and the outgoing waves are composed predominantly from waves corresponding to the main peak. To create such a layer in front of grill we suggest to use a so called box limiter (a rectangular graphite ring slid on the mouth of the grill covering waveguide) which partly protrude into the plasma. This idea was tested on Prague experiment with QOG on the small tokamak CASTOR [6]. The measured density profile in the shadow of the box-limiter decays exponentially in agreement with the simple theory and the predicted density scale length $L_n^{\mathrm{box-limiter}} = \sqrt{2Db/v_s}$ [7] (where D is the anomalous diffusion coefficient $\sim 1\mathrm{m}^2\mathrm{s}^{-1}$, b is the toroidal width of the grill and $v_s = \sqrt{k_B(T_e + T_i)/m_i}$ is the ion sound velocity). For TdeV parameters ($T_e = T_i$=25eV, b=24 or 18 cm) we obtain an estimate of $L_n^{\mathrm{box-limiter}} \approx$ 3mm. At the box-limiter mouth we suppose the density corresponding to the TdeV measured density at the separatrix $n_{\mathrm{wall}}/n_{\mathrm{crit}} = 3$ (n_{crit}=$1.7\times10^{12}\mathrm{cm}^{-3}$ for 3.7 GHz) and linear density gradient $\frac{dn}{dx}$ =$2.5\times10^{11}\mathrm{cm}^{-4}$. For the design of our quasi-optical grills we use a plasma surface impedance [8] corresponding to the density profile depicted in Fig.1 (an exponential grow followed by an linear increase).

We designed two structures: 1) 8 rod (a cross-section $4.05\times2.35\mathrm{cm}^2$ and gap 0.6cm) placed in the tapered main hyperguide $10\times39.2\times24.2\mathrm{cm}^3$ (TdeV port available for LHCD

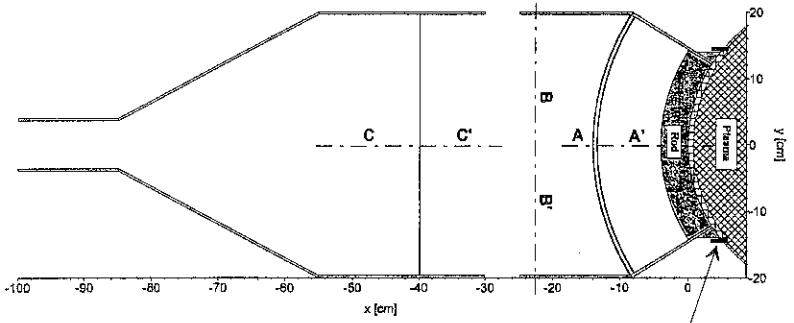

Fig 2 Poloidal section through the TdeV 8 rod QOG struture operating at 3.7GHz

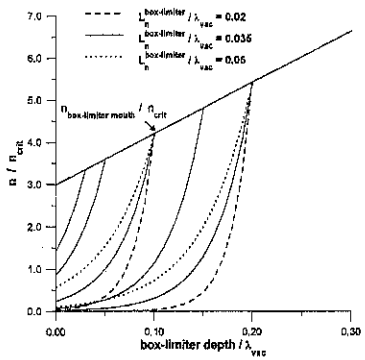

Fig. 1 Box-limiter density prpofile - n_{wall} / n_{crit} =3

dn /dx=2.5x10^{11}cm^{-4}

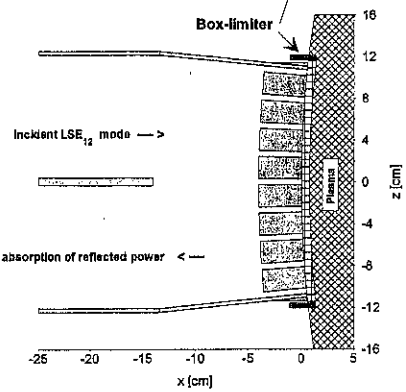

Fig. 3 Equatorial section (A-A') through 8 rod QOG structure for TdeV

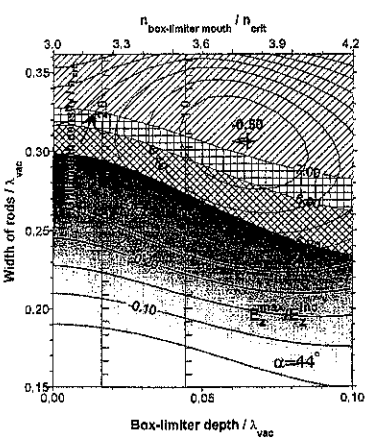

Fig. 4 Weighted directivity

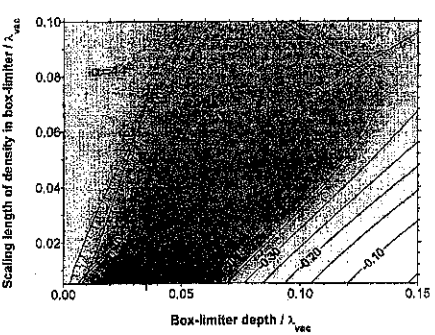

Fig. 5 Weighted directivity

$l_{rod\ cross\text{-}section}$ / λ_{vac} = 0.5 n_{wall} / n_{crit} = 3 dn /dx=2.5x10^{11}cm^{-4}

$N_{z,-1}$ = -2.0 Width of rods / λ_{vac} = 0.3

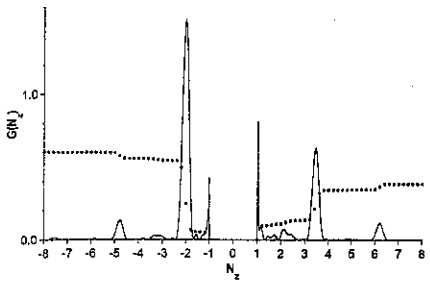

Fig. 6 Spatial power spectrum of 8 rod QOG for 3.7 GHz

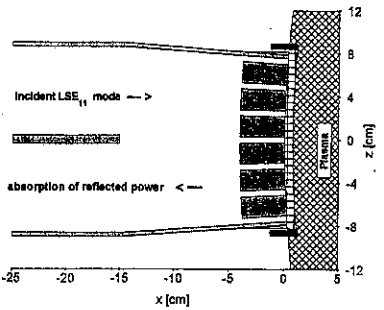

Fig. 7 Equatorial section through 6 rod QOG structure for TdeV

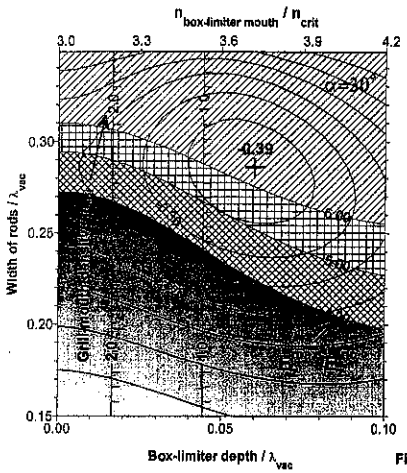

Fig. 8 Weighted directivity

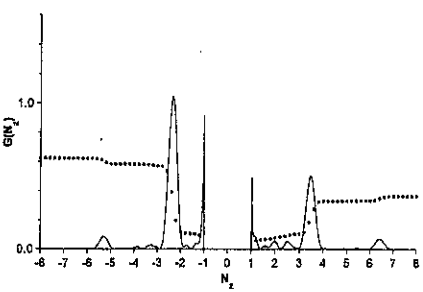

Fig. 9 Spatial power spectrum of 6 rod QOG for 3.7 GHz

experiment has toroidal width 28cm and poloidal height 43cm). The rods, bent poloidally and arranged radially in the equatorial plane to fit the plasma surface, are irradiated obliquely by LSE_{12} mode (a combination of standard TE and TM modes with zero poloidal component of the electric field ($E_y = 0$)) emerging from the $39.2 \times 11.7 cm^2$ auxiliary hyperguide and producing a plane wave with an angle of incidence $\alpha = 44°$. The second auxiliary hyperguide of the same dimensions is passive and absorbs the reflected power (Figs. 2-3).

The main peak in the power spectra (Fig. 6) is situated at $N_{||} = -2.03$, the power reflection coefficient R_{tot}=14% and the ratio of the maximum electric field between rods to the incident field in the auxiliary hyperguide $E_z^{max}/E_z^{incident}$ is 3.8 at the depth of box-limiter equal to 0.45cm. The weighted directivity of resulting spectrum is rather low (-33% if we truncate the fast waves with $N_{parallel} = \pm 1$, the coupled directivity is only 60%) because the reflections from walls, finite width of peaks and inhomogeneous irradiation of rods play dominant role in our rather small structure.

The Fig. 4 shows that the weighted directivity has a broad optimum (the box-limiter

depth varies from 3mm to 7mm; $L_n^{\text{box-limiter}} \approx 3$mm) and that the electric field between rods increases with rod width (decreasing gaps between rods). For TdeV at 650kW we have an electric field of 1.5kV/cm in the auxiliary hyperguide. A maximum field between rods must be lower than 7.5kV/cm (factor 5 in the Fig. 4). This value is the experimental maximum field obtained in the multijunction antenna of TdeV. At larger $L_n^{\text{box-limiter}}$ the directivity is lower but the optimum with respect of the box-limiter depth is broader (Fig. 5). These figures are based on the infinite grill theory [10] (an infinite number of rods irradiated obliquely by a plane wave with the electric field perpendicular to the rods) so both the directivity and the maximum electric field are higher than those for the structure with the finite number of rods mounted in hyperguide.

2) 6 rod (a cross-section $4.05\times2.17\text{cm}^2$ and gap 0.6cm) structure using LSE_{11} excited in $39.2\times8.2\text{cm}^2$ auxiliary hyperguide and having the optimum angle of incidence $\alpha = 29.8°$ (Fig. 7). The last structure is narrower (the main hyperguide is $11\times39.2\times17.2\text{cm}^3$) so that the field between rods could be only 4.2 times higher than the incident field in the auxiliary hyperguide. The excitation of the LSE_{11} mode can be done very efficiently with the simple structure consisting of only two $7.2\times3.4\text{cm}^2$ standard waveguide flared in 2m long sectoral horns to $39.2\times3.4\text{cm}^2$. A coupling structure of this type was successfully tested in Prague on CASTOR tokamak [6]. The power spectra are broader with a main peak at $N_{||} = -2.35$ (Fig. 9); R_{tot}=17%, $E_z^{\text{max}}/E_z^{\text{incident}}$=4 and the weighted directivity (truncated) is -28.5% (the coupled power directivity 63%) at the depth of box-limiter equal to 0.5cm. The dependance of the weighted directivity on the box-limiter depth and the rod width is demonstrated in Fig. 8 for $L_n^{\text{box-limiter}} \approx 3$mm.

The directivities are rather low for TdeV due to its small size. Nevertheless, a reactor size quasi-optical structure designed for an $N_{||} = 1.8$ and operating at 8 GHz could reach directivity as high as 70% fully comparable with the best contemporary multijunction grills.

The authors acknowledge many constructive remarks from R. Klíma, F. Žáček, J. Stöckel and M. Lokajíček. The work was partly supported by the U.S. - Czech Science and Technology Joint Fund in the cooperation with Czech Ministry of Education and DOE under Project Number 93067 and partly sponsored by the Grants No. 202/96/1350, 202/96/1355 and 202/97/0778 of Czech Grant Agency.

References

[1] Petelin, M.I. et al., Plasma Phys. Control. Fus. **38** (1996) 593-610.

[2] Côté, A. et al.,16th IAEA Fusion Energy Conf., Montréal (1996)

[3] V. Fuchs, P.T. Bonoli et al., Nucl. Fus. **35**

[4] Preinhaelter, J., Nucl. Fusion **36** (1996) 593-611.

[5] Preinhaelter, J. et al, Proc. of Joint Varenna- Lausanne Workshop (1996), pp. 87-100

[6] F. Žáček at al., Proc. of 1996 ICPP, Nagoya.

[7] J. Preinhaelter et al., 12th Topical Conf on RF Power in Plasmas, Savannah, 1997

[8] F. Romanelli, F. Santini, Nucl. Fus. **24** (1884) 219

[9] M. Hron: Diploma thesis, Czech Technical University, Prague, 1997.

[10] Hurťák, O. and Preinhaelter, J., IEEE Plasma Science **20** (1992) 425.

Analysis of Hydrogen Pellet Injection Experiments in RFX

L.Garzotti, **S.Martini**, B.Pégourié*, A.Canton, L.Carraro, D.Gregoratto, P.Innocente, R.Pasqualotto, R.Pugno

CONSORZIO RFX
Corso Stati Uniti, 4 - 35127 Padova, Italy

* Association EURATOM-CEA sur la Fusion Contrôlée,
C. E. Cadarache, 13108 Saint-Paul-lez-Durance, France

Introduction

Pellet injection experiments in Reversed Field Pinches (RFP) have been performed in the past on the ETA-BETA II, on the ZT40M and on the RFX devices [1,2,3], where some positive effects of the pellet refuelling on plasma β and confinement were seen. This paper presents a set of H pellet injection experiments performed on RFX, a large RFP (R=2 m, a=0.46 m), at currents of 0.6-0.8 MA. During the experimental campaign, the RFX 8-pellet injector [4] was used to fire mainly 'small' pellets of $1.5 \cdot 10^{20}$ atoms (typically 1 per pulse, but sequences of up to 4 pellets have been also used) at velocity of 400÷500 m/s, which were generally completely ablated in the plasma core. A database of ≈170 pellets has been gathered.

In RFX pellet injection proved to be useful on the one hand to peak significantly the density profiles, allowing to achieve transient improvements of the plasma β and confinement time, and, on the other hand, as a diagnostic tool for particle and energy transport analyses.

Behaviour of global parameters during pellet injection

As seen also in the past [3], when a pellet is injected in the RFX plasma, despite the relative large perturbation in the density profile and central value, very little effects are produced on the plasma current, loop voltage, total radiated power, H_α emission, reversal and pinch parameters F and Θ ($F \equiv B_\phi(a)/\langle B_\phi \rangle$ and $\Theta \equiv B_\theta(a)/\langle B_\phi \rangle$ are indicative of the shape of the RFP magnetic profiles).

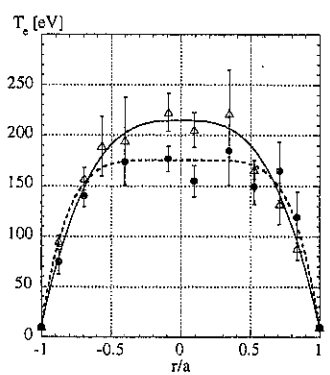

Fig.1 T_e profiles from Thomson scattering: triangles -> pre-pellet data, circles ->post pellet data

Based on measurements of soft X-rays emission with the double filter technique and on Si(Li) detector pulse-height-analysis system, a drop in the central electron temperature in the range 50÷130 eV is generally observed. The evolution of the electron temperature profile obtained from ensemble average data of the 10-points Thomson scattering system is shown in fig.1 and, besides confirming the aforementioned drop in the central region, it shows a transient flattening from a profile corresponding to $1-(r/a)^3$ to a profile well fitted by a $1-(r/a)^5$

dependence. The temperature recovers the pre-pellet central value and profile in 2-4 ms.

As for the density profile, an example of its time evolution derived from the inversion of the line integral profile measured by a 12 chords interferometer is given in fig.2. The initially flat or slightly hollow profile, which is typically found [5] in the medium/low density regimes where the pellet are injected, becomes centrally peaked with a maximum peaking factor n(0)/<n> which ranges between 1.5 and 2. The profile then diffuses back to the original one in a time ranging between 1 and 5 ms. The faster diffusion times are generally due to a MHD Dynamo Relaxation Event (DRE), which seems to be triggered when the pellet reaches and cools the plasma core [6]. While almost all pellets cause a transient increase in poloidal beta, β_Θ, and energy confinement time, τ_E, which slightly exceeds the standard RFX scaling with I/N [7], for most of them the improvement is seen only for the very short time before a DRE crash occurs (fig.3a). Yet in some DRE-free cases, a fast re-heating is seen and τ_E is found to increase by a factor ≈1.5, lasting for a few confinement times (fig.3.b).

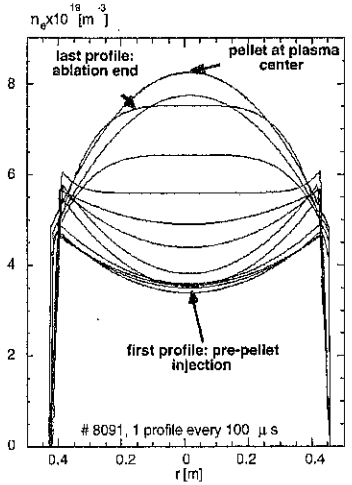

Fig.2 Typical evolution of density profile during pellet ablation.

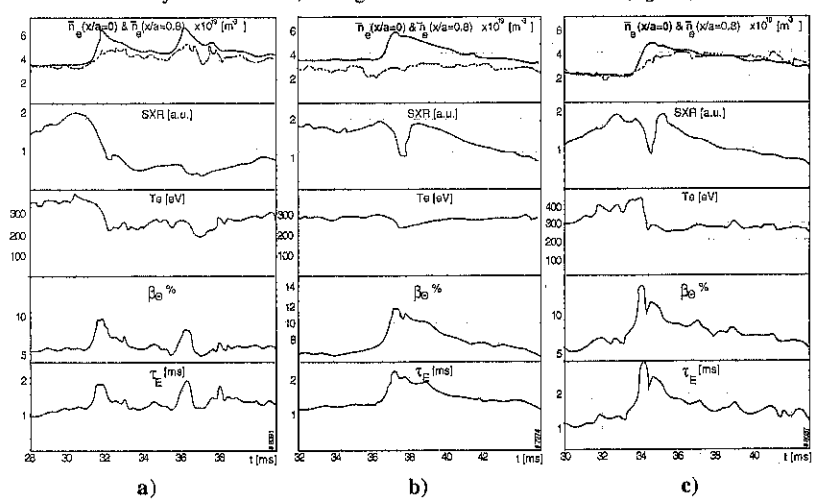

Fig.3 Time behaviour of line average density $n_e(0)$ and $n_e(x/a=0.8)$, SXR emission, T_e, β_Θ and τ_E for: a) two pellets which induce DRE,; b) one pellet with no DRE; c) Pellet on PPCD.

Similar positive results are obtained more frequently by injecting pellets during the improved confinement phase obtained by Pulse Poloidal Current Drive (PPCD) [8]. In this case, the occurrence of MHD relaxation events is made more unlikely by the stabilising effect of the PPCD and the injection of the pellet produces improved confinements regimes lasting for several milliseconds (fig.3c).

Transport simulations for standard pellets

The ablation of a pellet produces a large perturbation of the plasma density and temperature profile and this is obtained by adding a particle source and an energy sink which are well known, because of the accurate measurements of particle deposition [3]. Hence a transport analysis of the pellet ablation phase and of the following profile diffusion phase has been performed with the aim of gaining information on the transport mechanism in the core of an RFP plasma. A 1-dimensional particle and energy transport code has been used, which assumes a linear dependence of the fluxes on the gradients and an outward directed particle pinch velocity: $\Gamma=-D\cdot\nabla n+V\cdot n$, $\mathbf{Q}=-n\chi\cdot\nabla T$. The presence of an outward convective velocity is implied by the stationary density profiles, which in RFX are hollow in a large part of the I/N (I/N ≡ plasma current/line density) operation range [5]. In the code the source terms are: the pellet ablation rate and the recycling at the wall for the density, the Ohmic power for the temperature. The sinks are: the net particle outflux of the plasma for the density, the power used for ionisation and radiation and the global heat outflux for the temperature. The experimental data to be reproduced are: the Ohmic input power, the energy and particle confinement times, the density and temperature profiles.

With the aim of getting information on transport in standard plasmas, the simulation was focused on a pulse (# 8066) where a small pellet did not cause large change in plasma confinement. The code was used in a semi-interpretative mode, iterating for different choices on the transport coefficients until all of the control parameters could be matched. It was found that both the stationary (pre-pellet) and dynamic (during and after pellet injection) phases could be simulated with the same transport coefficients. Hence the results obtained may be considered as indicative of the stationary transport coefficients in the plasma. On the other hand, the constancy of V, D and χ indicates that the transient increase in β_Θ and τ_E observed in pulses like # 8066 is mainly caused by the increase of the particle confinement time due to the pellet fuelling in the plasma core. The best estimates of V, D and χ profiles, along with a shaded region indicative of the range values compatible with the experimental data (accounting for the error bars), are given in figg. 4 and 5.

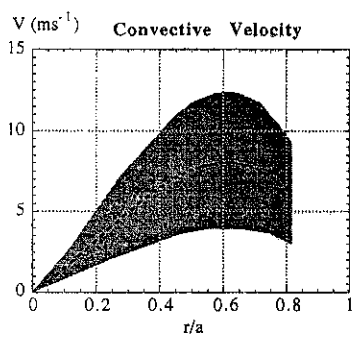

Fig.4 Range of outward convective velocity acceptable for transport simulations

The particle and energy diffusivity have high values in the central region of the plasma, which could be in agreement with a mechanism based on parallel transport along stochastic field lines as it

has been often proposed in the past. On the other hand, the Rechester-Rosenbluth scaling for transport along stochastic field line:

$$D = L_{//}\, v_{thi}\, (\delta B/B)^2 , \qquad \chi = D\, v_{the} / v_{thi}$$

assuming $T_e \approx T_i$, predicts a ratio $\chi/D \approx (m_H/m_e)^{0.5} = 44$, whereas the value derived from the simulation is significantly smaller. Indeed in the plasma core the simulations give $\chi/D \approx 3 \div 5$, which would imply an unrealistic condition $T_e << T_i$.

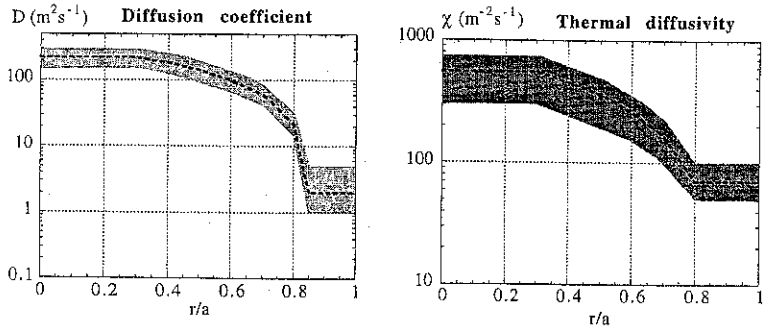

Fig.5 Range of acceptable particle and energy diffusion coefficients for transport simulations.

Conclusions

In RFX, $1.5 \cdot 10^{20}$ atom pellets fired at 400÷500 m/s ablate in the plasma core at $I \geq 600$ kA and are able to peak the density profiles. Little changes are observed in the discharge global parameters, except that in many cases the central cooling produced by the pellet induces a Dynamo Relaxation Event. In the DRE-free cases and, more frequently, in combined Pellet+PPCD experiments β_Θ and τ_E increase by a factor 1.5÷2, exceeding the empirical RFX scaling with I/N for standard pulses.

A transport analysis has been performed which took advantage of the well-diagnosed pellet ablation phase. Its results confirm the existence of an outward particle pinch velocity which sustains the stationary hollow density profiles. The ratio χ/D found to best simulate the data is apparently not completely consistent with the prediction of the Rechester-Rosenbluth model for transport along stochastic magnetic field lines, living an open question about the transport mechanism at work in the core of the RFP plasma.

References

[1] P.Innocente, S.Martini, *in "Physics of Mirrors, Reverse Field Pinches and Compact Tori"*, Int.School of Plasma Phys., Varenna 1987, vol. III 1043.
[2] G.A. Wurden, P.G.Weber, et al., Nuclear Fusion 27 (1987) 857.
[3] L.Garzotti, P.Innocente, S.Martini et al., 23rd EPS Fusion Conf., Kiev 1996, II p.637
[4] W.Baker, L.Garzotti, et al. 16th SOFE Champaign-Urbana, 1995,p.1570
[5] S.Martini, et al. 21th EPS Fusion Conf., Montpellier 1994, I p.454
[6] T.Bolzonella, P.Innocente, S.Martini, R.Paccagnella, *"Magnetic profiles behaviour, dynamo mechanisms and confinement in RFX"*, this Conference
[7] A.Buffa and RFX team, 23rd EPS Fusion Conf., Kiev 1996, II p.629
[8] T.Bolzonella, S.Martini, P.Innocente, S.Costa et al., *"Pulsed poloidal current drive experiments in RFX"*, this Conference

Magnetic profile behaviour, dynamo mechanisms and confinement in RFX

T.Bolzonella, **P.Innocente**, S.Martini, R.Paccagnella

Consorzio RFX -Corso Stati Uniti,4- 35127 Padova - Italy

Introduction

According to the experimental values of the pinch and reversal parameters, $\Theta \equiv B_\theta(a)/\langle B_\phi \rangle$ and $F \equiv B_\phi(a)/\langle B_\phi \rangle$, RFX [1] normally operates close to the fully relaxed Bessel Function Model (BFM) state described by Taylor [2]. In this work we analyse the behaviour of the magnetic profiles, as inferred from external magnetic measurements, in terms of the typical 'quasi-stationary' states and then we describe some spontaneous or induced transient modifications and their effects on plasma confinement.

Magnetic profiles during the current flat-top phase

The 'quasi-stationary' or 'equilibrium' magnetic field profiles in RFX lay in a well-defined F-Θ locus. The $\mu \equiv J \cdot B/B^2$ profile is nearly flat and, in terms of a fit as $1\text{-}r^\alpha$, it corresponds to values of α ranging from $\alpha \geq 10$ at marginal reversal to α=5-6 at deep reversal (see fig.1). Similarly to previous analyses on the ETA-BETA II experiment [3], no dependence on electron temperature, electron density, plasma collisionality or plasma current is found. This is shown e.g. in fig.1, where two data groups corresponding to different mean-free-path λ_o overlap completely.

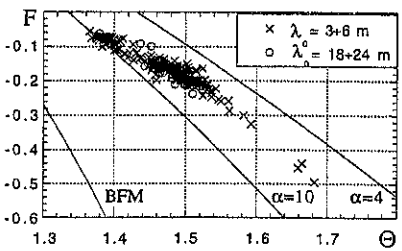

FIG.1 - F- Θ points during current flat-top phase for two groups of shots with different mean-free-path λ_o parameter.

The above insensitivity to parameters such as the plasma collisionality and the electron temperature suggests that a strong MHD mechanism compensates on the one hand for changes in Kinetic Dynamo [4] which are predicted for different values of the electron collisionality [5], and, on the other hand, for changes in plasma resistivity, which in principle could also alter the balance between dynamo action and diffusion processes.

Compared with those of other RFPs (fig.2a) in terms of F-Θ diagrams, the relative proximity of the RFX magnetic profiles to the ideal BFM is evident.

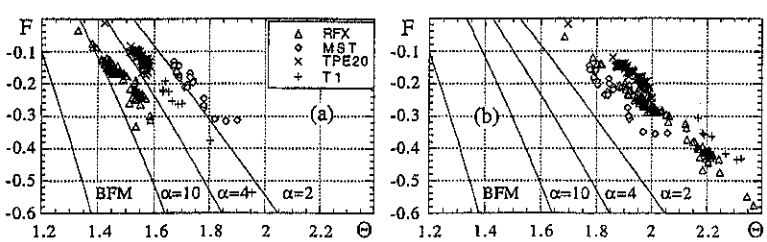

FIG.2 -Comparison of F- Θ loci for different RFP experiments: (a) F and Θ computed at inner wall; (b) F and Θ computed at stabilising shell. Data from [7]

The ranges of operation of different RFPs become more similar if the parameters are computed at the conducting shell surface (fig.2b).

To study the relationship between shell proximity and magnetic profiles one should change the plasma-shell distance in the same machine. To a certain extent this can be done by changing the horizontal shift of the plasma, Δ, applying a different vertical field. In fig.3 the Θ values for a set of RFX shots with the same F (both computed at plasma surface) are seen to decrease with Δ and, if the dependence is linearly extrapolated in terms of shell proximity, it indicates that RFX with a close fitting shell would have magnetic profiles similar to those of MST.

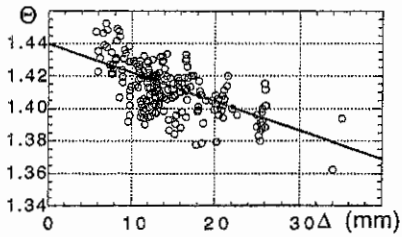

FIG 3 - Scaling of Θ with Δ for constant F=-0.145

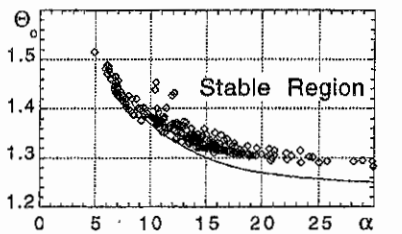

FIG.4 - Comparison of the RFX experimental values of α and Θ_0 parameters (from the μ&p model profiles) with marginal stability boundaries for internally resonant m=1 resistive modes

The above observations suggest that the shell proximity influences, via MHD stability constraints, the shape of the equilibrium magnetic profile. Indeed the RFX data lay very close to the marginal stability curve in the α-Θ_0 plane for m=1 internal resistive modes (fig.4). In particular the curve corresponds to the locus of the states for which the intability growth rate is of the order of the resistive diffusion time (σ-stable [6]) when $r_W/a=1.18$ (r_W = shell radius, a = plasma radius) and the wall has an high, but finite resistivity.

Study of magnetic transient phases

Deeper insight in the above subjects is provided by the analysis of the transient profile modifications. It has been already shown for RFX [8] as in other RFP's [9,10,11] that discrete relaxation events or 'SawTeeth' are often observed, during which the magnetic profiles evolve cyclically back and forth from the states closest to the fully relaxed ones.

If the occurrence of ST is analysed in the α-Θ_0 plane, the pre-crash values lay on a well-defined curve not too far from the marginal stability boundary previously discussed, whereas the post-crash points move well inside the stable region.

Except at high Θ, when ST are more frequent and larger, the occurrence of ST is not ubiquitous in RFX pulses, and indeed the events may appear and disappear even during the current flat-top of the same shot with constant pinch parameters. In fig.5 some points taken from ST-free phases show that in this cases the profiles are in an intermediate region of the α-Θ_0 plane.

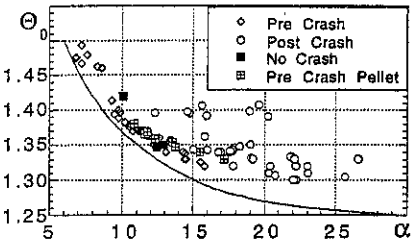

FIG 5 - Comparison of RFX experimental values of α and Θ_0 (pre and post ST crash and for ST-free phases) with marginal MHD stability boundaries

Forced modifications of the electron temperature profile T_e by pellet injection show clear influence on sawteeth. In particular, 85% of the pellets ablating in the core cause a ST-crash starting when the pellet is close to the magnetic axis (see fig.6a). Although its signature in terms of excited modes and F-Θ trajectory is similar to that of 'standard' sawteeth, the crash is not associated to a change of the magnetic profiles towards the typical pre-crash condition. In fact some pellet pre-crash points shown in fig.5 are on the 'stable' side of the 'standard' pre-crash boundary. On the contrary a large and slow pellet, which ablates completely at r/a>0.7, induces a strong peaking of the parallel current density profiles which finally results in a large sawtooth (fig.6b).

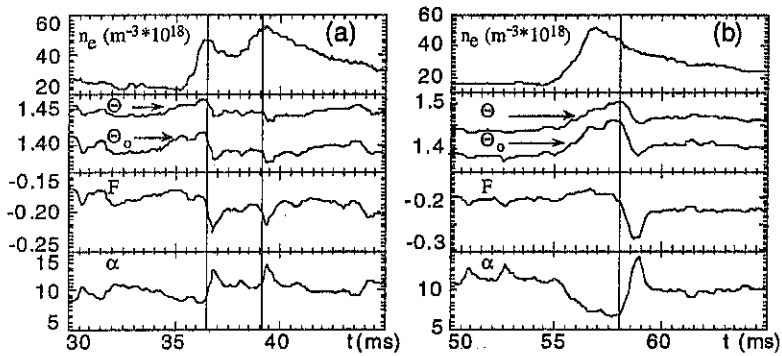

Fig.6 Effect of pellet on sawteeth activity: (a) a sequence of two pellets ablating in the plasma core, each of them causing a sawtooth crash; (b) a large and slow pellet completely ablated at r/a>0.7 first causes a strong peaking of the μ profiles which finally results in a large sawtooth.

The main effect of the pellets which could be linked with their action on the sawteeth is the local cooling associated to the strong particle source. The fact that only the pellet ablating in the core immediately triggers a ST crash without first inducing changes in the rate of magnetic profiles peaking suggests that, besides the threshold in terms of MHD stability, there could be a direct effect of the Lundquist number regime on the growth rates of the instabilities or on their non-linear coupling. The behaviour shown in fig.6b for the case of the large and slow pellet shows that, as long as the core plasma region is untouched (central SXR emission is unaffected), even a strong cooling of the plasma outer region does not excite a ST.

Whenever the dynamo action is reduced, as in the pre-crash phase, the lower magnetic fluctuations are associated to improved confinement [8,9]. Similarly, the confinement improvement observed in MST [12] and RFX [13] during Pulsed Poloidal Current Drive experiments is believed to be caused by the reduction of the power losses associated to the partial suppression of the

dynamo. During the PPCD both in MST and RFX, except in the very early phase, the μ profile does not flatten, but actually becomes more peaked. The stabilization of the profile by current drive works as a seed for the dynamo suppression, which then cause a peaking of the temperature profiles and triggers an improved confinement regime, ST-free and with low α.

Recently some spontaneous transitions to an improved confinement regime have been seen in RFX during normal Θ operations (fig.7). The regime is associated to a peaking of the μ profile and is characterised by a decrease of loop voltage and an increase of SXR emission. The amplitute of the locked magnetic modes in these conditions is reduced while their n-spectrum approaches a single elicity state, similarly to the Improved High Θ Mode of TPE [15].

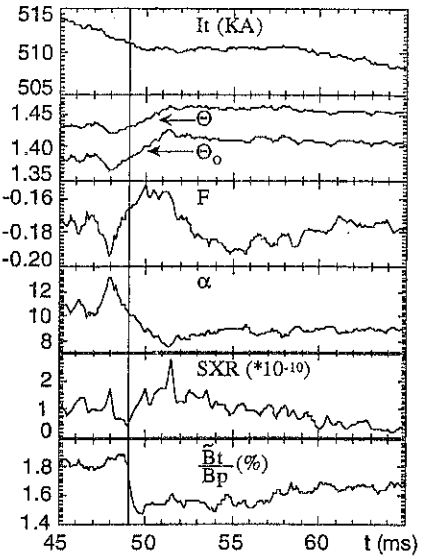

Fig.7 Example of RFX pulse with transition to Improved Confinement Peaked μ-profile Mode.

Conclusions

In RFX the stability criteria for internally resonant m=1 modes imposed by the plasma-shell distance larger than in other RFPs seems to be the cause for the quasi-stationary magnetic profiles closer to the BFM. An increased dynamo action is needed to drive the larger poloidal currents associated to such profiles. The price paid could be a higher level of turbulence, possibly leading to higher probability of mode locking to the wall. On the other hand, the MHD stability boundary can be trespassed, and RFX, as other RFP experiments [14,15], shows quasi-stationary improved confinement regimes, characterized by peaked T_e and μ profiles, where dynamo activity is reduced and the magnetic profiles get away from the fully relaxed ones without triggering relaxation events.

References

[1] G. Malesani, G. Rostagni, in Proc. 14th Fusion Technology Symp., Avignon , Vol.1 (1986) 173.
[2] J.B.Taylor, Phys. Rev. Lett. 33 (1974) 1139.
[3] Ch. Ferrer Roca, P.Innocente, S.Martini, R.Paccagnella, 18th EPS Conf. Berlin (1991) II, 305.
[4] A.R. Jacobson, R.W. Moses, Phys. Rev. A, 29 (1984) 3335.
[5] G.Giruzzi, E.Martines, Phys. Plasmas 1 (1994) 2653.
[6] J.P. Goedbloed, P.H. Sakanaka, Phys. Fluids 17 (1974) 908.
[7] S. Hokin et al. , 22th EPS Conf. Bournemouth (1995) I, 181.
[8] L.Marrelli, P. Martin, A. Murari, P. Franz, G.Spizzo ICCP Nagoya (1996) 974
[9] V.Antoni, P.Martin, S.Ortolani, Nucl. Fus. 29 (1989) 1759.
[10] K.Hattori, Y. Hirano, et al. Phys. Fluids B 3 (1991) 3111.
[11] P.R.Brunsell, Y.Yagi,Y. Hirano, et al. Phys. Fluids B 5 (1993) 3111.
[12] J.S.Sarff, S.A.Hokin, H. Ji, S.C. Prager and C.R.Sovinec, Phys. Rev.Lett. 72 (1994) 3670.
[13] T.Bolzonella et al. this Conference
[14] B.E. Chapman, A.F. Almagri, M. Cekic, et al. Phys. Plasmas 3, (1996) 709.
[15] Y. Hirano, Y. Maejima, T. Shimada, I. Hirota, and Y. Yagi, Nucl. Fus. 36, (1996) 721.

Pulsed Poloidal Current Drive experiments in RFX

T. Bolzonella, **S. Martini**, P. Innocente, S. Costa, A. De Lorenzi, E. Martines, A. Murari, R. Paccagnella, R. Pasqualotto, M.E. Puiatti, A. Sardella, M. Valisa.

Consorzio RFX - Corso Stati Uniti, 4 - 35127 Padova, Italy.

1. Introduction.

Active poloidal current profile control has been proposed as a promising way of improving confinement properties of the reversed field pinch (RFP) configuration. Indeed tests of this concept, performed by a technique named Pulsed Poloidal Current Drive (PPCD) on the MST reversed field pinch, support this hypothesis showing strong reduction of magnetic fluctuations measured at plasma edge and suppression of sawteeth MHD activity [1,2]. Magnetic fluctuations in particular are believed to be responsible for a large part of the measured global energy flux in RFP's. The origin of these magnetic fluctuations is mostly from resistive kink instabilities with m=1 and toroidal mode numbers n=2R/a. As these instabilities are driven by the current density gradient [3], its modification can stabilise them and reduce the associated particle and energy transport. Driving poloidal currents inductively is a simple way to induce transient modifications of current and magnetic fields profiles and to test the effectiveness of profile control on magnetic confinement.

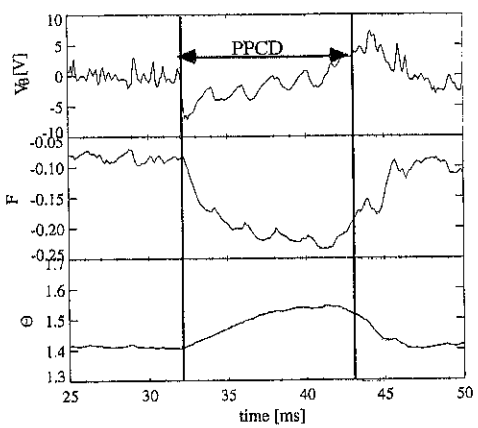

Fig.1. Time evolution during PPCD operation of: (a) poloidal loop voltage, (b) reversal parameter $F=B_\phi(a)/<B_\phi>$, (c) pinch parameter $\Theta = B_\theta(a)/<B_\phi>$ (shot #8183).

2. PPCD description.

Recently PPCD experiments were carried out in RFX [4], the largest (R=2 m, a=0.457 m) RFP in operation. Poloidal currents have been driven in the plasma outer region by applying a series of one to five poloidal voltage pulses on the toroidal magnetic system.

A parametric study has been done by varying the parameters of the single PPCD pulse (amplitude, time constant of the external circuit), the relative timing of the pulses during the discharge and the target plasma parameters (density, reversal parameter $F = B_\phi(a)/<B_\phi>$, plasma current) in order to determine the optimum performance.

An optimum range has been found operating at shallow reversal (-0.1<F<-0.05) and medium plasma densities (2.5 10^{-14}< I/N <4.5 10^{-14} Am). Effective PPCD, in terms of magnetic fluctuations reduction and soft X-ray increase, were realised at three different plasma currents: 400 kA, 600 kA and 800 kA. Some results of a 800 kA PPCD experiment are shown in Fig.2.

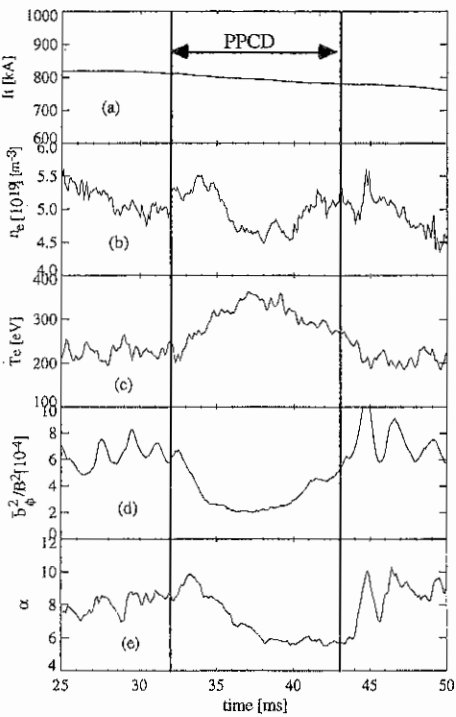

Fig. 2. Time evolution of : (a) plasma current, (b) central electron density,(c) electron temperature, (d) normalised energy of toroidal magnetic fluctuations, α parameter fro μ&p model (shot #8183).

3. Experimental results.

Optimising I/N and F, we can reproducibly obtain improvements in many plasma parameters lasting, in the best cases, for several milliseconds, i.e. for a time greater than the energy confinement time, which is of the order of 1 ms for standard RFX discharges.

We always find a strong increase of soft X ray flux measured by a 78 chords tomography, that detects also a peaking of the profile confirming that PPCD is able to drive changes in the whole plasma configuration and not only at the edge. Tomographic measurements in the double filter configuration and Si(Li) detector PHA system could follow the time evolution of on-axis T_e and confirmed an increase up to 75% with respect to the pre-PPCD value in the best cases. Electron temperature radial profiles have been measured near the maximum of the SXR flux by a single pulse 10-point Thomson scattering diagnostic. Profiles are measured along a diameter in the plasma equatorial plane, with a spatial resolution of 2.4 cm and up to r/a = 0.84. Two sets of discharges with and without PPCD, selected with the same macroscopic behaviour (plasma current, electron density, magnetic shift and Θ parameter), have been compared (Fig.3). Clear evidence is shown that T_e on axis is higher during PPCD, where an average increase $\Delta T_e/T_e \approx 30\%$ is found. Experimental T_e profiles appear to be more peaked during PPCD than without it. T_i, measured by NPA

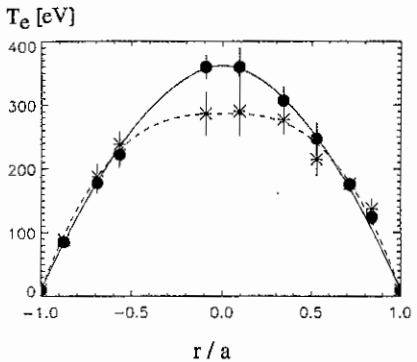

Fig.3. T_e profiles measured by Thomson scattering during PPCD (continuos line, average over 10 shots) and during conventional discharges (broken line, average over 15 shots) for the same I/N and Θ intervals.

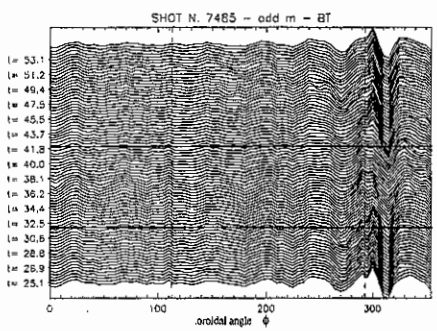

Fig.4. B_ϕ perturbation measured by two 72 coils arrays during PPCD. PPCD operation is between 32 and 42 ms (shown by horizontal lines).

diagnostic, presents little modifications due to PPCD application. In RFX we estimate T_i also from Doppler broadening of some impurity lines. These measurements show strong influence of PPCD on CIII temperature, implying an increase of edge (r/a≈0.9) ionic temperature.

Total (bolometric) radiation decreases, particularly in the outer equatorial edge region, where the main interaction with the wall is concentrated because of the Shafranov shift of the plasma. Electron density shows a little decrease and no profile modification. Z_{eff} does not show a reproducible behaviour. In some cases it decreases from 3 to 2 in agreement with a reduction found in the amplitude of influxes, particularly in the region where the MHD modes are locked to the wall.

As in MST, PPCD operations cause in RFX a strong reduction in magnetic fluctuations (Fig.4). Differently from MST, RFX discharges are affected by MHD modes which remain locked both in phase and to the wall. In none of the shots showing the greater reduction of magnetic fluctuations (≈50% in terms of global energy of magnetic modes) we found evidence of rotation of the most important modes (m=1, n=8,9). This could mean that, if there is a threshold on the magnetic fluctuation level to induce the rotation, we did not reach it during PPCD operations. Also spectroscopic measurements of plasma rotation do not show an evident and reproducible phenomenology during PPCD application.

It should be noted that during PPCD in RFX, except in the very early phase, the parallel current profile does not flatten, but actually becomes more peaked (see Fig 2e).

4. Discussion and conclusions.

A careful comparison with the performance of stationary discharges with high Θ values, comparable to the post-PPCD ones, shows that the positive effects on the central T_e and on magnetic fluctuations, which are present in both cases, are clearly more pronounced in the PPCD case. Also the peaking of the T_e profiles is greater during PPCD. These features can therefore be interpreted as due to the reduction of dynamo action induced by PPCD and not simply as an effect of a transition to higher values of Θ.

Taking into account the new values of the profile and on-axis value of temperature and electronic density, we can estimate an increase of the poloidal beta, $\beta_\theta=2\mu_0<nk_BT>/B_\theta(a)^2$, up to 30-40% (assuming $T_e=T_i$).

For the calculation of the energy confinement time, τ_E, the ohmic input power has been estimated using the equilibrium μ&p model [5] to compute the contribution fro the variation of the plasma internal magnetic energy: τ_E can double during the period of poloidal voltage application, reaching a value of 2.5 ms which can be maintained for more than 5 ms in the best cases. As an alternative approach we have estimated the ohmic input power by mean of the ohmic dissipation taking into account the Spitzer resistivity, the measured electron temperature and Z_{eff} and modelling the magnetic profiles with the μ&p model :

$$P_\Omega \propto T^{-3/2}\langle \eta J^2 \rangle$$

obtaining results in good agreement with the previous calculation.

To investigate the influence of PPCD on the dynamo mechanism, the F-Θ behaviour in RFX has been simulated using the resistive 1-D diffusion code RFXPORT. A good matching with experimental data was obtained (without temperature and density evolution) only by applying a 30% reduction of the dynamo action during PPCD, followed by a similar increase during the subsequent discrete relaxation phase.

The analysis of the first PPCD experiments on RFX confirm that this technique can lead to improvements in terms of magnetic fluctuations reduction, on-axis electron temperature increase and general confinement properties. The stabilisation of the profile by current drive appear to be necessary only as a seed for the dynamo suppression, which then causes a peaking of the temperature profiles and triggers an improved confinement regime as can be seen during other transient regimes in RFX [6].

References:

[1] J.S. Sarff *et al.*, Phys. Rev.Lett. **72**, 3670 (1994)

[2] J.S. Sarff *et al.*, Phys. Rev.Lett. **78**, 62 (1997)

[3] D.C. Robinson, Nucl. Fusion **18**, 939 (1978)

[4] L. Fellin, Fus. Eng. Des. **25**, 301 (1995)

[5] V. Antoni *et al.*, Nucl. Fusion **26**, 801 (1982)

[6] T. Bolzonella, P. Innocente, S. Martini, R.Paccagnella,*"Magnetic profile behaviour, dynamo mechanisms and confinement in RFX"* , this Conference.

Toroidal and poloidal plasma rotation in the Reversed Field Pinch RFX.

Carraro L.,Casarotto E.,Pugno R.,Puiatti M.E.,Sattin F.,Scarin P.,Valisa M.

Introduction

In tokamaks, changes of the radial electric field E_r and of the shear of the poloidal rotation velocity profile have been considered responsible for the suppression of turbulent fluctuations, and consequently related to improved confinement regimes such as the H mode and the reversed shear mode [1,2,3]. Analogously in RFP's the knowledge of the radial electric field profile at the edge, where large pressure gradients are observed, may provide information about the confinement properties of the outer region. In a stochastic plasma, as an RFP is supposed to be, if the ion radial flux is negligible and the electrons have a maxwellian distribution, the theory predicts an outward radial electric ambipolar field [4] . In RFX, an inward E_r has been measured at the wall by Langmuir probes [5,6]; the evaluation of the radial position where E_r changes its direction allows to characterize an outer region where, with the previous assumptions, the magnetic field is not completely stochastic and therefore, as in Tokamaks and Stellarators, a transport barrier may be established.

Plasma rotation velocity measurements are related to the radial electric field E_r through the momentum equation (neglecting viscous terms and inter-particle frictional forces):

$$E_r = -\frac{1}{n_i Z_i e}\cdot(\nabla p_i)_r - (\bar{v}\times\bar{B})_r \qquad (1)$$

where n_i and Z_i are the density and the charge number of the ion species, p_i is the ion pressure, $\bar{B}$ is the total magnetic field , $\bar{v}$ is the fluid velocity.

Actually, in RFP's plasma rotation measurements have been associated to the study of transport phenomena, and in particular to the presence of unstable MHD modes locked both in phase and in the laboratory frame [7,8].

In this paper, from the plasma rotation velocity measurements performed on RFX, E_r has been estimated from eq (1) using a 1-dim impurity diffusion model [9], coupled with a Monte Carlo code to simulate the impurity behaviour at the edge.

Results and discussion

Experimental results. Toroidal and poloidal rotation velocities have been spectroscopically measured on RFX from the Doppler shift of impurity lines; the considered lines are listed in table 1.

table I

ion	wavelength (Å)
C III	2296 5th order
O V	2781 4th order
B IV	2823 4th order
C V	2271 5th order

The emission along four chords (two for the toroidal velocity measurement and two for the poloidal one) is simultaneously collected by a spectrometer and recorded on a fast optical multichannel analyzer with a time resolution up to 0.25msec [10]. The uncertainty of the

measurement is essentially determined by the error in the numerical fit of the line profile, and ranges from $\approx 10^3$ m/sec (for strong signals, such as for the C V 2271Å line) to $\approx 2\ 10^3$ m/sec (for low signals).

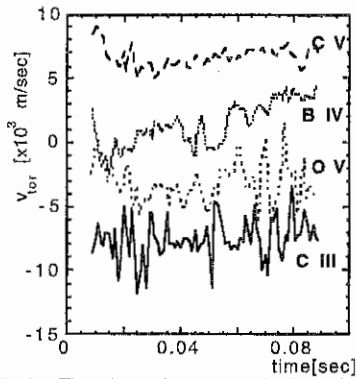

Fig.1 - Time behaviour of toroidal rotation velocity from different ions (I_p=600kA, n_e=4 10^{19} m^{-3}, Te=250eV)

Fig.1 shows an example of the temporal behaviour of the toroidal rotation velocity v_t, as obtained in similar RFX discharges for all the considered ions. Positive velocities have the same direction as the plasma current. CIII, that emits from the edge of the plasma, rotates toroidally opposite to CV, localized in a more internal region, while the other ions show intermediate values of v_t. All of the ions have similar poloidal velocities, around 2 10^3 m/sec, that, with the exception of B IV, are lower than the toroidal ones; in typical discharges, they have opposite direction with respect to the poloidal field. Fig. 2 shows the measured v_t and v_p as a function of ionisation potential, relative to discharges at 700kA of plasma current with electron densities between 3.5 and 4.5 10^{19} m^{-3}. The toroidal velocity increases with increasing ionisation potential, i.e. with decreasing distance from the plasma centre, and the point where the sign reverses corresponds about to the region where B IV is localized (r/a $\approx$ 0.9).

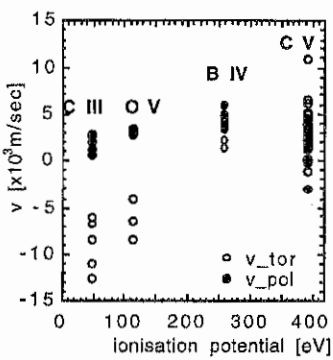

Fig. 2 - Toroidal and poloidal rotation velocities as a function of the ionisation potential.

It is worth mentioning that these fluid velocities are observed despite the fact that the MHD modes in RFX are always locked to the wall.

The measured rotation velocities have been correlated with the main plasma parameters. Fig.3 shows the toroidal and poloidal velocities of C V as a function of the electron density: while v_t decreases at high densities, v_p increases, reversing its direction around n_e= 3.5 10^{19} m^{-3}. However, the velocity module decreases with density, and this dependence cannot be interpreted in terms of C V radial profile variation, because neither multi-chord emission measurements nor the simulations by the impurity diffusion model show significant variations in C V profiles with density. It might be associated with

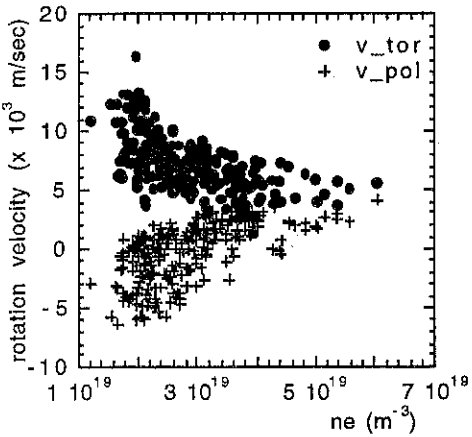

Fig. 3 - Toroidal and poloidal rotation velocities measured from CV as a function of the electron density

a viscous effect, as it is qualitatively consistent with the viscosity dependence on the density.

A scaling with plasma current has not been found for plasma rotation: in fact C V velocities measured at 600 kA may be observed also at lower plasma current.

C III rotation does not show any correlation either with the electron density or the plasma current. Lower toroidal velocities for C III are found when the modes are locked at a toroidal angle close to the region where the rotation measurements are carried out, showing a direct association between the C III toroidal rotation and the plasma-wall interaction.

Radial electric field The experimental data on toroidal and poloidal impurity ion velocities have been compared with a 1-dim impurity diffusion model simulation in order to estimate a profile for the radial electric field. The impurity line emissivities and the total radiated power as measured in a typical RFX discharge ($n_e(0)$= 4 10^{19} m^{-3}, $T_e(0)$=250 eV, Ip = 600kA) have been simulated to obtain the ion density and emissivity profiles. The radial profile of the toroidal velocity has been varied until for each ion the value averaged on the emissivity along the line of sight was consistent with the corresponding experimental v_t. The poloidal rotation velocity has been assumed to be uniform, since similar values have been measured for all ions. Assuming T_i=T_e, an estimate of the radial electric field has therefore been obtained from eq. (1). At the wall an inward E_r of ≈3000 V/m is found. It reverses at r/a≈0.9, and increases up to 1500 V/m, outward directed, at r/a≈0.85. For C V, the contribution of the diamagnetic term to E_r in eq.(1) reaches about 20% in the region of maximum ion density gradient.

This estimate of E_r has been used as input for a Monte-Carlo code , where the carbon production and transport in the edge region of the plasma is described with more detail. In fig.4 the line-integrated emissivity profile of the C III 4649Å line as obtained from the model assuming a diffusion coefficient D=5 m^2/sec and the experimental axisymmetric shift of the plasma of 1.4 cm is compared with the same emissivity measured by a multi-chord linear photodiode array coupled with an interference filter.

The C III velocities deduced from eq.(1) and averaged on the calculated emissivity profile are found -9.7 10^3 m/sec for the toroidal one and 3 10^3 m/sec for the poloidal, to be compared respectively with the

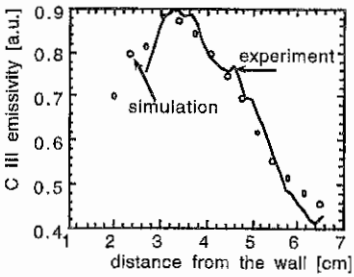

Fig. 4- Comparison between the measured and simulated C III 4649Å line profile

experimental values of -9 10^3 m/sec and 2 10^3 m/sec in these discharge conditions. The toroidal velocity shows an high shear between r/a=0.87 and r/a=0.92, of the order of 5 10^5 sec^{-1}.

While the value of the electric field obtained at the wall is well consistent with that measured by Langmuir probes [5,6], the plasma potential gradient measurements indicate that E_r reverses closer to the wall (r/a≈0.95) [11], suggesting that in RFX the field is practically everywhere stochastic [4]. This discrepancy is well within the uncertainty in the estimate of the E_r profile from the simulations; however, according to the Monte-Carlo code, such an external inversion radius for the electric field is compatible with Doppler-shift velocity measurements if a lower diffusion coefficient, of the order of 1 m^2/sec, and an higher inward E_r at the wall (4500 V/m) are assumed.

Conclusions

Toroidal and poloidal plasma velocities have been measured from Doppler shift of impurity line emissions in RFX, showing that:

- the toroidal velocity of the core ions is co-directed with the plasma current, while the velocity of the edge ones has the opposite sign, showing the presence of a velocity shear at the edge.
- the poloidal velocities are in general lower than the toroidal ones. They are opposite to the poloidal field, except for C V at low plasma densities
- a dependence of v_t and v_p on the electron density has been observed for CV.

The simulations performed by a 1-dim impurity diffusion model and by a Monte-Carlo edge model have shown that:

- the measured poloidal and toroidal velocities are compatible with a radial electric field of ≈3000-4000 V/m at the wall, inward directed. E_r changes direction at r/a ≈0.9-0.95
- a velocity shear of ≈5 10^5 sec^{-1} may be estimated.

References

[1] Shaing K.C.,Crume E.C., Houlberg W.A., Phys. Fluids B2, 6 (1990) 1492
[2] Biglari,H., et al., Plasma Physics and Controlled Nucl. Fus. Res., IAEA, Washington (1990), Nucl. Fus. Suppl. vol.2, 191
[3] Synakowski, E.J., et al., Phys. Rev. Lett., 78 (1997) 2972
[4] Harvey,R.W., et al., Phys. Rev. Lett. 47 (1981) 102
[5] Antoni V., et al., Nucl. Fus. 36 (1996) 435
[6] Antoni,V.,et al., Nucl.Fus. 36 (1996) 1561
[7] Den Hartog,D.J.,et al.,Phys. Plasmas 2 (1995) 2281
[8] Horling, P., et al., 23rd EPS Conf., Kiev (1996) vol.II, 672
[9] Carraro L., et al., Nucl. Fus. 36 (1996) 1623
[10] Haskovec,J.S.,et al.,Proc. of the 13th Symposium on Fus. Engineering, Knoxville, Tennessee, (IEEE,1989), Vol.I,p.153
[11] Antoni,V., this conference (invited paper TL08)

Z_{eff} measurements on the Reversed Field Pinch RFX

L.Carraro, M.E.Puiatti, F.Sattin, P.Scarin, M.Valisa
Consorzio RFX - Padova Italy

Introduction

In Reversed Field Pinch configuration spectroscopic methods are the only means to directly measure Z_{eff}. The alternative method that relies on the relation between effective charge, loop voltage and plasma resistivity in fact requires a detailed modelling of the complex dynamo mechanism that by transforming poloidal into toroidal flux generates and maintains the characteristic reversed configuration [1].
Among the spectroscopic methods the continuum measurements are the most suitable for yielding Z_{eff} estimate on a shot to shot basis, provided the spectra are not contaminated by molecular emission, atomic lines or blackbody radiation. However, the latter condition is not automatically met in RFX, where, due to the absence of limiters, the plasma interacts with the entire wall surface, covered all over by graphite tiles.
To verify the reliability of the Z_{eff} measurements from the continuum emission in RFX, two different spectral regions (λ=5235 ±5 Å and λ=10440 ± 40 Å) have been studied and the results have been compared with the estimates of a 1-dimensional Collisional Radiative model simulating the experimental H-like and He-like resonant line emissivities of carbon and oxygen [2], the main impurities in RFX, and the total radiated power [3].

Experimental set-up

Inspection of RFX emission spectrum in different standard operational regimes showed that the two spectral regions chosen to determine Z_{eff} are line free.
The bremsstrahlung emission in the VIS range is measured vertically along two lines of sight: the vertical diameter and a chord with impact parameter p/a=0.28. The opposite ends of the two lines of sight do not intersect the graphite tiles but the windows of the diagnostic ports.
The system of light collection is based on f/2 objective lenses (f=50 mm) imaging 10 mm of equatorial diameter on a 600 μm diameter optical fiber 35 m long.
The fiber is connected to two 3 cavity interference filters (at 5235 Å with 10 Å passband), serially coupled in order to maximize the rejection.
The detectors are Hamamatsu PMT R928 coupled to current-voltage amplifiers (including 3 pole active filters) with 5 KHz cut-off. The interference filters and the detector housing are maintained at a constant temperature of 30 °C.
The bremsstrahlung emission in the IR range is measured at the same poloidal section along 18 vertical chords with impact parameters p/a ranging from

-0.3 to 0.3. One third of these lines of sight do not intersect the graphite wall and pass through the quartz window of a diagnostic access.
The detector is a 38 photodiodes array Hamamatsu S411 (coupled to a C2334 evaluation board), placed on the focal plane of a f/2 objective lens (f=50 mm) with an interference filter to select the radiation wavelength. The maximum time resolution of the IR system is 1 ms.
The light collected by each pixel comes from an area of about 40 x 10 mm ^{2} centered on the intercepted equatorial diameter.

Results.

The effective charge is calculated from the absolute measurements of the continuum emissivities, in the VIS and IR spectral ranges, having evaluated the dependence of the free-free Gaunt factor on T_e and Z_{eff} for each spectral range [4].The resulting Z_{eff} values are averaged along the line of sight, taking into account the experimental profiles of n_e given by a CO_2 interferometer and of T_e given by a Thomson Scattering diagnostic.
A typical error of ±20% has been evaluated for the Z_{eff} measurements from bremsstrahlung, taking into account the absolute calibration of the detectors, the uncertainties on the electron density and temperature profiles and the fitting procedure applied to the calculation of the Gaunt factors.
An example of the time behaviour of Z_{eff} measured in RFX in the VIS range for the central line of sight (LOS) is shown in Fig.1. The increase in the electron density due to pellet injection [5] is well correlated with the decrease in the measured effective charge.
The ratio between Z_{eff} evaluated in the VIS and IR spectral regions along the vertical diameter of the plasma is drawn in Fig. 2 towards electron density for discharges with Ip=550-650 KA. The results of the Z_{eff} measurements in the two spectral ranges agree within 20% for $n_e \geq 2.10^{19} m^{-3}$ so that the value of Z_{eff} from bremsstrahlung measurements can be considered reliable for this range of electron density. At lower density the value of Z_{eff} obtained in the IR range results higher than that from VIS range perhaps associated to contamination of the spectra by unidentified radiation due to plasma wall interaction, that may become important at low density when the Bremsstrahlung signal is weaker.
In Fig. 3 the Z_{eff} values measured along the diameter in the VIS range and the Z_{eff} calculated with the 1-dim Collisional Radiative (CR) code for C and O are reported towards the electron density, for discharges with Ip=550-650 kA.
The Z_{eff} measured in the VIS spectral range and the predictions of the model agree within 20%, confirming that the measurements of continuum provides suitable estimates of the plasma effective charge in RFX for electron density $n_e \geq 2.10^{19} m^{-3}$.
The high Z_{eff} values in Fig. 2 at low density have to be considered unrealistic since in RFX no relevant emission from heavy elements has ever been detected; in some cases at the beginning of the discharge NiXI and NiXII lines have been observed, corresponding to Nickel concentration that never exceeded 10^{-4}, with a negligible contribution to Z_{eff}.

The 1-dim CR code for C and O has been run to reproduce the absolute emissivities of CV, CVI resonant lines, measured with an absolutely calibrated Grazing Incidence spectrometer [6] and OVII resonant line measured by a multi layer mirror system [7]. The best simulation of the experimental data results with a diffusion coefficient D of 10-20 m^2/s for $r/a \leq 0.8$ decreasing to 2-4 m^2/s at greater radii and a inward pinch velocity $V(r)=-S\ D\ r/a^2$ with S=1-2.
The total radiated power for the calculated concentration of C and O [2] is consistent with the measurements of bolometric system within a factor of 2. The agreement between the experimental and simulated data may be considered satisfactory taking into account that:
-radiation in RFX shows a strong poloidally asymmetry [8] while the CR 1-dim diffusion model is cylindrically symmetric.
-the absolute emissivities of the resonances of the most radiative low ionization states are not measured; so that their calculated populations are not so accurate as the H-like and He -like ones.
In Fig. 3 the effective charge measured in RFX just after a boronization [9] has been also reported. The effect of this conditioning procedure results in lower Z_{eff} values at all densities, well correlated with lower O and C influxes from the wall[10]. The variation in the Z_{eff} values obtained at a given density and plasma current depends in fact on the plasma wall interaction as shown in Fig. 4 where the correlation with the measured C and O influx is evident.
The described measurements have been performed also at high current discharges (Ip=750-850 KA) and no dependence of Z_{eff} on Ip has been found at fixed density.

Conclusions

In reliable measurements of Z_{eff} have been obtained shot by shot using measurements of continuum emission in 2 spectral regions .
The Z_{eff} values obtained in the 2 spectral ranges agree between them and with the simulation of a 1-dimensional CR code within 20% for $n_e \geq 2.10^{19} m^{-3}$, while at lower densities the experimental Z_{eff} data diverge towards unrealistic values due to contamination of the spectra by unidentified radiation, probably coming from the edge.
Typically values of Zeff=1.5-2. are found in RFX , the impurity content becomes very low (Zeff close to 1) after a boronization procedure.

References

[1]Carraro L. et al. 22nd EPS Conference on Controlled Fusion and Plasma Physics Bournemouth 1995, Vol.III p.161
[2] L. Carraro et al. Nucl Fusion 36 12, 1996, p.1623
[3] Summers and Mc Whirter J. Phys. B Vol 12 n.14 ,1979, p.2387
[4] W.J.Karzas R.Latter Astrophys.J.Suppl. 6, 1961, p.167 .

[5]L.Garzotti et al. This Conference
[6]L.Carraro et al. Rev.Sci.Instrum 66(1), 1995 p.613
[7]L.Carraro et al.Nucl. Rev. of Sci. Instrum. 68 (1) ,1997,p.1043
[8]L.Carraro et al J.Nucl.Mat 220-222 ,1995,p.646
[9]P.Sonato et al. J. Nucl. Mat. 227 ,1996,p.259
[10]M.E.Puiatti et al. 22nd EPS Conference on Controlled Fusion and Plasma Physics Bournemouth 1995, Vol. II p.317

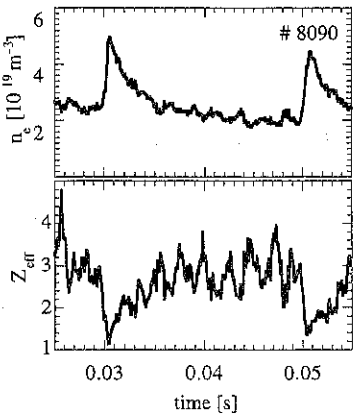

Fig.1 Time behaviours of electron density and Zeff (in the VIS range) in a RFX discharge with injection of two pellets

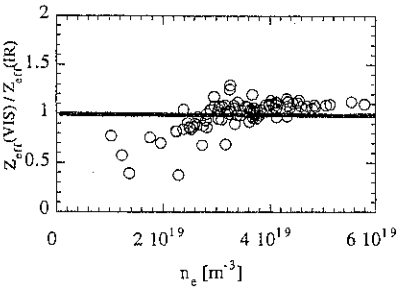

Fig.2 Ratio between Zeff evaluated from Bremsstrahlung emission in the VIS and IR ranges in discharges with Ip=550 kA-650 kA.

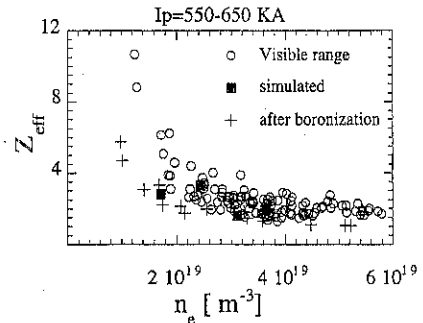

Fig.3- Zeff evaluated in the visible range and simulated with the 1-dim CR diffusion code vs electron density in RFX discharges with plasma current Ip=550-650 kA

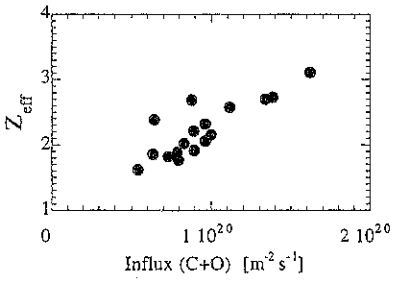

Fig.4 Zeff measured in the VIS range towards the sum of C and O influxes

TOTAL RADIATION EMISSIVITY PROFILES RECONSTRUCTED WITH TOMOGRAPHIC TECHNIQUES IN RFX

L.Marrelli, P.Martin, A.Murari
Consorzio RFX
Corso Stati Uniti 4, Padova, Italy

1 Introduction.

This paper presents a survey of the total radiation emissivity profiles measured in RFX [*Rostagni 95*], a large (a=0.46 m, R=2 m) Reversed Field Pinch (RFP) [*Bodin 90*] experiment, with a new remotely controlled bolometric tomographic system [*Martin et al. 97*] which uses up to 48 miniaturised metal resistor bolometers [*Mast et al. 84*] identical to those used in large tokamak experiments. Particular attention has been paid to the study of poloidal and toroidal asymmetries in the emissivity profiles, which are effectively reconstructed with a maximum entropy tomographic technique in the explored plasma current (I_p) interval which ranges between 0.2 and 0.8 MA. They are related to the non-symmetric plasma-wall interactions, which in the toroidal direction are due to stationary distortions of the main magnetic fields, the so called "locked modes" [*Antoni et al 95*], and in the poloidal direction are originated by the horizontal displacement of the plasma column. The effect of radiation losses, in particular those due to locked modes, on the global power balance will be analysed.

2 Toroidally symmetric emissivity

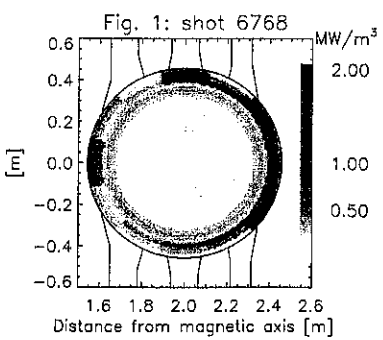

A general property of RFX total radiation emissivity profiles, away from the locked mode region, is that they are typically edge-peaked [*Marrelli et al 96*], as 80% of the bolometric power (which accounts for up to 30-40% of total input power) is radiated in an outer layer of width 0.15-0.3a. Previous investigations performed with a 8-chord bolometer, spanning 2/3 of the plasma diameter, indicated a poloidal asymmetry well correlated with the position of the plasma column. This is confirmed with more detail by the present measurements, as shown in fig. 1, where an example of emissivity profile is reported; to reconstruct the shape of the emissivity $\varepsilon(r,\theta)$ function from the finite set of brightness measurements $f(p,\phi)$, we have adopted a maximum entropy approach [*Buck 91*]: the emissivity is supposed constant over pixels of suitably chosen shape and the discretized Radon equation is solved imposing the maximum entropy constraint. The pixels in the plasma core are simple concentric rings whereas in the outer region (last 30 % of the plasma radius), where more poloidal resolution is required, they are also divided in 12 poloidal sectors.

The poloidal dependence of the total radiation can be highlighted with the help of the radially integrated bolometric emissivity, defined as $\sigma(\vartheta)=\int_0^a rdr\,\varepsilon(r,\vartheta)$ and shown in fig. 2 for three low current RFX discharges (electron density $n_e\approx 2\times10^{19}$ m^{-3} for these plasmas) characterised by different horizontal plasma positions: the horizontal magnetic shift is Δ_h=1.5 cm for the curve "A", Δ_h=0.3 cm for the curve "B" and Δ_h=-2.3 cm for "C". In this figure, 0° corresponds to the equatorial plane on the outer side of the torus, while 180° is the poloidal position nearest to the torus axis. A prominent maximum as a function of θ is

Fig. 2

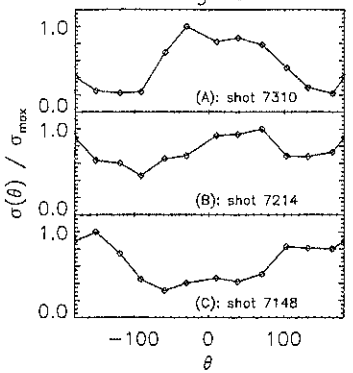

Fig. 3

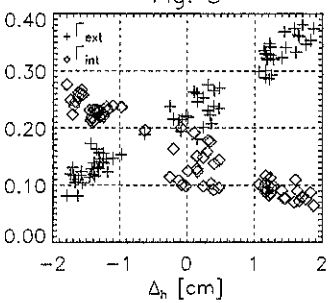

Fig. 4

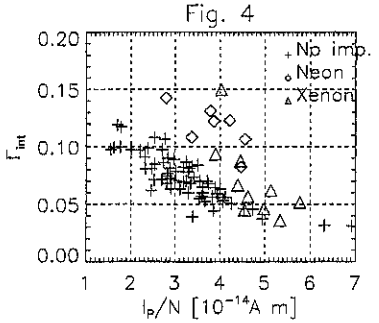

evident in the "A" ($\theta_{max}\approx$ 0°) and "C" ($\theta_{max}\approx$ 180°) cases, corresponding to outward and inward displaced plasmas respectively; for a well centred discharge ("B") the inner and the outer region exhibit the same level of emissivity. The shape of $\sigma(\theta)$ and its width require harmonics at least up to m=2 to be reproduced.

The poloidal extension of the emitting region can be quantified with the help of $\Delta\,\theta_{50\%}$ indicator, which determines the region emitting 50% of the power radiated on the whole cross-section $\left(\int_{\vartheta_{max}-\Delta\vartheta_{50\%}}^{\vartheta_{max}+\Delta\vartheta_{50\%}}\sigma(\vartheta)\,d\vartheta = 0.5\int_0^{2\pi}\sigma(\vartheta)\,d\vartheta\right)$. Discharge 7148 (plasma current 230 kA), whose magnetic shift is ~2 cm, is characterised by a poloidal extent $\Delta_{\theta 50\%}$= 150°, around the 180° maximum, while discharge 7310 , whose shift is 1.5 cm has a narrower peak around 0° extending over 97°.

The correlation between plasma displacement (and the related plasma-wall interaction) and poloidal asymmetries in the emissivity profiles can be described by analysing the ratios Γ_{ext} and Γ_{int} between the power emitted in the external and internal circular segments and the total radiated power P_{rad} (these two circular segments are both topologically defined by the chords whose impact parameter is p/a=±0.7). When plotted against the plasma shift (see fig. 3), Γ_{ext} shows a remarkable increase whereas Γ_{int} decreases (each point correspond to a 10 ms average around t=30 ms for discharges with similar I_p and n_e). For centred discharges ($\Delta_h\approx$0) on the other hand, Γ_{ext} is approximately equal to Γ_{int}. These results show that the local enhancement of the emissivity can be related to the increased wall interaction suffered by the plasma when its equilibrium is displaced: this leads to a larger localised influx of impurities, which in their lower ionisation states are mostly responsible for radiation.

The poloidal extent of the influence of impurities on the emissivity profiles is found to depend on electron density.

For typical 0.6 MA discharges (I_p=0.55-0.65 MA, Δ_h=1-1.5cm) at low density values (that is at high values of the I_p/N parameter, where N is the linear electron density) Γ_{int} ranges between 0.03 to 0.06, while at high densities it can be as high as 0.12-0.14 (fig. 4). On the other hand $\Gamma_{ext}\approx$ 0.2-0.3% does not change significantly for the same discharges: therefore at higher densities the outer radiating layer is more symmetric. The injection of extrinsic impurities (either Xenon or Neon) through gas puffing can induce similar but more dramatic

changes on bolometric profiles, which tend to be even more symmetric for the same values of I_p/N parameter. The most significant changes involve the emission of radiation in the internal region of the plasma cross-section, which increases significantly as may be seen in the fig. 4 (where measurements taken during impurity injection experiments are plotted with a different symbol); also Γ_{ext} is affected, since it becomes smaller, in particular when Xenon is the injected impurity.

The emissivity profiles vary also with plasma current. Γ_{ext} slightly decreases and profiles become more symmetric when the plasma current is raised. Also the radial width of the emitting layer changes: at low current (≈0.4 MA) 80% of total power is radiated in the last 15% of plasma radius, whereas at higher currents (≈0.8 MA) the emitting layer extends between $0.6<r/a<1$.

3 Emissivity from the locked mode region

Stationary magnetic perturbations, due to the locking to the wall of unstable MHD modes, affect all RFX discharges and cause an helical distortion of the magnetic fields, which is localised toroidally over 30-40° and whose toroidal component can be roughly modelled with an expression like $\tilde{B}_\phi(a,\vartheta,\phi) = B_1 \cdot \exp\left(-\left(\frac{\phi-\phi_{lock}}{\Delta\phi}\right)^2\right) \cdot \sin(n\vartheta+\varphi+\xi)$, where Φ_{lock} is the toroidal location of the maximum of the perturbation and n is in the range 10 to 15. The helical shaped region where the graphite wall is intersected by the distorted magnetic surfaces is interested by enhanced plasma wall interactions, causing a dramatic increase of

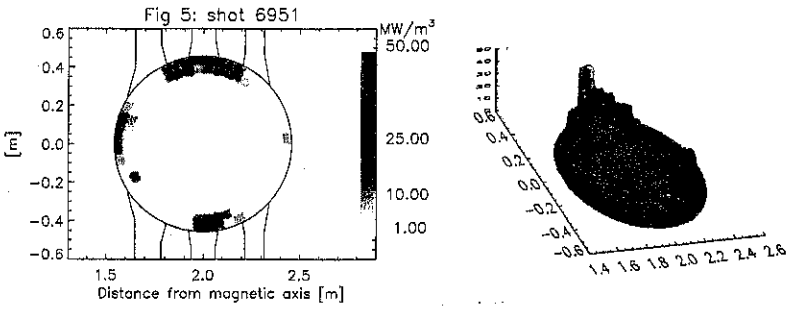

impurity influxes [*Valisa et al. 96*]. In this region, the spatial distribution of total radiation is rather variable: in some cases measured brightness does not seem significantly affected by the presence of the locked modes, whereas in other cases one or more poloidally localised highly emitting regions suddenly appear near the first wall, as in fig. 5 which shows an increased emission at $\theta = 90°$. Very often these small regions of enhanced emissivity, which may be characterised by consistent fluctuations in time, correspond to the edges in proximity of vessel portholes.

A characterisation of the toroidal distribution of radiation losses have been performed by studying the dependencies of the x component of the radiation barycenter $x_g(\phi) = \int d\vartheta dr\, r^2 \cdot \cos\vartheta \cdot \varepsilon(r,\vartheta) \big/ \Pi_{rad}$ on ϕ_{lock} and of the bolometric power linear density $\Pi_{rad}(\phi) = \int d\vartheta dr\, r\, \varepsilon(r,\vartheta,\phi)$. Time averages over a 60 ms interval, for a set of similar 0.6 MA discharges, are shown in fig. 6 and fig. 7, together with standard deviations. The radiation barycenter x_g is constant in toroidal regions far from the locked mode, and is

Fig. 6

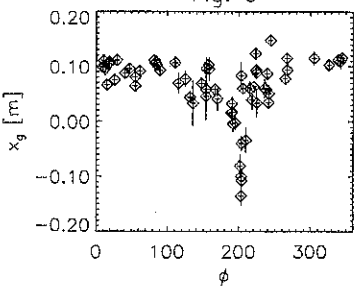

significantly altered between 160° and 240° (the bolometric diagnostic is located at ϕ=202°), indicating that the toroidal extent of bolometric emissivity asymmetry is comparable to the magnetic perturbation. The position of the maximum alteration of the bolometric barycenter corresponds to that of the maximum of the magnetic perturbation; moreover, bolometric emissivity perturbation is not symmetric around the maximum.

A consistent increase of Π_{rad}, neither systematic nor constant in time during the discharge, affects a narrower region whose extent is approximately $\Delta\Phi_{lock} = 30°$ (between 190° and 220°) (see fig. 7).

The results of fig. 7 can be applied to estimate the radiated power due to the presence of locked modes. In fact, total bolometric losses can be written as $P_{rad} = \int d\Phi R\Pi_{rad}(\Phi)$, with $\Pi_{rad}(\phi)=\Pi_{rad,sym}+\Pi_{rad,lock}(\phi)$. $\Pi_{rad,sym}$ represents the toroidally symmetric component that, for the discharges of fig. 7 ranges between 0.07 and 0.15 MW/m, whereas $\Pi_{rad,lock}(\phi)$ is a function sharply peaked around ϕ_{lock}. Assuming an average value for $\Pi_{rad,lock}(\phi)$, i.e. $<\Pi_{rad,lock}(\phi)>\approx$0.5 MW/m, constant over $\Delta\phi_{lock}$, we can estimate the bolometric power radiated in the perturbed region $P_{rad,lock}$= 0.5 MW, which may be of the same order of toroidally symmetric losses $P_{rad,sym}\approx$ 0.7-1.5MW.

Fig. 7

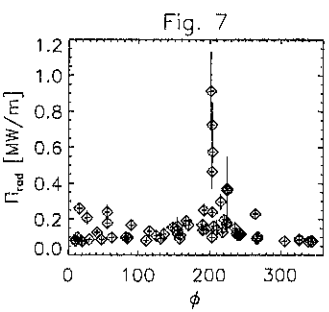

This information allowed us to better quantify the contribution of bolometric losses to the global power balance: for the particular set of 0.6 MA considered above, bolometric losses account for up to 5-8% of total input power (which varied in the range 20-24MW). We can therefore conclude that the static magnetic distortions can cause a significant modifications of the emissivity profiles an increase of radiation losses, but the impact on the average global power balance is not large, confirming that transport mechanisms are the main loss channel and determine the global energy confinement of RFX plasmas.

References

V.Antoni et al.*in Proc. of the 22nd EPS Conf. on Contr. Fus. and Plas. Phys.*, **19C part IV**, 181, Bournemouth, UK (1995).

H.A.B.Bodin, Nucl.Fusion **29**, 1717 (1990).

B.Buck ed., *Maximum Entropy in Action*, Clarendon Press, 1991, p.109

L.Marrelli, P.Martin, A.Murari *Proc. of the 23rd Conf. on Contr. Fus. and Plas. Phys.*, **20C part II**, 645, Kiev,Ukraine, 1996

P.Martin, A.Murari , L.Marrelli, *Rev.Sci.Instrum.* **68(2)** Feb 1997 p 1256

K.F.Mast, E.R. Müller, J. Appl. Phys, **55**, 7 (1984)

G. Rostagni et al., *Fusion Engineering and Design*, **25**, (1995) 301.

M.Valisa et al., "Locked Modes Induced Plasma-Wall Interactions in RFX" to be published on Journ. of Nucl. Materials (1996).

Dynamo and Superthermal Electrons in RFX

A.Murari, E.Martines, V.Antoni, D.Desideri, P.Franz, L.Marrelli, P.Martin, G.Serianni, G.Spizzo, L.Tramontin, F.Vallone.

Consorzio RFX.
Corso Stati Uniti 4, Padova, Italy

1. Introduction.

In the Reversed Field Pinch (RFP) configuration [1] the toroidal magnetic field at the wall $B_t(a)$ is in the direction opposite to the on axis toroidal field $B_t(0)$ and this B_t reversal can be achieved spontaneously and maintained against resistive diffusion. The sustainement of the magnetic field profiles implies the existence of a toroidal flux Φ regeneration mechanism internal to the plasma. The most important models that have been proposed and developed to describe this regeneration mechanism, usually called "dynamo", fall under two main categories; the kinetic dynamo theory (KDT) [2] and the MHD dynamo [3]. The KDT relies on the diffusion of energetic electrons, which escape from the core of the plasma following the wandering field lines of that highly stochastic region; once these so-called superthermal electrons reach the edge, they carry a substantial part of the current required to sustain the configuration [4]. According to the MHD dynamo, on the contrary, the configuration is the result of the dynamic interaction of a wide spectrum of low frequency coherent magnetic fluctuations, which create an electromotive force along the magnetic field through their non-linear coupling with the fluctuations of the plasma velocity; in this context the superthermal electrons could be generated in the regions where the reconnection of the fields, associated with the resistive tearing instabilities, takes place [5].

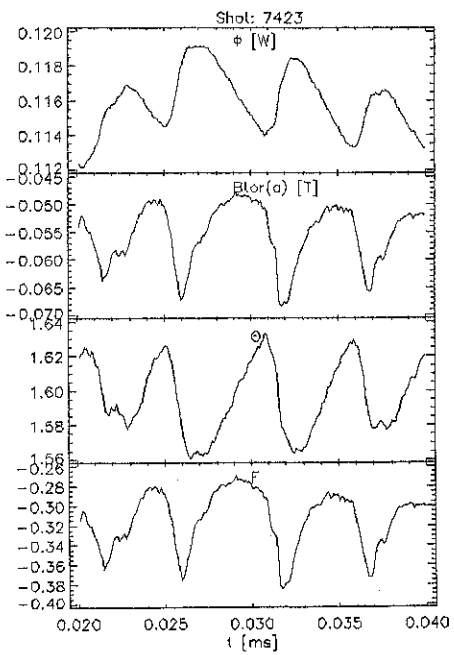

Fig.1: Discrete dynamo events in RFX

Discrete dynamo events (fig.1) have been detected in various RFP machines, particularly when they are operated at high Θ, a parameter defined as $\Theta = \pi a^2 B_p(a)/\Phi$ (here

$B_p(a)$ indicates the poloidal component of the magnetic field at the wall) and that is normally used together with the parameter $F = \pi a^2 B_t(a)/\Phi$ to describe the RFP configuration. The main purpose of this paper is to present the results of a high Θ experimental campaign of the RFX experiment [6] dedicated to the investigation of these discrete dynamo events. The trends of the various plasma parameters during the periodic oscillations have been studied with the help of several diagnostics: a set of 72 external magnetic coils, a 48 channels soft X rays (SXR) tomography, a 36 channels bolometric tomography calibrated absolutely, an electrostatic Electron Energy Analyzer (EEA) [4] and Langmuir probes. It is worth mentioning that all the discharges of the present database were affected by local stationary deformations of the main magnetic field normally referred to as "locked modes" [7]; on the other hand, since the discrete dynamo is generally less strong and therefore more difficult to detect in normal RFX discharges ($\Theta \cong 1.45$) [8], during this campaign the machine has been operated at high Θ (about 1.6). The obtained measurements provide a quite complete description of the evolution of the magnetic profiles and of its effects on the thermal quantities and also allow to insert the superthermal electrons behavior in the global picture of the discrete dynamo oscillations.

2 Experimental Evidence.

Evolution of the Magnetic Quantities

The typical time evolution of the magnetic quantities during a 600 kA, high Θ discharge of RFX is shown in fig.1, where several quasi-periodical oscillations of the quantities Φ, $B_t(a)$, Θ, and F are presented. The diffusion phase, which is characterized by a reduction of the total flux Φ and of the reversal ($B_t(a)$ becomes less negative) on a time scale of a few ms, is followed by a sudden (of the order of 1 ms) regeneration of the toroidal flux (often called relaxation phase) and the deepening of the reversal ($B_t(a)$ becomes more negative).

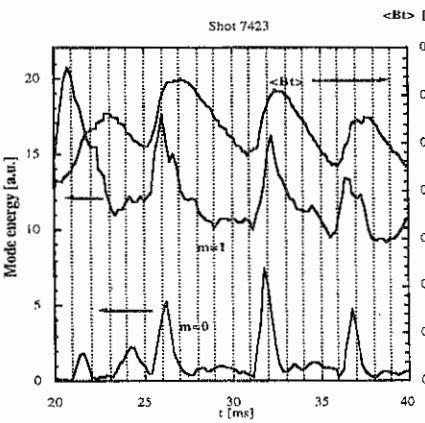

Fig.2: Evolution of the mode energy

With regard to the evolution of the MHD instabilities (fig.2), the energy in the toroidal component of both the m = 0 and the m = 1 modes, measured in the frequency range between 100 Hz and 5 kHz and between 0 and 5 kHz respectively, remains quite stationary during the diffusion phase and presents a sudden positive jump when the flux is

regenerated. It is worth mentioning that at slightly lower values of Θ (around 1.55), the m = 0 modes show the tendency to increase after the m = 1 modes, whereas in the more common case of Θ ranging between 1.45 and 1.5 the phenomenology is more varied.

The oscillations of the m = 1 modes, which do not rotate in the laboratory frame and are the ones that form the static local distortion of the main field, constitute an interesting new piece of evidence, proving the role played by locked modes in the discrete dynamo events. On the other hand, the strong dynamic evolution of the m = 0 modes at the moment of the flux regeneration confirms the assumption that the edge region, close to the presumable resonance location of these modes, is strongly affected during the relaxation phase.

Radiation and Temperature

As far as the thermodynamic quantities are concerned, the on axis electron temperature $T_e(0)$, determined with the double-foil technique, increases during the diffusion phase whereas the total radiation remains quite low (between 5 and 10 % of the input power); a sudden drop of the on axis temperature and a simultaneous increase of the total radiation are on the contrary typical of the interval in which the magnetic flux is regenerated [8]. With regard to the measured profiles, the SXR emission is higher and more peaked at the center during the first stage of the cyclical evolution (see fig.3 where a simple linear fit of the raw data is shown), whereas at the moment of relaxation the profiles are flattened and in several cases there is some evidence of an inversion radius at the plasma edge, where several instabilities are believed to resonate. The total radiation profiles are also remarkably modified by the discrete events; after relaxation indeed, even if the emissivity remains strongly peaked at the edge, the profiles appear more symmetric poloidally (the peak in the outer region of the equatorial plane is less relevant) and the emission from the plasma core can be higher than in normal stationary conditions.

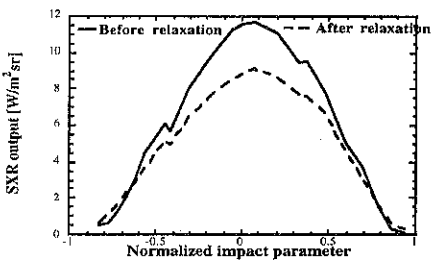

Fig.3: Integrated SXR profiles

Superthermal Electrons and Edge Density

The regeneration of the total magnetic flux coincides with a strong rise of the superthermal electron flux, as shown in fig.4, where the signal measured with the EEA at fixed repeller voltage is reported: the current associated with these superthermal electrons is estimated to increase up to a factor of two above a stationary level, which is always present also in the absence of periodic oscillations. The strong variation of the superthermal electron flux during the regeneration proves that these electrons are deeply influenced by the dynamics of the discrete dynamo. On the other hand the present experimental evidence does not allow to

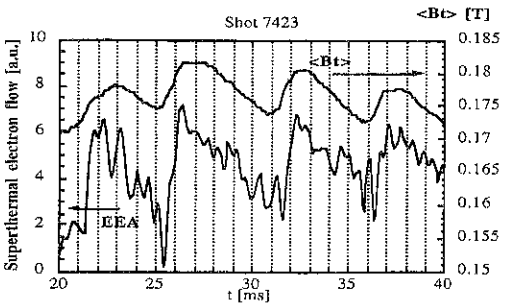

Fig.4: Flux of superthermal electrons

determine if they are generated locally or transported from the core. In any case, the rapid jump of their flux at the moment of relaxation seems to suggest a strong emission of particles toward the wall, an interpretation that is also sustained by the increase of both the H_α emission and the electron density at the edge. Moreover these measurements confirm that the superthermal electrons can play a significant role in the power balances of RFX, particularly during the regeneration phase of the coherent oscillations, when they can constitute a significant loss channel.

Conclusions.

The reported measurements allow a phenomenological description of the global magnetic and thermodynamic behavior of RFX plasmas during the cyclical oscillations. The usual phenomenology of both the magnetic and the thermodynamic quantities ([3], [8]) has been proved to coexist with locked modes. In particular it has been shown that the m = 1 modes, which form the stationary deformation of the mean fields, are strongly involved in the discrete dynamo events. On the other hand, the strong dynamics of the m = 0 modes indicates that, unlike tokamak saw-teeth, the edge region is deeply affected during the regeneration of the toroidal flux. Besides, the relaxation phase is contemporary to a remarkable increase of the flux of superthermal electrons, whose origin on the other hand has not been identified yet, leaving open the issue whether they are the result of the kinetic or the MHD dynamo. In any case, the superthermal electrons could constitute a significant power loss channel, particularly at low density operation, when their energetic role is believed to be higher.

References

[1] H.A.B.Bodin, Nucl.Fusion **29**, 1717 (1990)

[2] A.Jacobson and R.Moses Jr., Phys.Rev. A **29**, 3335 (1984).

[3] S.Ortolani and D.Schnack, *Magnetohydrodynamics of plasma relaxation*,.World Scientific, Singapore, 1993.

[4] Y. Yagi, V. Antoni, M. Bagatin et al., *Proc. 23rd Eur. Conf. on Contr. Fusion and Plasma Phys*, Kiev, 1996 (European Physical Society, Geneva, 1996), **20C**, **Part II**, p.707.

[5] M.Erba et al., Nucl.Fusion **33**, 1577 (1993).

[6] R.Fellin et al., Fusion Engineering and Design, **25**, (1995).

[7] V.Antoni et al.*in Proc. 22nd EPS Conf. on Contr. Fusion and Plasma Physics*, **19 C part IV**, 181, Bournemouth, UK (1995).

[8] L.Marrelli, P.Martin, A.Murari et al, Int. Conf. on Plasma Phys., Nagoya, **1**, 974 (1996).

Halo current measurements and their correlation with mode locking in RFX

S.Peruzzo, R.Bartiromo, N.Pomaro, P.Sonato
Consorzio RFX - C.so Stati Uniti, 4 - I-35127 Padova - Italy

1 Introduction

The presence of current flowing from the plasma to the first wall and vacuum vessel in the Reversed Field Pinch RFX has been evidenced during the last inspection of the vessel, carried out in 1995 [1]. Numerical simulations and experimental tests on a mock-up have been performed in order to evaluate the current necessary to reproduce the damage observed in some first wall components [2]. This paper reports the analysis of data collected with a set of probes recently installed to investigate the presence of halo currents.

The 72 poloidal stiffening rings of the vacuum vessel [3] represent preferential paths with low electric resistance for current flowing. A number of insulated wires have been electrically connected to some pumping and cooling ports, welded to the vessel between two stiffening rings, at three different toroidal positions. On each poloidal plane the probes provide three voltage measurements as described in fig.1.

2 Analysis of axially symmetric signals

Since the wires are located outside the thick shell surrounding the vessel, the voltage measurements experience not only the ohmic part due to the flowing of halo currents, but also two inductive parts related to the toroidal magnetic flux variation linked both within the vessel and with the coil formed by the vessel and the wires. After a correction based on local magnetic measurements, the signals turned out to be related with the horizontal position of the plasma column: with external shift ($\Delta h > 2$ cm) typical V_{be} and V_{et} signals, recorded at different toroidal positions during the whole pulse, range from 50 to 400 mV and show always opposite sign (fig.2), that means that top and bottom are almost equipotential; with lower shift and with negative shift no significant signals have been detected.

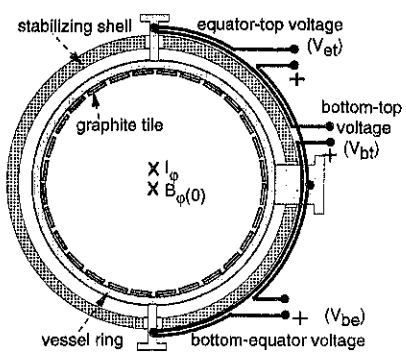

Fig.1 - Set of vessel voltage probes

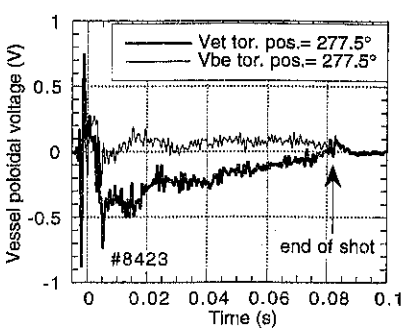

Fig.2 Axis-symmetric signals with external shift

3 Correlation with mode locking phenomena

In RFX all pulses are affected by a magnetic perturbation locked at the wall, which causes a displacement of the plasma column along a helical path and consequently an increased local plasma-wall interaction on a region that typically extend over about 40 toroidal degrees [4].

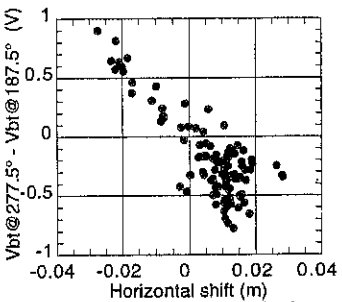

Fig.3 - correlation between vessel voltage and plasma mean horizontal position

When the mode locking occurs at a monitored section, the vessel voltage signals, measured at that section, present strong differences with the correspondent voltages measured at distant sections. Those voltage differences, cancelling all the symmetric components, can be ascribed to the flowing of current due to electric charges that intercept the wall in the region of the mode locking.

In order to obtain a correlation between halo currents and global plasma parameters, the maximum voltage signals, averaged out of 10 ms, have been analysed for each pulse. A clear correlation exists between vessel voltage and the mean plasma position: fig.3 shows that bottom-top voltage at the mode locking position, unlike the symmetric case, can vary both in magnitude and sign, showing a dependence on the mean shift. The extreme cases have been analysed in detail double-checking with toroidal magnetic field measurements, necessary to deduce the local position of the helical perturbation induced by the mode locking [5]. V_{bt} with positive sign has been detected in correspondence with an upper-external position of the perturbation (minimum of $B\Phi$, fig.4); V_{bt} with negative sign, on the contrary, fits a lower-internal position of the perturbation (maximum of $B\Phi$).

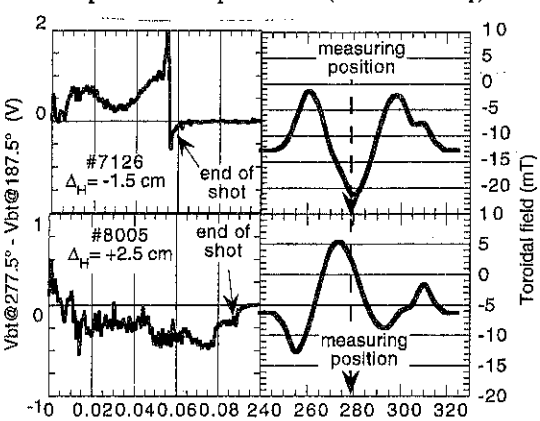

Fig.4 - correlation between vessel voltage and toroidal magnetic field at locking position

Despite a large range of plasma current was explored (300÷800 kA), a weak dependence on plasma current has been found. No systematic correlation has been found either with the amplitude of the perturbation or electron density, even if in some particular cases a relation seems to exist (fig.5).

Maximum V_{be} and V_{et} signals, related to mode locking, are typically about 1 V, but in some cases signals up to 2.5 V have been recorded.

4 Discussion

Unlike tokamak devices, where halo currents are observed exclusively during disruptive events [6], in RFX the phenomenon persists during the whole pulse because in the edge of an RFP plasma a large poloidal current is always present, being necessary for the maintenance of the magnetic configuration. The displacement of the plasma column, particularly enhanced in RFX in the region of mode locking, can thus determine the impact of charge particles to the wall and their circulation within the vessel structure.

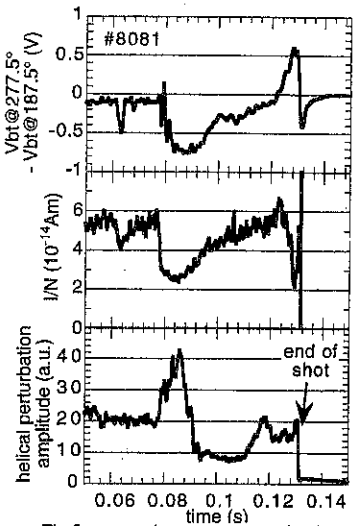

Fig.5 - comparison among vessel voltage, I/N and perturbation amplitude signals

The opposite sign of the voltage measured in the axial symmetric signals (fig.2), when the plasma column is outward shifted, is compatible only with a current, inside the vessel rings, that converges towards the contact point between the first wall and the Last Closed Flux Surface (LCFS). This can be explained with an electronic current that exits from the plasma in a region closely surrounding the contact point of the LCFS; whereas the ionic current, necessary to close the circuit, should appear in two approximately symmetric zones with respect to the contact point of the LCFS (fig.6).

This current circulation agrees with the assumption of a phenomenon dominated by the different ion and electron Larmor radii, which lead to the deposition of the electrons in a region close to the LCFS contact point and of the ions in a farther region. With this description the part of the vessel ring corresponding to the position where the LCFS is farther from the wall should be approximately equipotential, and this is in good agreement with the absence of signals when the plasma is inward shifted (see section 2).

This phenomenological interpretation can be applied also to the plasma column helical distortion due to mode locking: in this case the LCFS contact point, following a helical path, can be found at any poloidal position, and not only in the equatorial plane, providing various possibilities of voltage among the detected vessel points (see section 3).

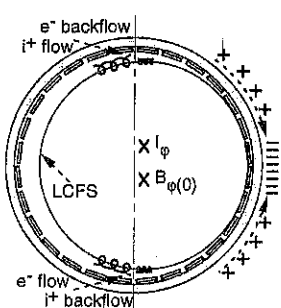

Fig.6 - sketch of the different impact regions for ions and electrons

In order to assess the total current flowing from the plasma to the vessel, a numerical estimate, fitting the voltage measurements, has been carried out: a radial ion current density, cosinusoidally distributed on a collection surface provided by the seven graphite tiles lying along 90° poloidal, has been assumed. A signal of 0.2 V is

compatible with a total current of 0.5 kA for each vessel ring, that corresponds to a maximum tile current of 0.12 kA.

This current should be limited by the total particle outflux from the plasma: considering an average particle outflux of $1 \cdot 10^{22}$ $s^{-1}m^{-2}$ [7] on the whole first wall surface (40 m^2), one can deduce a current of 0.8 kA per each vessel ring. A similar limit is also found considering the ion saturation current: the previous current estimation corresponds to a maximum current density of 40 kA/m^2 that is consistent with the average plasma edge characteristics (electron density: $1 \cdot 10^{19}$ m^{-3}; electron temperature: 20 eV) [7].

A signal of 2 V, detected in correspondence of the mode locking region, can be justified by a total current of 5 kA collected in a ring, corresponding to a maximum ion current in one tile of 1.2 kA. Considering that the electron flow intercepting the wall is more concentrated than the ion one, the maximum electron current for a single tile could reach 5 kA. These current values are in agreement with a particle flux ten times higher then the one considered for the symmetric phenomenon; they are also consistent with an ion saturation current density of 400 kA/m^2, that is compatible with the estimated electron density at the locking region (about 10^{20} m^{-3}) [5].

The evident dependence of the voltage measurement, in the helical perturbation region, from the average horizontal shift (fig.3) should indicate that, when the plasma shift increases (positively or negatively) also the volume outside the LCFS increases allowing an enhanced plasma deformation and, consequently, a higher radial current density.

6 Conclusions

Data collected with a set of voltage detectors installed on the vessel have been analysed in order to correlate the halo current phenomenon with local and global parameters. Both an axial symmetric and a non axial symmetric phenomenon has been evaluated; the latter, being related to the mode locking, is one order of magnitude larger than the former. The voltage difference along the poloidal direction could be a consequence of different region of impact between ions and electrons, because of their different Larmor radii. The phenomenon seems to be influenced more by local parameters (n, T, B, Γ) than by global parameters.

References

[1] P.Sonato et al., *"Investigation of plasma facing components and vacuum vessel in RFX"*, 12th PSI Conference (Saint Raphael, 1996), to be published on Journal of Nucl. Mat.
[2] S.Peruzzo et al., *"Numerical and experimental evaluations of halo currents in RFX plasma facing components"*, 19th Symposium on Fusion Technology (Lisbon, 1996)
[3] F.Gnesotto et al., Fusion Engineering and Design, **25**, 335-372, (1995).
[4] V. Antoni et al., Proc. 22nd EPS Conf. (Bournemouth, 1995), **19C**, Part IV, 181-184.
[5] M. Valisa et al., *"Locked Modes Induced Plasma-Wall Interactions in RFX"*, 12th PSI Conference (Saint Raphael, 1996), to be published on Journal of Nucl. Mat.
[6] F.C.Schüller, Plasma Phys. Control. Fusion, **37** (1995), A135-A162
[7] V. Antoni et al., Proc. 20th EPS Conf. (Lisboa, 1993), **17C**, Part II, 695-698.

Locked modes in the reversed-field pinch device TPE-1RM20

G. Zollino*, **Y. Yagi**, Y. Hirano and G. Serianni*
Electrotechnical Laboratory, 1-1-4 Umezono, Tsukuba-shi, Ibaraki, 305 Japan
* Consorzio RFX, Corso Stati Uniti 4, I-35127, Padova, Italy

1. Introduction

Wall locking of tearing modes in reversed-field pinch and tokamak plasmas has proven to have deleterious effects. So far locked modes have been extensively investigated on both MST [1] and RFX [2] and partially on TPE-1RM20 [3]. In particular, in MST tearing modes lock to the wall when magnetic field errors are higher than a threshold value. Keeping field errors below such value is a necessary condition to avoid locking. In RFX, all pulses have been affected so far by wall locking, even in presence of good field control at the shell gaps.

An experimental campaign was carried out on TPE-1RM20, in collaboration with RFX staff, in the framework of the IEA Working Group on Field Errors in Reversed Field Pinches. Field error was increased and its effect on wall locking was assessed. The same experiments were repeated with two shell layouts. At first, a close fitting shell was present, made of an inner double-layered thin shell and an outer thick shell. The time constant for the penetration of an external field orthogonal to the magnetic axis, τ_L, was 7 and 100 ms respectively. Then the inner shell was removed, thus proximity factor, b/a (where b is the minor radius of the inner-most shell layer and a is the plasma minor radius) changed from 1.08 to 1.12.

In the paper the first summary of the experimental results are reported.

2. Experimental conditions

Fig. 1 shows sections of the TPE-1RM20 shell [4]. The outer layer has one equatorial and one poloidal gap; each of the thin layers have two equatorial and four poloidal gaps. The latter are overlapped to each others. The field error (B_{err}) induced by eddy currents at the thick shell poloidal gap can be cancelled by both an axisymmetric pre-programmed vertical field and a local saddle coil field with feed-back control. B_{err} was increased on purpose, up to 25% with respect to the poloidal component of the magnetic field, by changing the programming of both correction systems.

The m=1 component of the radial field was measured by saddle probes located beneath the thick layer poloidal gap and 180° away in the toroidal direction (normal section), outside the thin shell, at $\vartheta=\pm 90°$. The difference between the signals at the gap and at the normal section was assumed as B_{err} . When the thin shell was present, the measured B_{err} was not actually seen by the plasma column, due to the shielding effect of the thin shell. For this case the measured value was numerically corrected accounting for the transfer function of a thin cylinder with 7 ms time constant. In the paper the corrected value is referred to.

Two toroidal arrays of 32 toroidal field probes are located outside the vacuum vessel at $\vartheta=0$ and $\vartheta=180°$. The signals of such probes were acquired at 500 kHz in order to have enough resolution for the time analyses of toroidal modes. For the analyses reported in the paper the shielding effect of the vacuum vessel was not taken into account. A numerical high-pass filter

was applied with 200 Hz cut-off frequency to cancel pick-up effects from the vertical field. All pulses analyzed in the paper are at plasma current, I_p~140 kA and pinch parameter, Θ~1.5.

3. Experimental results

Magnetic data analyses show that when B_{err} is well controlled tearing modes rotate, with both shell layouts. Fig. 2 shows the amplitudes of odd m toroidal modes, for four typical pulses with low and relatively high B_{err}, with and without the thin shell. The values are averaged from 4 to 8 ms, for the case of optimal B_{err} control (both discharges lasted more than 12 ms), and on a 3 ms interval (around the locking time) in the other case. The principal modes are approximately the same (n=11-14) at low B_{err}, but their amplitude seems to be higher without the thin shell. However we still need more statistical to quatify the average difference in the mode amplitude. When locking occurs, toroidal mode amplitudes increase and their spectrum slightly changes, with a shift of the peak to n=9-10 and n=11 with and without the thin shell, respectively.

All modes generally exhibit a smoother rotation with the thin shell, than without it. With the thin shell and optimal B_{err} control, odd m modes from n=7 to n=10 typically rotate at 40-100 km/s, while for n=11-13 the velocity ranges from 5 to 25 km/s. Due to such a difference in mode velocities, toroidal mode spectrum is expected to change if the filtering action of the vacuum vessel is taken into account. Without the thin shell, velocity is approximately the same for n=11-13, while it reduces by a factor of 2 approximately for lower n values. As B_{err} increases, mode amplitudes increase as well, their velocities reduce and finally phase and wall locking occur. In fig. 3, n=9 amplitude and phase are plotted versus time for a typical pulse with the thin shell and relatively high B_{err} (the same as in fig. 2), for which locking occurs at t~5.5 ms. Fig. 4 shows the time and spatial behaviour of toroidal modes n=9,10,11,12 and odd m for a typical discharge without the thin shell and relatively high B_{err} (the same as in fig. 2), where locking occurs at t~5 ms.

With the thin shell, the stationary perturbation is mostly located at the thin shell poloidal gaps closer to the thick shell one. Without the thin shell it occurs almost always in the proximity of the thick shell poloidal gap. A threshold value of B_{err} for locking to occur has been found by analyzing a set of discharges with relatively good B_{err} control, which exhibit mode rotation for at least 3 ms after the reversal (reversal time is 2-3 ms). For both shell layouts, the positive threshold value results higher than the negative one, as shown in Fig. 5. When the thin shell is present, modes still rotate with higher value of B_{err} (from -5% to 7%) than without the thin shell (from -1% to 5%). However, such a result could be affected by the correction operated on the B_{err} signal, as mentioned before, especially for the negative values of B_{err}. Moreover, it is not yet clear whether the asymmetry in the field error threshold values is due either to a systematic error in B_{err} measurement or to the fact that a positive B_{err} locally pushes the plasma column towards the machine axis, where no equatorial gap is present on the thick shell.

The resistive part of the loop voltage increases after locking (fig. 6), with a corresponding shortening of the discharge duration, due to limited volt-sec. It does not show a step-wise increase. Immediately after locking, it becomes ~15-20% approximately higher. Then, while plasma current has the same time evolution as in the optimized discharge, resistive loop voltage rapidly grows in ~1 ms up to a value a factor of two approximately larger then before locking.

4. Summary

Tearing modes in TPE-1RM20 rotate with both shell layouts, when the field error is below a threshold value. However, rotation results smoother and less sensitive to field error when the close fitting shell is present. Mode locking shortens the discharge duration. Resistive loop voltage increses immediately after locking by 15-20%, with respect to optimized discharges. Then, still before plasma current decay, it rapidily increases by 80-100%, likely due to enhanced plasma-wall interaction.

Acknowledgements

The authors wish to thank Dr. Emilio Martines of Consorzio RFX, for giving them many suggestions and some routines which were adapted for the present data analyses.

References

[1] A. F. Almagri et al., Phys. Fluids B, **4** (12), Dec. 1992, p. 4080.
[2] A. Buffa, et al., Proc. of the 21st EPS Conf. on Contr. Fus. and Plasma Physics, vol. I, July 1994, p. 458.
[3] P. R. Brunsell et al., Phys. Fluids B, **5** (3), Mar. 1993, p. 885.
[4] Y. Yagi, Y. Hirano et al., Jour. of Plasma and Fusion Research, **69** (6), 1993, p. 700.

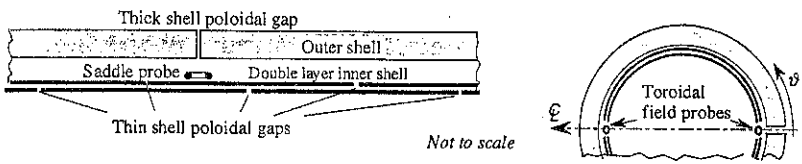

Fig.1: longitudinal (left) and cross sections of TPE-1RM20 shell

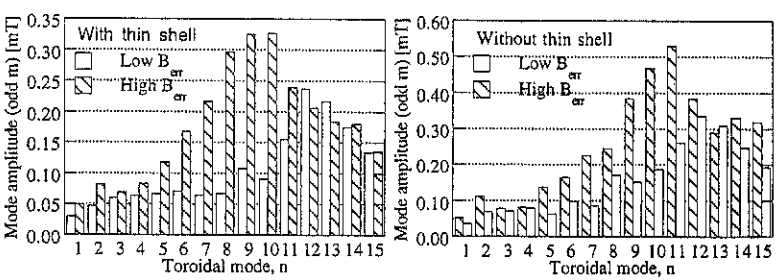

Fig.2: toroidal mode for typical discharges with low and relatively high B_{err}, with and without the thin shell.

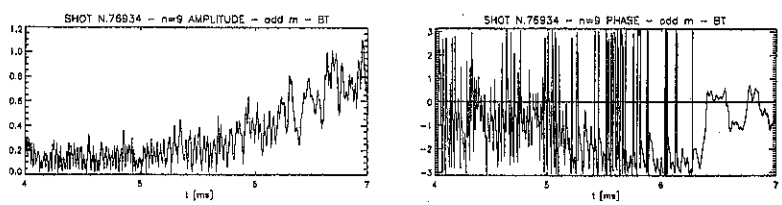

Fig.3: amplitude and phase of mode n=9 and odd m for a typical pulse with the thin shell and relatively high B_{err} (locking occurs at t~5.5 ms).

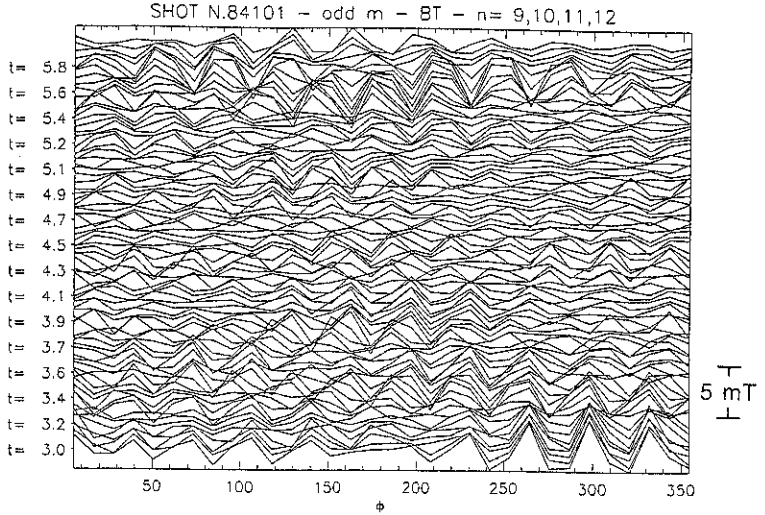

Fig.4: time and spatial behaviour of toroidal modes n=9,10,11,12 and odd m for a typical discharge without the thin shell and relatively high B_{err} for which locking occurs at t~5 ms.

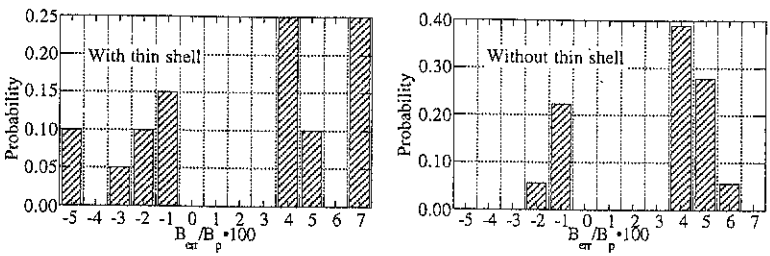

Fig.5: locking probability as a function of B_{err} at the locking time, with and without the thin shell.

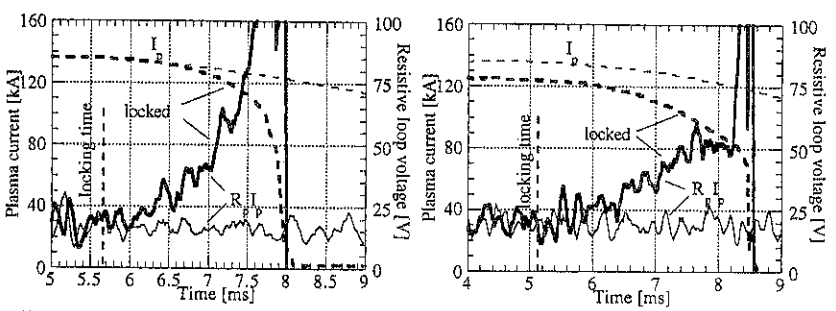

Fig.6: plasma current (Ip) and resistive toroidal loop voltage (RpIp) in four typical discharges with low and relatively high B_{err}, with (left) and without the thin shell.

Superthermal electrons and magnetohydrodynamic fluctuations in TPE-1RM20

Y. Yagi, G. Serianni* and H. Ji**

Electrotechnical Laboratory, 1-1-4 Umezono Tsukuba-shi, Ibaraki 305, Japan
* STA Fellow at ETL, Japan, on leave from Consorzio RFX, Padova 35127, Italy
** Princeton Plasma Physics Laboratory, Princeton, New Jersey 53706, United States

1. Introduction

In the edge plasma region of reversed-field pinch (RFP) experiments, superthermal electrons are observed flowing along local magnetic field lines with the temperature, T_h, parallel to local magnetic field lines, which is comparable to that in the core plasma region. It is of importance to understand the cause of the superthermal electrons in RFPs not only because it is desirable to prevent from enhanced plasma-wall interaction caused by them but also because such a study can give a deeper picture of transport physics in RFP plasmas. It should be noted that superthermal electrons are also observed outside the reversal surface of RFPs, which means they are not locally accelerated by the induction field, E, in the toroidal direction.

Recent study in RFX using an electron energy analyzer (EEA) [1] shows that T_h increases with E/E_c where E_c ($E_c \propto n_e/T_e$) is the critical electric field for electrons to run away, E here was calculated by $V_{loop}/(2\pi R)$ and the other variables have the usual meanings. This may indicate that the superthermal electrons are produced by relatively high E/E_c inside the reversal surface and they are transported to the plasma surface, plausibly along the stochastic magnetic field lines. There is another possibility: i.e., instead of externally applied electric field, the self-generated dynamo electric field can locally drive the fast electrons. The dynamo electric field acts to drive poloidal plasma current near the reversal region while suppressing the current in the core. To address this possibility, we have recently done experiments by measuring the coherency between the local dynamo electric field and the current density of superthermal electrons. This paper reports the first summary of the results.

2. Experimental Apparatus

TPE-1RM20 is a medium sized RFP with major and minor radii of 0.75 m and 0.192 m, respectively. The machine was originally constructed with a double-layered thin shell and a thick shell so that the shell proximity b/a of 1.08 was achieved with a vacuum vessel of ultra-high vacuum grade, where b is inner minor radius of the innermost shell and a is the minor radius of the plasma [2]. Recently, the double-layered thin shell was removed to study the effects of the shell proximity on the plasma confinement characteristics. The shell proximity after the modification has become 1.12. The first results of this modification are

reported in the separate papers in this conference. The experiments reported in this paper are carried out after the modification. We assume that this modification do not qualitatively alter the physical origin of superthermal electrons in RFP plasma.

To study the correlation between superthermal electrons and magnetic fluctuations, a complex probe has been developed, which has EEA, electro-static and electro-magnetic probes all installed into a small case (Fig. 1). The probe was mounted on a manipulator at an outer horizontal port on the equatorial plane. The manipulator can be manually driven linearly towards the plasma and can be also rotated around the insertion axis. The maximum insertion of the probe tip tried in the experiment was 25 mm deep into the plasma (r/a = 0.87).

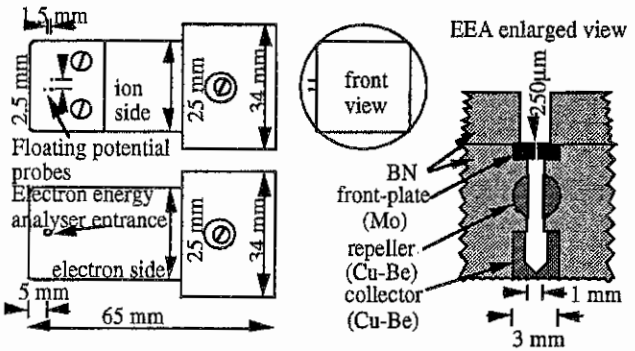

Fig. 1: Schematic of the probe system.

As shown in Fig. 1, the probe consists of a boron nitride case containing EEA and supporting four tungsten pins for floating potential measurements. Inside the probe, two magnetic coils are located for toroidal and radial magnetic field measurements; the magnetic coils are wound around an insulation core. The centre of the entrance hole of the EEA is 5 mm recessed from the tip of the probe. The EEA is made of three cylindrical-shaped electrodes: a molybdenum front-plate, for eliminating the ions, having a hole with 250 μm diameter and 1 mm thickness; a Cu-Be repeller, for selecting the electron energy, with 1 mm internal diameter and 3 mm thickness; a Cu-Be Faraday cup, for collecting the electron current, with 1.5 mm internal diameter. The pins for floating potential measurements are located on the opposite side of the probe in order to be protected from superthermal electrons when the EEA is exposed to the electron drift side; they constitute a rectangle whose centre is at 5 mm from the tip of the probe and are 1.5 mm spaced in the radial direction and 2.5 mm in the toroidal direction; the pin diameter is 0.5 mm and they protrude 2 mm into the plasma.

The floating potentials and the repeller voltage are measured by voltage dividers; the collector current by a shunt resistance. From the probe, the signals by coaxial cables go to a connection box. From there, the cabling for the magnetic signals consists of twisted pairs;

for the other signals, optical fibres are used. All of the signals are acquired at a sampling frequency of 500 kHz.

3. Results

In the computations, the following coordinate system has been used. The toroidal direction is along the toroidal field on axis, the poloidal field is along the local poloidal field and the radial direction points outwards. Experiments were conducted at low plasma current of about 50 kA in order to protect the probe from high heat flux of the superthermal electrons. Shot-averaged plasma parameters are; I_p = 52±4 kA, R_pI_p = 28±11 V, F = -0.22±0.05, Θ = 1.70±0.06, n_{el} = (0.9±0.4)×10^{19} m^{-3}, T_{e0} = 190±120 eV, $n_{e\text{-}edge}$ = (0.8±0.1) × 10^{19} m^{-3} and $T_{e\text{-}edge}$ = 38±4 eV, where the edge parameters were measured at r/a = 0.92. Note that the reversal surface with this F and Θ value is at r/a = 0.85 according to the Polynomial Function Model.

On assuming that the magnetic field at the edge is essentially poloidal, the parallel MHD dynamo electric field [3]:

$$\left(\tilde{\mathbf{v}}\times\tilde{\mathbf{B}}\right)_{//}=\left(\tilde{\mathbf{E}}_{\perp}\bullet\tilde{\mathbf{B}}_{\perp}\right)\frac{1}{B_{tot}}\approx\frac{E_{tor}B_{tor}+E_{rad}B_{rad}}{B_{pol}} \qquad (1)$$

can be computed by using the toroidal and radial components of the electric field, obtained from the average differences of the floating potentials divided by the probe distances, and multiplying by the magnetic fields, obtained by numerically integrating the magnetic coil signals. More accurately, plasma potential instead of floating potential should be used to calculate the electric field. However, for simplicity the floating potential only is measured because the contribution of the fluctuating electron temperature to the dynamo electric field was found to be negligible in the previous experiments [3]. It should also be noted that there is another dynamo term due to diamagnetism of electrons depending on collisionality of the plasma [3]. The normalized electron collisionality λ_e/a (λ_e is the electron mean free path) for the present experiment is calculated to be about 11±2 at r/a=0.92, which indicates that the diamagnatic dynamo term can be neglected according to Ref. [3].

The data collected for every shot have been divided into sub-sections containing 100 time points (200 μs) each. Every sub-section is treated as a separate sample, whose total amount is N_{sam}; from each of them the linear trend is subtracted and, after Hanning windowing, they are FFT-transformed and the coherency (κ) and phase (φ) spectra are computed between $\left(\tilde{\mathbf{v}}\times\tilde{\mathbf{B}}\right)_{//}$ and the superthermal electron current by applying the following formulas, for two general quantities a and b;

$$c(\nu)=\frac{\langle a^{*}(\nu)b(\nu)\rangle}{\sqrt{\langle|a(\nu)|^{2}\rangle\langle|b(\nu)|^{2}\rangle}}\quad \kappa(\nu)=|c(\nu)|\quad \varphi(\nu)=arctg\left(\frac{\mathrm{Im}(c(\nu))}{\mathrm{Re}(c(\nu))}\right) \qquad (2)$$

The error on the coherency spectrum is obtained from the following formula [4]:

$$\sqrt{\frac{A}{N_{sam}}\left(1-\kappa(\nu)^{2}\right)} \qquad (3)$$

where A = (3/8) for the Hanning window.

With the complex probe a set of different experimental conditions have been explored; the experiment that has been used as a reference is described by the following features: repeller voltage short-circuited; collector voltage short-circuited collector resistance 49.7 Ω; EEA facing the electron drift side; insertion of the tip of the probe 20 mm inside the plasma beyond the fixed limiter position; and plasma parameters as described above. Figure 2 shows the coherency and phase spectra for $\left(\tilde{\mathbf{v}}\times\tilde{\mathbf{B}}\right)_{//}$ and the collector current j_{col} for this reference condition. It can be noticed that the coherency, although its value is small, is nevertheless significantly different from zero below 100 kHz, as is shown by the statistical error overlaid on the figure.

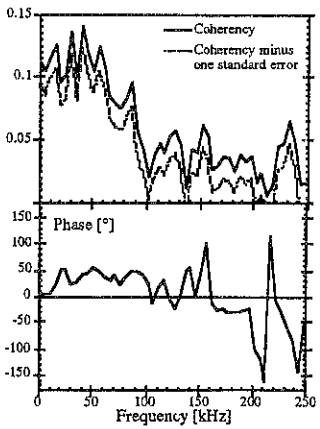

Fig. 2: Coherency and phase spectra for the reference experiment

With the same plasma conditions we scanned repeller voltage, V_R (= from 0 V to -300 V), collector voltage, V_C (= 0 V, 50 V), probe orientation angle, θ_P, (electron drift side and ion drift side) and the probe insertion depth, X_P. We also scanned I_p, Θ and n_{el}. Results of these scanning will be reported elsewhere.

4. Conclusions

It is experimentally shown in TPE-1RM20 that there is a statistically meaningful coherency between MHD dynamo electric field and the fluctuating part ($\nu > 2.5$ kHz) of the superthermal electron current density, j_{col}. It indicates that fluctuations often seen as spiky signals in j_{col} can be closely related to the MHD dynamo electric field. Note that it is still an open question about the origin of the slow change ($\nu < 2.5$ kHz for the analysis shown here) of j_{col}.

References

[1] Yagi Y., Antoni V., Bagatin M., Desideri D. et al., Proc. of 23rd Eur. Conf. on Controlled Fusion and Plasma Physics (Kiev, Ukraine), 1996

[2] Yagi Y., Hirano Y., Shimada T. et al., J. Plasma and Fusion Research **69**, 700 (1993)

[3] Ji H., Yagi Y., Hattori K. et al., Phys. Rev. Lett. **75**, 1086 (1995)

[4] Jenkins G. M. and Watts D. G., *Spectral analysis and its applications*, Holden-Day, Oakland, California, 1968

Effect of the shell proximity on confinement characteristics in a reversed-field pinch device, TPE-1RM20

Y. Yagi, Y. Hirano, Y. Maejima, T. Shimada, S. Sekine, H. Sakakita,
G. Zollino * and G. Serianni *
Electrotechnical Laboratory, AIST, 1-1-4 Umezono, Tsukuba-shi, Ibaraki 305 Japan
* Consorzio RFX, Corso Stati Uniti 4, 35127, Padova, Italy

1. Introduction

It has been shown both theoretically and experimentally that reversed-field pinch (RFP) plasma would have large instabilities without a conducting shell, with a resistive shell or a distant shell. To overcome this situation, we have been studying the shell configuration more quantitatively to find a design which is tolerable in terms of confinement properties and still is compatible with engineering requirements for the first wall design and space between the plasma and blanket for future reactors.

There have been many theoretical studies, numerical simulations [1,2] and experimental studies [3,4] about effects of non-ideal shell in RFP plasmas. However, the experiments have been carried out with extreme conditions having a resistive shell whose time constant for the external vertical field is much smaller than or at least comparable to the plasma discharge duration. From the experiences of those extreme cases, we made TPE-1RM20 [5] at Electrotechnical Laboratory (ETL) to be a solution for the close-fitting conducting shell system with an ultra-high vacuum grade chamber. It had a triple-layered conducting shell system which consisted of a double-layered copper thin shell and a copper thick shell. The shell proximity, b/a of 1.08 was realized, where b is the inner minor radius of the closest shell and a is the minor radius of the plasma. The machine showed a good confinement characteristics and it was speculated that the anomaly part of the loop voltage was in fact reduced due to the shell proximity [6]. However, some ambiguity remained whether the shell proximity of 1.08 was really effective than only having the thick shell at b/a = 1.12 keeping the same value of a. To study this subject more clearly, we have recently removed the thin shell to change b/a from 1.08 to 1.12. In this paper, we report the first summary of the experiments with this modified version of TPE-1RM20.

2. Change of the front-end system and experimental conditions

Figure 1 shows the original design of the front-end system of TPE-1RM20. The penetration time of the external vertical field of the double-layered thin shell is 7 ms while that of the thick shell is 100 ms. The modification was made by taking out the thin shell. Figure 2 shows the comparison of the typical waveforms of plasma current, I_p, loop voltage, V_{loop},

reversal parameter, F, and pinch parameter, Θ. Figure 2 shows that there is a quantitative difference in V_{loop} while the other quantities are almost unchanged.

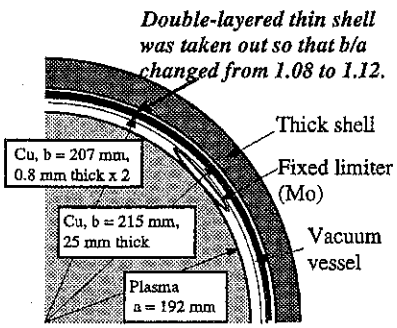

Fig. 1: Cross sectional view of the front-end system of TPE-1RM20

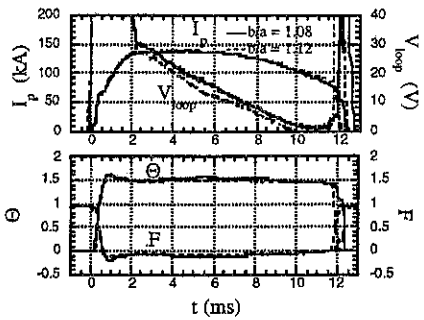

Fig. 2: Typical waveforms before and after the modification

Experiments were conducted after intensive main discharge cleanings. We mainly operated the machine at the 'reference discharge' where I_p = 130-140 kA, F = -0.1 and Θ = 1.5 with an optimized equilibrium control and error field compensation. In this paper, we report the comparison of the confinement characteristics mainly in this reference discharges before and after the modification. We have also studied a role of the shell proximity or a role of the overlapped poloidal gaps in the shell for the locked mode by an externally induced error field. The result is reported in a separate paper in this conference.

3. Experimental results

The first clear difference we noticed is the change in V_{loop}. Figure 3 shows non-inductive loop voltage, R_pI_p, averaged in $t = 4.5 \pm 0.25$ ms (about the center of the current flat-top) in about 500 of reference discharges. It is seen in Fig. 3 that R_pI_p increased by about 40% after the modification. Note that the about more than a hundred of main discharge cleaning shots were necessary to have the well reduced value of R_pI_p in each machine configuration.

Table I summarizes confinement properties such as; central electron temperature, T_{e0}, by a Thomson scattering, ion temperature, T_i, by a neutral particle energy analyzer and line-averaged electron density, n_{el}, by a CO_2 interferometer. Also listed are the apparent Z_{eff}, Z^*, which includes both actual Z_{eff} and an anomaly part in R_pI_p, poloidal beta, β_p, and energy confinement time, τ_E. There are relatively large standard deviations in T_{e0}, Z^*, β_p and τ_E, which are because of the large shot-to-shot deviations in T_{e0} due to the point-wise nature of the measurement both temporally and spatially. In the calculation of Z^*, we used a helicity balance equation to estimate the Spitzer part of R_pI_p assuming parabolic electron temperature profile and spatially uniform $Z_{eff}(r)/Z_{eff}(0)$ profile. The shot-averaged Z^* shows 30% increase after the modification. Since we have no experimental method to estimate absolute value of Z_{eff}

independently, identification of the cause is difficult. However, we discuss three major possibilities for the increment of Z^*, i.e., Z_{eff}, profile of the resistivity and V_{loop} anomaly.

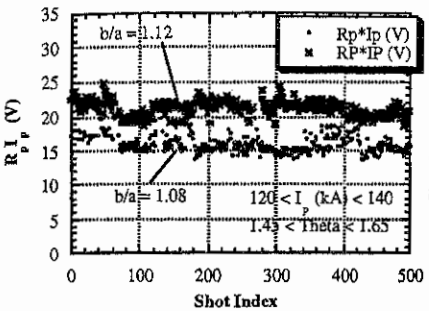

Fig. 3: Non-inductive loop voltage versus shot index

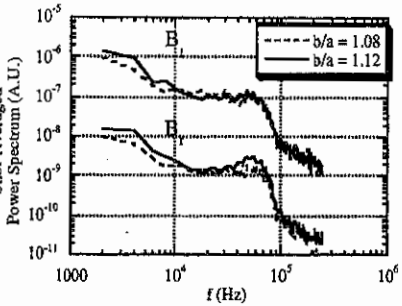

Fig. 4: Power spectrum of B_t and B_r

b/a (shots)	I_p (kA)	F	Θ	R_pI_p (V)	T_{e0} (eV)	Z^*	T_i (eV)	n_{el} ($10^{19}m^{-3}$)	β_p	τ_E (ms)
1.08 (13)	132 ± 7	-0.101 ± 0.01	1.54 ± 0.02	14.9 ± 0.7	541 ± 213	4.2 ± 1.7	352 ± 55	0.95 ± 0.10	0.09 ± 0.02	0.28 ± 0.08
1.12 (18)	142 ± 4	-0.106 ± 0.06	1.56 ± 0.01	21.0 ± 0.5	544 ± 278	5.6 ± 2.9	299 ± 63	1.40 ± 0.11	0.11 ± 0.04	0.22 ± 0.09

Table I : Confinement properties at t = 4.5 ± 0.25 ms of reference shots.

b/a	$(\delta B_r/B_{pa})$	$(\delta B_t/B_{pa})$	$(\delta B_p/B_{pa})$	$(\delta B/B_{pa})$
1.08	$(9.3 \pm 1.1) \times 10^{-4}$	$(8.2 \pm 0.7) \times 10^{-3}$	$(3.9 \pm 0.6) \times 10^{-3}$	$(9.1 \pm 1.9) \times 10^{-3}$
1.12	$(11.3 \pm 1.4) \times 10^{-4}$	$(8.6 \pm 1.4) \times 10^{-3}$	$(3.2 \pm 0.4) \times 10^{-3}$	$(9.2 \pm 2.2) \times 10^{-3}$

Table II : Comparison of r.m.s. of the magnetic field fluctuations measured at +20 mm from the plasma surface in t = 4.5 ± 0.25 ms. Average over 22 reference shots are listed.

Electron density has increased after the modification. It was difficult to reduce the density while keeping the same I_p after the modification. A larger input power and/or larger plasma-wall interaction due to a slight increase of magnetic fluctuations on the plasma surface might enhance the source term in the particle balance equation. The enhanced PWI might have made the profile of the plasma resistivity somewhat narrower than before. For example, a profile change of T_e from $(1-(r/a)^2)$ to $(1-(r/a)^{1.5})$ could enhance Z^* by 30%. Also, Increment of B_r fluctuation as is shown below might enhance the loop voltage anomaly through the edge helicity loss. However, more plausibly, increase of impurity content might be the case. The radiation fraction, P_{rad}/P_{oh}, measured by a bolometer increased by a factor of two from 20 % to 40%.

The ratio of the measure for Z_{eff} for the same T_e, i.e., P_{rad}/n_{el}^2, before and after the modification, has increased by 50% with a large error bar. The increase of impurity could enhance the electron density and Z_{eff}.

Finally, τ_E which includes all the loss channel decreased by 20 ± 10% mainly due to the increase of the loop voltage.

Magnetic field fluctuations are also compared before and after the modification. The three components of the magnetic field are measured by an insertable magnetic probe. Table II shows shot-averaged r.m.s. of each magnetic field component and the total amplitude. It shows 20% increase of δB_r while no clear changes are observed in the other components and the total r.m.s. The shot-averaged power spectrum for B_t and B_r is shown in Fig. 4. It is seen that B_t increases at $f < 10$ kHz while B_r increases in almost all f. Toroidal mode spectrum of the odd component (m=1) measured by the B_t-array on the equatorial plane showed a shift of the dominant modes from n=7, 8 to n=9, 10, 11. Note here that the shielding effect of the vacuum vessel was recovered by a reverse filtering in the FFT process. It is also noticed that the phase velocity of the previously dominant modes (n=7, 8) becomes slower. These modes were studied to be near-axis resonant tearing modes. Resonant surface positions are not very different after the modification since F and Θ are almost the same. The result indicates a close relation between the plasma rotation and the electro-magnetic boundary condition of the plasma. Explanation by a theory remains to be studied for a better understanding of the overall pictures.

4. Summary

The effect of the shell proximity was studied in TPE-1RM20 by taking out the double-layered thin shell to have b/a = 1.12 from 1.08. Though the relative difference of b/a is only 4%, there were finite differences in confinement characteristics and magnetic fluctuations. The results for the reference discharges show the increase of non-inductive loop voltage by 40%. This increase is mostly due to the increase of Z^*, which is plausibly due to the enhanced Z_{eff} due to higher PWI though relation with b/a is unclear. Root mean square of magnetic fluctuation amplitude shows 20% increase in δB_r, while other components are unchanged. Toroidal mode spectrum and phase velocity have change after the modification, indicating a close relation between the plasma rotation and the boundary condition.

References

[1] Gimblett C G, *Nucl. Fusion*, **26** 617 (1986)
[2] Ho Y L and Prager S C, *Phys. Fluids* **31** 1673 (1988)
[3] Alper B, Bevir M K, Bodin H A B et al, *Plasma Phys. and Control. Nucl. Fusion Res. (Proc. 13th Int. Conf., Washington,1990)* Vol.2 IAEA Vienna 431 (1991)
[4] Green P, Barrick G and Robertson S, **B4** 911 (1992)
[5] Yagi Y, Hirano Y, Shimada T et al, *J. Plasma and Fusion Research* **69** 700 (1993)
[6] Yagi Y, Brunsell P, Hirano Y et al, *Plasma Phys. and Control. Nucl. Fusion Res. (Proc. 14th Int. Conf. Würzburg, 1992)* Vol. 2 IAEA Vienna 611 (1993)

Mode Locking From An Applied Stationary Error Field in MST

P. Campostrini, G. Chitarin, and G. Zollino
Consorzio RFX, Padova (Italy)
A.F. Almagri, A.K. Hansen, D.J. Den Hartog, T.W. Lovell, S.C. Prager, J.S. Sarff, and M.A. Thomas
Physics Department, University of Wisconsin, Madison WI (USA)

Abstract

To gain a better understanding of mode locking resulting from magnetic field errors in the reversed field pinch (RFP), a stationary field error has been applied to MST to determine the locking threshold amplitude and dependence on the spatial structure of the field error. Mode locking could be robustly produced by an applied $m = 1$ field error, which is resonant with the core tearing modes. A dominantly $m = 0$ field error did not produce locking. The toroidal loop voltage V_{loop} was not significantly changed by the applied error field nor by the occurrence of locking.

Introduction

A set of experiments was carried out on the MST RFP device [1], in collaboration with RFX personnel, within the framework of the IEA RFP Working Group on Field Errors. The goal was to gain a better understanding of mode locking resulting from magnetic field errors in the reversed field pinch and specifically of the differences in mode locking observed in MST and RFX, two large RFP devices with similar geometric dimensions but different mode locking behaviour [2, 3].

A controlled stationary field error, provided by a toroidally localised set of three saddle coils mounted on the outside surface of the MST conducting shell, was applied in order to induce mode locking away from the poloidal gap.

In normal operation of MST, field errors are controlled through passive techniques to not exceed ~2% of the surface equilibrium field strength. However a few "mode locking" events are observed, always associated with errors at the poloidal gap in the conducting shell surrounding the plasma. In a locking event, a normally rotating, spatially localised magnetic perturbation in the plasma (formed by the coupling of several $m = 1$ tearing modes) slows down and locks underneath the gap, remaining in the same position for the rest of the pulse.

One of the aims of the experiments performed was to investigate the threshold of field error amplitude able to prevent the toroidal rotation of the tearing modes.

Applied error field characteristics

The stationary error field was provided by a toroidally localised set of three saddle coils mounted on the outside surface of the MST conducting shell ~75° from the poloidal gap (at $\phi = 285°$). Each coil consisted of 20 turns. A DC feedback controlled power supply (50 V, 600 A) produced a stationary radial field B_r under the coil with an amplitude $\leq 10\%$ of the equilibrium poloidal field B_θ. The winding was activated long before the plasma was formed, to

allow complete field penetration through the conducting shell. An array of magnetic pickup coils located on the outer surface of the conducting shell was used for measurement of the field error amplitude and structure.

By changing the coil interconnections, a field error with a dominant poloidal mode number $m = 1$ or $m = 0$ spatial structure could be produced. The toroidal mode spectrum was broad but peaked at $n = 11$ and was not strongly dependant on coil connections. The poloidal distribution of the radial component of the field on the coil symmetry plane, at the plasma edge are reported in Fig. 1 for both possible connections of the coil system.

The amplitude of the sinϑ harmonic (m = 1) is as large as 95% of Br at ϑ=90°.

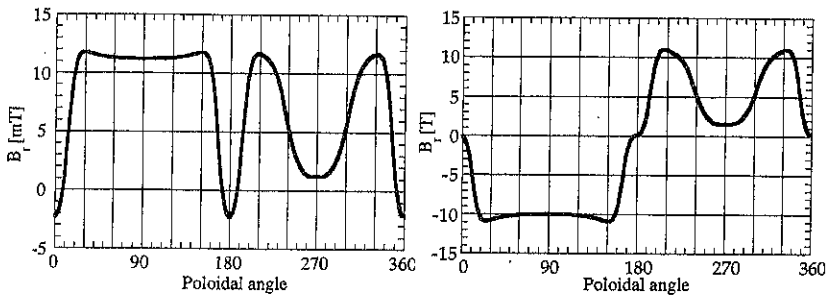

Fig. 1. Poloidal distribution of the radial component of magnetic field @ r/a=0.95, with prevalent m = 0 (a) or m = 1 (b).

Observation and results

Mode locking could be robustly produced by the applied field error, but only with the coils configured for a dominantly $m = 1$ structure; its position was generally underneath the field error coil set.

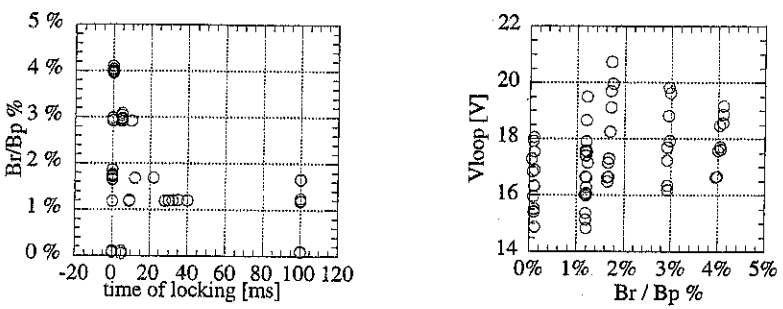

Fig. 2a-: locking time vs. error field Br/Bp% applied (t=100 means no locking).

Fig. 2b: loop voltage Vloop vs. error field Br/Bp% applied

$m = 1$ experiments

The applied error field is quantified as the ratio between the field produced by the external coil at the plasma edge ($r/a = 0.95$, $\theta = 90°$), considering only the $m = 1$ component, and the B_p field at the edge produced by the plasma. Its amplitude was set between 1% and 4% of B_p. The main results of this set of experiments can be summarised as follows:

a) RFP plasma formation was not a problem even in the presence of a large vacuum error field (≥5% of the toroidal field B_φ).

b) For an error field at plasma edge above 3%, mode locking always occurred within the first 10 ms of the start of the discharge; above 4% the discharge was locked from the beginning. When the error field was below 2%, some shots did not lock at all (fig. 2a).

c) The localized plasma magnetic perturbation generally locked underneath the field error coil set, not the poloidal gap.

d) The toroidal loop voltage V_{loop} rose less than 10% when the error field was applied or the modes locked (fig. 2b).

In all MST discharges the amplitude of the core tearing mode fluctuations peaks at sawtooth crashes, independent of the error field applied. The locking events caused by the external error field always occurred during a sawtooth crash at the peak of the fluctuation amplitude. After the sawtooth crash which caused the mode locking the fluctuation amplitude decreased to values close to those observed before the locking event.

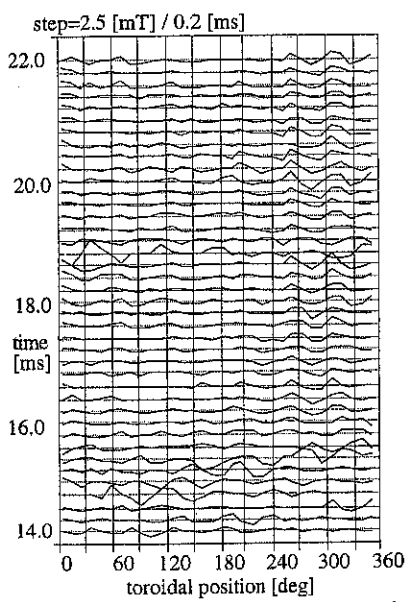

Fig. 3: Plot of Bp-<Bp> vs. toroidal position and time

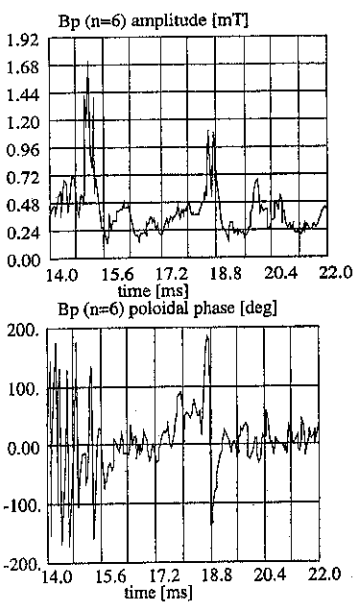

Fig. 4: Mode amplitude and phase around a locking event

Figures 3 and 4 show a typical example of a locking event induced by the applied field error: the Bp fluctuation amplitude is small (less than 0.5% of <Bp>) and the phase first rotates and than locks (at 15 ms in this case). At this moment the amplitude sharply increases (up to 1.5% of <Bp>) and crashes to the value had before the sawtooth. After the crash, the mode phase remains generally locked, even if other amplitude sawteeth events occur.

m = 0 experiments

Application of a predominantly $m = 0$ field error did not lock the rotating modes, presumably because the $m = 0$ error field was not resonant with the $m = 1$ core tearing modes. Even in the presence of a $m = 0$ field error as large as 4% of the main poloidal component Bp the core tearing modes rotate throughout the discharge.

Comparison with RFX

In RFX, the localised magnetic perturbation is always locked to the wall from the beginning of a discharge. When the field error at the gaps is well controlled, the perturbation is locked at random toroidal positions [4]. Locking in RFX causes a macroscopic, usually stationary, perturbation of the magnetic configuration of the plasma column [5].

The prevalent modes are m=1, n = 7-11, no evident sawtooth behaviour is present and the mode amplitude is larger than in MST (around 2% of <Bp>). This could be due to the higher plasma - shell distance, that allows less rigid paths for the magnetic field lines.

Conclusions

The relation between an external stationary field error and the mode locking was investigated on MST. An external m=1 error field is capable of locking the natural mode rotation (which normally occurs at the beginning of the pulse) when the error exceeds 2% of Bp at plasma edge. Sometimes the mode phase locks and then restarts rotation, but in most cases the phase remains locked. The locking events are always related with a mode amplitude increase and crash, but viceversa, the amplitude sawteeth sequence seems to be unaffected when the phase is locked. The locking phenomenology in MST is quite different from that of RFX, where the phase of the major field perturbation never rotates and the mode amplitude remains almost constant during the pulse.

References

[1] S. Hokin et al., "Reversed-field pinch studies in the Madison Symmetric Torus", J. of Fusion Energy 12, 281, 1993.

[2] A. Almagri, S. Assadi, S.C. Prager, J.S. Sarff, and D.W. Kerst, "Locked modes and magnetic field errors in the Madison Symmetric Torus", Ph. of Fluids B 4, 4080, 1992.

[3] A. Buffa et al, "Magnetic Field Configurations and Locked modes in RFX", Proc. of the 21 EPS conference on Controlled Fusion and Plasma Physics, Montpellier, France, Jun. 1994, vol. I, pp. 458 - 461.

[4] P.P. Campostrini, G. Chitarin, M. Guarnieri, N. Pomaro, F. Trevisan: "Methods of Magnetic Measurements in the RFX Fusion Experiment", IEEE Trans. on Magnetics, vol. 31, no.6, Nov. 1995, pp 3158 - 3160.

[5] V. Antoni et al. "Analysis of Wall Locking Phenomena and their consequences in RFX", Proc. of the 22 EPS conference on Controlled Fusion and Plasma Physics, Bournemouth, UK, Jun. 1995.

First reflectometric measurements on a RFP plasma with high density fluctuations

R. Cavazzana, F. Chino, M. Moresco, A. Sardella, E. Spada
Consorzio RFX, c.so Stati Uniti 4, I-35127 Padova - Italy

1. Introduction

Microwave reflectometry has been extensively applied on tokamaks and stellarators [1]. The attempt to apply this technique on a Reversed Field Pinch (RFP) plasma, turned out to be a difficult task due to the presence of strong density fluctuations in the outer plasma region. In this paper the results of a theoretical analysis on the degradation of the reflectometric signal caused by density fluctuations are reported and the estimated requirements to overcome the problem and correctly operate the diagnostic are pointed out. According to this result, part of the RFX homodyne reflectometer [2] has been modified to operate at ultra fast sweep rate (up to 4 GHz/μs) in the reduced range 34-38 GHz. Plasma measurements confirm the adopted criterion and show that correct phase information can be successfully recovered from the reflectometric signal even in presence of strong density fluctuations.

2. Requirements for correct phase reconstruction

The IF signal obtained from an homodyne reflectometer is:

$$s_{IF}(t) = A(t)\cos(\Delta\phi(t)) \qquad (1)$$

where $\Delta\phi$ is the phase difference for the electromagnetic radiation of frequency F, which is reflected at the critical cut-off layer r_c:

$$\Delta\phi(t) = \frac{2\pi}{c} F(t)\left[2\left(d_{vacuum} + \int_{r_0}^{r_c(F)} \mu_F(r;t)dr - \frac{\pi}{2}\right) - d_{reference}\right] \qquad (2)$$

The phase $\Delta\phi$ contains the information about the electron density profile, upon which depends the refraction index $\mu(r)$. The recovering of the phase from the IF signal $s_{IF}(t)$ is straightforward for a static profile, but becomes more complicated or even impossible if the profile is changing during the measurement. To understand the effect of the phase variation on the IF signal, one can consider a totally reflecting layer, placed at an average position d_0 oscillating with a displacement $\delta(t)$. Usually $F(t)$ has a linear law of the form $F(t) = F_0 + \nu_{sw} \cdot t$ with sweep rate ν_{sw} and $\Delta\phi$ can be written as:

$$\Delta\phi(t) = \frac{4\pi}{c}\left(F_0 + \nu_{sw}t\right)\left(d_0 + \delta(t)\right) = \phi_0 + \omega_S t + 4\pi\frac{\delta(t)}{\lambda_0} + \frac{4\pi}{c}\delta(t)\nu_{sw}t \qquad (3)$$

In the static case $\delta(t)=0$ and $s_{IF}(t)$ is a sinusoid with characteristic frequency $\omega_S = (4\pi/c)\, d_0\, \nu_{sw}$, which depends upon the sweep rate ν_{sw}, the geometry of the diagnostic and the average target position, summarised together in the parameter d_0. Considering a limited sweep range the second and third terms in eq. (3) dominate and neglecting the amplitude modulation $A(t)$, it is possible to refer the problem to the well-known theory of FM telecommunications. According to Carson's law [6], the typical spectrum of $s_{IF}(t)$ has a shape of width Bw_{IF} centered around ω_0. The bandwidth Bw_{IF} depends on the bandwidth Bw_δ of the displacement $\delta(t)$ and its amplitude:

$$Bw_{IF} \approx 2 \cdot Bw_\delta (1 + 2 \cdot \gamma \cdot \delta_{r.m.s.}/\lambda_0) \qquad (4)$$

The factor γ depends on the form of $\delta(t)$ and ranges between $\sqrt{2}$ for a sinusoidal signal to 3 in the case of pink noise. It should be pointed out that the IF signal spectrum broadening is always larger than the bandwidth of the phase variation caused by fluctuations.

If the bandwidth of the signal broadening due to fluctuations is higher than the typical IF frequency ($\omega_S/2\pi < Bw_{IF}/2$), the information of the signal phase is lost and the optical path can't be recovered. This situation appears in the time domain as spurious fringe jumps, while in the frequency domain it gives rise to the aliasing of frequencies below zero which distort the signal spectrum. Either points of view show an increase of the signal center frequency, which leads to overestimate the phase difference and consequently the measured optical path. So the phase $\Delta\phi$ can be recovered from the IF signal $s_{IF}(t)$ only if [3]:

$$\omega_S/2\pi > Bw_{IF}/2. \qquad (5)$$

To experimentally determine the value of Bw_{IF} is not necessary to know the details of $\delta(t)$: the bandwidth Bw_{IF} is the same bandwidth of the IF signal measured by the homodyne reflectometer with a constant probing frequency F [3]. The correct value of ω_S to satisfy the condition (5) can be obtained increasing either the sweep rate ν_{sw} or the distance d_0. The latter choice however causes a reduction in spatial resolution. On the contrary changing ν_{sw} preserves the spatial resolution and improves the temporal resolution.

3. The RFX case

During the first period in which RFX reflectometer operated, it was not possible to routinely reconstruct the density profiles. The IF signal level was adequate and the diagnostic correctly measured the maximum electron density [4]. Unfortunately no clear sinusoidal behaviour could be identified in the IF signal. This was very likely due to density fluctuations localised in the outer plasma region. The effect of the fluctuations on the IF signals was evaluated as above mentioned by means of reflectometric measurements at fixed frequency.

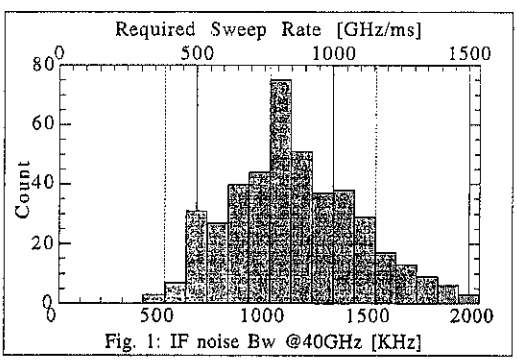

Fig. 1: IF noise Bw @40GHz [KHz]

Fig. 1 shows the histograms of the bandwidth for these signals, along with the minimum sweep rates required to extract correct phase information with d_0=20cm. A sweep rate of at least 1.5 GHz/μs should be adopted to recover most of our measurements.

4. Experimental Set-up

An IMPATT source in Ka band (Hughes 47171H) is modulated between 34 and 38 GHz by our fast IMPATT driver [H], modified to improve S/N ratio. An arbitrary waveform generator (LeCroy 9109) with two channels is used to drive all the system: the analog output of one channel is connected to the IMPATT driver; the digital outputs of the other channel are used to trigger the acquisition system. To achieve measurements at different sweep rates, the generator was programmed to operate during the same plasma pulse with triangular waveforms of a period ranging between 2 and 40 μs. The IF signal is recorded at 250 Ms/s by a digital sampling scope

(LeCroy 9374L) with 8 bit resolution and 8 Mbytes deep memory. A personal computer (Mac IIcx running LabView 3) controls both instruments through an IEEE-488 interface. The acquired signal is then transferred on an Alpha server for subsequent data processing.

5. Plasma Measurements

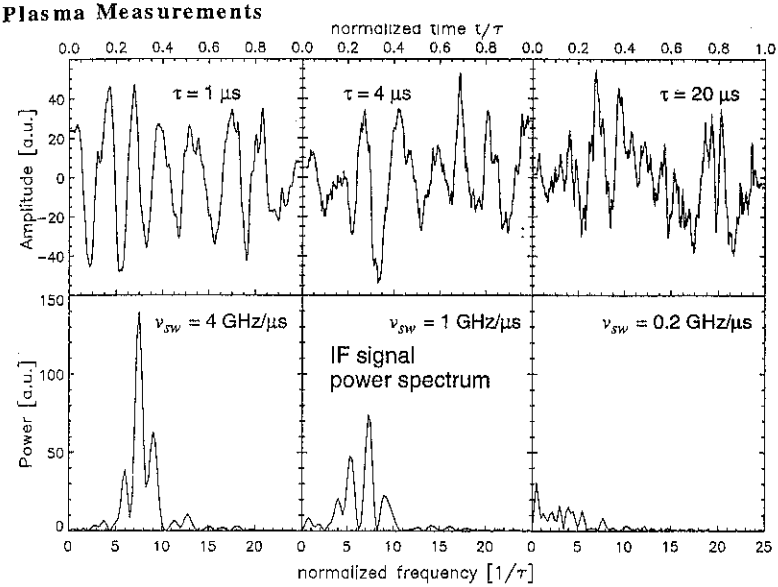

Fig. 2 - Deterioration of the IF signal due to fluctuations with increasing sweep time for a typical RFX discharge.

According to the measurements made at different sweep rates (Fig. 2), a value of 1 GHz/μs (4 μs sweep time), appears to be the lowest possible limit. At this sweep rate however only about the 35% of signals can be recovered, while at 4 GHz/μs more than 70% of signals are useful. The location of the critical density layer was usually found near the first wall in agreement with the flat profile of the present RFX plasma. The time evolution of the average reflection distance (calculated assuming a linear density gradient) is shown for some significant cases (Fig. 3 and 4).

6. Conclusions

In presence of density fluctuations in the region of the density gradient, the reflectometric homodyne diagnostic can give correct results only if the sweep rate is higher then a defined critical value.

[1] Laviron C. et al., Plasma Phys. Control. Fusion **38**, 905-936, 1996
[2] Moresco M., Dubhghaill O. and Spada E., Int. J. Infrared Millimiter Waves **12**, 609, 1992
[3] Cavazzana R. and Spada E., IGI Internal Report FB/71, 1996
[4] Moresco M. et al., Rev. Sci Instrum. **66**(1), 406-408, 1995
[5] Martini S. et al.:21 EPS Conf Control Fus. Plasma Phys. **18B I**, 454-457, 1994
[6] Carlson A. B.: Communication Systems, McGrawHill, 1975
[7] M. Moresco et al., Proc. Int. Conf. Millimeter Submillimeter Waves and Applications II, San Diego, SPIE **2558**, 319-325, 1995.

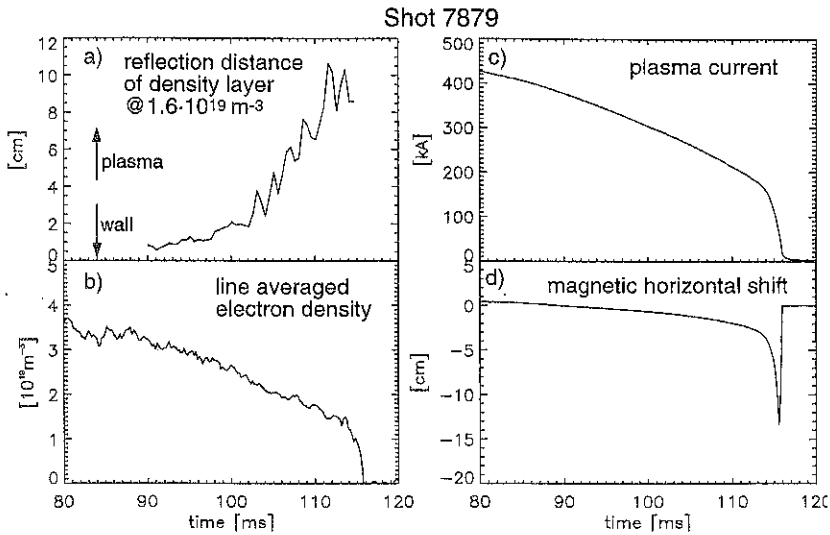

Fig. 3 - Reflection distance measured by the reflectometer (a) while the plasma is moving radially inward during the decay of the discharge.

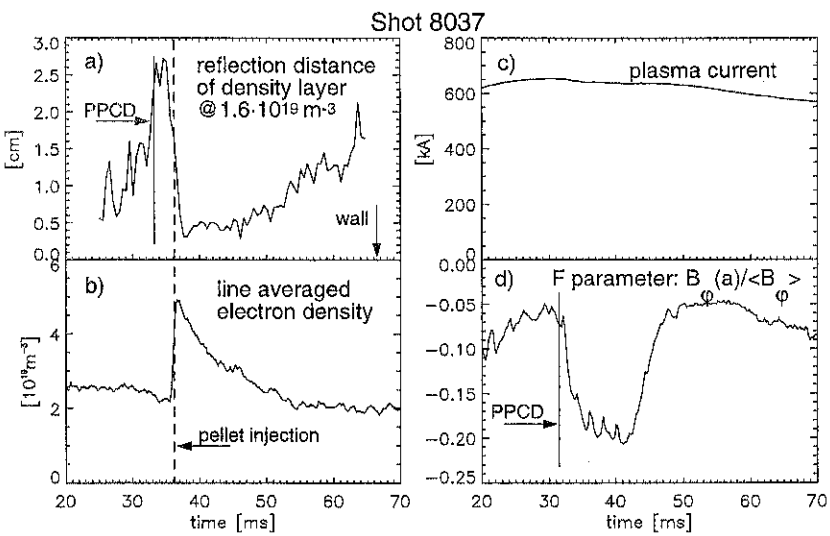

Fig. 4 - Effects of a combined Pulsed Poloidal Current Drive (PPCD) (32 ms), and pellet injection (35 ms).

Fast Flow Phenomena in the MST Reversed-Field Pinch

D. J. Den Hartog, A. F. Almagri, J. T. Chapman, C-S. Chiang, D. R. Craig, G. Fiksel, A. K. Hansen, C. C. Hegna, S. C. Prager, J. S. Sarff, and M. R. Stoneking
Department of Physics, University of Wisconsin, Madison, WI 53706 USA

In the MST RFP equilibrium and fluctuating plasma flow plays a critical role in toroidal flux generation via the MHD dynamo, and rotation and locking of the core resistive tearing modes.

INTRODUCTION—We have obtained these key results from the MST RFP: 1) The toroidal velocity fluctuations of the plasma are coherent with the large-scale magnetic tearing modes; during a sawtooth event the scalar product of $\tilde{v}_\phi$ and $\tilde{B}_r$ is similar to that expected for the MHD dynamo electromotive force. 2) Non-resonant external field errors do not cause magnetic mode locking. 3) Toroidal plasma flow closely tracks the toroidal rotation of the magnetic tearing modes, including the fast changes that occur during sawtooth and locking events. 4) The sawtooth change in mode rotation and plasma flow is not caused by external electromagnetic torque. 5) Plasma flow and mode rotation can be actively controlled, including rotation reversal and unlocking, by modifying E_r with a biased probe or plasma source electrode.

MST is a large RFP with major radius R = 1.5 m, minor radius a = 0.5 m, thick (5 cm) aluminum conducting shell [1], and standard discharge parameters T_e = 230 eV, n_e = 1.0 x 10^{19} m^{-3}, and τ_E = 1.1 ms at I_p = 340 kA. Plasma flow is measured with a fast Doppler duo-spectrometer (≤10 μs time resolution) which has been described in detail elsewhere [2,3]; it is a fiber-optically-coupled grating spectrometer with good luminosity and resolution which simultaneously records two independent chordal views of Doppler-shifted impurity line emission. Usually, measurements are made of the 227.1 nm C v emission (representative of the core ions) or the 229.7 nm C III emission (representative of the edge ions). On the time and spatial scales of interest, these impurities should mimic majority species behavior.

THE MHD DYNAMO—A series of experiments has been carried out in MST, both in the edge [4] and the core, to measure the magnetohydrodynamic (MHD) dynamo electric field parallel to the equilibrium magnetic field. This dynamo arises from the correlation between the fluctuating flow velocity and magnetic field, expressed as the flux surface averaged cross product $\langle \tilde{\mathbf{v}} \times \tilde{\mathbf{B}} \rangle$ [5]. In the RFP, the magnetic field, or plasma current parallel to the field, cannot be fully accounted for by the applied toroidal electric field. This is dramatically evident in the outer region of the plasma where the applied parallel electric field is either zero or actually points in the direction opposite to the observed current. This magnetic field configuration is sustained for times long compared to τ_R, the resistive decay time.

Dynamo activity in MST is most clearly manifested by the sawtooth "discrete dynamo" events [6,7,8]. Sawtooth events occur in MST with periods of 2 - 6 ms, depending on the plasma parameters. Strong spontaneous magnetic field generation is evident in the sudden

increase of toroidal flux Φ_ϕ during a sawtooth crash (at $t = 0$ in Fig. 1). Decreases in the pinch parameter $\Theta \equiv B_\theta(a)/(\Phi_\phi/\pi a^2)$ and the reversal parameter $F \equiv B_\phi(a)/(\Phi_\phi/\pi a^2)$ indicate that, during a crash, the plasma relaxes toward a minimum energy state with a flatter current profile, i.e., current decreases at the core and increases at the edge. Between crashes, a "continuous dynamo" may be operative at a low level.

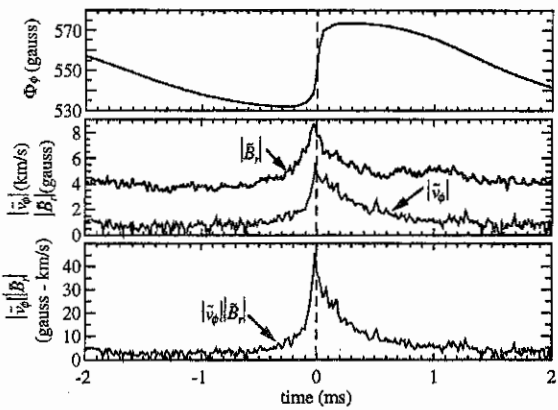

Fig. 1. An ensemble average illustrating the sawtooth change in toroidal flux Φ_ϕ, velocity and magnetic field fluctuations, and the scalar quantity $|\tilde{v}_\phi||\tilde{B}_r|$.

In order to estimate the level of dynamo activity expected in MST throughout a sawtooth period, we have done parallel Ohm's law modeling of the plasma: $E_\parallel = \eta_\parallel J_\parallel - E_{d\parallel} - E_{ind\parallel}$, where $E_\parallel$ is the applied parallel electric field, $\eta_\parallel$ is the parallel Spitzer resistivity, $J_\parallel$ is the parallel current density, $E_{d\parallel}$ is the MHD dynamo term $\langle \tilde{\mathbf{v}} \times \tilde{\mathbf{B}} \rangle_\parallel$, and $E_{ind\parallel}$ is the electric field induced by the evolving magnetic field (the current density profile continuously evolves throughout the sawtooth period). MST does not have a complete set of profile diagnostics, but with reasonable assumptions we obtain estimates of $E_{d\parallel}$ before the sawtooth crash and during the sawtooth crash (Fig. 2). Irrespective of the details, note that the dynamo electric field is expected to be small between sawteeth, but should be very large during the sawtooth flux generation event.

The velocity fluctuations in the core plasma and the core tearing mode magnetic fluctuations exhibit coherence around 15 kHz, indicating that both these quantities are large-scale MHD fluctuations of the order of the plasma size. Both velocity and magnetic fluctuations grow in magnitude and peak at the sawtooth crash, indicating enhanced dynamo activity (Fig. 1). The scalar product of $\tilde{v}_\phi$ and $\tilde{B}_r$ exhibits the sawtooth cycle time variation expected for the dynamo electromotive force in MST, although away from the sawtooth event this scalar product is larger than the dynamo electromotive force predicted by the Ohm's law calculations. However, the

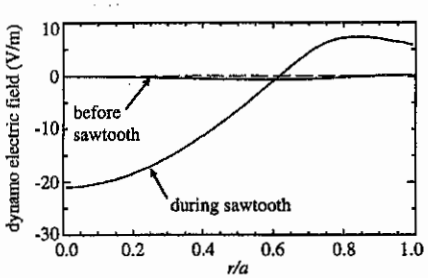

Fig. 2. Ohm's law estimates of the dynamo electric field before and during the sawtooth crash.

full picture requires comparison of these Ohm's law predictions to the actual dynamo product $\langle \tilde{\mathbf{v}} \times \tilde{\mathbf{B}} \rangle$, which includes phase information. Efforts are continuing to measure this product.

PLASMA FLOW AND MAGNETIC MODE LOCKING—Plasma flow, magnetic mode rotation, and radial electric field are tightly coupled in MST. Electromagnetic torques on the resistive tearing modes in the core of MST (m = 1, n = 5-8) are an important determinant of rotation and locking. Such torques may be classified into two types: external, arising from the interaction of a vacuum field error with the core modes [9,10,11]; and internal, from a non-linear interaction of the (m = 0, n = 1) mode at the reversal surface with the core modes [12]. Perhaps the simplest situation to describe is external field error induced locking that occurs between sawtooth events. On MST, we have applied both equilibrium [13] and pulsed field errors to study such locking events. These experiments demonstrated that only m = 1 external errors larger than approximately 2% of edge B_p consistently cause locking. Field errors which are not resonant with the core modes, e.g., m = 0, 2, do not cause locking. The threshold for locking caused by external m = 1 field errors appears to be the point at which the electromagnetic torque induced by the field error is roughly equal to the viscous torque exerted on the tearing mode magnetic islands by the rotating bulk plasma [14]. When a "between sawteeth" locking event is caused, both the core modes and bulk plasma decelerate on a 1 ms timescale, roughly as expected from a momentum diffusion calculation [15].

The behavior of the plasma flow and mode rotation during a sawtooth event is more complex and not simply explained by external electromagnetic braking. In MST, the core modes often (but not always) rotate together at the same phase velocity as a sort of "rigid rotor." The toroidal flow of the core plasma closely tracks the phase velocity of these dominant tearing modes even during sawtooth events. During such events, the deceleration time of the magnetic modes and the plasma is about 100 μs. In normal operation of MST (Fig. 3), between sawteeth the core modes and plasma reach a toroidal velocity of about 20 km/s, in a direction consistent with a positive E_r. At the sawtooth event, the phase velocity of the modes usually drops to a small value, while the plasma decelerates to about 5 - 10 km/s (about the expected magnitude of the ion diamagnetic drift). Typically, the modes do not lock during such sawteeth, but instead slowly accelerate along with the plasma after the event. It appears that external

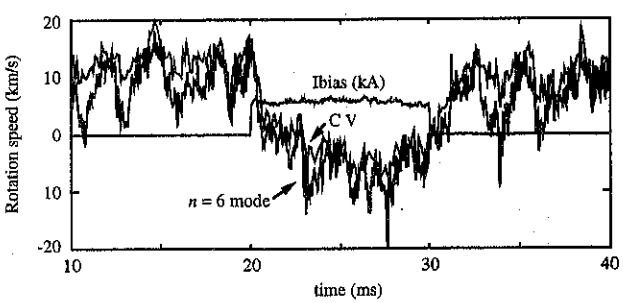

Fig. 3. The rotation of the core modes and plasma during normal operation (10 - 20 ms and 30 - 40 ms) and negative biasing (20 - 30 ms).

electromagnetic torques on the core modes are not responsible for the change in mode and plasma velocities during a sawtooth event, even though the amplitude of the core modes rises dramatically during a sawtooth. External electromagnetic torques can only decelerate the modes toward zero velocity in the lab frame. When the direction of the mode and plasma rotation is reversed from its normal direction by negatively biasing the plasma with either a material electrode [16] or an electrostatic plasma source [17], the magnitude of both the mode and plasma velocities *increases* during a sawtooth (Fig. 3). Therefore, it seems that external electromagnetic torques on the core modes cannot be responsible for the change in mode and plasma velocities during a sawtooth event. It appears that during sawtooth crashes the core and the edge try to match velocity; since the edge velocity is greatly increased by biasing (confirmed by observations of the C^{+2} ions), the core must accelerate during a sawtooth crash. Such coupling of the core to edge may be due to anomalous viscosity associated with increased momentum diffusion during a crash, or it may be due to an increase in the internal electromagnetic torque that couples the core modes to the edge modes. Another part of the explanation may be the acceleration force of the fluid stress term, $\langle \tilde{\mathbf{v}} \cdot \nabla \tilde{\mathbf{v}} \rangle$ [18]. As can be seen from Fig. 2, $\tilde{v}$ peaks during the sawtooth crash, suggesting that this term, which generates equilibrium plasma flow, may be large.

SUMMARY—Both velocity and magnetic field fluctuations peak during a sawtooth crash, indicative of MHD dynamo generation of toroidal flux. Locking is caused by external field errors which are resonant with the core tearing modes; non-resonant errors do not cause locking. External electromagnetic torques do not appear to determine plasma flow and mode rotation during a non-locking sawtooth event.

ACKNOWLEDGEMENT—This work was supported by the United States Department of Energy.

[1] R. N. Dexter *et al.*, Fusion Technol. **19**, 131 (1991).
[2] D. J. Den Hartog and R. J. Fonck, Rev. Sci. Instrum. **65**, 3238 (1994).
[3] J. T. Chapman and D. J. Den Hartog, Rev. Sci. Instrum. **68**, 285 (1997).
[4] H. Ji *et al.*, Phys. Plasmas **3**, 1935 (1996).
[5] S. Ortolani and D. D. Schnack, *Magnetohydrodynamics of Plasma Relaxation*,World Scientific, Singapore (1993), 95-127.
[6] R. G. Watt and R. A. Nebel, Phys. Fluids **26**, 1168 (1983).
[7] S. Hokin *et al.*, Phys. Fluids B **3**, 2241 (1991).
[8] C. C. Hegna *et al.*, Bull. Am. Phys. Soc. **40**, 1874 (1995).
[9] H. Zohm *et al.*, Europhys. Lett. **11**, 745 (1990).
[10] R. Fitzpatrick, Nucl. Fus. **33**, 1049 (1993); R. Fitzpatrick *et al.*, Nucl. Fus. **33**, 1533 (1993).
[11] D. J. Den Hartog *et al.*, Phys. Plasmas **2**, 2281 (1995).
[12] C. C. Hegna, Phys. Plasmas **3**, 4646 (1996).
[13] P. Campostrini *et al.*, these proceedings.
[14] A. K. Hansen *et al.*, Bull. Am. Phys. Soc. **41**, 1408 (1996).
[15] M. Yokoyama *et al.*, Nucl. Fusion **36**, 1307 (1996).
[16] A. F. Almagri *et al.*, Bull. Am. Phys. Soc. **41**, 1410 (1996).
[17] D. Craig *et al.*, Bull. Am. Phys. Soc. **41**, 1407 (1996).
[18] J. P. Wainwright *et al.*, Plasma Phys. Control. Fusion **37**, 1449 (1995).

Improved Confinement and β in an RFP with Reduced Turbulence

J. Anderson, B.E. Chapman, C-S. Chiang, D.R. Craig, **D.J. Den Hartog**, G. Fiksel, N.E. Lanier, S.C. Prager, J.S. Sarff, and M.R. Stoneking
Department of Physics, University of Wisconsin, Madison, WI 53706 USA

Improved confinement has been obtained in the Madison Symmetric Torus (MST) reversed field pinch (RFP) (1) by application of current profile control, (2) spontaneously, subject to constraints on toroidal field-reversal and plasma density, and (3) by application of electrostatic biasing. In all three cases, either or both magnetic and electrostatic fluctuations are reduced. Improved confinement coinciding with reduced turbulence in the RFP is expected, since magnetic fluctuations have been measured to produce large particle [1] and energy transport [2] in the RFP core (roughly defined interior to the reversal surface), while electrostatic fluctuations produce large particle transport in the edge [3,4,5,6]. (The cause of energy transport in the edge remains unidentified.) Here we briefly describe the important observations for each of these three cases of improved confinement in MST.

I. IMPROVED CONFINEMENT BY CURRENT PROFILE CONTROL

Transport in the RFP core [1,2] is caused by m=1, n~2R/a tearing instability-generated magnetic stochasticity. Since these instabilities result from the current density gradient, profile control using electrostatic [7], rf [8,9], or neutral beam [10] auxiliary current drive has been proposed to reduce the fluctuations and improve confinement. In MST, inductive poloidal current drive has been employed for this purpose, resulting in a halving of the m=1 fluctuation amplitude and a four- to five-fold increase in the energy confinement time [11]. A record high MST electron temperature of 600 eV is produced, and beta increases from 6% to 8%. In a conventional RFP plasma, the tearing instabilities produce current in the outer region of the plasma through a dynamo effect; the auxiliary current drive may be viewed as a replacement of dynamo, reducing fluctuations otherwise essential to sustain the RFP equilibrium. Poloidal inductive current drive is inherently transient (related to a changing toroidal flux), and the observed improvements last as long as the current drive is present. We therefore refer to this technique as pulsed poloidal current drive (PPCD).

A key result of PPCD is the reduction of the magnetic fluctuation amplitude to a record low value. The spatial rms magnetic fluctuation $\tilde{b}_{rms}$ measured by a 32-station toroidal array of pickup coils at the plasma surface is shown in Fig. 1, normalized to the equilibrium $B(a)$. The dominant wavelengths that compose $\tilde{b}_{rms}$ are m=1, n=6-10 modes, although the n=6 mode alone accounts for most of the fluctuation during PPCD. Before PPCD is applied, $\tilde{b}_{rms}$ cycles with the sawtooth oscillation (large bursts in the figure) at a cycle-averaged amplitude of $\tilde{b}_{rms}/B(a) \approx 1.5\%$, typical of conventional RFP plasmas. PPCD suppresses sawtoothing, and

the fluctuation amplitude remains small, falling below the sawtooth cycle minimum toward the end of PPCD. The $\tilde{b}_{rms}/B(a) \approx 0.8\%$ amplitude in Fig. 1a is the lowest ever observed in the MST RFP.

In addition to the magnetic field, other quantities show reduced fluctuations during PPCD. For example, the voltage $\tilde{\varphi}$ in Fig. 1b from a floating Langmuir probe at the plasma edge shows a reduction similar to $\tilde{b}_{rms}$. The parallel electric field $E_{\parallel} = \mathbf{E} \cdot \mathbf{B} / B \approx E_{\theta}$ measured at the surface is shown in Fig. 1c to emphasize the relationship of reduced fluctuations and poloidal current drive.

The energy confinement time τ_E increases up to five-fold during PPCD (to ≈5 ms), with both increased stored thermal energy and decreased Ohmic input power. Comparing PPCD and conventional RFP plasmas at the same current I_{ϕ}=350 kA

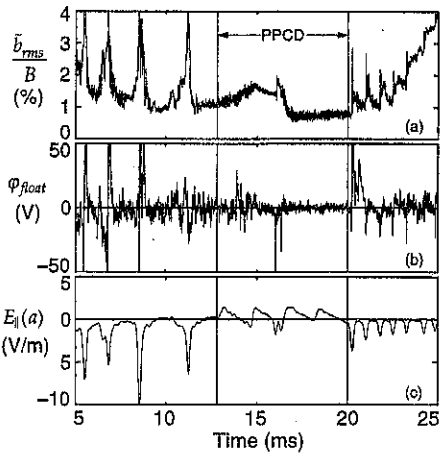

Fig. 1. The (a) spatial rms magnetic fluctuations, (b) edge floating probe voltage, and (c) parallel electric field in a PPCD plasma. PPCD is applied during shaded time span.

and density n=1×10^{19} m^{-3}, the central electron temperature T_{eo} increases from 230 eV to 390 eV, the charge exchange ion temperature is unchanged at $T_i^{cx} \approx 0.5\, T_{eo}$, poloidal beta β_{θ} increases from 6% to 9%, and the Ohmic input power decreases from 4.4 MW to 1.3 MW in an ensemble of 25 plasmas having the lowest fluctuation, as in Fig. 1. The confinement for an ensemble of essentially all 350 kA PPCD plasmas at n=1×10^{19} m^{-3} increases four-fold. Higher I_{ϕ}=440 kA ensembles reach T_{eo}=610 eV, but $\beta_{\theta} \approx 8\%$.

II. SPONTANEOUSLY IMPROVED CONFINEMENT

In some MST plasmas, characterized by large gaps in the usually regular sawtooth period, enhanced energy and particle confinement happens spontaneously [12]. These plasma conditions occur regularly, but subject to constraints of relatively low plasma density, good plasma cleanliness, and relatively deep toroidal field reversal. The energy confinement time improvement can reach three-fold (to ≈3 ms). The conditions for these MST plasmas are similar to those required for the enhanced confinement "improved high-Θ mode" reported for the TPE-1RM20 RFP [13].

Recent measurements [14] of the plasma potential profile and electrostatic fluctuations in the edge of these MST plasmas reveal a narrow, ~1 cm wide region of strongly sheared radial electric field, and the power in electrostatic fluctuations decreases by factors of 10-20 throughout the edge of the plasma. The global m=1 tearing fluctuations are also reduced. The

large, radially sheared electric field (and toroidal plasma flow) with reduced turbulence suggests the mechanisms of sheared-flow stabilization of turbulence might be at work [15]. A distinguishing feature of these plasmas, however, is that the fluctuation reduction includes modes with radial correlation lengths ≥10 cm, much larger than the ~1 cm wide shear layer. This suggests that localized sheared flow might influence non localized turbulence, unlike usual "H-mode" conditions observed in tokamaks and stellerators where small-scale turbulence is suppressed in and nearby the shear region.

The reduction of electrostatic fluctuations in these enhanced confinement plasmas occurs over the entire edge plasma and at all frequencies. Profiles of the fluctuation amplitudes and radial electric field are shown in Fig. 2. These ensembled data are obtained from similar plasmas using movable Langmuir probes. The profile labeled EC is for enhanced confinement plasmas, in which the electric field profile (dashed curve) is highly sheared. The profile labeled standard is for normal RFP plasmas, in which no narrow shear layer is observed. The electrostatic fluctuation power is reduced by a factor of 10 all radii, except for a factor of 20 reduction at r=43.5 cm adjacent to the maximum in the radial electric field. (The limiter radius is a=51.5 cm.) The frequency power spectrum (not illustrated) shows roughly the same factor reduction at all frequencies in the measured bandwidth 1-250 kHz.

Although the electrostatic fluctuation reduction is dramatic, improved energy confinement from reduced magnetic fluctuations is anticipated (measured dominance of $\tilde{b}$-induced transport [1,2]). In the best EC plasmas, $\tilde{b}_{rms}$ approaches the lowest observed in MST (*i.e.*, Fig. 1a). Reduced $\tilde{b}$ in EC plasmas might result from quasilinear edge current profile modifications that occur during new, dominantly m=0 dynamo events observed in EC plasmas [14]. Further measurements are required to understand the relative importance of electrostatic and magnetic fluctuations in these enhanced confinement discharges.

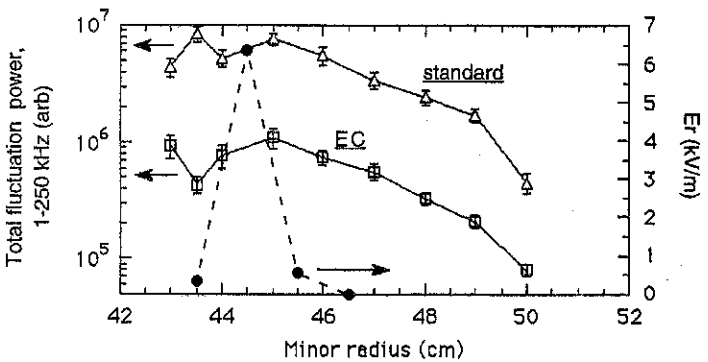

Fig. 2. Radial profiles of the total fluctuation power in the floating potential for the enhanced confinement (EC) case and standard RFP case. The profile of the radial electric field in the EC case is over laid for comparison.

III. IMPROVED PARTICLE CONFINEMENT BY ELECTROSTATIC BIASING

Motivated by MHD computation of dc current injection for RFP profile control [7], electrostatic current injection is being tested in MST. Current injection is achieved by electron current emission from ≤16 miniature plasma sources [16] distributed toroidally and poloidally around the torus. Each source, inserted 5 cm into the plasma edge, is biased with respect to the vacuum vessel and emits ≤1 kA, predominantly parallel to the magnetic field. The injected current returns through cross-field transport processes. By arranging the current injection to produce no net field-aligned current (even number of electrodes, alternating "forward" and "backward" orientation), the effects of electrostatic biasing are observed.

When biasing is applied (source potential ≤350 V), the global particle confinement is observed to roughly double [17]. This is indicated by both an increase in the density and decrease in H_α radiation (particle source) only when the bias is applied. (The plasma produced by the localized miniature sources is not substantially different during biasing.)

A possible cause for the improved particle confinement is turbulence suppression by sheared plasma flow. Clear evidence for strong modifications of the flow exist through Doppler measurements of various impurity charge states concentrated at different radii, and through modifications of the dispersion of magnetic turbulence. The electrostatic turbulence in the plasma edge is measured to decrease in biased plasmas, similar to the spontaneous reductions described above. In this case, however, the sheared flow is probably more gradual over the radii between 5 cm at the edge and is forced by the application of electrostatic biasing. Detailed measurements of flow and turbulence suppression in these plasmas will be reported in the near future.

This work was supported by the United States Department of Energy.

1. M.R. Stoneking, S.A. Hokin, S.C. Prager *et al.*, Phys. Rev. Lett. **73**, 549 (1994).
2. G. Fiksel, S.C. Prager, W. Shen, and M. Stoneking, Phys. Rev. Lett. **72**, 1028 (1994).
3. H. Ji, H. Toyama, K. Miyamoto *et al.*, Phys. Rev. Lett. **67**, 62 (1991).
4. H.Y.W. Tsui, Ch. P. Ritz, G. Miller *et al.*, Nucl. Fusion **31**, 2371 (1991).
5. T.D. Remple, C.W. Spragins, S.C. Prager *et al.*, Phys. Rev. Lett. **67**, 1438 (1991).
6. P.R. Brunsell, Y. Maejima, Y. Yagi *et al.*, Phys. Plasmas **1**, 2297 (1994).
7. Y.L. Ho, Nucl. Fusion **31**, 341 (1991).
8. E. Uchimoto, M. Cekic, R.W. Harvey *et al.*, Phys. Plasmas **1**, 3517 (1994).
9. S. Shiina, Y. Kondoh, and H. Ishii, Nucl. Fusion **34**, 1473 (1994).
10. K. Hattori, Y., Hirano, Y. Yagi *et al.*, Fusion Technol. **28**, 1619 (1995).
11. J.S. Sarff *et al.*, Phys. Rev. Lett. **78**, 62 (1997).
12. B.E. Chapman, A.F. Almagri, M. Cekic *et al.*, Phys. Plasmas **3**, 709 (1996).
13. Y. Hirano *et al.*, Nucl. Fusion **36**, 721 (1996).
14. B.E. Chapman, C-S. Chaing, S.C. Prager *et al.*, submitted to Phys. Rev. Lett.
15. For example, H. Biglari, P.H. Diamond, and P.W. Terry, Phys. Fluids B **2**, 1 (1990).
16. G. Fiksel, A.F. Almagri, D. Craig *et al.*, Plasma Sources Sci. Technol. **5**, 78 (1996).
17. D. Craig, A. Almagri, G. Fiksel *et al.*, Bull. Am. Phys. Soc. **41**, 1407 (1996).

Ion acceleration model in Reversed Field Pinch experiments

S. Costa, R. Paccagnella, M. Viterbo
Consorzio RFX, C.so Stati Uniti 4 - 35127 Padova - ITALY

1 Introduction

The NPA (Neutral Particle Analyzer) reveals the presence of a small population of non-thermal energetic ions ($E = 10^3 eV \div 10^4 eV$) in RFX plasma along the radial direction. Classical mechanisms, based on magnetic reconnection are not able to explain either such ion energies or their radial acceleration.
In this work supra-thermal electrons at the edge are considered to be the free energy source for ion acceleration, i.e. fast electrons, moving in the parallel direction, excite an $\omega \sim \omega_{pi}$ electrostatic wave which damps on ions in the perpendicular direction with respect to the equilibrium magnetic field at the plasma edge.

2 Ion plasma frequency electrostatic waves

The branch of waves we are investigating have frequency $\Omega_{ci} \ll \omega \ll \Omega_{ce}$ and the perpendicular wave number $1/\rho_i \ll k_\perp \ll 1/\rho_e$. Where $\Omega_{c\alpha}$ and ρ_α are respectively the gyrofrequency and the gyroradius of particles of type α.
We treat ions as an unmagnetized isotropic maxwellian population while we consider only the parallel dynamics of electrons [1]. Electrons are known to have two different populations: fast and thermal particles [7]. So we modelize the electron distribution function as the sum of two one-dimensional maxwellians [2].

$$f_e(v_\parallel) = n_0 \left(\frac{m_e}{2\pi T_{e0}}\right)^{1/2} exp\left[-\frac{v^2}{v_{the0}^2}\right] + n_1 \left(\frac{m_e}{2\pi T_{e1}}\right)^{1/2} exp\left[-\frac{(v-u_1)^2}{v_{the1}^2}\right] \qquad (1)$$

where the subscripts 0 and 1 refer respectively to thermal and fast electrons, $n_1 \ll n_0 = n - n_1$ and $T_{e0} \sim T_i \ll T_{e1}$.
The wave-particle resonance condition is

$$\vec{k} \cdot \vec{v}_i = k_\parallel v_{e\parallel} \qquad (2)$$

From the dielectric function it is seen that wave propagation occurs when

$$\frac{\omega}{k v_{thi}} \gg 1; \qquad \frac{\omega}{k_\parallel v_{the0}} \gg 1; \qquad \frac{k_\parallel u_1 - \omega}{k_\parallel v_{the1}} < 1 \qquad (3)$$

If $k_\perp \gg k_\parallel$, an elecrostatic wave at the ion plasma frequency propagates taking parallel energy from fast electrons and being damped in the perpendicular direction by ions. In fact the three contributions to the growth rate, normalized to ω_{pi} and approximating $\omega_R \sim \omega_{pi}$, are

$$\begin{aligned}
\gamma_i &= -\frac{2\omega_{pi}^3}{k_\perp^3 v_{thi}^3} exp\left[-\left(\frac{\omega_{pi}}{k_\perp v_{thi}}\right)^2\right] \\
\gamma_{e0} &= -\frac{n_0}{n}\frac{2\omega_{pe}^2}{k_\perp^2 v_{the0}^2}\frac{\omega_{pi}}{k_\parallel v_{the0}} exp\left[-\left(\frac{\omega_{pi}}{k_\parallel v_{the0}}\right)^2\right] \\
\gamma_{e1} &= \frac{n_1}{n}\frac{2\omega_{pe}^2}{k_\perp^2 v_{the1}^2}\frac{k_\parallel u_1 - \omega_{pi}}{k_\parallel v_{the1}} exp\left[-\left(\frac{k_\parallel u_1 - \omega_{pi}}{k_\parallel v_{the1}}\right)^2\right]
\end{aligned} \tag{4}$$

where the subscripts i, $e0$ and $e1$ refer to ions, thermal electrons and fast electrons respectively.

Taking into account the above approximations, the dispersion relation can be written as (see fig. 1 and 2)

$$\omega_R^2 = \left[\omega_{pi}^2 + \frac{n_0}{n}\frac{k_\parallel^2}{k_\perp^2}\omega_{pe}^2\right]\left[1 + \frac{n_1}{n}\frac{2\omega_{pe}^2}{k_\perp^2 v_{the1}^2}\right]^{-1} \tag{5}$$

For the value of $k_\parallel$ where γ_{e1} is maximum for any value of $k_\perp$, $|\gamma_{e0}| \ll \gamma_{e1}$. In figure 3 is plotted the growth rate $\gamma = \gamma_{e1} - \gamma_i$ as a function of $\omega_{pi}/k_\perp v_{thi}$.
The electrostatic wave is efficiently transferring energy from fast electrons to ions if

$$\Omega_{ci} < \gamma_i(k_\perp) < \gamma_{e1}(k_\perp) \tag{6}$$

since on one hand the gyration motion cannot take ions out of resonance and on the other hand ions cannot damp too quickly the wave. Using (2), this condition reads as

$$2.8 v_{thi} < v_{i,res} < 3 v_{thi} \tag{7}$$

Therefore such a narrow range of $v_{i,res}$ implicates a small density of ions involved in wave-particle interaction which can be determined by calculating

$$\begin{aligned}
n_{i,res} &= n_i\left(\frac{m_i}{2\pi T_i}\right)^{1/2}\left(\frac{m_i}{2\pi T_i}\right)\int_{-\infty}^{\infty} dv_\parallel\, exp\left(-\frac{v_\parallel^2}{v_{thi}^2}\right) \\
&\quad 2\pi\int_{2.8v_{thi}}^{3v_{thi}} dv_\perp\, v_\perp\, exp\left(-\frac{v_\perp^2}{v_{thi}^2}\right) \sim 10^{-4} n_i
\end{aligned} \tag{8}$$

A rough estimate of the energy density transferred by the wave from fast electrons can be done using quasilinear theory [3],[4] as

$$\epsilon \sim n_1 m_e u_1 v_{the1} \sim 10^{20} eV/m^3$$

At most all this energy density is transferred to resonant ions so

$$n_{i,res}\Delta E \sim \epsilon \Rightarrow \Delta E \sim 10^4 eV$$

Finally we address the transfer rate efficiency from fast electrons to the electrostatic wave. Imagining fast electrons to reach the edge by a radial stochastic diffusion [5], we can calculate the time (τ_{cr}) that takes a fast electron to cross the edge region ($\Delta r \sim 10^{-1} m$) and compare it with the time of growth of the instability. We find that

$$\tau_{cr} = \frac{\Delta r^2}{v_{thel} D_{st}} \gg \frac{1}{\gamma_{el}}$$

where $D_{st} \sim 10^{-5} \div 10^{-4} m$. So fast electrons stand in the edge region enough time to feed the wave.

3 Conclusions

Our model assumes that ion acceleration is due to the presence of a current driving fast electron population at the edge of the RFX plasma. The parallel energy of fast electrons is transferred through an electrostatic wave, and accelerates ions perpendicularly to the equilibrium magnetic field to an energy about $10^4 eV$ in accordance with NPA experimental results.
The NPA shows that the mean value of the ratio between fast ions and thermal ions measured as neutral fluxes [6] is $\langle \Delta \rangle \simeq 8.5 \cdot 10^{-5}$ with a dispersion $10^{-6} \leq \Delta \leq 10^{-3}$. Theoretical calculation, employing the mechanism proposed here, leeds to $\Delta \sim 10^{-3}$ which can be considered in good agreement with experimental data, taking into account that the process have an efficiency less than one.
This theory is approximately not sensitive to a change in the model's parameters, in the range of found experimental values, but the mechanism is no longer efficient if the electron distribution function shows a positive slope less steep than the one of a maxwellian [1]. As a result our model is a reasonable candidate to explain fast ion tail.

Acknowledgements
The authors are indebted with Prof. F. Pegoraro for the suggestion of considering the mechanism, here proposed, and for many other helpful discussions.

References

[1] B.Coppi, F. Pegoraro, R. Pozzoli, G, Rewoldt; "Slide-away distributions and relevant collective modes in high-temperature plasmas" - Nuclear Fusion 16 2 (1976)

[2] S. Takeji et al.; "Magnetic fluctuations in the range of ion cyclotron frequency in ULQ and RFP plasmas" - Plasma Phys. Control. Fusion 37 (1995) 1433-1448

[3] N. A. Kraal and A. W. Trevelpiece; "Principles of plasma physics" -(chap. 10 p. 530)

[4] W. E. Drummond, D. Pines, Nucl. Fusion, 1962 Suppl. Part 3, p. 1049, 1962

[5] F. D'Angelo and R. Paccagnella; "The stochastic diffusion process in Reversed-Field-Pinch" - Phys. Plasmas 3 (6), june 1996

[6] Hutchinson; "Plasma diagnostic techniques" (chap. 8 p. 284)

[7] Y. Yagi et al.; "Measurement of super thermal electron flow and temperature in RFX by an electrostatic Electron Energy Analyser" - submitted to Plasma Phys. and Contr. Fus.

Fig.1 $k_{\|} \sim 120m^{-1}$

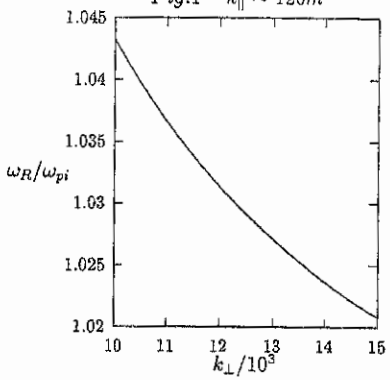

Fig.2 $k_{\perp} \sim 1.3 \cdot 10^4 m^{-1}$

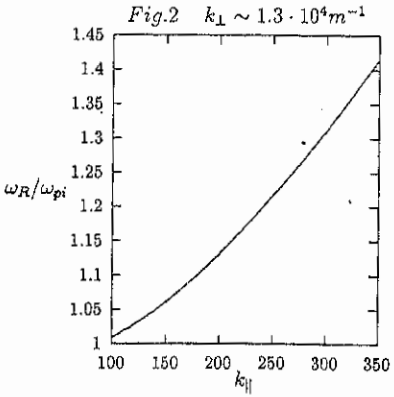

Fig.3 $k_{\|} \sim 120m^{-1}$

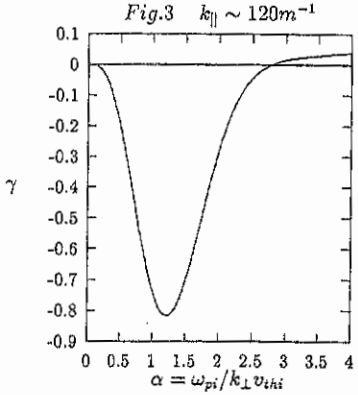

Two Aspects of Poloidal Plasma Current in Various Wave Form of Toroidal Plasma Current on ATRAS RFP Experiment

(Nihon University, Kanda -Surugadai, Chiyoda-ku ,Tokyo,101,Japan)

K. Saito, K. Ikeda, Y. Osanai and S. Shiina

Abstracts: ATRAS is a RFP device (major radius of 0.5 m and minor radius of 0.09 m) which has two independent OH circuits. We can obtain many types of the wave form of plasma current by controlling the discharge time and charging voltage of two OH condensers. In these discharges we can obtain many types of the plasma current wave form and see the many characteristics of the reversed field pinch plasma. We describe here two aspects of poloidal plasma current which maintain the structure of the reversed field pinch plasma. One of which is the reduction of the fluctuation level of the toroidal magnetic field when poloidal voltage is induced sufficiently by linearly decreasing toroidal magnetic flux. The other is surprising experimental result obtained universally on all ATRAS-RFP discharge having various current wave forms. It is that the value of $\Theta/(1-F)$ is almost constant of 1.5.

The reduction of the fluctuation level of the toroidal magnetic field.

The toroidal magnetic field on the plasma surface in usual discharge is shown with plasma current, loop voltage and toroidal magnetic flux in Fig. 1. It is clear that the fluctuation level of the magnetic field dose not reduce in the decaying phase of the toroidal flux. When toroidal loop voltage is added to the plasma which have had the peak of plasma current, the toroidal magnetic flux start to decrease linearly at the time when the loop voltage change the sign on the vacuum discharge and run out abruptly with current disruption as shown in Fig. 2. The loop voltage is low and sustains almost constant between these times. In this phase, fluctuation level of the magnetic field reduce to about 1/4 times of the usual discharge.

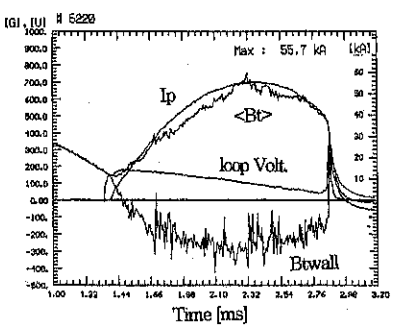

Fig. 1 Current wave form, averaged toroidal field, loop voltage and toroidal field on the plasma surface obtained in usual RFP discharge.

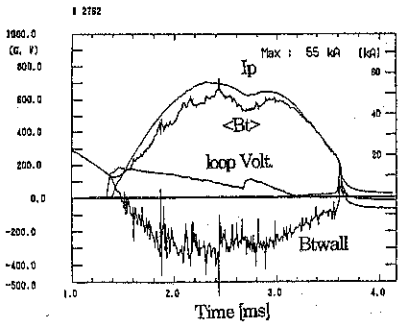

Fig. 2 Each wave form shown in Fig.1 are shown for the discharge which has linearly decreasing toroidal flux.

In these discharges, the fluctuation of the toroidal magnetic field on the plasma surface is analyzed by the wavelet method and the result show that low frequency fluctuation amplitude decreases more and earlier a little than high frequency one as shown in Fig. 3. The bottom three curves show behavior of the confinement field throughout the discharge.

The radial distribution of the poloidal loop voltages which are induced by decreasing toroidal flux is estimated from the assumed distribution (MBFM) of the toroidal magnetic field. Induced poloidal loop voltage increase almost linearly and have sufficient peak to drive the poloidal current calculated from the Spitzer resistivity at the reversal surface, and then it turn to decrease slowly. This shows that sufficient amount of the voltage to drive the poloidal current sustaining reversed field configuration appear in the needed region. These results suggest that a current-drive technique altered toroidal loop voltage which produce poloidal current through the magnetic fluctuation reduce not only the magnetic fluctuation and toroidal loop voltage itself but also the transport.

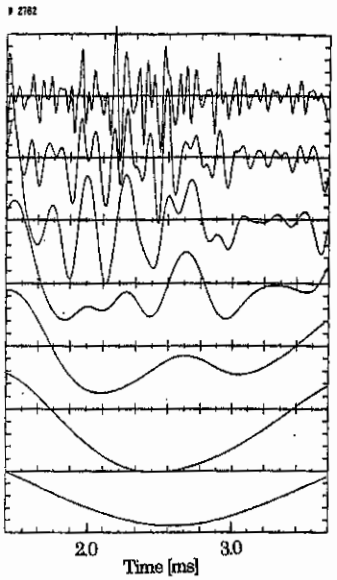

Fig.3. Wavelet analysis for the toroidal magnetic field on the plasma surface obtained by the same discharge of Fig. 2.

$\Theta/(1-F)$ is usually constant for all ATRAS-RFP discharges and in each discharge duration, where Θ and F are pinch parameter and reversal parameter, respectively. $\Theta/(1-F)$ means the ratio of toroidal plasma current, I_p, to toroidal magnetic flux, Φ_p, which is produced by the poloidal current flowing in plasma only excepting the proportional constant $2/(\mu_0 a)$, where μ_0 is magnetic permeability and a the minor radius of the plasma column. That is, $I_p/\Phi_p = \{2/(\mu_0 a)\}\Theta/(1-F)$.

On all ATRAS-RFP discharge ($1.8<\Theta<3.0$), the value of $\Theta/(1-F)$ is constant of 1.5 as shown in Fig.4. Here, the values are shown as a function of the Θ value for 450 discharges of the various current wave form. This value is also maintained to 1.5 excepting the small fluctuations while the RFP configuration is sustaining in discharge of every current wave form and shown in Fig. 5 (a)-(h) with the current wave form, loop voltage, F value and

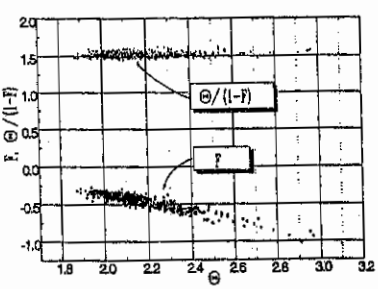

Fig.4. $\Theta/(1-F)$ and F values for various current wave form obtained on RFP discharge. Each point shows those values of each discharge.

Θ value. Fig.5 (a)-(d) show examples of that the values are independent for the current wave form. (a) shows the plasma current and loop voltage for the basic discharge, and (b) the value of Θ, F and Θ/(1- F) for the same discharge of (a). (c) shows a current wave form which is controlled by additional toroidal loop voltage and wave form of the loop voltage. (d) shows that Θ, F and Θ/(1- F) values do not depend on the current wave form. (e)and (f) show time dependency of each values mentioned above. We can see that the Θ/(1- F) value is also constant even if Θ value increase in after half period of discharge. (g) and (h) show the case of that the Θ/(1- F) value is constant for discharge having decreasing Θ value.

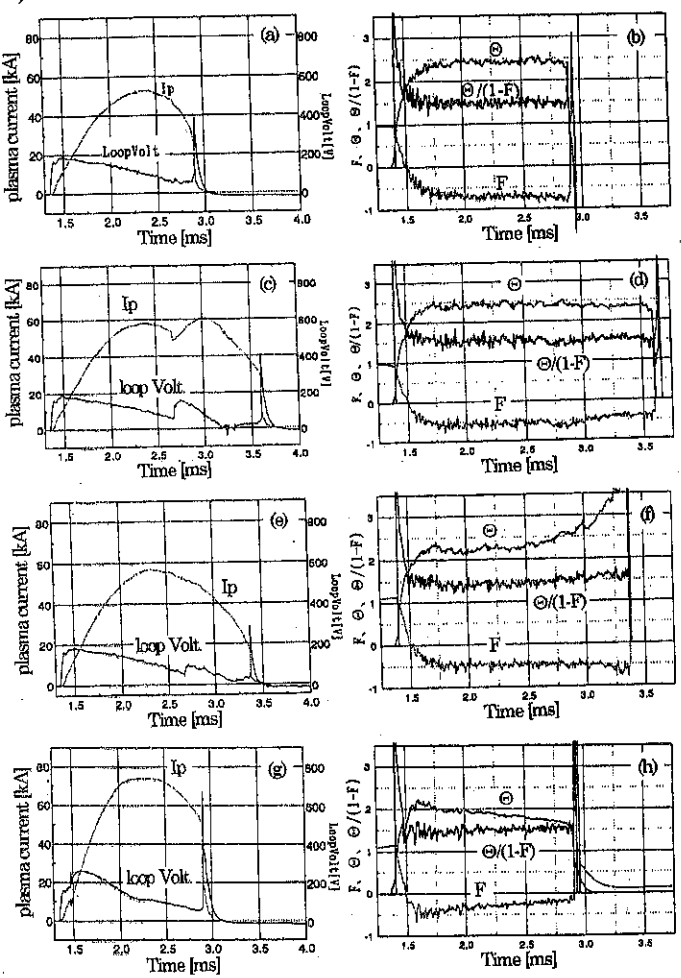

Fig.5. Θ/(1-F) value for the duration of various discharges having different current wave forms (a-d) and behavior of the Θ value (e-f). (a),(c),(e) and (g) show the plasma current and loop voltage for each discharge. (b),(d),(f) and (h) show the Θ, F and Θ/(1-F) value for each discharge.

Many field configurations were examined to explain this strange result of $\Theta/(1-F)=1.5$ ($1.8<\Theta<3.0$). One of the most reasonable configuration is as follows. Pinch following the Kadomtsev's paramagnetic model progress to high Θ($1.6<\Theta<2.0$)configuration with out field reversal. Then uniform negative toroidal field is added to produce a reversed field configuration by using of the toroidal field coil. These profile of the toroidal and poloidal field are shown in Fig.6 (a) ($\Theta=1.6$ at the reversal time and amount of additional field is 15% of the axis). Addition of this field does not change the current distribution produced before and the configuration is not now force free field. We plot the value of $\Theta/(1-F)$ as a function of Θ in Fig. 6 (b), where implicit variable is the Θ value of paramagnetic model and additional field is selected to the value mentioned above which coincide with the experimental result. We can see that $\Theta/(1-F)$ take almost constant value of 1.5 in the same region of Θ($1.8<\Theta<3.0$) obtained in experiment. We show the experimental Θ value at the field reversal time as versus of the usual Θ value in Fig.7. These results show that pinch proceed to the reversal time following the paramagnetic model then reversed by the boundary condition made by the current flowing in the toroidal field coil. Final field configuration is not sustained by the current explained by the paramagnetic model because the field configuration is not force free and that need poloidal current flowing same direction all over the plasma column. We must ask for the other mechanism driving unidirectional poloidal current to sustain static RFP configuration.

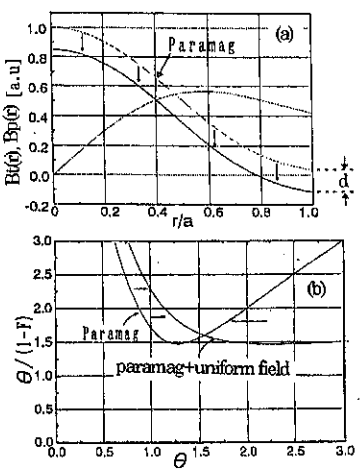

Fig.6. (a) Configuration made by addition of uniform reversed toroidal field (d=15% of the value on axis) to that obtained from Kadomtsev's paramagnetic model. (b)$\Theta/(1-F)$ values calculated from the field as a parameter of Θ.

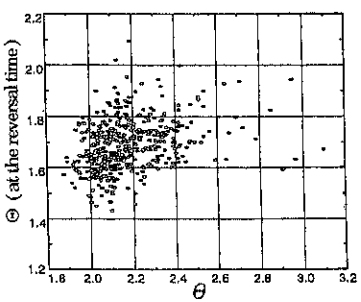

Fig.7. Θ values at the reversal time versus Θ values usually used.

Role of α-particles in Mirror Based Volumetric Neutron Source (FEF-II)

N.Mizuno

Department of Physics, College of Humanities and Sciences, Nihon University
Sakurajousui 2-25-40, Setagayaku, Tokyo, 156 Japan

S.Muramatsu, H.Midorikawa and T.Kawabe
Institute of Physics, University of Tsukuba
Tsukuba, Ibaraki, 305 Japan

Abstract

The behavior of the α-particles in the mirror based plasma neutron source FEF-II studied by use of the numerical simulation. The distribution function and the density of the α-particles by Fokker-Planck equation were obtained. We also studied that the contribution of α-particles to the beta value.

1. Introduction

It is recognized by the fusion community the importance and necessity of the 14MeV neutron sources for development of the fusion reactor materials and also fusion nuclear engineering. We have been proposed the FEF-II as a candidate of the neutron source[1][2]. FEF-II is two-component plasma system (target plasma and high energy sloshing ions). Configuration of magnetic field is formed basically by long solenoid with mirror field at both end. The sloshing ions are produced by oblique injection of NBI in mirror. The α-particles are produced by DT reaction in the two-component plasma. We studied the property of the sloshing ions and estimated the neutron flux in the earlier papers [3][4]. It was shown that the density of the sloshing ions reach 3.3×10^{13} cm^{-3}. We also proposed the plasma parameter for the class of neutron source with a neutron flux of 2MW/m^2.

In the present paper, we study the property of the α-particles in FEF-II by Fokker-Planck simulation. The Fokker-Planck equation for the α-particles is solved with the Fokker-Planck equation for the sloshing ions, simultaneously. We obtain the time evolution of the density and the energy density of the α-particles and estimate the effect of the α-particles to the beta value. We study the dependence of the parameters for α-particles on the electron temperature of the target plasma.

2. Plasma Model

We assume that the target plasma which consists of electrons and the nuclei of deuterium and tritium is isotropic and Maxwellian. The target plasma parameters are assumed to be constant throughout the simulation. The distribution of the sloshing ions is obtained by Fokker-Planck equation. We assume the sloshing ion is deuterium. The tentative parameters of FEF- II are listed in Table 1. The α-particles are produced by target(D)-target(T) reaction and sloshing(D)-target(T) reaction. The Fokker-Planck equation of the α-particles is given by

$$\frac{\partial f}{\partial t} = \frac{1}{v^2}\frac{\partial}{\partial v}\left[v^2\left(Af + D_{//}\frac{\partial f}{\partial v}\right)\right] + \frac{1}{v^2}D_{\perp}\frac{\partial}{\partial \zeta}\left[(1-\zeta^2)\frac{\partial f}{\partial \zeta}\right] + S_{\alpha} \qquad (1)$$

where f is the distribution function of the α-particles, ξ is the cosine of the pitch angle, $A, D_{//}, D_{\perp}$ are the Fokker-Planck coefficients which represent the slowing down, the energy diffusion and the pitch angle scattering, respectively[4][5]. $S\alpha$ is the production term by DT reaction expressed as

$$S_{\alpha} = \{n_D n_T \langle\sigma v\rangle_{DT} + n_S n_T \langle\sigma v'\rangle_{DT}\}\ h(v)\ \phi(\zeta) \qquad (2)$$

where $\langle\sigma v\rangle_{DT}$ is the rate of the DT reaction[4], the first term in the parentheses show the target-target reaction and second term show the target-sloshing reaction, ns is the density of the sloshing ions obtained by the Fokker-Planck equation. h(v) and $\phi(\xi)$ are the velocity and the angular distribution, respectively, of the produced α-particles as follows[5]:

$$h(v) = \frac{1}{4\pi v_{\alpha}^2}\left(\frac{a_0}{\pi}\right)^{1/2}\frac{1}{v}\left\{e^{-a_0(v-v_{\alpha})^2/v_{\alpha}^2} - e^{-a_0(v+v_{\alpha})^2/v_{\alpha}^2}\right\} \qquad (3)$$

with $a_0 = 5\ \varepsilon^0{}_{\alpha}/4Ti$, $\varepsilon^0{}_{\alpha} = m_{\alpha} v_{\alpha}{}^2/2 = 3.52MeV$,

$$\phi(\zeta) = \begin{cases} 1 & (\zeta < \zeta_c) \\ 0 & (\zeta \geq \zeta_c) \end{cases} \qquad (4)$$

where ξc is the cosine of the loss-cone angle.

target plasma density (cm^{-3})	4×10^{14}
ion temperature (keV)	20
electron temperature (keV)	1
plasma volume (cm^3)	9.4×10^4
plasma radius (cm)	10
mirror ratio	3.4
mirror to mirror distance (m)	3.3
magnetic field at midplane (T)	4.7
injection energy of NBI (keV)	100
injection angle of NBI	45°
injection current of NBI (A)	100

Table 1 Tentative parameters of FEF-II

3. Results and Conclusions

We obtain the distribution function of the α-particles in FEF-II by Fokker-Planck equation. In the simulation, the density of the sloshing ions is $2.37\times10^{13}(cm^{-3})$ at steady state. The temporal evolution of the α-particle density and the energy density is shown in Fig.1 (a) and (b), respectively. Fig.2 (a),(b) show the dependence of the density and energy density of the α-particles at steady state on the electron temperature. Fig.3 shows the contribution of the α-particles to the beta value at several value of the electron temperature. It is found that the accumulation of the α-particles in FEF-II does not increase its beta value for the MHD stability criteria, when the electron temperature is lower than a few keV. This assumption is reasonable for mirror confined plasma.

References

[1] T.Kawabe, S.Hirayama, et. al.: Fusion Technology, Nov./Dec. Vol.10, part 2B, (1986) 1102.

[2] T.Kawabe, H.Yamaguchi, N.Mizuno and S.Hirayama: Proc. International Conference on Open Plasma Confinement System for Fusion, (1994) 385.*S*

[3] N.Mizuno, H.Yamaguchi, T.Kawabe, A.A.Ivanov Yu.A.Tsidulko and S.Hirayama: Proc. 20th EPS Conference on Controlled Fusion and Plasma Physics, (1993) II-549

[4] N.Mizuno, S.Muramatsu, K.Tohrisawa and T.Kawabe: Proc. 1994 International Conference on Plasma Physics, Vol.1 (1996) 454.

[5] N.Mizuno, H.Irie and M. Sato: J. Phys. Soc. Jpn. 54 (1985) 1830.

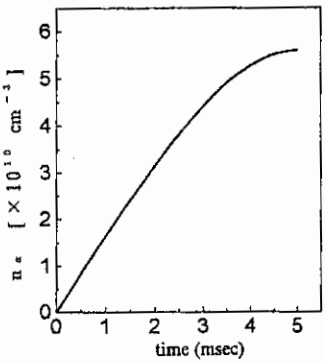

Fig.1(a) Temporal evolution of α-particle density

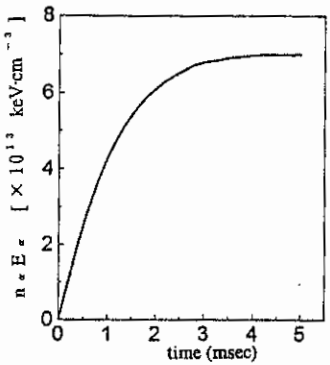

Fig.1(b) Temporal evolution of α-particle energy density

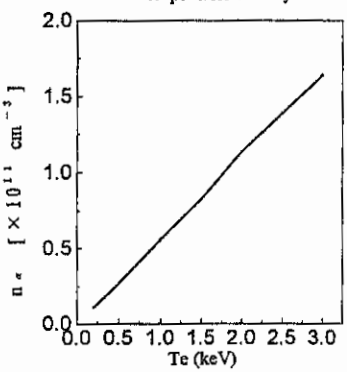

Fig.2(a) Dependence of α-particle density on Te

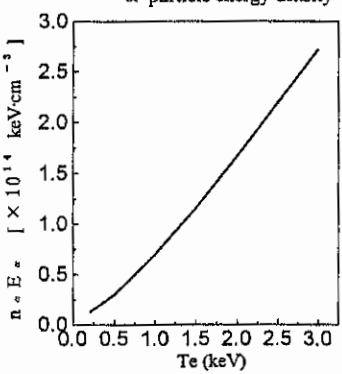

Fig.2(b) Dependence of α-particle energy density on Te

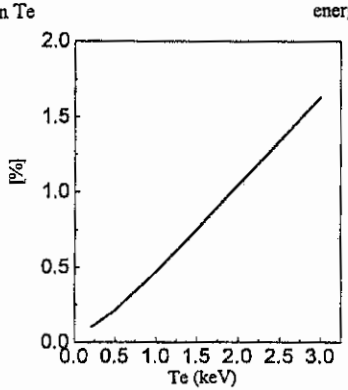

Fig.3 Contribution of α-particles to beta value

High Power Neutral Beam Heating Experiments in the Gas Dynamic Trap.

A.V.Anikeev, P.A.Bagryansky, P.P.Deichuli, A.A.Ivanov,A.N.Karpushov, S.A.Korepanov, A.A.Lizunov, V.V.Maximov, S.V.Murakhtin, K.N.Saunichev.
Budker Institute of Nuclear Physics, 630090 Novosibirsk, Russia.
K.Noack, G.Otto,
Research Center Rossendorf Inc., PO 510119 D-01314 Dresden, Germany.

The Gas Dynamic Trap (GDT) is an axisymmetric mirror device with a high mirror ratio (12.5-100) [1,2]. The plasma confined in the trap consists of two components. The main component is relatively dense and collisional whereas the other, fast ion minority, is collisionless. Fast ions are produced in the trap by 45° NB injection at the midplane. The collisional plasma component serves to stabilize MHD flute modes in the entire trap through feeding high enough density plasma in the external MHD-anchors where the field line curvature is favorable for stability. Experimental program of the GDT is mainly focused on generation of the plasma physics database, necessary for the GDT-based neutron source project [3].

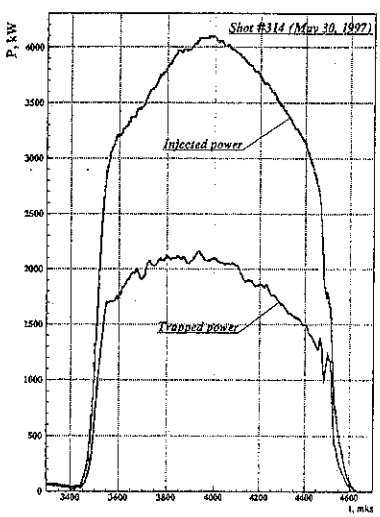

Figure 1: Time evolution of injected and trapped neutral beam power.

The GDT NB-system consists of six injectors [4]. The injectors are arranged azimuthally in the two opposite groups each occupying 90°. Recently, the NB system has been upgraded to achieve higher plasma parameters. The main technical improvements were the following:

1. The ion sources were equipped with additional puffing gas valves which are used to achieve higher gas efficiency of plasma production in the sources. This also enabled us to

obtain a rectangular pulse of extracted beam current rather than triangular as it was in the previous experiments [5];

2. We employed new control system based on transputers that allows more reliable control of the injectors and the other GDT systems;
3. Completely new beam lines were installed. These are designed to have a sufficiently large volume and baffles to increase the gas delay from injectors, so that the gas input into the central cell during plasma shot was reduced to negligible value;
4. Special beam dumps for each neutral beam were installed to reduce gas release from the walls;
5. The NB's power supplies were reconstructed to improve their reliability.
6. The gas puff into neutralizers was optimized to obtain higher neutral fraction of the beam and to reduce gas load from the neutralizers.

The above improvements resulted in a significant increase of the beam parameters and in a considerable increase of their reliability. Special measures were also taken to achieve axial symmetry of the injected power. Equivalent current of each neutral beam was set at 48-55A, so that total currents from the opposite groups of injectors are balanced within an accuracy of 10-20 eq. Amps. The beam energy was varied in the range of 13-16.5 keV and the duration of NB's was set 1-1.2 ms. Under these conditions, the total NB-power exceeded 4 MW (see. Fig.1). The achievable fast ion density was estimated by comparing the previous experimental results [5] with the parameters predicted by Monte-Carlo simulations. These considerations show that if the energy losses would remain on the same level as it was with moderate beam power the maximum density of fast ions should exceed $10^{13}\,cm^{-3}$ and their beta should be greater than 10%.

The first experiments with high-power neutral beam heating in the GDT were carried out in May 1997. The magnetic field at the midplane was set at 0.22 T, the initial mirror ratio was 12.5. The experimental shot scenario was as follows:

1) Initially, plasma gun was turned on and operated during 4ms;

3) The NBs started 2.9 ms after gun turn on;

4) During the NB-operation the mirror ratio increased from 12.5 to 45÷65.

Before the NB injection the radial density profile was close to Gaussian one with characteristic length of 10 cm and a maximum on-axis density of $10^{14}\,cm^{-3}$. It was measured

that 50-60% of the injected power was trapped. At initial stage of injection the target plasma rapidly expanded radially, so that the on-axis density fell down to $5 \div 6 \cdot 10^{13}\,cm^{-3}$. According

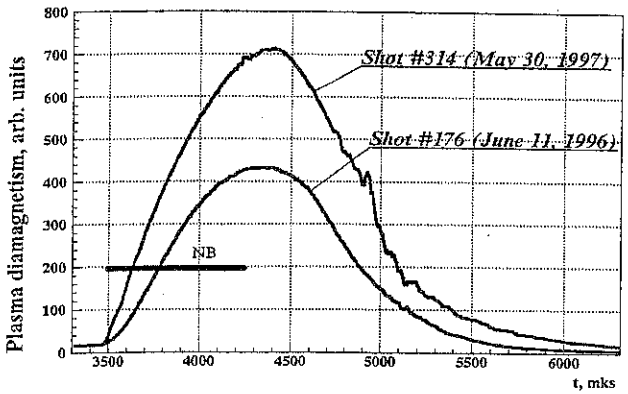

Figure 2: Plasma diamagnetism vs time in the shots before (SHOT 176) and after (SHOT 314) improvement of the NB-system.

to Thomson scattering data the electron temperature was about 70 eV during the gun operation and then increased up to 125eV after the gun was turned off.

The plasma diamagnetism was measured using diamagnetic loop located at GDT midplane. The results are shown in Fig. 2. For comparison, the data are given for the shots before and after the upgrade of the NB-system. It is seen from Fig.2 that the plasma diamagnetism increased by factor of 1.6 which is consistent with the increase of the NB energy deposited to the plasma. Thus it indicates that the total energy confinement time did not change with the increase of NB-power. The time variation of total radiated power and charge-exchange losses of the fast ions is shown in Fig.3. It is important to note, that the losses are negligible compared with the trapped NB-power. The detailed study of plasma parameters in experiments with high power NB- heating is now underway. According to the first experimental results, the achieved parameters of the plasma are as follows:

- density of fast ions - up to 10^{13} cm^{-3},
- mean energy of the fast ions - 3-8 keV,
- total plasma β - up to 15%
- maximum electron temperature – 125±15eV.

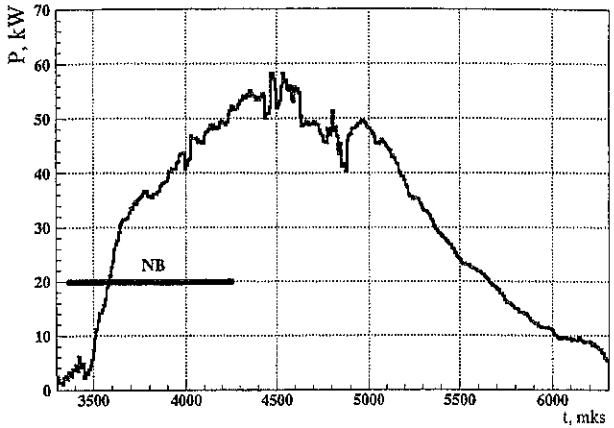

Figure 3: Total charge-exchange and radiative losses

Conclusions

The injected power in the GDT experiment was increased from 2.5 up to 4MW for 1.2ms pulse duration and injected current of about 300 eq.Amp. According to preliminary measurements, the energy content of the fast ions increased by a factor of 1.6 which is consistent with the power increase. Total radiative and charge-exchange losses from the central cell plasma did not substantially increase. They were limited to 2-3% of trapped neutral beam power and, therefore, did not affect global energy balance of the plasma. On the base of diamagnetic measurements and predictions of Monte-Carlo simulations, the fast ion density near the turning points was estimated to be $10^{13}cm^{-3}$. The maximum electron temperature of 125±15eV was measured.

References:

[1] V.V.Mirnov, D.D.Ryutov, Sov. Techn. Phys. Lett., v.5, p.279(1979)

[2] R.F.Post and D.D.Ryutov, Comments Plasma Phys. Controlled Fusion, 1995, v.16, p.375.

[3] A.A.Ivanov, et al., In: Proc. of 17th Symp. Fusion Techn. 2, p. 1394 (Rome, Italy, 1993)

[4] V.I .Davydenko, G.V.Roslyakov, V.Y.Savkin, Voprosy Atomnoy Nauki i Tekhniki-Termoyadernuj Sintez, v.12, 2, p.67 (1983) (in Russian)

[5] A.V.Anikeev, P.A.Bagryansky, E.D.Bender et al., In: Proc. 22nd EPS Conference Controlled Fusion and Plasma Phys., Bournemouth, UK, Cont. Papers, v.19C, part IV, p.193(1995)

Modelling equilibrium magnetic fields with plasma flows in the SPHEX spheromak and tight aspect ratio tokamak

D. M. Willett, P. K. Browning, G. Cunningham, S. J. Gee, K. J. Gibson,
J. Hugill, M. G. Rusbridge and S. Woodruff
Dept. of Physics, UMIST, P.O. Box 88, Manchester M60 1QD, U.K.

1 Introduction

The Spheromak Experiment, SPHEX, [1] at UMIST is a device for magnetic confinement of a topologically spherical plasma. Plasma is expelled from a magnetised Marshall gun into a copper flux conserver, carrying with it the magnetic field generated by the coaxial solenoid. This magnetic field reconnects to form a set of nested poloidal flux surfaces (the closed flux) while current driven on the open flux connecting the gun electrodes generates a toroidal magnetic field. As the plasma relaxes the closed poloidal flux is amplified and a large toroidal current arises which is sustained for ~ 0.5 ms by helicity injection; this phase is characterised by the appearance of an oscillation with toroidal mode number $n = 1$ [2]. The toroidal field may be enhanced by inserting a current carrying rod along the geometric axis and operating SPHEX as a helicity injected tight aspect ratio tokamak. We have written a code to model static equilibria at various rod currents using different forms for $\mu(\psi) = \boldsymbol{j} \cdot \boldsymbol{B}/B^2$, where ψ is normalised to the gun flux; the coefficients are determined by fitting to experimental data. We have also attempted to determine $\mu(\psi)$ with no rod present by direct measurement during intervals of reduced mode activity. The code has been generalised to include the effect of mass flow and further fits made to this data.

2 Static Equilibrium Fits

The time averaged configuration of the plasma is axisymmetric and is ideally described by the Grad-Shafranov equation [3]. Most previous studies of spheromak equilibria have assumed a force free ($dP/d\psi = 0$) configuration with a linear dependence of μ on the poloidal flux; $\mu = \alpha + \beta\psi$. However, internal measurements during sustainment have revealed a sharp drop in μ at the edge of a 25cm diameter region of high potential about the geometric axis. We therefore postulate that a tanh form, $\mu = \gamma + \delta\{\tanh[2(1-\psi)]-1\}$, which can accommodate this drop, may be more appropriate.

We have determined the coefficients for both cases by fitting to time averaged measurements of the internal magnetic fields for a range of rod currents, taken with an insertable probe at the flux conserver equator. The quality of the fit deteriorates as the rod current increases; the tanh fits are no better than the linear fits, though the corresponding μ profiles more closely resemble those measured.

Although the shapes of the q profiles are qualitatively dependent on the form chosen for $\mu(\psi)$ (Fig. 1), we do find that the calculated toroidal current, magnetic energy and total helicity are almost independent of the form of $\mu(\psi)$. The maximum toroidal current on the closed flux is 60 kA for zero rod current (for a gun current of 60 kA). It increases to reach a maximum of 140 kA for a rod current of 50 kA but falls off for higher rod currents.

3 Measurements of μ during Quiescent Periods

Recent work has shown that the $n = 1$ mode becomes intermittent after titanium gettering. We have determined the form of $\mu(\psi)$ during such quiescent periods when the plasma might be expected to be more axisymmetric. $\mu(r)$ was measured using the μ probe [4], whilst simultaneous measurements of the axial magnetic field, corrected to give zero flux penetration of the flux conserver, were integrated to obtain $\psi(r)$. These data were combined to give the plot of $\mu(\psi)$ shown in Fig 2. We found that μ is constant for $\psi > 1$ and rises sharply as $\psi \to 0$. There is no sign of the peak at $\psi = 1.4$ reported in [4] for measurements time averaged over periods of mode activity. Unfortunately, we have insufficient data to determine if μ is constant on a flux surface (i.e. is a unique function of ψ) as the static model requires.

4 Stationary Equilibrium with Flow

We have found that virtually all the current leaving the centre electrode crosses magnetic surfaces and returns via the flux conserver rather than along the open flux to the outer gun electrode — the generalised code incorporating mass flow admits the possibility of such cross-surface currents. The equations describing the axisymmetric equilibrium configurations of an incompressible, flowing, ideal magnetofluid may be reduced [5] to

$$A\frac{dA}{d\psi}\left[\left(\frac{\partial\psi}{\partial r}\right)^2+\left(\frac{\partial\psi}{\partial z}\right)^2\right]-\left(1-A^2\right)\left[\frac{\partial^2\psi}{\partial r^2}-\frac{1}{r}\frac{\partial\psi}{\partial r}+\frac{\partial^2\psi}{\partial z^2}\right]= \frac{1}{2}\frac{d}{d\psi}\left[\frac{F^2}{1-A^2}\right]+\frac{r^2}{2}\frac{d}{d\psi}\left[\frac{M^2}{1-A^2}\right]+\frac{r^4}{2}\frac{d}{d\psi}\left[\frac{L^2}{1-A^2}\right]. \quad (1)$$

$F(\psi)$ and $M(\psi)$ are generalised poloidal current and pressure functions; $A(\psi)$ is the Mach

Alfvén number of the poloidal flow and $L(\psi) = d\phi/d\psi$, the electric potential gradient with respect to ψ.

A simple specification which allows cross-surface currents is A = const and L = const; we tried $M(\psi) = 0$, and set $L(\psi) = -15$, corresponding roughly to the average potential gradient between the geometric axis and magnetic axis. The remaining functions were specified $F(\psi) = F_1\psi + (F_2/2)\psi^2$ and $A(\psi) = A_0$ with the coefficients F_1, F_2 and A_0 to be determined by minimising the difference between magnetic field strengths predicted by the model and measured experimentally with no current carrying rod present.

The best fit to experimental data was achieved when $A(\psi) = A_0 = -0.79 \pm 0.04$, suggesting parallel flow velocities approaching the Alfvén speed in the direction opposite to the sense of the poloidal field. The fit ($\chi^2 = 6.2$) improved somewhat from that obtained using the static model ($\chi^2 = 7.8$). The corresponding μ profiles are shown in Fig. 3.

5 Conclusions

Calculated global quantities such as the toroidal current, magnetic energy and helicity do not vary by more than 10% for different forms of $\mu(\psi)$ and so can be predicted accurately from internal equatorial magnetic field measurements; the q profiles cannot however be reliably determined from such data. A substantial increase in toroidal current on closed flux can be achieved by directly applying additional toroidal field and, for specified gun and solenoid currents, there exists some corrsponding optimum rod current.

The difference between the experimental μ profile averaged over quiescent periods (Fig. 2) and over periods of mode activity is consistent with the existence of a rotating asymmetric current channel which straightens during the quiescent periods.

The inclusion of one free parameter to specify poloidal mass flow permits a closer fit to the magnetic field data and allows a non-zero toroidal field at the flux conserver. This accounts for most of the poloidal current loss to the flux conserver. The model predicts an antiparallel mass flow comparable to the $\boldsymbol{E} \times \boldsymbol{B}$ drift speed resulting in an axial flow velocity (for a density of $4 \times 10^{19}\,\mathrm{m}^{-3}$) approaching $4 \times 10^5\,\mathrm{ms}^{-1}$ *towards* the gun near the geometric axis (Fig. 4).

The relevance of this surprising result is uncertain since our MHD model takes no account of plasma generation and loss processes. Future modelling work will however simulate the effect of non MHD current loss with an additional parameter in the poloidal current function.

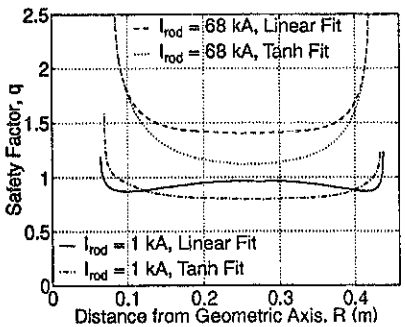

Figure 1: Static fit q profiles for linear and tanh forms of $\mu(\psi)$.

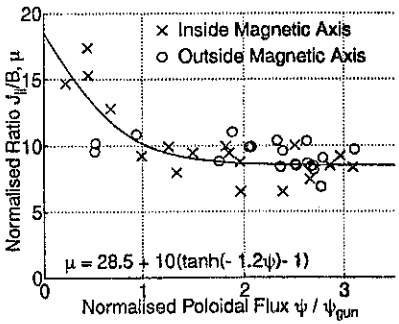

Figure 2: Experimental $\mu(\psi)$ data points with hand drawn tanh curve.

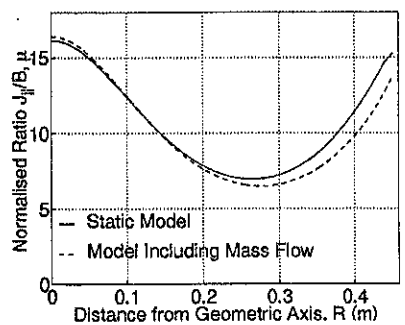

Figure 3: Simulation μ profiles with and without mass flow.

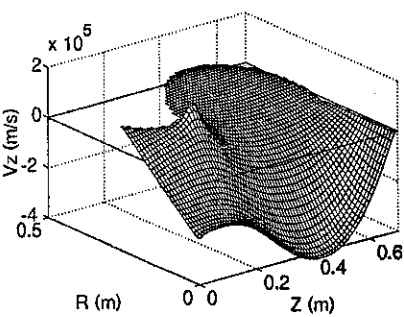

Figure 4: The best fit axial velocity field. Note fast reverse flow near z-axis.

Bibliography

[1] M. G. Rusbridge *et al.*, *Plasma Physics and Controlled Fusion* **39** p. 683 (1997).

[2] R. C. Duck *et al.*, *Plasma Physics and Controlled Fusion* **39** p. 715 (1997).

[3] H. Grad and H. Rubin, Proceedings of the Second International Conference on the Peaceful Uses of Atomic Energy **31** p. 190 (1958).

[4] R. Martin *et al.*, *Plasma Physics and Controlled Fusion* **35** p. 269 (1993).

[5] K. C. Tsinganos, *Astrophysical Journal* **245** p. 764 (1981).

VUV spectroscopic measurements of the impurity content and diffusion coefficient in the spheromak SPHEX

G. Cunningham
Dept of Physics, UMIST, PO Box 88, Manchester M60 1QD

Introduction

Passive spectroscopy of emission from impurity lines is commonly used to diagnose impurity content, but has rather gone out of favour as a technique for determining plasma parameters such as electron temperature and transport coefficient. However, some experiments are not equipped with Thomson scattering diagnostics, and, with care, and with good quality atomic physics data, spectroscopy can produce reliable results.

SPHEX is a spheromak where the plasma current is sustained by injection from electrodes which form a magnetised Marshall gun, by means of magnetic relaxation [3]. For this work, the available spectrometer was a normal incidence VUV instrument covering wavelengths from 60nm to the visible. For most of the impurity species present, this range includes only one resonance line, so that the usual line-ratio method for determining T_e is not possible. We have therefore simply measured the ionisation balance, and use a model to deduce the plasma parameters.

Analysis

With the VUV spectrometer absolutely calibrated, observed line intensities are fitted to an impurity transport model, by adjusting the model's free parameters, which are: $T_e(0)$, the central electron temperature, $D_\perp$, the radial diffusion coefficient for impurities, F_O and F_C , the flux of neutral oxygen and carbon from the wall. The model solves the diffusion equation in one dimension, using toroidal coordinates. It is time-dependent, and uses ADAS data (metastable resolved) for ionisation rates and emissivities [5].

Reliability of the fit

For the first (left hand) set of data shown in figure 1, the 'best fit' is obtained with

$$\begin{aligned} T_e(0) &= 30\ \text{eV} \\ D_\perp &= 1.41\times10^{6}\ \text{cm}^2\ \text{s}^{-1} \\ F_O &= 3.4\times10^{18}\ \text{cm}^{-2}\ \text{s}^{-1} \\ F_C &= 1.1\times10^{18}\ \text{cm}^{-2}\ \text{s}^{-1} \end{aligned}$$

and it is reassuring to note that the total radiated power for this model is within a factor 2 of the observed power.

To estimate the uncertainty in these parameters, we 'randomise' the observed intensities (σ = factor 2) and re-run the fitting algorithm. The variance in $T_e(0)$ and in $D_\perp$ is much less than in the observed intensities, and for the fluxes it is about the same. Therefore the estimates of these parameters are quite precise, even if there are significant

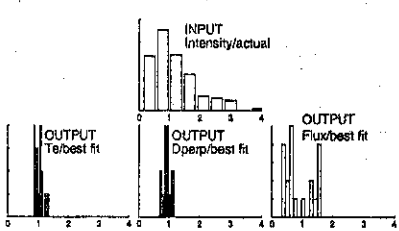

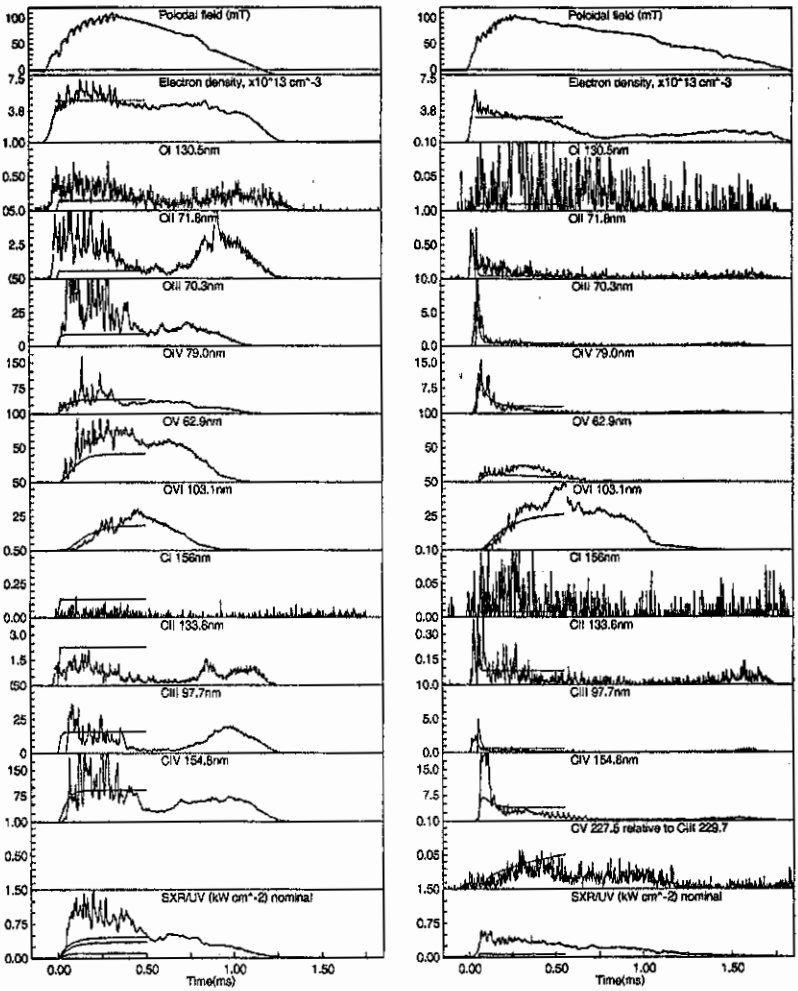

Figure 1: Typical shot data, as indicated. The data on the left is recorded under standard conditions, those on the right are for identical conditions except that titanium is evaporated onto the plasma-facing surface. The top traces are poloidal field at the edge of the plasma, which is approximately proportional to plasma current. The spectrometer data are line-integrated emissivities, units 10^{18} photons cm^{-2} s^{-1}. The bottom trace is from a SXR/UV photodiode, which functions as a bolometer. Overlayed on each is the result of the model calculation. The 3 lines shown for the modelled SXR/UV signal are, in increasing order, for carbon, oxygen, and their sum.

calibration and other errors in the observed intensities.

Nevertheless, this kind of technique cannot be applied as a 'black box'. For the data set on the right of figure 1 (obtained by evaporating titanium onto the plasma-facing wall), fitting the model to the oxygen line intensities gave $T_e(0) = 90$eV, but very weakly constrained, as this trial illustrates. The problem is that the O^{5+} and O^{4+} intensities do not vary much with T_e in this region.

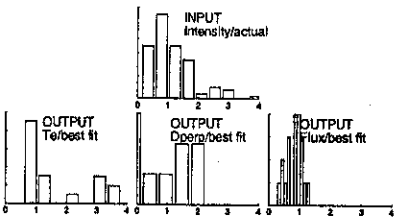

$T_e(0)$	ratio
40eV	271
50	37
55	19
60	11

However, the C^{4+} intensity *does* vary strongly, so we can get a reliable T_e by comparing C^{4+} 227.1nm with C^{2+} 229.7nm. The observed C^{2+} signal is 27 times the C^{4+} signal, whereas the modelled ratios areas shown here , almost independent of $D_\perp$. The 'best fit' T_e is clearly 53eV.

We can then go back and use this value to determine $D_\perp$ from the oxygen ionisation balance, with the following result:

$$\begin{aligned} T_e(0) &= 53 \text{ eV} \\ D_\perp &= 2.1\times10^{5} \text{ cm}^2 \text{ s}^{-1} \\ F_O &= 2.5\times10^{17} \text{ cm}^{-2} \text{ s}^{-1} \\ F_C &= 4.8\times10^{16} \text{ cm}^{-2} \text{ s}^{-1} \end{aligned}$$

Line ratio

We can check this temperature using a line-ratio measurement with O^{5+} ; the observed ratio for O^{5+} 381nm:103nm is 1.1×10^{-5}. This is plotted against the theoretical ratio, and intersects at $T_e = 51.5$eV, a remarkably good agreement.

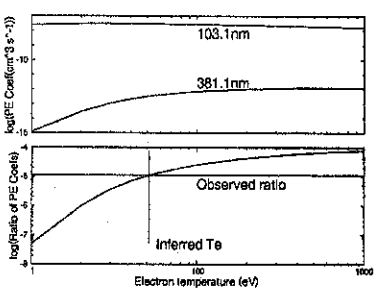

Discussion

- By considering a wide range of ionisation states, and by careful analysis, it has been possible to obtain reliable values for the electron temperature and the average impurity diffusion coefficient from spectroscopic measurement of the ionisation balance.
- In the ungettered condition, the impurity content in SPHEX is high, $\frac{n_i}{n_e} \simeq 10\%$, of which at least 50% is oxygen and carbon. At least half of the oxygen influx and two thirds of the carbon influx is recycling from the flux conserver wall rather than directly from the Marshall gun. This fraction is in the same region as the figure of 1 to 4% oxygen obtained in a similar sized version of CTX [1], who also conclude that 'the power and impurity levels are consistent with radiation still dominating the the global power balance in the first 100μs of the discharge' (the discharge appears to be decaying after this time).
- It should be noted that this is not the whole story on energy confinement in relaxed state devices; many experiments, reviewed by [2], have shown that at least as much power can go directly from magnetic fluctuations into ion heating, being lost mainly by charge exchange. Indeed, if radiation were the main energy loss channel, the decay time of the current would be substantially longer than is observed – other likely loss channels include edge losses which are tightly coupled to the central plasma by magnetic relaxation, as observed on other relaxed state devices, see [2] and [4].
- Application of titanium reduces the electron density and the impurity fraction to 3%, and increases the electron temperature. However its greatest effect is to reduce the impurity transport, by a mechanism which is not clear, but may include creation of more favourable pressure profile, reduced viscosity, or reduced turbulence.

Acknowledgements

I am indebted to Dr. P. Carolan (UKAEA Culham laboratory) for loan of the VUV spectrometer, and to Prof. H. Summers for access to the ADAS database. SPHEX has been funded by EPSRC, and ADAS is part of the JET Joint Undertaking, funded by Euratom.

References

[1] C W Barnes et al. Spheromak formation and operation with background filling gas and a solid flux conserver in CTX. *Nuclear Fusion*, 24:267, 1984.

[2] T R Jarboe. Review of spheromak research. *Plasma Physics and Controlled Fusion*, 36(6):945, 1994.

[3] M G Rusbridge et al. The design and operation of the SPHEX spheromak. *Plasma Physics and Controlled Fusion*, 1997. in press.

[4] J S Sarff et al. Increased confinement and β by inductive poloidal cuurent drive in the reversed field pinch. *Physical Review Letters*, 78:62, 1997.

[5] Summers and Wood. Ionization, recombination and radiation of impurities in plasmas. Technical Report JET-R(88)06, JET Joint Undertaking, 1988.

The Optimization and Design of a Small Aspect-Ratio Torsatron-Tokamak Hybrid (EPEIUS)

D. W. Ross, Huang He, W. H. Miner, Jr., P. E. Phillips,
P. M. Valanju, J. C. Wiley, **A. J. Wootton**, and Shao-Bai Zheng

Fusion Research Center, The University of Texas at Austin, Austin, Texas 78712, USA

Abstract. Studies for EPEIUS, a planned small aspect-ratio torsatron-tokamak hybrid, based on a concept developed at the Oak Ridge National Laboratory, are presented. We investigate magnetic geometries with aspect ratio $A \lesssim 3$, and an externally imposed rotational transform $\iota_{ext}(r)$ which decreases with increasing minor radius (i.e. uniquely tokamak-like), in a device with major radius $R_0 \approx 0.5$ m, toroidal field on axis $B_\phi \approx 1$ T, auxiliary heating and toroidal plasma current $I_p \lesssim 150$ kA.

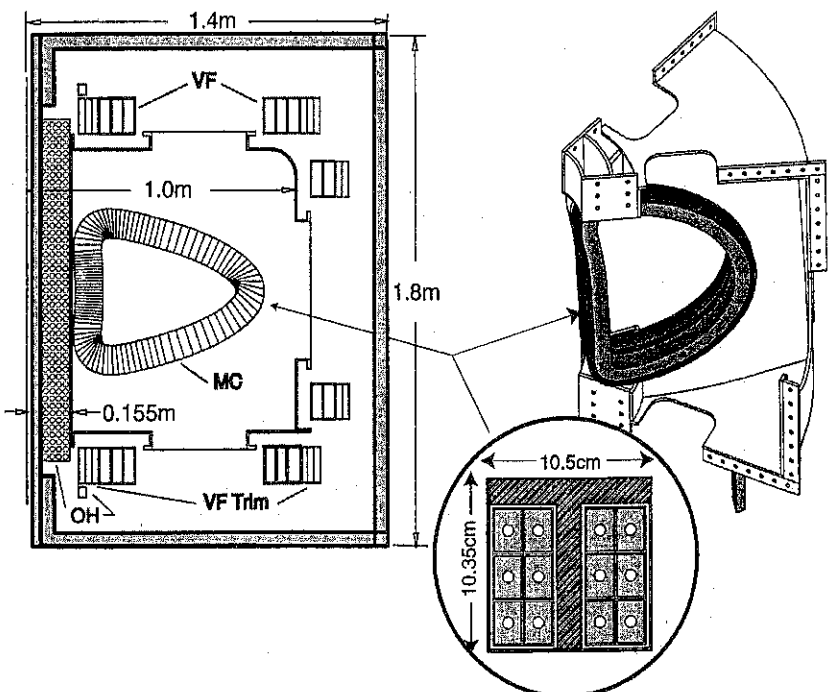

Figure 1. An elevation dimension view of EPEIUS, with details of the modular coils.

Fusion oriented motivation. The requirements that a low-A 3-dimensional system must satisfy, in addition to those common for normal-A systems, are 1) the coils must allow for a nuclear blanket, 2) they must operate at large β (introducing I_p to make a torsatron-tokamak hybrid has been proposed as one means to achieve this), and 3) neoclassical losses must not

exceed anomalous losses, or conclusions concerning reductions in size are negated. This is usually considered to imply strict optimization of the magnetic geometry. An alternative solution is to develop a partial magnetic optimization, and to rely on radial electric fields E_r for thermal plasma confinement. This is the SMARTH concept [1-5]. We envision a reactor-development path in which very low A is achieved with partial magnetic optimization sufficient for alpha-particle confinement in the very low collisionality regime. The alphas will have closed trapped particle orbits with excursions Δr_α such that the diffusion coefficient is $D_\alpha = (\Delta r_\alpha)^2 \nu_\alpha$ and the confinement time can exceed the slowing-down time (ν is a collision frequency). The thermal plasma, on the other hand, will be nominally in the $1/\nu$ regime, even with closed orbits, thus requiring naturally occurring or driven E_r to enter the ν/E_r^2 regime. This scenario has the added benefit of providing an ash-removal mechanism: after the alphas give up most of their energy they enter the $1/\nu$ regime and are lost before being affected by E_r. The ultimate objective is to design a compact reactor: will it be a torsatron, tokamak, or hybrid?

Optimization studies. We seek the lowest possible aspect-ratio toroidal device consistent with robust flux surfaces, stability and good confinement. Our premise is that the ultimate "generalized optimization" will not depend on the magnetic configuration alone, but will require some aspects of both tokamaks and stellarators.

As a first experimental step, to study thermal transport, we propose EPEIUS [5]. The basic eight fold symmetry, eight coil configuration was chosen from initial studies as a compromise between magnetic ripple, ϵ_{eff}, coil construction simplicity and diagnostic access. It still has large ripple, with an unfavorable poloidal gradient. Calculations at low-A employing the longitudinal bounce invariant $J = \oint m v_\parallel dl$, or an approximation J^* [6], can result in unconfined orbits [3], so that energetic trapped particles will be lost and radial diffusion will be large. E_r can drastically improve the confinement, however [3]. According to Monte Carlo and simplified transport calculations, our basic case yields interesting plasma parameters with confinement enhanced by the naturally occurring E_r.

The magnetic field of EPEIUS is generated by four separate coil systems, shown in *Figure 1*. The physics design studies focussed on the modular coils whose purpose is to generate the main toroidal field and a tokamak-like ι profile decreasing from about 0.3 on axis to 0.1 at the edge and having a magnetic well. The low ι at the edge helps generate a robust field structure. On a given flux surface, the field lines have a relatively higher pitch at the outside which is thought to help stabilize ballooning modes. We chose a coil parameterization that conveniently allows us to describe the necessary central hole for the central solenoid (the OH winding, for I_p). It is composed of three components: 1) an inner helical region which allows the coil to be closely fitted about the solenoid and to be wedged for support, 2) the outer curve which is described in terms of the ellipticity and triangularity, κ and δ, which describe the plane curve and $\sin\theta$ and $\sin 2\theta$ components which describe the rotation and twist out of the plane, and 3) a 3D Hermite cubic which smoothly joins the components to reduce mechanical stresses. In what we call "local optimization" we varied the coil parameters to obtain vacuum configurations

that have a magnetic well, moderate ripple, a rotational transform profile decreasing toward the edge, and a large plasma volume (low A).

Surface resilience. We have addressed the quality of the flux surfaces due to realistic current distributions in the windings, the effects of current feeds and crossovers, and the effects of manufacturing and assembly errors. We also asked what level of stochasticity could be tolerated at the edge. The criterion that the transport from any stochastic layer should be smaller than that due to other processes implied that the field should have a radial displacement of < 1 cm in 400 toroidal transits. Construction and assembly errors were investigated by moving a single coil radially, vertically, and toroidally. Large radial displacements (> 5 mm) clearly generated an $m = 5$ island at the $\iota = 0.2$ position (about half way out in r) but position errors in the 1-2 mm range did not generate islands or stochastic regions that exceeded the criterion. While orientation of winding cross section and feed location clearly affect plasma size, the conclusion was that construction and assembly tolerances of < 2 mm are adequate.

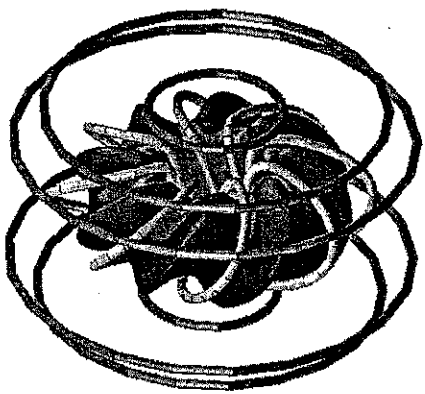

Figure 2. An outer flux surface obtained using the coils shown, computed by VMEC. Courtesy of D. Spong

Finite current and beta equilibrium. MHD equilibrium were calculated with VMEC [7] to determine the effects of I_p and β. Figure 2 shows an example, together with the modular and vertical field (B_z or VF) coil positions. Varying I_p, we can change EPEIUS from a torsatron ($Ip = 0$ kA) to a hybrid (20 to 60 kA) to a tokamak (100 kA). Even a small current allows significant variations in R_0, ι, equilibrium and MHD stable β [8]. The ι profile, helical ripple, R_0, A, and equilibrium and maximum stable β can be varied by using the three extra controls: I_p, B_z, and B_ϕ. The toroidal field (TF) coil allows the ι profile and the ratio of helical to toroidal ripple to be varied. The VF and OH coils allow the magnetic well depth to be varied. Many issues such as β limits, disruption control, and the role of helical ripple in transport can be systematically studied using this flexibility. We expect to access densities $> 5 \times 10^{19} m^{-3}$ [9].

Transport estimates. We solve the standard 1-D equations describing particle and energy transport, together with the ambipolarity condition, allowing for thermal and prompt losses.

For an example we take $I_p = 0$, $B_0 = 1\,\mathrm{T}$, $a = 0.17\,\mathrm{m}$, $R_0 = 0.51\,\mathrm{m}$, a broad density profile with $n_0 = 2.0 \times 10^{19}\ \mathrm{m}^{-3}$, centrally deposited power to electrons = 240 kW, and that to ions = 170 kW. The resulting ion-root temperatures are $T_{e0} = 440$ eV and $T_{i0} = 350$ eV, $E_r = -12$ V/cm at $r/a = 2/3$, confinement times are $\tau_{Ee} = 0.8$ ms and $\tau_{Ei} = 1.8$ ms, so that $\tau_E \approx 1.1$ ms. This is consistent with the ISS95 [10] and Lackner-Gottardi [11] scaling relations, which give 1.2 and 0.9 ms, respectively. The helical collisionalities in the core are $\nu_e^* \approx 0.05$ and $\nu_i^* \approx 0.005$.

Experimental program. EPEIUS is intended to answer the following questions:

- Can torsatron and torsatron-tokamak hybrid plasmas with acceptable magnetic surfaces operate at $A < 3$? No other machine design exists to do this.
- Can E_r ameliorate the neoclassical confinement consequences of the helical magnetic ripple? Can E_r be controlled? Can an H-mode be achieved?
- What are the tearing- and kink-mode stability properties associated with the particular combination of rotational transforms? The external transform profile is unique.
- How do confinement properties relate to local MHD stability?

In addition, the following more generic physics questions and issues can be addressed:

- Can an externally imposed ι profile decreasing with minor radius suppress disruptions in tokamaks?
- With a driven I_p simulating a bootstrap current (either peaked or hollow), what are the implications of a bootstrap current for tearing- and kink-mode stability?
- What are the effects of E_r and its gradients on anomalous transport?
- How do turbulence and anomalous transport compare among torsatrons, hybrids and tokamaks, i.e. with a plasma current varying from 0 to 150 kA ?

Conclusions. We have designed a compact torsatron-tokamak hybrid, with expected performance in the ion root comparable or greater than the predictions of present day scaling relations. We think that essential studies of the plasma thermal transport and stability with E_r and I_p can be completed with this relatively simple "locally optimized" design.

Acknowledgments. This work was supported by the USDoE under grant DE-FG03-94ER-5421, Grant DE-FG03-95ER54296, and the Texas Atomic Energy Research Foundation. We are indebted to D. B. Batchelor, B. A. Carreras, S. P. Hirshman, V. E. Lynch, D. A. Spong, A. S. Ware, and J. C. Whitson, of ORNL, for their assistance.

References.

[1] B. A. Carreras, N. Dominguez, L. Garcia, V. E. Lynch, J. F. Lyon, J. R. Cary, J. D. Hanson, and A. P. Navarro, Nucl. Fusion **28** (1988) 1195.
[2] B. A. Carreras, V. E. Lynch, and A. Ware, *Configuration Studies for a Small-Aspect-Ratio Tokamak Stellarator Hybrid*, Report ORNL/TM-13252, Oak Ridge National Laboratory (1996).
[3] D. A. Spong, S. P. Hirshman, and J. C. Whitson, Plasma Phys. Reports **23** (1997) 483.
[4] P. E. Moroz, Phys. Plasmas **3** (1996) 3055.
[5] D. W. Ross, P. M. Valanju, H. He, W. H. Miner, Jr., P. E. Phillips, J. C. Wiley, A. J. Wootton, and S. B. Zheng, Plasma Phys. Reports **23** (1997) 492.
[6] J. R. Cary, C. L. Hedrick, and J. S. Tolliver, Phys. Fluids **31** (1988) 1586.
[7] S. P. Hirshman, W. I. van Rij, and P. Merkel, Computer Phys. Comm. **43** (1986) 143.
[8] W. A. Cooper, personal communication (1997).
[9] S. Sudo, y. Takeiri, H. Zushi, K. Itoh, K. Kondo, and A. Iiyoshi, Nucl. Fusion **30** (1990) 11.
[10] U. Stroth, M. Murakami, R. A. Dory, H. Yamada, S. Okamura, F. Sano, and T. Obiki, Nucl. Fusion **36** (1996) 1063.
[11] K. Lackner and N. A. O. Gottardi, Nucl. Fusion **30** (1990) 767.

The influence of mode coupling on the rotation and locking of Tearing Modes

R. Coelho, M. F. F. Nave, F. Serra, E. Lazzaro[1], M.E.Manso

Associação EURATOM/IST, Centro de Fusão Nuclear, 1096 Lisboa Codex, Portugal
[1] Istituto di Fisica del Plasma, EURATOM-ENEA-CNR, Milan, Italy

Introduction

Magnetic islands have been observed in many tokamak discharges showing a strong influence on both global stability and transport and leading to confinement degradation. The understanding of how rotating islands evolve and interact with the plasma and surrounding vessel is of great importance in the avoidance of locked modes and disruptions, which are both key issues for ITER.

In order to assess the influence of mode coupling on island growth and rotation, a numerical model for the evolution of rotating tearing modes has been developed extending existing models /1,2/. In this paper, we are mainly interested on the electromagnetic nature of the mode coupling, thus viscous torques applied at an island in the Rutherford regime by the rotating plasma and the small stabilising contribution of plasma inertia are neglected. In toroidal geometry, magnetic islands with different poloidal and toroidal mode numbers (m,n) are expected to interact since a perturbation $\tilde{B}$ will not have a single (m,n) component but will also have side-band harmonics. The side-band harmonic (m±1,n) of an (m,n) mode can be regarded as an external current of helicity (m±1,n) which will interact with a (m±1,n) mode. Stability and toroidal rotation of both modes will be influenced by their phase difference and by the resistive vessel.

Helical sheet currents induced at the resistive vessel by the rotating modes or connected to mode coupling are shown to play an important role on both stability and toroidal rotation of the modes. These helical currents will modify the boundary conditions of the perturbed mode flux function or equivalently, induce eddy sheet currents $\delta\vec{j}$ around the rational surface of an island. The part of the eddy current that is in phase with the naturally occurring magnetic island at the rational surface affects the amplitude of the magnetic island. The part of the eddy current that is out of phase with the naturally occurring magnetic island yields electromagnetic forces around the rational surface.

Numerical Model

The first step to our analysis is the tearing mode equation for tokamak plasma discharges in the limit of large aspect ratio $\varepsilon \to 0$

$$\frac{1}{r}\frac{\partial}{\partial r}\left(r\frac{\partial \psi}{\partial r}\right) - \frac{m^2}{r^2}\psi = -\frac{q_s \mu_0 j_z'}{B_\theta (q - q_s)}\psi \qquad (1)$$

where the perturbed magnetic field of a (m,n) mode is described in terms of a perturbed flux function $\tilde{\vec{B}} = \nabla \times (\Psi \hat{z}) = (i\frac{m}{r}\Psi, -\frac{\partial \Psi}{\partial r}, 0)$ with $\Psi \equiv \psi(r)\exp(i(m\theta - n\phi - \int^{t} \omega(t')dt'))$ where ω is the instantaneous frequency of the mode. This equation is singular at r_s where $q = q_s$ and the solution will have a discontinuity on the radial derivative which may be characterised by the value of Δ' defined by $\Delta' . r_s = \left\{ \left[r\psi' \right]_{rs-}^{rs+} . \psi^*(r_s) + \left[r\psi'^* \right]_{rs-}^{rs+} . \psi(r_s) \right\} / (2\psi(r_s)\psi^*(r_s))$ where $r_{s\pm} = r_s \pm w/2$ refer to the radial locations of the edges of an island of width w (we follow the "constant ψ" approximation within the island region, valid when there is no forced reconnection /3/). We take into account the modifications to the perturbed flux function due to the resistive wall and mode coupling by making the expansion $\Psi = \Psi_{mode} + \Psi_{wall} + \Psi_{coupl}$ to a solution of (1) (the last two terms will satisfy suitable boundary conditions according to their nature).

To study the evolution of the island rotation with time, we must know the torques applied at the island. Since poloidal rotation is strongly damped /1, 4/ we will be mainly interested on the toroidal torques. However, due to the magnetic field line and perturbed current density geometry at the rational surface, the poloidal and toroidal torques due to $\tilde{\vec{\jmath}} \times \tilde{\vec{B}}$ forces are connected by $T_{\phi s} = \frac{n}{m} T_{\theta s}$ (torque at the rational surface of the island). Since the perturbed current densities are approximately "sheet-like", only the "toroidal" component of the perturbed current will contribute to the poloidal torque, which in terms of the perturbed flux function yields

$$T_{\phi s} = 4\pi^2 R_0 \frac{m}{\mu_0} \frac{i}{2} \left\{ \left[r\psi' \right]_{rs-}^{rs+} . \psi^*(r_s) - \left[r\psi'^* \right]_{rs-}^{rs+} . \psi(r_s) \right\} \qquad (2)$$

Considering a simple diffusion of the perturbed field lines the temporal evolution of the radial magnetic field perturbation is given by

$$\frac{d\tilde{B}_r}{dt} = -\frac{3.32}{\sqrt{\left| \frac{16rq}{mq'B_\theta} \right|_{r_s}}} \frac{Z_{eff}\eta}{\mu_0} \Delta' \sqrt{\tilde{B}_r} \qquad (3)$$

Once the toroidal moment of inertia of each island is calculated we can easily obtain the following set of coupled equations for the modes (m,n) and (m±1,n), which describes the temporal evolution of the amplitude of the radial magnetic perturbation ($\tilde{B}_r$) and the toroidal rotation frequency (ω) :

$$\left. \frac{d\tilde{B}_{rm}}{dt} \right|_{r_{sm}} = a_m \left[\left[\Delta'_m - \frac{2m}{r_{sm}} \left(\frac{r_{sm}}{r_w} \right)^{2m} \frac{(\omega\tau_{mw})^2}{1+(\omega\tau_{mw})^2} + \frac{2m}{r_{sm}} \frac{\tilde{B}^{(m)}_{rm\pm1}(r_{sm})}{\tilde{B}_{rm}(r_{sm})} \cos(\Delta\varphi_{m,m\pm1}) \right] \sqrt{\tilde{B}_{rm}(r_{sm})} \right] \qquad (4)$$

$$\frac{d\omega_m}{dt} = \frac{1}{I^{(m)}_\phi} \left(-b_m \tilde{B}^2_{rm}(r_{sm}) \left(\frac{r_{sm}}{r_w} \right)^{2m} \frac{\omega\tau_{mw}}{1+(\omega\tau_{mw})^2} - b_m \tilde{B}_{rm}(r_{sm}) \tilde{B}^{(m)}_{rm\pm1}(r_{sm}) \sin(\Delta\varphi_{m,m\pm1}) \right) \qquad (5)$$

Here, $\widetilde{B}^{(m)}_{rm\pm1}$ is the (m,n) harmonic of the (m±1,n) mode; $\Delta\varphi_{m,m\pm1}$ is the toroidal phase difference; $I^{(m)}_{\phi}$ is the moment of inertia of a (m,n) island in the toroidal direction. The function $\Delta'_m(\widetilde{B}_{rm})$ represents the stability parameter of the (m,n) mode, in the absence of the conducting vessel and coupling. The parameter τ_{mw} is given by τ_w/m where τ_w is the resistive time of the vessel ($\tau_w = (\mu_0\sigma_w\delta_w r_w)/2$).

Comparison with experimental results

Lower-hybrid current drive (LHCD) discharges in ASDEX indicate that the (2,1) tearing mode can be destabilised due to the change in the current density profile (caused by the localised power deposition of the waves), often leading to mode locking and a major plasma disruption /5/. During mode locking, a flattening of the electron density profile around the q=2 surface is observed from the microwave reflectometry diagnostic (figure 1) /6/. Although the magnetic signals could not detect a change in the growth rate of the m=2 mode after locking, reflectometry measurements show that the island continues to grow during locking. In addition, there is indication that a (m=3;n=1) mode has been destabilised and continues to oscillate while the (2,1) is locked.

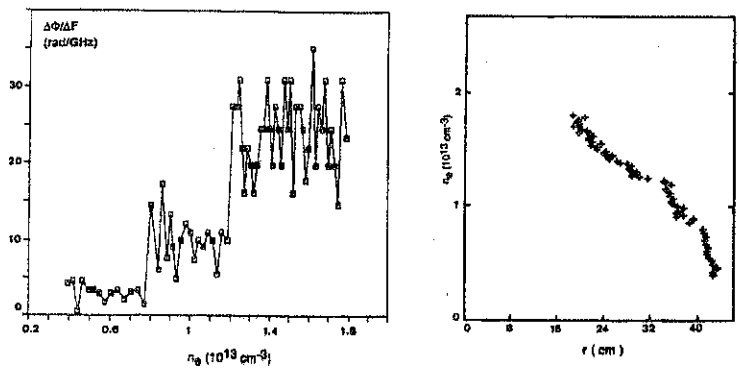

Figure 1 - Results from broadband reflectometry obtained in the ASDEX tokamak for the discharge 29285, at t=1580 ms, when locking of the m=2,n=1 occurred. The abrupt jumps in the phase derivative $\Delta\phi / \Delta F$ (a) correspond to the flattening of the plasma density in the evaluated density profiles (b), revealing the influence of magnetic islands located near the rational surfaces q=2 (r~30 cm) and q=3 (r~39 cm).

The model was therefore applied to the study of the time evolution of MHD observations in ASDEX lower-hybrid heated discharges. Numerical studies of the growth and toroidal rotation of modes (m=2;n=1) (unstable) and (m=3;n=1) (stable or unstable) were performed. It was found that the toroidal coupling between the (2,1) and (3,1) islands strongly affects the amplitude and rotation of the outer (3,1) island. A stable (3,1) is also shown to be destabilised after a critical (2,1) width. The simulations showed that after the m=2 island locks, the m=3

will continue to oscillate (as shown in figure 2), in agreement with the experimental data. After the locking of both islands, further growth of the modes leads to island overlap on a time scale that agrees with the time when ASDEX disruptions were observed (~10 ms after the locking).

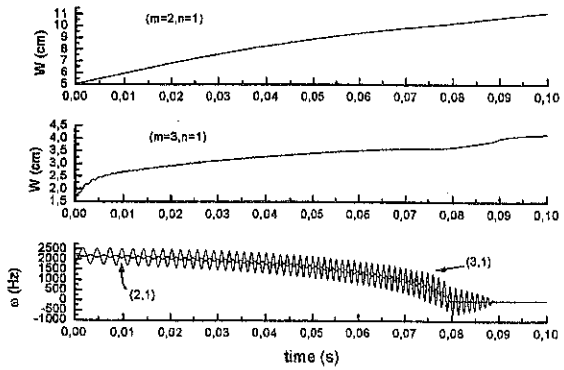

Figure 2 - Evolution of island widths and rotation frequencies for two coupled islands with mode numbers: (m=2, n=1) and (m=3, n=1). Each island rotates, as well as oscillates in the potential of the other. The (m=3, n=1) mode continues to oscillate after the locking of the (m=2, n=1) mode. In this simulation the following input parameters were used: r_{s2}=0.297m, r_{s3}=0.38m, $\Delta_2'(0)$=6, $\Delta_3'(0)$=4, $\phi_2(0)=\phi_3(0)$=0, $W_2(0)$=5cm, $W_3(0)$=1.5cm, $\omega_2(0)$=2.2 kHz, $\omega_3(0)$=1.8 kHz, τ_W=15ms

References

/1/ R.Fitzpatrick, Nucl. Fusion **33**,(1993)1049

/2/ E.Lazzaro, M.F.Nave, Phys. Fluids **31** (1988)1623

/3/ C.C.Hegna, Phys. Plasmas **3** (1996) 4646

/4/ A.I. Smolyakov et al., Phys. Plasmas **2** (1995) 1581

/5/ H.Zohm et al., Plasma Phys. Contr. Fusion **33** (1991)1423

/6/ M. E. Manso et al., Proc. 17th EPS Conf. on Contr. Fusion and Plasma Heating, Amsterdam, 14 B - II - (1990) 837

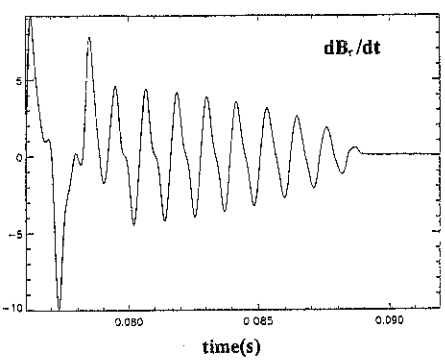

Figure 3 - Magnetic signal expected to be observed if the (3,1) island oscillates after the locking of the (2,1) island (for the simulation shown in figure 2)

The investigations of magnetic perturbation spatial structures behavior during major disruptions in tokamak T-11M

A.M. Belov, **S.V. Mirnov**, I.B.Semenov, E.A.Azizov, I.A. Kovan, V.B.Lazarev, I.N. Makashin, S.G.Maltsev, I.N. Monakhov, M.V.Morozov, A.P.Popryadukhin, A.P.Chernobai.
TRINITI,142092 Troitsk, Moscow region, Russia.

This report is devoted to the investigation of magnetic perturbation evolution during disruptions at I>Icr in T-11M tokamak. We guess, it is possible to follow the dynamics of magnetic islands formation at the column boundary on the basis of knowledge of the structure and the magnitude of magnetic perturbations near the boundary. Then we can make the estimations of plasma-wall interaction parameters (Te,Ti, peaking factor and others) in disruptions. This is important for modeling plasma-wall interaction and for the study of the major disruption mechanism.

The experiments were carried out at T-11M tokamak (R=0.7m, a=0.2m) [1] in following conditions: q(a)=2.5-3, $n_e<n_{ecr}$, Ip=80-100KA, Bt=0.8-1T. To study magnetic fluctuations at the vessel inside surface, 78 magnet probes in 4 toroidal cross-sections (φ =0,40.50, 180 degrees with 23, 32, 16, 7 probes correspondingly) were installed. The data acquisition system allowed to observe 63 signals with time resolution of 1 mks simultaneously.

The magnetic field visualization method suggested earlier in [2] was used for processing of the large data array. The region of high brightness (white) corresponded to the maximum positive B_θ-perturbations, the dark region - to negative ones. A visualization picture, the soft X-ray (SX) signal from the center, the total current ΔIp and plasma displacement (ΔR) for the typical major disruption in T-11M are shown in fig.1. The vertical displacement of the visualization picture corresponds to the poloidal angles from 0 to 360 degrees (the inner side of the plasma column), the middle line corresponds to the outer side (angle 180^0). The time window (the horizontal direction) corresponds to 320mks. The major disruption has a typical magnetic precursor in the mode of oscillation with m=2,3. Apparently, it is transformed to m=3,4 during the disruptions.

This transformation of magnetic perturbations from small m to big ones was discovered firstly in Merejkin's experiments [3] and then was observed in many tokamaks.

It is seen from fig.1, that this transformation is followed by the drastic drop of the SX signal in the column core, that means the flattening of Te profile in the core [4,5] and, as it was shown in [6] earlier, is result of the mode m=1/n=1 development in the core (deep sawtooth).

The explosion of the outer MHD-activity, accompanied by the current positive pulse (ΔIp) generation and column dropping inside (ΔR), occurs in 50-100μs after SX decrease in the core in our experiment. That's why we guess, that the main reasons of the disruption are events in the core, and

outer MHD-activity is the result of column r-extension (the drop of *li*). Apparently, the observed m rise can be the consequence of such extension.

The another consequence of the current channel extension is the rise of the total current Ip (ΔIp, fig.1). As was noted earlier [1], the weak increase of the current is observed already on the stage of helical perturbations. This process was interrupted by some "fast" event [1], then the short phase (10-30μs) of fast magnetic oscillation (fig.1, turbulization) comes. The drastic current rise and powerful plasma-wall interaction happen simultaneously with these oscillations. Probably, the overlapping of the magnetic island with different helical geometry occurs in this moment.

If the reason of these events is just the simple interaction between islands and the wall (limiters, antennas and so on), we could expect, that the "turbulizaton" moment (the rise ΔIp) has to be bonded with the boundary MHD-perturbations phase. However, it is not right. The serial of superposed oscillogramms ΔIp (t) and magnetic perturbations Bp(t), measured by one of magnetic probes for some T-11M discharges are shown in fig.2. It is easy to see, that "turbulization" comes in an arbitrary phase relatively to magnetic perturbations. That means, that it has the inner character and can be hardly explained by the simple interaction between magnetic islands and the wall.

The knowledge of the absolute values of magnetic perturbations ($\tilde{B}_\theta < 5\%$) allows us to make the estimations of possible sizes of magnetic islands, appearing in plasma column before a disruption. To take into account the influence of the conductive wall, the formula was used that describes connection of the poloidal field near the wall $B_\theta(r_p)$ and the radial component at resonant surface $B_r(r_s)$:

$$\frac{B_r(r_s)}{B_\theta(r_p)} = \frac{1-(r_s/b)^{2m}}{(r_s/r_p)^{m+1}+(r_s/b)^{m+1}(r_p/b)^{m-1}}$$

(b - is copper shell radius). Radii of the resonant surfaces and the corresponding shear values was calculated for the one parameter approximation for the current profile: $j = (I/pa^2)(\nu+1)(1-r^2/a^2)^\nu$. In this case $\nu=q_a/q_0-1=2.8$, the profile is peaked. The island semiwidths for the m=2/n=1, m=3/n=1 harmonics are 2.9 and 1.5cm respectively in this approximation, while the distance between these resonant surfaces is 4.7cm in stage long before the major disruption. The amplitudes of oscillations of these mode are increasing before disruption and we can suggest, that the islands are overlapping in this period. That corresponds with results obtained in ASDEX earlier [7].

The information about n-spectrum helical perturbations is very important for magnetic islands reconstruction. We had suggestions n=1 in our previous estimations. But that is not correct during disruption. At Fig.3 is shown B_θ-visualization picture for two different cross-sections of T-11M ($\Delta\phi$=40 degrees). We can see some different behavior of magnetic perturbations during disruption in very close toroidal cross-sections (toroidal asymmetry). That means development of n>1 perturbations.

(The n=2 perturbation was observed in T-11M earlier [1]) This problem will be the subject of our future work.

Conclusions.

1. The analysis of the behavior of magnetic perturbations before and during the major disruption allows to suggest, that the most fast and dangerous phase of a disruption - turbulization - is accompanied by the generation of the positive current pulse and powerful thermal and particle fluxes onto the wall and is the consequence of magnetic island m=3/n=1 and m=2/n=1 reconnection. We guess that the main reason of their formation before the disruption is the loss of magnetic shear in the center, as it was suggested in [4].
2. The absence of the connection between magnetic perturbation phase and the moment of the turbulization development can mean that the turbulization reason is not the direct plasma-wall interaction, but some other internal processes. Probably, it is the reconnection of magnetic islands m=3/n=1 and m=2/n=1.

References.

1. Mirnov S. et al., 16-IAEA Conf., (1996), N IAEA-CN-64/ AP1-23
2. Semenov I. et al., 22 EPS Conf., (1995), P11995, p.421.
3. Merejkin V.G. Plasma Phys. (Rus.) (1988), v.4, N2,p.275.
4. Mirnov S., Semenov I., 6-IAEA Conf (1977), v.1, p.291..
5. Karger F. et al., 6-IAEA Conf (1977), v.1, p.267.
6. Mirnov S., Semenov I., 8 EPS Conf., (1977), v.1, p.45.
7. Schittenhelm M., Zohm H., 23 EPS Conf., (1996), f011, p1027.

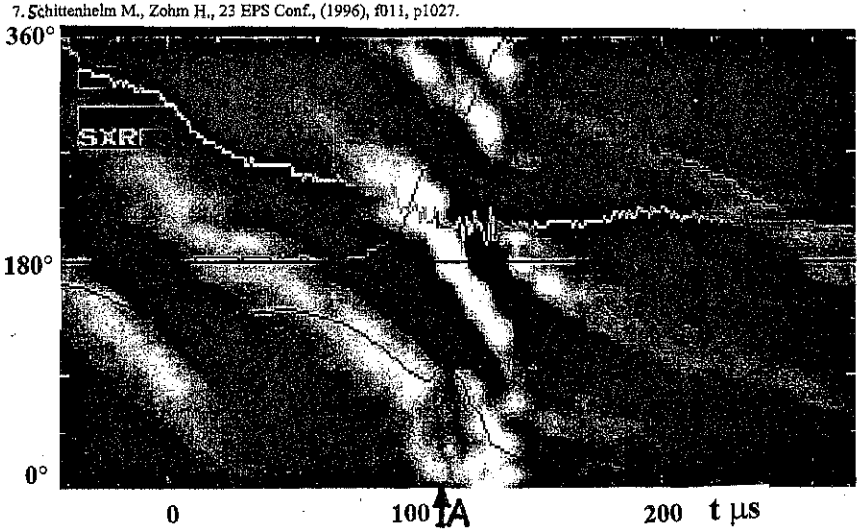

Fig.1 Typical $\tilde{B}p$ visualization picture for T-11M. A-begin of turbulization.

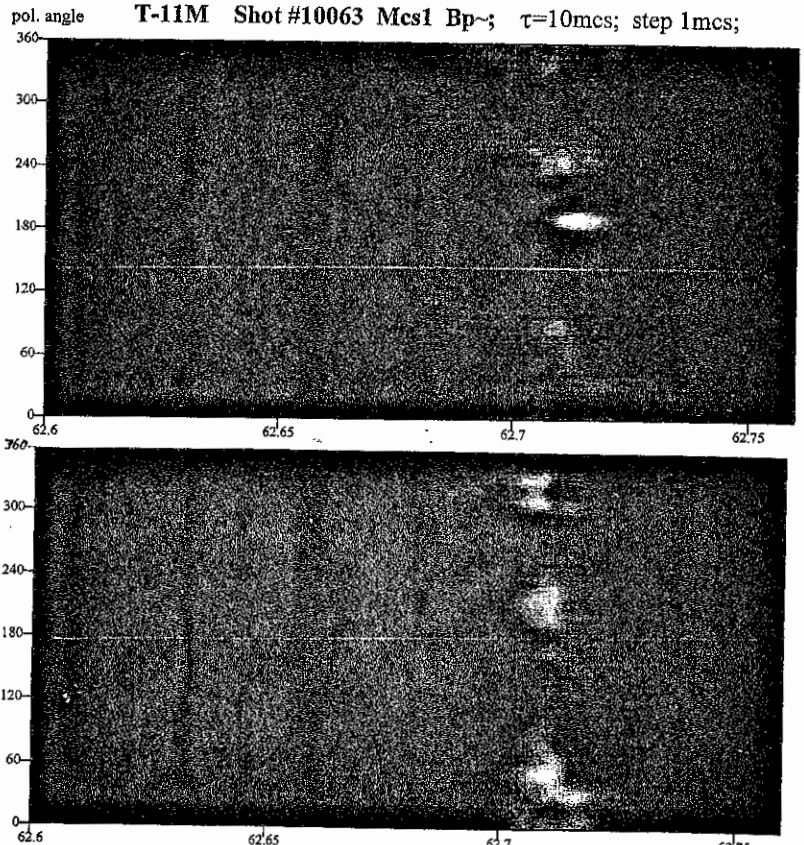

Fig.3 Bp visualization pictures for 2 toroidal crossections ($\Delta\varphi$=40°). Δt=160μs.

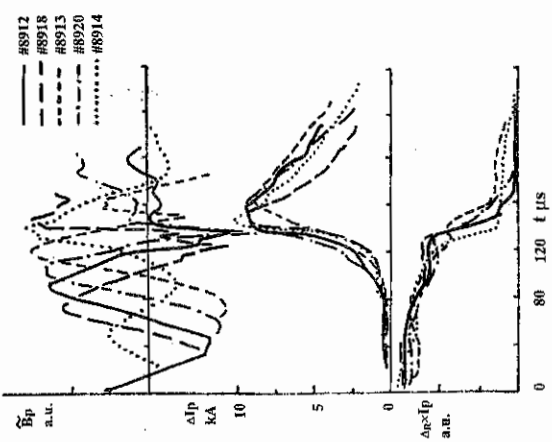

Fig.2 $\tilde{B}_p$ behaviour during several T-11M shots.

ON PECULIARITIES OF L-H TRANSITION IN T-11M TOKAMAK

Kovan I.A., Romannikov A.N., Petrov Yu.V.
TRINITI, Troitsk, Moscow region, Russia

INTRODUCTION

After the reconstruction of the limiter in spring, 1994, the regimes with improved energy confinement (L-H transition) have been revealed on T-11M tokamak, which were attended by D_α - emission intensity fall, by the loop-voltage and ohmic power drop, and by the energy content and the energy confinement time rise [1]. The transition occurred spontaneously at 35th ms of discharge as the plasma current attained the quasi-steady state, and was accompanied by flattening of the density profile and by increase of the electron temperature on plasma axis. The regime arose, by our opinion, due to formation of the negative electrical potential at the limiter during the discharge, which had the dielectric covering of B_4C with ~100μ thickness after the reconstruction. This suggestion is supported by sharp decrease (approximately in 100 times) of the current in the limiter-chamber circuit in comparison with conducting limiter (Mo) case. It was impossible to measure the radial distribution of potential in the plasma edge because of the quick destroy of Langmuir probe (for this reason the radial movement of the probe on T-11M is possible in SOL only, r≥21cm, where the potential responds weakly on L-H transition). That's why we focused our attention on contactless method of elucidating the electrical potential gradient in plasma, based on measuring of the poloidal plasma rotation. It is well known that during the transition to H-regime the plasma edge-layer gains the significant value of poloidal rotation velocity (~10^5 cm/s) [2]. The main method of this velocity measuring is based on estimating the frequency Doppler shift in impurity-ions spectra. However, since there is no high-resolution (~0.1Å) spectrometer on T-11M and because of the problem of adequate relation between impurity-ions and main plasma motion, we use the corpuscular diagnostic tools for the stated aims [3].

The dependence of the c.x. flux on the plasma poloidal rotation velocity V_p follows from the analysis of main ions distribution function in a moving coordinate system. The neutrals' flux I depends on the velocity V_p of the coordinate system as:

$$I \sim \exp\left(-M\cdot\left(V_i - V_p\right)^2/2T\right) ,$$

where $E=MV_i^2/2$ is energy, and T is the ion temperature in the observed point. In the case of small V_p , when the neutrals' flux I_0 for the stationary (V_p=0) coordinate system is known, one has the relation:

$$\frac{I}{I_0} \approx \exp\left(\sqrt{2M\cdot E}\cdot V_p/T\right) \qquad (1)$$

At high energies the c.x. flux drops exponentially, so that the restrictions in analyzer loading can turn critical for the measurements. That's why the compromise is necessary in choosing the neutrals' energy. Knowing the variation of fluxes before and after the L-H transition, it is possible to measure the poloidal rotation velocity V_p according to formula (1). The sensitivity of this method is maximum when measuring and comparing the fluxes in co-rotational direction and in counter-rotational direction.

EXPERIMENTAL RESULTS

The experiments have been carried out on T-11M in regimes with improved energy confinement, in conditions of boronized chamber walls. The typical discharge parameters were as following: toroidal magnetic field B_t=1.2T, plasma current $I_p \approx 90$kA, $q \approx 3.2$, average plasma density $\bar{n}_e \approx 2 \cdot 10^{13}$ cm^{-3}, $Z_{eff} \approx 1$, electron and ion (deuterium) temperature $T_{e0} \approx 450$eV, $T_{i0} \approx 120$eV, discharge duration $t \approx 120$ms, minor plasma radius a=19cm, major radius R_0=70cm. For the measurements of the c.x. fluxes the analyzer "Lakmus" was used, which allows to scan the plasma vertically up to radius $r \approx 0.6a$ above the midplane. The analyzer was working in the counting regime, the size of the spot, which could be seen by analyzer, was 2cm×1.5cm approximately. Fig.1 shows the temporal behavior of neutrals' fluxes at 300eV energy level, averaged over three discharges, on the chord Y=11cm, during L-H transition on T-11M. The curve 1 is the flux gained from the plasma region that moves as supposed towards the analyzer during the plasma rotation. The curve 2 is the flux obtained from the same region in case of its moving away from analyzer. The curve 3 is the flux measured in L-mode discharge (presumably without plasma rotation) which has been formed in conditions of metallic limiter and without the chamber walls boronization. Due to the fact of considerable fall of the overall fluxes after the boronization, the curve 3 had to be normalised by factor 1/3 in vertical scale. The altering of plasma poloidal rotation direction (curve 2 case) was achieved by reversing both the plasma current and toroidal magnetic field directions, leaving all the rest parameters identical to discharge in curve 1 case. It was done because of technical restriction for the analyzer to scan the plasma above the midplane only (Y>0). The comparison of fluxes in discharges with and without rotation yields $V_p \approx 10^6$ cm/s, according to formula (1), with ±50% accuracy. The similar measurements on Y=6cm chord did not reveal any difference in corresponding fluxes, in contrast to measurements on Y=11cm chord. In the plasma region observed by the analyzer the ion pressure gradient is rather small, so that the arising of poloidal plasma rotation may be attributed to radial electric field $E_r \approx 100$V/cm ($cE_r/B_t \approx 0.8 \cdot 10^6$ cm/s) appearing during the L-H transition.

THEORETICAL ANALYSIS IN SUPPORT OF THE MEASURING METHOD

The formula (1) used for calculating the poloidal rotation velocity V_p is valid, strictly speaking, for ions which move along the magnetic field lines rather than across them. In T-11M the collision rate is low enough, so that the 300eV ion can circle almost the whole drift trajectory before it will change its pitch angle considerably. Taking into account that only the ions with $V_z << V_\perp$ can fly into analyzer (it is directed perpendicular to magnetic axis), it may seem doubtful using (1) for these ions, because even when the radial electric field is present in the plasma, their drift orbits may look like "banana" in cross-section, meaning that their poloidal drift velocity changes the sign both in the lower and in the upper halfplane of the plasma column. The aim of the analysis given below is to justify the usage of formula (1) for the V_p-measuring method.

The condition of flying the particle into the analyzer is determined by the inclination of magnetic field line with respect to analyzer view line. From region X≈0, Y≈11cm only the particles which have $V_z/V_\perp \approx 0.1$ can fly into analyzer, and from region X≈0, Y≈-11cm - the particles with $V_z/V_\perp \approx -0.1$ (Z-axis and toroidal magnetic field B are directed clock-wise, if one looks from the top, and plasma current I_p - counter-clock-wise). On fig.2 the trajectories of two 300eV deuterons are shown, which were launched from the point X=0, Y=11.4cm with initial velocities $V_z/V_\perp = 0.08$

(first particle) and $V_z/V_\perp = -0.08$ (second particle). Besides, the radial homogeneous electric field E_r=100V/cm was set in plasma. From fig.2 it may seem that due to mirror symmetry with respect to Y=0 line, the analyzer will gain the particles with equal drift velocities V_x, both from Y≈11cm and from Y≈-11cm regions. However it is not so. On fig.3 the time evolution of coordinates X, Y and velocities V_x, $V_\parallel$ ($\approx V_z$) for the first particle are shown (left column). It can fly into analyzer if $V_\parallel \approx 1.4 \cdot 10^6$ cm/s and Y≈11cm, or if $V_\parallel \approx -1.4 \cdot 10^6$ cm/s and Y≈-11cm. Such points are marked with circles on fig.3. It is seen that in point Y≈11cm the particle has the drift velocity $V_x \approx 10^6$ cm/s (towards analyzer), and in the point Y≈-9cm it has the drift velocity $V_x \approx -0.4 \cdot 10^6$ cm/s (away from analyzer). As for the second particle, the analysis of the similar evolution curves (fig.3, right column) shows that it can fly into analyzer from region Y≈-11cm only, having $V_x \approx -0.6 \cdot 10^6$ cm/s (away from analyzer). Thus, the drift velocities V_x for the particles which can fly into analyzer, are opposite in sign in the upper and lower halfplanes of the plasma column. In the case of zero electric field the trajectories of these particles are "banana"-like, with turning points located at X≈0, Y≈±11.4cm (the trajectories of these particles are nearly coincide, in contrast to trajectories shown on fig.2). In this case each of these particles can fly into analyzer from Y≈11cm as well as from Y≈-11cm, having one and the same drift velocity $V_x \approx 0.16 \cdot 10^6$ cm/s (mainly due to $V_\parallel$ input), directed towards the analyzer in the upper and lower halfplanes of the plasma column, symmetrically with respect to Y=0 line. For the given analysis it is not very essential from which points the particles are launched. For instance, if they are launched from the point X=0, Y=-11.4cm, the same curves as those shown on figs.2,3 will be obtained, with some time-shift. In the case of another sign of electric field (E_r=-100V/cm) the result is opposite to the case given above: the first particle can fly into analyzer from region Y≈11cm, with drift velocity V_x<0, and the second particle can fly into analyzer from region Y≈-11cm, having V_x>0. The trajectories of these particles differ significantly from those shown on fig.2: the first particle looks like "banana" in cross-section, and the second one goes along the trajectory close to a circle. It should be mentioned that in numerical code, used for constructing the drift trajectories, special terms are present which describe the ripples of toroidal magnetic field. However, for the particles considered above ($V_z/V_\perp \approx \pm 0.1$ at t=0) the ripples did not reveal itself.

Discussion

The observed asymmetry in evolution of c.x. fluxes during the L-H transition for chords located on the opposite sides from the midplane, may be interpreted as the result of plasma rotation in arising radial electric field and can not be attributed to locally-trapped ions or to vertical shift of plasma column. Thus, it is shown that for the L-H transition in T-11M tokamak:

1.The H-mode is characterised by deep penetration of radial electric field (up to a/2).
2.The poloidal rotation velocity V_p on the Y≈11cm chord is order of 10^6 cm/s, corresponding to E_r ~100V/cm (directed outward from the plasma centre).
3.The neo-classical analysis of observed ions justifies the measuring method.

References

[1] Lazarev V.B., Alekseev A.G., Amosov V.N., et al., Proc. of the 15th Int. Conf. on Plasma Phys. and Contr. Nucl. Fus. Res., V.2, P.45, 1995.
[2] Groebner R.J. Phys.Fluids B 5 (7), 1993.
[3] Romannikov A.N., Chernobai A.P., Russ. journ. Fizika Plazmy, 1997, N.10 (in press).

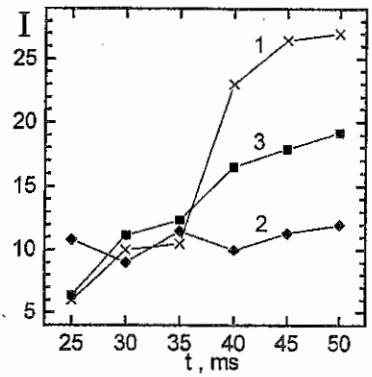

Fig.1. Temporal behavior of measured neutrals' flux (relative units) during L-H transition in T-11M tokamak:

1 - flux from plasma region which moves towards analyzer, averaged over discharges #9369, #9370, #9371.

2 - flux from plasma region which moves away from analyzer, averaged over discharges #9520, #9523, #9626.

3 - flux in L-mode, discharge #2617.

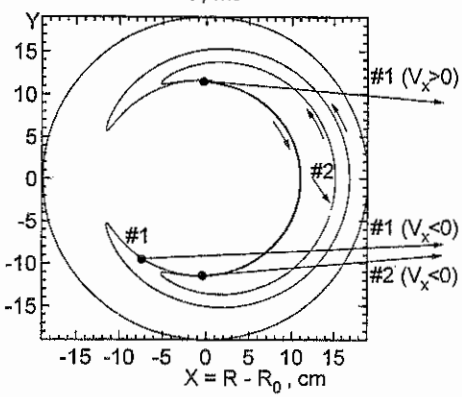

Fig.2. Cross-section view on drift trajectories of two 300eV deuterons with $V_z/V_\perp \approx \pm 0.1$ (at t=0) in radial electric field E_r = 100 V/cm. Long arrows show from which points of the drift trajectory the particle can fly into analyzer if it looks at Y≈11cm or at Y≈-11cm. The sign of drift velocity V_x at this moment is shown for each particle near the corresponding arrow. The evolution of coordinates and velocities see on fig.3.

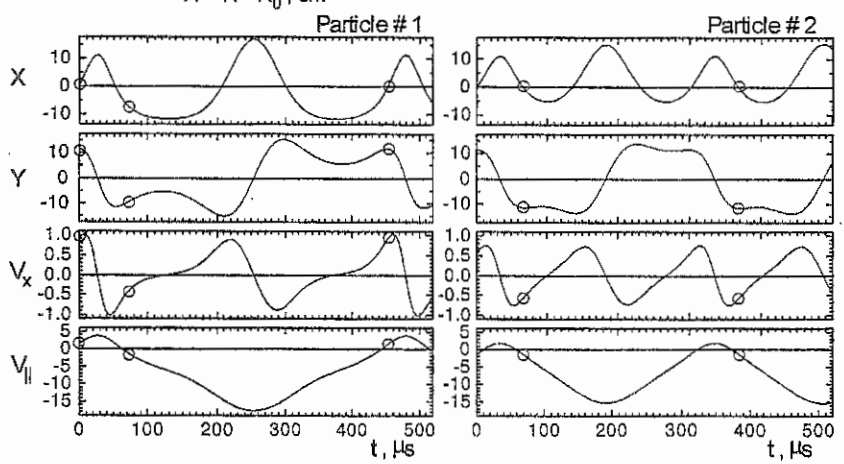

Fig.3. Time-evolution of coordinates X and Y (in cm), drift velocity V_x and velocity along magnetic field line $V_{||}$ (in 10^6 cm/s) for the first particle (left column) and for the second particle (right column). The small circles indicate the values of these variables with which the particle can fly into the analyzer.

On the Turbulent Transport in Tokamaks

Vladimir P. Pavlenko
Department of Materials Science, EURATOM-NFR Fusion Association, Uppsala University, Box 534, S - 751 21 Uppsala, Sweden

I. It is evident now that the ion thermal transport in tokamaks can be anomalous.[1] The evidence comes from experimental studies in large scale tokamak discharges aimed at the investigation of the ion thermal confinement properties. The mechanism responsible for the ion thermal transport is most probably thought to be the low frequency instability, which is a drift wave type electrostatic mode driven by the density and temperature gradients and inhomogeneity in the magnetic field. To describe the transport properties in such a plasma the conventional turbulent transport program is usually used. This program includes the deriviation of a complete set of equations describing the nonlinear dynamics of a drift type mode, the solution of the linear stability problem and determining the critical value of parameters for the onset of instability, the calculation of the transport coefficients based on the estimated saturation level of the turbulence, and finally the numerical calculation of the profiles.

Recently another program was suggested which starts from the Lagrangian invariants L_k (quantities that are concerved along trajectories) and leads to a turbulent attractor.[2] To demonstrate the basic idea of this program, let assume that there exist Lagrangian invariants (other than the energy and the total number of particles) that are held for a plasma in tokamaks and not destroyed by the turbulence.So, state the system is totally described by the Lagrangian invariants L_k, i.e. $\frac{d L_k}{d t} = 0$. It is naturally then to argue, in analogy with the Taylor theory of relaxation, that the turbulent transport of heat and particles drives the plasma towards the steady state $L_k = const.$ This steady state is called *Turbulent Equipartition* (TEP). TEP, which also refers to as a turbulent attractor, is the relaxed state of turbulent plasma in which Lagrangian invariants are uniformly distributed in the space.Therefore, the fluxes of conserved quantities vanish at TEP. It is worthwhile to note that to define the turbulent transport matrix in the convential transport theory, we expand the fluxes near the global attractor $n = const$, $T = const.$, which is determined by the energy conservation. In the TEP transport theory we expand the fluxes near the turbulent attractor $L_k = const.$

If the attractor is described by invariants, then the problem is what invariants to exploit. The frozen- in law is principal for the magnetic confinement, but the ideal frozen-in law in toroidal systems totally prohibits the turbulent diffusion. It was proposed that many transport properties of a turbulent plasma in large scale tokamak devices can be explained by one natural hypothesis: that the poloidal, but not toroidal component of the frozen-in low holds in tokamaks.[3] Based on this assumption one can obtain that in a tokamak plasma the appropriate Lagrangian invariant is given by $L = nr / B_\theta$, where n is the plasma density, r is the minor radius and B_θ is the poloidal magnetic field. A uniform distribution of L at TEP implies that the density distribution is then given by $n \cong 1 / q$, where q is the safety factor, which agrees well with experimental data.We note that this density distribution is not uniform in the space.

II. It has not been suggested yet the fluid equations suitable for the TEP description. In the present paper we derive the system of model equations, which holds the invariant L, using two fluid plasma description for low frequency electrostatic perturbations. Let the equilibrium magnetic field of a tokamak is $\mathbf{B} = \mathbf{e}_z B_T + \mathbf{e}_\theta B_\theta$. The basic assymptions are that the poloidal component of the magnetic field is frozen into the plasma, and there is no plasma motion in the poloidal direction. In these limits the frozen-in law, obtained from the equation of electron motion with zero electron inertia, is given by

$$\frac{\partial}{\partial r}(v_r B_\theta) + \frac{\partial}{\partial z}(v_z B_\theta) = 0 \qquad (1)$$

where v_r and v_z are components of the electron fluid velocity. Here z denotes the direction of the toroidal magnetic field B_T = const, r denotes the radial direction of a plasma torus, and θ denotes the poloidal direction. The equation (1) can be solved exactly, if one assumes that the two-dimensional velocity vector $\mathbf{v}_E$ (v_r , 0, v_z) is expressed through the gradient of potential function ϕ , i.e.

$$\mathbf{v}_E = -\frac{1}{B_\theta}(\nabla \phi \times \mathbf{e}_\theta) \qquad (2)$$

We consider low - β (the ratio of the plasma pressure to the magnetic field pressure) plasma and so, we can treat the electric field of the perturbation to be potential, $E = -\nabla \phi$. Since the frequency of the perturbations $\omega << \omega_c$ (ion cyclotron frequency), we neglect the charge separation and, instead of the Poisson equation, use the condition of quasineutrality, $n = n_i = n_e$.

We now define the quantity $L = n\,q$, where $q = (r B_T / R B_\theta)$ is the safety factor. Taking into account velocity (2) in the electron continuity equation, transforms this equation to the statement that L is the Lagrangian invariant. Indeed, by direct calculations we obtain

$$\frac{dL}{dt} = \frac{\partial L}{\partial t} + (\mathbf{v}_E \cdot \nabla) L = 0 \qquad (3)$$

where $\mathbf{v}_E$ is define by (2). In order to form the closed set of equations we need the equation for the potential function ϕ, which we obtain by considering the ion motion. The ion motion is assumed to be two-dimensional. The description of this motion is derived by the perturbation expantion of the ion fluid velocity in terms of the usual drift wave ordering. The relative size of the spatial and the time scales for the perturbation to those of equilibrium quatities, as well as the relative size of the perturbation to the equilibrium quantities, are $\varepsilon = \omega / \omega_c$. Then, to the lowest order in ε , the ion fluid velocity may be written as a sum of $\mathbf{v}_E$ drift and the ion diamagnetic drift velocity. To the next order, we have to include the polarization and the stress tensor (collisionless part) drift velocities. Taking then into account the condition of qusineutrality and the divergence of the ion fluid velocity in the ion continuity equation, yields

$$\frac{1}{\omega_i}\frac{3T_0}{m_i R_\theta}\frac{1}{q}\frac{\partial L}{\partial z}+\frac{1}{\omega_i}\frac{c n_0}{B_\theta}\left\{\frac{\partial}{\partial t}\nabla^2 U+\nabla\cdot\left[(v_E\cdot\nabla)\nabla U\right]\right\}=0 \qquad (4)$$

where

$$\omega_i = eB_\theta/m_i\,,\quad U=\phi+3\frac{T}{e}\ln N,\quad R_\theta^{-1}=\frac{r}{B_\theta}\frac{d}{dr}\left(\frac{B_\theta}{r}\right)$$

Equations (3) and (4) form a closed set of equations describing dynamics of low-frequency drift-flute type perturbations which are uniform with respect to the poloidal magnetic field.It is important that the invariant L is the Lagrangian invariant which is preserved by the turbulence due to these perturbations. In deriving Eqs (3) and (4) we have taken into account the effects of pressure gradient and finite ion Larmor radius, and assumed that the frequency of perturbations $\omega \ll \omega_i$.

III. In the linear limit, assuming the perturbed potential and density in Eqs (3) and (4) to be of the form $exp\,(-i\omega + i\boldsymbol{k}\boldsymbol{r})$, we obtain the mode dispersion relation

$$\omega(\omega+k_z v^*)+\kappa g\frac{k_z^2}{k^2}=0 \qquad (5)$$

where

$$v^*=\frac{3T_0\kappa}{m_i\omega_i},\quad \kappa=\frac{1}{n_0 q}\frac{d(n_0 q)}{dr},\quad g=\frac{3T_0}{m_i R_\theta}$$

Here the equilibrium plasma density n_0 and temperature T_0 are assumed to be slowly varying functions of r.

It is seen from (5) that for $\kappa g > \frac{k^2(v^*)^2}{4}$ the solution of the dispersion relation will correspond to instability which drives a plasma to the state of TEP (L = const) with the growth rate proportional to $\sqrt{\kappa g}$ The driving force of the instability is the pressure gradient combining with the shear of magnetic field. The finite ion Larmor radius effect, manifested by the term (k v*), leads to the boundary for the wavelength of unstable modes from below. The necessary condition for the instability to be developed is given by

$$-\frac{r}{n_0 q}\frac{d}{dr}(n_0 q)\cdot\frac{r}{q}\frac{dq}{dr}>0 \qquad (6)$$

The low-frequency drift type instability analyzed here is acknowledged to be leading candidates to account for the anomalous radial transport of particles and energy observed in the interior of tokamak experiments. If these modes can be linearly stabilized by the profiles that generate negative magnetic shear, i.e.

$$s=\frac{r}{q}\frac{dq}{dr}<0 \qquad (7)$$

it can suppress the source of drift turbulence in tokamaks and therefore, the transport in stabilized region should be reduced to the neoclassical (collisional) level. This effectively forms a "transport barrier" in a plasma interior which can sustain the peaked pressure profiles, shown here to be related to the turbulent attractor

$$L = n(r)\, q(r) = \text{const} \qquad (8)$$

So, the quantity (dq / dr) is responsible for the canonical plasma profiles which depend on q(r). These profiles have already been seen in many recent experiments and in gyro-particle simulations For example, the strong peaking of the pressure profiles has been observed in experimental discharges in JET and DIII-D within the negative magnetic shear region and suggests the existence of a "transport barrier" , i.e.localized region within the plasma where the thermal and particle transport are much smaller than in the surrounding regions.[4]

A new type of internal transport barrier (ITB) has been observed in JT - 60U reversed shear discharges. The ITB lies in the negative shear region and extended beyond 60% of the plasma minor radius. High density plasmas with high confinement have been obtained with the formation of ITB. [5]

References

1. F.Wagner and U.Stroth, Plasma Phys. Controlled Fusion, **35** , 1321 (1993)
2. J.Nycander and V.V.Yankov, Phys. Plasmas, **2**, 2874 (1995)
3. V.V.Yankov, JETP Lett., **60**, 169 (1994)
4. C.V.Forest, et al., Phys.Rev.Lett., **77**, 3141 (1996)
5. T.Fujita, S.Ide, et al, Phys.Rev.Lett., **78**, 2377 (1997)

CURRENT DRIVE EXPERIMENTS ON THE SPHERICAL TOKAMAK TST

H. Toyama, K. Hanada, K. Yamagishi, S. Shinohara, H.Totsuka, E. Ishiyama, H. Saito, S. Shiraiwa, S. Duorah, M. Hasegawa, I. Nakajima, M.Usigome, N. Uetake, K. Tanji

Department of Physics, School of Science, University of Tokyo
7-3-1 Hongo, Bunkyo-ku, Tokyo 113, Japan

The spherical tokamak (ST) sacrifices OH volt second for low aspect ratio, so that the role of the current drive is crucial for ST to be a volume neutron source(VNS) and an advanced reactor. Toroidally symmetrical electrodes with 16 cm wide have been installed in the vacuum chamber of Tokyo Spherical Tokamak(TST) [1] at the position of R=32.5 cm and 60.5 cm, respectively. The voltage of 500V is applied between up and bottom electrodes (R=32.5 cm), at 0.1ms after OH start. The duration of the plasma current increases from 0.7 ms to 1.0 ms. In the lower current operation, the plasma current of 8kA is sustained for 2.8 ms. Helicity balance at 2.4ms is estimated assuming electron density ~$10^{17}m^{-3}$, electron temperature ~ 10 eV [2].

The TST has been recently modified to TST-M in order to apply the helicity injection current drive on the plasma with better plasma performance and to check the feasibility on 1MA machines. The strength of the toroidal filed is increased to 0.18 T at the center of the vacuum chamber. The plasma current of 60 kA has been obtained with OH flux swing of 20 mVs. Two types of flux swing have been tried for the plasma production; one is to make the plasma by decreasing OH flux(Fig. 1(a)). The other is to make the plasma by increasing OH flux(Fig. 1(b)).

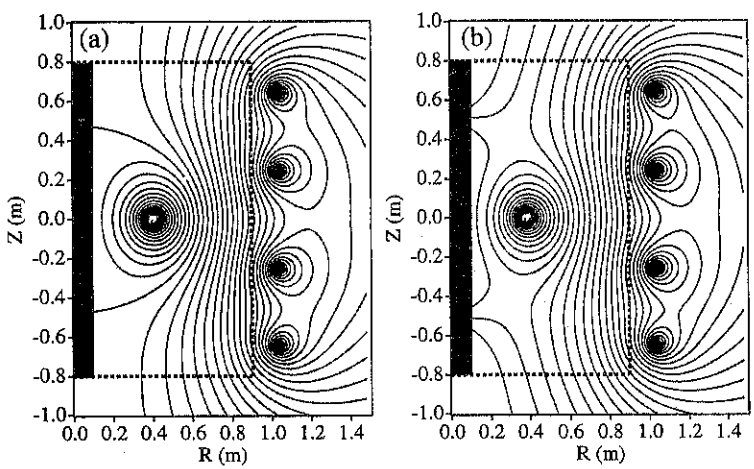

Fig.1 Flux surfaces of (a) decreasing OH flux and (b) increasing OH flux.
The gray areas show center posts and dotted lines show the cross section of the vacuum chamber.

The minor radius of the plasma is estimated by the radial profiles of the ion saturation current of the inserted Langmuir probe and the vertical magnetic field of the pickup coil. It change the sign at R=38 cm(Fig. 2(b));thus the magnetic axis sits at R=38 cm in both operations. But the ion saturation current drops sharply at R=20 cm in case of increasing OH flux(open circles in Fig. 2(a)), indicating the plasma boundary. The plasma is extended near the center post in case of decreasing OH flux(closed circles). The aspect ratio estimated by this method is 1.3 in case of decreasing OH flux and 2.5 in increasing case.

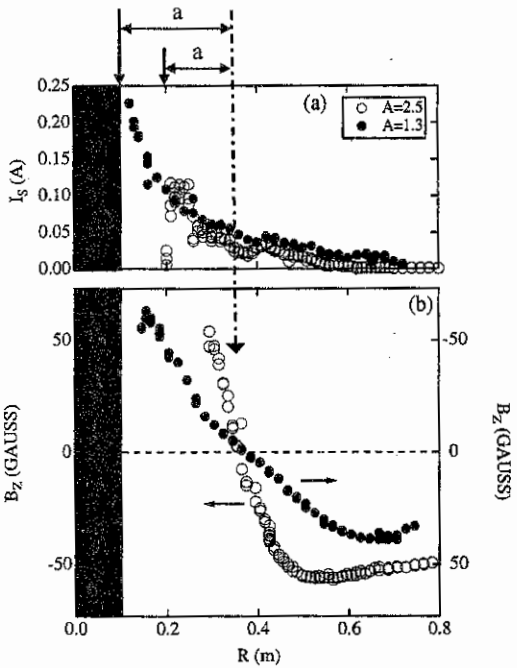

Fig.2 Radial profiles of (a) the ion saturation current of the Langmuir probe and (b) the vertical magnetic field. The gray areas show center posts. Open and closed circles show increasing OH flux and decreasing OH flux, respectively.

The electrostatic fluctuations are measured by triple Langmuir probes. The radial profiles of the relative fluctuation levels of the ion saturation current are plotted in Fig.3. The fluctuation levels are 5-10% in the central part of the plasma. There is little aspect ratio dependence in electrostatic fluctuations.

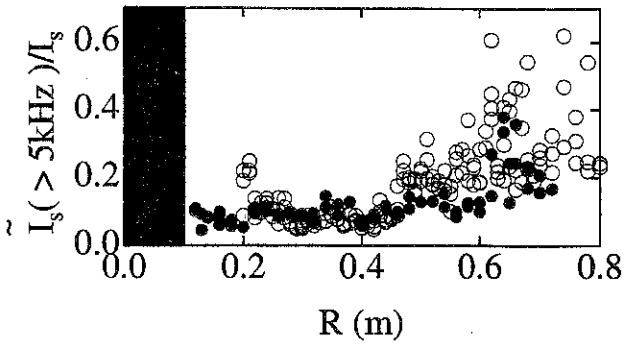

Fig.3 The radial profiles of the relative fluctuation level of the ion saturation current of the Langmuir probes. Open and closed circles show aspect ratio of 2.5 and 1.3, respectively.

The magnetic fluctuations are measured by inserting pickup coils into the plasma. The radial profiles of the relative fluctuation levels of vertical and radial magnetic field are shown in Fig.4. The magnetic fluctuations of the aspect ratio A of 1.3 is lower than A=2.5; the observed fluctuation level is 0.1% in the core plasma region; 1 order lower than REPUTE-1 RFP plasma. The electron heat transport estimated from the fluctuation level of 0.1% can not account for the electron heat transport of 50 kW/m^2; less than 1%.

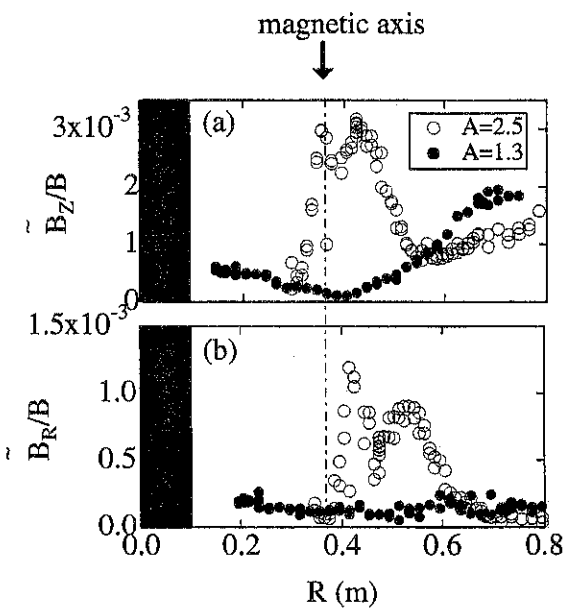

Fig.4 The radial profiles of the relative fluctuation level of the vertical (a) and radial magnetic field. Open and closed circles show aspect ratio of 2.5 and 1.3, respectively.

The voltage of 500V is applied between up and bottom electrodes (16 cm wide, set toroidally symmetrically at the position of 60.5 cm. The current density of the toroidal current is measured by inserting a Rogowskii coil into the plasma with and without the helicity injection. The toroidal current is observed to flow mainly under electrodes in this operation as shown in Fig.5. More detailed surveys of helicity injection experiments on upgraded TST-M plasmas are now under way.

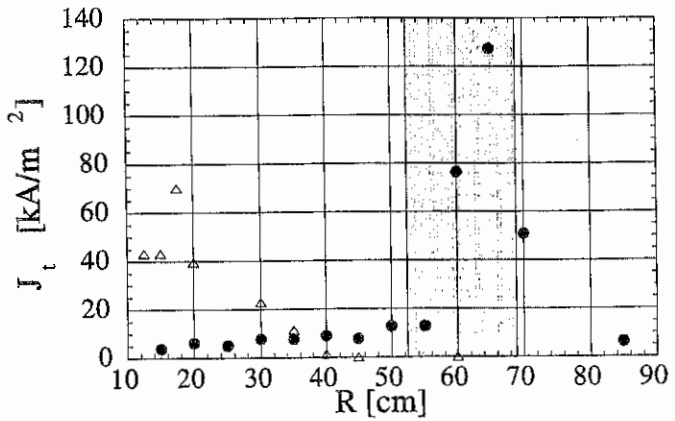

Fig.5 Comparison of toroidal current density between OH plasma (open triangles) and helicity injected plasma (closed circles). Gray area shows the space between up and bottom electrodes.

References

[1] K. Hanada, *et al.* : Transactions of Fusion Technology, 27,440 (1995).

[2] H.Toyama, K. Hanada, K. Yamagishi, H. Totsuka, *et al.* : in Proc. 16th IAEA Fusion Energy Conference,F1-CN-64/CP-15 (1997).

Effect of induced toroidal rotation on poloidal rotation and ion heat conductivity of tokamak edge plasmas.

V.S. Tsypin,[a] D.Kh.Morozov,[b] J.J.E.Herrera,[b] J.J.Martinell, [b]
M. Tendler,[c] I.F.Potapenko,[a] A.S. de Assis[d] C.A. de Azevedo,[a]

[a] *Institute of Physics, State University of Rio de Janeiro,*
20550-013, Maracanã, Rio de Janeiro, Rio de Janeiro, Brazil.
[b] *Instituto de Ciencias Nucleares, Universidad Nacional Autonoma de Mexico,*
a Postal 70-543, 04510 Mexico
[c] *The Alfvén Laboratory, Fusion Plasma Physics, Royal Institute of Technology, 10044 Stockholm, Sweden*
[d] *Institute of Mathematics-Group of Applied Mathematics,*
Fluminense Federal University, Niterói, Rio de Janeiro, Brazil.

The possibility of controlling plasma poloidal flows is very attractive, as the low-to-high confinement transition (L-H transition) in tokamaks depends on sheared plasma poloidal flows [1]. External radio frequency waves, plasma turbulence or biased electrodes are usually considered to control the plasma poloidal flows. Neutral beam injection can also strongly affect poloidal plasma velocities and transport processes in tokamaks, as has been shown both for collisional plasmas, as well as for the weakly collisional tokamak plasma.

It has been recently shown that the kinetic [2],[3] or slow [4] Alfvén waves (AW) can be used to create the localized sheared poloidal flows in the edge plasmas of tokamaks. Plasma rotation, induced by AW, was found out experimentally in the Phaedrus-T tokamak [5]. Calculations, performed in Refs.3,4, are in satisfactory coincidence with the experimental results [5].

We generalize these results for slightly rippled tokamaks with external forces, affecting the plasma, where the collisional parameter $b = \nu^{*2}$ is large enough for the ion-electron heat exchange and toroidal perturbations of the ion and electron temperatures to play an essential role in the ambipolarity condition. We analyze the possibility of controlling the plasma poloidal and toroidal velocities as well as ion heat fluxes by external forces. We

suppose that results obtained in this paper can be used in the future experiments on the TCA/Br tokamak [6].

Let us consider a slightly rippled tokamak, in which the angle dependence of the magnetic field is given by $B = B_0\,(1 + \epsilon\cos\theta + \delta\cos N\zeta)$, where θ and ζ are the poloidal and toroidal angles, ϵ is the inverse aspect ratio, δ is the ζ-modulation depth of the magnetic field, and N is the number of ripples. To find the poloidal and toroidal plasma velocities, we use the ambipolarity condition, in the well-known form that follows from the current continuity equation $\nabla\cdot\mathbf{j} = 0$,

$$< j^r >= 0, \tag{1}$$

where

$$< \ldots >= \int_0^{2\pi}\int_0^{2\pi} (\ldots)\,\sqrt{g}d\theta d\zeta \Big/ \int_0^{2\pi}\int_0^{2\pi}\sqrt{g}d\theta d\zeta.$$

From MHD equations we find

$$\left(M_i n\frac{d\mathbf{V}_i}{dt} + \nabla p + \nabla\cdot\hat{\pi} - \mathbf{F}^h\right)_{\theta,\zeta} = -\frac{\sqrt{g}}{c} j^r B^{\zeta,\theta}, \tag{2}$$

where $\mathbf{F}^h$ is an external force being exerted on the plasma. In the general case, this force can originate from any kind of rf wave, plasma turbulence or neutral beam injection. In particular, this force has been calculated for the case of slow Alfvén waves [2],[3]. We take the plasma viscosity in the form [4]

$$(\nabla\cdot\hat{\pi})_\theta = \frac{3}{2}\pi_\parallel\frac{\partial}{\partial\theta}\ln B - \frac{1}{2}\frac{\partial\pi_\parallel}{\partial\theta}, \quad (\nabla\cdot\hat{\pi})_\zeta = -\frac{3}{2}\pi_\parallel\frac{\partial}{\partial\zeta}\ln B + \frac{\partial\pi_\parallel}{\partial\zeta}, \tag{3}$$

Other quantities, depending on the angles θ and ζ can be found from the well-known MHD equations.

We take the parallel viscosity tensor $\pi_\parallel$ in the form derived in Refs.7

$$\pi_\parallel = -\frac{2}{3}\frac{p_i}{\nu_i}\,(0.96\beta - 0.59\gamma), \tag{4}$$

where

$$\beta = \frac{3}{r}\left\{\epsilon U_{\zeta i}\frac{\partial}{\partial\zeta}\ln B - U_{\theta i}\frac{\partial}{\partial\theta}\ln\left(\sqrt{g}n^{2/3}B\right) + U_{Ti}\frac{\partial}{\partial\theta}\ln\frac{B}{n}\right\}, \tag{5}$$

$$\gamma = -\frac{3}{r}\left\{0.34U_{\theta i}\frac{\partial}{\partial\theta}\ln n + U_{Ti}\left(1.36\frac{\partial}{\partial\theta}\ln B - 0.84\frac{\partial}{\partial\theta}\ln n\right)\right\}. \tag{6}$$

Then, the ion heat flux Γ_{Ti} can be derived by integrating the temperature evolution equation over the plasma volume

$$\Gamma_{Ti} =< q_i^r >, \tag{7}$$

where after the integration over the angle θ, we obtain

$$\Gamma_{Ti} = -\frac{2nT_i\nu_i}{M_i\omega_{ci}^2}\frac{\partial T_i}{\partial r} - \frac{5cB_s}{4\pi\epsilon e_i R}\int_0^{2\pi} d\theta \frac{p_i}{B^2}\frac{\partial T_i}{\partial \theta}. \tag{8}$$

As can be seen from Eq.(5),(6), it is necessary to calculate the ion poloidal velocities $U_{i\theta}$ and $U_{e\theta}$.

Now we can find the plasma rotation velocities using the ambipolarity conditions Eq.(1), the expressions for perturbed temperatures, and the ion viscosity Eqs.(4)-(6):

$$U_{i\zeta} = 1.39\frac{\nu_i R^2}{M_i n_0 v_{Ti}^2 (N\delta)^2} F_\zeta^h, \tag{9}$$

$$U_{i\theta} = G_{u1}(\alpha, b)U_{Ti} + G_{u2}(\alpha, b)\left(\frac{\epsilon}{q}\frac{j_\parallel}{e_i n_0} + U_p\right) + 1.39\frac{\nu_i R^2}{M_i n_0 v_{Ti}^2} G_{u3}(\alpha, b)F_\theta^h, \tag{10}$$

where

$$G_{u1}(\alpha, b) = -\frac{f_2(\alpha, b)}{f_1(\alpha, b)}, \qquad G_{u2}(\alpha, b) = 1.35\frac{M_e}{M_i}\frac{\alpha b^2}{f_1(\alpha, b)}, \qquad G_{u3}(\alpha, b) = \frac{d(b)}{f_1(\alpha, b)},$$

$$f_1(\alpha, b) = d(b)\left(1 + \frac{2}{3}\alpha\right)(1 + 0.19\alpha) + 0.18\alpha^2 b\left(1 + 15.2b\frac{M_e}{M_i}\right),$$

$$f_2(\alpha, b) = d(b)\left(1 + \frac{2}{3}\alpha\right)(1.83 + 1.52\alpha) - 0.9\alpha b, \qquad d(b) = 1 + 2.2b\sqrt{M_e/M_i}.$$

Functions $G_{u1}(\alpha, b), G_{u2}(\alpha, b), G_{u3}(\alpha, b)$ are plotted for the deuterium plasma case in Fig. We can conclude, analyzing Fig., that toroidal rotation does not allow the strong variations of poloidal rotation, when forces induced by radio frequency waves, plasma turbulence or neutral beam injection are present. The relevant regime for L-H transition, when the poloidal rotation is sufficient, occurs when $\alpha \ll 1$.

From Eqs.(8) we find the radial ion heat flux. We write this equation in the Shafranov form

$$\Gamma_{Ti} = -\frac{2nT_i\nu_i}{M_i\omega_{ci}^2}\frac{\partial T_i}{\partial r}\left\{1 + 1.6q^2\left[G_{T1}(\alpha, b) + G_{T2}\frac{1}{U_{Ti}}(\alpha, b)\left(\frac{\epsilon}{q}\frac{j_\parallel}{e_i n_0} + U_p\right) - \right.\right. \tag{11}$$

$$\left.\left. -1.39\frac{\nu_i R^2}{U_{Ti} M_i n_0 v_{Ti}^2} G_{T3}(\alpha, b)F_\theta^h\right]\right\},$$

where

$$G_{T1}(\alpha, b) = \frac{(1 + \alpha/2)\, f_3(\alpha, b)}{f_1(\alpha, b)}, \qquad G_{T2}(\alpha, b) = 0.76\frac{M_e}{M_i}\frac{\alpha b\,(1 + \alpha/2)}{f_1(\alpha, b)}\left[\left(1 + \frac{2}{3}\alpha\right)\times\right.$$

$$\left.\times\,(1 + 0.19\alpha) - \frac{0.18\alpha^2 b}{d(b)}\right], \qquad G_{T3}(\alpha, b) = \frac{\alpha\,(1 + 7.6bM_e/M_i)\,(1 + \alpha/2)}{5f_1(\alpha, b)},$$

$$f_3(\alpha,b)=\left(1+\frac{2}{3}\alpha\right)\left[1+0.19\alpha+\frac{\alpha}{5}\left(1.83+1.52\alpha\right)\left(1+7.6b\frac{M_e}{M_i}\right)\right]+1.4\frac{M_e}{M_i}\frac{\alpha^2b^2}{d(b)}.$$

If we suppose that b satisfies the inequality $1<b<\sqrt{M_i/M_e}$, we obtain the previously known expression for the radial ion heat flux.

As proper analysis shows, the quantity $G_{T2}(\alpha,b)$ is negligible under the condition $b\leq M_i/M_e$. The quantities $G_{T1}(\alpha,b)$ and $G_{T3}(\alpha,b)$ are plotted in Fig.2. As can be seen from Fig.2, the neoclassical contribution in the radial ion heat flux, as a function of α, is approximately of the same order for $b\geq\sqrt{M_i/M_e}$, dropping with increasing b. The influence of induced forces on the radial heat flux is usually small for $b\geq\sqrt{M_i/M_e}$.

[1] J.D.Callen, Phys. Fluids **B4**, 2142 (1992)

[2] G.G.Graddock and P.H.Diamond, Phys. Rev. Lett. **67**, 1537 (1991).

[3] V.S.Tsypin, A.G.Elfimov, C.A. de Azevedo, A.S. de Assis. Physics of Plasmas. **3**, 4606 (1996)

[4] V.S.Tsypin, A.G.Elfimov, C.A. de Azevedo, A.S. de Assis. Physics of Plasmas. **3**, 2818 (1996)

[5] S.Wukitch, C.Litwin, M.Harper, R.Parker, and N.Hershkovitz, Phys. Rev. Lett. **77**, 294 (1996).

[6] I.C.Nacimento, R.M.O.Galvaõ, A.G.Tuszel, F.T.Degasperi, L.F.Ruchko, TCA/Br team. In: Proc. of X Int. Conf. on Plasma Physics. Contr. Pap. Brasil, Foz do Iguacu, vol.1, p.69, 31.10.94-04.11.94, (1994)

[7] A.B. Mikhailovskii and V.S. Tsypin. Plasma Physics, **13**, 785 (1971)

Current drive by Alfvén waves in elongated cross section tokamak

V.S. Tsypin[1], **A.G. Elfimov**[2], **M.Tendler**[3],
F.M.Nekrasov[1], **C.A. de Azevedo**[1], **A.S. de Assis**[4]

[1]*State University of Rio de Janeiro, 20550-013, Rio de Janeiro, Brazil.*

[2]*University of São Paulo, Cx. Postal 20516, São Paulo, Brazil.*

[3]*The Alfvén Laboratory, Royal Institute of Technology, 10044 Stockholm, Sweden*

[4]*Fluminense Federal University, Niterói, Rio de Janeiro, Brazil.*

The problem of the noninductive current-drive in cylindrical plasma model and in circular cross-section tokamaks had already been discussed intensively [1,2]. At the beginning of the study of this problem it have been clear that there are significant difficulties in using of the current-drive in toroidal magnetic traps, especially in a tokamak reactor. For the Alfvén waves, there is an opinion that the efficiency of the current-drive drops as a result of waves absorption by the trapped particles. Now, the theory development of the Alfvén wave (AW) current drive is very important in the course of the future experiments on the TCA/Br tokamak [2]. In this paper, an attempt is made to clarify some general aspects of this problem. For large aspect ratio tokamaks, with an elongated cross-section, some general formulas in the model approximation concerning the untrapped and trapped particles dynamics and their input to the Landau damping of the Alfvén waves, are presented. They are supposed to be used for the further development of the Alfvén current drive theory for tokamaks.

To derive general expressions for the noninductive current induced by AW we proceed from the surface-averaged Ohm's law [1]. The angle dependence of the magnetic field, we get from the expression $B_0 = \sqrt{g_{ik}B^iB^k} = B_s(1 + \epsilon^* \cos\theta + A\epsilon^* \cos^2\theta/2)$, where g_{ik} is the metric tensor, $A = \epsilon^*(\exp(2\eta) - 1)/q^2, q = \phi'/\chi'$ is the safety factor. For the current calculation, we proceed from the drift kinetic equation supposing $\partial f/\partial\zeta = -inf, f = f_0 + f, W = v^2/2, \mu = v_\perp^2 B_s/2B_0, \lambda = \mu/W$

$$\frac{\partial f}{\partial\theta} - inqf - \frac{2\pi i\omega\sqrt{g}B_0}{v_\parallel\chi'}f - \frac{2\pi\sqrt{g}B_0}{v_\parallel\chi'}C = \frac{2\pi\sqrt{g}B_0}{v_\parallel\chi'}\frac{e}{T}v_\parallel E_\parallel f_0, \qquad (1)$$

where f_0 is the Maxwellian distribution function. We only take the right-hand side of Eq.(2) as afunction $E_\parallel$ as we further consider the kinetic Alfvén waves.

The roots $a_{1,2}$ of the equation $v_{\|} = 0$ are

$$v_{\|} = \pm\sqrt{2W}\sqrt{1 - \lambda\left(1 + \epsilon^* \cos\theta + \frac{\epsilon^* A}{2}\cos^2\theta\right)}, \qquad a_{1,2} = \frac{-1 \pm \sqrt{1 + \frac{2A}{\epsilon^*}\left(\frac{1}{\lambda} - 1\right)}}{A}. \quad (2)$$

Here, we suppose the parameter $A \leq 1$. The untrapped particles are under the conditions $0 \leq \lambda \leq \lambda_1$ and $0 \leq \theta \leq 2\pi$. The first region of the trapped particle (as in a circular cross-section tokamak) is $\lambda_1 \leq \lambda \leq \lambda_2$ and $\theta_1 \leq \theta \leq \pi - \theta_1$, where $\theta_1 = \arccos(a_1)$ and

$$\lambda_1 = \lambda_{cr}(0) = \frac{1}{1 + \epsilon^* + \frac{\epsilon^* A}{2}}, \qquad \lambda_2 = \lambda_{cr}(\pi) = \frac{1}{1 - \epsilon^* + \frac{\epsilon^* A}{2}}. \quad (3)$$

In the new variables, the rf current can be written in the form

$$j_{\|\alpha} = 2\pi e_\alpha \frac{B_0}{B_s}\int_0^\infty W dW \int_0^{\lambda_2} d\lambda (f_\alpha^+ - f_\alpha^-), \quad (4)$$

where f^+ and f^- are the distribution functions of the particles, moving along and against $\mathbf{h}_0$. The interval $0 \leq \lambda \leq \lambda_2$ is supposed to be divided in two intervals, for untrapped and trapped particles, $0 \leq \lambda \leq \lambda_1$, $\lambda_1 \leq \lambda \leq \lambda_2$.

Now, we can solve the ordinary differential equation Eq.(2), allowing for the dependence on the angle θ Eqs.(1),(3). For the untrapped particles with $0 \leq \lambda \leq \lambda_1$ and $0 \leq \theta \leq 2\pi$ the integration constant is determined from the condition $f^{\pm}_{\alpha u}(0) = f^{\pm}_{\alpha u}(2\pi)$ and for the trapped particles with $\lambda_1 \leq \lambda \leq \lambda_2$ and $\theta_1 \leq \theta \leq 2\pi - \theta_1$, from $f^+_{\alpha t}(\theta_1) = f^-_{\alpha t}(\theta_1)$, $f^+_{\alpha t}(2\pi - \theta_1) = f^-_{\alpha t}(2\pi - \theta_1)$. Then, we find the Fourier component of the distribution function $f^{\pm}_{\alpha u} = \sum f^{\pm}_{\alpha u m_0} \exp(i m_0 \theta)$, $\quad Q_\alpha = \sum Q_{\alpha m} \exp(im\theta)$.

For the untrapped particles, the substitution can be used

$$\xi_u = -\arcsin\sqrt{\frac{(1 - a_2)(1 + \cos\theta)}{2(\cos\theta - a_2)}}, \quad \theta = \arccos\left[-\frac{(1 - a_2) + 2a_2 sn^2(Ku)}{(1 - a_2) - 2cn^2(Ku)}\right], \quad (5)$$

where $u = F(\xi_u, \kappa)/K(\kappa) + 1$, $F(\xi_u, \kappa)$ and $K(\kappa)$ are the elliptic and complete elliptic integrals, respectively; sn(Ku) is the Jacobian elliptic function, the sine-amplitude.

For the trapped particles "t", we use the substitution in Eq.(2)

$$\xi_t = \arcsin\sqrt{\frac{2(a_1 - \cos\theta)}{(1 + a_1)(1 - \cos\theta)}} \quad \theta = \arccos\left[\frac{2a_1 - (1 + a_1)sn^2(Ku)}{2 - (1 + a_1)sn^2(Ku)}\right]. \quad (6)$$

where $u = F(\xi_t, 1/\kappa)/K(1/\kappa)$.

Let's at first make the further simplifications of the untrapped particle distribution function. The analysis shows that the resonant points of this function are described by

the equation $\beta_m \pm \alpha_u/\pi = s$, where $s = 0, \pm 1, \pm 2..., \beta_m = m - nq$. Note, that for a wide range of the values λ and A the function $\theta = \theta(u)$, Eq.(6), is close to the straight line $\theta = \pi u$, i.e. $(\theta - \pi u)/\theta \ll 1$. That is why at the first approximation we can assume that $\theta = \pi u$, i.e. we take into account only the bounce-resonances with $s = 0$. After some calculations, we find the rf distribution function of the untrapped particles $f^{\pm}_{\alpha um}$. As it can be seen from Eq.(7), the bounce-resonances for the trapped particles t are described by the equation $\alpha_t = \pi s/2$ with $s = 0, \pm 1, \pm 2$ and so on. Taking this into account, after analyzing of the dependence $\theta = \theta(u)$ for the further calculation simplification we can suppose that for the trapped particles "t" $\theta = -(\pi - \theta_1)\cos(\pi u/2) + \pi$.

Using the model substitutions instead of the exact quantities Eqs.(6),(7) gives the accuracy not more than several percents practically for all trapped particles except of the narrow region near the separatrix between untrapped and trapped particles where the accuracy go up to 20%. Eqs.(6),(7) gives us the possibility to find the functions $f^{\pm}_{\alpha tm_0}$.

As it is well-known[1] the noninductive current induced by KAW can be expressed through the absorbed power $P_w \approx \frac{\omega}{8\pi}\mathrm{Im}\epsilon_{\parallel}\left|E_{\parallel}\right|^2$ in this case. Using Eqs.(2),(6),(7), we can find the expression for the oscillating currents

$$j_{\parallel\alpha m} = -\frac{4ie_\alpha^2 qRE_{\parallel m}}{T_\alpha}\int_0^\infty f_{0\alpha}WdW\left(\int_0^{\lambda_1}\frac{\alpha_u d\lambda}{\beta_m^2 - \alpha_u^2/\pi^2} - \frac{\pi^2}{4\beta_m^2}\int_{\lambda_1}^{\lambda_2}\sum_{s=-\infty}^{\infty}\frac{s^2 J_s^2(x_{1m})}{\alpha_t + s\pi/2}d\lambda\right). \tag{7}$$

where $\kappa^2 = 2(a_1 - a_2)/(1 + a_1)(1 - a_2), S = 2\omega qR/\sqrt{2\epsilon^*\lambda WA(a_1 - a_2)}, \alpha_u = \kappa K(\kappa)S$, $\alpha_t = K(1/\kappa)S$.

As far as we are interested in the imaginary part of the permeability tensor $\epsilon_{\parallel m}$, after the integration on the variable W we have

$$\mathrm{Im}\epsilon_{\parallel m} = \frac{2\sqrt{\pi}\omega_{pe}^2 qR}{\omega\beta_m v_{Te}}\left[F_u(A) + F_t(A)\right], \tag{8}$$

where

$$F_u(A) = \int_0^{\lambda_1} d\lambda f_u^4(\lambda)\exp\left[-f_u^2(\lambda)\right], \qquad f_u(\lambda) = \frac{\alpha_u\sqrt{W}}{\pi\beta_m v_{Te}}, \qquad f_t(\lambda, s) = \frac{2\sqrt{2W}\alpha_t}{\pi s v_{Te}}$$

$$F_t(A) = \frac{1}{\beta_m}\sum_{s=1}^{\infty} s\int_{\lambda_1}^{\lambda_2} d\lambda f_t^4(\lambda, s)J_s^2(x_{1m})\exp\left[-f_t^2(\lambda, s)\right].$$

Now, we can estimate the relative absorption of AW by untrapped and trapped particles using the next tokamak plasma parameters: $c_A/v_{Te} = 0.2$, where $c_A = B_0/\sqrt{4\pi n_0 M_i}$ is Alfvén velocity; $\beta_m = m - nq = 6$. The dependence of absorbed power by different

kind of particles $F_u(\epsilon^*)$ and $F_t(\epsilon^*)$ Eq.(10) on the tokamak inverse aspect ratio $l_1/2R$ in the center of the semiminor axis is plotted on Fig.1. At $\epsilon^*/2 = 0$, we have the cylinder expression for absorbed power. At $\epsilon^*/2 \approx 0.065$, AW power, absorbed by untrapped and trapped particles, is approximately the same, $F_u(\epsilon^*) \approx F_t(\epsilon^*)$. The dependence of the ratio of absorbed powers $k(\epsilon, A) = F_t(\epsilon, A)/[F_u(\epsilon, A) + F_t(\epsilon, A)]$ as a function of the parameters ϵ and A for $c_A/v_{Te} = 0.2$, $\epsilon^*/2 = 0.125$, $\beta_m = m - nq = 6$ is shown on Fig.2 and Fig.3. This last dependence is weak for the tokamak low aspect ratio.

[1] A.G.Elfimov, A.G.Kirov and V.P.Sidorov. In: *High-Frequency Plasma Heating*, A.G.Litvak (Ed.), American Inst. of Physics Translation series, New-York p.239, (1992).

[2] I.C.Nacimento, R.M.O.Galvaõ, and TCA/Br team. In: Proc. of X Int. Conf. on Plasma Phys. Contr. Pap. Brasil, Foz do Iguacu, v.1, p.69, 31.10.94-04.11.94, (1994).

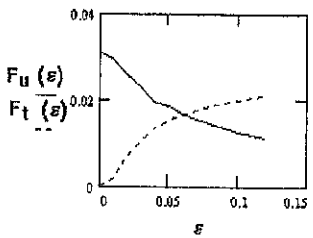

Fig.1

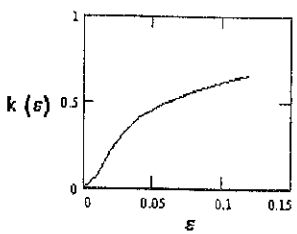

Fig.2

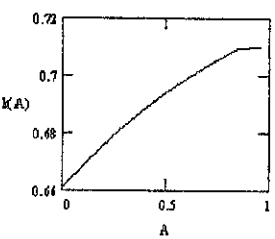

Fig.3

$$k(\varepsilon, A) = \frac{F_t(\varepsilon, A)}{F_u(\varepsilon, A) + F_t(\varepsilon, A)}$$

Fig.1. ***The dependence of absorbed powers on untrapped*** $F_u(\varepsilon)$ ***and trapped*** $F_t(\varepsilon)$ ***particles.***

Fig.2. ***The dependence of the ratio of absorbed powers on*** ε.

Fig.3. ***The dependence of the ratio of absorbed powers on*** A.

The Generation of Shear Flow at a Plasma Edge in the Finite Gyro-radius Guiding Center Approximation

M. Shoucri, J. Lebas[1], G. Knorr[2], P. Bertrand[1], A. Ghizzo[1], G. Manfredi, E. Sonnendrucker[1], H. Burbaumer[3], G. Kamelander[3] B. Krane[2], I. Christopher[2]

Centre canadien de fusion magnétique, Varennes J3X 1S1, Québec Canada

Numerical simulations are performed to study the effect of a viscous dissipation term on the generation of shear flow at a plasma edge in the finite Larmor radius guiding center approximation. The effect of the finite Larmor radius is to allow for a charge separation between electrons and ions to exist in the $\vec{E}\times\vec{B}$ flow. The equations also include the polarization drift, which has a different sign for ions and electrons, and consequently has a tendency to produce and accentuate a charge separation in a time varying electric field. A study of the asymptotic states of the finite Larmor radius guiding center system of equations was presented in Ref. [1], and it was shown that given certain initial conditions, energy can cascade to lower wave numbers, where it manifests itself macroscopically by the appearance of large scale structures [2]. This process in which energy condenses in the low k modes is known as an inverse cascade.

We present in this work results obtained in studying the effect of a viscous dissipation term of the diffusion type on the solution. The pertinent equations are given by:

$$\frac{\partial n_{e,i}}{\partial t}+\nabla\cdot\left[\left(\vec{V}_D+\vec{V}_{pe}\right)n_{e,i}\right]=\nu_{e,i}\nabla^2 n_{e,i} \tag{1}$$

$$\Delta\phi=-\frac{q}{\epsilon_o}\left(\bar{n}_i-\bar{n}_e\right);\quad E=-\nabla\phi \tag{2}$$

$$V_D=-\nabla\phi\times\vec{e}_z/B;\quad V_{pi,e}=\alpha_{i,e}\left\{\frac{\partial E}{\partial t}+V_D\cdot\nabla E\right\} \tag{3}$$

$$\alpha_{i,e}=\frac{1}{\Omega_{i,e}^2}\frac{q_{i,e}}{m_{i,e}};\quad q_i=q\quad\text{and}\quad q_e=-q$$

---

[1] Université Henri Poincaré, Nancy France
[2] Depart. of Physics and Astronomy, Univ. of Iowa, Iowa City, Iowa, U.S.A.
[3] Forschungszentrum Seibersdorf, Seibersdorf, Austria

The bar over the different quantities denotes the integral operation

$$\overline{a}(r) = \int G(r - r')\, a(r')\, dr' \tag{4}$$

which takes into account that the guiding centers and particle locations are not the same. G(r) is a symmetric kernel. In Fourier space, the integral in Eq. (4) becomes a filtering operation, which is numerically easy to perform on the different Fourier modes [1]. Mode $e^{i\vec{k}\vec{r}}$ is multiplied by a factor $g_k = \exp\left(-\frac{1}{2}k^2 r_{i,e}^2\right)$, where k is the wave number normal to the magnetic field and $r_{i,e}$ the Larmor radius for ions and electrons. Equations (1-4) are solved numerically using a method of fractional steps [1]. The results presented in the figures are normalized such that space is normalized to the ions gyro-radius $r_i = v_{thi} / \omega_{ci}$, time is normalized to ω_{ci}^{-1}, potential is normalized to T/e, where T is the temperature (we assume electrons and ions have the same temperature), and velocity is normalized to the ion thermal velocity v_{thi}. This system is solved using a slab model, periodic in the x direction, with an initial profile of guiding center density $n_e = n_i = 0.5\left(1 + \tanh(0.8y)\right)$. The length of the slab is $L_x = 20$ in the periodic direction and extends from $y = -8$ to $y = 8$ in the transverse direction. A grid of 128 points in y and 128 points in x is used.

It is common in the literature to model anomalous transport of particles by adding a diffusion term to the density equations. With this in mind, we consider an initially neutral plasma ($\overline{n}_i = \overline{n}_e$ in Eq. (2)), and consider a small transport of guiding centers. If $v_e = v_i$, the initially neutral equilibrium is conserved. If we set $v_e = 3 \times 10^{-4}$ and $v_i = 7 \times 10^{-5}$, this difference in the small transport of guiding centers between electrons and ions creates a charge separation at the edge of the plasma, which can be unstable. We present in Fig. 1 the time evolution of the first three Fourier modes of the potential growing from round-off errors (the plasma being initially neutral). In Fig. 2, we see the potential profile (averaged over x) due to the charge separation growing and modifying itself from a sine-like shape to a half-sine like shape. Note towards the end the rapid growth and the rapid inversion of the potential to a half-sine like shape. The fundamental Fourier mode in Fig. 1 is dominant, and the inversion of the potential to a half-sine like shape towards the end is consistent with an evolution of the energy to the largest scales available, an evolution characteristic of an inverse cascade. This is in agreement with a powerful statistical analysis of a set of equations close to the one we are studying, presented in Ref. [2]. If the polarization drift is neglected, it was shown in Ref. [2]

that the resulting guiding-center equations have three "rugged" invariants and that the canonical ensemble probability distribution for this system can have negative temperature states, characterized by an inverse energy cascade with energy accumulating in the low k modes in the asymptotic equilibrium. Once this stage has been reached, the energy remains in the lowest k modes, and high k modes fluctuations are negligible. Fig. 3 shows the charge separation resulting from the slow transport of the guiding centers building an initial sine-like shape, and redistributing itself rapidly towards the end so that the potential evolves to a half-sine like shape as presented in Fig. 2. In Fig. 4, the velocity $V_x \sim E_y$ associated with the shear of the flow is presented. It evolves from a bell-shaped structure to a profile decreasing smoothly across the gradient.

We have seen how a small difference in the diffusion term can create a charge separation at the plasma edge of an initially neutral plasma. This charge separation can be unstable, and the instability saturates with energy evolving to the longest wavelength associated with the system, and consistent with boundary conditions, an evolution characteristic of an inverse cascade. In addition, the resulting sheared flow is generated at a plasma edge, and the formation and existence of a charge separation and an electric field at the plasma edge is studied self-consistently with the shear.

We conclude that the present results which shows an unstable charge separation in the presence of a slow transport of guiding centers are relevant to the physics of the transition from a low flow velocity to a high flow velocity at the edge of a plasma. In addition, the present results, (supported by a strong theoretical analysis in Ref. [2]) suggest that inverse cascades (with energy condensing in the low k modes) is a physical mechanism which can play an important role in suppressing turbulence. Work is in progress to add a third dimension to Eq. (1) to include the effect of the motion along the magnetic field on the instability.

Acknowledgments

This work was funded by the Government of Canada, Hydro-Québec and the Institut national de la recherche scientifique.

References

[1] M. Shoucri, J. Lebas, G. Knorr, P. Bertrand *et al.*, Physica Scripta, 55, 617 (1997).

[2] G. Knorr and H. Pecseli, J. Plasma Phys. 41, 157 (1989).

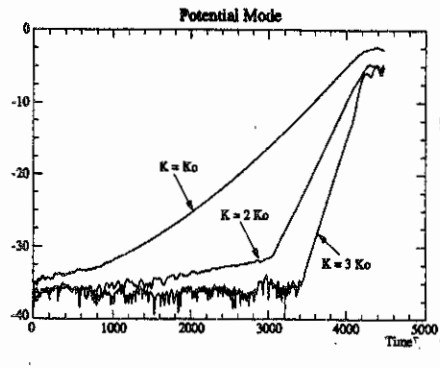

Figure 1

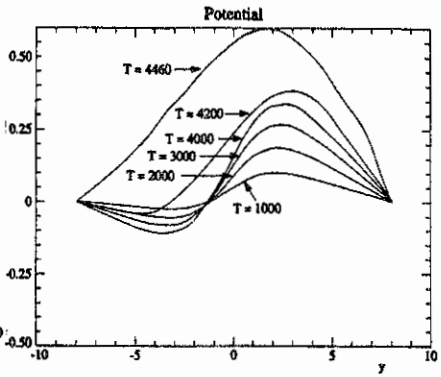

Figure 2

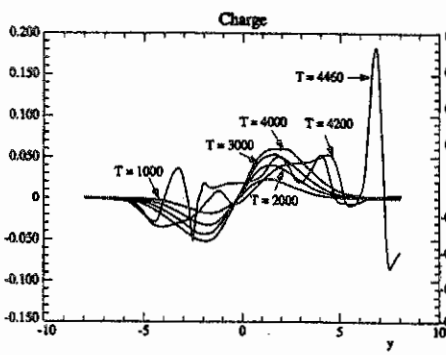

Figure 3

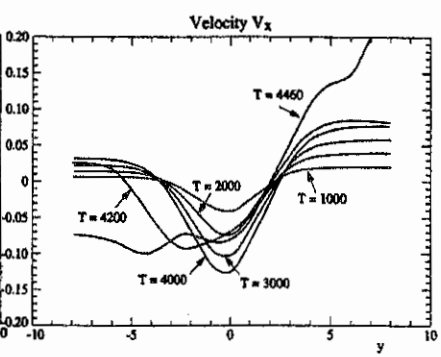

Figure 4

Surface relaxation of highly excited diatomic molecules in the plasma edge

V.N. Malnev[1], Eu.V. Martysh[1], and A.V. Nedospasov[2]

[1] Taras Shevchenko Kiev University, Kiev, Ukraine
[2] Institute for High Temperatures, Moscow, Russia

Recently, it was noted [1] that the plasma edge in tokamaks consists of some amount of diatomic (hydrogen) molecules. Unlike to a low temperature plasma, in this case, the vibration degrees of freedom can be excited by fast heavy particles - ions and atoms. The excitation occurs mostly at the border of highly ionized plasma and the near wall gas. The heat transport from the plasma bulk on the surface of a metal divertor, generally speaking, depends on the pasma edge properties and, particularly, on the accomodation coefficient. It is determined as a part of the total energy of a particle (associated with the kinetic and vibration deegrees of freedom)wich can be transferred into the surface.

The theory of accomodation of structureless particles colliding with the surface, which is modelled by a set of harmonic oscillators, was given by Landau [2].

The theory of accomodation of the vibration energy of low excited diatomic molecules was developed in [3, 4], where the transition probabilities in the vibration spectrum of a diatomic molecule interacting with the surface were obtained. The accomodation coefficient - a part of the vibration energy transferred to the surface oscillators - was calculated in the case of large and small molecular velocities, when a typical time of the molecule-surface interaction is smaller and larger in comparison with a typical time of the molecular vibrations $\frac{1}{\omega_0}$ (ω_0 is a frequency of the molecular vibrations). In both cases the accomodation coefficient of vibration energy happens to be small. This is understandable because a quant of the vibration energy $\hbar\omega_0$ of a diatomic molecule is much larger than the Debye frequency $\hbar\omega_D$ of the surface material.

Along with a time of the *V-T* relaxation (the typical time of establishing of the thermal equilibrium between vibration and kinetic degrees of freedom of a molecule in the gas bulk), we can introduce a time of the surface relaxation (*S-V*) for vibration excited molecules (the typical time of vibration deexcitation of a molecule when it collides with the surface).

A comparison of typical times of the bulk and surface relaxation shows that the *S-V* relaxation dominates over the bulk *V-T* relaxation in a low temperature plasma up to density numbers of the order of $10^{18} cm^{-3}$. We can state that this is also true in the case of the edge plasma.

An analysis of the experimental data shows that the probability of the *S-V* relaxation decreases on increasing of a vibration quantum $\hbar\omega_0$ and when passing from the metal to dielectric surfaces. The quantitative description of these processes must be based on the microscopic theory of interaction of a vibration

excited molecule with the surface. In many cases, and in particularly, in the plasma edge, this interaction has an adiabatic character because the typical time of interaction of a molecule with the surface is much larger than the period of the molecular vibrations. Therefore, the inequality $a\omega_0 / v >> 1$ holds true. Here the phenomenological parameter a corresponds to a typical length of the molecule-surface interaction, v is the mjlecular velocity. The parameter a must be determined from experiment.

In the case of a structureless wall a probability of transformation of the vibration energy $\hbar\omega_0$ into the kinetic energy of a single molecule when colliding with the surface is proportional to the Messi factor $\exp\{-\omega_0 a / v\}$ and is exponentially small.

However, the real *S-V* relaxation is accompanied by the transformation of some part of vibration energy into the energy of the surface oscillations. The phonon spectrum of solids is restricted by the Debye frequency ω_D and usually cases $\omega_0 > \omega_D$. If we take into account the surface oscillators, we can expect that in the Messi factor instead ω_0 must be a difference $\omega_0 - \omega_D$. Therefore, we can expect some increase in the probability of the vibration relaxation.

By using this model we can obtain a probability of the heterogeneous relaxation of the vibration energy. The corresponding results for low excited vibration molecules are given in [4]. The main conclusion which can be made from these results is that the probability of the *S-V* relaxation is comparatively small. This is true for low vibration excited molecules when the anharmonism can be neglected. The situation changes for highly excited molecules when the anharmonism becomes significant.

The adiabatic character of the surface-molecule interaction requires its analytic form . We use a model potential

$$V = A\left(e^{-z_1/a} + e^{-z_2/a}\right), \qquad (1)$$

where z_1 and z_2 are distances of the first and second atoms of the molecule from the surface.

Within a wide temperature diapason, the translation and rotation degrees of freedom are quantum. This assumption pertims to solve the problem of motion of the molecule center mass by using classic mechanics. The transitions in the quantum vibration degrees of freedom are determined by the time dependence of the classical motion of the molecule center of mass in the field (1). The probability of transitions in the vibration degrees of freedom we calculate in the first order of the time dependent perturbation theory. The matrix elements of perturbation, which depends on the normal coordinates of the surface oscillators and the vibration coordinate of the molecular vibrations are evaluated by using the functions of harmonic oscillators for both the surface and molecular vibrations.

The probability of deactivation of the one-quantum transition in the molecular vibration when interacting with the surface oscillators obtained in [4] may be written in the form

$$w_n^{n-1} = n\frac{16}{9}\sqrt{\frac{\pi}{3}}\frac{TT_s^2}{\rho c^3 a^2 \hbar\omega_0}\int_0^{\theta/T_s}\frac{\alpha^{7/3}e^{-3\alpha^{1/3}}}{e^x-1}x\,dx, \qquad (2)$$

$$\alpha = \frac{\omega_0 a}{v_T}\left(1-\frac{T_s}{\hbar\omega_0}x\right),$$

where n is the initial quantum number of the molecular oscillator, ρ is a density of the surface material, c is the sound velocity in the material, ω_0 is the molecular vibration frequency, T and T_s are the gas and the surface temperatures respectively, θ is the surface material Debye temperature, $v_T = \sqrt{2T/m}$ is the molecule heat velocity.

The probability (1) must be averaged with respect to a distribution of the molecule quantum states. In a general case, the usage of (2) is possible only after numerical culculations. Here we propose the qualitative considerations.

It is obviously that relation (2) gives the following leading dependence of the probability of the surface relaxation of the molecule vibrations

$$w_n^{n-1} \sim \exp\left\{-3\left[\frac{m(\omega_0-\omega_D)^2a^2}{2T}\right]^{1/3}\right\}. \qquad (3)$$

Such a type of dependence on a gas temperature is typical for the processes of the V-T relaxation which take place in the bulk of a molecular gas. Moreover, it corresponds qualitativly to available experimental data. To obtain a quantitative correspondens one has to correctly choose the parameter a which characterizes a typical length of the molecule-surface interaction

The obtained probability (3) allows us to take into account the anharmonicity of the molecular highly excited states. The simplest way of doing this is to introduce the reduced frequency of the molecular vibrations depending on quantum number n or substitute ω_0 with $\omega_n = \omega_0(1-\gamma n)$, where γ is the anharmonicity coefficient.

A large percent of excited molecules corresponds to high vibration temperatures. It is known that in this case the vibration population obeys the Treanor distribution which differs from the Boltzmann distribution. It has a typical plateu which starts with moderate n and lasts up to the so-called predissociation regime. After the quantum number $n_0 = \frac{D}{\hbar\omega_0}$ (D is the dissociation energy) the Treanor distribution decreases sharply.

For rough evaluations we can substitute in (3) ω_0 with the expression $\omega_0(1-\gamma n_0/2)$. A smallness of parameters γn_0 and ω_D/ω_0 allows us to obtaine that the probability of the *S-V* relaxation of higly vibration excited molecules increases by a factor $\exp\left\{\alpha^{1/3}\gamma\frac{D}{\hbar(\omega_0-\omega_D)}\right\}$. For highly excited hydrogen molecules (n=4) at the vibration temperature T_V=10^3K and carbon walls, we get that the *S-V* probability increases approximately by one order.

We have to note now that at the low gas temperatures a vibration excited molecule firstly is absorbed by the surface in a bond state and spending on it some time relaxes and leaving the surface. Taking account of this mechanism, we can show that the *S-V* relaxation probality increases by a factor $exp(q/T)$, where q is the absorption heat.

The high temperatures of the plasma edge make possible to assume that there are no absorbed molecules. Therefore, the probability of the *S-V* relaxation of highly vibration excited molecule at temperatures 1500-2000°*K* on a carbone divertor is of the order of 10^{-3}. It is approximately ten times more than the coorresponding probability of low excited vibrations.

At low temperatures when the absoption of molecules is important, we obtained the probability of vibration relaxation of highly excited hydronen molecules of the order of $5 \cdot 10^{-3}$. This enables us to note that collisions of highly vibration excited diatomic molecules with surfaces may be an efficient mechanism of their cleaning.

Conclusion

It is shown that the relaxation probability of higly vibration excited diatomic molecules colliding with a surface is much larger than the one of low excited molecules if the anharmonism is taken into account. This circumstance may be of interest in the plasma edge physics and in the plasmochemistry.

References

1. Krashennikov S.I., A.Yu. Pigarov, D.J. Sigmar, Plasma recombination and divertor detachment, Physics Letter A 214, 285(1996).
2. Landau L.D. On the theory of the accomodation coefficient, in the Collection of works, p. 146.. Nauka, Moscow, 1969.
3. Kogan E.Ya. and Malnev V.N., Accommodation coefficient of a diatomic molecular gas, Sov. Phys. JETP, v. 47 (2), 276 (1978).
4. Kogan E.Ya. and Malnev V.N., Heterogeneous relaxation of vibration excited molecules of a gas, Ukr. Fiz. Zhur., v. 28, No 3, 374 (1983).

Features of plasma edge turbulence in TBR tokamak

M. V. A. P. Heller, R. M. Castro, **I. L. Caldas**, Z.A. Brasilio, R. P. da Silva, I. C. Nascimento
Institute of Physics, University of São Paulo
C. P. 66318, 05315-970, São Paulo, SP, Brazil

1. Introduction

The relation between plasma transport and turbulence has been studied at TBR tokamak [1] by using a specially designed edge probe system, which measures the mean and fluctuating values of potential, temperature, density, and the radial and poloidal fluctuations of magnetic field. A modified triple probe confirmed the influence of temperature fluctuations on density and potential fluctuations and consequently on transport. Bispectral analysis techniques showed a quadratic mode coupling between temperature fluctuations and other quantities.

2. Experiment description

TBR [2] is an Ohmically heated tokamak with major radius R=0.30 m, minor radius a=0.08 m, toroidal magnetic field B_ϕ=0.4 T, plasma current I_p=10 kA, chord average density of $n_0=7x10^{18}m^{-3}$, and pulse length of 10 ms.

The probe assembly [1] (Figs.1a,b) is inserted at the top of the tokamak, 45^0 toroidally displaced from the poloidal limiter. This system is composed by four tips, a four-pin probe array, and a single probe tip. Two of the four tip configuration measure the floating potential fluctuations, $\tilde{\varphi}_f$ and the other two measure the ion saturation fluctuations, $\tilde{I}si$. These two pairs of pins were used for determining the spectrum S(k,f) and power weighed average values of poloidal wave vector, k_θ, frequency, f, phase velocity, v_{ph}. The single tip, at 3mm from the four tip configuration, measured the mean value of floating potential. Electron mean temperature, T_e, its fluctuation, ion saturation current, and its fluctuation, were obtained using a modified triple probe technique with four pins for phase delay error corrections. Two sets of magnetic coils (Fig.1a) measured poloidal, $\tilde{B}_\theta$, and radial, $\tilde{B}_r$, components of magnetic field fluctuations.

3. Discussion and Conclusion.

Taking into account the temperature fluctuation corrections ($T_e^{rms}/T_e \approx 0.15$ [1]), we obtained from spectral analysis the correlation between fluctuating parameters and the particle and energy transport.

Linear correlation between the fluctuations show that ion saturation current and floating potential fluctuations are in phase and present a linear coherence $\gamma \approx 0.5$ at frequencies below 100 kHz. The linear coherence between floating potential and temperature fluctuations is lower than coherence between ion saturation current and temperature fluctuations.

Fig.2 shows the superposition of similar power spectra for ion saturation current, temperature and poloidal magnetic fluctuations, suggesting a common driving force for these fluctuations. In TBR, as previously reported [3], the main frequencies observed in the spectra of electrostatic fluctuations are smaller than Mirnov frequencies, and there is a partial superposition between magnetic and electrostatic spectra. These characteristics encourage the investigation of possible correlation between these two kinds of oscillations.

Fig.3 shows the velocity profile with and without the temperature corrections (velocity is in the ion diamagnetic drift direction). Temperature fluctuations enhanced phase velocity. The absence of shear layer, as already reported [3], is confirmed in this experiment.

The fluctuation driven particle flux $\Gamma_{\tilde{r}\tilde{E}\theta}$ is derived from the cross correlation between density fluctuations ($\tilde{n}$) and the poloidal electric field fluctuations ($\tilde{E}_\theta$) [4]. The importance of particle fluxe correction can be seen in Fig.4. The diffusion coefficient is $D=\Gamma/\nabla n \approx 0.5$ m^2/s (at r/a=0.90), and the particle confinement time $\tau_p \approx 1.5$ ms.

The convective electron energy-flux is related to particle flux by $q_{conv.}=5T_e < \tilde{n}\,\tilde{E}_\theta > /(2B)$, and the conductive part by $q_{cond}=5n< \tilde{T}_e\,\tilde{E}_\theta > /(2B)$, and $q_{tot}=q_{conv.}+q_{cond}$ [4]. Fig.5 shows the total radial energy fluxes profiles with and without temperature corrections.

To investigate the nonlinear coupling we used bispectral analysis [5]. The autobicoherences of electrostatic and magnetic fluctuations showed non prominent peaks. However, they have a level much larger than the statistical uncertainty.

Fig.6 shows the integrated bicoherence Σb^2, for temperature and poloidal magnetic field fluctuations; where b^2 is the bicoherence corresponding to a triplet f_1, f_2 and $f=f_1+f_2$. Each value of Σb^2 is a sum of b^2 for all f_1 and f_2 satisfying the resonant condition $f=f_1+f_2$ within the spectral region $0 \le f_2 \le f_{N/2}$ and $f_2 \le f_1 \le f_N-f_2$, where f_N is the Nyquist frequency. The nonlinear coupling is lower for the poloidal magnetic field fluctuations. However, for temperature fluctuations the sum of bicoherence is close to 0.5 indicating the presence of nonlinear interactions at frequencies around 60 kHz.

The crossbicoherence between poloidal magnetic and electrostatic fluctuations is more significant for temperature and ion saturation current fluctuations. Figs.7a,b show the squared

crossbicohrence spectrum (surface and contour plot) of temperature and poloidal magnetic fluctuations, with maximum level of 0.19±0.02. The highest value appears in the same frequency region of the crossbicoherence peak observed for the two poloidal magnetic coils.

The inclusion of temperature fluctuations in the measured electrostatic parameters gives a better evaluation of the turbulent particle and heat flows and a more reliable description of the turbulence at plasma edge.

This work was partially supported by the Brazilian agencies FAPESP and CNPq.

References.

[1] R. M. Castro, M. V. A. P. Heller, I. L. Caldas, R. P. da Silva, Z. A. Brasilio, I. C. Nascimento, Phys. Plasmas **3**, 971 (1996); Phys. Plasmas **4**, 329 (1997).

[2] I. C. Nascimento, I. L. Caldas, and R. M. O. Galvão, J. Fusion Energy **12**, 295 (1993)..

[3] M. V. A. P. Heller, R. M. Castro, Z. A. Brasilio, I. L. Caldas, and R. P. da Silva, Nuclear Fusion **35**, 59 (1995).

[4] A. J. Wootton, B. A. Carreras, H. Matsumoto, K. McGuire, W. A. Peebles, Ch. P. Ritz, P. W. Terry, S. J. Zweben, Phys. Fluids **B2**, 2879 (1990).

[5] Ch. P. Ritz, E. J. Powers, and R. D. Bengtson, Phys. Fluids **B1**, 153 (1989)

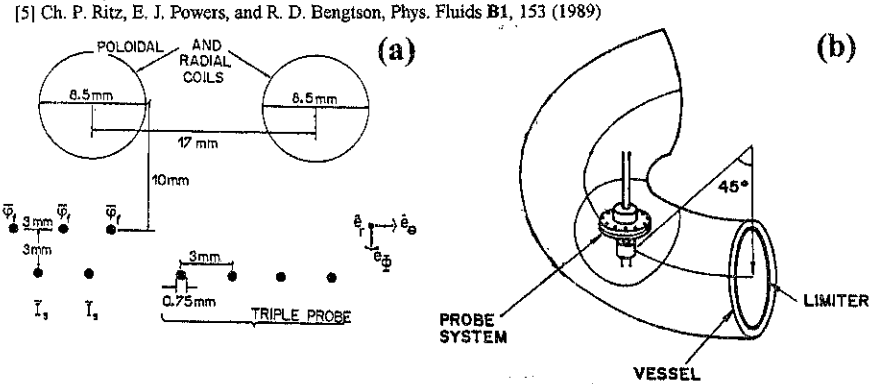

Fig.1 Scheme of probe assembly, (a). Section of the tokamak illustrating measurement position (b).

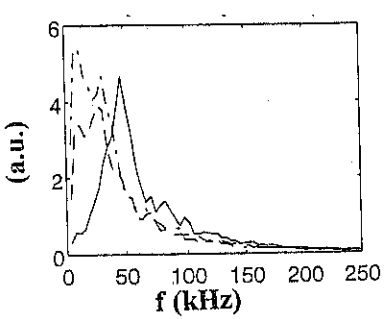

Fig.2 Spectra of ion saturation current (-.-.-),temperature fluctuations (——) at r/a=0.85 and poloidal magnetic fluctuations (—) at r/a=1.10.

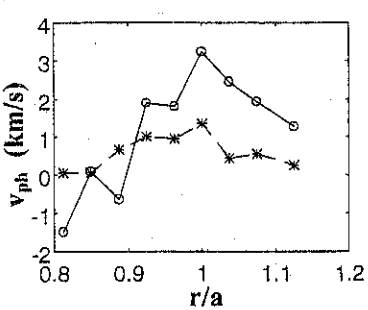

Fig.3 Radial profile of phase velocity for potential fluctuations with(o) and without (*) temperature fluctuation correction.

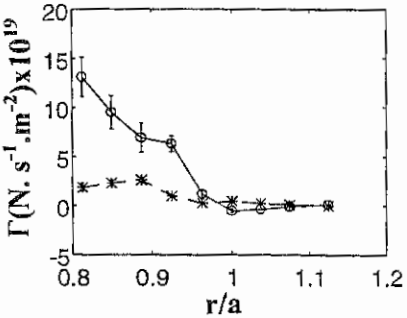

Fig.4 Radial profiles of particle fluxes with (o) and without (*) temperature fluctuation corrections.

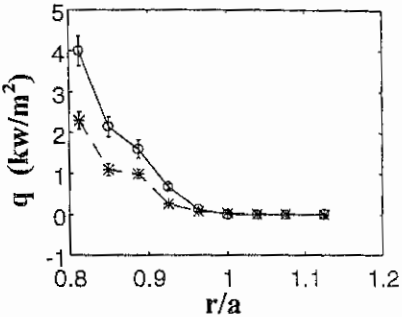

Fig.5 Radial profiles of total energy fluxes with (o) and without (*) temperature fluctuation corrections.

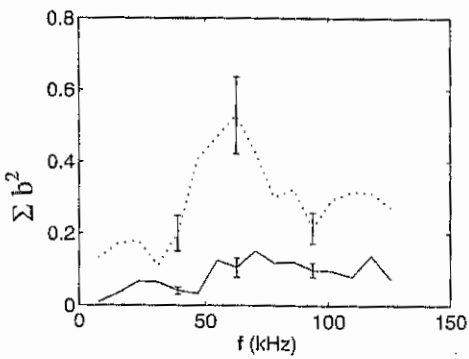

Fig 6 Integrated bicoherence for temperature (---) at r/a=0.92 and poloidal magnetic fluctuations at r/a=1.1.

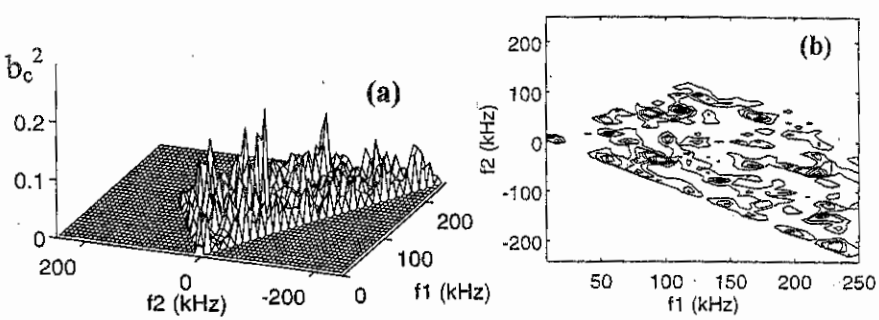

Fig.7 Squared crossbicoherence spectrum of temperature and poloidal magnetic field fluctuations (r/a=0.92 and r/a=1.10 respectively), (a) surface plot, (b) contour plot.

THE COLLISION LIMITS OF COLLISIONLESS BOUNCE-RESONANCE DISSIPATION OF WAVES IN MAGNETIZED TOROIDAL PLASMAS

F.M.Nekrasov, **A.G.Elfimov***, C.A. de Azevedo and A.S. de Assis+
Instituto de Física, Universidade do Estado do Rio de Janeiro, Rio de Janeiro, RJ, Brazil.
*Instituto de Física, Universidade de São Paulo, 05315-970, SP, Brazil
+Instituto de Matemática-GMA, Universidade Federal Fluminense, Niterói, RJ, Brazil.

Introduction. To study the effect of weak collisions on collisionless wave dissipation in plasmas is very important in connection with the radio-frequency (RF) plasma heating and current drive in large tokamaks like JET, TFTR and so on. The theoretical analysis of the effect of weak collisions on wave dissipation is presented in Ref.[1] where the collisional limits of the electron Landau damping are demonstrated for homogeneous magnetic field. Because of inhomogeneity of the tokamak magnetic field the parallel velocity of the untrapped particles suffers the poloidal modulation and trapped particle effect appear[2]. The theoretical analysis of the collisionless wave dissipation based on the Vlasov-Maxwell set of equations is rather difficult. For toroidal plasmas with circular magnetic surfaces and small toroidicity parameter, $\epsilon = r/R_0 \ll 1$, the analytical solution of Vlasov's equation have been developed in [2]. Finally, wave dissipation depended strongly on electron and ion bounce resonance frequency $\approx |j|\omega_b \approx |j|\sqrt{r/R_0}v_{Te,i}/q_t R_0$. The effect of weak collisions is important because the weak collisions may destroy phase correlation when the collision frequency is the order of frequency shift ($\approx \omega_b$) between two bounce resonance frequencies. The simplest model to account the Coulomb collisions is Krook model. This model gives us correct limit in the Landau pole method integration of collisionless wave dissipation[2] but it does not allow to analyze collision effects in the velocity space.

Hear, using the Boltzmann equation, we study the effect of weak Coulomb collisions on the parallel permeability of magnetized toroidal plasmas with circular magnetic surfaces. We begin to discuss the problem related to the evaluation of the oscillating part of the distribution function, which is governed by the Boltzmann equation with a collisional operator in Landau-Fokker-Planck form, in the toroidal plasma geometry with the circular cross section of magnetic surfaces. The Boltzmann equation can be reduced to two dimensional form in the drift approach, which means approximation of small ion and electron Larmor radii. Introducing variables related to a magnetic moment and an angle:

$$\lambda = \sin^2\gamma B_0^0/B_0(\rho,\theta) = \sin^2\gamma(1+\epsilon\cos\theta), \quad \Theta = \theta + \frac{\epsilon}{2}\sin\theta,$$

and renormalizing the distribution function, electric field and current with the formulae,

$$f_s = \bar{f}_s \exp\left(\mathrm{i}\frac{3\epsilon}{2} n q_t \sin\Theta\right), \quad E_3 = \bar{E}_3\sqrt{1+\epsilon\cos\Theta}\exp\left(\mathrm{i}\frac{3\epsilon}{2} n q_t \sin\Theta\right),$$

we obtain the drift kinetic equation for electrons with the accuracy of ϵ in the form,

$$\frac{\partial \bar{f}_s}{\partial t} + sk_0 v_\parallel\left(\frac{\partial \bar{f}_s}{\partial\Theta} + \mathrm{i}nq_t\bar{f}_s\right) - \frac{\nu v_T^2}{v}\frac{\partial^2\left(v\,\bar{f}_s\right)}{\partial v^2} = -\frac{sev_\parallel F_M}{T}\bar{E}_3, \qquad (1)$$

where $v_\parallel = v\sqrt{1+\epsilon\cos\Theta-\lambda}$ is the module of parallel velocity, $s = \pm 1$ means positive or negative direction of a velocity of charged particles along magnetic field, $q_t = rh_\zeta/R_0h_\theta$ is

the tokamak stability parameter, $k_0 = h_\theta/r$. Note that we study the electromagnetic fields and perturbed distribution function oscillating in time as $\exp(-\mathrm{i}\omega t)$. In Eq.(1), we use the diffusion form of the collision operator over the variable v only. Because the scattering term for the small wave phase velocities has the same order as the diffusion term, the diffusion approximation is enough to estimate the limits of collisionless approximation.

In the case of trapped particles, it is necessary to introduce an additional transformation of the angle variable Θ and new variables $\hat{w}$ via Jacobi function and $\hat{\kappa}$:

$$\hat{w}(\hat{\theta}) = \int_0^{\hat{\theta}} \frac{\mathrm{d}\eta}{\sqrt{1-\hat{\kappa}^2\sin(\eta)^2}}, \quad \hat{\kappa}^2 = \frac{1+\epsilon-\lambda}{2\epsilon}, \quad \sin\hat{\theta} = \frac{1}{\hat{\kappa}}\sin\frac{\Theta}{2}.$$

Eq.(1) with the boundary conditions, $\bar{f}_s^t(\hat{w}=\pm K) = \bar{f}_{-s}^t(\hat{w}=\pm K)$, has the form,

$$\begin{aligned} &-\mathrm{i}\omega\,\bar{f}_s^t + sk_0 v\sqrt{\frac{\epsilon}{2}}\left(\frac{\partial \bar{f}_s^t}{\partial \hat{w}} + 2\mathrm{i}\,nq_t\hat{\kappa}\,\mathrm{cn}\hat{w}\,\bar{f}_s^t\right) - \nu_e\frac{v_T^2}{v}\frac{\partial^2}{\partial v^2}\left(v\bar{f}_s^t\right) \\ &= -s\sqrt{2\epsilon}\frac{e\,vF_M}{T}\hat{\kappa}\,\mathrm{cn}\hat{w}\sum_{m=-\infty}^{\infty} E_m \exp\left[2im\hat{\kappa}\int_0^{\hat{w}}\mathrm{d}\eta\mathrm{cn}\eta\right], \end{aligned} \tag{2}$$

and the oscillating current induced by trapped electrons is

$$j_{3,p}^t = -4e\,\epsilon\sum_s s\int_0^\infty v^3\mathrm{d}v\int_0^1 \mathrm{d}\hat{\kappa}\hat{\kappa}^2\int_{-K}^{K}\mathrm{cn}\hat{w}\,\bar{f}_s^t\exp\left[-2ip\hat{\kappa}\int_0^{\hat{w}}\mathrm{d}\eta\mathrm{cn}\eta\right]\mathrm{d}\hat{w}. \tag{3}$$

Expanding the right hand side of Eq.(2) in Fourier series over $\hat{w}$,

$$\hat{\kappa}\,\mathrm{cn}\hat{w}\exp\left[2\mathrm{i}(m+nq_t)\hat{\kappa}\int_0^{\hat{w}}\mathrm{d}\eta\mathrm{cn}\eta\right] = \sum_{r=-\infty}^{\infty} C_{m,r}^t\exp\left(\mathrm{i}\,r\frac{\pi\hat{w}}{2K}\right),$$

we can obtain the solution in the form:

$$\bar{f}_s^t = \tilde{f}_s^t\exp\left[-2\mathrm{i}nq_t\hat{\kappa}\int_0^{\hat{w}}\mathrm{d}\eta\mathrm{cn}\eta\right], \quad \tilde{f}_{\pm 1}^t = \sum_{r=-\infty}^{\infty} g_{m,r}^t(v,\hat{\kappa})C_{m,\pm r}^t(\hat{\kappa})\exp\left(\pm\mathrm{i}\,r\frac{\pi\hat{w}}{2K}\right) \tag{4}$$

where the coefficients $C_{m,0}^t$ are zeros and the coefficients $C_{m,r}^t$ have symmetry properties:

$$C_{m,r}^t + (-1)^r C_{m,-r}^t = 0. \tag{5}$$

The function $g_{m,r}^t(v,\hat{\kappa})$ is a solution of the differential equation of the second order:

$$-\mathrm{i}\omega\,g_{m,r}^t + \mathrm{i}\,r\sqrt{\frac{\epsilon}{2}}\frac{\pi}{2K}k_0 v\,g_{m,r}^t - \nu_e\frac{v_T^2}{v}\frac{\partial^2}{\partial v^2}\left(vg_{m,r}^t\right) = -\sqrt{2\epsilon}\,e\frac{v\,F_M}{T}E_m. \tag{6}$$

To solve the above equation, we use the Laplace transformation:

$$\Gamma_{m,r}^t(y) = \int_0^\infty g_{m,r}^t\exp(\mathrm{i}uy)\,u\,\mathrm{d}u \tag{7}$$

where $u = v/v_T$ is the dimensionless velocity. The solution of the problem has the form:

$$\Gamma_{m,r}^t = -\frac{e\sqrt{\epsilon}N_0E_m}{2\pi\sqrt{\pi}m_e}\exp\left(\frac{3\mathrm{i}\,\omega y - \nu_e y^3}{3\bar{\omega}_{bt}^r}\right)\int_{-\mathrm{sign}\,r\cdot\infty}^{y}\mathrm{d}\bar{y}\int_0^\infty\frac{u^2\mathrm{d}u}{v_T^4\bar{\omega}_{bt}^r}\exp\left(\frac{\nu_e\bar{y}^3 - 3\mathrm{i}\omega\bar{y}}{3\bar{\omega}_{bt}^r} - \frac{u^2}{2} + \mathrm{i}uy\right)$$

where $\bar{\omega}^r_{bt}$ is the bounce frequency of trapped particles, $r\pi\sqrt{\epsilon/2}\,k_0 v_T/(2K)$. Using the general solving procedure shown above, we can write the total solution of Eq.(2) for the trapped particle distribution function, $\tilde{f}^t_s$, and the parallel component of the dielectric tensor (trapped particle part) expressed through this function is:

$$\varepsilon^{p,m}_{33(t)} = (2\epsilon)^{3/2}\omega^2_{pe}\sum_{r\neq 0}\int_0^1 K\,\mathrm{d}\hat{\kappa}^2\frac{C^t_{p,r}C^t_{m,r}}{\pi(\bar{\omega}^r_{bt})^2}\left[1+\frac{\mathrm{i}\omega}{|\bar{\omega}^r_{bt}|}\int_0^\infty \mathrm{d}\eta(1-\eta^2)\exp\left(\frac{\mathrm{i}\omega\eta}{|\bar{\omega}^r_{bt}|}-\frac{\nu_e\eta^3}{3|\bar{\omega}^r_{bt}|}-\frac{\eta^2}{2}\right)\right] \tag{8}$$

The untrapped particle part of the dielectric tensor can be found in the same manner:

$$\varepsilon^{p,m}_{33(u)} = 4\frac{\epsilon\sqrt{2\epsilon}}{\pi}\omega^2_{pe}\sum_{r=-\infty}^{\infty}\int_{\kappa_0}^1\frac{K\,\mathrm{d}\kappa}{\kappa^4}\frac{C^u_{p,r}C^u_{m,r}}{[\bar{\omega}^r_{bu}]^2}\left[1+\frac{\mathrm{i}\omega}{|\bar{\omega}^r_{bu}|}\int_0^\infty \mathrm{d}\eta(1-\eta^2)\exp\left(\frac{\mathrm{i}\omega\eta}{|\bar{\omega}^r_{bu}|}-\frac{\nu_e\eta^3}{3|\bar{\omega}^r_{bu}|}-\frac{\eta^2}{2}\right)\right] \tag{9}$$

Discussion. The imaginary part of the parallel permittivity of the toroidal plasmas is very important for the analysis of wave dissipation in plasmas, because density of wave dissipated power is proportional to it. The Coulomb collision effects on wave dissipated power is defined by real part of the integral in Eqs.(8):

$$I_r(\nu) = \int_0^\infty \mathrm{d}\eta(1-\eta^2)\exp\left(\mathrm{i}\,\Omega_r\eta-\frac{\nu_r\eta^3}{3}-\frac{\eta^2}{2}\right) \tag{10}$$

where parameters, $\Omega_r = \omega/|\bar{\omega}^r_{bu,t}|$, $\nu_r = \nu_e/|\bar{\omega}^r_{bu,t}|$, are introduced. To define the limits of collisionless dissipation, it is sufficient to find domain of parameters where dependence of $I_r(\nu)$ on ν is slight. For large tokamaks, $R_0 \approx 3$ m, when the density is of $\sim 10^{14}\mathrm{cm}^{-3}$ and temperature of $\sim 10^4$eV, the parameter ν_r is small, $\nu_e/|\bar{\omega}^r_{bu}| \approx 10^{-3}$. In this case, the exponential function under the above integral can be presented as, $\exp[-\bar{\nu}_r\eta^3/3] \approx 1-\bar{\nu}_r\eta^3/3$. Finally, we express the results of integration via the error function[3]:

$$\mathrm{Im}I_r \approx \Omega_r^2\sqrt{\frac{\pi}{2}}\exp\left(-\frac{\Omega_r^2}{2}\right)+\frac{\nu_r}{3}\left[6-8\Omega_r^2+\Omega_r^4-\Omega_r(12-9\Omega_r^2+\Omega_r^4)\int_0^{\Omega_r}\mathrm{d}\Omega\exp\left(\frac{\Omega^2-\Omega_r^2}{2}\right)\right] \tag{11}$$

In low frequency domain, $\Omega_r < 1$, the limits of collisionless dissipation related to imaginary part of $\varepsilon^{p,p}_{33(u,t)}$ are defined by conditions:

$$\nu_e \ll \omega^2/|\bar{\omega}^r_{bu,t}|. \tag{12}$$

From these conditions we can find maximal number of bounce-resonances, which can be used for calculations of collisionless dissipation in Eqs.(8). In particular, for trapped particles we obtain, $r_{max} = \omega^2/\nu_e\omega_{bt}$. For high frequency, $\omega \gg |\bar{\omega}^r_{bu,t}|$, using asymptotic of large argument of the error function, we can obtain the condition:

$$\nu_e \ll \nu_{max} = \sqrt{\frac{\pi}{8}}\frac{\omega^6}{|\bar{\omega}^r_{bu,t}|^5}\exp\left[-\frac{\omega^2}{2(\bar{\omega}^r_{bt})^2}\right]. \tag{13}$$

Here, we note that the most restricted condition is appear for the collisionless dissipation related to the first bounce-resonance ($r = 1$). The numerical calculations of Eqs.(10,11), which are fulfilled for different values of ν_r and Ω_r, confirm the theoretical estimations.

For untrapped particles the condition of a collisionless dissipation will be the same as for trapped particles in Eq.(12) if we change the number r on $r + nq_t$ in the expression of the bounce-resonance frequency. For $nq_t \sim 1$, we have the same result as for trapped particles. A novelty appear for the case $|r + nq_t| \ll 1$, when the collisionless dissipation is exponentially small. It should be noted, that conditions (37) and (38) are necessary, but not sufficient. The sufficient conditions can be moderated. To obtain them, we should perform integration over κ and summarize over r in the equations for $\varepsilon^{p,m}_{33(u)}$. Expanding the function $\widetilde{am}$ in q-series, we show these results for large parallel number, $\epsilon|m+nq_t| \gg 1$,

$$C^u_{m,r} = \frac{\pi}{2K}\frac{r+nq_t}{m+nq_t} J_{r-m}[4q(m+nq_t)]. \tag{14}$$

Because of large index of Bessel function we can carry out summation in Eq.(9) from $-r_{max}$ to $r_{max} \approx \epsilon|m+nq_t|$. As a result we obtain:

$$\varepsilon^{p,m}_{33(u)} = \frac{\sqrt{2\epsilon}\,\omega^2_{pe}R^2_0 q^2_t}{\pi v^2_T}\int_{\kappa_0}^1 \frac{K\,\mathrm{d}\kappa J_{m-p}[4q(p-m)]}{\kappa^2(p+nq_t)(m+nq_t)}\left\{1 + \mathrm{i}\tilde{\Omega}_m I_r\right\} \tag{15}$$

$$\tilde{\Omega}_m = \frac{2K}{\pi}\frac{\kappa\,\omega\,R_0 q_t}{\sqrt{2\epsilon}\,(m+nq_t)v_T};\quad \tilde{\nu}_m = \frac{2K}{\pi}\frac{\kappa\,\nu_e\,R_0 q_t}{\sqrt{2\epsilon}\,(m+nq_t)v_T}.$$

In low frequency and weak collision domain, $\Omega_m \ll 1$ and $\nu_m \ll 1$, expanding $K(\kappa)$ in Taylor series taking into account only three terms, the imaginary part of the diagonal tensor components ($p = m$) can be found with the accuracy of $\sim 10\%$:

$$\mathrm{Im}\,\varepsilon^{m,m}_{33(u)} = \frac{\omega^2\,\omega^2_{pe}R^4_0 q^4_t}{2\epsilon(m+nq_t)^4 v^2_T}\left(\frac{1.1\,\omega R_0 q_t}{\sqrt{2\epsilon}\,|m+nq_t|\,v_T} + 1.7\frac{\nu}{\omega}\right) \tag{16}$$

and the condition, $\nu_e \ll \omega^2/|\bar{\omega}_{bu}nq_t|$, of the collisionless dissipation will be the same as in Eq.(12) when $r = 0$. The tensor elements ($m \neq p$) can be analyzed in the same manner.

Here, we note that it is possible to use only the diffusion form of the collision operator over the variable v in Eq.(1) where the scattering term was disregarded. This approach is valid for analysis of the deeply trapped electrons when the dependence of bounce-resonance frequency over κ is very weak. In this case the perturbed distribution function in Eq.(2) is strongly affected by the diffusion term of the collision operator only. For untrapped particles the scattering term is important because it has the same order as the diffusion term but the diffusion approximation is enough for qualitative estimations.

In synthesis, on the basis of the study of the imaginary part of parallel plasma permittivity in tokamaks with the circular cross section of magnetic surfaces, we find that the weak collisions can strongly affect on the collisionless wave dissipation. In the low frequency wave band, $\omega < \omega_b$, the sufficient condition for the collisionless wave dissipation is defined by the inequality, $\nu_e \ll \omega^2/\omega_b$. For waves with large phase velocity, $\omega/k_\parallel \gg v_{Te}$, the sufficient condition for the collisionless dissipation defined by Eq.(13) is only qualitative because the coefficients in collisional operator used in Eq.(1) are valid for $v < v_{Te}$. We use these coefficients because number of particles in the velocity space, $v \sim v_{ph}$ is exponentially small and the main contribution is defined by particles with $v < v_{Te}$.

[1] S.P.Auerbach , Phys. Fluids, **20**, 1836 (1977).

[2] F.M.Nekrasov, Sov.J.Plasma Phys., **18**(8) (1992) p.520.

[3] M. Abramowitz, I.A. Stegun: Handbook of mathematical functions (Dover Publication Inc., New York, 1972) p.555-587.

The Influence Of Light Impurity Ions On Alfvén Wave Dispersion And Alfvén Wave Plasma Heating

A.G.Elfimov, R.M.O. Galvão, I.C.Nascimento, and G.Amarante-Segundo

Departamento Física Aplicada, Instituto de Física, USP, São Paulo - SP, BRASIL

Introduction. Alfvén wave heating and current drive are attractive for tokamaks because of the availability of high power radio frequency (RF) generators, the simplicity of antenna structures, possibility to heat the plasma core and there is no any density limits for current drive operation. In the past, Alfvén wave plasma dispersion and heating was intensively investigated in the stellarators, and TCA and Phaedrus-T tokamak experiments[1-3]. The best heating results were obtained by employing a surface Alfvén wave (SAW) resonance with mode conversion into kinetic Alfvén (KA) waves in stellarators[1] and the regime of global Alfvén wave (GAW) resonance in TCA tokamak[2]. The main problems of these experiments are growth of plasma density and partially ionized heavy impurities, such as oxygen and iron, supplied by chamber wall during RF pulse. The impurities cause large radiation energy loses and introduce zones of ion cyclotron resonance. If the wave frequency is the order of the impurity ion cyclotron frequency, an ion-ion Alfvén continuum appear and the dispersion characteristics of Alfvén waves may be strongly modified [4]. To avoid impurity problems, a boronization procedure was used in the Phaedrus-T experiments [3] where Alfvén wave heating and current drive was demonstrated in low density plasmas. In the nearest future, the Alfvén wave heating and current drive will be under investigation in the TCA/Br -Brazilian tokamak with Alfvén wave excitation [5], utilizing a modified version of the experimental configuration previously used in Lausanne[2]. To increase antenna impedance and central power deposition for effective current drive, an antenna with multiple phasing elements has been designed, that produces different combinations of toroidal ($n=\pm 4, \pm 6$) and poloidal ($m=\pm 1$) wavenumbers. The boronization procedure is also considered to stabilize density growth, which is necessary for the best conditions for the eigenmode resonance excitation, and to reduce energy loss caused by partially ionized heavy impurities, such as oxygen and iron.

Here, applying one-dimensional kinetic code[4], we extend the analyses of the Alfvén spectrum in tokamak. We take into account the effects of boron and carbon impurities fully ionized on Alfvén wave dispersion characteristics and wave dissipated power. We show this effect via a series of numerical calculations of the characteristic parameters of the TCA/BR.

Plasma model and results of calculations. The 1-D kinetic code[4], calculates Alfvén wave fields and dissipation in a two ion-species cylindrical plasmas. This code solves the coupled Maxwell-linearized Vlasov equations, posed as a boundary value problem, for the RF wave fields produced by an external antenna in a magnetized plasma column. This cylindrical model can serve as an approximation of a tokamak. The plasma is proposed to be a cylinder of radius a surrounded by a vacuum region which is bounded by a conducting wall of radius d. In the vacuum region, there is a sheet current antenna located on a cylindrical surface of radius b. The z and θ -components of the sheet current have the Fourier series representations, it can also serve as a model of a frame multi-mode antenna (Nagoya-III type).

We have calculated distribution of RF fields and the dependence of the real part of the antenna loading impedance as a function of the generator frequency. The geometry and plasma parameters that we assumed are characteristics of TCA/Br: $a=18$ cm, $b=18.5$ cm, $d=23$ cm, and $R_0=61$cm, corresponding to an aspect ratio of 3. For the plasma, we assumed

that the electron and ion temperatures are, respectively, T_e=*500 eV* and T_i=*300 eV*, while we varied the peak electron density, n_0, between *1. 10^{13}* and *5. 10^{13} cm^{-3}*. The ion density was chosen so that the condition of charge neutrality is satisfied, $Z\,n_Z + n_i = n_e$, where n_Z and n_i designate, respectively, the densities of the impurity (or deuterium) ions and hydrogen ions. Finally, we varied the toroidal magnetic field, B_t, between *10* and *15 kG*, assumed a q of *1.01* at the magnetic axis, and varied q between *3* and *4* at the plasma edge.

In Fig. 1, we present a plot of the resistive part of the frame antenna loading impedance versus frequency for a hydrogen plasma with variation of full ionized carbon impurity, where the carbon density relative to the total ion density (n_C/n_{0i}) is varied from *0.0* to *0.03*. The frequency is measured in *MHz*. The following parameters were considered in Fig.1: B_t = *10. kG*, q =*1.1*, n_0 = *3. $10^{13}cm^{-3}$*, density profile is parabolic, current profile is parabolic in square.

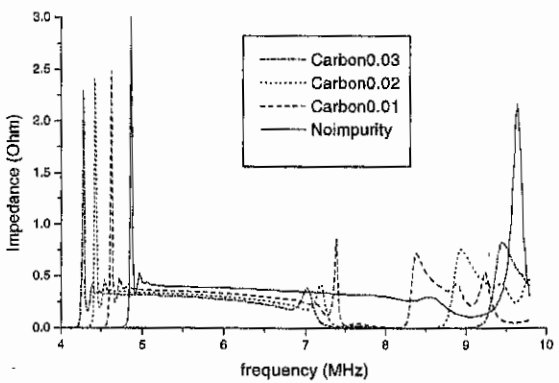

Fig. 1. Antenna impedance versus frequency *(MHz)* for a hydrogen plasma with carbon impurity. The curves (solid, dashed, doted, dash-doted lines) are correspond to the relative carbon concentrations, n_C/n_{0i}=*0.0;0.01; 0.02; 0.03*, respectively. One mode antenna configuration are chosen (a poloidal m=*-1* and toroidal mode number n= *-4*). The plasma parameters are B_t = *10. kG*, q =*1.1*, n_0 = *3.$10^{13}cm^{-3}$*

With a small population of impurities added to the plasma, gaps will appear in the impedance curves (dashed, doted, dash-doted lines) about the cyclotron resonance of the impurity ions, $\omega \approx \omega_{cZ}$ = *7.65MHz*. This gap is strongly correlated with the Alfvén wave continuum gap described by the equation, $\varepsilon_\perp \omega^2/c^2 - k_\parallel^2 = 0$, where $\varepsilon_\perp = \Sigma_i\, \omega_{pe}^2/(\omega_{ci}^2 - \omega^2)$. Just below the continuum gap there are surface eigenmode spikes. The sharp spikes presented at the threshold of the low Alfvén continuum in Fig.1, correspond to the GA eigenmodes, suggesting central heating of the plasma. Small changes in the GA frequency are produced by variations in the plasma density through the impurity concentration. Above the threshold of ion-ion Alfvén continuum, we can see maximums of the impedance, which are correspond to SAW situated deeply in the continuum. The frequency of this SAW moves down to the threshold of the ion-ion Alfvén continuum if the plasma ion density is reduced from *3. 10^{13}* to *1.3$10^{13}cm^{-3}$*. Near the i-i continuum threshold, the surface Alfvén wave changes its wave field structure to that of a combined Alfvén mode (CAM). The RF field structure of the CAM has an intermediate character, that is between the surface and global Alfvén wave (see **Ref.**[1,4]) suggesting central heating of the plasma through mode conversion into the kinetic Alfvén wave. This means that the Alfvén mode has the conversion point as the SAW but it heats the plasma core as global waves. This regime is very good for Alfvén wave heating and current drive but the plasma density and the real carbon impurity concentration (*0.01*) are too low for TCA standard conditions. Finally, the global Alfvén wave appear below the ion-ion Alfvén continuum if the density is below the value of *1. $10^{13}cm^{-3}$*. This effect is illustrated in Fig. 2.

For poloidal and toroidal wavenumbers (m=*-1*, n=*-6*) and generator frequency of *9.1MHz*,

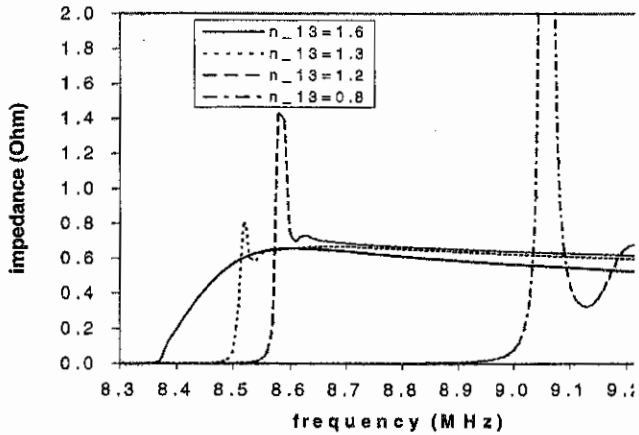

Fig.2. Antenna impedance versus frequency for different plasma densities, with the relative carbon concentration - *0.01*. The lines (solid, doted, dashed, dash-doted) correspond to the plasma densities, *1.6· 10¹³*, *1.3· 10¹³*, *1.2·10¹³*, *0.8·10¹³ cm⁻³*, respectively. One mode antenna configuration with a poloidal (*m= -1*) and toroidal (*n=-4*) mode numbers are chosen. The other plasma parameters are the same as in Fig.1.

We also find the optimal wave heating and current drive conditions in the TCA plasmas with the ion density of *2.3 10¹³ cm⁻³* and the relative carbon impurity concentration of *0.02*.

In Fig. 3, we present the dispersion characteristics of SAW and GA modes and illustrate the gap in the Alfvén continuum for a hydrogen plasma with the carbon impurity ion species (n_C/n_{0i} *=0.02)*, which have parabolic density profile. We have plotted the threshold frequency of the Alfvén continuum for *m=±1*, GAW frequency for *m=-1* and SAW for *m=+1*, which are normalized to the cyclotron frequency of carbon, versus the normalized negative toroidal wavenumber, $\kappa = -n\,c/R_0\,\omega_{pi}$. We show that GAW, which are usually situated below the continuum, enter into ion-ion Alfvén continuum as the density of the hydrogen ions increases (or the parameter κ decreases).

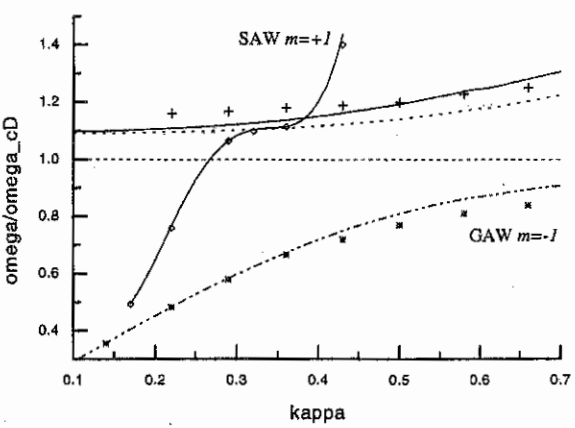

Fig. 3. Plot of the normalized eigenmode frequencies in a hydrogen plasma with the 2% carbon impurity versus the normalized negative toroidal wavenumber κ. For *m=-1*, the threshold frequency of the low Alfvén continuum is labeled with dot-dash-dot line, the i-i Alfvén continuum is labeled with solid line and GAW frequency is labeled with crosses; for *m=+1*, the i-i Alfvén continuum is labeled with dotted line and SAW (*m= +1*) is labeled with diamonds fitted by solid line. The other plasma parameters are the same as in Fig.1.

We can also point out, in Fig.3, that SAW for *m=+1* actually crosses the Alfvén continuum, the continuum gap and the i-i Alfvén continuum. If the frequency of this mode is in the continuum, its RF field structure is a typically surface mode with the conversion point. An

important feature of the positive *m*-Alfvén mode is that its character changes from a surface mode when it is far from the continuum to a global mode when it approaches the continuum threshold. Near the threshold of the i-i Alfvén continuum the eigenfrequency of this mode is elongated the continuum line and, here, the SA mode structure is dramatically changed on a combination of the global wave and SAW with the conversion point in the continuum. In this case, the plasma core can be also heated effectively as the combined Alfvén wave for *m=-1*.

Discussion and Conclusion. Generally, *1-D* cylindrical model is a reasonable approximation for the analyses of the global Alfvén wave and the mode-conversion phenomena in a tokamak plasma with multi-ion species when the generator frequency lies at the Alfvén continuum threshold. In this case, the toroidicity parameter is very small and toroidal effects are not important. To avoid cyclotron resonance effects in the i-i Alfvén continuum, we need to chose the frequency band, $\omega_{cZ,HFS} < \omega < \omega_{cH,LFS}$, between the impurity cyclotron frequency on the high field side and the hydrogen cyclotron frequency on the low field side of a tokamak plasmas. This frequency band limitation is imposed by the spatial inhomogeneity of the tokamak magnetic field for negative *m*-surface Alfvén waves since these modes are suppressed in zones of ion cyclotron resonances. There is no frequency band limitation for the positive *m*-Alfvén mode because dissipation of these waves is very weak in the ion cyclotron resonance.

Our calculations of Alfvén wave dissipation and dispersion, in the i-i Alfvén continuum of the two-ion species plasma, have demonstrated a strong influence of the other plasma species (or impurities) on the value of the antenna impedance, the position of the dissipated power, and the dispersion of Alfvén eigenmodes. The condition of strong dependence on parallel wavenumber has an important implication that the efficient plasma heating is possible by an antenna that has a narrow toroidal wavelength spectrum.

We have found conditions for central heating in a two species plasmas of the medium size TCA/BR tokamak when the GA modes fall within the shear Alfvén continuum. If either of these conditions are satisfied, most of the dissipated RF power is delivered to the plasma core via mode-conversion into the kinetic Alfvén wave. Specifically, with a toroidal modenumber *n=-4* and a poloidal modenumber *m=-1*, and a generator frequency *0.29* times the hydrogen cyclotron frequency ($n_0 = 3\ 10^{13} cm^{-3}$ for the low Alfvén continuum) and *0.57* times the hydrogen cyclotron frequency ($n_0 = 1.2\ 10^{13}\ cm^{-3}$ for the i-i continuum) central plasma heating will occur in a hydrogen plasma with a carbon concentration of *0.02*. These optimal conditions is also found for the other toroidal modes, from *n=-9* to *-5*, according to the diagram in Fig. 3.

For positive poloidal modenumbers, we have also found conditions for central heating of a two species plasmas with combined Alfvén waves when these modes fall near the threshold of the i-i Alfvén continuum. Specifically, with toroidal (*n=-4*) and poloidal (*m=+1*) modenumbers and a generator frequency of *0.83* times the hydrogen cyclotron frequency (the plasma density is of $1.9\ 10^{13}\ cm^{-3}$) central plasma heating will occur in a hydrogen plasma with a $^3He^{+2}$ admixture concentration of *0.34*. In this case, the wave phase velocity, $2\pi f k_{\|}^{-1}$, is approximately 2.5 times the electron thermal velocity and the Alfvén wave current drive can be produced very effectively as a lower hybrid current drive. These experiments in the TCA/BR tokamak can simulate the i-i hybrid current drive in D-T tokamak- reactor plasmas.

[1] A. G. Elfimov, A. G. Kirov, V. P. Sidorov In: *High Frequency of Plasma Heating*, edited by A. G. Litvak (Translation Series, American Institute of Physics, New York, 1992) 239.

[2] G.A. Collins, F. Hofmann, B. Joye, *et al, Phys. Fluids*, **29**, 2260 (1986).

[3] T.Intrator, P. Probert, S. Wukitch, *et al Physics of Plasmas*, **2**, 2263 (1995).

[4] A.G. Elfimov, J.A.Tataronis, N. Hershkowitz, *Physics of Plasmas*, **1**, 2637 (1994).

[5] L. Ruchko, M.C.R. Andrade, R.M.O. Galvao, I.C. Nascimento, In: *Proceedings of Intern Conf. on PLASMA PHYSICS*, Foz do Iguaçu (BRAZIL), November 1994, **1**, 365 (1994).

Plasma dynamics in box of unshielded fast wave antenna

V.I. Zasenko*, D.W. Faulconer, and R. Koch
Laboratoire de Physique des Plasmas - Laboratorium voor Plasmafysica
Association "Euratom-Etat Belge" - Associatie "Euratom-Belgische Staat"
Trilateral Euregio Cluster
Ecole Royale Militaire-Koninklijke Militaire School
Brussels, Belgium

*on leave from Bogolyubov Institute for Theoretical Physics, Kiev, Ukraine

1. Introduction Since an early date ICRF experiments have been conducted with a Faraday shield placed between antenna and plasma. Positive effects of the Faraday shield are accompanied by adverse ones which include suppression of magnetic flux of the antenna central conductor and sputtering of heavy ion impurities from the shield surface due to radio frequency (RF) sheath effect. After re-evaluation of the role of the Faraday shield [1], successful operation of an unshielded ICRF antenna was demonstrated on the medium-size tokamak TEXTOR [2,3]. This work motivates the present study of plasma dynamics in an unshielded antenna box.

2. Model

2.1 Basic equations Periodic potential ≈20 kV applied to the central conductor produces a strong local electrostatic field which is taken to dominate inductive effects in the near region. The plasma dynamics in the antenna box is then determined by a balance between particle transport in the radial (x) direction across the magnetic lines and particle escape to the walls of the box along the magnetic lines (Fig.1).

The system under consideration is strongly varying in the radial (x) direction but quite uniform along the magnetic lines (//z) due to the difference in transverse and longitudinal box dimensions, whence our introduction of z-averaged quantities, $\bar{}$. Neglecting poloidal (y) dependence, the equations for averaged densities and potential follow from species momentum and Poisson equations with omission of inertial terms in the former:

$$\frac{\partial \bar{n}_\alpha}{\partial t} - \frac{\partial}{\partial x} D_\alpha \left(\frac{\partial \bar{n}_\alpha}{\partial x} + \bar{n}_\alpha \frac{e_\alpha}{T_\alpha} \frac{\partial \bar{\varphi}}{\partial x} - \bar{n}_\alpha \frac{\omega_{c\alpha}}{\nu_{\perp\alpha}} \frac{e_\alpha \bar{E}_y}{T_\alpha} \right) + \frac{2}{L} [n V_z]_\alpha = 0 , \qquad (1)$$

$$\frac{\partial^2 \bar{\varphi}}{\partial x^2} = -\frac{e}{\varepsilon_0} (\bar{n}_i - \bar{n}_e) \qquad (2)$$

Here, E_x, E_z are components of field characterized by potential φ, E_y - poloidal component of inductive field, α - species index, $\omega_{c\alpha}$ - cyclotron frequency. The effective collision frequency $\nu_{\perp\alpha}$ describes the change in particle momentum due to collisions with turbulent field and is chosen consistent with $D_\alpha = 4\,m^2/s$. To close the set of Eqns.(1),(2) the fluxes to the walls at $z=\pm L/2$, $[nV_Z]_\alpha$, should be written in terms of $\bar{n}_\alpha$ and $\bar{\varphi}$.

2.2 *Particle fluxes to the wall* Almost all drop of potential along the magnetic lines between plasma and grounded antenna box ($\varphi=0$) occurs at the box walls - in the oscillating sheath. In accordance with probe theory and studies of the RF sheath we assume that in the absence of substantial accelerating field in the bulk or sheath regions particles escape from the plasma with the thermal velocity $v_{Te} = \left[T_e/m_e\right]^{1/2}$ for electrons, and the sound speed $c_s = \left[\left(T_e + \gamma T_i\right)/m_i\right]^{1/2}$ for ions with $\gamma=2$. When the potential difference between the bulk plasma and the wall (i.e. across the sheath) is retarding, the flux is reduced by the Boltzmann factor:

$$\begin{aligned}
[nV_Z]_e = {} & (\bar{n}_e v_{Te}/\sqrt{2\pi})\exp(-e\bar{\varphi}/T_e) && (\bar{\varphi}>0); \\
& (\bar{n}_e v_{Te}/\sqrt{2\pi}) && (\bar{\varphi}<0,\ \bar{n}_i > \bar{n}_e); \\
& (\bar{n}_e v_{Te}/\sqrt{2\pi}) + \bar{n}_e\sqrt{-2e\bar{\varphi}/m_e}\,\vartheta(1-\bar{n}_e/\bar{n}_i) && (\bar{\varphi}<0,\ \bar{n}_i < \bar{n}_e)
\end{aligned} \qquad (3)$$

$$[nV_Z]_i = [nV_Z]_e(\bar{\varphi} \to -\bar{\varphi},\ v_{Te} \to c_s,\ \text{e index} \leftrightarrow \text{i index}) \qquad (4)$$

The last term in Eqns.(3),(4) models enhanced particle expulsion occurring when a layer at given x has charge of the same sign as the antenna's; $\vartheta\left(1-\left(\bar{n}_\alpha/\bar{n}_\beta\right)\right)$, with properties $\vartheta(0)=0$ (charge of opposite sign) and $\vartheta(1)=1$ (same sign), smoothens the transition between the two cases.

2.3 *Boundary conditions at central conductor and in front of the box* Boundary conditions taken for potential and particle densities at the position of the central conductor, x=d(=3 cm), are: $\bar{\varphi}(d)=\varphi_o \sin(2\pi ft)$ or $\bar{\varphi}_{fl}$ [=floating potential=$(T_e/e)\ln(v_{Te}/c_s)$] when RF is respectively applied or not, and $n_\alpha(d)=0$. To avoid an arbitrary specification of boundary condition at the mouth of the box, x=0, we also consider the plasma dynamics in front of the box. The same Eqns.(1),(2) are applied over the same region in z as inside the box, but with modified fluxes along the magnetic lines:

$$\begin{aligned}
[nV_Z]_e = {} & (\bar{n}_e v_{Te}/\sqrt{2\pi})[-1+\exp(-e(\bar{\varphi}-\bar{\varphi}_{fl})/T_e)] && (\bar{\varphi}>\bar{\varphi}_{fl}); \\
& (\bar{n}_e v_{Te}/\sqrt{2\pi})[1-\exp(e(\bar{\varphi}-\bar{\varphi}_{fl})/T_e)] && (\bar{\varphi}<\bar{\varphi}_{fl})
\end{aligned} \qquad (5)$$

$$[nV_z]_i = [nV_z]_e(v_{Te} \to -c_s, \text{ e index} \to \text{ i index}) \qquad (6)$$

These fluxes describe the flow of charged particles in front of the box through imaginary surfaces at $z=\pm L/2$. The first terms represent free-streaming fluxes out of the region of higher particle potential energy, the second, particle influxes into the same region suitably reduced by the Boltzmann factor where potential is taken as φ_{fl} at large $|z|$ (corresponding to the scrape-off plasma making contact with the grounded (φ=0) tokamak limiter). Particle density and potential profiles are rather insensitive to the boundary conditions imposed at x=-d (=-3 cm): $\partial\overline{\varphi}(-d)/\partial x = k(\overline{\varphi}(-d)-\varphi_{fl})$, $n_\alpha(-d)=n_o$.

3. Particle densities and potential The equations obtained in the previous section have been solved numerically and results are given below. Deuterium plasma parameters taken in the numerical simulations are as follows: $n_e(x=-3cm)\equiv n_o=2\times10^{18}m^{-3}$, $m_i=2m_p$, $T_i=60eV$, $T_e=30eV$, $B_o=3T$, $f=3\times10^7Hz$, $\varphi_o=20kV$, $D_\alpha=4m^2/s$, $k=12.08m^{-1}$. In the figures the particle density is normalized to $2\times10^{18}m^{-3}$ and $U=e\overline{\varphi}/T_e$ is dimensionless potential. For the calculations we omit the poloidal component of inductive field E_y from Eqn.(1).

3.1 Evolution in the early stage The early stage of evolution of particle density and self-consistent potential inside the box, from the stationary state without RF ($\overline{\varphi}=\varphi_{fl}$), is presented in Figs.2-4. The first 45 periods are shown, f being the applied frequency. The greatly reduced number of oscillations is due to stroboscopic sampling at intervals of 1.125 period. Fig.2 shows n_i to be rapidly evacuated from in front of the central conductor as has been seen in experiment [4]; note that $n_i(x,t=0)$ already descends from n_o to $.116n_o$ at the box mouth (off-scale at x=0). The penetration of potential into the plasma shown in Fig.3 (note changed direction of axes) proceeds simultaneously with the above expulsion of particles from the density tail. The species density difference ($\propto$ charge density) plotted in Fig.4 shows peaked structure in the same region where the potential field indeed is shielded (where $\partial U/\partial x \to 0$ in Fig.3). This charge density layer gravitates toward the mouth of the box with time.

4. Conclusions This model points to the sole presence of an RF potential electric field as sufficient to cause a strong initial evacuation of plasma from the high potential region immediately in front of the antenna central conductor. Though further analysis is in order, one can anticipate a salutary influence of this on phenomena linked to ion bombardment of the box walls (sputtering; power loss in sheaths). An RF charged layer plays the role of a Faraday shield, limiting perturbation of the scrape-off layer for the times examined. These findings support the idea that ICRF antennas can be operated without a Faraday shield.

Acknowledgement One of the authors (V.I.Z.) has benefitted from a grant of the Federale Diensten voor Wetenschappelijke, Technische en Culturele Aangelegenheden.

References

[1] Van Nieuwenhove R., Koch R., Van Oost G. LPP-ERM/KMS Brussels Report nr.93, "Reevaluation of the role of ICRH Faraday Shields", (1990).

[2] Van Nieuwenhove R., Koch R., Van Oost G. *et al.* 1991 *Nucl.Fusion* **31** 1770.

[3] Van Nieuwenhove R., Koch R., Van Oost G. *et al.* 1992 *Nucl.Fusion* **32** 1913.

[4] Van Nieuwenhove R., Koch R., Van Oost G. 1994 *Controlled Fusion and Plasma Physics (Proc. 21th Eur. Conf. Montpellier, 1994)* Vol. 18B, part II (Geneva: EPS) p.976.

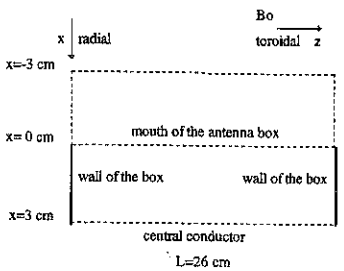

Fig.1 Poloidal view of the antenna box with toroidal extension 26 cm and radial extension 3 cm. The central conductor is modelled as a surface of width L=26 cm at x=3 cm.

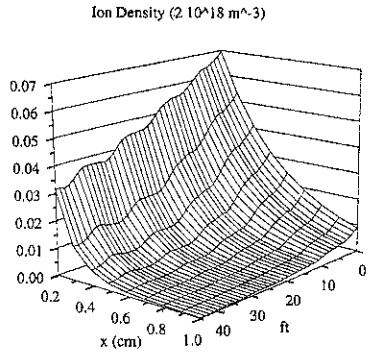

Fig.2 Evolution of ion density over first 45 periods after RF voltage is applied, showing evacuation of antenna box. The front part of the box is shown.

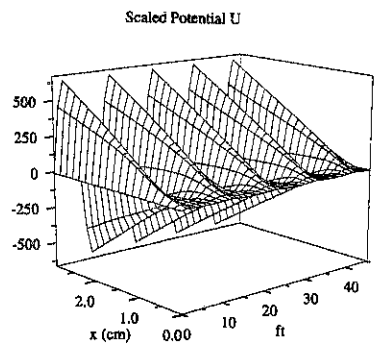

Fig.3 Evolution of the potential $U=e\overline{\varphi}/T_e$. The penetration of potential into the plasma corresponds to relative depletion of the density tail with time.

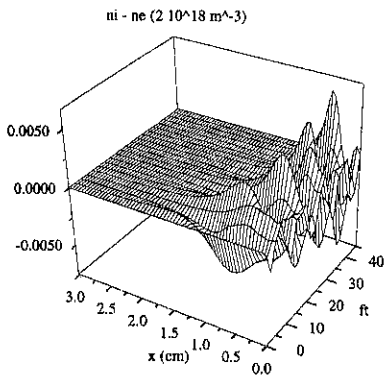

Fig.4 Difference in ion and electron densities. Charge separation is localized to a layer with thickness of several mm coinciding with the position where potential (Fig.3) has large radial second derivative.

Nonlinear Weighting Scheme for Monte Carlo Computation of the Particle Distribution Function During rf Heating[1]

Sergei V. Kasilov*, Vladimir E. Moiseenko*, **Martin F. Heyn**†, and Winfried Kernbichler†

*Institute of Plasma Physics, National Science Center "Kharkov Institute of Physics and Technology", Ul. Akademicheskaya 1, 310108 Kharkov, Ukraine
†Institut für Theoretische Physik, Technische Universität Graz, Petersgasse 16, A–8010 Graz, Austria

Introduction

At present, Monte Carlo (MC) methods are successfully used to model radio-frequency heating in various magnetic geometries. Compared to finite-difference schemes or other regular methods, MC modeling has several advantages. First, the numerical diffusion in stiff problems can be avoided. Such a diffusion develops in regular solution methods for the kinetic equation with strong convection because of averaging within finite mesh cells. Second, except for time constraints, MC modeling imposes practically no restrictions when increasing the dimensionality of the problem. Third, the MC method is fairly simple.

However, a disadvantage of traditional MC implementations is their poor statistics in regions with a small particle population, in particular, in the tail region of the distribution function. An increased resolution in this region is desirable for various problems in magnetic fusion theory, primarily in scenarios with rf heating. E.g., particles in the tail contribute significantly to the fusion power output in D-D or D-T low temperature experimental plasmas. Therefore, in order to be able to use these fusion products for diagnostic purposes, one needs a highly accurate method able to compute that part of the distribution function. Another important case is the computation of the distribution function in systems with a finite loss cone present in the suprathermal region of velocity space, e.g., in stellarators and in tokamaks with magnetic field ripples.

For slightly disturbed Maxwellian distribution functions, the resolution problem can be handled by introducing different forms of particle weighting schemes known as δf-methods [1-3] which significantly reduce the noise. However, these methods are not applicable to model the distribution function in the high energy region during rf heating because in that case this function no longer can be described in form of a perturbed Maxwellian. In the present paper, a nonlinear weighting scheme is implemented into the MC modeling algorithm and, as a result, a much better resolution of the distribution function in the tail phase space region is obtained.

Weighting Scheme

In the present context it is convenient to formulate the MC modeling of the quasilinear kinetic equation with a Fokker-Planck collision term in integral form,

$$f(t,\mathbf{z}) = \hat{P}_z f(t-\Delta t,\mathbf{z}) = \int \mathrm{d}^n z'\, P_z(\Delta t,\mathbf{z}',\mathbf{z}-\mathbf{z}')f(t-\Delta t,\mathbf{z}'). \qquad (1)$$

[1]This work was partly supported by the Association EURATOM-OEAW under contract number ERB 5004 CT 96 0020 and by the Ukrainian Foundation of Fundamental Research.

Here, f is the distribution function, $\mathbf{z}$ is a set of phase-space variables, and $\hat{P}_z$ is a dynamic phase space integral operator with kernel P_z, the Green's function of the underlying process. In particular, the stochastic mapping equation [4] which is the counter-part of the bounce averaged kinetic equation for the case of a general magnetic geometry and non-integrable particle motion, is of this form. In the numerical realization of the Monte Carlo algorithm, the function P_z is to be interpreted as the probability density for the transition from phase space point $\mathbf{z}'$ to $\mathbf{z}$. If the stochastic orbits are modeled directly, the Green's function P_z for small Δt can be approximated by a simpler function which has, up to linear order terms in Δt, the same moments in $\mathbf{z} - \mathbf{z}'$ as P_z .

In order to introduce the weighting scheme, the phase space is extended by one additional variable w, the weight of test particles, such that the distribution of real particles f is related to the distribution of test particles g in extended space by

$$f(t, \mathbf{z}) = \int_0^\infty \mathrm{d}w\, w\, g(t, \mathbf{z}, w). \tag{2}$$

The evolution equation for g,

$$\begin{aligned} g(t, \mathbf{z}, w) &= \hat{P}_z \hat{P}_w g(t - \Delta t, \mathbf{z}, w) && (3) \\ &= \int \mathrm{d}^n z'\, P_z(\mathbf{z}', \mathbf{z} - \mathbf{z}') \int_0^\infty \mathrm{d}w'\, P_w(w, w', w_0(\mathbf{z}'))\, g(t - \Delta t, \mathbf{z}', w'), && (4) \end{aligned}$$

includes now both, the dynamics in phase space described by operator $\hat{P}_z$ [see (1)], and the dynamics in the space of weights described by weighting operator $\hat{P}_w$,

$$P_w(w, w', w_0) = \int_0^\infty \mathrm{d}w''\, P_k(w, w'', w_0) P_s(w'', w', w_0). \tag{5}$$

A particular realization of the weighting operation would be in form of a splitting operator P_s and a killing operator P_k (like in the roulette procedure, see, e.g. [5])

$$\begin{aligned} P_s(w, w', w_0) &= \Theta\left(\alpha - \frac{w'}{w_0}\right) \delta(w - w') + \Theta\left(\frac{w'}{w_0} - \alpha\right) \frac{w'}{w_0} \delta(w - w_0), && (6) \\ P_k(w, w', w_0) &= \Theta\left(\frac{w'}{w_0} - \beta\right) \delta(w - w') + \Theta\left(\beta - \frac{w'}{w_0}\right) \frac{w'}{w_0} \delta(w - w_0). && (7) \end{aligned}$$

Here, Θ is the Heaviside step function, $w_0(\mathbf{z})$ is a prescribed weight for any given phase space point $\mathbf{z}$, whereas $\alpha \gtrsim 1$ and $\beta \lesssim 1$ are the upper and lower weighting boundaries. It is easy to check that multiplication with w and subsequent integrating of (3) over w leads immediately back to (1). Therefore, the weighting procedure does not change the original dynamics in phase space.

If the distribution function is known to be of the order of some "unperturbed" function $f_0(\mathbf{z})$ everywhere in phase space beforehand, then the choice of the prescribed weight in the form $w_0(\mathbf{z}) = C(f_0(\mathbf{z}) + \epsilon)$ will produce a more or less uniform distribution of the relative statistical error within phase space regions of interest. Here, C is a constant which determines the average number of test particles and the finite value of ϵ determines a minimum value of the distribution function to be resolved during the computation.

For the nonlinear weighting scheme, the distribution function $f(\mathbf{z})$ itself is used for the construction of the prescribed weight $w_0(\mathbf{z}) = C(f(\mathbf{z}) + \epsilon)$. In this case, this value can either be taken from the previous time step or from its time averaged value (average over all previous time steps) if one looks for a stationary solution.

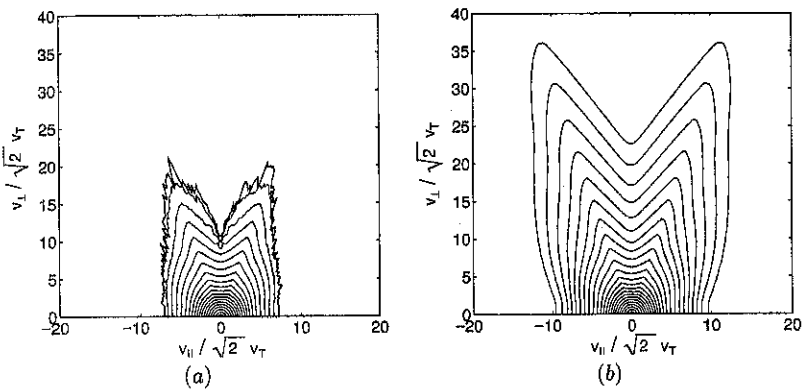

Figure 1. Contour lines of the ^{3}He minority ion distribution function during fundamental ICRH in a tokamak. Here, $v_\parallel$ and $v_\perp$ are the parallel and perpendicular velocity in the magnetic field minimum point, and $v_T \equiv \sqrt{T_i/m_\alpha}$.

Modeling of Minority Heating

The nonlinear weighting scheme has been implemented into the Monte Carlo mapping code [4] in order to study the fundamental ion minority cyclotron resonance heating in a tokamak. In the considered case, the rf field is assumed in form of one single toroidal harmonic and, therefore, the rf diffusion coefficients are symmetric with respect to the toroidal angle. In this case, the stochastic mapping equation [4] coincides with the conventional bounce-averaged equation,

$$\frac{\partial f}{\partial t} = \hat{L}_C f + \hat{L}_{QL} f, \tag{8}$$

where $\hat{L}_C$ is the bounce-averaged Coulomb collision operator for the Maxwellian distribution of the background particles and $\hat{L}_{QL}$ is the quasilinear diffusion operator (for details see [6]),

$$\hat{L}_{QL} f = \frac{1}{\tau_b^* v_\perp} \frac{\partial}{\partial v_\perp} \left(\tau_b^* v_\perp D_\perp \frac{\partial f}{\partial v_\perp} \right), \quad D_\perp = \frac{\pi e_\alpha^2 \left| E^+ \right|^2 qR}{4 m_\alpha^2 \varepsilon_t \omega \left| v_\parallel \right| \tau_b^*}. \tag{9}$$

Here, the independent variables $v_\perp, v_\parallel$ are the perpendicular and parallel velocity components in the minority ion cyclotron resonance point, τ_b^* is the particle return time to the magnetic field minimum point on a given magnetic surface (half bounce time for trapped and bounce time for passing particles, respectively), and E^+, e_α, m_α, ω, ε_t, q and R are the left polarized component of the wave electric field, minority ion charge and mass, wave frequency, toroidicity, safety factor and the big tokamak radius, respectively. The parameter set used in the computation is, $R = 300$ cm, plasma density $n_e = 10^{14}$ cm^{-3}, plasma temperature $T_i = T_e = 7$ keV, toroidicity $\varepsilon_t = 0.1$, surface averaged absorbed rf-power density $< p >= 0.5$ W/cm^3, and ^{3}He minority ion concentration $n_\alpha/n_e = 5\%$.

In Figure 1 the contours of the minority ion distribution function are shown as functions of parallel and perpendicular velocity in the magnetic field minimum point. In Figure 1a

the region of enhanced resolution by weighting has been chosen to be $f/f_{\max} \leq 10^{-10}$ ($f_{\max}$ is the value of f for zero energy). In Figure 1b this region has been increased to $f/f_{\max} \leq 10^{-20}$ without significantly increasing the number of steps. These results from Monte Carlo computations using the nonlinear weighting scheme stay in good agreement in the whole phase space with results from a computation with a finite difference code using a similar parameter set [6].

Conclusion

A dynamic weighting scheme has been used to improve the statistics of Monte Carlo computations of the minority ion distribution function during RF heating in the high energy region of phase space. This scheme makes the MC method much more effective so that it becomes comparable to finite difference methods. The main objective for future studies will be the application of this method to actual high dimensional problems not accessible by finite difference or other regular methods.

References

[1] Dimits, A. M. and Lee, W. W., *J. Comp. Phys.*, **107**, 309–323 (1993).

[2] Parker, S. E. and Lee, W. W., *Phys. Fluids B*, **5**, 77–86 (1993).

[2] Sasinowski, M. and Boozer, A. H., *Phys. Plasmas*, **2**, 610–619 (1995).

[4] Kasilov, S. V., Moiseenko, V. E., Heyn, M. F., and Kernbichler, W., In Gressilon, D., et al., editor, *Europhysics Conference Abstracts* (23rd EPS Conference on Controlled Fusion and Plasma Physics, Kiev, 24-28 June, 1996), Vol. 20c, Part II, 559-562 (1997).

[5] Khisamutdinov, A. I., *Zhurnal Vychislitel'noi Matematiki i Matematicheskoi Fiziki*, **29**, 289–293 (1989).

[6] Kasilov, S. V., Marushchenko, M. B., Pyatak, A. I., and Stepanov, K. N., In Gressilon, D., et al., editor, *Europhysics Conference Abstracts* (23rd EPS Conference on Controlled Fusion and Plasma Physics, Kiev, 24-28 June, 1996), Vol. 20c, Part II, 906-909 (1297).

A MW LHCD System and its First Operation on HT-7 Superconducting Tokamak

LHCD group of ASIPP, presented by Guang-Li Kuang
Institute of Plasma Physics, Academia Sinica (ASIPP)
P. O. Box 1126 Hefei 230031, P. R. China

Abstract

A Lower Hybrid Current Drive (LHCD) system was constructed on HT-7 superconducting tokamak to deliver 1.2 MW for 3 sec every 8 min at a frequency of 2.45 GHz. Its first operation demonstrated that the system can work effectively. A large percentage of plasma current in HT-7 tokamak can be sustained by LHCD. Besides, it was demonstrated that MHD activities and plasma confinements can be considerably influenced by LHCD.

1. The LHCD System on HT-7

The LHCD system is composed of the following main subsystems:

- 1 RF exciter module with phase and amplitude control for 12 klystrons;
- 12 High Power klystron Amplifiers (HPA);
- 12 microwave transmission lines;
- 1 grill coupler (an arrarys of 2 × 12 subwaveguides);
- 2 High Voltage Power Supplies (HVPS);
- wave monitoring & phase feedback control;
- system protections;
- water cooling system.

The 12 klystron amplifiers in the LHCD system are fed by 2 identical high voltage power supplies and driven by one RF exciter module. Their waves are launched to HT-7 plasmas by one grill coupler. The $N_{//}$-spectrum can be feed-back controlled in a preset value from $N_{//} = 1$ to $N_{//} = 4.4$. At the present the system can be operated in the following parameters:

Frequency	2.45GHz
Power output	1.2 MW
Pulse length	3 sec
Pulse repetition period	8 min
Power density in the coupler	< 3.5 KW / cm^2 averaged
$N_{//}$-spectrum	$N_{//}$ peak from 1 to 4.4

The layout of the LHCD system is shown in Fig.1.

The RF exciter module consists of one master oscillator, one PIN modulator, one 1:12 power divider, and 12 identical RF drive chains. Each of the chains consists of a digital phase shifter, a semiconductor RF balance amplifier, a voltage control attenuator, a power detector, etc. The master oscillator has three outputs, one among the three delivers 100 mw for phase reference, either of other two delivers 1 w. The PIN modulator can switch off RF power in 10μs with a cut-off level of 20 dB. The phase adjustment range of the digital phase shifter is 360^0 with an adjustment step of 2.8^0. The semiconductor amplifier has a constant output about 3 w when its input (a few mw) changes in a range of 5 dB. The attenuator has a dynamic range of 20 dB. Each of the 12 RF drive chains connects to the input of one klystron amplifier.

The klystron amplifiers (Type KU-2.45, 2.45GHe,100KW, CW) were designed and constructed by a Russian company. Each klystron is protected from a high reflected microwave by a 4-port differential phase shift circulator with an insertion loss of 0.3 dB max. After the circulator, the microwave is transmitted to the grill coupler through a standard rectangular waveguide (WR430) which is changed in sizes by a step transformer and then divided into two subwaveguides by a 3dB divider at the grill. The two subwaveguides compose one column of the grill. By such arrangement, adjacent subwaveguides in either row of the grill emit waves from different klystrons, therefore, the $N_{//}$-spectrum can be flexibly controlled. There is one BeO ceramic window in the standard rectangular waveguide section on each of the 12 transmission lines. The grill coupler is evacuated by a turbo-pump and cooled by a cooling water jacket.

The high voltage power supplies normally acquire about two third of electrical power from a flying wheel AC generator and the left from the electricity network. Ignitrons are used for fast switching-off the high DC voltage on klystrons cathodes. The klystron beam voltage can be controlled by a star point voltage regulator.

The wave phase and power in each of the 12 waveguides at the coupler are detected by a 12-channel detecting system. The 11 phase signals (the 12th is taken as a reference) are compared with their pre-set values by a PC which generates the digital signals for the control of the 11 phase shifters in the RF exciter module. The time to complete one cycle control of the 11-channel RF phases is less than 180 μs. The phase control of the system has an accuracy of 5^0 over a range of 360^0. The RF power control is realized by pre-setting a proper klystron

cathode voltage and corresponding proper control voltages to the 12 attenuators in the RF exciter module.

A RF protection system is developed to switch off the RF signals to the 12 semiconductor amplifiers in less than 20μs and to switch off klystron cathode voltage in less than 50ms in any case of high reflection, ARC in the waveguides or the grill, as well as faulty flow rate of the cooling water. The ignitrons of the HVPS are triggered to fast switch off the klystron cathode voltage in less than 150μs in case of overcurrent in any of klystron cathode circuits or klysron resonator circuits.

The klystron collectors and resonators, solenoides, circulators, waveguide ceramic windows, and the grill coupler are cooled by circulating pure water with total about 4 m^3 /min in two different presures, 4 Atm. and 8 Atm. respectively.

2. Main experimental results from the first operation of the system

The whole LHCD system was constructed in the fall of the 1996 and was first operated in the December, 1996. Before the first time operation of the system, the inner stainless steel surfaces of the subwaveguide grill was cleaned by continuous short pulse RF glow discharge in helium for about two hours. By adjusting launched wave spectrum and the antenna position, a current drive efficiency $\eta_{CD} = N_e R p I_{CD} / P_{CD} = 0.5 \times 10^{19}$ (M^{-2} A/W) in the RF power level of 400 KW (with a pulse length of 1 sec) and the line averaged plasma electron density of 1.5 $\times 10^{19}$ M^{-3} was achieved. A typical shot was shown in Fig.2 in which 75% of the plasma current was driven by the lower hybrid wave (~300 KW). The plasma particle confinement was in some cases improved by LHCD considerably with reduced edge density fluctuations and decreased edge electron temperature.. The suppression of Mirnov oscillations were frequently observed in a LHCD phase.

3. Summary

A LHCD system with a maximum output of 1.2 MW was already constructed on HT-7 superconducting tokamak. Its wave source consists of 12 klystrons and the launched wave spectrum can be flexibly adjusted. The first performance of the system demonstrated that it can be operated effectively and plasma confinement could be influenced by LHCD.

Acknowledgements:

The authors would like to thank the Center of Construction of ASIPP for technical support which made the construction of the LHCD system possible. The authors are also indebted to our colleagues who operated the HT-7 machine or made the diagnostics working.

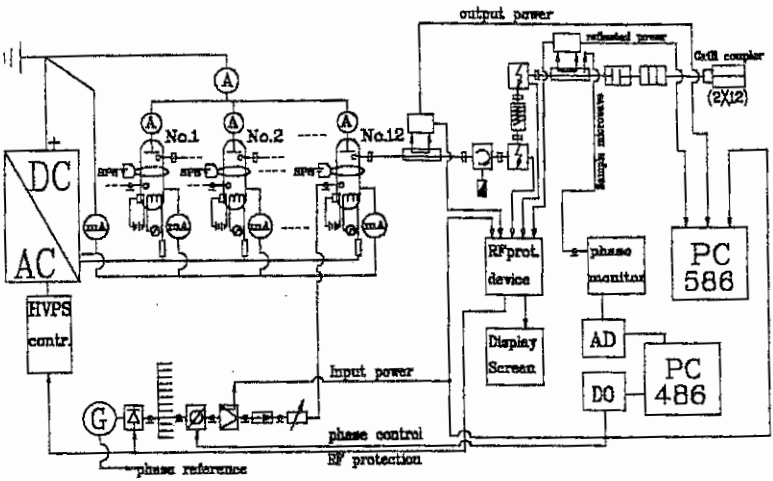

Fig.1: The layout of the LHCD system on HT-7 Tokamak.

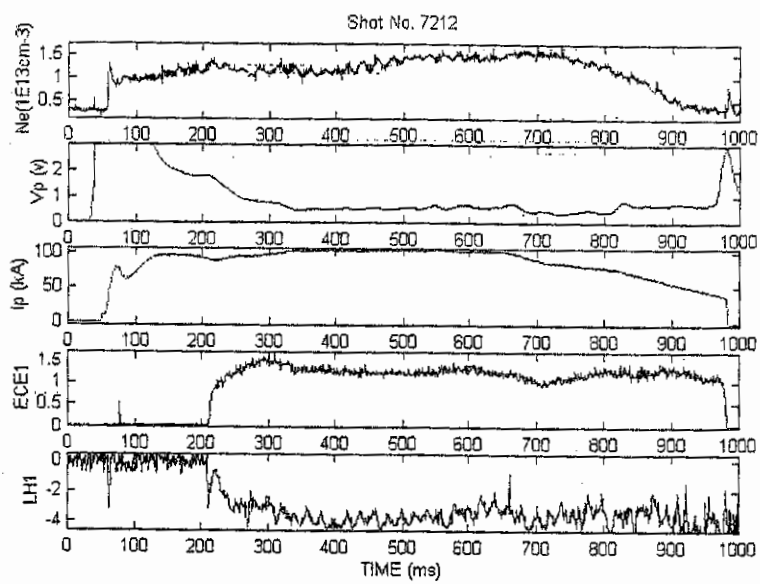

Fig.2: A typical shot with LHCD on HT-7. The loop voltage maintained a small value during the LHCD phase. The discharge terminated after hard x-ray radiation became very strong.

Role of Secondary Processes in Neutralization of Fast Protons During He^0 Neutral Beam Injection into Plasma

A.V.Khudoleev, V.I.Afanassiev, M.I.Mironov, I.Yu.Stepanov*
A.F.Ioffe Physical-Technical Institute, 194021, St.Petersburg, Russia
*State Maritime Technical University, 198262, St. Petersburg, Russia

Introduction

The study of the fast particles behavior in MeV energy range in a contemporary plasma experiments is one of the key questions for the thermonuclear reactor design. For this purpose recently designed neutral particle diagnostics has been implemented on the several large tokamaks [1,2,3]. It has been shown that in the energy range of interest fast protons are mostly neutralized in the charge-exchange (CX) processes with light impurity ions such as He^+, Be^{3+}, C^{5+} [1,4]. Neutral flux is observed both in "passive"(without beam injection) and in "active"(with beam injection) mode.

There are several experimental applications where He^0 beam injection was used either for the plasma heating or for the diagnostic purposes. For the neutral particle analysis (NPA) it is important to take into account all of those processes which lead to the neutralization target formation in plasma. Another important question is the spatial localization of the measurements. For protons with different energies the different impurities play dominant role in the neutralization. For such impurities as Be^{3+} and C^{5+} ionization the length $\lambda_{ion} \geq 2\pi R_{tor}$ for typical plasma parameters. It means that these ions will be able to fill all magnetic surfaces and it is necessary to calculate the ionization balance in the whole plasma volume. For He^+ the situation is opposite $\lambda_{ion} < 2\pi R_{tor}$ and we need to consider the local balance in the vicinity of the beam. Both the secondary processes and spatial localization of neutralization target should be taken into account since they directly affect the accuracy of the ion distribution function reconstruction from experimental data.

In present paper we analyze the relative role of different secondary processes including ion-ion atomic collisions having impact on the neutralization target formation during He^0 beam injection into pure He-plasma. This case is considered to be the most interesting because the helium target is localized near the beam so the spatially resolved CX

measurements are feasible. Besides the cross-sections between helium atoms and ions are well known. It allows to make the model calculations more reliable.

Model Calculations

The model is based on Monte-Carlo simulation code similar to those one used in [5]. Both the ionization and all of the CX processes between helium particles (Fig.1 [6]):

$$He^{2+} + He^0 = He^0 + He^{2+} \quad (1)$$

$$He^{2+} + He^0 = He^+ + He^+ \quad (2)$$

$$He^{2+} + He^+ = He^+ + He^{2+} \quad (3)$$

were taken into account. Reaction (1) is important for thermal He^0 halo formation. Reaction (2) produces He^+ ions with thermal and beam energies. Since the distribution function of secondary He^+ beam ions has a strong spatial anisotropy we average their motion over Larmour rotation using the similar procedure described in [7]. For the beam He^+ ions reaction (3) is the dominant absorption process. For thermal He^+ (3) does not change the total number of these particles but it can substantially modify their spatial distribution [5] and has to be taken into account.

To approach the real experimental conditions we have analyzed He^0/He^+ density formation using the layout of JET neutral beam injection. The plasma parameters were taken as typical for large tokamaks: $n_e=3\cdot10^{13}$ cm^{-3}, $T_i=T_e=5$ keV, $E_{NBI}(He^0)=45$ keV/amu, $P_{NBI}=5$ MW. The result of calculations is presented in Fig.2. One can see that all of the helium species are located in the vicinity of the beam as it was expected. The He^0 thermal halo density does not exceed 20 % of initial beam density so it plays an insignificant role. The He^+ beam density is comparable with the beam. The production of He^+ thermal halo ions is the dominant process. Density of these ions exceeds density of He^0 beam by factor of 4. It should be noted that the evaluation with a simple ionization balance equations described in [4] gives only $n_{He^+thermal}/n_{He^0beam}\sim0.8$ because the important secondary processes such as He^+ ion beam halo formation and He^+/He^{2+} ion-ion collisions were not included into the analysis.

The injection of He^0 beam into He plasma seems to be a very suitable test of the shortage in absolute flux which was found in experiments [8,9]. The estimates show that for impurity density of carbon $n_C/n_e\leq1$ % the neutralization of fast protons on C^{5+} ions is negligible in comparison with that on the helium target in wide (0.2-0.7) MeV energy range. Cross-section of ion-ion CX between He^+ and C^{6+} was taken from [10].

To evaluate a counting rate of hydrogen atoms expected in experiment we assumed that density of fast protons is equal to n_p/n_e=5 %. Their energy distribution function was taken as exponential (see Fig.3) which was close to observed in H-minority ICRF heating discharges [1,4,9]. For simplicity we used the isotropic distribution of the function so our calculations correspond to the minimum estimate. The CX NPA parameters were as follows: detection efficiency ~0.2, energy resolution $\Delta E/E$~0.05-0.11, solid angle $\omega s \sim 5 \cdot 10^{-5}$ $cm^2 st$ [11]. The resulted counting rates in the CX NPA channels are presented in Fig.4. For energies $E_p \sim T_{tail}$ the calculated counting rates are high $\sim 10^6$ s^{-1} and weakly dependent on the tail temperature. But if the experimentally observed in [8,9] shortage is valid then this estimate should be reduced by factor of 30.

Conclusions

The model including both atom-ion and ion-ion collisions and describing the formation of combined He^0/He^+ population produced by He^0 beam injection into He-plasma has been developed. It is shown that the fast proton neutralization target is mainly dominated by He^+ ion thermal halo which is spatially located in the vicinity of the beam. The contribution of the secondary processes such as He^+ ion beam halo formation and ion-ion helium charge-exchange is found to be substantial. The considered plasma discharge scenario is found to be appropriate to perform experimental test of the absolute value of CX flux. The production of C^{5+}, Be^{4+} and B^{3+} in collisions with He^+ requires more data on the cross-sections.

References

[1] Petrov M.P. et al., *19th EPS Conf. on Contr. Fus. and Pl. Phys.*, **16C(II)** 1031 (1992)
[2] Medley S.S. et al, *20th EPS Conf. on Contr. Fus. and Pl. Physics* **17C(III)** (1993) 1183.
[3] Kusama Y. et al, *Rev. Sci. Instrum.* **66** (1995) 339.
[4] Korotkov A.A. and Gondhalekar A., *JET Report JET-P(95)* **47** (1995).
[5] Khudoleev A.V. et al.,*23rd EPS Conf. on Contr. Fus. and Pl. Phys.*, **20C(III)** 1047 (1996).
[6] Barnett C.F.,editor, *Atomic data for fusion* , ORNL-6086 1 (1990).
[7] Mironov M.I. et al., *23rd EPS Conf. on Contr. Fus. and Pl. Phys.*, **20C(III)** 1043 (1996).
[8] McChesney J.M. et al, *Rev. Sci. Instrum.* **66** (1995) 339.
[9] Afanassiev V.I. et al., to be published in *Plasma Physics and Controlled Fusion.*
[10] Stepanov I.Yu., to be published in ICPEAC.
[11] Kislyakov A.I. et. al., to be published in *Fusion Engineering and Design.*

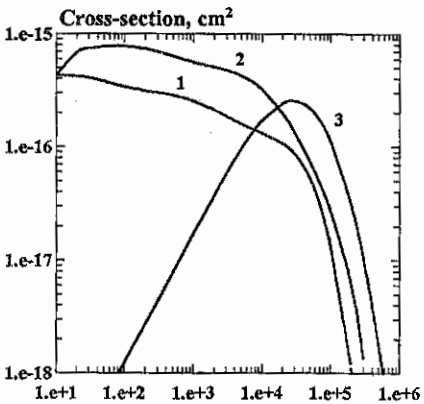

Fig.1 Charge-exchange cross-sections for helium ions and atoms: 1- $He^{2+}+He^{0}=He^{0}+He^{2+}$, 2- $He^{2+}+He^{+}=He^{+}+He^{2+}$, 3- $He^{2+}+He^{0}=He^{+}+He^{+}$.

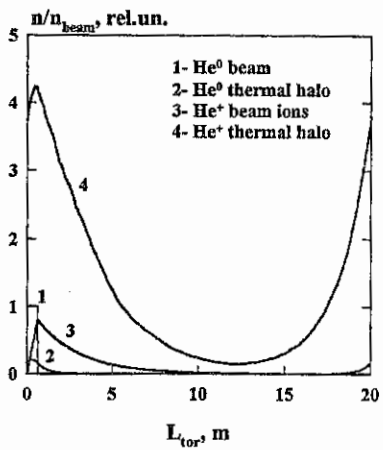

Fig.2 Particle densities as a function of distance along the field line produced by He^{0}-beam injected into pure He-plasma which make the contribution to fast proton neutralization.

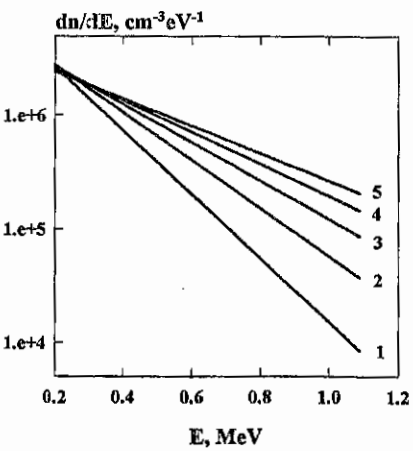

Fig.3 Model energy distribution function of fast protons for different tail temperatures (n_p/n_e=5 %): 1- 150 keV, 2- 200 keV, 3- 250 keV, 4- 300 keV and 5- 350 keV.

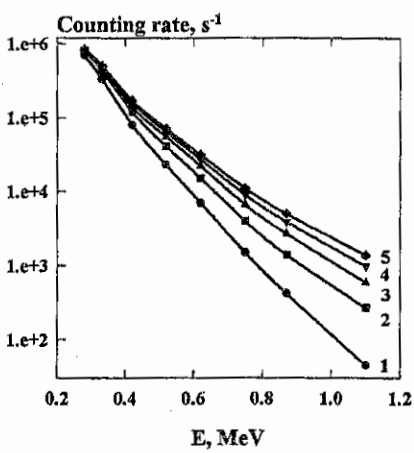

Fig.4 Expected counting rate of H^{0} atoms in high energy NPA produced in charge-exchange of fast protons on He^{0} beam. The curves correspond to different tail temperatures given in Fig.4.

Gamma-Ray Diagnostic Project

V.G.Kiptily*

A.F.Ioffe Physical Technical Institute, 194021 St.Petersburg, Russia

Gamma spectrometry is a non-routine plasma diagnostics, based on detection and analysis of MeV gamma-rays, following thermonuclear fusion and other nuclear reactions between fast ions and nuclei of light elements both background impurities and ones artificially injected into plasma. It may be used for study of fast ion confinement and for density control of fuel and impurities.

This paper presents the summary of the activity on gamma-ray spectrometry of tokamak plasma that is realized during last years in the frame of a project of the International Science and Technology Center (ISTC).

The general directions of the project activity are the following: study of diagnostic reactions using accelerator beams; research and developments of new diagnostic methods based on these reactions; simulation of diagnostic gamma-ray spectra, using the produced nuclear database; development of advanced gamma-ray spectrometer, diagnostic collimator and radiation shield; study of behavior of fast alpha particles and other ions in tokamak plasma by means of the gamma-ray spectrometry technique.

Development of gamma diagnostics

Considered methods of gamma diagnostics are based on nuclear reactions partially presented in the Table. In the process of an analysis of various approaches, two principal methods were selected for study of fast ions in the tokamak plasma, namely, integral and spectral ones. According to the first method, the integral intensity of gamma radiation resulting from diagnostic reactions is detected. This approach can be realized in the form of a multidetector tomographic system consisted of two gamma camera. Information on time-depended spatial distribution of fast particles may be deduced from tomographic reconstruction of experimental data.

For application of the second method, it is necessary to use gamma-ray spectrometers with fine energy resolution. In this case information on a distribution function of fast particles in the plasma can be obtained from the Doppler broadened lines in PHA spectra. For example, to study protons and alpha-particles the $^{9}Be(p,\alpha\gamma)^{6}Li$, $^{9}Be(\alpha,n\gamma)^{12}C$ and $^{10}B(\alpha,p\gamma)^{13}C$ reactions may be used. This kind of nuclear reactions are accompanied by energetic particle emission that leads to a high kinematic scatter of the recoil nuclei and, correspondingly, to more stronger Doppler broadening of gamma lines manifested in PHA spectra of the collimated detector. For example, in the reaction $^{9}Be(p,\alpha\gamma)^{6}Li$, the FWHM of the 3.56-MeV line varies within 45-240 keV for proton energies in the range 1.5-7.0 MeV. Since the Doppler broadening directly depends on energy of particles, this diagnostic technique can provide the study of the velocity distribution of the fast ions. Estimations show that in the case of alpha-particle reactions the broadening can be measured in future D-^{3}He reactors.

FUSION REACTIONS	
$D(p,\gamma)^{3}He$	γ5.5 MeV
$T(p,\gamma)^{4}He$	γ20 MeV
$D(d,\gamma)^{4}He$	γ24 MeV
$D(t,\gamma)^{5}He$	γ17 MeV
$D(^{3}He,\gamma)^{5}Li$	γ17 MeV
BACKGROUND REACTIONS	
$^{9}Be(p,p'\gamma)^{9}Be$	γ1.7, 2.4, 3.05, 4.7 MeV
$^{9}Be(p,\gamma)^{10}B$	γ5.1, 6.7, 7.5, 7.8 MeV
$^{9}Be(p,\alpha\gamma)^{6}Li$	γ3.56 MeV
$^{9}Be(d,n\gamma)^{10}B$	γ2.8, 2.15 MeV
$^{9}Be(d,p\gamma)^{10}Be$	γ3.4 MeV
$^{9}Be(^{3}He,p\gamma)^{11}B$	γ7.3, 4.44 MeV
$^{9}Be(^{3}He,n\gamma)^{11}C$	γ6.3-6.9, 4.3 MeV
$^{9}Be(\alpha,n\gamma)^{12}C$	γ4.44 MeV
"PELLET" REACTIONS	
$^{7}Li(p,p'\gamma)^{7}Li$	γ0.478 MeV
$^{7}Li(p,\gamma)^{8}Be$	γ17.6 MeV
$^{11}B(p,p'\gamma)^{11}B$	γ2.43, 4.44, 5.02 MeV
$^{11}B(p,\gamma)^{12}C$	γ4.44, 11.7 MeV
$^{19}F(p,\alpha\gamma)^{16}O$	γ6.1, 6.9, 7.1 MeV
$^{10}B(\alpha,p\gamma)^{13}C$	γ3.1, 3.7, 3.85 MeV

Resonance capture reactions $^{9}Be(p,\gamma)^{10}B$ and $^{9}Be(p,\alpha\gamma)^{6}Li$ can be a powerful tool for study of velocity distribution of ICRF driven protons in He/H or D/H plasma. In the case of spatial emissivity profile measurements a localization of the fast ions can be determined.

To assess a feasibility and efficiency of the gamma diagnostic techniques a code GAMMAS is worked out. Estimation of experimental conditions and simulation of gamma-ray yield from plasma are performed for different discharge scenarios in ITER. Spectrometer count-rates corresponded to the diagnostic reactions and background are calculated.

In-beam study of diagnostic reactions and database

A complete using of the gamma diagnostics is impeded by the lack of basic gamma-ray production cross-section data for fast ions interacting with light impurities. Furthermore, the spectral diagnostic approach developed in the frame of the project requires a precise data on gamma-ray spectra for simulation of the experiments and processing data.

According to the work plan of the project, detailed investigation of $^{9}Be(p,\alpha\gamma)^{6}Li$, $^{9}Be(\alpha,n\gamma)^{12}C$ and $^{10}B(\alpha,p\gamma)^{13}C$ reactions are carried out using accelerators. Information on integral and differential cross sections and gamma-ray spectra have been obtained. The Doppler gamma-lines recorded by HP Ge detectors have been processed and characteristic parameters have been deduced by means of least square fitting. The data have been included to nuclear reaction database FUSION developed for gamma diagnostic experiments. Beside of this information, cross sections of basic nuclear reactions used in fusion research are inserted too. This database can be utilized in diagnostic simulation and data processing.

Diagnostic gamma detector

One of the general objective of the project is development of a special detector for gamma diagnostics in the reactor environment. A total energy peak spectrometer GAMMACELL is worked out as a prototype of the device. The spectrometer consists of nine optically independent scintillation BaF_2 detectors (42x42x142 mm) assembled in a single housing. Gamma radiation from the plasma through a collimator impinges only on central section of the array. All detectors are included in a circuit which is ensure summation of full energy of gamma ray, falling on a central crystal.

In front of the central crystal, it is supposed to establish one more BaF_2 detector with the sizes 60x60x40 mm (passive-active gamma-ray filter), which must functionate as an absorber of low energy gamma radiation and, simultaneously, as a rejecter of scattered and annihilation radiation found the central unit of the spectrometer. This is needed to reduce background load to the basic detector.

Developed data acquisition and processing system allow to accumulate gamma-ray spectra with count-rate more than 2 MHz.

In ignition experiment all diagnostic devices will be in a strong neutron flux. It is supposed that the gamma-ray spectrometer will be surrounded by radiation shield, nevertheless, to reduce neutron flux through the collimator is needed. Our calculation shows that the ^{6}LiH plug in collimator is suitable for the gamma-ray measurements. Three samples of the plug have been manufactured and tested. A factor of the neutron reducing of this material is measured with d-d and d-t neutron generator. The attenuation is tested with sharp and wide beams of the neutrons. These experiments confirmed our Monte-Carlo calculations, and the ^{6}LiH plug is recommended to utilize in the gamma diagnostic experiment.

During optimization of the gamma-ray collimator it is found out that some part of neutron flux will irradiate the detector. That is why neutron examination of using scintillation crystal has been carried out. The measurements of neutron registration efficiency of the BaF_2 crystal have been performed, using d-d and d-t reactions in calibrated neutron generator. The results show that the neutron sensitivity of the BaF_2 scintillator is low, and this material is acceptable for fusion diagnostics.

Results of the research and development that carried out in the project can be applied in the large operated tokamaks JET (UK), JT-60U (Japan) and DIII-D (USA). In prospect, the obtained results may be used for diagnostic system design and study of the ITER plasma. It is necessary to note that gamma diagnostics can be a powerful instrument for research and plasma control in future thermonuclear reactors with low neutron yield, such as D-^{3}He.

---

* ISTC Collaboration: Ioffe Institute (St.Petersburg) - Kurchatov Institute (Moscow)- Russian Federal Nuclear Center VNIIEF (Sarov)

Modeling of ion-dynamic effects in Stark-broadening theory of hydrogenic emitters

I.O. Golosnoy
Institute for Mathematical Modeling, Miusskaya sq. 4-A, Moscow 125047, Russia
E-mail: golosn@kiam.ru

1. Introduction

The problem of calculating optical properties of hot, dense plasmas (the shape and intensity of spectra lines, the opacity) and Stark-broadening diagnostics of these plasmas arise in various physical experiments and technical processes and in astrophysics. The computation of the line shapes is an important task in this problem, because of the profiles of spectra lines, broadened mostly by Stark effects from electric microfield of plasma, have been long used for determining electron and ion densities and for calculating photoemission and photoabsorption by hot matter.

Plasma broadening of spectra lines arises from interaction of the radiator with electric microfield both electrons and ions of plasma. It is assumed to distinguish two types of electric fields, a high-frequency field of electrons and low-frequency field of shielded ions. It is now customary to treat the electrons with an impact theory and to obtained the ions contribution by quasistatic approximation. This assumptions allow to describe the far wings of spectra lines. However, the motion of ions can produce significant discrepancy near the line center. The experiment [1] have shown that this ion-dynamic effects can change the halfwidth of the lines with unshifted components, such as $Ly_{\alpha,\gamma}$, $H_{\alpha,\gamma}$, by a factor of 2 or more with respect to quasistatic approximation for ions. Computer simulations [2] were performed to study the effects of ion dynamics on spectra line shape of charged hydrogenic emitters. It was shown [2] that considerably large effects due to ion motion are observed near the line center at this case.

It was shown in [3] that the main factor of broadening near the line center is the rotation of the ionic microfield. The perturbation theory was used for calculations of the corrections on thermal motion of ions [3,4]. That is why this corrections are suitable for the low temperature plasma only, when they are small. The influence of ions motion on the line broadening in hot plasma is so hard that the perturbation theory is not suitable. The difficult model [5] was constructed for this case. In spite of its difficult, this model gives rather accurate results only for Ly_α lines. For more complicated lines, such as Ly_β its accuracy falls off. Moreover model [5] is suitable in the case of charged emetters only.

Often the models mentioned above not suitable for practical applications, because the simple, suitable for large scale numerical calculations, applied at wide rang of temperature and densities models are needed for plasma diagnostics and opacity calculations.

2. The model of ion-dynamic broadening

The new universal analytic semiempirical model of ion-dynamic broadening for all intermediate region between the impact limit and the perturbation theory corrections to the

static approximation of ion broadening was obtained. This model was constructed by to steps:

1) Simple physical model was used for extracting the general functional relation between the broadening and the plasma temperature and density. We used the one-particle approach [6] for determining this relation. The line profile is reduced to quadratures with special functions at this case. The analytic approximation for this quadratures have been constructed. This model gives only the general proportions between the line halfwidth and the plasma conditions:

$$\Delta\omega_{1/2} \sim \frac{N_i C^2}{v_i} \ln\left[\frac{v_i^2 R_i^2 + C^2}{C^2}\right], \tag{1}$$

where N_i is the concentration of ions in plasma, T and m_i there temperature and mass, $\frac{4\pi}{3} N_i R_i^3 = 1$, $v_i^2 = \frac{2k_B T}{\mu}$, $\mu^{-1} = m_i^{-1} + m_0^{-1}$, μ is the reduced mass for ion-emitter pair.

$$C = 1.5n\left[n_1 - n_2\right]_{eff} \frac{Z\hbar}{m_e(Z_0 + 1)}, \quad n_1 \geq n_2, \tag{2}$$

n, n_1, n_2 are the principal and parabolic quantum numbers, Z and Z_0 denote the charges of plasma ions and of emitter respectively. We use so-called three level approximation in (1), (2) (as in Ly_α line) to model ion-dynamic effects because the quadratures mentioned above are extremely difficult for more complicated cases. In this approximation the real system of Stark sublevels are replaced by three components: the central and two shifted ones with Stark constants $\pm C$ from (2). The average $\left[n_1 - n_2\right]_{eff}$ in (2) is determined by taking into account the relative intensities and shifts of all Stark components of a given spectral line. So we have to determine the coefficient of the proportion in (1), which due to many-particle effects in plasma.

Let us use the approximation of isolated Stark components [7]. In this approximation the spectral line shape is given by the following formula:

$$I(\Delta\omega) = \frac{1}{\pi} \operatorname{Re} \int_0^\infty \sum_{\alpha,\beta} \Phi_{ion}^{\alpha\beta}(t)\, \Phi_{el}^{\alpha\beta}(t)\, \exp(-\Delta\omega\, t)\, dt, \tag{3}$$

where $\Phi_{ion}(t)$ and $\Phi_{el}(t)$ denote the reduced auto-correlation functions of the atomic dipole moment in the cases of emitters interactions with ions and electrons respectively. For example, $\Phi_{el}^{\alpha\beta}(t) = \exp(-w_{\alpha\beta} t)$, where $w_{\alpha\beta}$ is the electron impact half-width. The sum in (3) is made over all Stark components $\alpha \to \beta$. It is known that $\Phi_{ion}^{\alpha_0\beta_0}(t) \equiv 1$ for unshifted component $\alpha_0 \to \beta_0$ in quasistatic model. At the present paper we use the exponential approximation for this quality

$$\Phi_{ion}^{\alpha_0\beta_0}(t) = \exp(-s_i t^2), \; s_i^{1/2} = \xi^{1/2} \frac{N_i C^2}{v_i} \ln\left[\frac{v_i^2 R_i^2 + C^2}{C^2}\right]. \tag{4}$$

Just the coefficient ξ takes into account many-particle effects in plasma.

2) The analytic approximation for ξ which connected the impact and quasistatic limits was constructed:

$$\xi = \frac{\eta + 22x \lg\left[\frac{C}{\nu_i R_i} + 1\right]}{1 + x \lg\left[\frac{C}{\nu_i R_i} + 1\right]}, \qquad (5)$$

where η response to the impact limit for ions. For example, η=2, $C = 3Z\hbar(Z_0+1)^{-1}m_e^{-1}$ for Ly_α and η=2.74, $C = 14.7\ Z\hbar(Z_0+1)^{-1}m_e^{-1}$ for Ly_γ. The single free parameter x at this model was selected to provide the best agreement of the results obtained with the experiment [1] or with calculations of the lines shape by molecular dynamic (MD) method [2]. It was found x=0.4 for Ly_α and x=0.6 for Ly_γ.

3. Results

We tested our model to compare our results with experiments in hydrogen [1] at T~10^4(K), N_e~10^{17}(cm^{-3}) and with MD calculations [2,8] for hydrogen at the same conditions and for Al^{+12}, Ar^{+17} at T~10^6(K), N_e~10^{22}(cm^{-3}). In spite of the very different plasma conditions at this cases our model gave good accuracy (Fig.1,2,3). Emphasize that the quasistatic model is rather well for a far wings of spectral line (Fig.1,3), but there are significant deviations between this model and experiment or MD results near the line center. As opposed to this result, the model, presented here, describe well as the line center as the far wings of the line.

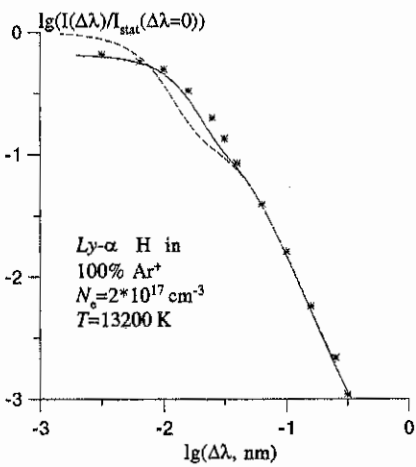

Fig.1. Comparison of measured (, *, *) and calculated: the present model (——), static ions (- - -), Ly_α hydrogen Stark profiles. The intensity of the line calculated by the static model for ions is equal to 1 for Δλ=0. We use log-log coordinates for more detailed comparison as the line center as the far wings of the line.*

Halfwidths measured [1] and calculated by quasistatic and dynamic models are listed in Table I. Although the calculated widths are smaller than measured ones, they are within the errors of experiment [1].

Also we tested the variation of the line profile with changing the reduced mass of radiator–perturbing-ion pair. It was founded in experiment [9] that the ratio I_D/I_H of the profiles Ly_α of D in Ar^+ and H in Ar^+ respectively, at the line center is equal to 1.17 for T=15500(K), N_e= =2·10^{17}(cm^{-3}). The proposed model give the close result (1.18) for this conditions. So the discrepancy is less than 1%.

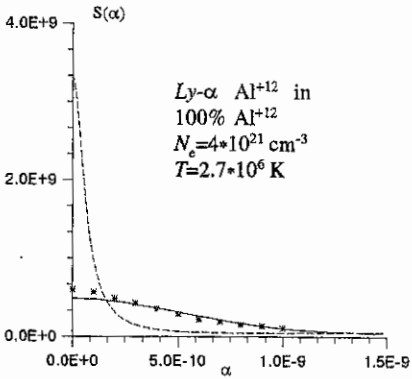

Fig.2. Ly_α spectral line of Al^{+12} for the present model (——), MD (, *, *) and static ions (– – –), $\alpha=\Delta\lambda/E_0$, $\Delta\lambda$ in angstroms, $E_0=eI R^2$, $(4\pi/3)N_e R^3=1$.*

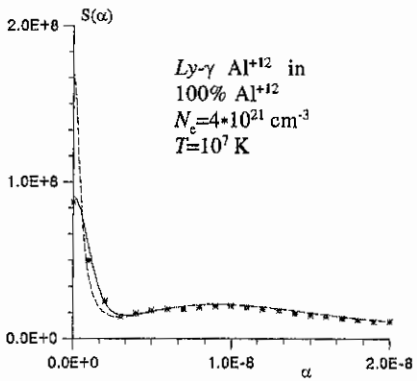

Fig.3. Ly_γ spectral line of Al^{+12}. The markings are the same as Fig.2.

TABLE I. Full-width (in nm) at half maximum for Ly_α H in Ar^+. $\Delta N_e/N_e<\pm0.1$; $\Delta T/T<\pm0.03$

N_e (10^{17} см$^{-3}$)	T (K)	Calculated		Measured (±0.002)
		Quasistatic model	Present calculations	
1	12700	0.014	0.021	0.023
2	13200	0.016	0.028	0.030
3	13200	0.019	0.034	0.036
4	14000	0.022	0.040	0.042

4. Acknowledgments

This research was supported by Russian Foundation for Basic Reseach, Grant N 96-01-00305

5. References

1. K.Gruntzmacher, B.Wende. *Phys.Rev.A*, **16**, 243, 1977.
2. R.Stamm, B.Talin, E.L.Pollock, C.A.Iglesias. *Phys. Rev. A*, **34**, 4144, 1986.
3. A.V.Demura, V.S.Lisitsa, G.V.Sholin. *Zh. Eksp. Teor. Fiz. (USSR)*, **73**, 400, 1977.
4. R.Gauble, H.R.Griem. *Phys. Rev. A*, **27**, 3187, 1983.
5. D.B.Boercker, C.A.Iglesias, J.W.Dufty. *Phys. Rev. A*, **36**, 2254, 1987.
6. V.S.Lisitsa, G.V.Sholin. *Zh. Eksp. Teor. Fiz. (USSR)*, **61**, 912, 1971.
7. G.V.Sholin, A.V.Demura, V.S.Lisitsa. *Zh. Eksp. Teor. Fiz. (USSR)*, **64**, 2097, 1973.
8. R.Stamm, E.W.Smith, B.Talin. *Phys. Rev. A*, **30**, 2039, 1984.
9. M.Geisler, K.Gruntzmacher, B.Wende. In *Spectral Line Shapes II*, ed. by Burnett p.37, 1983.

A 5-Chord VUV Spectrometer for Impurity Study

C.Giroud, G.Cunningham
Dept. of Physics, UMIST, P.O. Box 88, Manchester M60 1QD, U.K.

1 Introduction

If the light from 5 different lines of sight of the Spheromak annulus is collected simultaneously, a quantity of information (all time resolved) can be deduced about the sustained phase of SPHEX: the impurity concentration can be mapped, and the impurity transport and impurity influx can be estimated with the help of a computer model.

A 5-chord VUV spectrometer has been developed for the spectral range 600 $\AA$ to the visible, using a normal incidence mount. Its design is presented below, followed by the initial results on the emissivity profiles of C, O species in the SPHEX annulus.

2 Design Constraints

Two main constraints of this design are due to the use of the VUV light and the choice of the channel separation configuration.

The VUV spectrum is of interest because it includes the most intense impurity lines, ie the resonant lines. However, the main problem of this spectrum is that the light cannot be transmitted through optical fibre or lenses due to absorption. Therefore, mirrors have to be used for the channel selection. If the light is reflected near normal incidence, CVD-SiC is the coating with best reflectance, see figure 4 of [1]. This latter being so expensive, a gold coating used at high angle of incidence is preferred even if it allows less freedom in the design. At high angle of incidence, the reflectance of gold and CVD-SiC are comparable for the spectral region of concern, see figure 6 of [1]. So, gold coated mirrors are chosen and have to be used with an angle of incidence greater than 80° for a reflectance greater than 75 % (cannot deviate rays by more than 20°).

Two configurations are possible for the channel separation: the slit division or the solid angle: the best is the one with the maximum intensity for each channel, and minimum overlapping between channels. The étendue being the same for both configurations, there is no difference of intensity . However, the overlapping consideration is able to discard one configuration. Actually, the main problem of the concave grating is astigmatism. A point at the entrance slit is imaged by a line of length $\Delta L(\lambda)$. For a slit division system, the

entrance slit (20 mm long) is divided in 5, ie each channel is 4 mm long. The overlapping between channels at the exit slit is tolerable if it is less than 30 %, so $\Delta L(\lambda) \geq 3$ mm. With the help of the ray-tracing program Zeemax, we determined the latter condition to be valid if $\lambda \geq 2300$ $\AA$. Since, the visible spectrum is needed for the absolute calibration, the slit division configuration is inadequate, and the solid angle is chosen to be divided .

3 Description of the instrument

The solid angle division configuration is presented on figure 1. The five lines of sight from 5 different regions of the plasma are selected with the help of gold coated mirrors, specially shaped for this experiment, see figure 2.

For the arrangement of this instrument, two points need to be considered. Since the spectrometer needs to be absolutely calibrated, the mirrors, the collecting optics and the spectrometer must form a fixed assembly that can be moved in and out of the tank. Secondly, the distance between the mirrors and the flux conservers needs to be adjustable, so a flexible pipe is used. The arrangement is shown on figure 3. The mirrors are held in an aluminium box whose walls have machined recesses allowing the mirrors to be positioned to within an accuracy of 1 deg of angular separation. Leaf springs were used to hold the mirrors securely in place, without causing any distortion. A stainless hollow pipe maintains the mirrors box at an fixed position in respect to the spectrometer (internal pipe). A flexible pipe allows the distance between the mirrors and the flux conserver to be adjusted. The spectrometer is a 1 m normal incidence (Hilger and Watts E766), with a 600 $l.mm^{-1}$ Osmium grating. The ray-tracing program Zeemax is used to determine the image of each channel including overlapping, at a distance of 110 mm from the exit slit. The light from each channel is collected by Perspex light pipe whose cross-section has been manufactured such as to transmit light from only one channel. The exposed tip of each light pipe is coated with sodium salicylate, whilst the other end is cemented to a photomultiplier. To eliminate interference, the collecting optics assembly is electrically isolated from the spectrometer.

Some characteristics of the instrument can be deduced from figure 4. It shows the intensity detected by each channel against the distance travelled by a mercury lamp (4 mm wide) along a vertical line at 550 mm from the mirrors, with a slit width of 50 μm. One can see that the light contribution from neighbouring channels represents less than 30 % of the total intensity of a channel. An accurate determination of the degree of overlapping

requires the use of a diffuser in order to illuminate the whole channel. These measurements also showed a level of overlapping below 30 %. At 550 mm from the mirrors, the channel width is $\sim$ 40 mm (see figure 4), and its length is $\sim$ 100 mm. The wavelength resolution is $\sim$ 1 $\AA$. A problem of this instrument is that the focus needs to be accurate in order to avoid any correction to the relative intensity of the channels.

4 Initial results

Shots are taken at the centre of the CI line 1930.90 $\AA$, and the CIV line 2296.87 $\AA$, see figure 5; a definite change in the profile of impurity concentration is clearly visible.

Even if the absolute calibration has not been performed yet, we can still deduce an emissivity profile for C, O species since the relative intensity calibration has been done. Figure 6 shows that the concentration of the lower ionisation level species increases towards the wall, whilst the concentration of the higher ionisation level species decreases, as expected. The relative calibration is not yet complete, which may explain the behaviour of region 3.

For future work, the instrument will be absolutely calibrated. The impurity concentration profile for different plasma conditions will be measured. With the help of an existing computer model, the temperature profile and information on the impurity transport will be deduced.

Bibliography

[1] V.Rehn, *Nuclear Inst. and Methods* **177** p. 173 (1980).

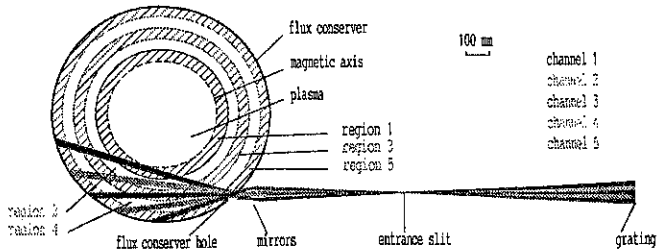

Figure 1: A 5-chord vuv spectrometer with solid angle division

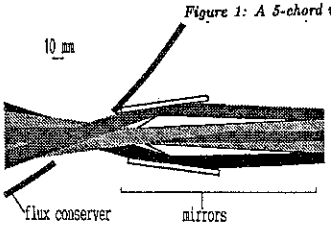

Figure 2: Enlargement of figure 1 on the mirrors

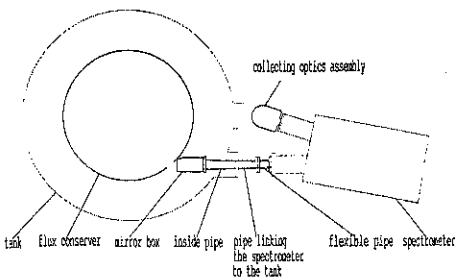

Figure 3: Arrangement of the instrument

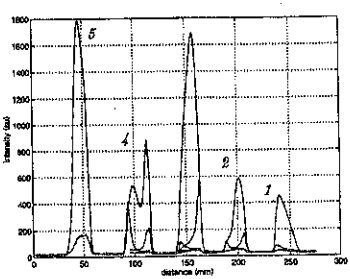

Figure 4: Channel separation.

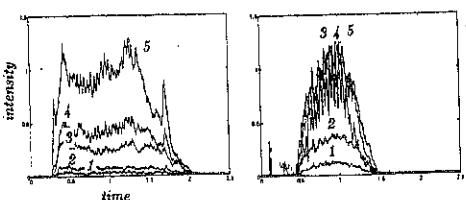

Figure 5: Intensities at 1930.90 Å, CI species, and at 2296.87 Å, CIV species.

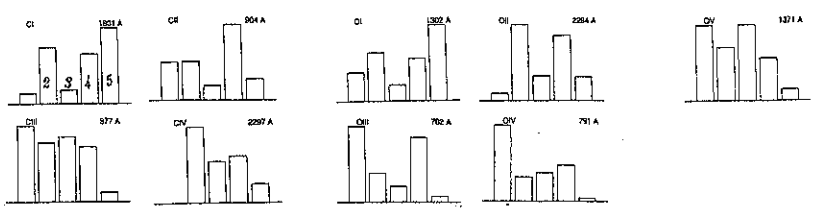

Figure 6: Emissivity profile for Carbon, Oxygen species:

Extension and optimization of lithium beam diagnostic methods

R. Brandenburg[1)], S. Fiedler[2)], K. McCormick[2)], G. Petravich[3)], F. Aumayr[1)], HP. Winter[1)], J. Schweinzer[2)] and W7-AS Team

1) Institut für Allgemeine Physik, TU Wien, Association EURATOM-OEAW, A-1040 Wien

2) Max-Planck-Institut für Plasmaphysik, EURATOM Association, D-85748 Garching

3) KFKI-Research Inst., Dept. of Plasma Physics, P.O.Box 49, H-1140 Budapest

Introduction

Lithium beam diagnostics are a multi-facetted technique for investigating fusion edge plasmas. While the determination of electron densities by lithium impact excitation spectroscopy (Li-IXS) has already reached a satisfying standard on both large fusion experiments at IPP Garching [1,2], a neutral lithium beam can also be used to determine local concentrations as well as temperatures of impurity ions by charge exchange spectroscopy (Li-CXS) [3,4]. In order to achieve simultaneous Li-IXS and Li-CXS measurements, both existing IPP setups for electron density measurements have been extended. First results prove the feasibility of Li-CXS in W7-AS plasmas.

In order to check the modelling of the lithium beam we have also investigated the population of higher LiI energy levels.

Experimental setup on W7-AS

The existing lithium beam diagnostic on the stellarator W7-AS has been extended by a 14 channel CXS observation system. Two achromats ($\Omega/4\pi \approx 2.9\text{x}10^{-4}$sr) are used to image the light onto 14 bundles of quartz fibers, each bundle consisting of 8 single fibers (400μm). The detection region covers a radial range of about 13cm from the plasma center to the last closed flux surface of standard plasma configurations. For these investigations the bundles are coupled one by one to the entrance slit of a monochromator (ACTON, Czerny-Turner, f=0.75m). A two-dimensional detector (Proscan CCD camera, 512x512 pixels, each 19x19μm^2) is directly connected to the monochromator exit. The spectral resolution is up to 0.018nm/pixel using a 1800g/mm holographic grating. An additional system of photomultipliers equipped with interference filters (λ=529.0nm) has been introduced, which can be coupled to the same light guides for simultaneous measurements at 14 radial locations. We used the improved extraction geometry of the ion source [1,2] to inject a beam ($I_{Li}\leq$3mA) in the energy range of 20-66keV.

Experimental setup on ASDEX Upgrade

On the ASDEX Upgrade tokamak the lithium beam diagnostic has a new location 33cm above midplane. It is equipped with a completely rebuilt 35 channel electron density optics, a 16 channel charge exchange optics and a 3 channel neutral density monitoring system (fig. 1). At

the new position of the ion gun, which is similar to the one on W7-AS, the magnetic field is weaker. There is also additional μ-metal shielding around the ion beam. Thus, we expect magnetic field effects on the lithium beam (E=35keV, I=1.2mA) to be reduced considerably.

Electron density measurement setup

In the former optical system each spatial channel consisted of three 400μm fibers. The light collection/transmission efficiency varied drastically from fiber to fiber and the system was sensitive to the beam position [5]. To overcome these difficulties, a new head for the fiberguides was built with each spatial channel corresponding to a bundle of 35 quartz fibers (100/130μm). The light from each bundle is coupled to a 48m long, 600μm monofiber (N.A.=0.37) that carries the light to the detection units. About seven percent of the incoming light can be detected this way. A new BK7 optical system -a wedge and two lenses- was built to gather light into 35 channels from about 16cm along the beam path. The observation region can be radially shifted by a couple of centimeters, allowing it to be adjusted to different plasma scenarios. Each detection unit is equipped with an interference filter (T>40%, FWHM≤0.7nm) followed by a photomultiplier. We expect 5 to 10 times more signal with the new detection system which will permit increased temporal resolution and investigations of density fluctuations outside the separatrix.

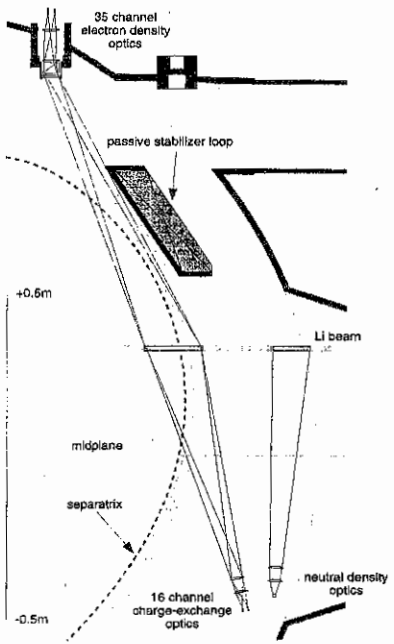

Fig. 1: Optical observation systems of extended lithium beam diagnostics on ASDEX Upgrade.

CXS measurement setup

Two quartz lenses ($\Omega/4\pi \approx 1.5\times10^{-3}$sr) focus the light onto an array of 16 quartz fibers (400μm) enabling the radial distribution of the emitted light in a 16cm region around the separatrix to be measured with 1cm spatial resolution. The fibers are coupled to the entrance slit of the same CXS spectroscopic system as described for W7-AS. Temporal resolution is limited by the readout time of the CCD detector for 16 channels (13 ms).

Neutral density measurement setup

Two BK7 lenses ($\Omega/4\pi \approx 1.8\times10^{-3}$sr) focus the light onto an array of 21 quartz fibers (400μm) that are grouped into three bundles. The light is gathered from a region far from the separatrix where lithium excitation by collision with neutrals is the dominant process [2]. Each channel is equipped with an interference filter (T>40%, FWHM≤0.7nm) to select the Li(2p→2s) line.

Results

Lithium beam composition

Because of highly different cross sections for charge exchange processes, depending on the excitation state of the donor atom, the composition of the lithium beam is an important parameter for evaluating CXS data. We have therefore investigated several LiI spectral lines ($2p \rightarrow 2s$, $3d \rightarrow 2p$, $4s \rightarrow 2p$, $4d \rightarrow 2p$) in W7-AS discharges. While the measurements of the most relevant line Li($2p \rightarrow 2s$) at λ=670.8 nm were performed for calibrating the CXS setup relatively to the Li-IXS photomultiplier setup, all other LiI lines were investigated to check the attenuation model of the lithium beam [6]. Measured intensities of emission from higher levels were found to differ considerably (30-60%) from corresponding theoretical values. We observed no dependence on magnetic field strength and beam energy, whereas changing plasma densities had strong effects on the conformity of experimental and theoretical values with the deviation becoming larger at higher densities.

Inadequate scaling relations for excitation and ionization processes involving protons and impurity ions in the underlying database [7] have been identified as the major reason for these disagreements. These are now being recalculated by more advanced means. First results for the Li($3l \rightarrow 2l$) transitions show a significant decrease of theoretical values of Li(3d)/Li(2p) ratios (fig.2) when using the improved cross section data. However, since the relative population of the Li(3d) level in the lithium beam is in the range of 1% only, with populations of all other Li(nl) levels (n>2) even smaller, the influences on electron density calculations remain below 10%.

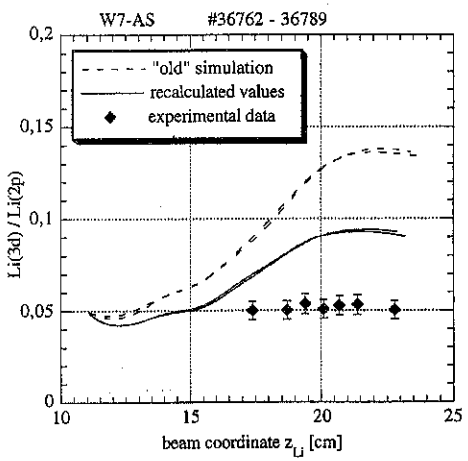

Fig.2: Population ratios of the Li(3d) and Li(2p) energy levels. Comparison of experimental data and beam simulation results for a series of similar W7-AS discharges. Plasma center at z_{Li}≈26cm.

Furthermore, recent simulations have suggested that the population of higher excited states depends on Z_{eff}. Thus, the measurement of only one additional line besides the resonance line offers a possibility to determine an estimate for Z_{eff} -under the assumption of a reasonable radial charge state distribution of the impurities and if the present disagreement for n=3 populations between simulation and experiment further diminishes as a consequence of more accurate cross sections.

CXS investigations

Measurements of spectral lines of impurity ions have proven the feasibility of charge exchange spectroscopy on W7-AS plasmas with the extended setup. The photomultiplier system has been introduced for simultaneous measurements of C^{6+} concentrations at 14 radial locations, while the spectrometer system has been used for the determination of temperature profiles of C^{6+} ions (fig. 3).

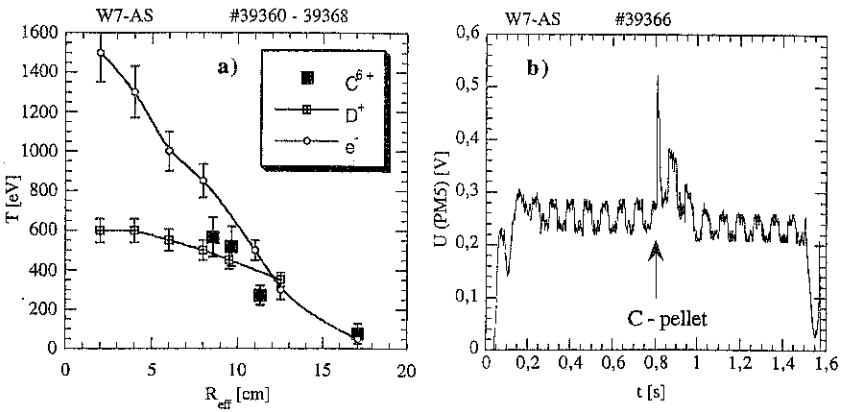

Fig. 3: a) Radial temperature profiles of C^{6+} compared to e^- [8] and D^+ [9]. All data were obtained during a series of similar W7-AS discharges. b) Raw photomultiplier signals for concentration evaluation at R_{eff}=12.3cm. Injection of a carbon pellet at t=0.8s increases the charge exchange induced signal significantly. Injected lithium current I_{Li} ≈2mA at E=48kV.

Temperature values, which were corrected for line broadening effects such as Zeeman splitting and l-level mixing [10], are similar to proton/deuteron as well as electron temperature profiles. Evaluation of impurity ion concentration values requires extension of the charge exchange cross section database, which is presently being carried out.

Acknowledgements

This work has been supported by Friedrich Schiedel - Stiftung für Energietechnik and by Kommission zur Koordination der Kernfusionsforschung at the Austrian Academy of Sciences.

References

1. K. McCormick et al., *IPP Report III/211* (1996)
2. S. Fiedler, *IPP Report III/209* (1995)
3. E. Wolfrum et al., *Rev. Sci. Instrum.* **64** (1993) 2285
4. F. Aumayr et al., *J. Nucl. Materials* **196-198** (1992) 928
5. J. Schweinzer et al., *22th EPS Conf., Europhys. Conf. Abstr.* **19C** III (1995) 253
6. J. Schweinzer et al., *Plasma Phys. Contr. Fusion* **34** (1992) 1173
7. D. Wutte et al., *At. Nucl. Dat. Tables* **65** (1997) 155
8. H.J. Hartfuss et al., *Proc. 8th Workshop on ECE and ECRH, Oxford* (1987) 281
9. M. Kick et al., *20th EPS Conf., Europhys. Conf. Abstr.* **17C** I (1993) 357
10. R.P. Schorn et al., *Nucl.Fusion* **32** (1992) 351

ELECTRON TEMPERATURE PROFILE MEASUREMENTS BY HEAVY ION BEAM PROBING ON THE TOKAMAK ISTTOK

A. Malaquias, J.A.C. Cabral, C.A.F. Varandas, I. Nedzelskii and R. Canário
Associação EURATOM/IST, Centro de Fusão Nuclear, 1096 Lisboa Codex, Portugal

1. Introduction

A Heavy Ion Beam Diagnostic (HIBD) could be a suitable tool for the measurement of the electron temperature of a magnetised plasma with good spatial and temporal resolutions [1]. This parameter has been determined from the ratio of the tertiary to the secondary ion currents that attain a single detector cell[2]. The radial profile has been obtained by sweeping the beam through the plasma in different discharges. Therefore this method does not allow the determination of the temporal evolution of the T_e profile in a single discharge.

This paper presents measurement of the electron temperature of the ISTTOK plasma with the set-up described in section 2. Section 3 contains the study of the evolution of the T_e profile obtained by the classical method taking advantage of a new detection system. Section 4 describes a new method under development for the measurement of the evolution of this profile in a single discharge using a two species mixed ion beam.

2. Experimental set-up

ISTTOK is a small (R = 0.46 m; a = 0.085 m; B_T = 0.45 T; $n_e \approx 8\times10^{18}$; $T_e \approx 180$ eV) circular cross section, iron core transformer, limiter tokamak [3]. Its HIBD, whose operating principles are described in [1], is based on a plasma source ion gun and a detection system composed by two Multiple Cell Array Detectors (MCAD), one for the primary beam (5×3 copper cells with dimensions of 6×5 mm^2) and the other for the secondary ions (14×6 copper cells of 5×4 mm^2). Fig. 1 presents the schematic of the ISTTOK HIBD.

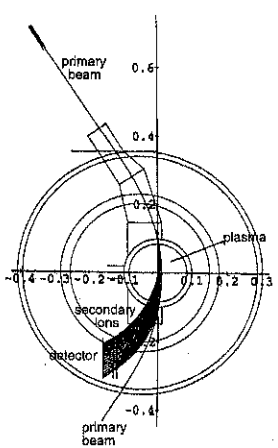

Fig. 1

3. Evolution of the T_e profile from the secondary and tertiary ion currents

The electron temperature can be obtained by comparison of the ratio between the secondary

$$I_j^{++} = 2I^+ n_e(r_j)\hat{\sigma}_{12}(r_j)dl \qquad (1)$$

and the tertiary

$$I_j^{+++} = 3I^+ n_e(r_j)\hat{\sigma}_{13}(r_j)dl' \qquad (2)$$

ion currents collected at one detector cell and the ratio of the corresponding cross sections. I^+ represents the primary beam current, $n_e(rj)$ is the plasma density and $\sigma_{12}(rj)$ ($\sigma_{13}(rj)$) is the effective cross section for single to double (triple) ionisation at the plasma position rj where this process occurs. dl and dl' are the primary beam paths for double and triple ionisation.

Due to geometric constrains it was not possible to install in the tokamak an additional MCAD for tertiary ion detection. Therefore, both types of ions were collected by the same MCAD in two similar discharges. From numerical simulations made taking into account the energy range of our ion beam (0 - 20 keV) and the expected T_e values we have concluded that the best choice was a Hg^+ beam with the following characteristics: 15.5 (20) keV energy and a current of 350 (580) nA for detection of the secondary (tertiary) ions.

The best measurements were performed in shots #6115 and #6116 in three different times during the best matching of plasma currents within an average density of 5×10^{18} to 8×10^{18} m^{-3} (measured by interferometer). The experimental ratio was normalised to the primary beam current and to the average plasma density. The results (Fig. 2a) show that the T_e profile decreases along the plasma shot in agreement with the increase of plasma resistivity (Fig. 2b).

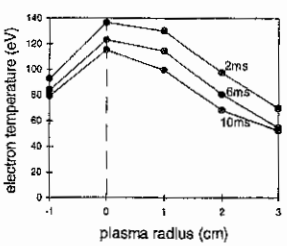

Fig. 2a

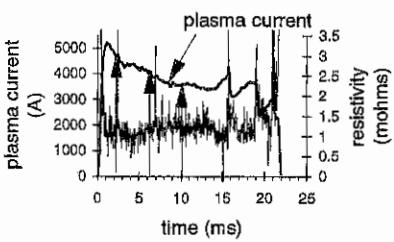

Fig. 2b

4. Temperature measurements using a mixed beam technique

The use of a mixed beam could allow the simultaneous measurement of several profiles of the electron temperature, plasma density and poloidal magnetic field during the same tokamak discharge

The method consists in the alternating injection of a mixed beam composed by two ion species (A^+ and B^+) of similar masses with a pure beam of one of the species (A^+ for instance). This condition ensures 'perveance match' at the beam accelerator optics and that both beams will be injected into the plasma at the desired energy. From the pure beam injection, we measure I_A^+ (A^+ beam current) and I_A^{++} (A^{++} beam current) in the detecting cells and the $(n_e \times \sigma_{12})_A{}^+$ profile can be determined. When the mixed beam is injected, we measure I_{A+B}^+ (primary mixed beam current) and I_{A+B}^{++} (secondary mixed beam current). Assuming that the plasma parameters remain constant during the commutation time from pure to mixed beam injection, $(n_e \times \sigma_{12})_A{}^+$ does not significantly change. The $I_{A(m)}^{++}$ (secondary current of species A on the mixed beam) that arrives to each detector cell can be calculated from

$$I_{A(m)}^{++} = I_A^{++} \frac{I_{A(m)}^{+}}{I_A^{+}} \qquad (3)$$

where $I_{A(m)}^{+}$ is determined from the relative positioning of the mixed beam and the known positions of the pure beams at the detector. The difference between I_{A+B}^{++} and $I_{A(m)}^{++}$ gives $I_{B(m)}^{++}$ at each secondary detector cell allowing the determination of $(n_e \times \sigma_{12})_B{}^+$. The electron temperature is calculated once again by comparison of the theoretical cross sections ratio with the experimental ratio between $(n_e \times \sigma_{12})_A{}^+$ and $(n_e \times \sigma_{12})_B{}^+$.

The implementation of this method on ISTTOK was studied for two types of mixed beams: $Cs^+ + Xe^+$ and $Xe^+ + Ba^+$. The first one is very easy to produce with our present ion gun. We inject Xe gas on a heated chamber containing the Cs vapor. The mixed plasma from which the mixed beam is extracted is produced by accelerating thermoelectrons between a hot filament and the chamber wall. A potential variable between 10V and 50V is applied to the hot filament modulating in this way the thermoelectrons energy. This technique allows the production of a pure Cs plasma (at 10V) alternated with a Xe/Cs mixed one (50V). The primary beam current arriving at the primary detector is presented in Fig. 3.

However it has three main difficulties: (i) we can only diagnose the plasma edge since the theoretical calculations show that the ratio of the cross sections is only temperature dependent for T_e lower than 50 eV; (ii) the contribution of the Xe^+ current in the mixed beam was too small, probably due to the large difference of the ionisation energy between the Cs and Xe species; (iii) since we are measuring at the plasma edge, the collected secondary Xe^{++} ion currents were too low and the results were masked by the noise.

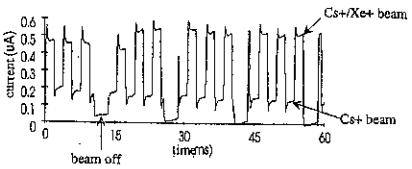

Fig.3 - Primary beam current at the detector. The beam is injected in a pulsed mode

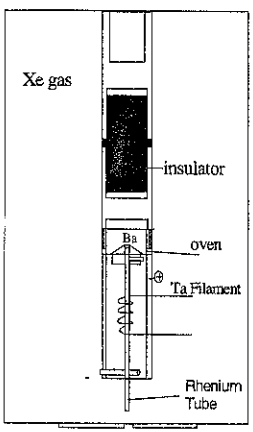

Fig. 4

The use of the $Xe^+ + Ba^+$ mixed beam is expect to increase the range of the T_e measurements until 250 eV. However the generation of a mixed beam of $Xe^+ + Ba^+$ implies major changes in the ion gun. The Ba^+ beam has to be produced from a thermal contact ionisation source which operates inside the Xe plasma ion source (Fig. 4). The Xe^+ beam will be commuted by modulating the hot filament potential while the Ba^+ will be continuously injected.

Acknowledgements - This work has been carried out in the frame of the Contract of Association between the European Atomic Energy Community and "Instituto Superior Técnico" and has also received financial support from "Junta Nacional de Investigação Científica e Tecnológica" and PRAXIS XXI.

References:

[1] - *J.A.C. Cabral et al.* "The Heavy Ion Beam Diagnostic for the Tokamak ISTTOK" IEEE Transations on Plasma Science 22, 4, 350, 1994.

[2] - *T. P. Crowley et al.* "Rensselear Heavy Ion Beam Probe Diagnostic Methods and Techniques" IEEE Transations on Plasma Science 22, 4, 291, 1994

[3] - *C.A.F. Varandas et al.* "Engineering Aspects of the tokamak ISTTOK" Fusion Technology 29, 105, 1996

Fast Multichannel Plasma Radiation Losses Measuring System

A.Alekseyev*, G.Perov, A.Kurnosov, A.Chernobai,
A.Romannikov, V.Lazarev, V.Amosov, D.Portnov, A.Belov
TRINITI, Troitsk, Moscow reg. 142092 Russia,
*E-mail: alexag@triniti.troitsk.ru
Raj Korde
International Radiation Detectors, Torrance CA, 90505 USA

1. Introduction

Bolometers are considered to be a standard diagnostic for fusion experiments, mainly for measuring the total radiated power and spatial profiles of the local radiation power density. Thin film metal foil resistors [1, 2] and pyroelectric detectors [3] are commonly used for these purposes due to non-selective sensitivity in wide spectral range of incident radiation, provided by thermal nature of their response. Their low sensitivity, susceptibility to EMI noises and poor rise/fall time lead to serious limitations for the space/time resolution of multichannel systems. Their high absolute measuring accuracy could be achieved for relatively slow processes only, generally at >10 ms timescale. The dynamic accuracy remains questionable since the numerical solutions of thermal conduction equations are necessary for fast heating power variations in the absorption layer to be derived from the temperature response of thermal sensitive layer behind.

Radiation induced current in semiconductor detectors is known to be independent on the incident particle energy in the range well above its energy bandgap E_g. Since plasma radiation losses spectrum is located within 20...5,000 eV energy range, semiconductors with $E_g < 2$ eV would be suitable if the input protection and high surface recombination rate layers are eliminated. Some attempts were made earlier in this direction with the use of InP:Fe photoconductors [4]. Applications of common Si photodiodes (PD) for UV-imaging are limited by the presence of a front dead layer providing low-energy response cutoff. Recent advances in Si technologies for eliminating this front dead layer and enhanced PD quantum efficiency stability pioneered by *International Radiation Detectors Inc.* (USA) have resulted in AXUV series Si PD manufactured for absolute radiometry applications in vacuum ultraviolet, extreme ultraviolet and soft X-ray spectral regions (7...6,000 eV) [5-7]. National standard laboratories: NIST (USA) and PTB (Germany) have approved use of AXUV-series IRD photodetectors as secondary standards with ±4% uncertainty in 30...6,000 eV range. Developed by IRD advanced nitridation technology resulted in low rate of detector surface carrier recombination yielding ultimate internal quantum efficiency preserved stable under 1 Grad radiation dose (with respect to 10.2 eV photons) and 4-week exposure to 100% relative humidity atmosphere [6].

Taking into account a number of attractive features, AXUV PD implementation to plasma radiation losses diagnostics seems to be worthwhile, although ~50% responsivity drop in 10...30 eV energy range could result in some systematic errors of plasma radiation intensity absolute measurements (Fig.1).

Fast Multichannel Plasma Radiation Losses Measuring System (MRLMS) have been developed for T-11M (Troitsk, Russia) and HL-1M (Chengdu, China) environments. Its main advantages are improved S/N-ratio and fast response achieved by the use of AXUV-16ELO Si 16-element detector array.

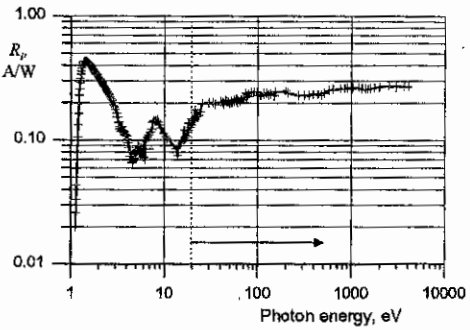

Fig.1. AXUV Si PD spectral response. Arrow marks the usual position of radiation losses spectra.

2. MRLMS Design

The system contains three main parts: Detector Unit (pinhole camera) including Si PD array + 16-channel preamplifier hybrid assembly to be placed into the vacuum port (Fig.2), remote ADC/Isolation Unit (1-3 m apart from the port) and IBM PC interface Control Card.

Detector Unit Specifications

■ Detector rise/fall time	0.5 μsec
■ Field of view (FOV)	40...90°
■ Sensitive area	2x5(x16) mm^2
■ Output sensitivity	10^3-10^6 V/W
■ Frequency band	0...100 kHz
■ Max.baking temperature	200°C
■ Power supply:	+6...18 V
■ Quescent current:	14 mA
■ - shutdown mode	20 μA
■ Power startup delay	≤ 10 msec
■ Total weight	250 g

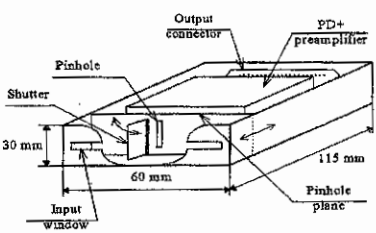

Fig.2. Detector Unit assembly.

MRLMS Detector Unit (pinhole camera) design is shown in Fig.2. Aluminium-made casing box is used for low weight electric shielding. Teflon and ceramic fixing elements provide high-voltage isolation to suspend holder and shutter drive mechanism. Pinhole shutter prevents detector surface contamination during the glow discharge vessel treatment.

MRLMS Data Acquisition system includes remote ADC/Isolation Unit connected via data transmission cable to the Control Card plugged into IBM PC internal bus expansion slot. Main advantages of the remote design assume high immunity to external EMI noises and wide range input common-mode floating potential achieved by means of shortened length of input wires in couple with total 1.5 kV galvanic isolation of analog circuits in the vicinity of primary signal source location. Common mode rejection ratio of >120 dB value have been proved in 0...100 kHz frequency band with up to 700 V_{pp} analog ground potential variations.

General system design provides multichannel functioning at up to 100 kS/sec ADC sampling rate with 12-bit resolution. Additional CAMAC modules with 1 μs sampling time were used in parallel for special studies of plasma disruptions and other fast processes.

3. Results and discussion

MRLMS was installed to T-11M tokamak environment in May 1996 for preliminary testing and plasma radiation profile evolution measurements. No remarkable deviations in detector sensitivity along a year of operation have been observed after a number of vacuum vessel treatments including baking up to 150-200°C, cleaning discharges, boronization and more than 1000 deuterium shots. Excellent signal-to-noise performance achieved by novel design of plasma radiation losses diagnostic have been demonstrated, no external interference induced signals were observed even at plasma disruptions and initial breakdown.

Preliminary MRLMS data obtained at T-11M on plasma radiation losses evolution were shown to be in agreement with conventional pyroelectric bolometer, D_α/SXR - emission and MHD activity measurements (Fig.3). In general, simple Abel inversion procedure could not be used, unfortunately, for the profile reconstruction due to its considerable vertical asymmetry. Additional devices are necessary for applicability of deconvolution technique. Anyway, owing to advanced dynamic properties, even a qualitative temporal/spatial behaviour analysis in comparison with evolution of various plasma parameters have proven MRLMS helpfulness for better imaging of radiation losses location and fast processes of plasma-limiter interactions during the disruptions (Fig.4). Fourier transform and correlation analysis technique were used also for MHD activity and plasma rotation induced radiation losses variations.

An experimental testing of MRLMS accuracy for radiation losses measurements is planned at T-10 environment. The design of a combined system including foil bolometers and AXUV Si detector array with the same FOV is under consideration also. This complementary approach seems to be the most promising for advanced accuracy and dynamic performance.

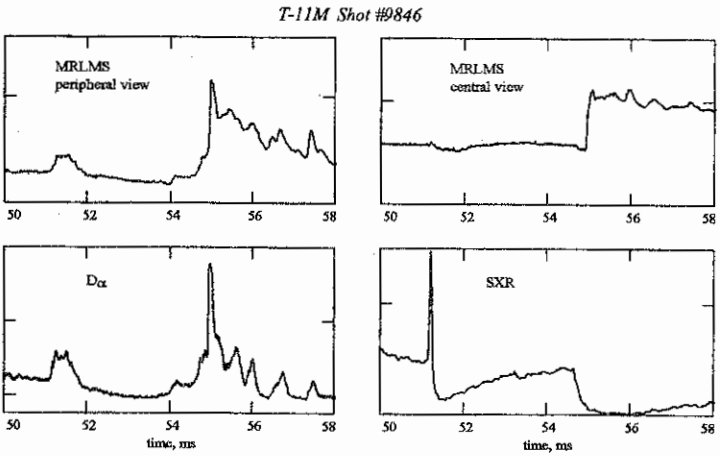

Fig. 3. Typical MRLMS, D_α and SXR traces during disruption. ADC sampling time - 5 μs.

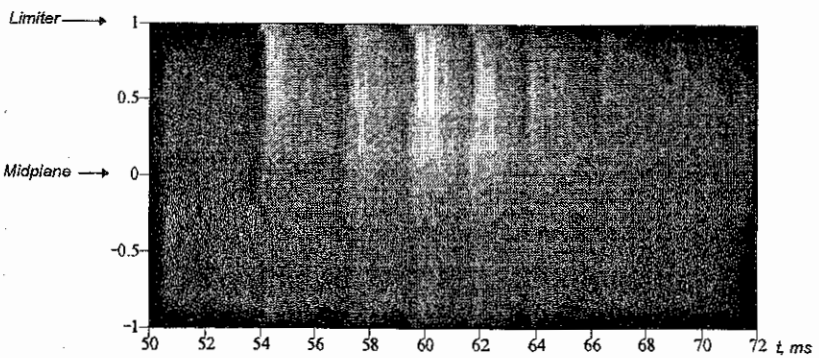

Fig.4. Radiation losses vertical profile evolution along the disruption processes. Frame cycle - 0.2 ms.

4. References

1. E.R.Muller and F.Mast, J.Appl.Phys. 1984, v.55, pp.2635-2641.
2. A.Murari, K.F.Mast *et al.* Rev.Sci.Instr. 1995 v.66, pp.665-667.
3. A.N.Vertiporokh, S.N.Zvonkov, Yu.S.Maksimov, Plasma Diagnostics v.5, ed. by M.I.Pergament, Energoatomizdat, Moscow 1986, pp.75-77 (rus).
4. D.R.Kania, L.A.Jones *et al.*, Rev.Sci.Instr. 1985, v.56, p.846.
5. L.R.Canfield, J.Kerner and R.Korde, Appl.Optics 1989, v.28, pp. 3940-3943.
6. R.Korde, J.S.Cable and L.R.Canfield, IEEE Trans.Nucl.Sci., 1993, v.40, pp.1655-1659.
7. E.M.Gullikson, R.Korde *et al.*, J.Electr.Spectr.Rel.Phen. 1996, v.80, pp.313-316.

Author Index

Author Index

Author Index

Author Index

Author Index

Author Index

Author Index

Author Index

Author Index

Author Index

Author Index

Author Index

Author Index

Author Index

Author Index

Author Index

Author Index

Author Index

Author Index

Author Index